TECHNISCHE UNIVERSITÄT WIEN
Vienna | Austria

DISSERTATION

Linear Stability of the Flow in Thermocapillary Liquid Bridges in the Presence of the Gas Phase

carried out for the purpose of obtaining the degree of
Doctor technicae (Dr. techn.), submitted to the TU Wien,
Faculty of Mechanical and Industrial Engineering,
by

Mario Stojanović

Mat. Nr.: 01125142

under the supervision of
Univ.-Prof. Hendrik C. Kuhlmann
Institute of Fluid Mechanics and Heat Transfer

Reviewed by

Univ.-Prof. F. Gallaire
École Polytechnique Fédérale
de Lausanne

Univ.-Prof. A. Oron
Technion – Israel Institute
of Technology

This work has been supported by the Austrian Research Promotion Agency (FFG) in the framework of the ASAP14 programme under contract no. 866027.

I confirm that going to press of this thesis needs the confirmation of the examination committee.

Affidavit

I declare in lieu of oath, that I wrote this thesis and performed the associated research myself, using only literature cited in this volume. If text passages from sources are used literally, they are marked as such.
I confirm that this work is original and has not been submitted elsewhere for any examination, nor is it currently under consideration for a thesis elsewhere.
I acknowledge that the submitted work will be checked electronically-technically using suitable and state-of-the-art means (plagiarism detection software). On the one hand, this ensures that the submitted work was prepared according to the high-quality standards within the applicable rules to ensure good scientific practice "Code of Conduct" at the TU Wien. On the other hand, a comparison with other student theses avoids violations of my personal copyright.

Vienna, September 2023

Mario Stojanović

Zusammenfassung

Die lineare Instabilität der achsensymmetrischen stationären Strömung in thermokapillaren Flüssigkeitsbrücken mit hoher Prandtlzahl wurde numerisch untersucht. Die Strömung wird primär durch den thermokapillaren Effekt angetrieben, welcher Schubspannungen proportional zum Gradienten der Oberflächentemperatur erzeugt. Die Flüssigkeitsbrücke ist von einem geschlossenen oder offenen Zylinder umgeben. Im Falle eines offenen Zylinders wird die Flüssigkeitsbrücke einem axialen Gasstrom mit vorgegebener Temperatur ausgesetzt. Im Grundzustand wird die deformierbare Grenzfläche zwischen der Flüssig- und Gasphase entweder als hydrostatisch bestimmt oder als dynamisch deformierbar angenommen, wobei die Deformation durch die Flüssigkeits- und Gasströmung verursacht wird. Generell wird die Strömung in beiden Phasen gekoppelt berechnet. Basierend auf dem achsensymmetrischen Grundzustand wird eine lineare Stabilitätsanalyse durchgeführt, um die kritische thermokapillare Reynoldszahl in Abhängigkeit des Länge-zu-Radius Seitenverhältnisses, des Flüssigkeitsvolumens, der Gravitationskraft und der Durchflussrate zu berechnen. Dabei werden verschiedene Näherungen der Grundgleichungen herangezogen, die von der Oberbeck–Boussinesq Approximation bis hin zum realitätsnahen Modell reichen, bei dem die Temperaturabhängigkeit aller thermophysikalischen Parameter berücksichtigt wird. Unter allen Kontrollparametern ist die kritische Reynoldszahl besonders empfindlich gegenüber der Richtung der Gasströmung, da das Gas hauptsächlich die Grenzflächentemperatur beeinflusst, die für den thermokapillaren Antrieb entscheidend ist. Sowohl für geschlossene als auch für offene Zylinder mit aufgedrängter axialer Gasströmung haben dynamische Oberflächenverformungen lediglich einen mäßigen Einfluss auf die kritische Reynoldszahl. Für zu hohe Temperaturunterschiede innerhalb der Flüssigkeitsbrücke führt die Oberbeck–Boussinesq Approximation aufgrund der starken Viskositätsschwankungen zu ungenauen Vorhersagen.

Neben den Stabilitätsanalysen wird ein reduziertes Einphasenmodell für die flüssige Phase entwickelt, welches herkömmliche Einphasenmodelle verbessert. Im verbesserten Einphasenmodell wird die üblicherweise konstant angenommene Biotzahl durch eine von der Höhe abhängige Biotfunktion ersetzt, die basierend auf zahlreichen Zweiphasensimulationen durch den räumlich aufgelösten Wärmestrom gewonnen wird. Durch die Verwendung der Biotfunktion profitiert das neue Einphasenmodell zum einen von zusätzlich gewonnener Genauigkeit (bedingt durch das Zweiphasenmodell) und zum anderen von den reduzierten Rechenkosten bezogen auf Zweiphasenberechnungen.

Alle Berechnungen wurden mit dem Code `MaranStable` durchgeführt, welcher im Rahmen dieser Arbeit entwickelt wurde. Der Code wurde einschließlich einer graphischen Benutzeroberfläche als Open Source veröffentlicht, wofür umfangreiches Zusatzmaterial wie z.B. Tutorials bereitgestellt wurde.

Abstract

Numerical calculations have been carried out to investigate the linear instability of the axisymmetric steady flow in high-Prandtl-number thermocapillary liquid bridges covering a wide range of length-to-radius aspect ratios, liquid volumes and gravity levels. The full two-phase problem is solved in which the liquid bridge and its support rods are surrounded by an annular gas duct that can either be sealed or open. For an open gas tube, the liquid bridge can be exposed to an axial gas flow of given temperature. The deformed liquid–gas interface is treated either as hydrostatically determined, or dynamically deformed by the liquid and gas flow (basic state only). Accurate critical data are provided for different approximations of the governing equations ranging from the Oberbeck–Boussinesq approximation to the more realistic model in which the full temperature dependence of all thermophysical parameters is taken into account. Among all control parameters, the critical conditions are particularly sensitive to the direction of the gas flow because the gas mainly affects the interfacial temperature, which is crucial for the thermocapillary driving. Dynamic surface deformations were found to have only a moderate influence on the critical conditions, even if the liquid bridge is exposed to an axial gas flow. When the imposed temperature difference between the two support rods is sufficiently large, the Oberbeck–Boussinesq approximation yields inaccurate predictions because of the large viscosity variation of the liquid.

Apart from the linear stability analyses, a reduced single-fluid model is devised for the liquid phase, which improves on the standard single-fluid models that are based on Newton's law with a constant Biot number. In the improved single-fluid model, the Biot number is replaced by a Biot function depending on the axial coordinate. The Biot function is obtained by extracting the space-resolved heat flux from two-phase simulations for a wide range of aspect ratios and Reynolds numbers by fitting a large set of two-phase simulations. Since the flow instability is almost always triggered in the liquid phase, the use of the Biot function inherits the accuracy of the two-fluid model while requiring only a single-phase solver at much lesser computational cost.

All calculations have been carried out using the code `MaranStable`. It has been developed as part of this thesis. The code, including a graphical user interface, has been made publicly available as open-source, together with extensive documentation and tutorial files.

Acknowledgments

Several people played a decisive role in supporting me during the past five years and helped me to accomplish this doctoral thesis, for whom I would like to express my gratitude. I shall start by thanking my supervisor Prof. Hendrik C. Kuhlmann for the opportunity to work under his guidance and for teaching me his scientific approach to proper research.

I want to thank Prof. François Gallaire and Prof. Alexander Oron for agreeing to review this thesis and Prof. Manuel García-Villalba for being the head of the jury.

I am deeply grateful to Prof. Francesco Romanò, who was a kind of co-supervisor for me. Thank you, Francesco, for teaching me your coding skills, helping me debug the code, and for a nice collaboration in all our joint papers that are part of this thesis. Writing this amount of papers would not have been possible without your support.

I cannot leave TU Wien without acknowledging my old and new colleagues who have contributed to a friendly atmosphere in the institute. I truly enjoyed our social gatherings among which we played laser tag, bowling and billiards or did a cycling tour to Lower Austria (still waiting for the go-cart event). In particular, it was a pleasure participating in our Friday's tradition and let us not forget its special edition: the Seidl rally.

I would like to extend my thanks to my friends for the fun we always have and for a true friendship. A special thanks goes to Lea, who accompanied me during my PhD. Thank you for cheering me up during the hard periods of the project and for carefully listening to my research progress without having a clue about fluid dynamics.

I am especially grateful to my parents, Danira and Zdravko, and to my brother Ivo for supporting me not only during my PhD but during my whole life. Hvala vam na svemu! I was lucky to share my workplace with Ivo during the last years and whish him all the best for his PhD.

I dedicate my work to my grandma Lovorka, who always believed in me but unfortunately passed away too early.

Panta rhei. – Everything flows.

Heraclitus of Ephesus

Contents

I General Introduction

During my research project at TU Wien, I progressed in understanding and modeling the flow in thermocapillary liquid bridges. Thanks to the numerous papers I achieved to publish, I was given the opportunity to compose my thesis as a cumulative dissertation. Throughout the thesis, the wording "*we*" is used, which is justified by the co-authorship.

Following the guidelines of TU Wien, the introductory Chapter I includes the motivation for our research, our research objectives, the problem formulation, and the methods for solving the given problem. Chapter I terminates with a summary of the published (and submitted) research results and explains the scientific contribution of the dissertation. The thesis is based on the publications which are presented in Chapter II.

1 Motivation

1.1 The Role of Flow Stability in Fluid Mechanics

It was around 500 years BC when the Greek philosopher Heraclitus of Ephesus said that nothing stays still but constantly changes in time, for which he used the words *Panta rhei* meaning *everything flows*. This wisdom best applies to the field of fluid dynamics, which deals with the motion of liquids and gases. In general, fluid motion can be classified into laminar and turbulent flows depending on the patterns and characteristics of the flow. While laminar flows are smooth and predictable, turbulent flows are chaotic and irregular. This behavior arises due to the nonlinearity of the equations of fluid motion, namely the Navier–Stokes equations. Essentially, for small driving forces, typically measured by a suitable Reynolds number Re, the nonlinear terms become negligible such that the Navier–Stokes equations reduce to linear equations, for which the solution is unique. In contrast, multiple solutions may exist for higher Re, not all of which must necessarily be known. However, a solution can only be observed if it is stable and, thus, robust against perturbations. For many flow configurations, the transition from a stable laminar to an unstable turbulent flow can

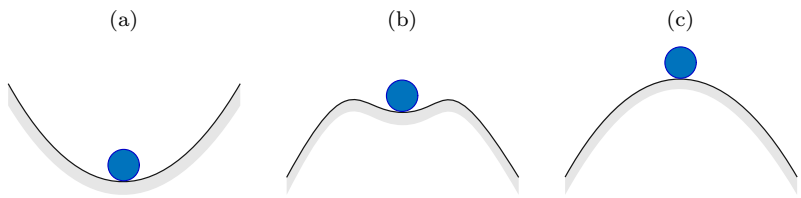

Figure I: Sketch illustrating the concept of stability by means of equilibrium states of point particles in different potentials. (a) Globally stable. (b) Conditionally or linearly stable. (c) Unstable.

Figure II: Capillary break-up of a liquid jet in air after Van Dyke [61].

be described with the hydrodynamic stability theory, which deals with the stability or the onset of instability of a fluid flow. Analyzing a flow regarding its stability starts with computing the unique solution for small Re. We call this solution *basic state* or *basic flow*. We then superpose the basic state with a perturbation to mimic possible imperfections that may occur in the real flow for whatever reason. If the perturbation decays for an infinite time $t \to \infty$, the system is said to be asymptotically stable. There exist different sub-categories subdividing the stability according to the temporal or spatial behavior of the perturbations. For a detailed description, the interested reader is referred to one of the classical textbooks [see e.g. 5, 9, 35]. Different methods exist to analyze the stability of the flow. We shall focus on the linear stability analysis relying on the assumption of infinitesimally small perturbations. This method has the advantage that the resulting so-called perturbation equations are linear. As a certain drawback, the linear stability analysis can merely predict whether a system is unstable or conditionally (linearly) stable, where the condition is related to the magnitude of the perturbation. Figure I illustrates the difference between global and conditional stability using a simple mechanical problem with one degree of freedom. However, the linear stability theory sometimes fails to predict the onset of instability. One example is circular pipe flow which is linearly stable for any pressure gradient. Despite its apparent limitations, the linear stability analysis often agrees well with experimental observations and is therefore used in the present thesis. Moreover, it provides a powerful tool not only for detecting critical thresholds but also for analyzing the mechanisms leading to instability.

Flow instabilities occur everywhere, whether in nature or industrial applications. Although different mechanisms are responsible for different types of instabilities, the common characteristic among all flow instabilities is their ability to change the flow structure. We shall demonstrate the significance of hydrodynamic instability for system dynamics through two representative scenarios for both an industrial application

Figure III: Photography of the von Kármán vortex street around the volcanic islands of Cape Verde taken by NASA on December 20, 2020, from the International Space Station.

and a natural phenomenon, respectively. In inkjet printing, the so-called Rayleigh instability initiates the capillary break-up shown in Fig. II, which can be successfully predicted by the linear stability theory. As an example of natural instabilities, we show a picture of a wake instability named after Theodore von Kármán (see Fig. III).

1.2 Thermocapillary Flow in Liquid Bridges

The aim of this thesis is to study thermocapillary flows. Flows are termed thermocapillary flows if interfaces between two immiscible fluids are present in non-isothermal systems. Now the question arises what is the driving force in multiphase systems when fluidic interfaces come across temperature gradients? The answer can be given by the temperature dependence of the interfacial free energy leading to a temperature-dependent surface tension. Hence, the presence of temperature gradients produces interfacial tension gradients that, if significant, can represent a major driving of the multiphase system [19]. Thermocapillary flows are a special case of the more general *Marangoni flows*, where the cause for the interfacial-tension gradients can also be gradients of, e.g., the concentration of a dissolved species or the electrical potential. The underlying *Marangoni effect* is named after the Italian physicist Carlo Marangoni (1840–1925) [39], who discovered a fast spreading of oil droplets on the surface of clean water [22]. Thermocapillary flows arise in several industrial applications. Examples are e.g. welding [25], combustion of fuels [46], droplets in microfluidics [67], crystal growth from the melt [36], inkjet printing [30] or manipulation of fluid in micro-electromechanical devices [11]. These flows are also relevant in space technology because the thermocapillary effect provides one of the most efficient natural forces by which fluid can be manipulated under weightlessness [29]. Regarding crystal growth from the melt, the so-called *floating-zone technique* was developed to produce *pure* crystals from the melt that are free of heterogeneous nucleation and to avoid contam-

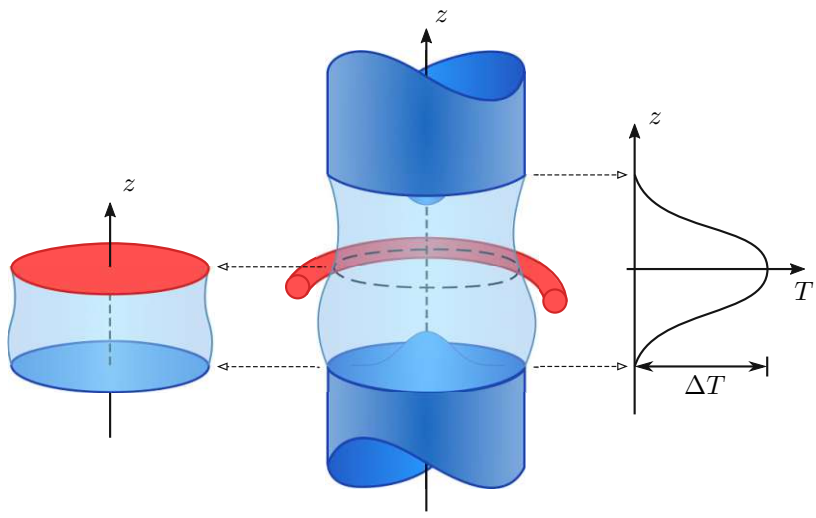

Figure IV: Simplification of the floating-zone (middle) to the half-zone (left) configuration recovered from Leypoldt *et al.* [21]. Right: Surface temperature distribution of the full-zone model.

inations due to the crucible [31]. In the course of this process, the melt is supported by solid crystalline or poly-crystalline rods of temperatures close to the melting point. However, the liquid–gas interface of the melt is exposed to radiation by means of a coaxially mounted heat source, keeping the melt above its melting point. As Fig. IV indicates, the heating ring is placed midway between the two supports, where the interface temperature exhibits its maximum. Thus, the melt solidifies to a crystalline structure at a certain distance from the heat source. During the solidification process, it is essential to suppress the onset of time-dependent melt flow because it leads to a time-dependent propagation of the solidification front, which is associated with an uneven distribution of impurities (striations) in the desired single crystal [4]. In order to prevent crystal growth from undesired inhomogeneous chemical composition, it is important to understand the physical mechanism of flow instabilities. The desire to better understand the thermocapillary flow in models of crystal growth raised the researchers' attention, who simplified the *full-zone* problem while retaining the essential flow physics. This led to the *half-zone* model, introduced by Schwabe *et al.* [38] and shown on the left of Fig. IV. In his half-zone model, the upper crystalline rod was replaced by a heating block inducing a temperature difference along the interface. This temperature difference is directly proportional to the strength of the flow. Disregarding the solidification process and focusing on the fluid motion allowed to further simplify the half-zone model by keeping the fluid volume bounded between two coaxial cylindrical rods far above the pour point. Thus, the configuration of the differentially heated *liquid bridge* was born, which has become one of the most popular paradigms of thermocapillary flow [13]. From the 1970s until today, a large number of scientific papers have been published devoted to thermocapillary liquid bridges.

1.3 Literature Review

The numerical analysis of thermocapillary flows in crystal growth was first introduced by Chang & Wilcox [2, 3], who addressed the original full-zone problem in which the free surface is heated symmetrically with respect to the equator. However, the simplified half-zone model turned out to be more appealing for researchers (especially for experimentalists) since it enables a better control of the driving force, typically measured by the thermocapillary Reynolds number. By today, the half-zone model has emerged as the most crucial paradigm for studying thermocapillary convection [13]. Despite its simple geometry, the stability problem in thermocapillary liquid bridges is highly complex owing to the coupling along the deformable interface between the liquid and the gas phase, as well as to the number of independent parameters that influence the basic state and the instability mechanisms of such a multiphase flow. Therefore, simplifying assumptions have been made to make the problem theoretically and numerically tractable.

A frequently used approximation is to consider only the liquid phase (single-fluid model) by neglecting viscous stresses from the gas phase. This model requires the heat transfer through the free surface to be modeled, commonly achieved by applying Newton's cooling law with a suitable ambient reference temperature and a selected constant Biot number or, even more restrictive, by neglecting the heat transfer into the gas, assuming an adiabatic free surface [63]. The latter approach allowed Wanschura *et al.* [63] to predict the onset of instability semi-quantitatively by means of linear stability analyses. For small Prandtl numbers, the instability was found to be purely inertial, while for high-Prandtl-number liquid bridges, Wanschura *et al.* [63] identified the critical mode as a pair of azimuthally traveling hydrothermal waves, a concept introduced by Smith & Davis [47] and first discovered for plane layers. However, the results of Wanschura *et al.* [63] obtained for an indeformable adiabatic free surface under zero gravity significantly deviate from the extensive measurements conducted by Velten *et al.* [62], which indicates the need for a more realistic modeling. The experiments of Kamotani *et al.* [10] revealed the impact of the heat transfer across the liquid–gas interface for the critical Reynolds number. To better regulate the thermal environment in the gas, the liquid bridge is, therefore, typically mounted inside a concentric shield cylinder, a setup first used by Preisser *et al.* [32]. The high sensitivity concerning the thermal conditions in the ambient atmosphere stimulated new experiments [60] and numerical investigations [66] where the liquid bridge is exposed to a well-defined gas flow. This approach can be used to manipulate the system's stability and, thus, to control the onset of oscillations.

Another prevalent assumption is concerned with the dynamics of the free surface. Early half-zone models assumed the free surface shape to be cylindrical, thus, free of deformations [see e.g. 18, 20, 63]. This ansatz is justified for tiny liquid bridges or microgravity environments, leading to negligible gravitational forces. Nevertheless, even for millimetric liquid bridges under earth gravity conditions, static surface deformations may affect the flow significantly and need to be taken into account. Assuming an adiabatic free surface, the study of Nienhüser & Kuhlmann [28] represents a significant advancement in stability analyses, as it extends beyond the previous limitation of cylindrical bridges. Flow-induced interface deformations, however, have been studied

numerically to a much lesser extent. Experiments revealed that the magnitude of the dynamic (flow-induced) interfacial deformation due to the subcritical thermocapillary flow close to the critical threshold is less than the static deformation [26, 42]. Moreover, oscillatory deformations due to the supercritical three-dimensional flow were found to be even smaller with an amplitude below micron size [6]. Surface deformations due to supercritical flow may, however, cause surface-wave instabilities, potentially arising from shear flow caused by mechanical stresses from the gas phase. However, no experimental observations of surface-wave instabilities have yet been made in the current flow system. They are more likely to arise in form of long-wave instabilities [48]. Surface waves are expected to be stabilized by the finite length of the liquid bridge. In fact, Carrión *et al.* [1] performed a linear stability analysis accounting for dynamic deformations of both the basic state and the perturbation flow but disregarded the gas flow and used Newton's law of cooling. They found a very weak effect of the dynamic deformations on the stability limits.

When investigating supercritical oscillatory flows in liquid bridges, experimentalists typically seed small particles into the liquid in order to track their position. In the three-dimensional oscillatory flow of a high-Prandtl-number liquid bridge, the particles can de-mix rapidly and form closed line-like structures which rotate in the liquid [37]. This phenomenon is termed **P**article **A**ccumulation **S**tructure (PAS). PAS may be used to separate particles from a fluid when other methods, e.g. centrifugation, are not applicable. With the approach of Romanò & Kuhlmann [33], it was possible to predict coherent particle structures numerically for which expensive three-dimensional simulations are required.

Depending on the size of the liquid bridge, a three-dimensional or time-dependent flow state can require a relatively large temperature difference, where the temperature dependence of the material properties is no longer negligible. Among all thermophysical fluid properties, the liquid's viscosity typically suffers the most significant variation. Therefore, the temperature dependence of the viscosity has been included in numerical simulations [e.g. 23, 41, 43] and stability analyses [1, 12]. Except for the results of Carrión *et al.* [1], the viscosity was taken to depend linearly on the temperature.

2 Open Questions and Research Objectives

Single-fluid models are still frequently used, especially for expensive three-dimensional simulations for which a coupled two-phase simulation is not affordable. Three-dimensional simulations are necessary to study the supercritical flow [see e.g. 16, 20]. However, applying Newton's cooling law can lead to poor predictions of the real dynamics of the liquid flow, mainly because of two reasons. On the one hand, the environmental reference temperature needs to be assumed, for which the heat transfer coefficient remains unknown. On the other hand, Newton's law does not accurately account for the spatial variation of the local heat transfer rate. The question arises: *Can the very complex two-phase stability problem be simplified to obtain the stability limits in a more efficient but still reliable way by employing a single-fluid model?* Hence, the aim is to derive an improved single-fluid model combining Newton's cooling law with

a space-dependent heat-transfer coefficient or local Biot number based on accurate two-fluid model calculations.

Owing to the limited availability of accurate numerical studies on high-Prandtl-number liquid bridges, we shall perform linear stability analyses to understand the effect of heat transfer through the liquid–gas interface on the onset of oscillatory three-dimensional flow. To that end, different parameters that are important to experimentalists shall be varied, such as e.g. the length-to-radius aspect ratio and the volume of the liquid bridge. Particular attention shall be paid to the influence of an external gas flow on the linear stability limits, for which an extensive linear stability analysis has never been carried out, except for the brief results of Shevtsova *et al.* [40].

To drive the forced gas flow, an additional imposed pressure gradient in the gas tube is required that may lead to significant dynamic deformations of the liquid–gas interface. However, the majority of previous numerical studies, including the linear stability analysis of Shevtsova *et al.* [40], neglected dynamic, i.e. flow-induced surface deformations. Since the findings of Carrión *et al.* [1], who reported a negligible effect of dynamic surface deformations, are based on a single-fluid model, the open question remains: *To what extent do flow-induced surface deformations influence the linear stability boundaries?* Thus, the aim is to compare stability analyses obtained by first neglecting and then including dynamic surface deformations. However, we focus solely on interfacial deformations caused by the axisymmetric basic flow, which is motivated by experimental evidence.

Most numerical results have been obtained for constant material properties or in the framework of the well-established Oberbeck–Boussinesq approximation [e.g. 8, 20, 27, 28, 57]. More realistic approaches assumed a linearly temperature-dependent viscosity of the liquid [12, 23]. By today, to the best of our knowledge, no numerical investigations have accounted for the full temperature dependence of all thermophysical parameters. Hence, the aim is to fill this gap by answering the question: *How much do critical Reynolds numbers obtained with either the Oberbeck–Boussinesq approximation or a linear temperature model deviate from more accurate data employing a fully non-linear temperature dependence of the liquid and the gas?*

It is well known that experiments on the ground can yield different stability boundaries than the ones under microgravity conditions. In order to study the pure thermocapillary flow in the absence of a gravity-induced buoyant flow and hydrostatic deformation, experiments under microgravity conditions are necessary. Therefore, the JEREMI space experiment (Japanese European Research Experiment on Marangoni Instability) has been developed, which was planned to be carried out in the Fluid Physics Experiment Facility of the Japanese module KIBO on the ISS [40]. Since experiments conducted on the ISS are very expensive, ground experiments are used for predicting the instability under microgravity conditions despite the additional driving force due to buoyancy. However, the question is: *What error is incurred when stability boundaries obtained experimentally under terrestrial buoyancy be used for predicting the instability under microgravity conditions?* Since buoyancy forces (measured by the Grashof number) scale cubically with the liquid bridge's height, the effect of buoyancy on the flow and its stability diminishes strongly with decreasing size of the liquid bridge. Hence, the aim is to perform a systematic analysis regarding the effect of buoy-

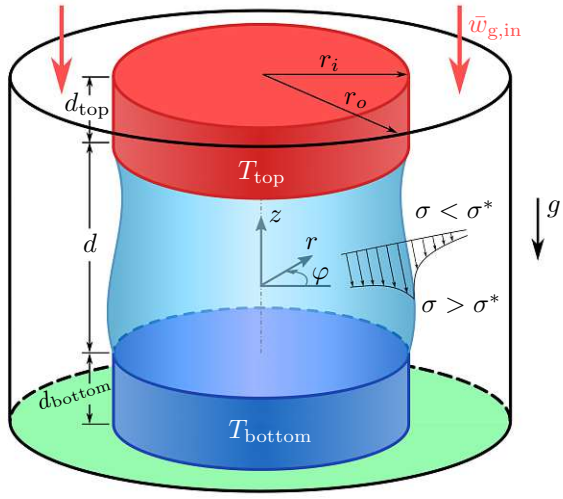

Figure V: Schematic of the axisymmetric thermocapillary liquid bridge. The cylindrical coordinate system originates in the center of the differentially heated liquid bridge. The gravity vector $\boldsymbol{g}$ is always aligned with the negative z-axis. The thermocapillary effect is illustrated schematically through velocity vectors close to the interface. The sketch shows the situation when the liquid bridge is heated from above and exposed to a hot gas stream with the mean value $\bar{w}_{\mathrm{g,in}}$.

ancy on the stability limits to indicate how small the liquid bridge on the ground must be to serve as a basis for reliable planning of the space experiment. Associated with a decreasing importance of gravity, the importance of varying parameters increases.

3 Problem Formulation

3.1 Setup

We consider a droplet of an incompressible Newtonian fluid captured between two coaxial, cylindrical rods of radius r_{i} and heights d_{top} and d_{bottom}, respectively, which are axially separated by a distance d (see Fig. V). The droplet is kept in place by forces due to the surface tension σ, forming a liquid bridge. Its volume V_{l} is typically normalized by the volume $\pi r_i^2 d$ of an upright cylindrical liquid bridge, yielding the volume ratio $\mathcal{V} = V_l/\pi r_i^2 d$. Depending on the wetting conditions, short liquid bridges can be hydrostatically stable, even in a terrestrial gravity field. Gravity forces, whenever present, act parallel to the symmetry axis of the axisymmetric geometry. Owing to the necessity of accounting for the ambient atmosphere [10], the liquid bridge is mounted in a concentric shield cylinder of radius $r_{\mathrm{o}} > r_{\mathrm{i}}$ and height $d_{\mathrm{top}} + d + d_{\mathrm{bottom}}$, radially confining the Newtonian gas, which surrounds the liquid bridge and the support rods. The gas tube can either be closed or open depending on the target of the

investigation.

The support rods are assumed to be perfect thermal conductors and are kept at different but constant temperatures $T_{\mathrm{top}} = \bar{T} + \Delta T/2$ and $T_{\mathrm{bottom}} = \bar{T} - \Delta T/2$ around the mean working temperature $\bar{T} = (T_{\mathrm{top}} + T_{\mathrm{bottom}})/2$, chosen as the reference temperature $T^* = \bar{T}$. The temperature difference $\Delta T = T_{\mathrm{top}} - T_{\mathrm{bottom}}$ can be either positive or negative, indicating heating from above or below, respectively. As the imposed temperature difference affects the temperature-dependent surface tension $\sigma(T)$, tangential interfacial stresses are induced via the thermocapillary effect driving a flow in both the liquid and the gas phase [13], as sketched in Fig. V. Expanding $\sigma(T)$ by means of a Taylor series yields the surface tension gradient

$$\begin{aligned}\nabla_{\parallel}\sigma(T) = \frac{\partial\sigma}{\partial T}\nabla_{\parallel}T = \frac{\partial}{\partial T}\left[\sigma^* - \gamma_1^*(T-T^*) + \frac{\gamma_2^*}{2}(T-T^*)^2 + \dots\right]\nabla_{\parallel}T \\ = \left\{-\gamma_1^* + \gamma_2^*(T-T^*) + O\left[(T-T^*)^2\right]\right\}\nabla_{\parallel}T, \end{aligned} \tag{1}$$

where $\nabla_{\parallel} = \boldsymbol{t}(\boldsymbol{t}\cdot\nabla)$ is the Nabla operator in direction of the unit tangent vector to the interface $\boldsymbol{t}$, $\gamma_1^* = -\partial\sigma/\partial T|_{T=T^*}$ is the negative linear surface-tension coefficient, $\gamma_2^* = \partial^2\sigma/\partial T^2\big|_{T=T^*}$ is the quadratic surface-tension coefficient, and $\sigma^* = \sigma(T^*)$ denotes the surface tension at the reference temperature T^*. Henceforth, all temperature-dependent thermophysical properties marked with an asterisk indicate reference values evaluated at T^*. Although our model includes higher corrections to the commonly used linear temperature dependence of $\sigma(T)$, accurate measurements of the full functional dependence are available only for a few liquids. However, for liquid bridges made of typical silicone oils, we must neglect quadratic and higher order contributions to $\sigma(T)$.

The conditions in the gas phase have a significant impact on the main thermocapillary flow in the liquid phase. Open gas containers allow for passive flow control in the liquid phase by adjusting parameters such as magnitude, temperature, and direction of the forced gas flow. The forced gas flow modifies the thermal conditions at the interface and induces mechanical shear stresses along the interface. Depending on the direction of the through-flow, the mean value $\bar{w}_{\mathrm{g,in}}$ of the inlet velocity $w_{\mathrm{g,in}}(r)$ can be positive or negative. In addition to the thermocapillary flow and forced gas flow, a buoyancy-driven flow occurs due to the temperature-dependent density of the liquid $\rho(T)$ and the gas $\rho_{\mathrm{g}}(T)$, respectively. Note that quantities related to the gas are indicated by a subscript 'g', while quantities referring to the liquid carry no subscript. In the case of tiny liquid bridges, surface forces typically outweigh volume forces. However, for millimetric liquid bridges studied under normal terrestrial conditions, buoyancy can significantly influence the shape of the interface and the fluid motion. Within our modeling, we assume conditions far from phase-change critical points allowing us to neglect the pressure dependence of *all* thermophysical fluid properties.

3.2 Governing Equations

General Transport Equations

The fluid motion in both the liquid and the gas phase is governed by the Navier–Stokes and energy equations. For the problem at hand, it seems reasonable to consider the

simplified version of the governing equations, namely the well-established **O**berbeck–**B**oussinesq (OB) equations [15, 24]. This approximation only considers density variations due to temperature differences if they lead to a buoyant flow. Thus, volumetric variations due to the temperature-dependent densities are neglected, and other thermophysical properties such as the dynamic viscosities μ and μ_g, the thermal conductivities λ and λ_g and the specific heat capacities c_p and c_{pg} are assumed constant. While the OB approximation is adequate to predict a wide range of buoyancy-driven flows, its validity range is certainly limited to sufficiently small temperature variations [7]. However, to properly take care of larger temperature differences, we include the **F**ull **T**emperature **D**ependence (FTD model) of all thermophysical properties in the governing equations. To that end, we use the strong conservative form of the Navier–Stokes and energy equations

$$\frac{\partial \rho}{\partial t} + \nabla \cdot (\rho \boldsymbol{u}) = 0, \tag{2a}$$

$$\frac{\partial (\rho \boldsymbol{u})}{\partial t} + \nabla \cdot (\rho \boldsymbol{u}\boldsymbol{u}) = -\nabla p + \rho \boldsymbol{g} + \nabla \cdot (\mu \boldsymbol{\mathcal{T}}), \tag{2b}$$

$$\frac{\partial (\rho c_p T)}{\partial t} + \nabla \cdot (\rho c_p T \boldsymbol{u}) = \nabla \cdot (\lambda \nabla T), \tag{2c}$$

where t denotes time, $\boldsymbol{u}$ the flow velocity, T the temperature, p the pressure, and $\boldsymbol{\mathcal{T}} = \nabla \boldsymbol{u} + (\nabla \boldsymbol{u})^\mathrm{T} - 2/3 (\nabla \cdot \boldsymbol{u}) \boldsymbol{\mathcal{I}}$ is (twice) the deformation rate tensor with the identity matrix $\boldsymbol{\mathcal{I}}$. The pressure work, the viscous dissipation, and the pressure contribution to the enthalpy ($p/\rho \ll |c_p T|$) have been disregarded in the energy equation (2c), which is well justified for liquid bridge problems [55]. To describe the gas motion, we shall replace the fluid properties (ρ, μ, λ, c_p) with (ρ_g, μ_g, λ_g, c_{pg}) in (2a)–(2c) and indicate the field quantities $\boldsymbol{u}_\mathrm{g}$, p_g and T_g by a subscript 'g'. However, as long as the formulation is formally identical for both phases, we do not distinguish between them.

Since the geometry is axisymmetric, we use cylindrical coordinates (r, φ, z) with the corresponding unit vectors ($\boldsymbol{e}_r$, $\boldsymbol{e}_\varphi$, $\boldsymbol{e}_z$) centered in the middle of the liquid bridge, within which the velocity field is represented by $\boldsymbol{u} = u\boldsymbol{e}_r + v\boldsymbol{e}_\varphi + w\boldsymbol{e}_z$. To compute the two-phase flow including the temperature fields, we need to solve the governing transport equations subject to appropriate boundary and coupling conditions. On all solid rods, we impose no-slip and no-penetration conditions. On the surface of the support rods, we prescribe constant but different temperatures $T_\mathrm{top} \neq T_\mathrm{bottom}$, while the outer shield is typically assumed adiabatic. In the case of an open gas tube, the gas enters the system with a given velocity profile $w_\mathrm{g,in}(r)$ and temperature, ensuring that outflow conditions are met at the outlet. Conversely, sealed gas containers confine the surrounding gas by either conductive or adiabatic annular walls. The detailed mathematical formulation of the respective boundary conditions is given in [34, 53, 52, 54] for each problem separately. However, we shall pay particular attention to the coupling conditions along the dynamically deformed liquid–gas interface. On the a priori unknown location of the interface described by $r = h(\varphi, z, t)$, three kinds of coupling conditions have to be satisfied:

(i) The thermal coupling conditions

$$T = T_\mathrm{g} \quad \text{and} \quad \lambda \boldsymbol{n} \cdot \nabla T = \lambda_\mathrm{g} \boldsymbol{n} \cdot \nabla T_\mathrm{g} \tag{3}$$

ensure continuity of the temperature and the heat flux across the interface.

(ii) The kinematic coupling conditions

$$\boldsymbol{u} = \boldsymbol{u}_{\mathrm{g}} \quad \text{and} \quad u = \frac{\mathrm{d}h}{\mathrm{d}t} \tag{4}$$

imply the no-slip condition at the interface and force material elements on the interface to remain on the interface.

(iii) The dynamic coupling conditions

$$-(p - \rho g z) + \mu \boldsymbol{n} \cdot \boldsymbol{\mathcal{T}} \cdot \boldsymbol{n} + \sigma \nabla \cdot \boldsymbol{n} = -(p_{\mathrm{g}} - \rho_{\mathrm{g}} g z) + \mu_{\mathrm{g}} \boldsymbol{n} \cdot \boldsymbol{\mathcal{T}}_{\mathrm{g}} \cdot \boldsymbol{n}, \tag{5a}$$

$$\mu \boldsymbol{t} \cdot \boldsymbol{\mathcal{T}} \cdot \boldsymbol{n} - \boldsymbol{t} \cdot \nabla \sigma = \mu_{\mathrm{g}} \boldsymbol{t} \cdot \boldsymbol{\mathcal{T}}_{\mathrm{g}} \cdot \boldsymbol{n}, \tag{5b}$$

are decomposed into a normal and a tangential stress balance, respectively, and express the continuity of stresses.

Note that the location of the interface h appears explicitly in (4) and also implicitly in (3) and (5) via the outward-pointing unit vector

$$\boldsymbol{n} = \frac{1}{N}\left(\boldsymbol{e}_r - \frac{1}{h}\frac{\partial h}{\partial \varphi}\boldsymbol{e}_\varphi - \frac{\partial h}{\partial z}\boldsymbol{e}_z\right) \quad \text{with} \quad N = \sqrt{1 + \left(\frac{1}{h}\frac{\partial h}{\partial \varphi}\right)^2 + \left(\frac{\partial h}{\partial z}\right)^2} \tag{6}$$

and in any of the linearly independent orthogonal vectors $\boldsymbol{t}_{1,2} = \boldsymbol{t}_{1,2}(h) \perp \boldsymbol{n}$. Since h is part of the solution, the governing equations (2) need to be solved simultaneously with the coupling conditions (3)–(5).

A typical approach in scientific research is to non-dimensionalize the governing equations in order to facilitate identifying and studying the key parameters that govern the behavior of a system. In [53, 52, 54], we followed this approach for different approximations of the governing equations, where all variables and coordinates have been made dimensionless by using suitable scales derived from the relevant physical quantities. Among all arising dimensionless parameters governing the problem, the thermocapillary Reynolds, Prandtl and dynamic Bond numbers

$$\mathrm{Re} = \frac{\rho^* \gamma_1^* \Delta T d}{\mu^{*2}}, \qquad \mathrm{Pr} = \frac{\mu^* c_p^*}{\lambda^*}, \qquad \mathrm{Bd} = \frac{\rho^* g \beta^* d^2}{\gamma_1^*} \tag{7}$$

have the most significant influence on the flow structure. While Pr is a material parameter describing the ratio of viscous diffusion to heat diffusion, Re and Bd measure the strength of different driving forces. More precisely, Re measures the relative strength of the thermocapillary surface forces compared to the viscous forces per unit surface, whereas Bd characterizes the strength of buoyancy forces relative to that of thermocapillary forces. Occasionally, the Marangoni number $\mathrm{Ma} = \mathrm{PrRe}$ is used instead of Re. Re and Ma can take positive and negative values correspondently to the imposed temperature difference ΔT. Owing to the symmetries of the underlying problem, an axisymmetric and time-independent solution can be stably realized for a sufficiently low driving (small |Re|). In other words, if Re exceeds the critical Reynolds number

Re_c in magnitude, i.e. $|\mathrm{Re}| > |\mathrm{Re}_c|$, the flow becomes unstable due to symmetry breaking, meaning that the flow develops a time-dependent and/or three-dimensional structure. In contrast, the subcritical basic flow is characterized by the symmetries $\partial_t(\cdot) = \partial_\varphi(\cdot) = 0$ resulting in $v_0 = v_{g0} = 0$, where the index 0 indicates the basic state. To obtain Re_c, which is of key interest in our study representing the linear stability boundary, we perform linear stability analyses, for which the equations are derived in the following.

Linear Stability Equations

Let us decompose the general three-dimensional and time-dependent solution vector $\boldsymbol{q} = (\boldsymbol{u}, p, T, h)$ into an axisymmetric time-independent part $\boldsymbol{q}_0 = (\boldsymbol{u}_0, p_0, T_0, h_0)$ (index 0) and a three-dimensional time-dependent perturbation flow $\tilde{\boldsymbol{q}} = (\tilde{\boldsymbol{u}}, \tilde{p}, \tilde{T}, \tilde{h})$. In component notation, the decomposition reads

$$u = u_0(r,z) + \tilde{u}(r,\varphi,z,t), \tag{8a}$$
$$v = 0 + \tilde{v}(r,\varphi,z,t), \tag{8b}$$
$$w = w_0(r,z) + \tilde{w}(r,\varphi,z,t), \tag{8c}$$
$$p = p_0(r,z) + \tilde{p}(r,\varphi,z,t), \tag{8d}$$
$$T = T_0(r,z) + \tilde{T}(r,\varphi,z,t), \tag{8e}$$
$$h = h_0(z) + \tilde{h}(\varphi,z,t). \tag{8f}$$

Motivated by experimental observations revealing that interfacial deformations due to the supercritical three-dimensional flow are very small [65], we assume that the perturbation flow does not affect the interfacial shape, i.e. $\tilde{h} \equiv 0$. By adopting this approximation, surface-wave instabilities are excluded beforehand.

The linear stability analysis presumes slightly supercritical flow conditions justifying the assumption of infinitesimally small perturbations. This assumption enables linearizing the governing equations with respect to all perturbation quantities after inserting (8) into (2). However, the full temperature dependence of the fluid properties in (2) induces additional non-linearities and, thus, requires the functional dependence of $\rho(T)$, $\mu(T)$, $\lambda(T)$ and $c_p(T)$ to be Taylor expanded about the local basic state temperature. Using $\rho(T)$ as a representative property, the expansion up to first order yields

$$\rho(T) = \rho(T_0 + \tilde{T}) = \rho(T_0) + \left.\frac{\partial \rho}{\partial T}\right|_{T=T_0} \tilde{T} + \mathcal{O}(\tilde{T}^2) = \rho_0 + \rho_0' \tilde{T} + \mathcal{O}(\tilde{T}^2), \tag{9}$$

where the prime indicates derivatives with respect to T and the index 0 denotes scalar fields which depend continuously on the basic state temperature $T_0(r,z)$, i.e. $\rho_0 = \rho(T_0(r,z))$. Inserting (8) and (9) into (2) and linearizing with respect to the perturbation quantities, we finally arrive at the perturbation equations

$$\rho_0' \frac{\partial \tilde{T}}{\partial t} + \nabla \cdot \left(\rho_0 \tilde{\boldsymbol{u}}\right) + \nabla \cdot \left(\rho_0' \tilde{T} \boldsymbol{u}_0\right) = 0, \tag{10a}$$

$$\boldsymbol{u}_0\rho_0'\frac{\partial\tilde{T}}{\partial t}+\rho_0\frac{\partial\tilde{\boldsymbol{u}}}{\partial t}+\nabla\cdot\left(\rho_0'\tilde{T}\boldsymbol{u}_0\boldsymbol{u}_0\right)+\nabla\cdot\left[\rho_0(\boldsymbol{u}_0\tilde{\boldsymbol{u}}+\tilde{\boldsymbol{u}}\boldsymbol{u}_0)\right]= \\ =-\nabla\tilde{p}+\rho_0'\tilde{T}\boldsymbol{g}+\nabla\cdot\left(\mu_0'\tilde{T}\boldsymbol{\mathcal{T}}_0\right)+\nabla\cdot\left(\mu_0\tilde{\boldsymbol{\mathcal{T}}}\right), \quad (10b)$$

$$\left[T_0(\rho_0'c_{p0}+\rho_0c_{p0}')+\rho_0c_{p0}\right]\frac{\partial\tilde{T}}{\partial t}+\nabla\cdot\left[(\rho_0'c_{p0}+\rho_0c_{p0}')T_0\boldsymbol{u}_0\tilde{T}\right] \\ +\nabla\cdot\left(\rho_0c_{p0}\tilde{T}\boldsymbol{u}_0\right)+\nabla\cdot\left(\rho_0c_{p0}T_0\tilde{\boldsymbol{u}}\right)=\nabla\cdot\left(\lambda_0'\tilde{T}\nabla T_0\right)+\nabla\cdot\left(\lambda_0\nabla\tilde{T}\right), \quad (10c)$$

where the beforehand computed basic state solution enters the equations parametrically. Due to the homogeneity of the basic state in t and φ, the perturbations $\tilde{\boldsymbol{q}}$ can be further decomposed into normal modes with azimuthal wave number $m\in\mathbb{N}$. The superposition of all normal modes can be written as

$$\tilde{\boldsymbol{q}}=\sum_{j,m}\hat{\boldsymbol{q}}_{j,m}(r,z)e^{\psi_{j,m}t+\mathrm{i}m\varphi}+\text{c.c.}, \quad (11)$$

where $\psi_{j,m}\in\mathbb{C}$ denotes the complex growth rates of the normal modes with amplitudes $\hat{\boldsymbol{q}}=(\hat{\boldsymbol{u}},\hat{p},\hat{T})$. The index j enumerates the different solutions for a given wave number m. The complex conjugate (c.c.) is needed to render the perturbations real. Inserting (11) into (10a)–(10c) yields the equations for the perturbation amplitudes $\hat{\boldsymbol{q}}$

$$\psi\rho_0'\hat{T}+\nabla\cdot\left(\rho_0\hat{\boldsymbol{u}}\right)+\nabla\cdot\left(\rho_0'\boldsymbol{u}_0\hat{T}\right)+\frac{\rho_0\mathrm{i}\hat{v}m}{r}=0, \quad (12a)$$

$$\psi\left(\boldsymbol{u}_0\rho_0'\hat{T}+\rho_0\hat{\boldsymbol{u}}\right)+\nabla\cdot\left(\rho_0'\hat{T}\boldsymbol{u}_0\boldsymbol{u}_0\right)+\nabla\cdot\left[\rho_0(\boldsymbol{u}_0\hat{\boldsymbol{u}}+\hat{\boldsymbol{u}}\boldsymbol{u}_0)\right]+\frac{\rho_0\mathrm{i}\hat{v}m\boldsymbol{u}_0}{r}= \\ =-\nabla\hat{p}+\rho_0'\hat{T}\boldsymbol{g}+\nabla\cdot\left(\mu_0'\hat{T}\boldsymbol{\mathcal{T}}_0\right)+\nabla\cdot\left(\mu_0\hat{\boldsymbol{\mathcal{T}}}\right)+\left(\mu_0'\hat{T}\boldsymbol{\mathcal{T}}_0+\mu_0\hat{\boldsymbol{\mathcal{T}}}-\hat{p}\right)\frac{\mathrm{i}m\boldsymbol{e}_\varphi}{r} \quad (12b)$$

$$\psi\left[T_0(\rho_0'c_{p0}+\rho_0c_{p0}')+\rho_0c_{p0}\right]\hat{T}+\nabla\cdot\left[(\rho_0'c_{p0}+\rho_0c_{p0}')T_0\boldsymbol{u}_0\hat{T}\right]+\nabla\cdot\left(\rho_0c_{p0}\hat{T}\boldsymbol{u}_0\right) \\ +\nabla\cdot\left(\rho_0c_{p0}T_0\hat{\boldsymbol{u}}\right)+\frac{\rho_0c_{p0}\mathrm{i}\hat{v}m}{r}=\nabla\cdot\left(\lambda_0'\hat{T}\nabla T_0\right)+\nabla\cdot\left(\lambda_0\nabla\hat{T}\right)-\frac{\lambda_0\hat{T}m^2}{r^2}, \quad (12c)$$

which can be identified as a linear eigenvalue problem with an infinite number of eigenmodes $\tilde{\boldsymbol{q}}$ and eigenvalues ψ [52]. The flow is *linearly stable* if the real parts of all complex growth rates $\psi_{j,m}$ are negative ($\forall_{j,m}\Re(\mu_{j,m})<0$), meaning that all perturbation modes decay in time. On the other hand, the flow is *unstable* if at least one growth rate exists with a positive real part ($\exists_{j,m}\Re(\mu_{j,m})>0$). In this scenario, the unstable perturbation flow will grow exponentially in time until finite-size effects come into play and change the dynamics of the flow. The flow is said to be *neutrally stable* if the perturbation mode with the largest real part neither grows nor decays for a given wave number m, which is characterized by a vanishing real part of the eigenvalue $\Re(\max_j\psi_{j,m})=0$. The corresponding control parameter, typically Re, is then called neutral Reynolds number Re_n^m and is assigned to a specific wave number m. The minimum neutral Reynolds number above which the flow becomes unstable defines the critical Reynolds number Re_c.

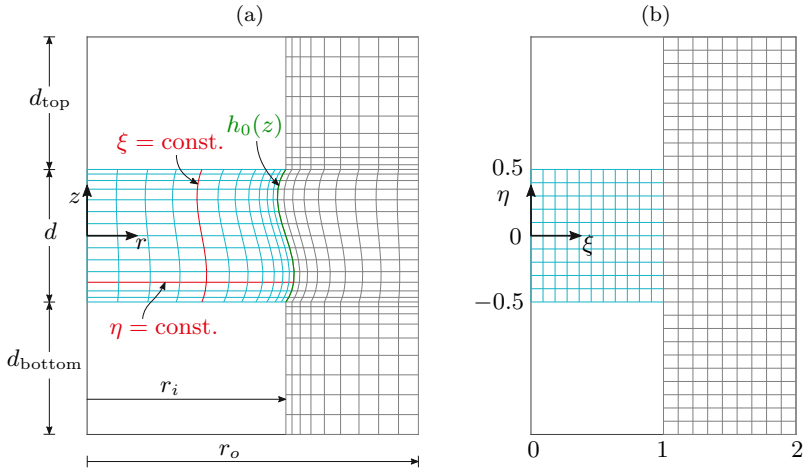

Figure VI: Illustrative examples for the physical mesh (a) and the correspoding transformed computational mesh (b) of the liquid (blue) and the gas (gray) phase. The liquid–gas interface is indicated by green color.

4 Mathematical and Numerical Methods

All required numerical operations to solve the differential equations presented in Section 3 are implemented in our MATLAB code `MaranStable`, initially developed by M. Lukasser within the project Engineering Marangoni Flows [14]. Years later, within the SAJE project (Stability Analysis for the JEREMI experiment) [51], we revised the code by removing several bugs and further developed the solver from its initial version `MaranStable` 1.0, up to `MaranStable` 3.1 where we extended the code by many features (concerning e.g. advanced heat transfer functions, Boussinesq approximation, energy budgets, surface impurities, optical ray tracking). Moreover, we created a graphical user interface (GUI) for `MaranStable` 3.1, which we recently introduced in [56] and made publicly available as open-source from `https://github.com/fromano88/MaranStable`. Although `MaranStable` uses the same discretization method for both the basic state and linear stability analysis, the discretized equations require different solution techniques.

4.1 Basic Flow

The steady axisymmetric versions of (2)–(5) (together with the boundary conditions) are discretized by second-order finite volumes on a structured and staggered grid, which is refined towards all boundaries either by hyperbolic tangent or geometric progression [59, 64]. `MaranStable` employs body-fitted coordinates (ξ,η), as shown in Fig. VI, where the physical mesh fitted to the interface shape h_0 is mapped to an

orthogonal computational mesh. The corresponding coordinate transformation reads

$$\xi(r,z) = \begin{cases} \dfrac{r}{h_0(z)} F_\mathrm{l}(r) & \text{for the liquid phase,} \\ \left[1 + \dfrac{r - h_0(z)}{r_o - h_0(z)}\right] F_\mathrm{g}(r) & \text{for the gas phase,} \end{cases} \tag{13a}$$

$$\eta(z) = \frac{z}{d}\, G(z), \tag{13b}$$

where $F_\mathrm{l}(r)$, $F_\mathrm{g}(r)$ and $G(z)$ are inverse stretching functions that are applied to rearrange the cells equidistantly. Since h_0 is computed simultaneously with the flow field, `MaranStable` updates the physical and computational meshes after every iteration step, which is described next. For a detailed description of the employed mesh parameters, we refer to [52].

Discretizing the governing equations results in a set of nonlinear algebraic equations that are solved iteratively by means of the Newton–Raphson method. If $\boldsymbol{q}_0^{(k)}$ is a known approximation of the solution $\boldsymbol{q}_0$ at the k-th iteration step, we obtain an improved approximation

$$\boldsymbol{q}_0^{(k+1)} = \boldsymbol{q}_0^{(k)} + \delta\boldsymbol{q}, \tag{14}$$

by solving the set of linear equations

$$\boldsymbol{J}\left(\boldsymbol{q}_0^{(k)}\right) \cdot \delta\boldsymbol{q} = -\boldsymbol{f}\left(\boldsymbol{q}_0^{(k)}\right) \tag{15}$$

for the increment $\delta\boldsymbol{q}$, where $\boldsymbol{J}\left(\boldsymbol{q}_0^{(k)}\right)$ is the Jacobian operator and $-\boldsymbol{f}\left(\boldsymbol{q}_0^{(k)}\right)$ is the nonlinear residual of the Navier–Stokes equations. In order to obtain (15), also the fully temperature-dependent parameters need to be linearized. For e.g. the density, the linearization reads

$$\rho\left(T_0^{(k+1)}\right) = \rho\left(T_0^{(k)} + \delta T\right) \approx \rho\left(T_0^{(k)}\right) + \left.\frac{\partial\rho}{\partial T}\right|_{T_0^{(k)}} \delta T := \rho_0^{(k)} + \rho_0'^{(k)}\delta T, \tag{16}$$

where the increment δT is contained in $\delta\boldsymbol{q}$. After inserting ansatz (14) into the basic state equations and linearizing with respect to small $\delta\boldsymbol{q}$ under consideration of (16), we end up with

$$\nabla\cdot\left(\rho_0^{(k)}\delta\boldsymbol{u} + \rho_0'^{(k)}\boldsymbol{u}_0^{(k)}\delta T\right) = -\nabla\cdot\left(\rho_0^{(k)}\boldsymbol{u}_0^{(k)}\right), \tag{17a}$$

$$\begin{aligned}\nabla\cdot\left[\rho_0^{(k)}\left(\boldsymbol{u}_0^{(k)}\delta\boldsymbol{u} + \delta\boldsymbol{u}\boldsymbol{u}_0^{(k)}\right) + \rho_0'^{(k)}\boldsymbol{u}_0^{(k)}\boldsymbol{u}_0^{(k)}\delta T\right] - \nabla\cdot\left(\mu_0^{(k)}\delta\boldsymbol{\mathcal{T}} + \mu_0'^{(k)}\boldsymbol{\mathcal{T}}_0^{(k)}\delta T\right) \\ + \nabla\delta p - \rho_0'^{(k)}\delta T\boldsymbol{g} = -\nabla\cdot\left(\rho_0^{(k)}\boldsymbol{u}_0^{(k)}\boldsymbol{u}_0^{(k)}\right) - \nabla p_0^{(k)} + \rho_0^{(k)}\boldsymbol{g} + \nabla\cdot\left(\mu_0^{(k)}\boldsymbol{\mathcal{T}}_0^{(k)}\right),\end{aligned} \tag{17b}$$

$$\begin{aligned}\nabla\cdot\left[\rho_0^{(k)}c_{p0}^{(k)}\left(\boldsymbol{u}_0^{(k)}\delta T + T_0^{(k)}\delta\boldsymbol{u}\right) + \left(\rho_0'^{(k)}c_{p0}^{(k)} + \rho_0^{(k)}c_{p0}'^{(k)}\right)T_0^{(k)}\boldsymbol{u}_0^{(k)}\delta T\right] - \nabla\cdot\left(\lambda_0^{(k)}\nabla\delta T\right. \\ \left. + \lambda_0'^{(k)}\delta T\nabla T_0^{(k)}\right) = \nabla\cdot\left(\lambda_0^{(k)}\nabla T_0^{(k)}\right) - \nabla\cdot\left(\rho_0^{(k)}c_{p0}^{(k)}\boldsymbol{u}_0^{(k)}T_0^{(k)}\right),\end{aligned} \tag{17c}$$

where $\delta\boldsymbol{\mathcal{T}} = \nabla\delta\boldsymbol{u} + (\nabla\delta\boldsymbol{u})^\mathrm{T} - 2/3(\nabla\cdot\delta\boldsymbol{u})\boldsymbol{\mathcal{I}}$. Besides (17), the Newton–Raphson iteration involves an additional iteration loop to update the surface shape $h_0(z)$ after

each iteration step. To that end, the normal stress balance (5a) is linearized in an analogous way, yielding

$$\begin{aligned}
&-(\delta p-\delta p_{\mathrm{g}})+\left(\rho_0^{\prime(k)}-\rho_{\mathrm{g}0}^{\prime(k)}\right) g\delta T z+\mu_0^{\prime(k)}\boldsymbol{n}^{(k)}\cdot\mathcal{T}_0^{(k)}\cdot\boldsymbol{n}^{(k)}\delta T+\sigma_0^{\prime(k)}\delta T\nabla\cdot\boldsymbol{n}^{(k)}+\sigma_0^{(k)}\nabla\cdot\delta\boldsymbol{n}\\
&-\mu_{\mathrm{g}0}^{\prime(k)}\boldsymbol{n}^{(k)}\cdot\mathcal{T}_{\mathrm{g}0}^{(k)}\cdot\boldsymbol{n}^{(k)}\delta T+\mu_0^{(k)}\left(\boldsymbol{n}^{(k)}\cdot\delta\mathcal{T}\cdot\boldsymbol{n}^{(k)}+\boldsymbol{n}^{(k)}\cdot\mathcal{T}_0^{(k)}\cdot\delta\boldsymbol{n}+\delta\boldsymbol{n}\cdot\mathcal{T}_0^{(k)}\cdot\boldsymbol{n}^{(k)}\right)\\
&-\mu_{\mathrm{g}0}^{(k)}\left(\boldsymbol{n}^{(k)}\cdot\delta\mathcal{T}_{\mathrm{g}}\cdot\boldsymbol{n}^{(k)}-\boldsymbol{n}^{(k)}\cdot\mathcal{T}_{\mathrm{g}0}^{(k)}\cdot\delta\boldsymbol{n}-\delta\boldsymbol{n}\cdot\mathcal{T}_{\mathrm{g}0}^{(k)}\cdot\boldsymbol{n}^{(k)}\right)=-\left(\rho_0^{(k)}-\rho_{\mathrm{g}0}^{(k)}\right)gz\\
&+p_0^{(k)}-p_{\mathrm{g}0}^{(k)}-\mu_0^{(k)}\boldsymbol{n}^{(k)}\cdot\mathcal{T}_0^{(k)}\cdot\boldsymbol{n}^{(k)}-\sigma_0^{(k)}\nabla\cdot\boldsymbol{n}^{(k)}+\mu_{\mathrm{g}0}^{(k)}\boldsymbol{n}^{(k)}\cdot\mathcal{T}_{\mathrm{g}0}^{(k)}\cdot\boldsymbol{n}^{(k)}, \qquad (18)
\end{aligned}$$

where the surface increment

$$\delta h_0=h_0^{(k+1)}-h_0^{(k)} \qquad (19)$$

appears implicitly in the increment of the surface normal vector

$$\delta\boldsymbol{n}=\boldsymbol{n}^{(k+1)}-\boldsymbol{n}^{(k)} \qquad (20)$$

with

$$\delta\boldsymbol{n}=-\frac{1}{N^{(k)^3}}\frac{\mathrm{d}h_0^{(k)}}{\mathrm{d}z}\frac{\mathrm{d}\delta h_0}{\mathrm{d}z}\boldsymbol{e}_r-\frac{1}{N^{(k)}}\left[1-\frac{1}{N^{(k)^2}}\left(\frac{\mathrm{d}h_0^{(k)}}{\mathrm{d}z}\right)^2\right]\frac{\mathrm{d}\delta h_0}{\mathrm{d}z}\boldsymbol{e}_z \qquad (21)$$

and its divergence

$$\begin{aligned}
\nabla\cdot\delta\boldsymbol{n}=\frac{1}{h_0^{(k)^3}N^{(k)^3}}\Bigg[&-h_0^{(k)^3}\frac{\mathrm{d}^2\delta h_0}{\mathrm{d}z^2}\\
&+\left(\frac{3h^{(k)^3}}{N^{(k)^2}}\frac{\mathrm{d}^2h_0^{(k)}}{\mathrm{d}z^2}-h_0^{(k)^2}\right)\frac{\mathrm{d}h_0^{(k)}}{\mathrm{d}z}\frac{\mathrm{d}\delta h_0}{\mathrm{d}z}-h_0^{(k)}N^{(k)^2}\delta h_0\Bigg]. \qquad (22)
\end{aligned}$$

`MaranStable` solves the Newton iteration (15) using the parallelized MATLAB operator `backslash`, where the Jacobian operator $\boldsymbol{J}\left(\boldsymbol{q}_0^{(k)}\right)$ and the nonlinear residual $-\boldsymbol{f}\left(\boldsymbol{q}_0^{(k)}\right)$ can readily be identified from (17) and (18). We consider the basic state solution converged as soon as both the L_2 norm $\|\delta\boldsymbol{q}\|_2$ and the infinity norm $\|\delta\boldsymbol{q}\|_\infty$ of the residual have dropped below 10^{-6}.

4.2 Linear Stability Analysis

To perform a linear stability analysis of the previously computed basic state $\boldsymbol{q}_0$, `MaranStable` numerically solves the linear perturbation equations (12) for the amplitudes $\hat{\boldsymbol{q}}$ (and $\hat{\boldsymbol{q}}_{\mathrm{g}}$). Although `MaranStable` employs the same mesh and discretization scheme used for the basic state, we now end up with a large complex eigenvalue problem. By introducing $\check{v}=\mathrm{i}\hat{v}$, the complex eigenvalue problem turns into a generalized eigenvalue problem with real matrices $\mathcal{A}$ and $\mathcal{B}$ [58], i.e.

$$\mathcal{A}\cdot\hat{\boldsymbol{q}}=\chi\mathcal{B}\cdot\hat{\boldsymbol{q}}, \qquad (23)$$

where the perturbation amplitudes $\hat{\boldsymbol{q}}_{j,m}$ and the decay rate $\chi_{j,m} = -\mu_{j,m}$ represent the eigenvectors and eigenvalues, respectively. To solve the eigenvalue problem, `MaranStable` makes use of the parallelized MATLAB operator `eigs`, which relies on the functions implemented in the ARPACK library [17] for linear algebra. A detailed description for detecting neutral and critical Reynolds numbers is given in [52], where we also elaborated on the arclength continuation method to track the neutral curves under a parameter variation.

5 Summary of the Research Results

Table I provides an overview of our papers that are either published or submitted for publication (see column 'Status'). The blue-marked papers are included in Chapter II and accompanied by graphical abstracts. In all publications, I performed all numerical (and analytical) calculations and developed the software for paper 6. However, the multi-stage fitting algorithm for the heat transfer model in paper 5 was developed by F. Romanò, who is the first author of this paper. All authors contributed equally to analyzing data, reaching conclusions, and writing the paper. We note that the papers are not given in chronological order of appearance but are instead sorted by content.

Paper 1: Stability Boundary for Constant Material Parameters Paper 1 can be considered the starting point of our investigations. Owing to the large parameter space of our flow model, we defined a common reference case serving as an origin for all quasi-continuous parameter variations not only for paper 1 but also for more realistic flow models examined in papers 2 and 4. The common reference case is characterized by the liquid–gas couple and the geometrical configuration given in Table II (c.f. sketch in Fig. V). Starting our investigations in paper 1 with a sealed gas tube, we assumed all material parameters to be constant, except for the density in the buoyancy term, within the well-established framework of the Oberbeck–Boussinesq (OB) approximation as commonly done when the temperature differences are small. We further neglected flow-induced surface deformations, which allowed us to focus on the leading order instability mechanisms. Originating from the reference case, we performed linear stability analyses varying the aspect ratio $\Gamma = d/r_i$ and the volume ratio $\mathcal{V}$, one at a time. Also the gravity level was varied quasi-continuously investigating the effect of buoyancy forces on the critical threshold, including conditions of weightlessness and liquid bridges that are heated from below (inverted gravity). The energy transfer between the basic flow and the critical mode was investigated by means of kinetic and thermal energy budgets to gain insights into the instability mechanism. Except for liquid bridges heated from below under strong buoyancy forces, the axisymmetric two-dimensional flow was found to become unstable to hydrothermal waves [47] throughout the range of parameters considered.

Paper 2: Influence of a Coaxial Gas Flow on the Critical Point Although the gas phase was found to play only a passive role for the instability, it strongly affects the linear stability boundary Re_c by the amount and structure of the heat transfer

Table I: Publication list. Blue-marked papers are included in Chapter II.

No.	Title [Ref.]	Journal	Status
1	Stability of thermocapillary flow in liquid bridges fully coupled to the gas phase [52]	*J Fluid Mech*	published
2	High-Prandtl-number thermocapillary liquid bridges with dynamically deformed interface: Effect of an axial gas flow on the linear stability [54]	*J Fluid Mech*	submitted
3	Instability of axisymmetric flow in thermocapillary liquid bridges: Kinetic and thermal energy budgets for two-phase flow with temperature-dependent material properties [55]	*Eur J Appl Math*	published
4	Flow instability in high-Prandtl-number liquid bridges with fully temperature-dependent thermo-physical properties [53]	*J Fluid Mech*	submitted
5	Scaling and modeling of the heat transfer across the free surface of a thermocapillary liquid bridge [34]	*Int J Numer Method H*	submitted
6	`MaranStable:` A linear stability solver for multiphase flows in canonical geometries [56]	*SoftwareX*	published
7	Stability of thermocapillary flow in high-Prandtl-number liquid bridges exposed to a coaxial gas stream [50]	*Microgravity Sci Tec*	published
8	Flow instability in high-Prandtl-number thermocapillary liquid bridges exposed to a coaxial ambient gas stream [49]	*Proc Appl Math*	published

Table II: Working fluids (2 cSt silicone oil, air) and geometrical configuration of the common reference case used in papers 1, 2 and 4. Values for d, r_i, r_o, d_{top} and d_{bottom} are given in mm.

Liquid	Gas	$\mathcal{V}$	d	r_i	r_o	d_{top}	d_{bottom}
2 cSt	Air	1	1.65	2.5	10	1	1

through the liquid–gas interface. Based on this finding, which Kamotani *et al.* [10] and others noticed before, we dedicated paper 2 to the potential of controlling Re_c via an externally imposed axial gas flow, which has the same temperature at the annular inlet as the adjacent support rod. Allowing the gas to enter the open gas tube through the top or bottom open end, we established the linear stability boundary as function of the gas flow rate for liquid bridges that are heated from either below or above. Since the forced gas flow implies an additional imposed pressure gradient also affecting the liquid–gas interface, we questioned the assumption of statically shaped liquid bridges. To estimate the impact of flow-induced surface deformations on the stability boundary, we carried out stability analyses for both cases, first neglecting and then including dynamic surface deformations caused by the axisymmetric flow. To properly take care of flow-induced deformations, we used an extended OB approximation in which the density of both fluids depends linearly on the temperature in all equations. Throughout, we found that neither the gas flow nor the thermocapillary flow leads to significant deviations from the static shape for the setup given in Table II. Thus, the influence of dynamic surface deformations on the critical thermocapillary Reynolds number is relatively modest. However, our results for moderate gas flow rates confirmed the potential of controlling the onset of oscillatory flow, where the linear stability boundary strongly depends on the imposed gas flow rate and direction. The sensitivity can be explained through the change of the thermal environment at the interface caused by the hot or cold gas flow manipulating the surface temperature profile, which is crucial for the structure of the basic vortex and temperature field. This results in a modification of the energy supply to the perturbation mode, which arises as a hydrothermal wave.

The critical data presented in papers 1 and 2 are in good qualitative agreement with experimental measurements from the literature. However, despite the high accuracy of our applied numerical method, we observed a quantitative difference in a few cases, which can have several reasons. On the one hand, experimental measurements of the critical Reynolds numbers for thermocapillary liquid bridges are challenging due to the small liquid bridge size, possible interface contaminations, and the difficulty in precisely controlling the thermal environment, all contributing to measurement uncertainties. On the other hand, we must note that the validity range of the OB approximation is limited to a certain imposed temperature difference, above which the assumption of constant material parameters fails. This assumption is proped in papers 3 and 4.

Paper 3: Impact of Temperature-Dependent Material Parameters on the Critical Onset The primary objective of paper 3 was the derivation of the full closed-form kinetic and thermal energy budgets for variable material properties. Evaluating the budgets for critical conditions, it turned out that the temperature dependence of the material parameters does not alter the general instability mechanism. However, Melnikov *et al.* [23] reported a significant impact of a linearly temperature-dependent viscosity on the linear stability boundary, which cannot be captured by the OB approximation. Therefore, we first examined the validity range of the OB approximation by considering a low- and high-Prandtl-number liquid bridge. Regarding the former, which was represented by molten tin, it turned out that the OB approximation is indeed sufficient to properly describe the flow. However, this was not the case for the high-Prandtl-number liquid bridge made from 2 cSt silicone oil and surrounded by air (see Table II, but $\mathcal{V} = 0.9$) since the obtained critical temperature difference provokes non-negligible changes of e.g. the thermal conductivities and the dynamic viscosities. Extending the model of Melnikov *et al.* [23], we introduced a more realistic model that accounts for the **L**inear **T**emperature **D**ependence (LTD) of all properties and derived a formula to estimate its validity range. Although the validity range of the LTD model is significantly larger compared to the OB approximation, it is still bounded to relatively small temperature differences owing to the exponential variation of the liquid's viscosity. To properly take care of temperature differences beyond the validity range of the LTD model, we further increased the complexity of the flow model by taking the **F**ull **T**emperature **D**ependence (FTD) of all material parameters into account. For the considered high-Prandtl-number test case, we found a deviation of almost 25% in the predicted critical Reynolds numbers between the OB and the FTD model. This large deviation arises due to the reduced viscosity in the FTD model near the hot wall and along the free surface, providing less resistance and thus leading to a stronger basic vortex and subsequently to a less stable flow.

Paper 4: Stability Boundary for Fully Temperature-Dependent Fluid Properties For a more comprehensive comparison between the OB, LTD and FTD models, we performed in paper 4 quasi-continuously variations of the volume ratio, the aspect ratio and the gas flow rates originating from the reference case from Table II and exploiting all three flow models. Moreover, we varied the domain's size to study the impact of the length scale on the critical Reynolds number, which is affected by the relative importance of buoyancy forces and by the range and character of the variability of the fluid's properties. In general, the variability of the material parameters increases with increasing ΔT. This means that for moderate critical temperature differences ($\Delta T_c \lesssim 10\,\mathrm{K}$), the OB approximation can be considered accurate enough to predict the onset of instability since the critical conditions compare well with the ones obtained by our reference FTD model. For higher ΔT_c, the critical curve obtained by the OB model may deviate significantly from the critical data resulting from the FTD model. Since the OB approximation may either under or overestimate the critical threshold, it is difficult to establish a consistent correlation for the critical data across larger ranges of aspect or volume ratios. As specific examples, we examined two different volume ratios more closely, where the FTD model predicted almost the same critical temperature difference of about 50 K. Despite the similar thermal conditions,

the OB approximation led to a good agreement in one case but to a severe overestimation in the other case. This indicates that competing effects on the critical threshold are at work that either compensate or reinforce each other. Thus, it is concluded that the deviations in ΔT_c (or Re_c) among the different approximations are due to subtle differences in the basic flow and the critical perturbation mode, which need to be examined separately for each parameter setup. For parameter variations related to the aspect ratio of the liquid bridge, we observe a qualitatively similar behavior of the deviations but at a much lesser extent owing to the smaller ΔT_c. If, instead, axial gas flows with variable gas flow rates are imposed at the inlet of the open gas tube (as in paper 2), the critical curve resulting from the OB approximation is not even comparable in terms of its shape with the one obtained by the FTD model. The LTD model, however, is able to qualitatively reproduce the critical threshold in all parameter variations but typically underestimates the critical instability onset. Throughout, the deviations in Re_c between the LTD and FTD can reach up to 25%, whereas the results obtained by the OB model can deviate by more than 100% from the data obtained by the FTD model.

Paper 5: Heat Transfer Model with a Space-Dependent Biot Function For high Prandtl numbers, it was shown that the gas phase mainly influences the critical onset due to the amount and structure of the heat transfer through the liquid–gas interface affecting the surface temperature, which is crucial for the thermocapillary driving. Although the heat flux density exhibits sharp peaks, single-fluid models considering only the liquid phase routinely model the heat flux by applying Newton's cooling law with a suitable ambient reference temperature and a constant Biot number Bi. This assumption may lead to a poor numerical prediction of the real flow and its stability. Still, the single-phase approach is appealing due to its computational efficiency, especially for fully-resolved three-dimensional simulations. In paper 5, we present an improved single-fluid model that combines the advantage of a standard single-fluid model (computational cost) with the benefit of a two-fluid model (accuracy). In our improved model, we replace the conventionally used constant Biot number Bi with a Biot function $\mathrm{Bi}(z)$ to better represent the space-dependent heat flux density through the interface. To that end, we extracted the space-resolved heat flux from two-phase simulations for various aspect ratios and Reynolds numbers. The collected data was fed to our derived multi-stage algorithm to establish closed-form expressions for the fitted Biot functions that can subsequently be used in single-phase simulations. This way, the correct thermal conditions are incorporated into the single-fluid model while the (less important) viscous coupling is still being neglected. To analyze the performance of the improved single-fluid model, we compared different heat transfer models regarding the linear stability boundaries with the reference two-fluid model. We showed that this approach yields more accurate results than the classical Newton law with a constant Biot number. Moreover, it has to be noted that an appropriate constant Biot number is typically unknown a priori and needs to be guessed. However, our derived model also provides improvement for the case of a constant Biot number, which was found to be best approximated with the average of the Biot function over the free surface excluding the thermal boundary layers. The linear stability analysis using this constant but case-dependent Biot number also yields a good approximation to Re_c.

Paper 6: MaranStable All calculations have been carried out using the MATLAB code `MaranStable`, which has been made publicly available with paper 6. Operating the software is facilitated by means of an easy-to-use graphical user interface, which has been developed as part of this thesis. `MaranStable` computes steady two-dimensional flows in canonical geometries and inspects their stability behavior by performing three-dimensional linear stability analyses. `MaranStable` can deal with both cylindrical and Cartesian coordinates and offers users a highly adaptable geometry setup, allowing for a wide range of configurations, such as e.g. channels, annular pipes, cavities or liquid bridges. Moreover, the user can select between the single-phase and multiphase solvers. `MaranStable` stands out due to its numerous features compared to commonly used solvers in the community of thermocapillary-driven flows, including three different models for the interface deformations with increasing complexity: (i) straight indeformable surface shape, (ii) hydrostatic surface shape and (iii) dynamically deformed surface shape. This allows for studying the impact of the often-neglected dynamic interface deformations. Regarding the governing equations, three approximations to the continuity, Navier–Stokes, and energy equations are implemented in `MaranStable` for both single-phase and immiscible multiphase flows, which have already been introduced and analyzed in papers 1–5. To summarize, the models are in increasing order of complexity: (i) the well-known OB approximation, (ii) the LTD model, where all fluid properties depend linearly on T and (iii) the FTD model accounting for the full temperature dependence of all fluid properties. Using the FTD model, the user can choose among over a hundred implemented liquids and gases, while for the OB and LTD model, additional fluids can be defined by the user with custom fluid properties. `MaranStable` can be further customized by activating or deactivating Marangoni stresses by using the Stokes flow approximation, where the inertia terms in the physical model are set to zero, or by skipping the energy equation. Apart from the basic state computation and the linear stability analysis, `MaranStable` provides a module to trace optical rays in the liquid, where the diffraction index $\mathcal{N}$ is non-homogeneous owing to its temperature dependence $\mathcal{N}(T)$. This tool can be especially useful for experimentalists measuring particle trajectories in non-isothermal liquids.

6 Scientific Contribution of the Dissertation

The knowledge of the linear stability limit is of great interest for experiments. For low-Prandtl-number liquids such as molten metal, the linear stability analysis allows to predict the first transition from the two-dimensional basic flow to the three-dimensional stationary flow [20]. For high-Prandtl-number liquids such as our primarily investigated 2cSt silicone oil, the linear stability analysis is sufficient to describe the instability to hydrothermal waves [63]. Since high-Prandtl-number liquids are transparent and easier to handle, they have been investigated experimentally to a greater extent both on the ground and under zero gravity. The importance of critical data becomes evident when considering the limited availability of accurate numerical studies on high-Prandtl-number liquid bridges in the existing literature. With the present work, we have accurately established the dependence of the linear stability boundary on parameters that are typically varied in laboratory experiments, namely the aspect and

the volume ratio of the liquid bridge. Moreover, we have shown to which extent the stability of the thermocapillary flow can be controlled via an externally imposed gas flow.

As members of the JEREMI project, we have carried out linear stability analyses to guide planning the upcoming space experiment. To that end, we have numerically studied the dependence of the linear stability on the gravity level including conditions of weightlessness. With the help of our critical data, the time-consuming search for the critical point can be sped up, saving valuable time on the ISS. As additional guidance for preparing the space experiment, we have conducted a systematic analysis concerning the size of the liquid bridge. Our study reveals the length scale below which the flow in the thermocapillary liquid bridge is practically unaffected by gravity forces, even under terrestrial conditions. Thus, ground experiments following our restrictions can serve as a basis for reliable planning of the space experiment.

Within the framework of this research project, we have systematically increased the complexity of our computational model, starting from the well-established Oberbeck–Boussinesq approximation with a solely hydrostatically deformed liquid–gas interface. By this means, we were able to estimate the error made by routinely used assumptions in numerical investigations. Inspecting flow-induced interface deformations, we found a moderate impact on the instability threshold. Thus, we conclude that previously reported critical data assuming a statically deformed surface are reliable. However, we have proven that the Oberbeck–Boussinesq approximation may lead to poor numerical predictions for sufficiently large critical temperature differences owing to the high variability of the liquid's viscosity. To get more accurate results, one may follow the approach of Melnikov *et al.* [23] and account for a linearly temperature-dependent viscosity. However, for very large temperature variations, we strongly recommend using a model which accounts for the full nonlinear temperature dependence of at least the viscosity.

Regarding single-phase solvers omitting the gas phase, we have analyzed standard single-fluid models incorporating a constant Biot number in Newton's cooling law. We have shown that for high-Prandtl-number liquid bridges, this assumption may cause unacceptable discrepancies from the actual flow, especially because the most suitable Biot number is typically unknown and, therefore, needs to be guessed. As a remedy, we have developed an improved single-phase model in which the heat transfer is still modeled by Newton's cooling law but with a space-dependent Biot function derived from numerous two-phase simulations and fitted for a wide range of aspect and Reynolds numbers. The resulting closed-form expressions are provided to the community under `https://github.com/fromano88/BiotFunction_LB.git`. They can be implemented in existing single-phase solvers to significantly improve their accuracy without increasing the computational cost. For solvers restricted to constant Biot numbers, we also provide a MATLAB code that computes the best-suitable value based on the average heat flux. Therefore, if the average heat flux would be measured in experiments in addition to the critical Reynolds number, the Biot number based on the measured heat flux should provide a good approximation to the proper constant Biot number to be used in numerical single-fluid linear stability analyses. It would be interesting to test this hypothesis in future investigations.

Despite all, our MATLAB software `MaranStable` undoubtedly makes the most significant scientific contribution. The extensively verified and validated software has been made operable via a graphical user interface allowing usage by non-expert programmers. It is freely accessible to scientists and students under https://github.com/fromano88/MaranStable, where we also provide many documentation and tutorial files to help users get started with the software. Concerning the flow in liquid bridges surrounded by gas, the user has the flexibility to set up the desired geometry parameters, gravity conditions, working liquid and gas, boundary conditions, etc., to compute the axisymmetric basic flow and its linear stability, or can seek for the critical mode at the given set of parameters. Experimentalists can profit from the results obtained with `MaranStable` when building the experimental design for experiments conducted in space (e.g. JEREMI) or on Earth. They typically study the thermocapillary flow in liquid bridges by seeding particles into the liquid in order to track their position. The resulting measurements, however, might be misleading since the index of refraction depends on the temperature field, which can exhibit strong gradients especially in high-Prandtl-number liquids. `MaranStable` provides a tool to correct the measured particle position by accounting for the temperature dependence of the diffraction index. The true scientific value of `MaranStable` is understood when considering that the software is not only restricted to liquid bridges but can deal with a wide range of canonical geometries including both planar and cylindrical geometries. Owing to the versatility of `MaranStable`, the user can carry out state-of-the-art research in complex multiphase hydrodynamic stability. The computed data can be visualized by the embedded visualization toolbox. Alternatively, the data can be exported in VTK or DAT, enabling external post-processing via software such as e.g. `Paraview`, `gnuplot` or `xmgrace`. In view of the advanced capabilities, `MaranStable` bears great potential to broaden the user community and facilitate advancements in understanding multiphase flow instabilities.

Some of the implemented features of `MaranStable` are still in the beta version and, thus, yet to be available in the GUI. This includes the computation of kinetic and thermal energy budgets of the critical mode, and the improved heat transfer model for single-fluid models. Apart from that, the computational model would benefit from further extensions to account for other important influence factors. For large temperature differences, evaporation may play an important role, which was found to have a stabilizing effect for highly volatile liquids [45]. Regarding the future space experiments where larger liquid bridges can be investigated, it would be useful to account for dynamic surface deformations in the perturbation flow. This would allow the detection of surface wave instabilities, which have been exlcuded beforehand in the present analysis. In general, experimental measurements may be affected by possible chemical contaminations of the interface [44]. Hence, it would also be desirable to numerically account for experimental errors related to surface contaminations by surfactants.

Bibliography

[1] Carrión, L. M., Herrada, M. A. & Montanero, J. M. 2020 Influence of the dynamical free surface deformation on the stability of thermal convection in high-Prandtl-number liquid bridges. *Intl J. Heat Mass Transfer* **146**, 118831 (10pp).

[2] Chang, C. E. & Wilcox, W. R. 1975 Inhomogeneities due to thermocapillary flow in floating zone melting. *J. Crystal Growth* **28**, 8–12.

[3] Chang, C. E. & Wilcox, W. R. 1976 Analysis of surface tension driven flow in floating zone melting. *Intl J. Heat Mass Transfer* **19**, 355–366.

[4] Cröll, A., Müller-Sebert, W., Benz, K. W. & Nitsche, R. 1991 Natural and thermocapillary convection in partially confined silicon melt zones. *Microgravity Sci. Technol.* **3**, 204–215.

[5] Drazin, P. G. & Reid, W. H. 1981 *Hydrodynamic Stability*. Cambridge: Cambridge University Press.

[6] Ferrera, C., Mialdun, A., Shevtsova, V. M., Cabezas, M. & Montanero, J. M. 2008 Measurement of the dynamical free surface deformation in liquid bridges. *Acta Astronaut.* **62**, 471–477.

[7] Gray, D. D. & Giorgini, A. 1976 The validity of the Boussinesq approximation for liquids and gases. *Intl J. Heat Mass Transfer* **19**, 545.

[8] Imaishi, N., Yasuhiro, S., Akiyama, Y. & Yoda, S. 2001 Numerical simulation of oscillatory Marangoni flow in half-zone liquid bridge of low Prandtl number fluid. *J. Crystal Growth* **230**, 164–171.

[9] Joseph, D. D. 1976 *Stability of Fluid motions I*, *Springer Tracts in Natural Philosophy*, vol. 27. Berlin, Heidelberg: Springer.

[10] Kamotani, Y., Wang, L., Hatta, S., Wang, A. & Yoda, S. 2003 Free surface heat loss effect on oscillatory thermocapillary flow in liquid bridges of high Prandtl number fluids. *Intl J. Heat Mass Transfer* **46**, 3211–3220.

[11] Karbalaei, A., Kumar, R. & Cho, H. J. 2016 Thermocapillarity in microfluidics — a review. *Micromachines* **7**, 13–1–13–41.

[12] Kozhoukharova, Z., Kuhlmann, H. C., Wanschura, M. & Rath, H. J. 1999 Influence of variable viscosity on the onset of hydrothermal waves in thermocapillary liquid bridges. *Z. Angew. Math. Mech.* **79**, 535–543.

[13] Kuhlmann, H. C. 1999 *Thermocapillary Convection in Models of Crystal Growth*, *Springer Tracts in Modern Physics*, vol. 152. Berlin, Heidelberg: Springer.

[14] Kuhlmann, H. C., Lukasser, M. & Muldoon, F. H. 2011 Engineering Marangoni flows (EMA). ASAP6 819714. FFG.

[15] Landau, L. D. & Lifschitz, E. M. 1959 *Fluid Mechanics*. New York: Pergamon Press.

[16] Lappa, M., Savino, R. & Monti, R. 2001 Three-dimensional numerical simulation of Marangoni instabilities in non-cylindrical liquid bridges in microgravity. *Intl J. Heat Mass Transfer* **44**, 1983–2003.

[17] Lehoucq, R. B., Sorensen, D. C. & Yang, C. 1998 *ARPACK Users' Guide: Solution of Large-Scale Eigenvalue Problems with Implicitly Restarted Arnoldi Methods*. Philadelphia: SIAM.

[18] Levenstam, M., Amberg, G. & Winkler, C. 2001 Instabilities of thermocapillary convection in a half-zone at intermediate Prandtl numbers. *Phys. Fluids* **13**, 807–816.

[19] Levich, V. G. & Krylov, V. S. 1969 Surface tension-driven phenomena. *Annu. Rev. Fluid Mech.* **1**, 293–316.

[20] Leypoldt, J., Kuhlmann, H. C. & Rath, H. J. 2000 Three-dimensional numerical simulation of thermocapillary flows in cylindrical liquid bridges. *J. Fluid Mech.* **414**, 285–314.

[21] Leypoldt, J., Kuhlmann, H. C. & Rath, H. J. 2002 Stability of hydrothermal-wave states. *Adv. Space Res.* **29**, 645–650.

[22] Marangoni, C. 1871 Ueber die Ausbreitung der Tropfen einer Flüssigkeit auf der Oberfläche einer anderen. *Ann. Phys. Chem.* **143**, 337–354.

[23] Melnikov, D. E., Shevtsova, V. M. & Legros, J. C. 2002 Numerical simulation of hydro-thermal waves in liquid bridges with variable viscosity. *Adv. Space Res.* **29**, 661–666.

[24] Mihaljan, J. M. 1962 A rigorous exposition of the Boussinesq approximation applicable to a thin layer of fluid. *Astrophys. J.* **136**, 1126–1133.

[25] Mills, K. C., Keene, B. J., Brooks, R. F. & Shirali, A. 1998 Marangoni effects in welding. *Phil. Trans. Roy. Soc. London A* **356**, 911–925.

[26] Montanero, J. M., Ferrera, C. & Shevtsova, V. M. 2008 Experimental study of the free surface deformation due to thermal convection in liquid bridges. *Exp. Fluids* **45**, 1087–1101.

[27] Motegi, K., Fujimura, K. & Ueno, I. 2017 Floquet analysis of spatially periodic thermocapillary convection in a low-Prandtl-number liquid bridge. *Phys. Fluids* **29**, 074104 (14pp).

[28] Nienhüser, C. & Kuhlmann, H. C. 2002 Stability of thermocapillary flows in non-cylindrical liquid bridges. *J. Fluid Mech.* **458**, 35–73.

[29] Ostrach, S. 1982 Low-gravity fluid flows. *Annu. Rev. Fluid Mech.* **14**, 313–345.

[30] Park, J., & Moon, J. 2006 Control of colloidal particle deposit patterns within picoliter droplets ejected by ink-jet printing. *Langmuir* **22**, 3506–3513.

[31] Pfann, W. G. 1962 Zone melting. *Science* **135**, 1101–1109.

[32] Preisser, F., Schwabe, D. & Scharmann, A. 1983 Steady and oscillatory thermocapillary convection in liquid columns with free cylindrical surface. *J. Fluid Mech.* **126**, 545–567.

[33] Romanò, F. & Kuhlmann, H. C. 2019 Finite-size coherent structures in thermocapillary liquid bridges: A review. *Int. J. Microgravity Sci. Appl.* **36**, 360201 (17pp).

[34] Romanò, F., Stojanović, M. & Kuhlmann, H. C. 2023 Scaling and modeling of the heat transfer across the free surface of a thermocapillary liquid bridge (submitted). *Int. J. Numer. Method H.* .

[35] Schmid, P. J. & Henningson, D. S. 2001 *Stability and Transition in Shear Flows*, *Appl. Math. Sci.*, vol. 142. New York, Berlin: Springer.

[36] Schwabe, D. 1981 Marangoni effects in crystal growth melts. *Physicochem. Hydrodyn.* **2**, 263–280.

[37] Schwabe, D., Mizev, A. I., Udhayasankar, M. & Tanaka, S. 2007 Formation of dynamic particle accumulation structures in oscillatory thermocapillary flow in liquid bridges. *Phys. Fluids* **19**, 072102 (18pp).

[38] Schwabe, D., Scharmann, A., Preisser, F. & Oeder, F. 1978 Experiments on surface tension driven flow in floating zone melting. *J. Crystal Growth* **43**, 305–312.

[39] Scriven, L. E. & Sternling, C. V. 1960 The Marangoni effects. *Nature* **187**, 186–188.

[40] Shevtsova, V., Gaponenko, Y., Kuhlmann, H. C., Lappa, M., Lukasser, M., Matsumoto, S., Mialdun, A., Montanero, J. M., Nishino, K. & Ueno, I. 2014 The JEREMI-project on thermocapillary convection in liquid bridges. Part B: Overview on impact of co-axial gas flow. *Fluid Dyn. Mat. Proc.* **10**, 197–240.

[41] Shevtsova, V., Melnikov, D. E. & Nepomnyashchy, A. 2009 New flow regimes generated by mode coupling in buoyant-thermocapillary convection. *Phys. Rev. Lett.* **102**, 134503–1–134503–4.

[42] Shevtsova, V., Mialdun, A., Ferrera, Ermakov, M., Cabezas, M. G. & Montanero, J. M. 2008 Subcritical and oscillatory dynamic surface deformations in non-cylindrical liquid bridges. *Fluid Dyn. Mat. Proc.* **4**, 43–54.

[43] Shevtsova, V. M., Melnikov, D. E. & Legros, J. C. 2001 Three-dimensional simulations of hydrodynamic instability in liquid bridges: Influence of temperature-dependent viscosity. *Phys. Fluids* **13**, 2851–2865.

[44] Shmyrov, A., Mizev, A., Demin, V., Petukhov, M. & Bratsun, D. 2018 On the extent of surface stagnation produced jointly by insoluble surfactant and thermocapillary flow. *Advances in Colloid and Interface Science* **255**, 10–17.

[45] Simic-Stefani, S., Kawaji, M. & Yoda, S. 2006 Onset of oscillatory thermocapillary convection in acetone liquid bridges: The effect of evaporation. *Intl J. Heat Mass Transfer* **49**, 3167–3179.

[46] Sirignano, W. A. & Glassman, I. 1970 Flame spreading above liquid fuels: Surface-tension-driven flows. *Combust. Sci. Tech.* **1**, 307–312.

[47] Smith, M. K. & Davis, S. H. 1983 Instabilities of dynamic thermocapillary liquid layers. Part 1. Convective instabilities. *J. Fluid Mech.* **132**, 119–144.

[48] Smith, M. K. & Davis, S. H. 1983 Instabilities of dynamic thermocapillary liquid layers. Part 2. Surface-wave instabilities. *J. Fluid Mech.* **132**, 145–162.

[49] Stojanović, M. & Kuhlmann, H. C. 2020 Flow instability in high-Prandtl-number thermocapillary liquid bridges exposed to a coaxial ambient gas stream. *PAMM* **20**, e202000123.

[50] Stojanović, M. & Kuhlmann, H. C. 2020 Stability of thermocapillary flow in high-Prandtl-number liquid bridges exposed to a coaxial gas stream. *Microgravity Sci. Technol.* **32**, 953–959.

[51] Stojanović, M. & Kuhlmann, H. C. 2021 Stability analysis for the JEREMI experiment (SAJE) – Final Report. FFG Report (ASAP) Project no. 866027. Institute of Fluid Mechanics and Heat Transfer.

[52] Stojanović, M., Romanò, F. & Kuhlmann, H. C. 2022 Stability of thermocapillary flow in liquid bridges fully coupled to the gas phase. *J. Fluid Mech.* **949**, A5 (51pp).

[53] Stojanović, M., Romanò, F. & Kuhlmann, H. C. 2023 Flow instability in high-Prandtl-number liquid bridges with fully temperature-dependent thermophysical properties (submitted). *J. Fluid Mech.* .

[54] Stojanović, M., Romanò, F. & Kuhlmann, H. C. 2023 High-Prandtl-number thermocapillary liquid bridges with dynamically deformed interface: Effect of an axial gas flow on the linear stability (submitted). *J. Fluid Mech.* .

[55] Stojanović, M., Romanò, F. & Kuhlmann, H. C. 2023 Instability of axisymmetric flow in thermocapillary liquid bridges: Kinetic and thermal energy budgets for two-phase flow with temperature-dependent material properties. *Eur. J. Appl. Math.* pp. 1–27.

[56] Stojanović, M., Romanò, F. & Kuhlmann, H. C. 2023 MaranStable: A linear stability solver for multiphase flows in canonical geometries. *SoftwareX* **23**, 101405.

[57] Tang, Z. M., Hu, W. R. & Imaishi, N. 2001 Two bifurcation transitions of the floating half zone convection in a fat liquid bridge of larger Pr. *Intl J. Heat Mass Transfer* **44**, 1299–1307.

[58] Theofilis, V. 2003 Advances in global linear instability analysis of nonparallel and three-dimensional flows. *Prog. Aerospace Sci.* **39**, 249–315.

[59] Thompson, J. F., Warsi, Z. U. & Mastin, C. W. 1985 *Numerical Grid Generation: Foundations and Applications*. Amsterdam: Elsevier North-Holland.

[60] Ueno, I. & Torii, T. 2010 Thermocapillary-driven flow in a thin liquid film sustained in a rectangular hole with temperature gradient. *Acta Astronaut.* **66**, 1017–1021.

[61] Van Dyke, M. 1982 *An Album of Fluid Motion*. Stanford, California: Parabolic Press.

[62] Velten, R., Schwabe, D. & Scharmann, A. 1991 The periodic instability of thermocapillary convection in cylindrical liquid bridges. *Phys. Fluids A* **3**, 267–279.

[63] Wanschura, M., Shevtsova, V. S., Kuhlmann, H. C. & Rath, H. J. 1995 Convective instability mechanisms in thermocapillary liquid bridges. *Phys. Fluids* **7**, 912–925.

[64] Wesseling, P. 2009 *Principles of Computational Fluid Dynamics*. Springer.

[65] Yano, T., Nishino, K., Matsumoto, S., Ueno, I., Komiya, A., Kamotani, Y. & Imaishi, N. 2018 Report on microgravity experiments of dynamic surface deformation effects on Marangoni instability in high-Prandtl-number liquid bridges. *Microgravity Sci. Technol.* **30**, 599–610.

[66] Yasnou, V., Gaponenko, Y., Mialdun, A. & Shevtsova, V. 2018 Influence of a coaxial gas flow on the evolution of oscillatory states in a liquid bridge. *Int. J. Heat Mass Transfer* **123**, 747–759.

[67] Young, N. O., Goldstein, J. S. & Block, M. J. 1959 The motion of bubbles in a vertical temperature gradient. *J. Fluid Mech.* **6**, 350–356.

II

Publications

Paper 1

Stojanović, M., Romanò, F., Kuhlmann, H. C. (2022), 'Stability of thermocapillary flow in liquid bridges fully coupled to the gas phase', *J. Fluid Mech.* **949**, A5-1–A5-51

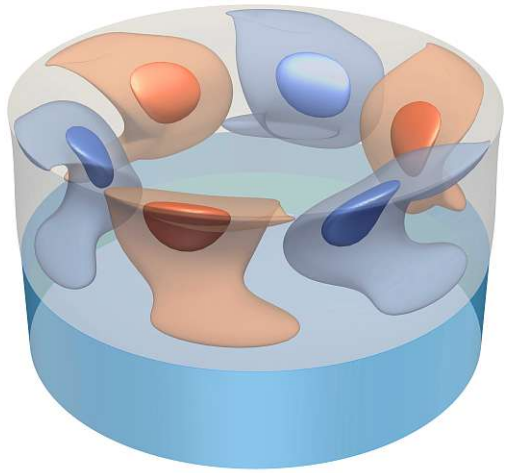

J. Fluid Mech. (2022), *vol*. 949, A5, doi:10.1017/jfm.2022.724

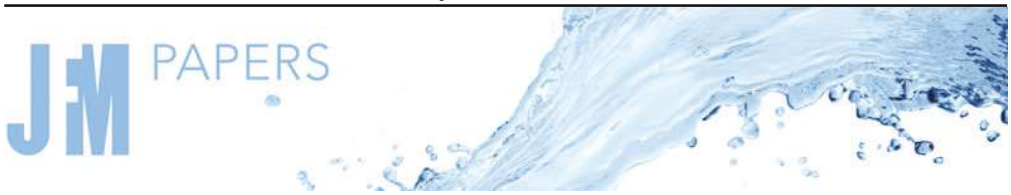

Stability of thermocapillary flow in liquid bridges fully coupled to the gas phase

Mario Stojanović[1],†, **Francesco Romanò**[2],† **and Hendrik C. Kuhlmann**[1],†

[1]TU Wien, Getreidemarkt 9-BA, 1060 Vienna, Austria

[2]Univ. Lille, CNRS, ONERA, Arts et Métiers Institute of Technology, Centrale Lille, UMR 9014 – LMFL – Laboratoire de Mécanique des Fluides de Lille – Kampé de Fériet, F-59000 Lille, France

(Received 9 April 2022; revised 7 July 2022; accepted 5 August 2022)

The linear stability of the axisymmetric steady thermocapillary flow in a liquid bridge made from 2 cSt silicone oil (Prandtl number 28) is investigated numerically in the framework of the Boussinesq approximation. The flow and temperature fields in the surrounding gas phase (air) are taken into account for a generic cylindrical container hosting the liquid bridge. The flows in the liquid and in the gas are fully coupled across the hydrostatically deformed liquid–gas interface, neglecting dynamic interface deformations. Originating from a common reference case, the linear stability boundary is computed varying the length of the liquid bridge (aspect ratio), its volume and the gravity level, providing accurate critical data. The qualitative dependence of the critical threshold on these parameters is explained in terms of the characteristics of the critical mode. The heat exchange between the ambient gas and the liquid bridge that is fully resolved has an important influence on the critical conditions.

Key words: thermocapillarity, instability, liquid bridge, gas/liquid flow

1. Introduction

The interfacial free energy between two immiscible fluids depends on the local temperature. If the temperature varies along the interface, then the associated energy gradients lead to variations of the line tension. This is the thermocapillary effect (Thomson 1855; Scriven & Sternling 1960; Levich & Krylov 1969), which can be a major driving force for fluid motion in pure fluids. Thermocapillary flows are of great importance for industrial applications such as welding (Mills *et al.* 1998), combustion (Sirignano &

† Email addresses for correspondence: mario.stojanovic@tuwien.ac.at, francesco.romano@ensam.eu, hendrik.kuhlmann@tuwien.ac.at

Glassman 1970), crystal growth (Schwabe 1981) and droplet manipulation in microfluidics (Young, Goldstein & Block 1959).

To better understand thermocapillary flows, a number of paradigmatic configurations have been investigated, ranging from flows in thin films (Smith & Davis 1983*a*, *b*; Oron, Davis & Bankoff 1997; Diez & Kondic 2002; Craster & Matar 2009), flows in liquid-filled cavities with a non-isothermal interface (Carpenter & Homsy 1989; Ohnishi, Azuma & Doi 1992; Xu & Zebib 1998; Kuhlmann & Albensoeder 2008; Romanò & Kuhlmann 2017), and axisymmetric liquid bridges kept in place by the mean surface tension and aligned with the gravity vector (Chun & Wuest 1979; Preisser, Schwabe & Scharmann 1983; Kuhlmann 1999; Kawamura & Ueno 2006; Schwabe 2014; Kumar 2015; Romanò & Kuhlmann 2018). The canonical system of a liquid bridge is often employed to model the fundamental transport processes in the floating-zone technique of crystal growth (Pfann 1962; Hurle & Jakeman 1981). A major aspect in floating-zone crystal growth is the onset of time-dependent melt flow, because it is associated with a time-dependent propagation of the solidification front, which leads to an uneven distribution of impurities (striations) in the desired single crystal (Cröll *et al.* 1991).

In the floating-zone technique, the liquid bridge is supported by solid crystalline or polycrystalline rods whose temperature near the melt zone is close to the melting point, while the temperature of the interface, which is heated, exhibits a maximum midway between the two supports. To simplify the problem while retaining the essential flow physics, the half-zone model has been introduced by Schwabe *et al.* (1978). In their half-zone model, two support rods of a material with a higher melting point than the liquid are used and kept at different temperatures. The strength of the flow in the half-zone depends on the applied temperature difference, often measured by a suitable Reynolds number Re. As the Reynolds number is increased, the axisymmetric steady flow in the half-zone becomes unstable. As these flow instabilities are related to the striations found in crystals produced by the floating-zone technique, much effort has been devoted to flow instabilities in the half-zone model (Kuhlmann 1999), which led to numerous experimental (Preisser *et al.* 1983; Velten, Schwabe & Scharmann 1991; Takagi *et al.* 2001; Ueno, Tanaka & Kawamura 2003; Kawamura & Ueno 2006; Gaponenko, Mialdun & Shevtsova 2012; Yano *et al.* 2017; Kang *et al.* 2019) and numerical (Wanschura *et al.* 1995; Leypoldt, Kuhlmann & Rath 2000; Levenstam, Amberg & Winkler 2001; Lappa, Savino & Monti 2001; Nienhüser & Kuhlmann 2002; Shevtsova, Gaponenko & Nepomnyashchy 2013; Li *et al.* 2015; Motegi, Fujimura & Ueno 2017*a*) investigations, only a few of which can be cited here. Investigations of the full-zone problem are sparse (see, however, Wanschura, Kuhlmann & Rath 1997*a*; Kasperski, Batoul & Labrosse 2000; Lappa 2003, 2004, 2005; Hu, Tang & Li 2008; Motegi, Kudo & Ueno 2017*b*).

The stability of the flow in a thermocapillary liquid bridge is a complex problem, because the flow and temperature fields in the gas and the liquid phase are coupled via a deformable interface. For this reason, most of the theoretical and numerical studies have made simplifying assumptions. The most popular approximation is to consider the interface indeformable (Shevtsova & Legros 1998; Nienhüser & Kuhlmann 2002) or even cylindrical (see e.g. Neitzel *et al.* 1993; Wanschura *et al.* 1995). Furthermore, the ambient atmosphere is often considered a passive gas that does not exert any viscous stresses on the interface and which may even be considered adiabatic. In this way, the two-phase problem is approximated by a single-phase problem that depends on only a few non-dimensional parameters. Within the single-fluid model, the dependence on the Prandtl number of the critical Reynolds number at which the instability arises has been established numerically by Wanschura *et al.* (1995) and Levenstam *et al.* (2001): for large Prandtl

numbers ($Pr \gtrsim 1$), the axisymmetric flow becomes unstable to hydrothermal waves upon increasing the Reynolds number, while the first instability at low Prandtl numbers ($Pr \lesssim 1$) is three-dimensional but steady.

The stationary three-dimensional instability was discovered by Levenstam & Amberg (1994, 1995) using numerical simulation, and by Wanschura *et al.* (1995) using linear stability analysis. The instability has been compared with the instability of vortex rings, and its mechanics was further detailed by Wanschura *et al.* (1995) who noted that the instability is purely inertial, while the temperature field serves only to drive the basic flow. Leypoldt, Kuhlmann & Rath (2002) carried out numerical simulations and explained the second instability at low Prandtl numbers when the steady three-dimensional flow becomes time-dependent. The second critical Reynolds number was further investigated by Motegi *et al.* (2017*a*) using a numerical Floquet stability analysis. Further investigation of the low-Prandtl-number instabilities are due to Takagi *et al.* (2001), Imaishi *et al.* (2001), Li *et al.* (2007, 2008) and Fujimura (2013).

For high Prandtl numbers, Wanschura *et al.* (1995) identified numerically the critical mode as a hydrothermal wave, a concept first introduced by Smith & Davis (1983*a*). Hydrothermal waves are characterised by locally strong temperature extrema in the bulk while the thermal wave is very weak on the interface. At the onset, a weak perturbation flow is driven primarily by azimuthal temperature gradients (thermocapillary stresses). The associated return flow transports basic state temperature in the bulk, which leads to the large internal perturbation temperature extrema that feed back on the free surface. Preisser *et al.* (1983) found experimentally the approximate correlation $m \approx 2.2/\Gamma$ for the dependence of the critical wavenumber m on the length-to-radius aspect ratio $\Gamma = d/R$ at the onset of oscillations. This dependence was confirmed within the linear stability analysis of Wanschura *et al.* (1995) and others. However, the results of Wanschura *et al.* (1995) were obtained for moderate Prandtl numbers, zero gravity and an indeformable adiabatic free surface. Therefore, they deviate from the extensive measurements of Velten *et al.* (1991), indicating that much finer and more realistic modelling is necessary.

The effect of the shape (slender/fat) of high-Prandtl-number liquid bridges on the critical Reynolds number has been investigated experimentally by Hu *et al.* (1994), Masud, Kamotani & Ostrach (1997) and Sakurai, Ohishi & Hirata (2004). Shevtsova & Legros (1998) carried out numerical simulations. Using the assumption of an adiabatic free surface, Nienhüser & Kuhlmann (2002) and Nienhüser (2002) calculated numerically the impact of the static shape of the liquid bridge and of buoyancy forces on the linear stability of an axisymmetric flow. Their study overcame the limits of stability analyses, which were restricted before to cylindrical bridges. For volumes of liquid of approximately 90 % of the straight cylindrical volume, the high-Prandtl-number axisymmetric steady flow is remarkably stable (see e.g. Sakurai, Ohishi & Hirata 1996; Chen & Hu 1998).

Even though Fu & Ostrach (1985) computed rudimentarily a coupled liquid–gas flow, early numerical attempts to model the heat transfer across the interface were typically based on Newton's law of heat transfer (see e.g. Shen 1989; Neitzel *et al.* 1993; Nienhüser & Kuhlmann 2001; Fujimoto *et al.* 2019; Carrión, Herrada & Montanero 2020). A recent study by Romanò & Kuhlmann (2019) has shown, however, that modelling the heat transfer across the interface by Newton's law tends to underestimate the thermocapillary driving, except very close to the cold rod. Motivated by the experimental evidence of the strong impact of the heat transfer across the interface (Kamotani *et al.* 2003; Yano *et al.* 2017), and with improved computing capabilities, more recent numerical approaches take into account the flow and heat transport in the surrounding gas phase (Shevtsova *et al.* 2014; Watanabe *et al.* 2014). Also, the possibility of imposing an external gas flow shows

promise for a control of the onset of hydrothermal waves. This perspective stimulated new experiments (Ueno, Kawazoe & Enomoto 2010; Irikura *et al.* 2005; Gaponenko *et al.* 2021) and numerical investigations (Yasnou *et al.* 2018) with imposed axial gas flow.

The present work is aimed at a linear stability analysis of the flow in a thermocapillary liquid bridge including the gas phase. To that end, we use our linear stability code MaranStable, which has been significantly extended and improved since its earlier version (see e.g. Shevtsova *et al.* 2014). Owing to the large parameter space, a liquid bridge made of 2 cSt silicone oil is considered ($Pr = 28$), which has often been employed in experiments (Yano *et al.* 2018*c*), fully coupled to the surrounding air. The material parameters are assumed constant, and the interface is indeformable. Stability analyses are carried out quasi-continuously varying the aspect ratio, the volume fraction and the gravity level. The relevance of such data is understood when considering that accurate numerical studies in such high-Prandtl-number liquid bridges are hardly reported in the literature, even though they are of great interest for experiments on stability and particle accumulation studies on the ground and under zero gravity. On the ground buoyancy-driven flow is always coupled to and interferes with a thermocapillary flow. Under zero gravity, however, buoyancy can be eliminated. This property is utilised in space experiments like MEIS (Kawamura *et al.* 2012), Dynamic Surf (Yano *et al.* 2018*b*) and JEREMI (planned; Barmak, Romanò & Kuhlmann 2021).

To compute the linear stability of the axisymmetric flow and its dependence on the parameters, we first formulate the governing equations and boundary conditions in § 2. Thereafter, in § 3 the linear stability approach and the post-processing are described. The results are presented and discussed in § 4, interpreting the stability boundaries in the light of the multi-phase energy budgets. We close with a discussion and conclusions in § 5.

2. Problem formulation

2.1. *The setup*

We consider an axisymmetric liquid bridge of a Newtonian liquid captured between two coaxial cylindrical rods both of length d_{rod}. The liquid bridge has axial length d and is assumed to be pinned to the sharp circular edges of the rods of radius r_i, as shown in figure 1. The rods are aligned parallel to the acceleration of gravity $\boldsymbol{g} = -g\boldsymbol{e}_z$, where $\boldsymbol{e}_z$ is the axial unit vector, and mounted coaxially in a closed cylindrical chamber of radius $r_o > r_i$ and height $2d_{rod} + d$ filled with a gas. We use cylindrical coordinates (r, φ, z) centred in the middle of the liquid bridge, and corresponding unit vectors $(\boldsymbol{e}_r, \boldsymbol{e}_\varphi, \boldsymbol{e}_z)$ such that the position vector is $\boldsymbol{x} = r\boldsymbol{e}_r + z\boldsymbol{e}_z$, and the velocity field is represented by $\boldsymbol{u} = u\boldsymbol{e}_r + v\boldsymbol{e}_\varphi + w\boldsymbol{e}_z$. The characteristic geometrical parameters are

$$\Gamma = \frac{d}{r_i}, \quad \Gamma_{rod} = \frac{d_{rod}}{r_i}, \quad \eta = \frac{r_o}{r_i}, \tag{2.1a–c}$$

where Γ and Γ_{rod} are the aspect ratio of the liquid bridge and of the rods, respectively, and η is the radius ratio of the chamber.

While the cylindrical sidewall and the annular top and bottom walls of the chamber are assumed to be adiabatic, the cylindrical support rods are kept at different but constant temperatures $T_{hot} = T_0 + \Delta T/2$ and $T_{cold} = T_0 - \Delta T/2$, respectively, where $T_0 = (T_{hot} + T_{cold})/2$ is the mean temperature, hereinafter used as the reference temperature. The enforced temperature variation across the liquid bridge creates a variation of the

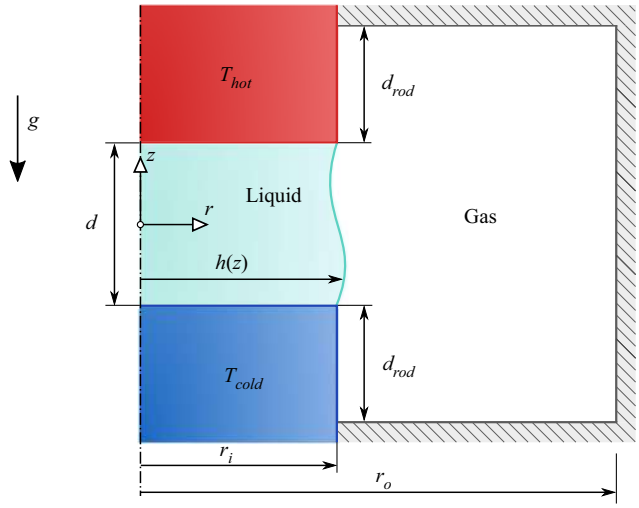

Figure 1. Schematic of the problem set-up and coordinates. The hot (red) and cold (blue) solid rods supporting the liquid bridge (light blue) are mounted coaxially in a closed cylindrical gas container (grey, hatched). Gravity acts in the negative z direction and leads to the hydrostatic shape $h(z)$ of the liquid bridge. The system is axisymmetric with respect to the dash-dotted line ($r = 0$).

surface tension that can be described, to first order, by the linear dependence

$$\sigma(T) = \sigma_0 - \gamma(T - T_0) + O[(T - T_0)^2], \tag{2.2}$$

where $\sigma_0 = \sigma(T_0)$ is the surface tension at the mean temperature, and $\gamma = -\partial\sigma/\partial T|_{T=T_0}$ is the negative surface tension coefficient. The resulting surface tension gradients induce tangential shear stresses via the thermocapillary effect, which lead to an axisymmetric thermocapillary flow on both sides of the interface (Kuhlmann 1999).

In addition to the thermocapillary stresses, the flow in the liquid is driven by buoyancy forces due to the temperature dependence of the density of the liquid:

$$\rho(T) = \rho_0\{1 - \beta(T - T_0) + O[(T - T_0)^2]\}, \tag{2.3}$$

where $\rho_0 = \rho(T_0)$ is the liquid density at the reference temperature, and $\beta = -\rho_0^{-1}(\partial\rho/\partial T)_p$ is the thermal expansion coefficient. Buoyancy forces also act in the gas phase due to the temperature-induced density variation of the gas in contact with the liquid–gas interface. For short liquid bridges employed in terrestrial laboratories, thermocapillary surface forces typically dominate over buoyant volume forces.

2.2. *Governing equations*

To compute the axisymmetric flow and temperature fields, and to investigate the hydrodynamic stability of the flow, the governing transport equations must be solved subject to the respective boundary conditions.

2.2.1. *Transport equations*

To non-dimensionalise the governing equations, we adopt the thermocapillary diffusive scaling given in table 1 (see e.g. Kuhlmann 1999), where ν is the constant kinematic viscosity of the liquid at the reference temperature. The temperature dependence of the

Variable	$\boldsymbol{x}$	t	$\boldsymbol{u}$	p	T
Scale	d	d^2/ν	$\gamma\,\Delta T/\rho_0\nu$	$\gamma\,\Delta T/d$	ΔT

Table 1. Scaling.

density in the liquid and in the gas is taken into account within the Oberbeck–Boussinesq approximation (Landau & Lifschitz 1959; Mihaljan 1962). In this formulation, the Navier–Stokes, continuity and energy equations for the liquid phase read

$$\frac{\partial \boldsymbol{u}}{\partial t} + Re\,\boldsymbol{u}\cdot\boldsymbol{\nabla}\boldsymbol{u} = -\boldsymbol{\nabla}p + \nabla^2\boldsymbol{u} + Bd\,\vartheta\boldsymbol{e}_z, \tag{2.4a}$$

$$\boldsymbol{\nabla}\cdot\boldsymbol{u} = 0, \tag{2.4b}$$

$$\frac{\partial \vartheta}{\partial t} + Re\,\boldsymbol{u}\cdot\boldsymbol{\nabla}\vartheta = \frac{1}{Pr}\nabla^2\vartheta, \tag{2.4c}$$

where $\vartheta = (T - T_0)/\Delta T$ is the normalised deviation from the reference temperature. The fluid motion depends on the thermocapillary Reynolds, Prandtl and dynamic Bond numbers defined as

$$Re = \frac{\gamma\,\Delta T\,d}{\rho_0\nu^2}, \quad Pr = \frac{\nu}{\kappa}, \quad Bd = \frac{\rho_0 g\beta d^2}{\gamma}, \tag{2.5a–c}$$

where κ is the constant thermal diffusivity of the liquid at the reference temperature. Instead of Re, the Marangoni number $Ma = Re\,Pr$ can be used.

Using the same scaling, the flow in the gas phase is governed by

$$\frac{\partial \boldsymbol{u}_g}{\partial t} + Re\,\boldsymbol{u}_g\cdot\boldsymbol{\nabla}\boldsymbol{u}_g = -\frac{1}{\tilde{\rho}}\boldsymbol{\nabla}p_g + \tilde{\nu}\,\nabla^2\boldsymbol{u}_g + \tilde{\beta}\,Bd\,\vartheta_g\boldsymbol{e}_z, \tag{2.6a}$$

$$\boldsymbol{\nabla}\cdot\boldsymbol{u}_g = 0, \tag{2.6b}$$

$$\frac{\partial \vartheta_g}{\partial t} + Re\,\boldsymbol{u}_g\cdot\boldsymbol{\nabla}\vartheta_g = \frac{\tilde{\kappa}}{Pr}\nabla^2\vartheta_g, \tag{2.6c}$$

where the non-dimensional field quantities are indicated by the subscript g. The additional non-dimensional parameters are the gas-to-liquid ratios of the density $\tilde{\rho} = \rho_g/\rho_0$, the kinematic viscosity $\tilde{\nu} = \nu_g/\nu$, the thermal diffusivity $\tilde{\kappa} = \kappa_g/\kappa$, and the thermal expansion coefficient $\tilde{\beta} = \beta_g/\beta$. Introducing

$$\boldsymbol{\alpha} = \left(\alpha_\rho, \alpha_\nu, \alpha_\kappa, \alpha_\beta\right) = \begin{cases} (1,1,1,1), & \text{for the liquid phase,} \\ (\tilde{\rho},\tilde{\nu},\tilde{\kappa},\tilde{\beta}), & \text{for the gas phase,} \end{cases} \tag{2.7}$$

allows us to refer to both phases at the same time, while keeping the notation succinct.

2.2.2. *Boundary conditions*

(i) Support rods. To be able to control experimentally the temperatures imposed on the liquid bridge, the heating rods are typically made from good thermal conductors.

Accordingly, the surfaces of the rods are modelled as isothermal, no-slip and no-penetration walls,

$$\text{hot rod:} \quad \boldsymbol{u} = \boldsymbol{u}_g = 0, \quad \vartheta = \vartheta_g = 1/2, \tag{2.8a,b}$$

$$\text{cold rod:} \quad \boldsymbol{u} = \boldsymbol{u}_g = 0, \quad \vartheta = \vartheta_g = -1/2, \tag{2.8c,d}$$

being in contact with the liquid along the faces of the rods and with the gas phase along the cylindrical surface.

(ii) Chamber walls. The outer cylindrical wall and the top and bottom walls of the closed chamber are considered as no-slip and adiabatic boundaries satisfying

$$r = \eta/\Gamma: \quad \boldsymbol{u}_g = 0, \quad \frac{\partial \vartheta_g}{\partial r} = 0, \tag{2.9a,b}$$

$$z = \pm\,(1/2 + \Gamma_{rod}/\Gamma): \quad \boldsymbol{u}_g = 0, \quad \frac{\partial \vartheta_g}{\partial z} = 0. \tag{2.9c,d}$$

(iii) Liquid–gas interface. The contiguous non-axisymmetric liquid–gas interface is described by a unique radial position $r = h(\varphi, z, t)$ on which coupling conditions for $\boldsymbol{u}$ and ϑ must be provided. The continuity of temperature and heat flux requires

$$r = h(\varphi, z, t): \quad \vartheta = \vartheta_g \quad \text{and} \quad \boldsymbol{n} \cdot \boldsymbol{\nabla} \vartheta = \tilde{\kappa}\, \boldsymbol{n} \cdot \boldsymbol{\nabla} \vartheta_g, \tag{2.10a,b}$$

where $\boldsymbol{n}$ is the local unit vector normal to the interface directed from the liquid into the gas phase. The kinematic coupling

$$r = h(\varphi, z, t): \quad \boldsymbol{u} = \boldsymbol{u}_g \quad \text{and} \quad u = \frac{1}{Re}\,\frac{\partial h}{\partial t} + \frac{v}{r}\,\frac{\partial h}{\partial \varphi} + w\,\frac{\partial h}{\partial z}, \tag{2.11a,b}$$

forces material elements on the interface to remain on the interface. Finally, the dynamic condition provided by the tangential stress balance

$$r = h(\varphi, z, t): \quad \boldsymbol{n} \cdot \boldsymbol{S} \cdot \boldsymbol{t} = -\boldsymbol{\nabla} \vartheta \cdot \boldsymbol{t} + \tilde{\rho}\tilde{\nu}\, \boldsymbol{n} \cdot \boldsymbol{S}_g \cdot \boldsymbol{t} \tag{2.12}$$

must be satisfied, where $\boldsymbol{S} = \boldsymbol{\nabla u} + (\boldsymbol{\nabla u})^{\mathrm{T}}$ and $\tilde{\rho}\tilde{\nu}\boldsymbol{S}_g$ are the viscous stress tensors in the liquid and the gas, respectively. The vector $\boldsymbol{t}$ can be any of the two orthogonal unit vectors tangent to the interface.

2.3. *Solution structure*

2.3.1. *Shape of the interface*

The non-dimensional radial position $r = h(\varphi, z, t)$ of the interface is part of the solution and therefore *a priori* unknown. Motivated by the very small capillary numbers $Ca = \gamma\, \Delta T/\sigma_0$ in typical experiments, we consider the limit of asymptotically large mean surface tension σ_0 in which $Ca \to 0$. In this limit, dynamic free-surface deformations can be neglected, and the problem of determining the liquid–gas interface decouples from solving (2.4) and (2.6) together with (2.8)–(2.12). These circumstances allow for an axisymmetric and stationary interface $h(\varphi, z, t) \to h(z)$ that is determined solely by

the normal-stress balance, yielding the Young–Laplace equation

$$\Delta p_h = \frac{\boldsymbol{\nabla}\cdot\boldsymbol{n}}{Ca} + \frac{Bo}{Ca}z, \tag{2.13}$$

where $\boldsymbol{n} = (1, 0, -h_z)^{\mathrm{T}}/\sqrt{1+h_z^2}$ is the outward surface normal vector, Δp_h is the hydrostatic (subscript h) pressure jump across the liquid–gas interface, and

$$Bo = \frac{(\rho_0 - \rho_{g0})gd^2}{\sigma_0} \tag{2.14}$$

is the static Bond number. Note that the ratio $\lambda = Bd/Bo = \rho_0\beta\sigma_0/[\gamma(\rho_0 - \rho_{g0})]$ is a material parameter. The Young–Laplace equation (2.13) for h is of second order in z and φ, and needs to be closed by additional conditions. The pinned contact lines require

$$h\,(z = \pm 1/2) = \frac{1}{\Gamma}. \tag{2.15}$$

Owing to these constraints, (2.13) has an axisymmetric solution $h(z)$, which we consider within its stability limits (Slobozhanin & Perales 1993). To determine $h(z)$ and the pressure jump p_h uniquely, (2.13) is solved subject to the volume constraint

$$\Gamma^2\int_{-1/2}^{1/2} h^2(z)\,\mathrm{d}z = \mathcal{V}, \tag{2.16}$$

where $\mathcal{V} = V_l/V_0$ is the liquid volume V_l normalised by the volume $V_0 = \pi r_i^2 d$ of an upright cylindrical liquid bridge. Within the range of $\mathcal{V}$ considered, the contact angle is a bijective function of $\mathcal{V}$ (Nienhüser & Kuhlmann 2002).

2.3.2. *Basic flow*

For a given axisymmetric hydrostatic shape $h(z)$ of the liquid bridge, the symmetries of the problem allow for a steady axisymmetric flow ($\partial_t = \partial_\varphi = 0$) with $v_0 = v_{g0} = 0$, which is denoted $\boldsymbol{q}_0(r, z) = (u_0, w_0, p_0, \vartheta_0)$ (liquid phase) and $\boldsymbol{q}_{g0}(r, z) = (u_{g0}, w_{g0}, p_{g0}, \vartheta_{g0})$ (gas phase). The pressure fields p_{g0} and p_0 are flow-induced and add, respectively, to the ambient pressures p_a (gas) and $p_a + \Delta p_h$ (liquid).

The flows $\boldsymbol{q}_0$ and $\boldsymbol{q}_{g0}$ are obtained by solving the steady axisymmetric versions of the differential equations (2.4) and (2.6), subject to the steady axisymmetric versions of the boundary conditions. On $r = 0$, axisymmetry requires

$$u_0 = \frac{\partial w_0}{\partial r} = \frac{\partial \vartheta_0}{\partial r} = 0, \tag{2.17}$$

while on the free surface we obtain, from (2.11*a*,*b*),

$$\frac{u_0}{w_0} = h_z. \tag{2.18}$$

2.3.3. *Linear stability analysis*

For small Reynolds numbers Re, the basic flow $(\boldsymbol{q}_0, \boldsymbol{q}_{g0})$ is stable. When Re exceeds a critical Reynolds number Re_c, the basic flow becomes unstable. In order to calculate the critical threshold, a linear stability analysis is carried out. To that end, the general three-dimensional time-dependent flow $\boldsymbol{q} = (u, v, w, p, \vartheta)$ and $\boldsymbol{q}_g = (u_g, v_g, w_g, p_g, \vartheta_g)$ is written as

$$u = u_0(r,z) + u'(r,\varphi,z,t), \qquad u_g = u_{g0}(r,z) + u'_g(r,\varphi,z,t), \tag{2.19a,b}$$

$$v = 0 + v'(r,\varphi,z,t), \qquad v_g = 0 + v'_g(r,\varphi,z,t), \tag{2.19c,d}$$

$$w = w_0(r,z) + w'(r,\varphi,z,t), \qquad w_g = w_{g0}(r,z) + w'_g(r,\varphi,z,t), \tag{2.19e,f}$$

$$p = p_0(r,z) + p'(r,\varphi,z,t), \qquad p_g = p_{g0}(r,z) + p'_g(r,\varphi,z,t), \tag{2.19g,h}$$

$$\vartheta = \vartheta_0(r,z) + \vartheta'(r,\varphi,z,t), \qquad \vartheta_g = \vartheta_{g0}(r,z) + \vartheta'_g(r,\varphi,z,t), \tag{2.19i,j}$$

where deviations from the basic flow are indicated by a prime ($'$). Inserting this decomposition into (2.4) and (2.6), and linearising with respect to the perturbation quantities, yields the linear stability equations that have the same form,

$$\frac{\partial \boldsymbol{u}'}{\partial t} + Re(\boldsymbol{u}_0 \cdot \boldsymbol{\nabla}\boldsymbol{u}' + \boldsymbol{u}' \cdot \boldsymbol{\nabla}\boldsymbol{u}_0) = -\frac{1}{\alpha_\rho}\boldsymbol{\nabla}p' + \alpha_\nu \boldsymbol{\nabla}^2\boldsymbol{u}' + \alpha_\beta\, Bd\, \vartheta' \boldsymbol{e}_z, \tag{2.20a}$$

$$\boldsymbol{\nabla}\cdot\boldsymbol{u}' = 0, \tag{2.20b}$$

$$\frac{\partial \vartheta'}{\partial t} + Re(\boldsymbol{u}_0 \cdot \boldsymbol{\nabla}\vartheta' + \boldsymbol{u}' \cdot \boldsymbol{\nabla}\vartheta_0) = \frac{\alpha_\kappa}{Pr}\boldsymbol{\nabla}^2\vartheta', \tag{2.20c}$$

for both phases. The subscript 'g' (for the gas phase) no longer appears, because the distinction between the two phases is made, henceforth, by the set of coefficients $\boldsymbol{\alpha}$ defined in (2.7).

Due to the homogeneity of (2.20) in φ and t, the general solution $\boldsymbol{q}' = (u', v', w', p', \vartheta')$ of (2.20) can be written as a superposition of normal modes

$$\boldsymbol{q}' = \sum_{j,m} \hat{\boldsymbol{q}}_{j,m}(r,z)\exp(\mu_{j,m}t + \mathrm{i}m\varphi) + \text{c.c.}, \tag{2.21}$$

where $\mu = \mu_{j,m} \in \mathbb{C}$ is a complex growth rate, and $m \in \mathbb{N}_0$ is the azimuthal wavenumber. The index j numbers the discrete part of the spectrum, and c.c. denotes the complex conjugate. Inserting the ansatz (2.21) into the linear perturbation equations (2.20), one obtains linear differential equations for the perturbation amplitudes $\hat{\boldsymbol{q}} = (\hat{u}, \hat{v}, \hat{w}, \hat{p}, \hat{\vartheta})$ that depend only on r and z:

$$\mu\hat{u} + Re\left[\left(\frac{1}{r} + \frac{\partial}{\partial r}\right)(2u_0\hat{u}) + \frac{u_0 \mathrm{i}\hat{v}m}{r} + \frac{\partial(u_0\hat{w} + \hat{u}w_0)}{\partial z}\right]$$
$$= -\frac{1}{\alpha_\rho}\frac{\partial \hat{p}}{\partial r} + \alpha_\nu\left[\frac{1}{r}\frac{\partial}{\partial r}\left(r\frac{\partial \hat{u}}{\partial r}\right) - (m^2+1)\frac{\hat{u}}{r^2} - \frac{2}{r^2}\mathrm{i}\hat{v}m + \frac{\partial^2\hat{u}}{\partial z^2}\right], \tag{2.22a}$$

$m=0:$	$\hat{u}=0$	$\hat{v}=0$	$\partial\hat{w}/\partial r=0$	$\partial\hat{\vartheta}/\partial r=0$
$m=1:$	$\partial\hat{u}/\partial r=0$	$\partial\hat{v}/\partial r=0$	$\hat{w}=0$	$\hat{\vartheta}=0$
$m>1:$	$\hat{u}=0$	$\hat{v}=0$	$\hat{w}=0$	$\hat{\vartheta}=0$

Table 2. Boundary conditions for the perturbation flow on $r=0$.

$$\mu\hat{v}+Re\left[\left(\frac{2}{r}+\frac{\partial}{\partial r}\right)(u_0\hat{v})+\frac{\partial(\hat{v}w_0)}{\partial z}\right]$$
$$=-\frac{1}{\alpha_\rho}\frac{1}{r}\hat{p}\mathrm{i}m+\alpha_\nu\left[\frac{1}{r}\frac{\partial}{\partial r}\left(r\frac{\partial\hat{v}}{\partial r}\right)-(m^2+1)\frac{\hat{v}}{r^2}+\frac{2}{r^2}\mathrm{i}\hat{u}m+\frac{\partial^2\hat{v}}{\partial z^2}\right], \tag{2.22b}$$

$$\mu\hat{w}+Re\left[\frac{1}{r}\frac{\partial(w_0\hat{u}+\hat{w}u_0)}{\partial r}+\frac{w_0\mathrm{i}\hat{v}m}{r}+2\frac{\partial w_0\hat{w}}{\partial z}\right]$$
$$=-\frac{1}{\alpha_\rho}\frac{\partial\hat{p}}{\partial z}+\alpha_\nu\left[\frac{1}{r}\frac{\partial}{\partial r}\left(r\frac{\partial\hat{w}}{\partial r}\right)-m^2\frac{\hat{w}}{r^2}+\frac{\partial^2\hat{w}}{\partial z^2}\right]+\alpha_\beta Bd\,\hat{\vartheta}, \tag{2.22c}$$

$$\frac{1}{r}\frac{\partial(r\hat{u})}{\partial r}+\frac{1}{r}\mathrm{i}\hat{v}m+\frac{\partial\hat{w}}{\partial z}=0, \tag{2.22d}$$

$$\mu\hat{\vartheta}+Re\left[\frac{1}{r}\frac{\partial(\vartheta_0\hat{u}+\hat{\vartheta}u_0)}{\partial r}+\frac{\vartheta_0\mathrm{i}\hat{v}m}{r}+\frac{\partial(\vartheta_0\hat{w}+\hat{\vartheta}w_0)}{\partial z}\right]$$
$$=\frac{\alpha_\kappa}{Pr}\left[\frac{1}{r}\frac{\partial}{\partial r}\left(r\frac{\partial\hat{\vartheta}}{\partial r}\right)-m^2\frac{\hat{\vartheta}}{r^2}+\frac{\partial^2\hat{\vartheta}}{\partial z^2}\right]. \tag{2.22e}$$

Using polar coordinates, the perturbation flow must satisfy boundary conditions on the axis $r=0$. These are provided in table 2 and can be derived from uniqueness conditions for $\partial\boldsymbol{u}/\partial\varphi$ and $\partial\vartheta/\partial\varphi$ as $r\to 0$ (Batchelor & Gill 1962; Xu & Davis 1984). Since the imposed constant temperatures on the cylindrical rods are taken care of by the basic flow, all perturbation quantities must vanish on the support rods:

$$\hat{\boldsymbol{u}}=\hat{\boldsymbol{u}}_g=0 \quad\text{and}\quad \hat{\vartheta}=\hat{\vartheta}_g=0. \tag{2.23a,b}$$

Like the basic flow, the velocity and heat flux of the perturbations must vanish on the solid adiabatic walls of the gas container:

$$\hat{\boldsymbol{u}}_g=0 \quad\text{and}\quad \boldsymbol{n}\cdot\nabla\hat{\vartheta}_g=0. \tag{2.24a,b}$$

In the limit $Ca\to 0$ considered, the liquid–gas interface is indeformable. From (2.10*a*,*b*)–(2.12), the coupling on the axisymmetric interface at $r=h(z)$ between the liquid- and gas-phase perturbations is provided by

$$\hat{\boldsymbol{u}}=\hat{\boldsymbol{u}}_g,\quad \hat{\vartheta}=\hat{\vartheta}_g,\quad \boldsymbol{n}\cdot\nabla\hat{\vartheta}=\tilde{\kappa}\boldsymbol{n}\cdot\nabla\hat{\vartheta}_g \quad\text{and}\quad \boldsymbol{n}\cdot\hat{\boldsymbol{S}}\cdot\boldsymbol{t}=-\nabla\hat{\vartheta}\cdot\boldsymbol{t}+\tilde{\rho}\tilde{\nu}\boldsymbol{n}\cdot\hat{\boldsymbol{S}}_g\cdot\boldsymbol{t}, \tag{2.25a–d}$$

with $\hat{\boldsymbol{S}}=\nabla\hat{\boldsymbol{u}}+(\nabla\hat{\boldsymbol{u}})^{\mathrm{T}}$.

For each azimuthal wavenumber m, (2.22)–(2.25*a–d*) represent a linear eigenvalue problem with an infinite number of eigenmodes $\boldsymbol{q}'$. The eigenmodes and the corresponding

eigenvalues

$$\mu_{j,m} = \mu(j, m; Re, \Gamma, \mathcal{V}, Pr, \lambda, \tilde{\rho}, \tilde{\nu}, \tilde{\kappa}, \tilde{\beta}) \tag{2.26}$$

depend on a number of parameters. Neutral values Re_n (using subscript n) of the Reynolds number associated with each mode (j, m) are characterised by a vanishing real part (Re) of the eigenvalue, $\mathrm{Re}[\mu_{j,m}(Re_n)] = 0$. These conditions define neutral hypersurfaces $Re_n^{j,m}(\Gamma, \mathcal{V}, Pr, \lambda, \tilde{\rho}, \tilde{\nu}, \tilde{\kappa}, \tilde{\beta})$ in the parameter space. The envelope of all neutral hypersurfaces $Re_c = \min_{j,m} Re_n^{j,m}$ is the critical Reynolds number $Re_c(\Gamma, \mathcal{V}, Pr, \lambda, \tilde{\rho}, \tilde{\nu}, \tilde{\kappa}, \tilde{\beta})$. For slightly supercritical Reynolds numbers with $\epsilon = (Re - Re_c)/Re_c \ll 1$, the basic flow is guaranteed to be unstable, because at least one eigenmode exists that has a positive growth rate $\mathrm{Re}(\mu) > 0$. This does not preclude the rare case of isolated islands in parameter space for larger Reynolds numbers ($Re/Re_c > 1$) for which the basic flow can be linearly stable, i.e. for which $\forall_{j,m}\, \mathrm{Re}(\mu_{j,m}) < 0$. However, within the present linear stability approach, which does not take care of nonlinear effects in the perturbation flow, it cannot be decided if the basic flow $\boldsymbol{q}_0$ is stable to finite-amplitude perturbations, either in these linearly stable islands or for $Re < Re_c$. Experimental and numerical evidence (Velten *et al.* 1991; Leypoldt *et al.* 2000; Sim & Zebib 2002) suggests, however, that the first instability of the basic flow is typically supercritical.

2.4. *Post-processing*

Analysing the energy transfer between the basic flow and the neutral mode can provide insights regarding the instability mechanism and helps us to understand the underlying physics. To that end, we build on the energy analysis derived in Nienhüser & Kuhlmann (2002) for a non-cylindrical axisymmetric liquid bridge, where the gas phase was neglected, and extend the equations to the present two-phase model. Multiplying the linearised momentum equation (2.20*a*) by the perturbation velocity vector $\boldsymbol{u}'$, the resulting equations for the liquid and gas are integrated over the volumes V_l and V_g, respectively, occupied by each phase. After splitting all terms into volume and surface integrals by means of Green's theorem, we obtain the balance

$$\frac{\mathrm{d}E_{kin}}{\mathrm{d}t} = \frac{1}{\mathcal{D}_{kin}} \frac{\mathrm{d}}{\mathrm{d}t} \int_{V_i} \frac{\boldsymbol{u}'^2}{2}\, \mathrm{d}V = -1 + M_r + M_\varphi + M_z + \sum_{j=1}^{5} I_j + B, \quad i \in [l, g], \tag{2.27}$$

for the (normalised) rate of change of the kinetic energy E_{kin}, where all terms on the right-hand side have been normalised by the mechanical dissipation rate $\mathcal{D}_{kin}$. Similarly, multiplication of (2.20*c*) by ϑ' and integration over the volume occupied by each phase yields the thermal energy balance

$$\frac{\mathrm{d}E_{th}}{\mathrm{d}t} = \frac{1}{\mathcal{D}_{th}} \frac{\mathrm{d}}{\mathrm{d}t} \int_{V_i} \frac{\vartheta'^2}{2}\, \mathrm{d}V = -1 + \sum_{j=1}^{2} J_j + H_{fs}, \quad i \in [l,\ g], \tag{2.28}$$

where all terms now have been scaled by the thermal dissipation rate $\mathcal{D}_{th}$. Thus the scaled dissipation rates $D_{kin} = D_{th} = 1$ are constant. The subscripts l and g have been omitted for all terms arising in (2.27) and (2.28) with the understanding that the balances are valid separately for both the liquid and gas phases. Detailed expressions for the individual terms are provided in Appendix A. The terms $\sum I_j = \sum \int i_j\, \mathrm{d}V$ and $\sum J_j = \sum \int j_j\, \mathrm{d}V$ (see (A2)) represent the scaled total production rates of kinetic and thermal

Fluid	ρ (kg m^{-3})	ν (m^2 s^{-1})	κ (m^2 s^{-1})	σ_0 (N m^{-1})	γ (N m^{-1} K^{-1})	β (K^{-1})
2 cSt	871	2.00×10^{-6}	7.14×10^{-8}	18.3×10^{-3}	7×10^{-5}	1.24×10^{-3}
Air	1.184	1.56×10^{-5}	2.22×10^{-5}			3.38×10^{-3}

Table 3. Thermophysical properties of the working fluids 2 cSt silicone oil KF96L-2cs and air at 25 °C.

energy, respectively, which is transferred between the basic and perturbation flows, with corresponding local production densities i_j and j_j. The terms M_r, M_φ and M_z in the kinetic energy balance (2.27) represent the work done per unit time by Marangoni forces in the respective spatial directions. Furthermore, the contribution B (see (A4)) accounts for the work done per unit time by buoyancy forces. In the thermal budget (2.28), H_{fs} (see (A5)) denotes the heat transferred through the liquid–gas interface. It appears in the budgets for both the liquid and gas phases, albeit with opposite signs.

It is generally accepted to refer to E_{th} and $E_{th,g}$ as thermal energies, even though it contradicts the definition of the thermodynamic thermal energy. Hence, what we call thermal energy is rather a measure for the temperature deviation from the axisymmetric temperature field.

2.5. *Reference case and parameter variation*

Due to the large number of parameters governing the linear stability problem, it is computationally too demanding to cover the whole parameter space. Therefore, we consider the liquid–gas couple made of 2 cSt silicone oil (KF96L-2cs, Shin-Etsu Chemical Co., Ltd., Japan) and air with constant material parameters, evaluated at $T_0 = 25\,^\circ$C for both fluids. This selection determines the non-dimensional material parameters Pr, λ, $\tilde{\rho}$, $\tilde{\nu}$, $\tilde{\kappa}$ and $\tilde{\beta}$. The thermophysical properties of both working fluids are listed in table 3.

Furthermore, we keep the aspect ratio of the support rods as well as the chamber radius ratio constant at $\Gamma_{rod} = 0.4$ and $\eta = 4$, respectively. This configuration corresponds to the experiments carried out by Romanò *et al.* (2017). We are left with the important geometrical parameters $\mathcal{V}$ and Γ representing the volume of liquid and the geometric aspect ratio of the liquid bridge, respectively. Finally, the gravity level can be varied via the Bond number Bd.

The origin of all parameter variations is a common reference case. It is based on the experimental geometry investigated by Romanò *et al.* (2017) with support rods of radius $r_i = 2.5$ mm and terrestrial gravity. Different from our objectives, however, Romanò *et al.* (2017) kept the temperature difference constant at $\Delta T = 10\,\mathrm{K} < \Delta T_c$, which is far subcritical. We define the reference case by $\Gamma_{ref} = 0.66$, $\mathcal{V}_{ref} = 1$ and $Bd_{ref} = 0.41$. All reference parameters are collected in table 4. Starting from the reference case, we perform three parameter variations.

(i) A first variation, which is typically made in laboratory experiments, is a variation of the length d of the liquid bridge (Velten *et al.* 1991; Monti, Savino & Lappa 2000; Nienhüser & Kuhlmann 2003; Melnikov *et al.* 2015), corresponding to a variation of Γ. Owing to the dependence of $Bd \sim d^2$, we simultaneously vary Bd such that $Bd = Bd_{ref}(\Gamma/\Gamma_{ref})^2$, corresponding to a constant acceleration of gravity. The range of variation is $\Gamma \in [0.5, 1.8]$ and $Bd \in [0.236, 3.07]$.

Γ_{ref}	$\mathcal{V}_{ref}$	Bd_{ref}	Pr	λ	$\tilde{\rho}$	$\tilde{\nu}$	$\tilde{\kappa}$	$\tilde{\beta}$
0.66	1	0.41	28	0.32	1.36×10^{-3}	7.80	310.16	2.73

Table 4. Constant non-dimensional parameters; Γ, $\mathcal{V}$ and Bd are varied around the reference values given.

(ii) In a second series of calculations, we vary $\mathcal{V} \in [0.65, 1.3]$ for $\Gamma = \Gamma_{ref}$ and $Bd = Bd_{ref}$. This type of variation has also been used in experiments (Hu *et al.* 1994; Sakurai *et al.* 1996; Tang & Hu 1999; Nienhüser & Kuhlmann 2002; Yano *et al.* 2016).

(iii) In a third step, we vary the acceleration of gravity for $\Gamma = \Gamma_{ref}$ and $\mathcal{V} = \mathcal{V}_{ref}$. In this series of calculations, the Bond number is varied in the range $Bd \in [-1.25, 1.25]$. This variation is intended to show how the instabilities for heating from above (reference case) and below are related to each other and to the case of zero gravity in which buoyancy forces and hydrostatic pressure are eliminated (Velten *et al.* 1991; Wanschura, Kuhlmann & Rath 1997*b*; Kawamura *et al.* 2012).

3. Numerical methods

To compute the basic state and its linear stability, a revised version of the numerical code MaranStable (Kuhlmann, Lukasser & Muldoon 2011; Stojanovic & Kuhlmann 2020*b*) is used. It is based on an earlier version developed by M. Lukasser (see § 4.2 of Shevtsova *et al.* 2014).

3.1. *Shape of the interface*

In a first step, the static axisymmetric shape $h(z)$ of the liquid–gas interface is computed. To that end, the Young–Laplace equation (2.13) is reformulated as a system of two ordinary differential equations:

$$h_{zz} = (1 + h_z^2)\left[\frac{1}{h} - (Ca\,\Delta p_h - Bo\,z)\sqrt{1 + h_z^2}\right], \tag{3.1a}$$

$$\Delta p_{h,z} = 0, \tag{3.1b}$$

where the subscript z denotes differentiation with respect to z. These equations, together with the pinning conditions (2.15), represent a boundary value problem, which is discretised by central finite differences on a uniform mesh. The pressure jump Δp_h is determined by the volume constraint (2.16). The discretised set of nonlinear equations is solved using the Newton–Raphson method. The iteration is terminated as soon as both the L_∞ and L_2 norms of the residual have dropped below 10^{-6}.

3.2. *Basic flow*

The steady axisymmetric versions of the nonlinear equations (2.4) and (2.6) determining the basic state are discretised on a structured and staggered grid using second-order finite volumes (Wesseling 2009). In order to implement the boundary conditions on the liquid–gas interface, the grid is body-fitted to the interface, transforming the radial coordinate to $\xi = r/h(z)$. To perform this transformation, the previously determined

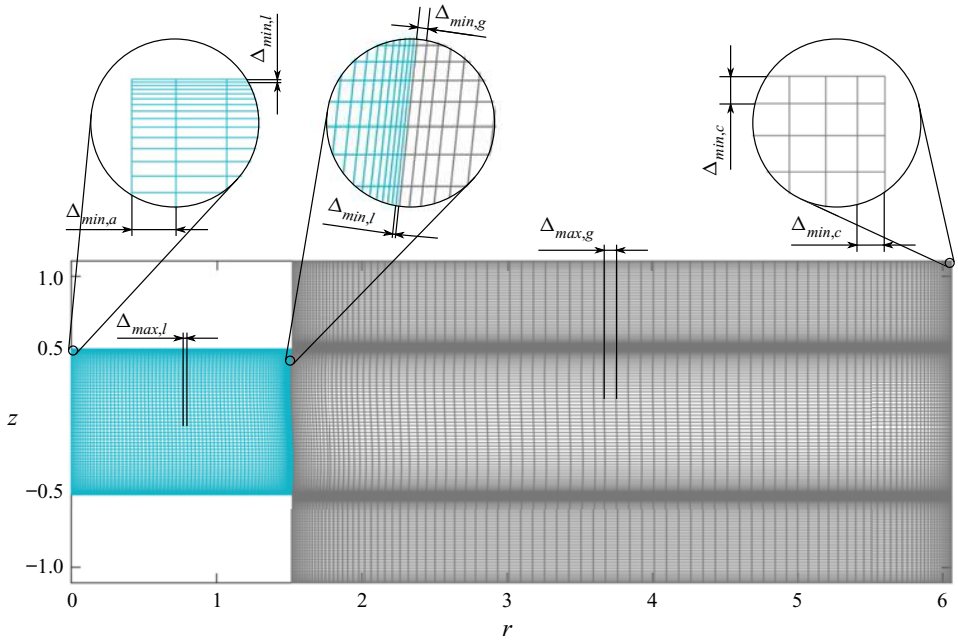

Figure 2. Example for the physical mesh inside the liquid (light blue) and the gas (grey). For better visualisation, the total number of nodes was reduced to $N_{tot} = 18\,852$, which is a reduction of more than 80 % compared to the mesh used for the calculations.

$h(z)$ is interpolated to the current grid using splines. Furthermore, the grid is refined towards all boundaries using a hyperbolic-tangent profile (Thompson, Warsi & Mastin 1985). Inside the liquid, a minimum cell width of $\Delta_{min,l} = 5 \times 10^{-5}$ was chosen for the wall-bounded cells and along the interface in order to guarantee that thermal boundary layers will be resolved for all calculations. On the axis of symmetry (subscript a), moderate temperature and velocity gradients are expected, justifying the larger minimum cell width in radial direction $\Delta_{min,a} = 10^{-3}$. The spatial resolution in the gas phase was set to $\Delta_{min,g} = 3\Delta_{min,l}$ along the interface, and $\Delta_{min,c} = 10^{-3} \times \Gamma_{rod}/\Gamma$ close to the adiabatic chamber walls (subscript c). The cells are stretched towards the interior with a stretching factor $f = 1.15$ until maximum cell widths $\Delta_{max,l} = 0.0075 = 150\,\Delta_{min,l}$ and $\Delta_{max,g} = 0.02(\eta - 1)/\Gamma = 150\,\Delta_{min,c} \approx 600\,\Delta_{min,g}$ are reached in the bulk of the liquid and the gas, respectively. These conditions lead to a total of $N_{tot} = 103\,613$ cells, of which $N_r \times N_z = 244 \times 197$ cells belong to the liquid, and $N_r \times N_z = 115 \times 483$ cells belong to the gas phase. Figure 2 shows the physical mesh, but at much lower resolution than used for the actual calculations.

The nonlinear algebraic equations resulting from the discretisation are solved by Newton–Raphson iteration:

$$\boldsymbol{J}(\boldsymbol{q}_0^{(k)}) \cdot \delta\boldsymbol{q} = -\boldsymbol{f}(\boldsymbol{q}_0^{(k)}), \tag{3.2a}$$

$$\boldsymbol{q}_0^{(k+1)} = \boldsymbol{q}_0^{(k)} + \delta\boldsymbol{q}, \tag{3.2b}$$

where $\delta\boldsymbol{q}$ is the increment of the approximation of the basic flow from the kth to the $(k+1)$th iteration step. Inserting (3.2b) into the steady axisymmetric versions of (2.4)

and (2.6) yields the equations governing $\delta\boldsymbol{q}$:

$$Re(\delta\boldsymbol{u}\cdot\boldsymbol{\nabla}\boldsymbol{u}_0^{(k)}+\boldsymbol{u}_0^{(k)}\cdot\boldsymbol{\nabla}\delta\boldsymbol{u})+\frac{1}{\alpha_\rho}\boldsymbol{\nabla}\delta p-\alpha_\nu\,\nabla^2\delta\boldsymbol{u}-\alpha_\beta\,Bd\,\delta\vartheta\,\boldsymbol{e}_z$$

$$=-Re\,\boldsymbol{u}_0^{(k)}\cdot\boldsymbol{\nabla}\boldsymbol{u}_0^{(k)}-\frac{1}{\alpha_\rho}\boldsymbol{\nabla}p_0^{(k)}+\alpha_\nu\,\nabla^2\boldsymbol{u}_0^{(k)}+\alpha_\beta\,Bd\,\vartheta_0^{(k)}\,\boldsymbol{e}_z, \tag{3.3a}$$

$$\boldsymbol{\nabla}\cdot\delta\boldsymbol{u}=-\boldsymbol{\nabla}\cdot\boldsymbol{u}_0^{(k)}, \tag{3.3b}$$

$$\delta\boldsymbol{u}\cdot\boldsymbol{\nabla}\vartheta_0^{(k)}+\boldsymbol{u}_0^{(k)}\cdot\boldsymbol{\nabla}\delta\vartheta-\frac{\alpha_k}{Ma}\nabla^2\delta\vartheta=-\boldsymbol{u}_0^{(k)}\cdot\boldsymbol{\nabla}\vartheta_0^{(k)}+\frac{\alpha_k}{Ma}\nabla^2\vartheta_0^{(k)}, \tag{3.3c}$$

where the nonlinear terms have been linearised with respect to $\delta\boldsymbol{q}$. The Jacobian operator $\boldsymbol{J}(\boldsymbol{q}_0^{(k)})$ and the nonlinear residual $-\boldsymbol{f}(\boldsymbol{q}_0^{(k)})$ are identified readily from (3.3). The Newton iteration (3.2) is considered converged as soon as both the infinity norm $\|\delta\boldsymbol{q}\|_\infty$ and the L_2 norm $\|\delta\boldsymbol{q}\|_2$ of the residual have dropped below 10^{-6}.

3.3. *Linear stability of the basic flow*

Once the basic state $\boldsymbol{q}_0$ is computed, it parametrically enters the linear stability equations (2.22), which are discretized on the same mesh using the same finite volume method. The resulting large generalised complex eigenvalue problem is converted into a generalised eigenvalue problem with real matrices by introducing $\check{v}=\mathrm{i}\hat{v}$ (Theofilis 2003). Defining the decay rate $\chi=-\mu$, the generalised real eigenvalue problem has the form

$$\boldsymbol{A}\cdot\hat{\boldsymbol{q}}=\chi\boldsymbol{B}\cdot\hat{\boldsymbol{q}}, \tag{3.4}$$

where $\boldsymbol{B}$ is singular. For a Reynolds number $Re\approx Re_n$ close to a neutral stability boundary (subscript n), the most dangerous modes (numbered by i) belong to the eigenvalues χ_i with the smallest real parts, satisfying $\mathrm{Re}(\chi_i)\approx 0$. To find the most dangerous eigenvalue, i.e. the one with the smallest real part of χ, twelve eigenvalues $\tilde{\chi}_i$ with the smallest absolute value are computed, in a first step, via an implicitly restarted Arnoldi method implemented in ARPACK (Lehoucq, Sorensen & Yang 1998) and available under MATLAB. A Krylov subspace of dimension $K=100$ is employed. Based on the eigenvalue $\tilde{\chi}_{sr}$ with the smallest real part among the twelve eigenvalues $\tilde{\chi}_i$, i.e. $\tilde{\chi}_{sr}:\mathrm{Re}(\tilde{\chi}_{sr})=\min[\mathrm{Re}(\tilde{\chi}_i)]$, we adopt the method proposed by Meerbergen, Spence & Roose (1994) to validate that the eigenvalue $\tilde{\chi}_{sr}$ is indeed the one with the smallest real part among all the eigenvalues χ_i and not only among the twelve eigenvalues $\tilde{\chi}_i$ with the smallest absolute value. To that end, 17 eigenvalues $\zeta=(\chi-a_2)(\chi-a_1)$ with the largest magnitude of the Cayley transform

$$(\boldsymbol{A}-a_2\boldsymbol{B})\cdot\hat{\boldsymbol{q}}=\zeta(\boldsymbol{A}-a_1\boldsymbol{B})\cdot\hat{\boldsymbol{q}} \tag{3.5}$$

are computed, as described in Meerbergen *et al.* (1994). The parameters a_1 and a_2 are determined by the five real eigenvalues with the smallest absolute value and a user-defined parameter $b=|(\chi_i-a_2)/(\chi_i-a_2)|=1.2$, where χ_i is one of the eigenvalues with the smallest real part. The resulting 17 eigenvalues containing the most dangerous mode are then sorted according to the magnitudes of their real parts.

At the neutral Reynolds number Re_n, the real part of the eigenvalue of the most dangerous mode, identified from the above procedure, crosses zero. To determine Re_n for a given azimuthal wavenumber m, the Reynolds number is varied in small steps, typically by approximately 5 % of its value, until the sign of $\min_i\mathrm{Re}(\chi_i)|_m$ changes, signalling that at least one root exists within this interval of Re. The root Re_n is then computed

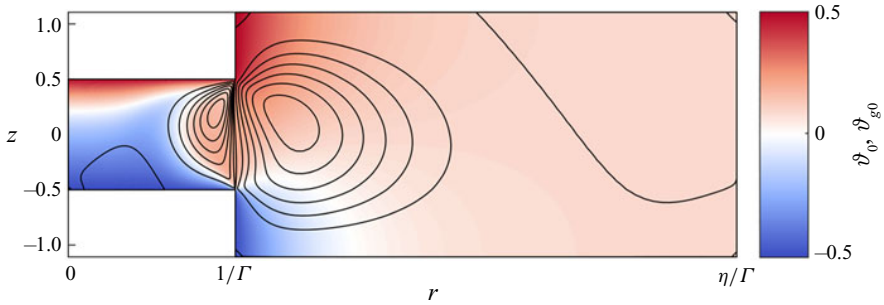

Figure 3. Streamlines and temperature fields ϑ_0 and ϑ_{g0} (colour) of the basic state for the reference case ($\Gamma = 0.66$, $\mathcal{V} = 1$, $Bd = 0.41$) at criticality $Re_c = 731$. Streamline levels differ in the liquid and the gas, but they are drawn equidistantly in each phase.

by the bisected direct quadratic *regula falsi* as described in Gottlieb & Thompson (2010), using the convergence condition $|\min_i \mathrm{Re}(\chi_i)|_m| < 10^{-5}$, i.e. a sufficiently small absolute value of the growth rate's real part. Repeating this procedure for a series of wavenumbers $m = 0, 1, 2, \ldots, M$ allows us to detect the critical Reynolds number Re_c as the envelope gathering the lowest neutral Reynolds numbers over all $Re_n(m)$.

In order to track the neutral curves under a variation of one of the parameters Γ, $\mathcal{V}$ or Bd, a natural continuation technique is used. The converged basic state and neutral Reynolds number are used as initial conditions for the Newton iteration to compute the basic state for the incremented parameter, followed by solving the new eigenvalue problem. The step change of the parameter is typically 1 % of its value. If necessary, the parameter variation is refined, e.g. near intersection points of neutral curves or when Re_n depends sensitively on the parameter varied.

The numerical code has been tested extensively. Grid convergence, verification and validation are described in detail in Appendix B.

4. Results

4.1. *Reference case*

4.1.1. *Basic flow*

Since the basic two-dimensional flow enters the linear stability analysis parametrically, it is important to examine its characteristics closely. Figure 3 shows the streamlines and the temperature field at criticality for the reference case ($\Gamma = 0.66$, $\mathcal{V} = 1$, $Bd = 0.41$). The hydrostatic shape of the interface deviates only slightly from the cylindrical shape. The thermocapillary stresses along the interface, directed from the hot corner to the cold one, lead to a streamline crowding at the interface and drive a clockwise vortex in the liquid phase (figure 3). Even though the absolute Rayleigh number for the liquid phase is $|Ra| = |Pr\,Bd\,Re| = 8392$, buoyancy forces do not cause the instability, because of the overall stable thermal stratification (see also Wanschura *et al.* 1997*b*). Buoyancy forces are, however, responsible for the vortex in the liquid, which is more slender than under zero gravity, because the hot fluid transported near the free surface to the cold wall has the tendency to rise in the bulk. This causes the large separation bubble on the cold wall (Romanò & Kuhlmann 2018), also visible in figure 3.

Owing to the geometry of the gas space, a much larger vortex is created in the gas phase (counterclockwise in figure 3). Because the thermal diffusivity of the gas is much higher

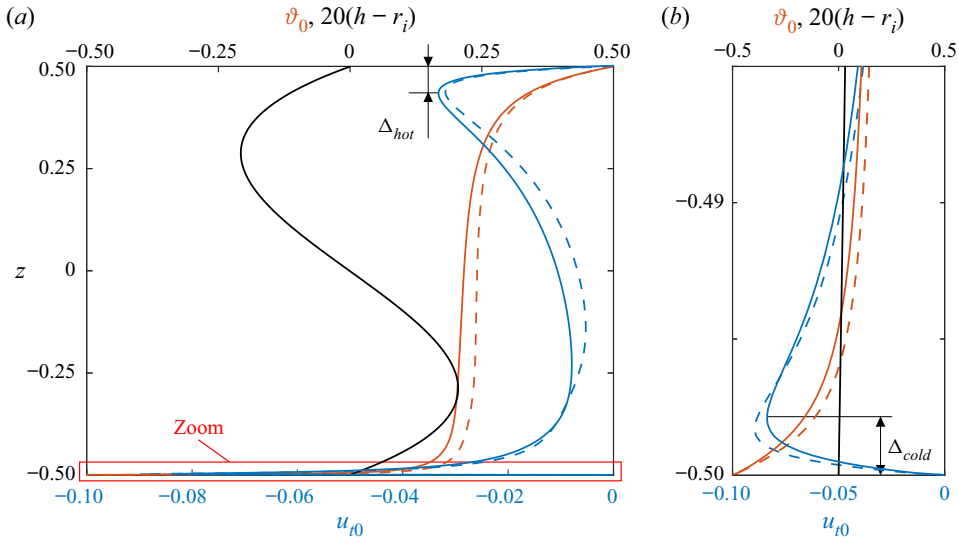

Figure 4. Tangential velocity $u_{t0} = \boldsymbol{t} \cdot \boldsymbol{u}_0$ (solid blue lines) and temperature distribution ϑ_0 (solid red lines) of the basic flow along the free surface (parametrised by z) for the reference case at criticality ($\Gamma = 0.66$, $\mathcal{V} = 1$, $Bd = 0.41$, $Re = Re_c = 731$). Also shown, as dashed lines, are the corresponding profiles for the single-fluid model at the same Reynolds number, and for an adiabatic free surface, neglecting viscous stresses from the gas. (*a*) Profiles along the whole free surface. (*b*) Zoom into the red rectangle shown in (*a*). The black curve indicates the shape $h(z)$ of the interface.

than that of the liquid (table 4), the convective effect on the temperature distribution in the gas phase is very weak. The temperature distribution along the interface (figure 4), being larger than T_0 on average, causes a mean temperature $\vartheta_{g0} > 0$ in the gas phase far away from the liquid bridge. Furthermore, a weak flow arises in a large separation bubble, while much smaller viscous eddies can be identified close to all four corners of the annular gas container. Buoyancy in the gas phase is even weaker than in the liquid phase. The ratio $Ra_g/Ra = \tilde{\beta}\tilde{d}^3/(\tilde{\nu}\tilde{\kappa}) \approx 10^{-2}$, where $\tilde{d} = 1 + 2\Gamma_{rod}/\Gamma$, suggests that buoyancy is negligible in the gas.

The distributions of the velocity (blue) and temperature (red) on the free surface are shown in figure 4(*a*) for the reference case (solid lines). Also shown are the profiles for the single-fluid model with an adiabatic free surface (dashed lines), neglecting viscous stresses from the gas. For both models, the boundary layer character is obvious from the steep variation of the temperature near the hot and cold corners. Associated with the temperature gradients are peaks of the surface velocity very close to the hot and cold corners. Of these, the cold-corner peak is particularly sharp, because the fluid at the interface is accelerated towards the wall, where it must get decelerated to zero. Since the finite volume method employed does not require any regularisation of the boundary conditions near the corners, the velocity peaks are fully resolved (zoom in figure 4*b*). The temperature is almost constant along the free surface midway between the two surface velocity peaks (figure 4*b*) as well as inside the main vortex in the liquid (figure 3). The two-fluid model exhibits a lower surface temperature in the plateau region than the adiabatic single-fluid model. This indicates that the two-fluid model exhibits a heat loss, i.e. a net heat flux outwards through the free surface (free-surface Nusselt number $Nu_{fs} < 0$ defined in (B2)), a stronger thermocapillary driving along the hotter part of the interface as compared to the

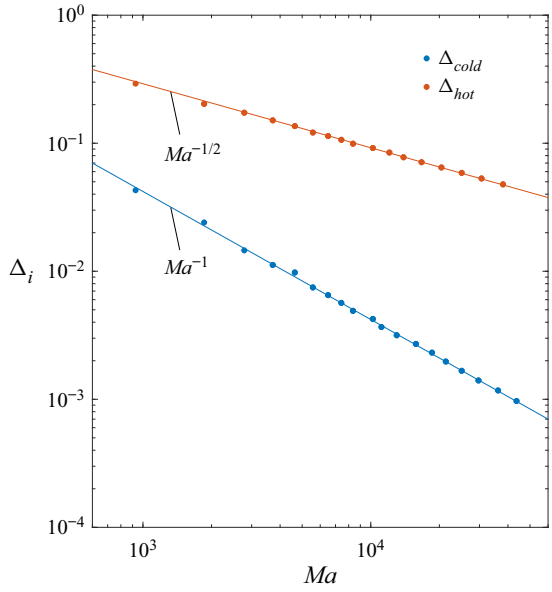

Figure 5. Distances Δ_i of the surface velocity peaks of the basic flow from the cold corner (blue dots, $i = \text{cold}$) and the hot corner (red dots, $i = \text{hot}$) compared to the theoretical scalings of the respective thermal boundary layer thicknesses (lines).

single-fluid model, and thus a larger surface velocity along most parts of the free surface. As a consequence, the flow obtained with the adiabatic single-fluid model is approximately twice as stable than the one obtained with the two-fluid model for the same conditions; cf. figure 29 in § B.1.

For high-Prandtl-number flows, the thermal boundary layers in the liquid near the hot and cold corners, i.e. on the circular rigid end walls and at the interface, are more relevant than the viscous boundary layers. For pure thermocapillary flow in the single-fluid model with contact angle $\alpha = 90^\circ$, the thermal boundary layer thickness on the cold wall near the contact line is expected to scale $\sim Ma^{-1}$ in the viscous convective limit ($Ma \to \infty$, $Re \ll Ma$) (Canright 1994). On the hot wall, the thermal boundary layer thickness should scale $\sim Ma^{-1/2}$ in this limit (Kamotani & Ostrach 1998). The thickness of the thermal boundary layers can be measured by the distances Δ_{hot} and Δ_{cold} of the velocity peaks from the hot and cold corners, respectively. Both distances are shown in figure 5 as functions of Ma for the present two-fluid model. The locations of the velocity peaks $\Delta_{hot}(Ma)$ and $\Delta_{cold}(Ma)$ exhibit the same scaling with Ma as predicted theoretically for the single-fluid model in the viscous convective limit.

4.1.2. *Hydrothermal wave instability*

At $Re_c = 731$, the basic flow becomes unstable with respect to a pair of azimuthally propagating modes with $\omega_c = \text{Im}(\gamma_c) = \pm 14.85$ and $m = 3$. One of the two critical modes is illustrated in figure 6. The global temperature distribution in the horizontal plane at $z = 0.20$ shown in figure 6(*a*) indicates that the temperature perturbations arise essentially in the liquid phase, while the gas phase temperature perturbations are weak. A close-up, including the velocity vector field, is shown figure 6(*b*). It reveals the characteristic structures of the internal perturbation temperature field and axial vortices known from

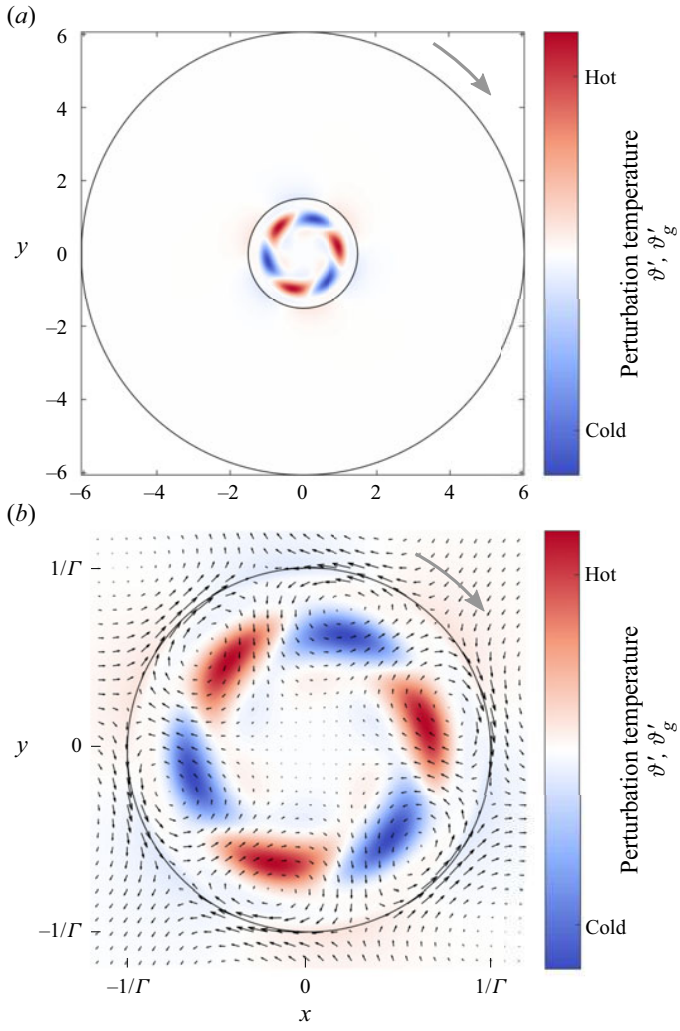

Figure 6. Critical velocity field (black arrows) and critical temperature field (colour) for the reference case ($Re_c = 731$, $m_c = 3$) in the horizontal plane $z = 0.20$ in which the local thermal production $\vartheta' \boldsymbol{u}' \cdot \boldsymbol{\nabla} \vartheta_0$ takes its maximum in the bulk of the liquid. The grey arrow indicates the rotation direction of the mode. (*a*) Complete domain. (*b*) Close-up of the liquid phase.

smaller Prandtl numbers (Wanschura *et al.* 1995). The perturbation vortices are driven in the azimuthal direction by the mainly azimuthal temperature gradients on the free surface (figure 7). These vortices transport cold (hot) fluid (note the basic state temperature distribution shown in figure 3) from the interior (from the free surface) just ahead of the cold (hot) interior perturbation temperature extrema, thus feeding the existing extrema and determining the azimuthal direction of propagation (indicated by the grey arrow) of the wave. The perturbation flow, on the other hand, is maintained by radial conduction of perturbation temperature from the internal extrema to the free surface such that the (mainly axial) perturbation vortices seen in figure 6(*b*) are driven by (mainly azimuthal) thermocapillary stresses. The structure of the perturbation flow confirms its character as a hydrothermal wave (Smith & Davis 1983*a*; Wanschura *et al.* 1995).

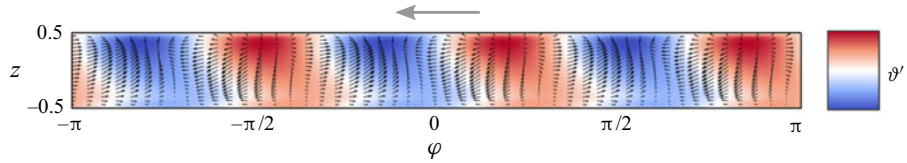

Figure 7. Critical mode (black arrows, colour) for the reference case evaluated on the free surface and projected radially ($Re_c = 731$, $m_c = 3$). The arrow indicates the direction of propagation.

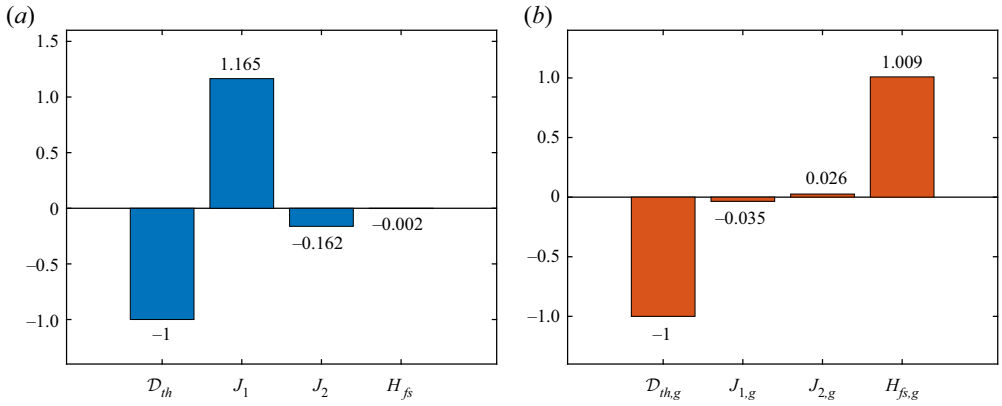

Figure 8. Thermal energy budget of the critical mode for the reference case ($Re_c = 731$, $m_c = 3$). (*a*) Liquid phase. (*b*) Gas phase.

The relevance of the temperature transport described is also confirmed by the total thermal energy budgets shown in figure 8. From figure 8(*a*), thermal perturbation energy in the liquid phase is produced mainly by J_1 (production due to radial convection of basic state temperature; see (A2*b*)) and dissipated in the bulk. Note that the instability cannot be due to axial temperature gradients, because their total contribution to the thermal energy budget is negative: $J_2 < 0$. Only a very small fraction of thermal perturbation energy (H_{fs}) is lost to the gas phase (in accordance with figure 6*a*), which appears as the major source term $H_{fs,g} = -H_{fs}(\mathcal{D}_{th}/\mathcal{D}_{th,g})$ in the gas phase (figure 8*b*) and which gets dissipated readily. In the present two-phase system with a cylindrical gas confinement, the gas phase thus merely plays a passive role when it comes to the instability mechanism. Moreover, due to the very high Prandtl number, inertial effects are not causing the instability (Wanschura *et al.* 1995). Likewise, buoyancy is not of key importance for the instability for the reference case (for stronger buoyancy, see Wanschura *et al.* 1997*b*).

The three-dimensional structure of the travelling temperature perturbation field and of the total thermal energy production is shown by isosurfaces in figure 9. A cross-section at an azimuthal angle at which the local thermal energy production in the bulk reaches its maximum is shown in figure 10. It is seen that the thermal energy production is strong where large interior gradients of the basic temperature field arise, i.e. near the region $\vartheta_0 \approx 0$ (white colour in figure 3), which is aligned with the streamlines on the interior side of the basic vortex in the liquid phase. Further, from figure 9, one can notice that the perturbation temperature isosurfaces and those for the energy production form an approximate spiral around the basic vortex. The phase relation between the internal temperature perturbations and the thermal energy transfer rate j is shown in

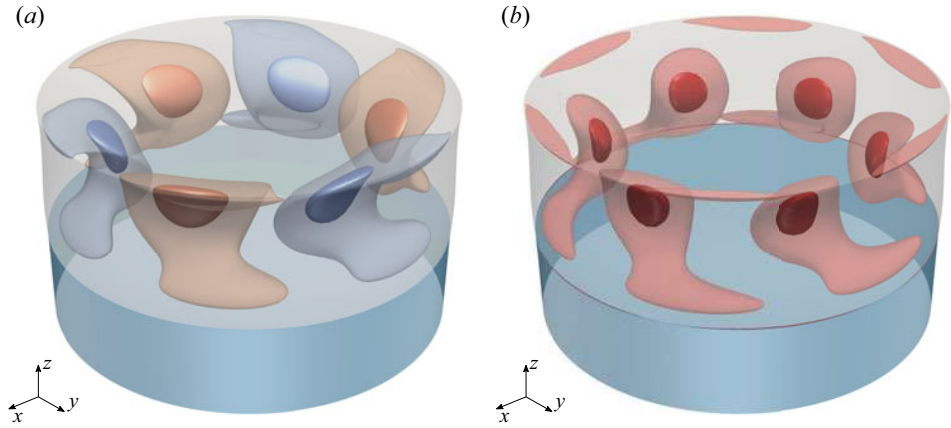

Figure 9. (*a*) Contours of the perturbation temperature ϑ' in the liquid. The isosurface values are $\pm 0.25 \times \max|\vartheta'|$ (light colours) and $\pm 0.75 \times \max|\vartheta'|$ (dark colours). (*b*) Contours of the local thermal production rate $j_1 + j_2 = \vartheta' \boldsymbol{u}' \cdot \nabla \vartheta_0$ shown at the isosurface values $0.1 \times \max|\vartheta' \boldsymbol{u}' \cdot \nabla \vartheta_0|$ (light red) and $0.7 \times \max|\vartheta' \boldsymbol{u}' \cdot \nabla \vartheta_0|$ (dark red).

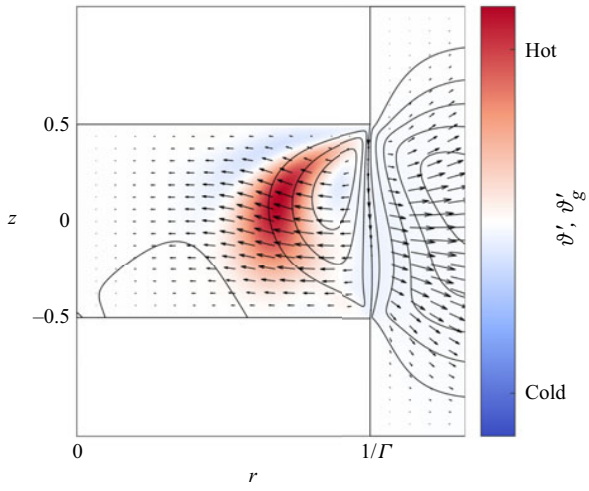

Figure 10. Critical mode $m_c = 3$ for the reference case at $Re_c = 731$. Shown are streamlines of the basic flow, the critical velocity field (arrows) and the critical temperature field (colour) in the (r, z) plane in which the local thermal production $\vartheta' \boldsymbol{u}' \cdot \nabla \vartheta_0$ takes one of its maxima in the bulk.

figure 11 for $z = 0.20$. Similar to the $Pr = 4$ case (Wanschura *et al.* 1995), the thermal perturbation energy is created just ahead of the instantaneous perturbation temperature extrema, consistent with the clockwise propagation of the hydrothermal wave.

We find that the critical Reynolds number for the single-fluid model and $\Gamma = 0.66$, $\mathcal{V} = 1$, $Bo = 0.41$ is more than twice that for the present two-fluid model (see also figure 29 in § B.1). The basic flow for the single-fluid model with adiabatic interface exhibits a higher surface temperature than the two-fluid model. This might suggest that the radial basic state temperature gradients are higher for the single-fluid model, thus providing a better source of energy for the instability. This effect, however, is counteracted by the lower surface and

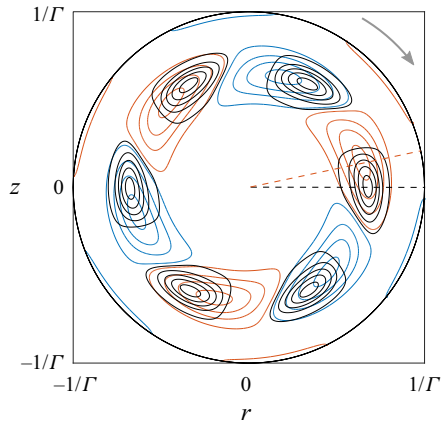

Figure 11. Isolines of the positive (red) and negative (blue) perturbation temperature, and of the local production density $j = j_1 + j_2$ (black) in the horizontal plane $z = 0.20$. Dashed lines are central lines through the maxima of the perturbation temperature (red) and of the related energy transfer (black). The grey arrow indicates the rotation direction of the mode.

return-flow velocity (figure 4), which tends to reduce the radial temperature gradients at midplane. While we cannot pinpoint exactly the reason for the large difference in Re_c, we notice that the critical temperature field in case of the single-fluid model is distinct from that of the present two-fluid model, exhibiting a finer structure with a much more pronounced spiral character (not shown, but similar to the mode for $Pr = 68$ reported in Stojanovic & Kuhlmann 2020*a*). It is thus expected that the relative importance of the thermal dissipation for the critical mode in the single-fluid model is considerable larger than for the critical mode of the two-fluid model, resulting in a considerable stabilisation of the basic flow in the single-fluid model.

4.2. *Dependence of the linear stability boundary on the length of the liquid bridge*

Figure 12 shows the dependence of the critical Reynolds number Re_c (figure 12*a*) and the critical oscillation frequency ω_c (figure 12*b*) on the length of the liquid bridge, expressed by the aspect ratio Γ. The relative volume of the liquid bridge is kept constant at $\mathcal{V} = \mathcal{V}_{ref} = 1$ and $Bd = Bd_{ref} \times (\Gamma/\Gamma_{ref})^2$. In addition, neutral Reynolds numbers and associated neutral frequencies are displayed as thin lines for $Re > Re_c$. The critical azimuthal wavenumber m is coded by colour.

Within the range of Γ considered, only critical modes with $m = 1$, $m = 3$ and $m = 4$ arise. The aspect ratios at which the critical mode changes are $\Gamma^{3,4} = 0.5590$ ($m = 3 \leftrightarrow 4$) with $Re_c(\Gamma^{3,4}) = 643.1$, and $\Gamma^{1,3} = 0.9020$ ($m = 1 \leftrightarrow 3$) with $Re_c(\Gamma^{1,3}) = 1645.9$. We find the basic flow to be particularly stable near $\Gamma^{1,3}$. The variation of the critical wavenumber with Γ follows the well-known trend according to which m_c decreases as Γ increases (as the liquid bridge becomes longer). For $Pr = 7$, Preisser *et al.* (1983) found experimentally that $m_c \approx 2.2/\Gamma$ (for $Pr = 28$; see also Ueno *et al.* (2003), and others). A mode with $m = 2$ does not become critical in the range of Γ. But near $\Gamma = 0.9$, the many neutral Reynolds numbers do not differ much, with $Re_n(m = 1) = 1690$, $Re_n(m = 2) = 1681$ and $Re_c(m = 3) = 1635$, such that a complicated supercritical dynamics can be expected near this aspect ratio.

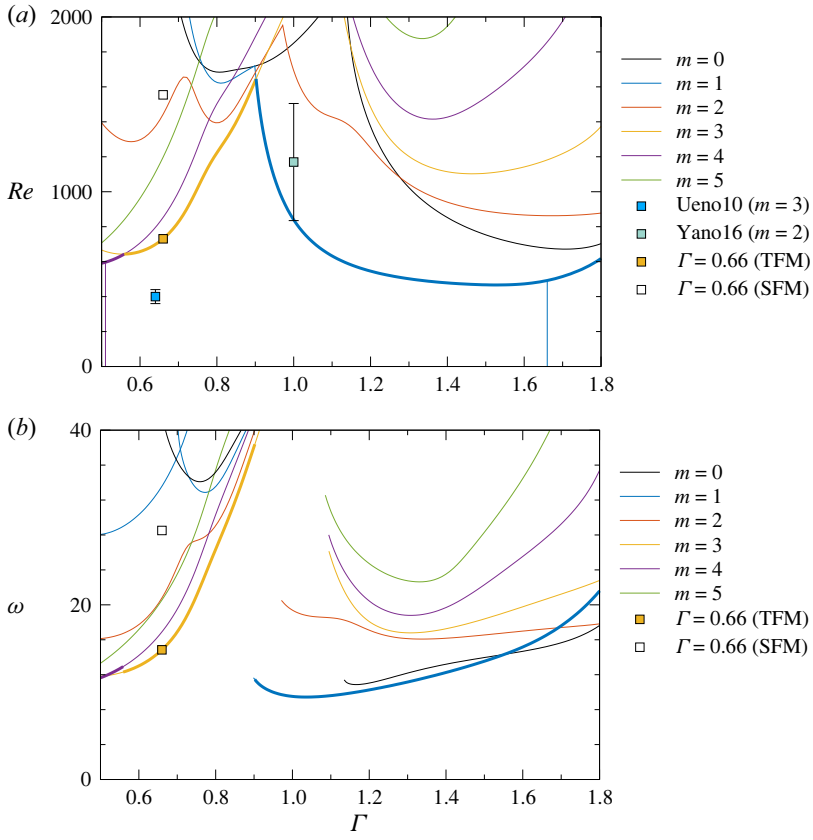

Figure 12. (*a*) Neutral Reynolds numbers (thin lines) and critical Reynolds numbers Re_c (thick lines) as functions of the aspect ratio Γ for $\mathcal{V} = 1$ and $Bd = Bd_{ref} \times (\Gamma/\Gamma_{ref})^2$. (*b*) Corresponding neutral (thin lines) and critical (thick lines) frequencies ω. The wavenumbers (colour), symbols and abbreviations are explained in the legend, with TFM meaning two-fluid model, SFM meaning adiabatic single-fluid model, Ueno10 meaning Ueno & Torii (2010), and Yano16 meaning Yano *et al.* (2016).

In addition to the critical mode for the reference case $\Gamma = 0.66$ with $m_c = 3$ discussed above, two other critical modes are visualised in figures 13 and 14 for a short ($\Gamma = 0.51$, $m_c = 4$) and a long ($\Gamma = 1.66$, $m_c = 1$) liquid bridge, respectively. These aspect ratios are indicated in figure 12(*a*) by vertical thin lines. Note that the interface is deformed in both cases. However, the static surface deformation is hardly visible for $\Gamma = 0.51$ (figure 13), because the liquid bridge is much shorter and lighter than for the longer bridge with $\Gamma = 1.66$ (figure 14), because the radius is the same in both cases. Even though the flow for $\Gamma = 1.66$ is affected much more strongly by the hydrostatic deformation of the liquid bridge and by buoyancy forces for the present parameter variation, all critical modes show the generic structure of axial vortices and internal perturbation temperature extrema of hydrothermal waves. The instability mechanism is qualitatively the same for all modes, and similar arguments hold as for the reference case discussed in § 4.1. In particular, from figure 15, the energy budgets do not change very much with Γ. While there is a visible jump of the energy terms in the liquid at $\Gamma^{1,3}$, as expected for a modal change, the jump at $\Gamma^{3,4}$ is hardly visible. The jump at $\Gamma^{1,3}$ is related to the particular structure of the $m = 1$ mode, which admits a flow across the axis of symmetry (cf. table 2) representing a

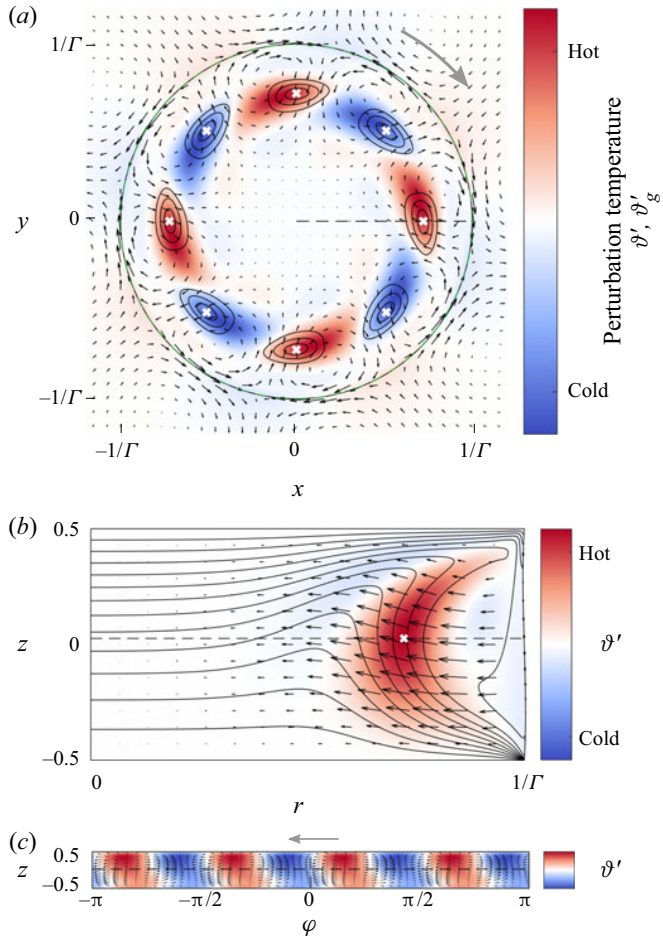

Figure 13. Critical velocity (black arrows) and temperature (colour) fields for $\Gamma = 0.51$, $Re_c = 597$, $Bd = Bd_{ref} \times (\Gamma/\Gamma_{ref})^2$ and $m_c = 4$. (*a*) Horizontal cross-section at $z = 0.03$ in which the local thermal production $\vartheta' \boldsymbol{u}' \cdot \boldsymbol{\nabla}\vartheta_0$ (isolines) takes its maximum (white crosses) in the bulk. (*b*) Vertical (r, z) plane in which the local thermal production $\vartheta' \boldsymbol{u}' \cdot \boldsymbol{\nabla}\vartheta_0$ (not shown) takes its maximum (white cross) in the bulk. Lines indicate isotherms of the basic state. (*c*) Perturbation velocity and temperature fields on the free surface. The grey arrows in (*a*,*c*) indicate the direction of propagation of the critical mode. The black dashed lines represent the locations of the corresponding cuts. The green circle in (*a*) indicates the diameter of the support rods.

qualitative difference compared to all other three-dimensional modes. Due to this property, the role of the radial transport of basic state temperature, hence J_1, is more important for $m = 1$ and $\Gamma > \Gamma^{1,3}$, associated with a particularly strong stabilising effect by J_2 in the liquid (figure 15*a*). As Γ increases beyond $\Gamma^{1,3}$, the critical Reynolds number reduces drastically due to the geometrical constraint that rules the wavenumber selection, and the stabilising effect of J_2 diminishes. For $\Gamma > 1.66$ (liquid) and $\Gamma > 1.24$ (gas), both J_1 and J_2 become positive (not shown).

Also shown in figure 12(*a*) is a critical Reynolds number (green square) for $\Gamma = 1$ obtained by Yano *et al.* (2016) for the same volume, and a similar radius ratio and Bond number. Note, however, that the thermal conditions on $r = \eta/\Gamma$ differ in that Yano *et al.* (2016) have imposed a constant temperature $T(r = \eta/\Gamma) = 20\,^{\circ}\mathrm{C}$ on the outer cylindrical

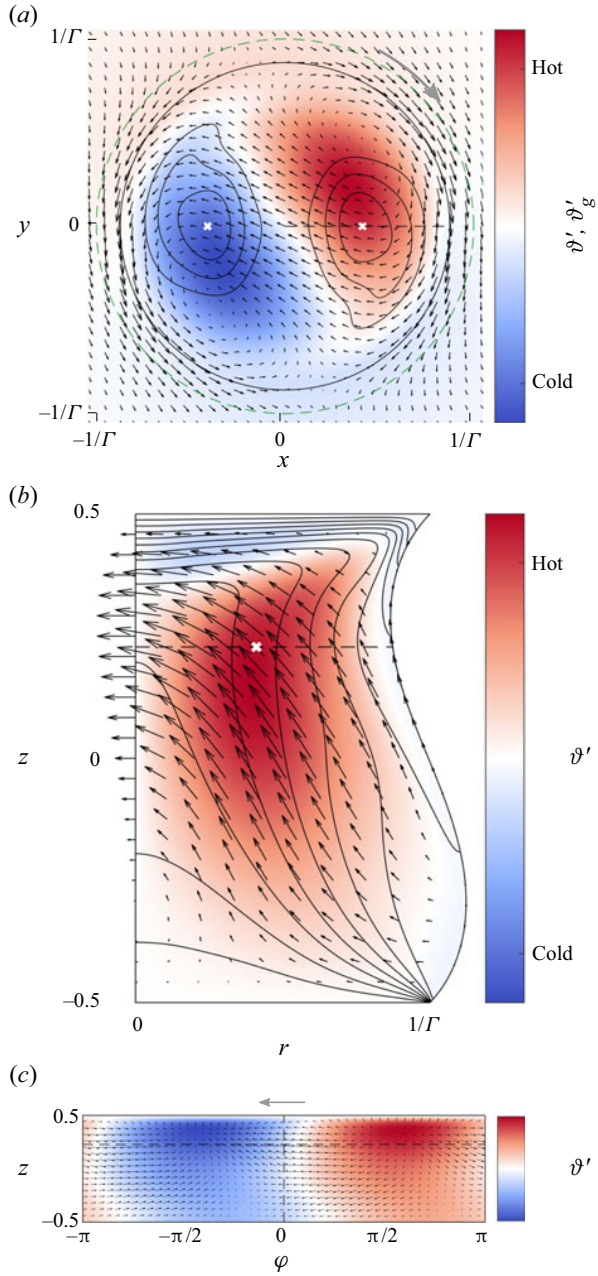

Figure 14. Same as figure 13, but for $\Gamma = 1.66$, $Re_c = 492$, $Bd = Bd_{ref} \times (\Gamma/\Gamma_{ref})^2$, $m_c = 1$ and $z = 0.23$.

wall of the gas container, and fixed $T_{cold} = 14\,^{\circ}\mathrm{C}$. These conditions lead to a cooling of the liquid bridge from the outer shield as soon as $T_{hot} \gtrsim 26\,^{\circ}\mathrm{C}$, which is indeed the case in the reported experiments. Also, the aspect ratio $\Gamma_{rod} = 4.8$ of the support rods in Yano *et al.* (2016) is much larger than the present value $\Gamma_{rod} = 0.4$. In view of the importance of the gas phase for the critical Reynolds number (orange and white squares in figure 12, see also Kamotani *et al.* 2003), it is not surprising that Re_c and m_c obtained by Yano *et al.*

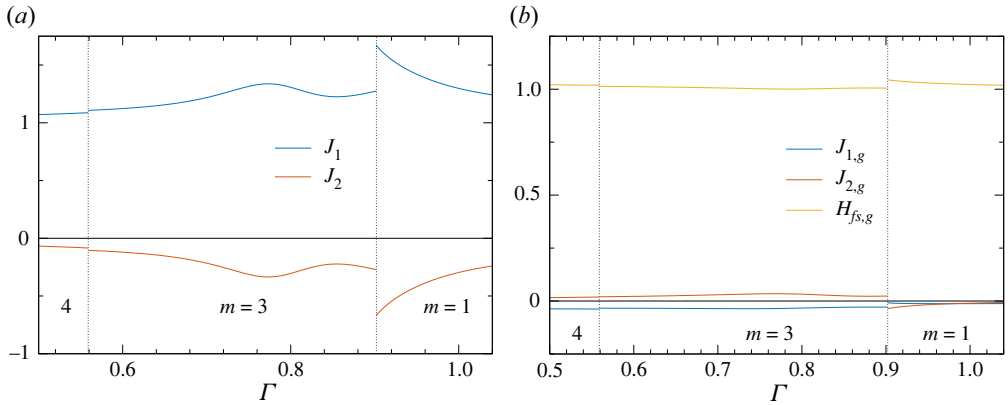

Figure 15. Normalised contributions J_1, J_2 and H_{fs} to the thermal energy budget as functions of Γ for the critical conditions shown in figure 12(*a*). The vertical dotted lines indicate $\Gamma^{1,3}$ and $\Gamma^{3,4}$ where m_c (indicated by labels) changes. (*a*) Liquid phase; throughout $-0.0037 < H_{fs} < 0$. (*b*) Gas phase.

(2016) differ from the present critical data. The deviation of the critical Reynolds number obtained by Ueno *et al.* (2010) for $\Gamma = 0.64$ (bright blue square in figure 12*a*) from the present data may be due to similar reasons. These comparisons demonstrate the important influence of the geometrical and thermal properties of the gas phase on the critical onset.

The effect on the critical Marangoni number of a partial confinement of the gas phase by partition disks was investigated experimentally by Irikura *et al.* (2005) in a geometry similar to the present one, also using the same working fluids. Since the critical temperature difference was always less than 17 °C, the thermal properties of the gas phase near the onset are comparable to the present ones. However, the geometry was slightly different: in our computations, the gas phase is radially confined by an adiabatic rigid wall, whereas it was open to the ambient in the experiments of Irikura *et al.* (2005). In their experiments, the effective length of the hot support rod was varied by axially moving a partition disk on the rod. For comparison, we adapted our geometry accordingly by selecting $\Gamma = 1$, $\eta = 6.55$ and $d_{rod,c} = 1$ mm, and computed the critical Marangoni number as a function of the length $d_{rod,h}$ of the hot (upper) support rod for the data provided by Irikura *et al.* (2005). The result is shown as a line in figure 16. In qualitative agreement with Irikura *et al.* (2005) (circles in figure 16), we find a reduction of the critical Marangoni number (line) as the length of the hot rod $d_{rod,h}$ is increased. The systematically larger numerical critical Marangoni numbers are attributed mainly to the different radial boundary conditions: an adiabatic wall in the numerics versus a gas phase open to the ambient atmosphere in the experiment. The coupling of the gas phase to the ambient air in the experiment may have caused mechanical and thermal perturbation, which may explain the scatter of the experimental data.

4.3. *Effect of the volume ratio*

The influence of the volume ratio $\mathcal{V}$ on the stability of the basic flow with $\Gamma_{ref} = 0.66$ and $Bd_{ref} = 0.41$ is shown in figure 17. The critical curve is made of segments of neutral Reynolds number belonging to all wavenumbers from $m = 0$ to $m = 4$. The critical modes change at the codimension-two points given in table 5. The well-known strong stabilisation of the flow near $\mathcal{V} = 0.9$ for 2 and 10 cSt silicone oils found by Sakurai *et al.* (1996) and Hu *et al.* (1994), respectively, is confirmed (see also Tang & Hu 1999). We find the maximum stabilisation at $\mathcal{V}^{0,1} = 0.8917$ with $Re_c = 2319$. The experimental critical data of Sakurai

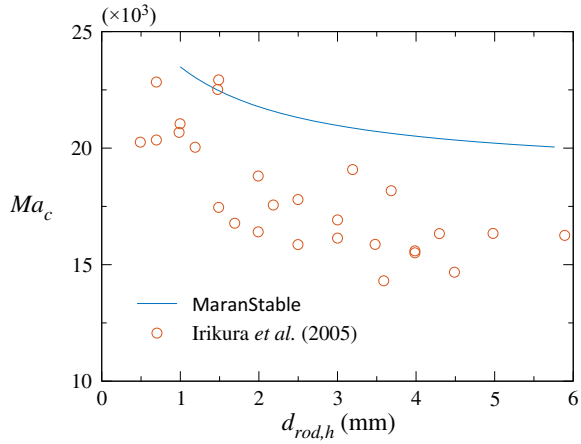

Figure 16. Critical Marangoni number $Ma_c = Pr\,Re_c$ ($m = 1$, line) as a function of the length $d_{rod,h}$ of the upper (hot, subscript h) supporting rod. The length of the lower (cold, subscript c) support rod was kept constant at $d_{rod,c} = 1$ mm, corresponding to the experiment of Irikura *et al.* (2005) whose data are reproduced as circles. The liquid bridge has length $d = 2.5$ mm and aspect ratio $\Gamma = 1$. The radius ratio $\eta = 6.55$ is estimated from figure 1 of Irikura *et al.* (2005).

et al. (1996) for 2 cSt silicone oil, with $\Gamma = 1$, $Bd = 0.95$ and otherwise uncontrolled ambient conditions, are shown in figure 17 as crosses. They agree qualitatively (despite the deviation in Γ and Bd), but differ quantitatively.

Surprisingly, a very small window of the volume ratio exists within which the critical mode is axisymmetric with $m = 0$. A similar axisymmetric oscillatory mode near the so-called gap region was found by Xun, Li & Hu (2010) near $\mathcal{V} \approx 0.8$ by a linear stability analysis, although for a single-fluid model with $Pr = 68.6$ (5 cSt silicone oil) and an adiabatic free surface.

Similarly to before, the contribution to the thermal energy budget is dominated by J_1 (building on radial gradients of ϑ_0) for all critical modes, with J_2 (building on axial gradients of ϑ_0) being small or negative (stabilising; figure 18). This indicates the predominance of axial vorticity in the critical mode, except for the axisymmetric mode. As another observation, the critical wavenumber does not depend monotonically on $\mathcal{V}$. Considering the structure of the neutral modes, it is possible to understand qualitatively the non-monotonic dependence of the critical Reynolds number on $\mathcal{V}$: for a small volume fraction $\mathcal{V} = 0.8$ ($m_c = 2$; figure 19), the internal temperature extrema of the hydrothermal wave are located quite close to the free surface. This facilitates the coupling between the temperature and velocity perturbations, because the free-surface temperature spots are more easily created by the internal temperature extrema. Hence the critical Reynolds number is relatively small for small $\mathcal{V}$. As $\mathcal{V}$ increases, the internal temperature extrema must be stronger to be able to heat/cool the more distant free surface and to generate the perturbation flow ($\mathcal{V} = 0.87$, $m_c = 1$; figure 20). This may explain the increase of the critical Reynolds number with $\mathcal{V}$ before reaching its maximum. However, as the volume gets very large ($\mathcal{V} = 1.3$, $m_c = 3$; figure 21), the basic flow and the perturbation flow suffer less viscous dissipation, because the liquid volume is bounded mainly by a free surface, only coupled to the gas phase. As a result, the critical Reynolds number decreases again after $\mathcal{V}$ has exceeded the point of maximum stabilisation (for $\mathcal{V} > 0.8917$).

Near the volume ratio $\mathcal{V} > 0.8917$ at which the maximum stabilisation is observed, a small window arises in which the critical mode is axisymmetric. Contrary to the other

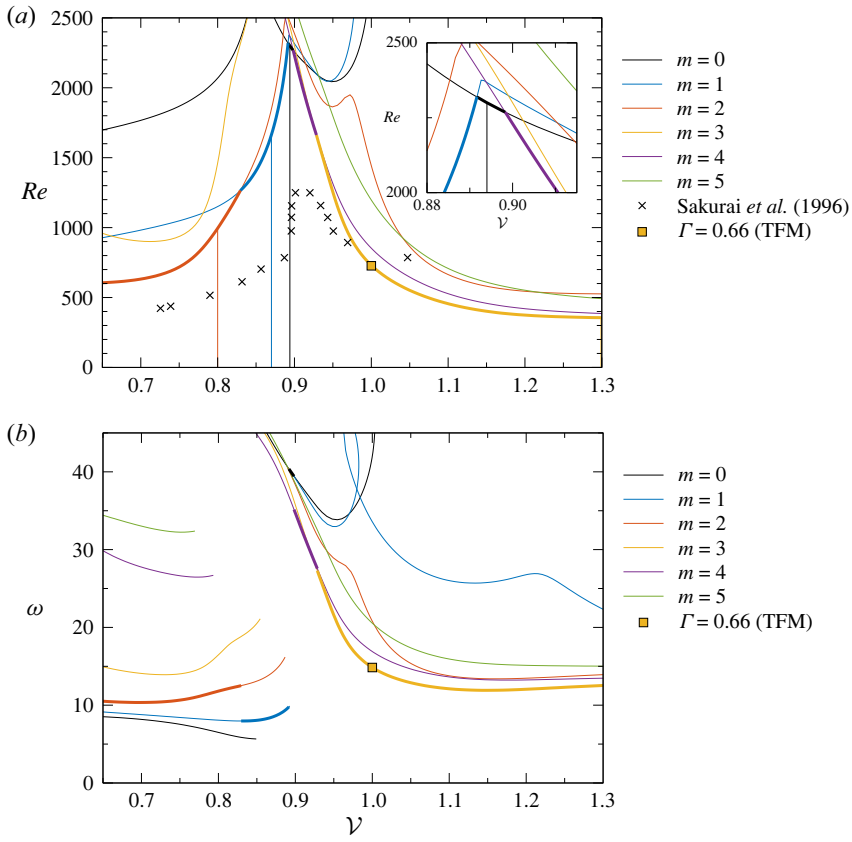

Figure 17. (*a*) Neutral Reynolds numbers (thin lines) and critical Reynolds numbers Re_c (thick lines) as functions of the volume ration $\mathcal{V}$ for $\Gamma = 0.66$ and $Bd = 0.41$. Crosses indicate data taken from Sakurai *et al.* (1996) for $\Gamma = 1$ and $Bd = 0.95$. (*b*) Corresponding frequencies ω. The yellow square indicates the reference case.

m	$1 \leftrightarrow 2$	$0 \leftrightarrow 1$	$0 \leftrightarrow 4$	$3 \leftrightarrow 4$
$\mathcal{V}^{m_1,m_2}$	0.8296	0.8917	0.8983	0.9286
$Re_c(\mathcal{V}^{m_1,m_2})$	1264	2319	2268	1662

Table 5. Codimension-two points where critical curves for constant m intersect, with $\Gamma = 0.66$, $Bd = 0.41$.

modes, the axisymmetric mode $m_c = 0$ draws its thermal energy from both axial and radial temperature gradients, with both J_1 and J_2 being positive (figure 18). The mode arises as a toroidal vortex ($\mathcal{V} = 0.8939$; figure 22) whose sense of rotation oscillates with $\omega_c(m = 0)$. The total nonlinear flow in an experiment would thus appear as a toroidal vortex whose strength, position and size change periodically in time.

4.4. *Effect of buoyancy*

The linear stability boundary and oscillation frequency as functions of the dynamic Bond number for $\Gamma_{ref} = 0.66$ and $\mathcal{V}_{ref} = 1$ are displayed in figure 23 for heating from above

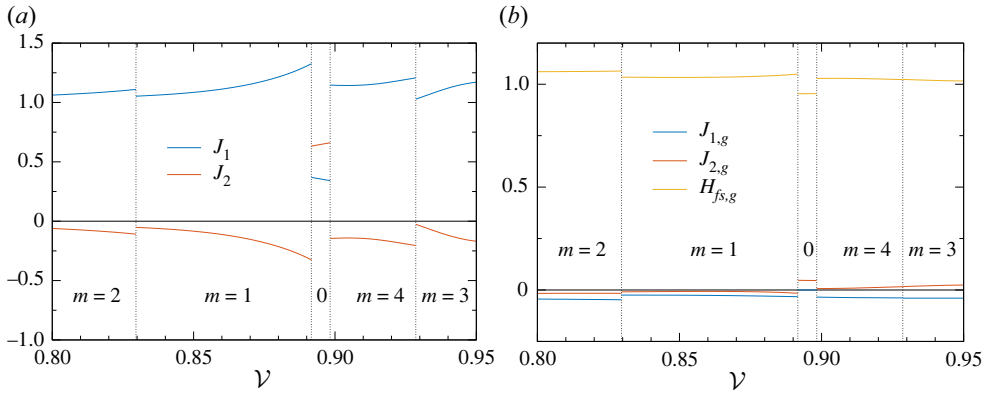

Figure 18. Normalised contributions J_1, J_2 and H_{fs} to the thermal energy budget as functions of $\mathcal{V}$ along the critical curve shown in figure 17(*a*). The vertical dotted lines indicate $\mathcal{V}^{1,2}$, $\mathcal{V}^{0,1}$, $\mathcal{V}^{0,4}$ and $\mathcal{V}^{3,4}$ at which m_c (indicated by labels) changes. (*a*) Liquid phase; throughout $-0.007 < H_{fs} < 0$. (*b*) Gas phase.

($Bd > 0$) and heating from below ($Bd < 0$). The crossover points at which the wavenumber of the critical mode changes are listed in table 6. It should be noted that a quiescent liquid bridge of $\Gamma = 0.66$ and $\mathcal{V} = 1$ would break mechanically due to the capillary instability at $Bo = \pm 31.75$ (Slobozhanin & Perales 1993). For the present working fluid, this limit corresponds to $Bd = \pm 10.31$. Therefore, the range shown in figure 17 is safely within the mechanical stability limits of the liquid bridge, even if dynamic surface deformations were taken into account.

In the range $-0.25 \lesssim Bd \lesssim 0.35$, buoyancy has only a small effect on the shape of the liquid bridge and on the magnitude of the critical Reynolds number. Since the governing equations are not invariant under $Bd \to -Bd$, the slope of the critical curve at zero gravity ($Bd = 0$) does not vanish. This was also found by Wanschura *et al.* (1997*b*) for small values of Bd and a cylindrical liquid bridge with $Pr = 4$, $\Gamma = 1$ and an adiabatic free surface. For weak stabilising buoyancy and $Bd > Bd^{2,3}$, the critical mode has $m_c = 3$ (yellow), whereas for $Bd < Bd^{2,3}$ and for destabilising buoyancy, the critical wavenumber is $m_c = 2$ (red). The Bond numbers corresponding to the gravity levels on the Moon, Mars and Earth are indicated by yellow vertical dashed lines. For zero gravity conditions, the critical mode with $m_c = 2$ is illustrated in figure 24. The basic flow in an upright cylindrical liquid bridge, exclusively driven by thermocapillarity, is a standard case within the single-fluid model. Here, however, the flow is modified by the presence of the ambient gas phase. The properties of the hydrothermal wave are similar to those discussed in § 4.1.2 for the reference case, which differs by the Bond number.

As the Bond number is increased beyond $Bd > 0.41$ (Earth gravity level), the critical Reynolds number increases significantly. This seems to be consistent with a more stable density stratification as Bd increases. However, for $Bd > Bd^{1,5} \approx 0.91$, the critical Reynolds number decreases again, mainly due to an $m = 2$ mode. A possible explanation is that the hot fluid transported downward along the free surface by the thermocapillary surface flow has a strong tendency to rise in the bulk, owing to its buoyancy. As a result, the basic thermocapillary-driven vortex has little radial extent, and the internal temperature gradients, which provide the source of the thermal perturbation energy, arise in the close vicinity of the free surface. This can be seen in figure 25, which shows the critical mode for $Bd = 1.1$. Since the thermocapillary flow does not penetrate very much inwards from

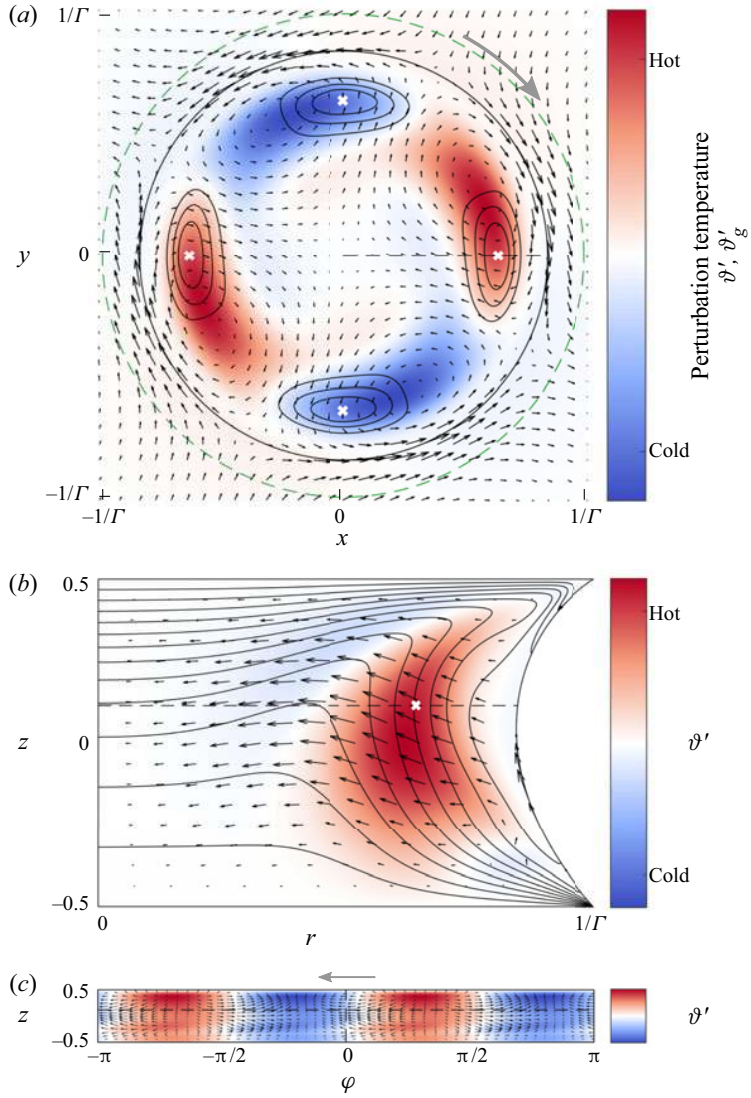

Figure 19. Same as figure 13, but for $\Gamma = 0.66$, $\mathcal{V} = 0.8$, $Re_c = 995$, $m_c = 2$ and $z = 0.12$.

the free surface, the free-surface temperature perturbations of the critical mode are much easier to create as compared to lower Bond numbers, in particular as compared to $Bd \approx 0$ (figure 24). This facilitates the coupling between temperature and velocity perturbations, and leads to a reduction of the critical Reynolds number despite the nominally stabilising buoyancy forces.

The critical mode for $Bd = 1.1$ is also affected by buoyancy. To analyse this effect, we separate the buoyancy effect on the critical mode from the buoyancy effect on the basic flow, by using the same basic state solution ($Bd = 1.1$), but artificially setting $Bd \equiv 0$ in the perturbation equations. Compared to figure 25, the spatial structure of the perturbation temperature ϑ' remains similar, while the vertical perturbation velocity is very small everywhere ($w' \approx 0$), except close to the free surface (not shown). Due to the nearly

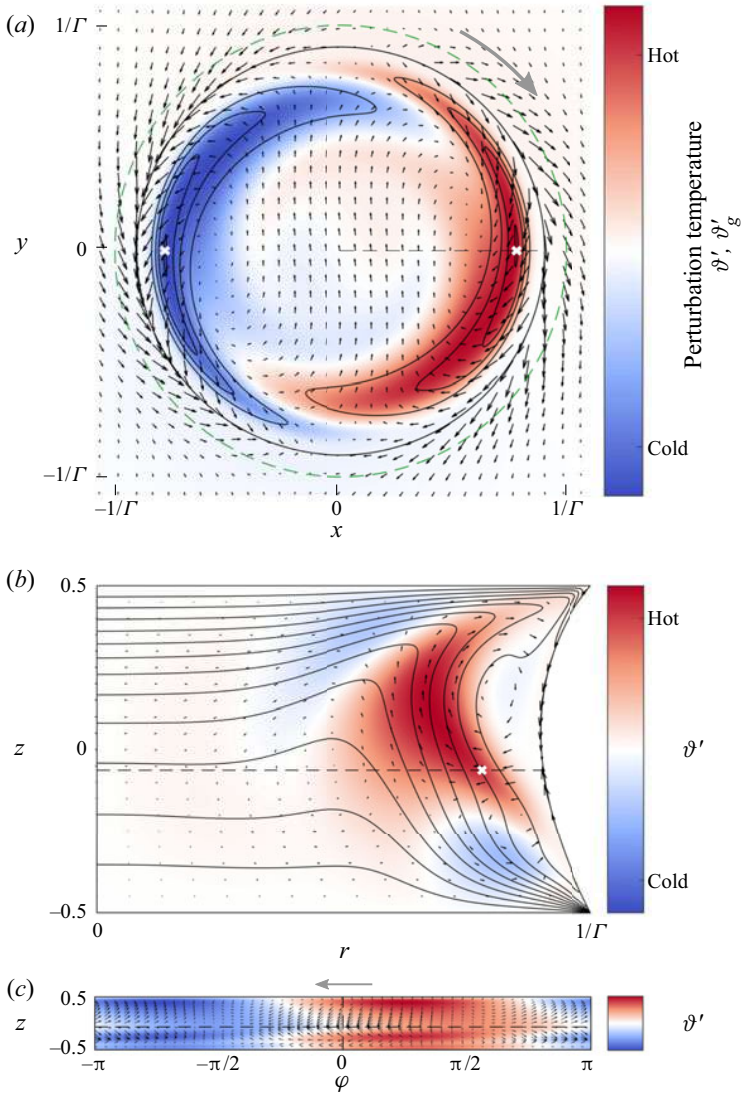

Figure 20. Same as figure 13, but for $\Gamma = 0.66$, $\mathcal{V} = 0.87$, $Re_c = 1664$, $m_c = 1$ and $z = -0.06$.

horizontal velocity perturbation in the bulk (axial vorticity), more thermal perturbation energy is generated, which would destabilise the basic state. This means that for $Bd = 1.1$, the action of buoyancy in the perturbation flow has a stabilising effect on the basic state. Therefore, the destabilising trend for increasing Bond number for $Bd > Bd^{1,5} = 0.9083$ is caused by the facilitated feedback between internal and surface temperature extrema due to the structure of the basic flow, and not by the action of buoyancy on the perturbation flow.

Contrary to what one would expect for destabilising buoyancy (heating from below, $Bd < 0$) the critical Reynolds number also increases as Bd is decreased. This effect is related to a similar mechanism as discussed before: the hot fluid that is transported to the cold wall along the free surface has little tendency to return to the hot wall in the bulk due

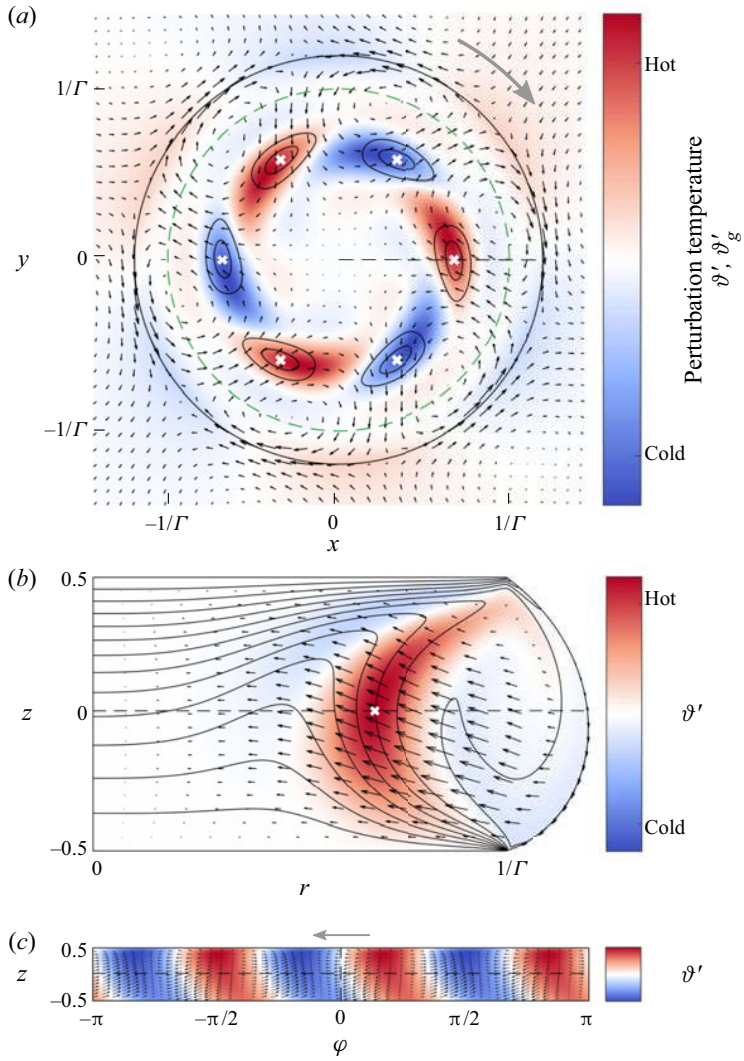

Figure 21. Same as figure 13, but for $\Gamma = 0.66$, $\mathcal{V} = 1.3$, $Re_c = 356$, $m_c = 3$ and $z = 0.01$.

to buoyancy. As a result, the thermocapillary basic state vortex (not shown) has a larger radial extension and the energy source for the hydrothermal wave arises closer to the axis of the liquid bridge. Therefore, the internal perturbation temperature extrema cannot easily heat/cool the distant free surface to drive the velocity field necessary for the hydrothermal wave feedback mechanism. As a result, Re_c increases.

The black dotted curve in figure 23(*a*) indicates a Rayleigh number $Ra = 1700$, where $Ra = -Pr\,Bd\,Re$ is defined in agreement with the usual convention for pure buoyancy-driven flows. This is roughly the Rayleigh number at which the flow becomes buoyantly unstable in a cylindrical adiabatic liquid bridge in the absence of thermocapillarity (Wanschura, Kuhlmann & Rath 1996). To the left of it, destabilising buoyancy forces get even stronger. However, pure buoyant instabilities are absent here, mainly because the basic thermocapillary flow significantly deforms the basic temperature field that would be conducting in the absence of thermocapillarity. Nevertheless,

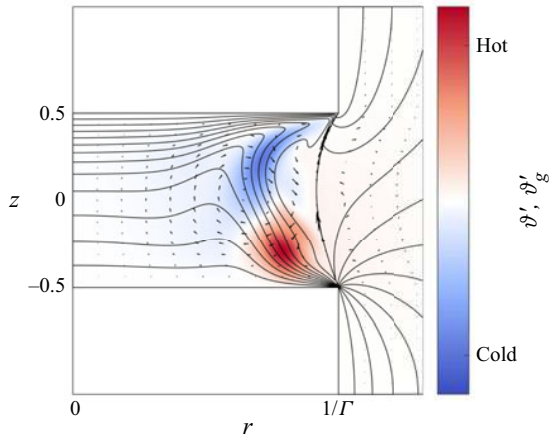

Figure 22. Axisymmetric critical mode for $\mathcal{V} = 0.8939$, $Re_c = 2301$ and $m_c = 0$. Shown are the basic state isotherms (lines), the critical velocity field (arrows) and the critical temperature field (colour).

destabilising buoyancy is expected to promote the instability of the basic flow for decreasing Bd. Such destabilisation is not seen, however, until $Bd = Bd^{1,2}$.

Only for $Bd < Bd^{1,2} = -0.5645$, a critical mode with $m_c = 1$ (blue) arises that seems to be affected by destabilising buoyancy. The critical mode for $Bd = -1.25 < Bd^{1,2}$ is shown in figure 26. At a first inspection of figures 26(*a*,*c*), the critical mode seems to be driven by an azimuthal thermocapillary effect. The associated radial flow in the bulk crosses the axis and creates a cold spot and a hot spot very close to the axis, since this is the region of largest radial gradients of the basic temperature field. However, in the absence of the action of buoyancy on the perturbation flow, there would be no obvious reason why the perturbation flow should not be essentially horizontal near the axis, as for $Bd = 0$ (figure 24*b*). Instead, we find a strong vertical upward (downward) flow near the hot (cold) near-axis perturbation temperature spots. This leads to a localised convection role in the plane of maximum thermal energy production shown in figure 26(*b*). Artificially switching off the Bond number in the perturbation equation only (setting $Bd \equiv 0$), while keeping $Bd = -1.25$ for the basic state, reveals (not shown) that the perturbation flow in this artificial case is indeed horizontal near the axis. Thus the vertical component of the velocity of the perturbation vortex near the axis must be driven essentially by buoyancy acting on the perturbation mode. The buoyancy effect on the perturbation mode should be particularly high in this case, because the horizontal temperature gradient of the perturbation flow (generated by the thermocapillary return flow) is particularly large when the perturbation temperature spots arise over a very small distance close to the axis.

This interpretation is confirmed by inspecting the major terms of the kinetic energy budget. These terms, corresponding to the work per time driving the perturbation flow, are given in table 7. Compared to $Bd = 0.41$, the work done by buoyant forces in case of $Bd = -1.25$ is more than ten times as large and amounts to approximately 14 % of the total kinetic energy production. But the major driving of the perturbation flow field is still caused by the work done by thermocapillary forces M_z and M_φ. Among these, the production M_z due to axial thermocapillary stresses for $Bd = -1.25$ is surprisingly more important than the azimuthal production. This might be related to the strong vertical component of the perturbation flow near the axis.

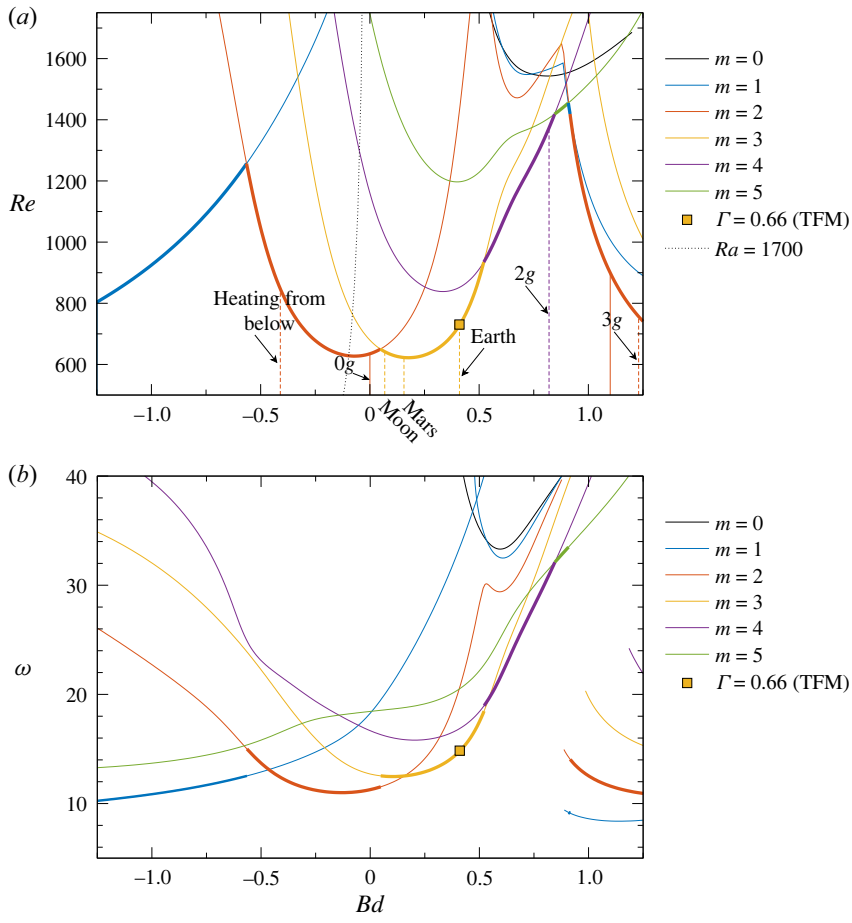

Figure 23. (*a*) Neutral Reynolds numbers (thin lines) and critical Reynolds numbers Re_c (thick lines) as functions of the dynamic Bond number Bd for $\Gamma_{ref} = 0.66$ and $\mathcal{V}_{ref} = 1$. (*b*) Corresponding neutral and critical frequencies ω.

m	$1 \leftrightarrow 2$	$2 \leftrightarrow 3$	$3 \leftrightarrow 4$	$4 \leftrightarrow 5$	$1 \leftrightarrow 5$	$1 \leftrightarrow 2$
Bd^{m_1,m_2}	−0.5645	0.0483	0.5214	0.8457	0.9083	0.9162
$Re_c(Bd^{m_1,m_2})$	1257	650	935	1420	1455	1419

Table 6. Codimension-two points where critical curves for constant m intersect, with $\Gamma_{ref} = 0.66$, $\mathcal{V}_{ref} = 1$.

The thermal energy budget as function of the Bond number is shown in figure 27. As in the previous cases, the thermal energy per time $H_{fs,g}$ supplied to the gas phase through the interface is essentially dissipated, with the thermal energy production rates $J_{1,g}$ and $J_{2,g}$ being insignificant. Therefore, the instability is always triggered in the liquid phase. While for $Bd < Bd^{2,3} \approx 0.05$ both J_1 and J_2 are positive and contribute to the destabilisation of the basic flow, J_2 is negative for $Bd > Bd^{2,3}$, which, on the stability boundary, is compensated by a much larger positive value of J_1. This indicates the dominant role for the instability of radial temperature gradients of the basic state when the liquid bridge

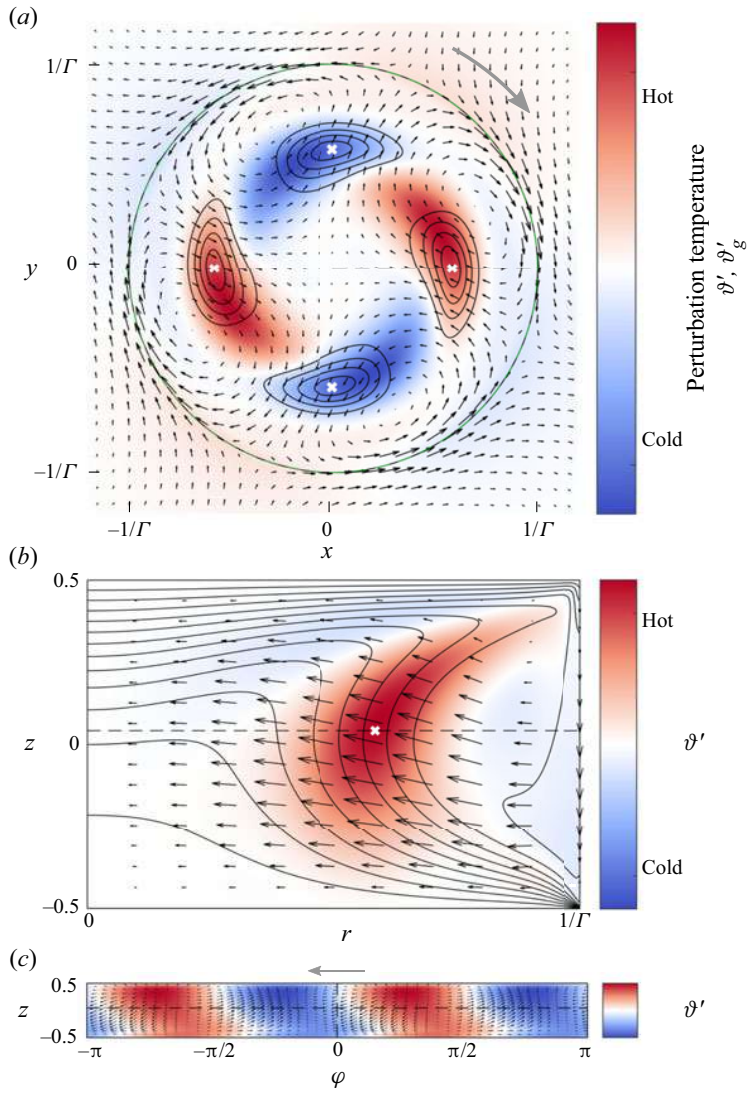

Figure 24. Same as figure 13, but for $\Gamma = 0.66$, $Bd = 0$, $Re_c = 635$, $m_c = 2$ and $z = 0.04$.

is heated from above (buoyancy forces are opposing basic state thermocapillarity forces on the free surface, $Bd > 0$), consistent with the above-described small radial penetration depth of the basic flow when buoyancy forces are large. For heating from below (buoyancy forces are augmenting the basic state thermocapillary forces on the free surface, $Bd < 0$), the perturbation flow can also extract thermal energy from the axial gradients of the basic temperature field via $J_2 > 0$, albeit radial temperature gradients of the basic state remain more important.

For heating from below and in the absence of thermocapillary effects, Wanschura *et al.* (1996) found that the onset of thermal convection in cylindrical liquid bridges is always non-axisymmetric. Nevertheless, steady axisymmetric solutions exist for Rayleigh numbers $Ra = g\,\beta\,\Delta T d^3/\nu\kappa$ larger than the neutral stability boundary for $m = 0$. These axisymmetric flows have either up- or down-flow at the free surface. Thermocapillary

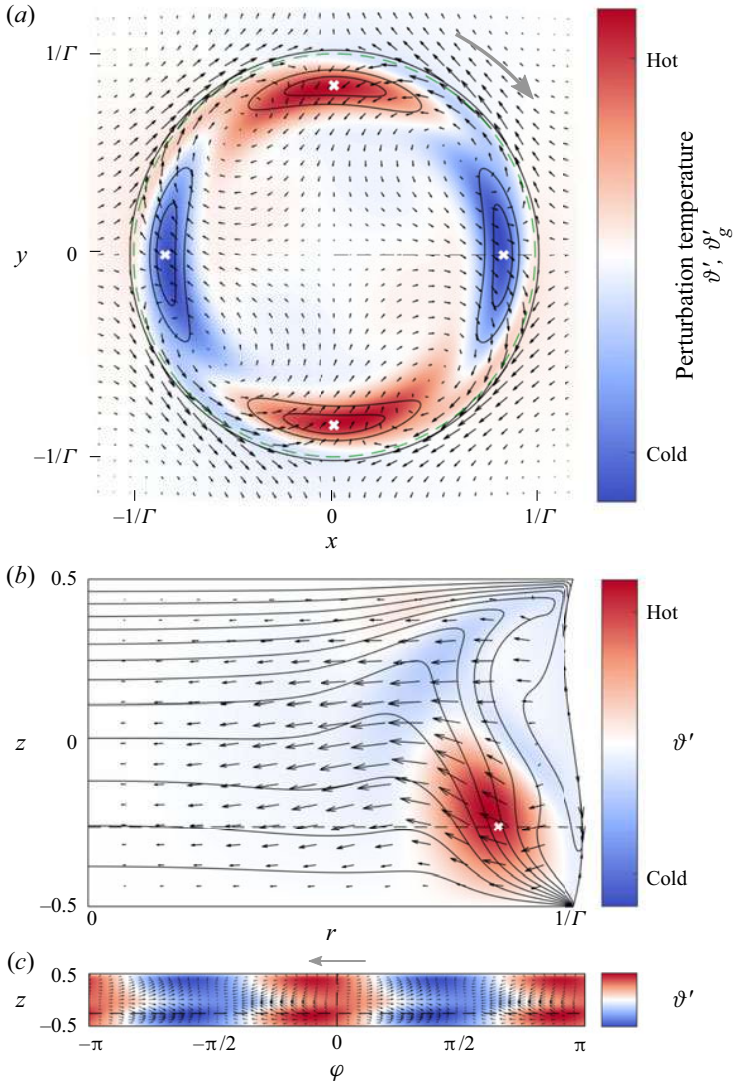

Figure 25. Same as figure 13, but for $\Gamma = 0.66$, $Bd = 1.1$, $Re_c = 900$, $m_c = 2$ and $z = -0.26$.

forces can either augment or oppose the buoyant flow on the free surface. To illustrate the resulting buoyant-thermocapillary flows, the coefficient $\gamma = -3.828 \times 10^{-7}\,\mathrm{N\,m^{-1}\,K^{-1}}$ is selected small due to e.g. impurities or surfactants dissolved in the liquid. For $\Gamma = 0.66$, $\mathcal{V} = 1$, $Ra = 3200$, $Re = 0.5$ and $Bd = -229$, the augmenting and opposing axisymmetric flows are illustrated in figures 28(*a*) and 28(*b*), respectively. For the opposing case (figure 28*b*), the direction of the surface flow is reversed near each of the two triple-phase contact lines such that a small eddy arises in the hot as well as in the cold corner. In addition to these two states, an intermediate weak state exists (figure 28*c*) in which the velocity field near the liquid–gas interface is very weak and which is unstable with respect to two-dimensional perturbations. This result is similar to the behaviour in adiabatic cylindrical liquid bridges using the single-fluid model (Wanschura *et al.* 1997*b*). We find that the flow in the augmenting case (strong solution; figure 28*a*) is linearly stable

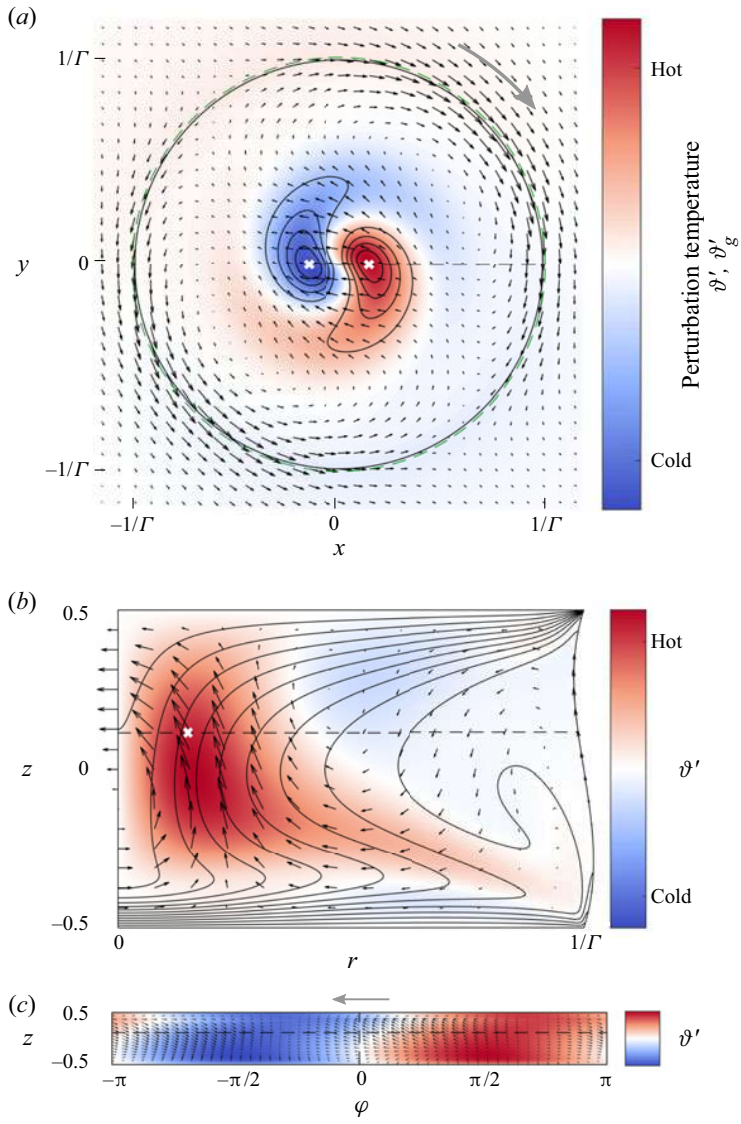

Figure 26. Same as figure 13, but for $\Gamma = 0.66$, $Bd = -1.25$, $Re_c = 804$, $m_c = 1$ and $z = 0.12$. Note that for $Bd < 0$, the hot wall is located at the bottom (heated from below).

with respect to all modes, with $m \in [0, 5]$, the most dangerous mode having $m = 3$ and a growth rate $\mu = -0.03 + 0i$. The flow in the opposing case (weak solution; figure 28*b*) is stable with respect to $m \in [0, 2]$, but unstable for $m \in [3, 5]$, with the most dangerous mode $m = 4$ and $\mu = 0.15 + 0i$. Finally, the third weak state (figure 28*c*) is unstable to all modes with $m \in [0, 5]$, the most dangerous having the wavenumber $m = 4$ with $\mu = 0.53 + 0i$.

5. Discussion and conclusions

The linear stability of axisymmetric steady flow in liquid bridges of silicone oil with $Pr = 28$ in air has been investigated numerically. This pair of fluids is used also in

Bd	M_r	M_φ	M_z	B
+0.41	0.002	0.531	0.481	0.013
−1.25	0.040	0.185	0.521	0.142

Table 7. Main contributions to the kinetic energy production at the critical point for $\Gamma_{ref} = 0.66$ and $\mathcal{V}_{ref} = 1$.

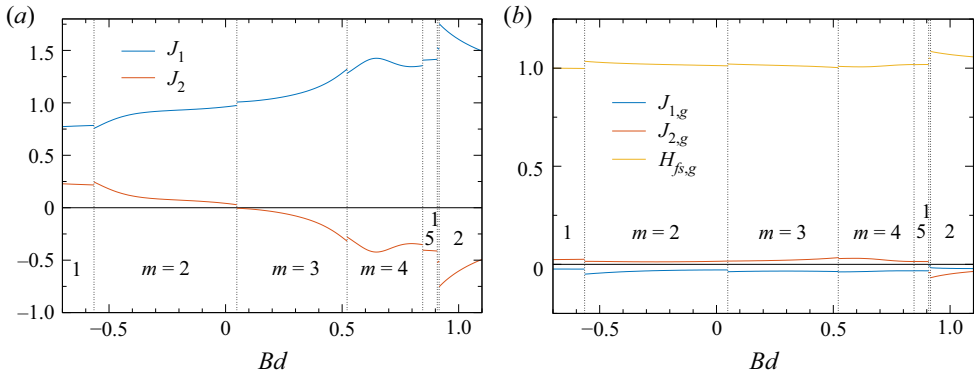

Figure 27. Normalised contributions J_1, J_2 and H_{fs} to the thermal energy budget at criticality (figure 23*a*) as functions of Bd for $\Gamma_{ref} = 0.66$ and $\mathcal{V}_{ref} = 1$. The vertical dotted lines indicate $Bd^{1,2}$, $Bd^{2,3}$, $Bd^{3,4}$, $Bd^{4,5}$, $Bd^{1,5}$ and $Bd^{1,2}$ where m_c (indicated by labels) changes. (*a*) Liquid phase; throughout $-0.0035 < H_{fs} < 0$. (*b*) Gas phase.

many experimental investigations (see e.g. Ueno *et al.* 2003; Irikura *et al.* 2005; Tanaka *et al.* 2006; Yano, Hirotani & Nishino 2018*a*). While taking into account the hydrostatic deformation of the liquid bridge, the liquid and gas flows are treated in Boussinesq approximation in order to reduce the large parameter space. Furthermore, the radii of the support cylinders and the cylindrical gas container relative to the radius of the liquid bridge were kept fixed. This set-up allowed us to investigate the effects of the relative length of the liquid bridge (Γ), the relative volume of liquid ($\mathcal{V}$), and buoyancy forces (Bd) on the threshold for the onset of three-dimensional flow. The linear stability boundary of the basic axisymmetric flow was calculated quasi-continuously varying these three parameters. All parameter variations originated from a common reference case, defined by $\Gamma_{ref} = 0.66$, $\mathcal{V}_{ref} = 1$ and $Bd_{ref} = 0.41$.

Throughout the range of parameters considered, the flow becomes unstable to hydrothermal waves, except for sufficiently strong heating from below when the critical mode arises as a convection roll in the centre of the liquid bridge. Quite generally, the hydrothermal waves exhibit $2m$ strong azimuthally periodic temperature extrema in the bulk of the liquid. As expected for hydrothermal waves, inertia effects are insignificant for the critical mode, which can hardly extract momentum from the basic vortex flow. On the other hand, advection of basic state temperature by the weak perturbation flow is of key importance for the creation of the characteristic internal temperature extrema. Considering the thermal energy budget of the critical mode, and its spatial structure, allowed us to understand the global trends of the critical Reynolds number Re_c.

The critical wavenumber m is found to depend on Γ, $\mathcal{V}$ and Bd. Within the parameter space considered, the critical wavenumber cannot be predicted based on a simple

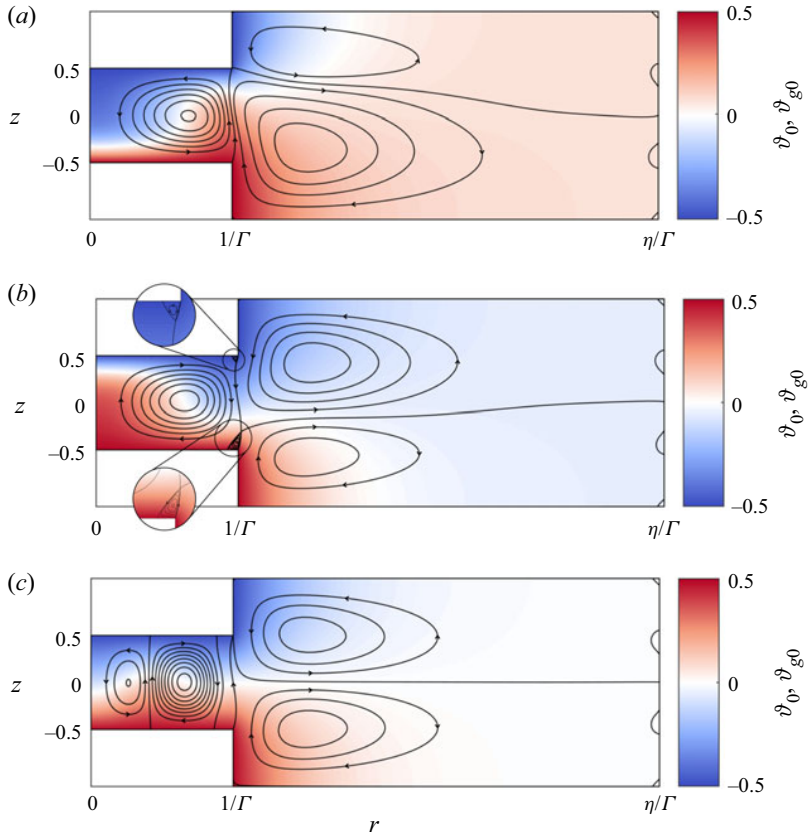

Figure 28. Three different axisymmetric flows for $\Gamma = 0.66$, $\mathcal{V} = 1$, $Ra = 3200$, $Re = 0.5$ and $Bd = -229$. (*a*) Thermocapillarity is augmenting the buoyant flow. (*b*,*c*) Thermocapillarity is opposing the buoyant flow with the strong state shown in (*b*) and the weak state shown in (*c*).

correlation like $m_c \approx 2.2 \times \Gamma$ proposed by Preisser *et al.* (1983) for the instability in $NaNO_3$ ($Pr \approx 7$), normal gravity and $\mathcal{V} \approx 1$, because the Preisser *et al.* (1983) correlation does not include the gravity level and the volume fraction of the liquid. For $Pr = 28$ and including the surrounding air in the analysis, we find that the critical wavenumber increases with decreasing Γ (for $\mathcal{V} = 1$ and $Bd = 0.41 \times (\Gamma/\Gamma_{ref})^2$), but misses out $m_c = 2$. The dependence of m_c on $\mathcal{V}$ does not exhibit any monotonic trend, while the critical wavenumbers are well ordered from $m_c = 1$ to $m_c = 5$ when the Bond number is increased from $Bd = -1.25$ (heating from below) to $Bd = 0.9083$ (heating from above). Interestingly, we find an axisymmetric oscillatory instability ($m = 0$) for $\Gamma = 0.66$ and $Bd = 0.41$ within a small window of $\mathcal{V} \in [0.8917, 0.8983]$ where the basic flow is extremely stable with a critical Reynolds number of approximately $Re_c \approx 2300$.

As a major result, the gas phase has a strong effect on the stability boundary. For instance, the critical Reynolds number taking into account the gas phase can be less than one-half of the critical Reynolds number for a single-fluid model with a passive adiabatic interface (cf. figures 12*a* and 29). This effect is caused primarily by the change of the thermal environment of the liquid bridge, i.e. by the heat exchange characteristics between the liquid and the gas. The gas phase, however, does not play an active role for the

instability, because neither mechanical nor thermal perturbation energy is produced from the velocity or temperature gradients of the basic state in the gas phase.

Since the Prandtl number of the liquid is quite large, the basic flow exhibits pronounced thermal boundary layers. The scalings of the boundary layer thicknesses on the cold and hot walls that we find in our numerical calculations for the reference case ($\Gamma_{ref} = 0.66$, $\mathcal{V}_{ref} = 1$, $Bd_{ref} = 0.41$) are in excellent agreement with theoretical scalings predicted for a contact angle $\alpha = 90^\circ$ and the single-fluid model. This finding is particularly notable for two reasons. First, in the presence of gravity, the hydrostatic free surface exhibits a contact angle $\alpha = 84^\circ$ for the reference case. Second, in our model the liquid bridge is surrounded by a gaseous phase, which was excluded in the theoretical investigations.

The mathematical model employed (Oberbeck–Boussinesq approximation) is based on the assumption of constant thermophysical properties of the fluids, evaluated at $T_0 = 25\,^\circ$C, except for ρ, ρ_g and σ, which are linearised around T_0. Despite the relatively moderate critical temperature differences ΔT_c found throughout our numerical investigation, the peak values reach $\Delta T_c \approx 36\,^\circ$C, $70\,^\circ$C and $44\,^\circ$C when varying Γ, $\mathcal{V}$ and Bd, respectively. Additional preliminary computations taking into account the full temperature dependence of all thermophysical properties of the fluids indicate that the temperature dependence can become important near sharp peaks of the critical curve, because it can suffer a certain shift with respect to the parameters varied (Γ, $\mathcal{V}$ or Bd). But the linear stability boundaries computed for $\mathcal{V} \geq 1.05$ using temperature-dependent fluid properties deviate only less than 1 % from the present results. Taking into account temperature-dependent fluid properties affects the linear stability boundary in a non-trivial way. Therefore, it deserves a comprehensive analysis that is beyond the scope of this paper. A dedicated study of the linear stability analysis for a multiphase liquid bridge with variable fluids properties is currently underway and will be reported in the future.

The 2 cSt silicone oil used in our study has a pour point below $-120\,^\circ$C and boiling temperature $88\,^\circ$C (Shin-Etsu 2004). All critical temperatures found in the present investigation go into this range. For ΔT close to the highest critical values computed ($\Delta T_c \approx 70\,^\circ$C), evaporation, which is not included in our model, may play a significant role. In fact, Simic-Stefani, Kawaji & Yoda (2006) found a strong stabilising effect due to evaporation using the highly volatile liquid acetone ($Pr = 4.3$). On the other hand, Yano *et al.* (2016) claim that the effect of evaporation for the 2 cSt silicone oil is negligible for typical critical temperature differences found in their experiments. Their statement is confirmed by figure 31, as our estimate of the linear stability boundary is in agreement with their experimental data. Nevertheless, the numerical model would benefit by including the mass exchange between the liquid and gas phases, in particular, for large critical temperature differences.

An experimental measurement of the critical Reynolds number for thermocapillary liquid bridges is usually quite error-prone due to the small size of the bridge in terrestrial laboratories, possible chemical contaminations of the interface, and the difficulty to control accurately the thermal environment. The current results provide accurate numerical stability data (Re_c, m_c, ω_c) for a particular geometrical setting, and the dependence of these data on the important control parameters Γ, $\mathcal{V}$ and Bd. Since the critical onset is affected by the gas phase due mainly to the amount and structure of the heat transfer through the liquid–gas interface, a variation of the relative geometry of the axisymmetric gas space (radius, height) is expected to have only a minor influence on the critical data as long as the heat transfer characteristics are not much affected. This can be expected, for example, if only the radius is increased from the current value. If, however, the heat transfer between the liquid and the gas phase is changed – e.g. by a forced axial gas flow

with a given temperature (Gaponenko *et al.* 2021), or by natural convection in a cold gas (Kamotani *et al.* 2003) – then the critical Reynolds number can be modified strongly. While the control of the critical onset by an imposed gas flow is the objective of ongoing work in the framework of the JEREMI project (Shevtsova *et al.* 2014), a systematic study of the effect of the temperature contrast between the liquid bridge and the gas environment would be an interesting problem for future investigations.

Funding. This work has been supported by the Austrian Research Promotion Agency (FFG) in the framework of the ASAP14 programme under contract no. 866027.

Declaration of interests. The authors report no conflict of interest.

Author ORCIDs.
Mario Stojanović https://orcid.org/0000-0003-0072-8563;
Francesco Romanò https://orcid.org/0000-0002-9511-4718;
Hendrik C. Kuhlmann https://orcid.org/0000-0003-1783-3255.

Author contributions. All authors contributed equally to analysing data and reaching conclusions, and in writing the paper.

Appendix A. Kinetic and thermal energy budgets of the perturbation flow

Here, we present all terms entering the kinetic (2.27) and the thermal energy budget (2.28). The structures of the budgets for the liquid and gas phases are identical, i.e. formally the same terms arise. However, the budgets are obtained by integration over different volumes that the liquid and the gas occupy. In the following equations, the distinction between the liquid and gas phases is taken care of by using the integration volume V_i occupied by the liquid or the gas, $i \in [l, g]$, and by using the corresponding set of coefficients $\boldsymbol{\alpha}$ (see (2.7)). Furthermore, the integrals over the free surface carry different signs, where the lower sign applies to the gas phase.

The viscous and thermal energy dissipations can be expressed as

$$\mathcal{D}_{kin} = \frac{\alpha_\nu}{2}\int_{V_i} |\boldsymbol{S}'|^2 \,\mathrm{d}V = \alpha_\nu \int_{V_i} (\boldsymbol{\nabla}\times\boldsymbol{u}')^2 \,\mathrm{d}V \pm 8\pi\alpha_\nu \int_{-1/2}^{1/2} (hh_{zz}\hat{w}^2 - \hat{v}^2)\mathrm{d}z \qquad \text{(A1}a\text{)}$$

where $\boldsymbol{S}' = \boldsymbol{\nabla}\boldsymbol{u}' + (\boldsymbol{\nabla}\boldsymbol{u}')^{\mathrm{T}}$ and

$$\mathcal{D}_{th} = \frac{\alpha_\kappa}{Pr}\int_{V_i} (\boldsymbol{\nabla}\vartheta')^2 \,\mathrm{d}V, \qquad \text{(A1}b\text{)}$$

respectively. Since the neutral modes are determined only up to an arbitrary factor, $\mathcal{D}_{kin}$ and $\mathcal{D}_{th}$ are used to normalise all terms in the respective kinetic and thermal energy balances. This allows us to determine the relative importance of each term in the budget for the instability mechanism.

The normalised mechanical and thermal production terms in (2.27) and (2.28), respectively, are defined as

$$\sum_{j=1}^{5} I_j = -\frac{Re}{\mathcal{D}_{kin}}\int_{V_i}\left(v'^2\frac{u_0}{r} + u'^2\frac{\partial u_0}{\partial r} + u'w'\frac{\partial u_0}{\partial z} + u'w'\frac{\partial w_0}{\partial r} + w'^2\frac{\partial w_0}{\partial z}\right)\mathrm{d}V, \qquad \text{(A2}a\text{)}$$

$$\sum_{j=1}^{2} J_j = -\frac{Re}{\mathcal{D}_{th}}\int_{V_i}\vartheta'\left(u'\frac{\partial\vartheta_0}{\partial r} + w'\frac{\partial\vartheta_0}{\partial z}\right)\mathrm{d}V, \qquad \text{(A2}b\text{)}$$

with j consecutively numbering the individual integrals I_j and J_j of the sums. The works done per unit time by thermocapillary forces acting at the liquid–gas interface are obtained as

$$M_r = \pm\frac{4\pi\alpha_v}{\mathcal{D}_{kin}}\int_{-1/2}^{1/2} hh_z\hat{u}\left(\frac{\partial\hat{w}}{\partial r}-\frac{\partial\hat{u}}{\partial z}\right)\mathrm{d}z, \tag{A3a}$$

$$M_\varphi = \pm\frac{4\pi\alpha_v}{\mathcal{D}_{kin}}\int_{-1/2}^{1/2} h\hat{v}\left(\frac{\partial\hat{v}}{\partial r}-\frac{\hat{v}^2}{h}-h_z\frac{\partial\hat{v}}{\partial z}\right)\mathrm{d}z, \tag{A3b}$$

$$M_z = \pm\frac{4\pi\alpha_v}{\mathcal{D}_{kin}}\int_{-1/2}^{1/2} h\hat{w}\left(\frac{\partial\hat{w}}{\partial r}+h_z\hat{w}-h_z\frac{\partial\hat{w}}{\partial z}\right)\mathrm{d}z. \tag{A3c}$$

The quantity

$$B = \frac{\alpha_\beta\, Bd}{\mathcal{D}_{kin}}\int_{V_i} w'\vartheta'\,\mathrm{d}V \tag{A4}$$

represents the work done per unit time by buoyancy forces. Further, the heat transfer across the liquid–gas interface can be written as

$$H_{fs} = \pm\frac{2\pi\alpha_\kappa}{\mathcal{D}_{th}\,Pr}\int_{-1/2}^{1/2} h\left(\frac{\partial\hat{\vartheta}^2}{\partial r}-h_z\frac{\partial\hat{\vartheta}^2}{\partial z}\right)\mathrm{d}z. \tag{A5}$$

The sign of the rate of change of the total kinetic (and thermal) energy is related directly to the growth rate of the normal mode for which the energy budget is evaluated. Thus if one of the integral terms in (2.27) or (2.28) is positive (negative), then it contributes to a destabilisation (stabilisation) of the basic flow. Since each of the above integrands describes a particular local transport process, each term can be associated with a particular physical mechanism, either stabilising or destabilising the basic flow.

As in Nienhüser & Kuhlmann (2002), the normalised residuals of the kinetic and thermal energy budgets are defined as

$$\delta E_{kin} := \left|-\frac{\mathrm{d}E_{kin}}{\mathrm{d}t}-1+M_r+M_\varphi+M_z+\sum_{j=1}^{5} I_j+B\right|, \tag{A6a}$$

$$\delta E_{th} := \left|-\frac{\mathrm{d}E_{th}}{\mathrm{d}t}-1+\sum_{j=1}^{2} J_j+H_{fs}\right|, \tag{A6b}$$

respectively. They serve as an additional verification for the numerics. Since (2.27) and (2.28) must be satisfied exactly, the residuals must vanish. We typically find $\delta E_{kin} < 0.03$ and $\delta E_{th} < 0.01$.

For the high Prandtl number $Pr = 28$ investigated, we find the inertial terms to be always small with $I_j < 0.05$. Therefore, the velocity field of the basic flow does not enter practically the energy budget of the linear mode, and the work done by thermocapillary stresses M_r, M_φ and M_z is almost perfectly balanced by the viscous dissipation. The basic velocity field merely serves to create a basic temperature field from which temperature perturbations can gain thermal energy via J_1 and J_2.

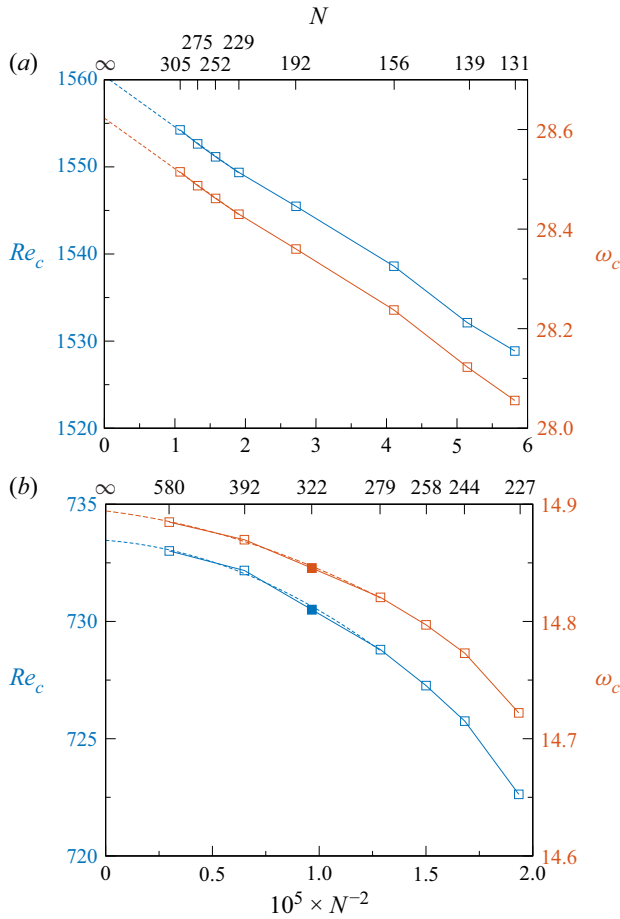

Figure 29. Critical data Re_c (blue symbols) and ω_c (red symbols) as functions of the grid size N for the reference case with $Pr = 28$, $\Gamma_{ref} = 0.66$, $\mathcal{V}_{ref} = 1$ and $Bd_{ref} = 0.41$. (*a*) Single-fluid model with adiabatic free surface, disregarding viscous stresses in the gas phase. The linear extrapolated critical data, using the four finest grids (dashed curves), are $(Re_c, \omega_c)^{extra} = (1560, 28.62)$. (*b*) Reference case (two-fluid model) including the gas phase. The critical data extrapolate quadratically (dashed curves) to $(Re_c, \omega_c)^{extra} = (733.5, 14.89)$. The solid symbols in (*b*) indicate the resolution used for production runs.

Appendix B. Numerical tests

B.1. *Grid convergence*

To prove grid convergence, we carry out a linear stability analysis for the reference case defined in § 2.5 – i.e. for $Pr = 28$, $\Gamma_{ref} = 0.66$, $\mathcal{V}_{ref} = 1$ and $Bd_{ref} = 0.41$ – and monitor the dependence of the critical Reynolds number Re_c and the critical frequency $\omega_c = \mathrm{Im}(\mu_c)$ as functions of $N = \sqrt{N_{tot}}$, where N_{tot} is the total number of finite volumes employed. For a second-order numerical scheme, the critical Reynolds number Re_c should scale $\sim N^{-2}$ for large N. This behaviour is confirmed for the single-fluid model in which viscous stresses in the gas phase are neglected and the free surface is assumed to be adiabatic. The critical data for this simplified model ($m_c = 4$) are shown in figure 29(*a*). It should be noted that the difference between $Re_c(m = 4)$ and the closest neutral Reynolds number $Re_n(m = 3)$ is less than 1 %. Linear regression of the data for the four

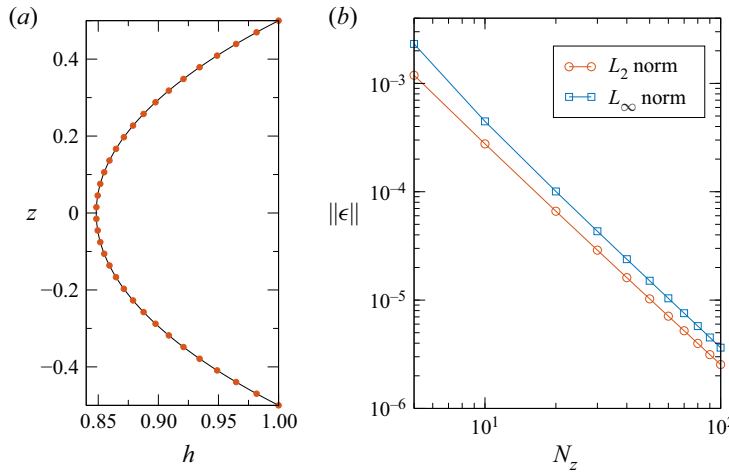

Figure 30. (*a*) Comparison of the catenoid profile $h_{cat}(z)$ (line) according to (B1) with the numerical solution $h(z)$ (red dots) of (3.1) for $\Gamma = 1$ and $h_0 = 0.848$ using an equidistant grid with $N_z = 34$ grid points. (*b*) L_2 and L_∞ norms of the deviation ϵ of the numerical solution from the exact catenoid as functions of the number of grid points N_z.

finest grids (dashed lines in figure 29*a*) yields the extrapolated values $(Re_c, \omega_c)^{extra} = (1560, 28.62)$. These extrapolated values deviate by only (0.4 %, 0.4 %) from the critical data $(Re_c, \omega_c)^{N=305} = (1554, 28.52)$ obtained on the finest mesh.

For the present two-fluid model that takes into account the gas phase, the critical wavenumber changes to $m_c = 3$ and the Reynolds number is remarkably lower. The data do not show a linear convergence (figure 29*b*), because the grid is not homogeneous and involves grid points in the gas as well as in the liquid phase that are refined differently. Nevertheless, a regression with a polynomial of second order (dashed lines in figure 29*b*) yields $(Re_c, \omega_c)^{extra} = (733.5, 14.89)$. Since the finest mesh used in figure 29(*b*) is numerically too expensive for the intended quasi-continuous parameter variations, production runs were carried out using the resolution $N = 322$ (solid symbols in figure 29*b*). The error is estimated by comparison of the extrapolated values $(Re_c, \omega_c)^{extra}$ with the result $(Re_c, \omega_c)^{N=322} = (730.5, 14.85)$. Again, we arrive at an error estimate of at most 0.4 % for both the critical Reynolds number and the critical frequency. From these results, we conclude grid convergence and proceed using the grid $N = 322$ for all stability analyses.

B.2. *Code verification*

In a first verification step the interfacial shape is considered. In the case of weightlessness ($Bo = 0$) the Young–Laplace equation (3.1) has the closed-form solution of a catenoid (Kenmotsu 1980; Langbein 2002):

$$h_{cat}(z) = h_0 \cosh\left(\frac{z}{h_0}\right), \tag{B1}$$

where $h_0 = h(0)$ is related to Γ by $h_0 \cosh(1/2h_0) = 1/\Gamma$ (cf. (2.15)). In figure 30(*a*), we compare the numerically computed shape of the free surface with the catenoid profile for $\Gamma = 1$ and $h_0 = 0.848$. The L_2 and L_∞ norms of the deviation $\epsilon = h(z) - h_{cat}(z)$ of the

Grid/	$Re = 3000$		$Re = 5000$		$Re = 7000$	
Reference	$\tilde{\psi}_{max}$	$\log(\lvert\delta Nu\rvert)$	$\tilde{\psi}_{max}$	$\log(\lvert\delta Nu\rvert)$	$\tilde{\psi}_{max}$	$\log(\lvert\delta Nu\rvert)$
121×121	2.1093	−12.3	2.0274	−12.2	1.9567	−12.4
160×160	2.1171	−12.2	2.0306	−12.2	1.9622	−12.4
260×260	2.1188	−13.1	2.0321	−12.9	1.9632	−12.5
360×360	2.1193	−12.3	2.0324	−12.3	1.9634	−12.4
Leypoldt *et al.* (2000)	2.09	—	1.97	—	1.86	—
Nienhüser (2002)	—	—	2.03	−2.52	—	—
Romanò *et al.* (2017)	2.1783	—	2.0605	—	1.9735	—

Table 8. Scaled maximum absolute value of the Stokes stream function $\tilde{\psi}_{max} = \max|\psi| \times 10^3$ and relative (logarithmic) error $\delta Nu = \sum_i Nu_i / \max|Nu_i|$ of the total Nusselt number for the flow in a cylindrical liquid bridge with $\Gamma = 1$, $\mathcal{V} = 1$, $Pr = 4$, $Bd = 0$ and an adiabatic free surface for different grid resolutions. The comparison is made with Leypoldt *et al.* (2000), Nienhüser (2002) and Romanò *et al.* (2017).

numerical solution $h(z)$ from the analytical counterpart $h_{cat}(z)$ are displayed in figure 30(*b*) as functions of the number of grid points N_z, distributed uniformly over the height of the liquid bridge. From the graphs, a second-order convergence is obvious.

To verify the computations of the basic flow, the maximum absolute value of the Stokes stream function ψ arising in the centre of the thermocapillary vortex is compared with literature data of Leypoldt *et al.* (2000), Nienhüser (2002) and Romanò *et al.* (2017) for the single-fluid model. Data for different grids $N_r \times N_z$ and Reynolds numbers are provided in table 8 for $\Gamma = 1$, $\mathcal{V} = 1$, $Bd = 0$ and an adiabatic free surface. As can be seen, the present results are in good agreement with the literature data.

Apart from this local test, we checked the energy preservation by computing the total heat flux through the liquid bridge in non-dimensional form:

$$\sum_i Nu_i = -\sum_i \int_{S_i} \boldsymbol{n}_i \cdot \nabla\vartheta \, \mathrm{d}S = 0, \tag{B2}$$

where Nu_i is the Nusselt number for the circular hot and cold walls in contact with the liquid, and for the free surface ($i \in [h, c, fs]$). Since the free surface is adiabatic, $Nu_{fs} = 0$ and the heat flux through the cold wall must balance the heat flux through the hot wall. The relative error in the energy preservation of the basic state expressed by $\delta Nu = \sum_i Nu_i / \max|Nu_i|$ is also provided in table 8. We find that the thermal energy of the basic state is conserved up to $\delta Nu < 10^{-12}$ for all presented calculations. The same order of magnitude of δNu was also obtained for cases with a non-vanishing heat flux through the free surface ($Nu_{fs} \neq 0$, not shown).

Finally, the linear stability analysis is verified by comparing with the critical parameters for the common benchmark of a cylindrical liquid bridge with $\Gamma = 1$, $Pr = 4$, $Bd = 0$ and adiabatic free surface. Table 9 shows that our results for Re_c and ω_c, and a resolution of $N = 176 \times 197$ grid points in the radial and axial directions, respectively, deviate less than 0.2 % from the data of Levenstam *et al.* (2001) and Carrión *et al.* (2020). The deviation of Re_c by 0.8 % from the result of Levenstam *et al.* (2001) for $Pr = 7$ is slightly larger. The somewhat larger deviation by 4.5 % of Re_c from the result of Wanschura *et al.* (1995) for $Pr = 4$ can be explained by the regularisation of the thermocapillary stresses within 10 % of d from each corner employed by Wanschura *et al.* (1995). Since the regularisation tends to reduce the driving force, a higher critical Reynolds number was obtained by these authors. Furthermore, the deviation of Re_c by 2.8 % with respect to the result of Shevtsova,

Authors	Resolution	$Pr = 4$		$Pr = 7$	
		Re_c	ω_c	Re_c	ω_c
Present	176 × 197 (FV)	1002	28.43	876	22.91
Wanschura *et al.* (1995)	20 × 80 (Spectral, FD)	1047	27.9	—	—
Shevtsova *et al.* (2001)	$(N_r, N_\varphi, N_z) = (25, 16, 21)$ (FV simulation)	1030	28.72	—	—
Levenstam *et al.* (2001)	41 × 41 (FE)	1002	28.5	869	22.9
Carrión *et al.* (2020)	91 × 91 (FD)	1000	28.45	—	—

Table 9. Critical data for common benchmarks ($Pr = 4$ and 7) of a cylindrical liquid bridge with $\Gamma = 1$, adiabatic free surface, zero gravity, and negligible viscous stresses from the gas phase. A comparison is made with Wanschura *et al.* (1995), Shevtsova *et al.* (2001), Levenstam *et al.* (2001) and Carrión *et al.* (2020). Here, FV indicates finite volumes, FD indicates finite differences, and FE indicates finite elements.

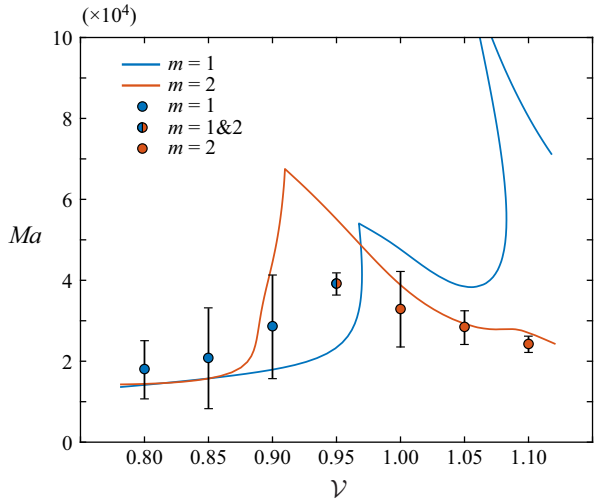

Figure 31. Neutral Marangoni numbers (lines) as function of the volume ratio $\mathcal{V}$ for $Pr = 28$, $Bd = 0.92$, $\Gamma = 1$, $\Gamma_{rod} = 4.8$ and $\eta = 5$. A comparison is made with the experimental critical Marangoni numbers (symbols) extracted from figure 6(*a*) of Yano *et al.* (2016) for zero gas flow rate in the ambient air. The wavenumbers are $m = 1$ (blue symbols) and $m = 2$ (red symbols).

Melnikov & Legros (2001) could be related to their method of determining the critical onset by numerical simulation and by using a coarser mesh (25 × 21) in the (r, z) plane. In view of these comparisons, we consider our code verified.

B.3. *Code validation*

For the purpose of validation, we also compared our linear stability analysis for $Pr = 28$, $\Gamma = 1$ and $Bd = 0.92$ with the experimental data measured by Yano *et al.* (2016). To match with the experimental geometry, we adopted not only Γ and Bd, but also $\eta = 5$ and $\Gamma_{rod} = 4.8$. Figure 31 shows the neutral and critical Marangoni numbers as functions of the volume ratio $\mathcal{V}$. As can be seen, the numerical critical Marangoni numbers, using resolution $N = 322$, agree with the experimental data within the experimental error bar.

Only for $\mathcal{V} = 0.95$ does some deviation exist. This can be explained, however, by the nearby codimension-two points at which the azimuthal wavenumber of the critical mode changes from $m = 1$ to $m = 2$. Near these points, the dynamics of the supercritical flow can be complicated. In fact, for $\mathcal{V} = 0.95$, Yano *et al.* (2016) found what they called a mixed mode with $m = 1$ and $m = 2$, which must be a result of supercritical nonlinear interactions. Moreover, the critical curve for $m = 1$ has a large slope with respect to $\mathcal{V}$ such that small uncertainties in $\mathcal{V}$ result in large deviations of the critical data. When comparing with the experiments, one has to keep in mind that the detailed experimental conditions may deviate to some degree from the numerical ones, and that the effect of temperature-dependent material parameters is not taken into account within the present modelling (except for ρ, ρ_g and σ). Given the remaining differences between experiment and numerics, and the relatively large error bar for the experimental critical Marangoni numbers measured by other authors, our code can also be considered validated.

References

Barmak, I., Romanò, F. & Kuhlmann, H.C. 2021 Finite-size coherent particle structures in high-Prandtl-number liquid bridges. *Phys. Rev. Fluids* **6**, 084301.

Batchelor, G.K. & Gill, A.E. 1962 Analysis of the stability of axisymmetric jets. *J. Fluid Mech.* **14**, 529–551.

Canright, D. 1994 Thermocapillary flow near a cold wall. *Phys. Fluids* **6**, 1415–1424.

Carpenter, B.M. & Homsy, G.M. 1989 Combined buoyant–thermocapillary flow in a cavity. *J. Fluid Mech.* **207**, 121–132.

Carrión, L.M., Herrada, M.A. & Montanero, J.M. 2020 Influence of the dynamical free surface deformation on the stability of thermal convection in high-Prandtl-number liquid bridges. *Intl J. Heat Mass Transfer* **146**, 118831.

Chen, Q.S. & Hu, W.R. 1998 Influence of liquid bridge volume on instability of floating half zone convection. *Intl J. Heat Mass Transfer* **41**, 825–837.

Chun, C.H. & Wuest, W. 1979 Experiments on the transition from the steady to the oscillatory Marangoni-convection of a floating zone under reduced gravity effect. *Acta Astronaut.* **6** (9), 1073–1082.

Craster, R.V. & Matar, O.K. 2009 Dynamics and stability of thin liquid films. *Rev. Mod. Phys.* **81**, 1131–1198.

Cröll, A., Müller-Sebert, W., Benz, K.W. & Nitsche, R. 1991 Natural and thermocapillary convection in partially confined silicon melt zones. *Microgravity Sci. Technol.* **3**, 204–215.

Diez, J.A. & Kondic, L. 2002 Computing three-dimensional thin film flows including contact lines. *J. Comput. Phys.* **183** (1), 274–306.

Fu, B.-I. & Ostrach, S. 1985 Numerical solution of thermocapillary flows in floating zones. In *Transport Phenomena in Materials Processing*, Power Engng Div. vol. 10, Heat Transfer Div. vol. 29, p. 1. ASME.

Fujimoto, S., Ogasawara, T., Ota, A., Motegi, K. & Ueno, I. 2019 Effect of heat loss on hydrothermal wave instability in half-zone liquid bridges of high Prandtl-number fluid. *Intl J. Microgravity Sci. Appl.* **36**, 360204.

Fujimura, K. 2013 Linear and weakly nonlinear stability of Marangoni convection in a liquid bridge. *J. Phys. Soc. Japan* **82**, 074401.

Gaponenko, Y., Mialdun, V.Y.A., Nepomnyashchy, A. & Shevtsova, V. 2021 Hydrothermal waves in a liquid bridge subjected to a gas stream along the interface. *J. Fluid Mech.* **908**, A34.

Gaponenko, Y., Mialdun, A. & Shevtsova, V. 2012 Shear driven two-phase flows in vertical cylindrical duct. *Intl J. Multiphase Flow* **39**, 205–215.

Gottlieb, R.G. & Thompson, B.F. 2010 Bisected direct quadratic *regula falsi*. *Appl. Maths Sci.* **4**, 709–718.

Hu, W.R., Shu, J.Z., Zhou, R. & Tang, Z.M. 1994 Influence of liquid bridge volume on the onset of oscillation in floating zone convection. I. Experiments. *J. Crystal Growth* **142**, 379–384.

Hu, W.R., Tang, Z.M. & Li, K. 2008 Thermocapillary convection in floating zones. *Appl. Mech. Rev.* **61**, 010803.

Hurle, D.T.J. & Jakeman, E. 1981 Introduction to the techniques of crystal growth. *PCH Phys. Chem. Hydrodyn.* **2** (4), 237–244.

Imaishi, N., Yasuhiro, S., Akiyama, Y. & Yoda, S. 2001 Numerical simulation of oscillatory Marangoni flow in half-zone liquid bridge of low Prandtl number fluid. *J. Crystal Growth* **230**, 164–171.

IRIKURA, M., ARAKAWA, Y., UENO, I. & KAWAMURA, H. 2005 Effect of ambient fluid flow upon onset of oscillatory thermocapillary convection in half-zone liquid bridge. *Microgravity Sci. Technol.* **16** (1), 176–180.

KAMOTANI, Y. & OSTRACH, S. 1998 Theoretical analysis of thermocapillary flow in cylindrical columns of high Prandtl number fluids. *Trans. ASME J. Heat Transfer* **120**, 758–764.

KAMOTANI, Y., WANG, L., HATTA, S., WANG, A. & YODA, S. 2003 Free surface heat loss effect on oscillatory thermocapillary flow in liquid bridges of high Prandtl number fluids. *Intl J. Heat Mass Transfer* **46**, 3211–3220.

KANG, Q., WU, D., DUAN, L., HU, L., WANG, J., ZHANG, P. & HU, W. 2019 The effects of geometry and heating rate on thermocapillary convection in the liquid bridge. *J. Fluid Mech.* **881**, 951–982.

KASPERSKI, G., BATOUL, A. & LABROSSE, G. 2000 Up to the unsteadiness of axisymmetric thermocapillary flows in a laterally heated liquid bridge. *Phys. Fluids* **12**, 103–119.

KAWAMURA, H., NISHINO, K., MATSUMOTO, S. & UENO, I. 2012 Report on microgravity experiments of Marangoni convection aboard international space station. *Trans. ASME J. Heat Transfer* **134** (3), 031005.

KAWAMURA, H. & UENO, I. 2006 Review on thermocapillary convection in a half-zone liquid bridge with high *Pr* fluid: onset of oscillatory convection, transition of flow regimes, and particle accumulation structure. In *Surface Tension-Driven Flows and Applications* (ed. R. Savino), chap. 1, pp. 1–24. Research Signpost.

KENMOTSU, K. 1980 Surfaces of revolution with prescribed mean curvature. *Tôhoku Math. J.* **32** (1), 147–153.

KUHLMANN, H.C. 1999 *Thermocapillary Convection in Models of Crystal Growth*. Springer Tracts in Modern Physics, vol. 152. Springer.

KUHLMANN, H. & ALBENSOEDER, S. 2008 Three-dimensional flow instabilities in a thermocapillary-driven cavity. *Phys. Rev.* E **77**, 036303.

KUHLMANN, H.C., LUKASSER, M. & MULDOON, F.H. 2011 Engineering Marangoni flows (EMA). ASAP6 819714. FFG.

KUMAR, S. 2015 Liquid transfer in printing processes: liquid bridges with moving contact lines. *Annu. Rev. Fluid Mech.* **47**, 67–94.

LANDAU, L.D. & LIFSCHITZ, E.M. 1959 *Fluid Mechanics*. Pergamon Press.

LANGBEIN, D. 2002 *Capillary surfaces: shape – stability – dynamics, in particular under weightlessness*. Springer Tracts in Modern Physics, vol. 178. Springer.

LAPPA, M. 2003 Three-dimensional numerical simulation of Marangoni flow instabilities in floating zones laterally heated by an equatorial ring. *Phys. Fluids* **15**, 776–789.

LAPPA, M. 2004 Combined effect of volume and gravity on the three-dimensional flow instability in noncylindrical floating zones heated by an equatorial ring. *Phys. Fluids* **16**, 331–343.

LAPPA, M. 2005 Analysis of flow instabilities in convex and concave floating zones heated by an equatorial ring under microgravity conditions. *Comput. Fluids* **34**, 743–770.

LAPPA, M., SAVINO, R. & MONTI, R. 2001 Three-dimensional numerical simulation of Marangoni instabilities in non-cylindrical liquid bridges in microgravity. *Intl J. Heat Mass Transfer* **44**, 1983–2003.

LEHOUCQ, R.B., SORENSEN, D.C. & YANG, C. 1998 *ARPACK Users' Guide: Solution of Large-Scale Eigenvalue Problems with Implicitly Restarted Arnoldi Methods*. SIAM.

LEVENSTAM, M. & AMBERG, G. 1994 Hydrodynamical instabilities of thermocapillary flow in a half zone. Supplement of the PhD Thesis of M. Levenstam, KTH Stockholm.

LEVENSTAM, M. & AMBERG, G. 1995 Hydrodynamic instabilities of thermocapillary flow in a half-zone. *J. Fluid Mech.* **297**, 357–372.

LEVENSTAM, M., AMBERG, G. & WINKLER, C. 2001 Instabilities of thermocapillary convection in a half-zone at intermediate Prandtl numbers. *Phys. Fluids* **13**, 807–816.

LEVICH, V.G. & KRYLOV, V.S. 1969 Surface tension-driven phenomena. *Annu. Rev. Fluid Mech.* **1**, 293–316.

LEYPOLDT, J., KUHLMANN, H.C. & RATH, H.J. 2000 Three-dimensional numerical simulation of thermocapillary flows in cylindrical liquid bridges. *J. Fluid Mech.* **414**, 285–314.

LEYPOLDT, J., KUHLMANN, H.C. & RATH, H.J. 2002 Stability of hydrothermal-wave states. *Adv. Space Res.* **29**, 645–650.

LI, K., IMAISHI, N., JING, C.J. & YODA, S. 2007 Proper orthogonal decomposition of oscillatory Marangoni flow in half-zone liquid bridges of low-*Pr* fluids. *J. Crystal Growth* **307** (1), 155–170.

LI, K., MATSUMOTO, S., IMAISHI, N. & HU, W.-R. 2015 Marangoni flow in floating half zone of molten tin. *Intl J. Heat Mass Transfer* **83**, 575–585.

LI, K., XUN, B., IMAISHI, N., YODA, S. & HU, W.R. 2008 Thermocapillary flows in liquid bridges of molten tin with small aspect ratios. *Intl J. Heat Fluid Flow* **29**, 1190–1196.

MASUD, J., KAMOTANI, Y. & OSTRACH, S. 1997 Oscillatory thermocapillary flow in cylindrical columns of high Prandtl number fluids. *AIAA J. Thermophys. Heat Transfer* **11**, 105–111.

MEERBERGEN, K., SPENCE, A. & ROOSE, D. 1994 Shift-invert and Cayley transforms for detection of eigenvalues with largest real part of nonsymmetric matrices. *BIT Numer. Maths* **34**, 409–423.

MELNIKOV, D.E., SHEVTSOVA, V., YANO, T. & NISHINO, K. 2015 Modeling of the experiments on the Marangoni convection in liquid bridges in weightlessness for a wide range of aspect ratios. *Intl J. Heat Mass Transfer* **87**, 119–127.

MIHALJAN, J.M. 1962 A rigorous exposition of the Boussinesq approximation applicable to a thin layer of fluid. *Astrophys. J.* **136**, 1126–1133.

MILLS, K.C., KEENE, B.J., BROOKS, R.F. & SHIRALI, A. 1998 Marangoni effects in welding. *Phil. Trans. R. Soc. Lond.* A **356**, 911–925.

MONTI, R., SAVINO, R. & LAPPA, M. 2000 Influence of geometrical aspect ratio on the oscillatory Marangoni convection in liquid bridges. *Acta Astronaut.* **47**, 753–761.

MOTEGI, K., FUJIMURA, K. & UENO, I. 2017*a* Floquet analysis of spatially periodic thermocapillary convection in a low-Prandtl-number liquid bridge. *Phys. Fluids* **29** (7), 074104.

MOTEGI, K., KUDO, M. & UENO, I. 2017*b* Linear stability of buoyant thermocapillary convection for a high-Prandtl number fluid in a laterally heated liquid bridge. *Phys. Fluids* **29** (4), 044106.

NEITZEL, G.P., CHANG, K.-T., JANKOWSKI, D.F. & MITTELMANN, H.D. 1993 Linear-stability theory of thermocapillary convection in a model of the float-zone crystal-growth process. *Phys. Fluids* A **5**, 108–114.

NIENHÜSER, C. 2002 Lineare Stabilität achsensymmetrischer thermokapillarer Konvektion in Flüssigkeitsbrücken mit statisch und dynamisch deformierbarer Grenzfläche. PhD thesis, Fachbereich Produktionstechnik. Universität Bremen.

NIENHÜSER, C. & KUHLMANN, H.C. 2001 Dynamic free-surface deformations caused by steady axisymmetric and by time-dependent three-dimensional critical flows in thermocapillary half-zones. *Tech. Rep.* TMR-010015E. NASDA.

NIENHÜSER, C. & KUHLMANN, H.C. 2002 Stability of thermocapillary flows in non-cylindrical liquid bridges. *J. Fluid Mech.* **458**, 35–73.

NIENHÜSER, C. & KUHLMANN, H.C. 2003 Corrigendum of *Stability of thermocapillary flows in non-cylindrical liquid bridges*, J. Fluid Mech. **458**, 35–73 (2002). *J. Fluid Mech.* **480**, 333–334.

OHNISHI, M., AZUMA, H. & DOI, T. 1992 Computer simulation of oscillatory Marangoni flow. *Acta Astronaut.* **26**, 685–696.

ORON, A., DAVIS, S.H. & BANKOFF, S.G. 1997 Long-scale evolution of thin liquid films. *Rev. Mod. Phys.* **69**, 931–980.

PFANN, W.G. 1962 Zone melting. *Science* **135**, 1101–1109.

PREISSER, F., SCHWABE, D. & SCHARMANN, A. 1983 Steady and oscillatory thermocapillary convection in liquid columns with free cylindrical surface. *J. Fluid Mech.* **126**, 545–567.

ROMANÒ, F. & KUHLMANN, H.C. 2018 Finite-size Lagrangian coherent structures in thermocapillary liquid bridges. *Phys. Rev. Fluids* **3**, 094302.

ROMANÒ, F. & KUHLMANN, H.C. 2019 Heat transfer across the free surface of a thermocapillary liquid bridge. *Tech. Mech.* **39**, 72–84.

ROMANÒ, F., KUHLMANN, H.C., ISHIMURA, M. & UENO, I. 2017 Limit cycles for the motion of finite-size particles in axisymmetric thermocapillary flows in liquid bridges. *Phys. Fluids* **29** (9), 093303.

ROMANÒ, F. & KUHLMANN, H.C. 2017 Particle–boundary interaction in a shear-driven cavity flow. *Theor. Comput. Fluid Dyn.* **31**, 427–445.

SAKURAI, M., OHISHI, N. & HIRATA, A. 1996 Effect of liquid bridge form on oscillatory thermocapilllary convection under normal gravity and microgravity conditions – drop shaft experiments. In *47th International Astronautical Congress*, paper number IAF–96–J.4.06. International Astronautical Federation.

SAKURAI, M., OHISHI, N. & HIRATA, A. 2004 Effect of liquid bridge form on oscillatory thermocapillary convection under 1 g and μg conditions. *Acta Astronaut.* **55**, 977–983.

SCHWABE, D. 1981 Marangoni effects in crystal growth melts. *Physicochem. Hydrodyn.* **2**, 263–280.

SCHWABE, D. 2014 Thermocapillary liquid bridges and Marangoni convection under microgravity – results and lessons learned. *Microgravity Sci. Technol.* **26**, 1–10.

SCHWABE, D., SCHARMANN, A., PREISSER, F. & OEDER, F. 1978 Experiments on surface tension driven flow in floating zone melting. *J. Crystal Growth* **43**, 305–312.

SCRIVEN, L.E. & STERNLING, C.V. 1960 The Marangoni effects. *Nature* **187**, 186–188.

SHEN, Y. 1989 Energy stability of thermocapillary convection in a model of float-zone crystal growth. PhD thesis, Arizona State University.

SHEVTSOVA, V., GAPONENKO, Y., KUHLMANN, H.C., LAPPA, M., LUKASSER, M., MATSUMOTO, S., MIALDUN, A., MONTANERO, J.M., NISHINO, K. & UENO, I. 2014 The JEREMI-project on

thermocapillary convection in liquid bridges. Part B: overview on impact of co-axial gas flow. *Fluid Dyn. Mater. Process.* **10**, 197–240.

SHEVTSOVA, V., GAPONENKO, Y.A. & NEPOMNYASHCHY, A. 2013 Thermocapillary flow regimes and instability caused by a gas stream along the interface. *J. Fluid Mech.* **714**, 644–670.

SHEVTSOVA, V.M. & LEGROS, J.C. 1998 Oscillatory convective motion in deformed liquid bridges. *Phys. Fluids* **10**, 1621–1634.

SHEVTSOVA, V.M., MELNIKOV, D.E. & LEGROS, J.C. 2001 Three-dimensional simulations of hydrodynamic instability in liquid bridges: influence of temperature-dependent viscosity. *Phys. Fluids* **13**, 2851–2865.

SHIN-ETSU 2004 *Silicone Fluid KF-96 – Performance Test Results*. 6-1, Ohtemachi 2-chome, Chioda-ku, Tokyo, Japan.

SIM, B.C. & ZEBIB, A. 2002 Thermocapillary convection in liquid bridges with undeformable curved surfaces. *J. Thermophys. Heat Transfer* **16**, 553–561.

SIMIC-STEFANI, S., KAWAJI, M. & YODA, S. 2006 Onset of oscillatory thermocapillary convection in acetone liquid bridges: the effect of evaporation. *Intl J. Heat Mass Transfer* **49**, 3167–3179.

SIRIGNANO, W.A. & GLASSMAN, I. 1970 Flame spreading above liquid fuels: surface-tension-driven flows. *Combust. Sci. Technol.* **1**, 307–312.

SLOBOZHANIN, L.A. & PERALES, J.M. 1993 Stability of liquid bridges between equal disks in an axial gravity field. *Phys. Fluids* A **5**, 1305–1314.

SMITH, M.K. & DAVIS, S.H. 1983*a* Instabilities of dynamic thermocapillary liquid layers. Part 1. Convective instabilities. *J. Fluid Mech.* **132**, 119–144.

SMITH, M.K. & DAVIS, S.H. 1983*b* Instabilities of dynamic thermocapillary liquid layers. Part 2. Surface-wave instabilities. *J. Fluid Mech.* **132**, 145–162.

STOJANOVIC, M. & KUHLMANN, H.C. 2020*a* Flow instability in high-Prandtl-number thermocapillary liquid bridges exposed to a coaxial ambient gas stream. *Proc. Appl. Maths Mech.* **20**, e202000123.

STOJANOVIC, M. & KUHLMANN, H.C. 2020*b* Stability of thermocapillary flow in high-Prandtl-number liquid bridges exposed to a coaxial gas stream. *Microgravity Sci. Technol.* **32**, 953–959.

TAKAGI, K., OTAKA, M., NATSUI, H., ARAI, T., YODA, S., YUAN, Z., MUKAI, K., YASUHIRO, S. & IMAISHI, N. 2001 Experimental study on transition to oscillatory thermocapillary flow in a low Prandtl number liquid bridge. *J. Crystal Growth* **233**, 399–407.

TANAKA, S., KAWAMURA, H., UENO, I. & SCHWABE, D. 2006 Flow structure and dynamic particle accumulation in thermocapillary convection in a liquid bridge. *Phys. Fluids* **18**, 067103.

TANG, Z.M. & HU, W.R. 1999 Influence of liquid bridge volume on the onset of oscillation in floating half zone convection. III. Three-dimensional model. *J. Crystal Growth* **207**, 239–246.

THEOFILIS, V. 2003 Advances in global linear instability analysis of nonparallel and three-dimensional flows. *Prog. Aerosp. Sci.* **39**, 249–315.

THOMPSON, J.F., WARSI, Z.U. & MASTIN, C.W. 1985 *Numerical Grid Generation: Foundations and Applications*. Elsevier North-Holland.

THOMSON, J. 1855 On certain curious motions observable at the surfaces of wine and other alcoholic liquors. *Lond. Edinb. Dublin Philos. Mag. J. Sci.* **10**, 330–333.

UENO, I., KAWAZOE, A. & ENOMOTO, H. 2010 Effect of ambient-gas forced flow on oscillatory thermocapillary convection of half-zone liquid bridge. *Fluid Dyn. Mater. Process.* **6** (1), 99–108.

UENO, I., TANAKA, S. & KAWAMURA, H. 2003 Oscillatory and chaotic thermocapillary convection in a half-zone liquid bridge. *Phys. Fluids* **15**, 408–416.

UENO, I. & TORII, T. 2010 Thermocapillary-driven flow in a thin liquid film sustained in a rectangular hole with temperature gradient. *Acta Astronaut.* **66**, 1017–1021.

VELTEN, R., SCHWABE, D. & SCHARMANN, A. 1991 The periodic instability of thermocapillary convection in cylindrical liquid bridges. *Phys. Fluids* A **3**, 267–279.

WANSCHURA, M., KUHLMANN, H.C. & RATH, H.J. 1996 Three-dimensional instability of axisymmetric buoyant convection in cylinders heated from below. *J. Fluid Mech.* **326**, 399–415.

WANSCHURA, M., KUHLMANN, H.C. & RATH, H.J. 1997*a* Instability of thermocapillary flow in symmetrically heated full liquid zones. In *Proceedings of the Joint Xth European and VIth Russian Symposium on Physical Science in Microgravity* (ed. V.S. Avduevsky & V.I. Polezhaev), vol. 1, pp. 172–173. St Petersburg.

WANSCHURA, M., KUHLMANN, H.C. & RATH, H.J. 1997*b* Linear stability of two-dimensional combined buoyant-thermocapillary flow in cylindrical liquid bridges. *Phys. Rev.* E **55**, 7036–7042.

WANSCHURA, M., SHEVTSOVA, V.S., KUHLMANN, H.C. & RATH, H.J. 1995 Convective instability mechanisms in thermocapillary liquid bridges. *Phys. Fluids* **7**, 912–925.

WATANABE, T., MELNIKOV, D.E., MATSUGASE, T., SHEVTSOVA, V. & UENO, I. 2014 The stability of a thermocapillary-buoyant flow in a liquid bridge with heat transfer through the interface. *Microgravity Sci. Technol.* **26**, 17–28.

WESSELING, P. 2009 *Principles of Computational Fluid Dynamics*. Springer.

XU, J.-J. & DAVIS, S.H. 1984 Convective thermocapillary instabilities in liquid bridges. *Phys. Fluids* **27**, 1102–1107.

XU, J. & ZEBIB, A. 1998 Oscillatory two- and three-dimensional thermocapillary convection. *J. Fluid Mech.* **364**, 187–209.

XUN, B., LI, K. & HU, W.-R. 2010 Effect of volume ratio on thermocapillary flow in liquid bridges of high-Prandtl-number fluids. *Phys. Rev.* E **81**, 036324.

YANO, T., HIROTANI, M. & NISHINO, K. 2018*a* Effect of interfacial heat transfer on basic flow and instability in a high-Prandtl-number thermocapillary liquid bridge. *Intl J. Heat Mass Transfer* **125**, 1121–1130.

YANO, T., MARUYAMA, K., MATSUNAGA, T. & NISHINO, K. 2016 Effect of ambient gas flow on the instability of Marangoni convection in liquid bridges of various volume ratios. *Intl J. Heat Mass Transfer* **99**, 182–191.

YANO, T., NISHINO, K., MATSUMOTO, S., UENO, I., KOMIYA, A., KAMOTANI, Y. & IMAISHI, N. 2018*b* Overview of 'dynamic surf' project in Kibo – dynamic behavior of large scale thermocapillary liquid bridges in microgravity. *Intl J. Microgravity Sci. Appl.* **35**, 350102.

YANO, T., NISHINO, K., MATSUMOTO, S., UENO, I., KOMIYA, A., KAMOTANI, Y. & IMAISHI, N. 2018*c* Report on microgravity experiments of dynamic surface deformation effects on Marangoni instability in high-Prandtl-number liquid bridges. *Microgravity Sci. Technol.* **30**, 599–610.

YANO, T., NISHINO, K., UENO, I., MATSUMOTO, S. & KAMOTANI, Y. 2017 Sensitivity of hydrothermal wave instability of Marangoni convection to the interfacial heat transfer in long liquid bridges of high Prandtl number fluids. *Phys. Fluids* **29** (4), 044105.

YASNOU, V., GAPONENKO, Y., MIALDUN, A. & SHEVTSOVA, V. 2018 Influence of a coaxial gas flow on the evolution of oscillatory states in a liquid bridge. *Intl J. Heat Mass Transfer* **123**, 747–759.

YOUNG, N.O., GOLDSTEIN, J.S. & BLOCK, M.J. 1959 The motion of bubbles in a vertical temperature gradient. *J. Fluid Mech.* **6**, 350–356.

Paper 2

Stojanović, M., Romanò, F., Kuhlmann, H. C. (2023), 'High-Prandtl-number thermocapillary liquid bridges with dynamically deformed interface: Effect of an axial gas flow on the linear stability (submitted)', *J. Fluid Mech.*

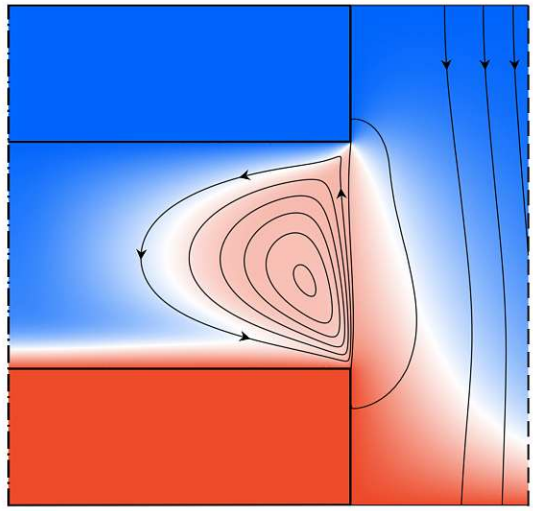

High-Prandtl-number thermocapillary liquid bridges with dynamically deformed interface: Effect of an axial gas flow on the linear stability

Mario Stojanović[1] †, Francesco Romanò[2] ‡, Hendrik C. Kuhlmann[1] ¶,

[1]Institute of Fluid Mechanics and Heat Transfer, TU Wien, Getreidemarkt 9-BA, 1060 Vienna, Austria
[2]Univ. Lille, CNRS, ONERA, Arts et Métiers Institute of Technology, Centrale Lille, UMR 9014 - LMFL - Laboratoire de Mécanique des Fluides de Lille - Kampé de Fériet, F-59000, Lille, France

(Received xx; revised xx; accepted xx)

The linear stability of the axisymmetric steady flow in a thermocapillary liquid bridge made from 2-cSt silicone oil (Pr = 28) is investigated numerically. The liquid bridge is heated either from above or below and exposed to an axial air flow which is confined to a concentric tube surrounding the bridge. At the annular inlet, the air flow is fully developed and has the same temperature as the adjacent support rod. Using an extended Oberbeck–Boussinesq approximation in which the density of both fluids depends linearly on the temperature in all equations, critical thermocapillary Reynolds numbers are obtained depending on the strength of the imposed axial air flow. The critical conditions are sensitive with respect to the direction of a weak air flow, because the air flow changes plateau value of the interfacial temperature midway between the hot and cold ends. For stronger air flow the critical thermocapillary Reynolds number almost saturates at moderate values. Throughout, the instability arises as a hydrothermal wave with the gas phase being passive. The dynamic interface deformations for axisymmetric flow caused by the thermocapillarity flow in the liquid and by the stresses from the air flow are considered separately. Apart from turning points of the critical curve, the impact of dynamic surface deformations on the critical thermocapillary Reynolds number is moderate.

Key words: Liquid bridges; Thermocapillarity; Instability; Gas/liquid flow

1. Introduction

When the temperature varies along the interface between two immiscible fluids, the thermocapillary effect generates a tangential shear stress that drives a motion in both fluids. This effect is important in many systems like, e.g., welding (Mills *et al.* 1998) or crystal growth from the melt (Hurle 1994). Crystals grown by the floating-zone technique (Pfann 1962) can exhibit impurity inhomogeneities caused by the onset of a time-dependent flow in the opaque melt. To understand the underlying physics, the model problem of a liquid bridge between coaxial cylindrical solid support rods has been devised. The original full-zone problem in which the cylinder-like free surface is heated symmetrically with respect to the equator (Chang & Wilcox 1975) was further simplified to a half-zone problem

† Email address for correspondence: mario.stojanovic@tuwien.ac.at
‡ Email address for correspondence: francesco.romano@ensam.eu
¶ Email address for correspondence: hendrik.kuhlmann@tuwien.ac.at

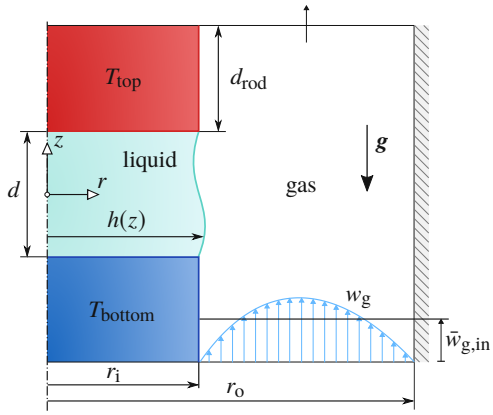

Figure 1: Schematic of a differentially heated liquid bridge (cyan) with a deformed interface $h(z)$ between the support rods (both with the same radius r_{i} and length d_{rod}) which are concentrically mounted in a tube (radius r_{o}, gray, hatched). The sketch shows the situation when the liquid is heated from above ($T_{\mathrm{top}} > T_{\mathrm{bottom}}$, red) and an imposed gas flow (bright blue) with velocity profile $w_{\mathrm{g}}(r)$ enters the annular region from below with a temperature T_{bottom} (blue). The polar coordinate system is centred in the liquid bridge and the gravity vector is always directed in the negative z direction.

(Schwabe *et al.* 1978). In the half-zone problem, which is more amenable to experimentation, the liquid bridge is differentially heated via the support rods. A sketch is shown in figure 1. Basic numerical models assuming a fixed cylindrical interface were able to qualitatively predict the instability of the steady axisymmetric basic flow. For low Prandtl numbers, the first instability is inertial and leads to a steady three-dimensional flow (Levenstam & Amberg 1995; Wanschura *et al.* 1995), while for high Prandtl numbers, the first instability arises as a pair of azimuthally travelling hydrothermal waves (Wanschura *et al.* 1995), first discovered for plane layers by Smith & Davis (1983*a*). Parallel to numerical investigations, experiments have been carried out, mainly for transparent high-Prandtl-number liquids. By today, the half-zone problem, or the thermocapillary liquid bridge, has become the most important paradigm for thermocapillary convection (Kuhlmann 1999). Apart from the Prandtl number Pr, the thermocapillary Reynolds number Re, or the Marangoni number Ma = PrRe, is the most important parameter measuring the strength of the driving force, which is proportional to the total variation of the surface tension along the interface.

Some features of real experiments have been very difficult to implement in numerical analyses. These are the dynamics of the free surface and the heat (and mass) transfer across it. The importance of the heat transfer for the critical Reynolds number has been pointed out by Kamotani *et al.* (2003). Its significance is also reflected by the scatter of critical Reynolds numbers for the onset of hydrothermal waves in high-Prandtl-number liquid bridges obtained in different experiments and by different investigators. The sensitivity with respect to the thermal conditions in the ambient atmosphere has been proposed to be utilised for controlling the onset of oscillations by exposing the liquid bridge to a well-defined gas flow (Yasnou *et al.* 2012; Shevtsova *et al.* 2014).

In early numerical investigations, the heat transfer across the interface has been treated by Newton's law of cooling (Neitzel *et al.* 1992; Kuhlmann & Rath 1993). Even for an adiabatic-free surface, this model was successful in qualitatively describing the instability and its mechanism (Wanschura *et al.* 1997). Melnikov & Shevtsova (2014) calculated the critical Marangoni number for the onset of hydrothermal waves for different variants of Newton's law. They tested models using different ambient reference temperatures: (a) the temperature

of the hot wall, (b) the temperature of the cold wall and (c) an ambient temperature linearly depending on the axial coordinate. The critical Marangoni numbers as a function of the Biot number strongly depended on the heat transfer model used because neither the heat transfer coefficient for an assumed environmental reference temperature is known nor does Newton's law correctly capture the spatial dependence of the local heat transfer rate.

The sensitivity of the critical conditions on the unknown model parameters thus calls for a more accurate treatment of the problem by including the flow in the gas phase into the analysis. The present work is intended to understand how a gas flow affects the critical Reynolds number and the instability mechanism. To that end a numerical linear stability analysis of the axisymmetric steady basic two-phase flow is carried out. In addition, the influence of the dynamic deformability of the liquid–gas interface on the critical conditions is studied.

Axisymmetric two-phase flow

The typical setup enabling a better control of the heat transfer is to mount the liquid bridge inside of a concentric shield cylinder (Preisser *et al.* 1983). But even if the shield cylinder is closed, sealing the gas phase, the critical Marangoni number and the modal structure depend on the wall temperature of the shield cylinder (Yano *et al.* 2017). For high-Prandtl-number liquids Romanò & Kuhlmann (2019) demonstrated the strong dependence of the local interfacial heat flux density on the axial coordinate. Moreover, by carrying out a large number of calculations of the steady axisymmetric thermocapillary flow in the presence of the surrounding gas, being confined to an adiabatic sealed cylindrical container, they developed fit functions for the true local interfacial heat flux valid for a wide range of Reynolds numbers and height-to-radius ratios of the liquid bridge (aspect ratio Γ). The fit function can be implemented in a single-fluid model using Newton's law with a space-dependent Biot function. This approach promises a significant reduction of the numerical effort as compared to the two-phase approach, while the thermal conditions are accurately represented.

When the shield tube has open ends, the liquid bridge can be exposed to a defined gas flow without swirl, which has the same temperature at the inlet as the adjacent support rod. In this case, the radius ratio $\eta = r_o/r_i$ (figure 1) becomes important: For large η, viscous stresses exerted on the interface by the gas flow are small and may be negligible. In this case, the effect of the gas flow on the liquid flow is mainly thermal. If, on the other hand, the air gap $\eta - 1$ is small, viscous stresses become important and may even dominate.

Gaponenko *et al.* (2012) investigated the effect of viscous stresses from the gas flow experimentally and numerically by considering the isothermal problem in which a toroidal vortex is solely driven by a gas flow through a relatively narrow annular gap with $\eta = 1.\bar{6}$. Depending on the strength of the gas flow, they found the axisymmetric toroidal vortex slightly displaced. Furthermore, when the dynamic viscosity of the liquid is more than 100 times that of the gas, the strength of the vortex scales linearly with the gas flow Reynolds number Re'_g, based on the mean gas velocity and twice the width of the air gap. Similar results were reported by Gaponenko *et al.* (2011*b*). Gaponenko *et al.* (2011*a*) used the same isothermal setup, but concentrated on the effect of the gas flow on the shape of the liquid bridge. For all cases considered, the gas-flow-induced deformation of the liquid bridge was much smaller than the one due to the hydrostatic pressure difference.

The same setup, but now with differentially heated support cylinders to include the thermocapillary effect, was considered by Shevtsova *et al.* (2013). Using Fluent, they numerically simulated the axisymmetric flow in liquid bridges made from n-decane and 5-cSt silicone oil in air, which had a temperature identical to the upstream support rod. For a tight gap with $\eta = 1.\bar{6}$, $\mathrm{Re}'_g \gtrsim 100$, and a liquid bridge with an indeformable interface and twice as long as its radius, the strength and structure of the flow in the liquid are strongly

affected by viscous stresses from the gas, even leading to multiple flow separations on the interface such that the surface flow is locally directed opposite to the thermocapillary stress. Furthermore, they found axisymmetric instabilities for large gas flow rates, leading to a time dependent flow. When the air comes from the cold side, the axisymmetric waves propagate to the cold side, i.e. upstream of the gas flow. Even though the mechanical shear stress was large, the waves were interpreted as being due to a modification of the Pearson mechanism (Pearson 1958), because the gas is cooling the interface, potentially leading to Marangoni rolls superimposed to the basic flow which could be advected by the basic surface flow. Part of these results have been published earlier by Gaponenko & Shevtsova (2012). Also Gaponenko *et al.* (2011*c*) reported similar results.

In their numerical study using STAR-CCM+, Yano & Nishino (2020) considered the axisymmetric flow in a thermocapillary liquid bridge for a moderately wide gap with $\eta = 3$. The gas at the inlet had the same temperature as the adjacent support rod. They found viscous stresses have a negligible effect on the flow in the liquid. But the flow direction and the temperature of the shield cylinder (which was varied) had a strong influence on the interfacial heat transfer and thus on the flow, even deep inside of the liquid.

Instability of the axisymmetric two-phase flow

In one of the first experimental investigations of the effect of an axial gas flow on the onset of hydrothermal waves, Ueno *et al.* (2010) used a 2-cSt liquid bridge heated from above in air with a shield tube of $\eta = 5$ and a gas temperature equal to the temperature of the support rod upstream of the airflow. They found a significant and almost linear dependence of the critical parameters on the mean gas flow rate measured by the gas flow Reynolds number $\mathrm{Re}'_g \in [-100, 100]$. For the wide air gap used, the change of the critical onset is mainly due to thermal effects, because the gas temperature differs from that of the surface of the liquid. For the same wide air gap, Yano *et al.* (2016) carried out experiments with liquid bridges heated from above under a weak airflow and an air temperature as in Ueno *et al.* (2010). The temperature of the cylindrical shield was kept constant. Likewise, the critical Marangoni numbers depended sensitively on the gas flow rate. The critical Marangoni numbers Ma_c obtained could be well correlated by the normalised total heat flux through the interface, which was obtained by numerically computing the basic axisymmetric flow for the measured values of Ma_c. However, in terms of the total normalised heat flux through the interface, the critical Marangoni number can be extremely sensitive. This indicates, once again, that the total heat flux is not a suitable parameter to characterise the onset conditions and that the heat flux must be considered space resolved.

As a first step towards a three-dimensional linear stability analysis, Ryzhkov & Shevtsova (2012) simplified the problem by considering an indeformable infinitely long liquid bridge similar as in (Xu & Davis 1984), but with an axial gas flow inside an annulus. An additional thermocapillary flow is driven by an imposed linear variation of the axial temperature in the whole system, while a zero axial mean flow was enforced in the liquid phase. A linear stability analysis shows that a gas flow parallel to the thermocapillary stress (co-flow) acts destabilising. A counter-flow can act stabilising or destabilising, depending on its strength. The first three-dimensional linear stability analysis for the two-phase flow in a system of finite length is reported in Shevtsova *et al.* (2014). For a 5-cSt liquid and an air gap with $\eta = 2$, it was demonstrated that the linear stability boundaries in the plane made by the thermocapillary and the gas Reynolds numbers $(\mathrm{Re}, \mathrm{Re}'_g)$ can be quite complex. For the same liquid, argon gas and $\eta = 3$, Stojanovic & Kuhlmann (2020*b*) obtained linear stability boundaries for moderate co- and counter flow. A representative critical hydrothermal wave which exhibits a strong spiral character was characterised and discussed by Stojanovic & Kuhlmann (2020*a*). The first more comprehensive linear stability analysis of the two-phase flow is due to Stojanovic *et al.*

(2022). They carried out a linear stability analysis of the flow in a liquid bridge of 2-cSt silicone oil inside of a sealed adiabatic air-filled shield tube with a radius ratio $\eta = 4$.

Targeting the supercritical behaviour, Gaponenko *et al.* (2021) carried out experiments on the fully developed three-dimensional flow in a liquid bridge of n-decane (Pr = 14) in nitrogen using a narrow gap with $\eta = 1.\bar{6}$. Certain cases were also numerically simulated taking into account the cooling of the interface due to evaporation of the liquid. The distinguished feature of their experiments was a constant gas flow rate with a mean velocity of 0.5 m/s ($\mathrm{Re}_g' = \text{const.}$) from the cold to the hot side of the liquid bridge, but the inlet temperature of the gas was varied. This was accomplished by the heating and cooling devices of the liquid bridge being realised by very thin plates mounted on the end faces of the support rods. Depending on the inlet gas temperature travelling and standing waves were found, as well as periodic and different quasi-periodic states. An isolated window of stability of the axisymmetric flow was detected when the gas flow was considerably hotter (28 °C) than the mean temperature of the liquid bridge (25 °C) which was kept constant. Hysteresis was not observed. Practically the same results have been reported earlier by Yasnou *et al.* (2018) who used the same setup and the same conditions. They also measured stability boundaries as a function of the gas temperature. A similar study was undertaken by Gaponenko *et al.* (2023) using the same setup and methods, but for the smaller mean gas velocity of 0.1 m/s.

Dynamic deformations and surface waves

The interest in dynamic surface deformations of thermocapillary liquid bridges was partly stimulated by Kamotani & Ostrach (1998), who proposed that the onset of flow oscillations in high-Prandtl-number liquid bridges is due to the coupling between the flow and the flow-induced dynamic surface deformations via an essentially two-dimensional mechanism. Today, however, it is generally accepted that the very small dynamic surface deformations in the oscillatory supercritical flow are only passive in the absence of a gas flow (Kuhlmann & Nienhüser 2002), merely reflecting the hydrothermal wave which is created by a different mechanism (Smith & Davis 1983*a*; Wanschura *et al.* 1997), independent of dynamic deformations.

In a series of publications Ferrera *et al.* (2008), Montanero *et al.* (2008) and Shevtsova *et al.* (2008) experimentally studied dynamic surface deformations due to the thermocapillary flow for a 5-cSt liquid (Pr = 68) for sub- and supercritical conditions. The magnitude of the dynamic (flow-induced) interfacial deformation due to the thermocapillary flow was found to be less than the static deformation at the threshold, and the oscillatory deformations in the supercritical flow were below micron size. Very small supercritical oscillatory dynamic deformations with amplitudes of the order of 0.1 microns were also measured for large liquid bridges ($r_\mathrm{i} = 5.15$ mm) of high Prandtl numbers under microgravity conditions by Yano *et al.* (2018*b*).

These results established that interfacial deformation induced by the liquid flow is typically small compared to the size of the liquid bridge (mm scale). In fact, the linear stability analysis of Carrión *et al.* (2020) including dynamic deformations due to the perturbation flow, but in the absence of a gas flow and using Newton's law of cooling, has shown that dynamic deformations have very little effect on the eigenvalues and eigenvectors resulting from the linear stability problem. But the presence of a gas flow may change this picture and surface wave instabilities may be triggered by the gas flow. Surface waves have been observed in low-Prandtl-number thermocapillary layers (Smith & Davis 1983*b*; Bach & Schwabe 2015) and in two-dimensional shallow droplets with low surface tension migrating on a flat wall under a constant temperature gradient (Hu *et al.* 2023). Surface waves in the plane return flow have a rather long wavelength when the surface tension is small (Davis 1987). Based on the analysis of Smith & Davis (1983*b*) surface waves are not expected to become critical

for high-Prandtl-number liquid layer and, in particular, not in axially confined liquid bridges of high Prandtl number.

Except for the brief results of Shevtsova *et al.* (2014) and Stojanovic & Kuhlmann (2020*b*) for liquids with Pr = 67, a numerical linear stability analysis of the flow in thermocapillary liquid bridges under the influence of an axial gas flow has never been carried out. The present work intends to fill this gap and compute the influence of the gas flow on the stability of a set of typical parameters. In section 2, the problem is formulated. The popular combination of 2-cSt silicone oil and air is selected and the case of a wide gap with $\eta = 4$ is considered. Section 3 explains the numerical methods employed. Results are presented in section 4. First, the influence of the axial gas flow rate on the linear stability boundary and the critical modes is presented and analysed. Thereafter, free surface deformations due to the basic flow are discussed and their effect on the linear stability boundary is established. We close with a discussion of the results in section 6.

2. Problem Formulation

2.1. *Setup*

We consider a liquid bridge between two coaxial cylindrical rods, both of lengths $d_{\mathrm{rod}} = 1$ mm and radius $r_{\mathrm{i}} = 2.5$ mm, which are separated by a distance $d = 1.65$ mm, as shown in figure 1. The rods are aligned parallel to the acceleration of gravity $\boldsymbol{g} = -g\boldsymbol{e}_z$ with $g = 9.8\,\mathrm{m/s^2}$. The liquid bridge is surrounded by an ambient gas which is confined to a cylindrical tube of radius $r_{\mathrm{o}} = 10\,\mathrm{mm} > r_{\mathrm{i}}$ (i: inner, o: outer). The geometry is characterised by the aspect ratio of the liquid bridge Γ, the rod aspect ratio Γ_{rod} and the radius ratio η which are defined, respectively, as

$$\Gamma = \frac{d}{r_{\mathrm{i}}} = 0.66, \quad \Gamma_{\mathrm{rod}} = \frac{d_{\mathrm{rod}}}{r_{\mathrm{i}}} = 0.4 \quad \text{and} \quad \eta = \frac{r_{\mathrm{o}}}{r_{\mathrm{i}}} = 4. \tag{2.1}$$

These geometry parameters are identical to the ones of the experimental setup used by Romanò *et al.* (2017) and they are kept constant throughout.

The liquid bridge is made of 2-cSt silicone oil KF96L-2cs produced by Shin-Etsu Chemical (Japan), while the surrounding gas is air. Both are considered Newtonian fluids. The liquid bridge is kept in place by capillary forces due to the surface tension between the liquid and the gas and by pinning of the three-phase contact lines to the sharp circular edges of the support rods. The support rods are assumed to be perfect thermal conductors and are kept at different but constant temperatures $T_{\mathrm{top}} = T_0 + \Delta T/2$ and $T_{\mathrm{bottom}} = T_0 - \Delta T/2$ with $\Delta T = T_{\mathrm{top}} - T_{\mathrm{bottom}}$ and $T_0 = (T_{\mathrm{top}} + T_{\mathrm{bottom}})/2$. The temperature difference ΔT can accept positive or negative values corresponding to heating from above or from below, respectively. Since the imposed temperature difference leads to a surface tension variation along the interface, tangential interfacial stresses are induced via the thermocapillary effect. These thermocapillary stresses drive a flow both in the liquid and in the gas phase (Kuhlmann 1999).

The dependence of the surface tension

$$\sigma(T) = \sigma_0 - \gamma(T - T_0) + O\left[(T - T_0)^2\right] \tag{2.2}$$

on the temperature T is considered up to first order in $T - T_0$, where $\sigma_0 = \sigma(T_0)$ is the surface tension at the reference temperature T_0 and γ the negative surface tension coefficient. Apart from thermocapillary surface forces, the flow is also driven by body forces caused by the

Property	Dimension	KF96L-2cs	Air
density ρ_0	[kg/m^3]	871	1.184
dynamic viscosity μ	[Pa s]	1.742×10^{-3}	1.846×10^{-5}
thermal conductivity λ	[W/(mK)]	0.11	2.637×10^{-2}
specific heat c_p	[J/(kgK)]	1768.1	1005.7
thermal expansion coefficient β	[1/K]	1.24×10^{-3}	3.38×10^{-3}
surface tension σ_0	[N/m]	18.3×10^{-3}	
surface tension coefficient γ	[N/(mK)]	7×10^{-5}	

Table 1: Thermophysical properties of the working fluids 2-cSt silicone oil KF96L-2cs and air at 25°C.

thermal expansion of the liquid and the gas. Therefore, the densities

$$\rho(T) = \rho_0 \left\{1 - \beta\,(T - T_0) + O\left[(T - T_0)^2\right]\right\}, \tag{2.3a}$$

$$\rho_{\mathrm{g}}(T) = \rho_{\mathrm{g}0} \left\{1 - \beta_{\mathrm{g}}\,(T - T_0) + O\left[(T - T_0)^2\right]\right\}, \tag{2.3b}$$

of the liquid and the gas, respectively, are also considered up to first order in the temperature deviation from its algebraic mean T_0, where $\rho_0 = \rho(T_0)$ and $\rho_{\mathrm{g}0} = \rho_{\mathrm{g}}(T_0)$ are the reference densities at the mean temperature. The respective thermal expansion coefficients are $\beta = -\rho_0^{-1}(\partial\rho/\partial T)_p$ and $\beta_{\mathrm{g}} = -\rho_{\mathrm{g}0}^{-1}(\partial\rho_{\mathrm{g}}/\partial T)_p$.

A third driving force of the fluid motion is an imposed axial pressure difference between the inlet and the outlet of the gas (figure 1). The pressure difference leads to a forced flow in the annular gap between the rods and the shield tube. The direction of the mean gas flow depends on the sign of the pressure difference. Here we assume that the gas enters the annular space with a temperature equal to the rod temperature upstream of the gas flow.

For millimetric liquid bridges of the above silicone oil which can be realised under terrestrial gravity the main driving force is thermocapillarity. As long as the imposed temperature difference and the gas flow rate are small the flow in the liquid and in the gas will be axisymmetric and steady, reflecting the symmetry of the problem. Here we are interested in the stability of this steady axisymmetric flow and the dependence of its stability boundary on the forced flow in the gas phase. In order to keep this problem manageable we assume the dynamic viscosities of both fluids μ and μ_{g} as well as their thermal conductivities λ and λ_{g} and their specific heat capacities c_p and $c_{p,\mathrm{g}}$ to be constant. Moreover, the mean temperature is kept constant at $T_0 = 25°\mathrm{C}$. All physical properties for both working fluids are given in table 1.

2.2. *Governing equations and boundary conditions*

2.2.1. *Transport equations*

The flow in both, the liquid and the gas phase, is governed by the Navier–Stokes, continuity and energy equations. For the problem at hand it seems reasonable to simplify the governing equations and consider the Oberbeck–Boussinesq approximation (Landau & Lifschitz 1959; Mihaljan 1962) which takes into account density variations only in the buoyancy term. However, a proper treatment of flow-induced deformations of the liquid–gas interface requires higher-order corrections to the Oberbeck–Boussinesq approximation (Simanovskii & Nepomnyashchy 1993). Therefore, we consider the linear temperature dependence of the densities not only in the buoyancy term, but also in the entire momentum equations, the continuity equations and in the energy equations for both the liquid and the gas.

$\tilde{\rho}$	$\tilde{\mu}$	$\tilde{\lambda}$	$\tilde{c}_p$	$\tilde{\beta}$
1.359×10^{-3}	0.010597	0.23973	0.5688	2.7258

Table 2: Ratios of the thermophysical parameters between air and 2-cSt silicone oil as defined in (2.6).

Within this approximation we consider the following equations for the velocity $\boldsymbol{u}$, pressure p and temperature field T for the liquid phase

$$\rho\frac{\partial \boldsymbol{u}}{\partial t} + \rho\boldsymbol{u}\cdot\nabla\boldsymbol{u} = -\nabla p - \rho g\boldsymbol{e}_z + \mu\nabla\cdot\mathcal{T}, \tag{2.4a}$$

$$\frac{\partial \rho}{\partial t} + \nabla\cdot(\rho\boldsymbol{u}) = 0, \tag{2.4b}$$

$$\rho\frac{\partial T}{\partial t} + \rho\boldsymbol{u}\cdot\nabla T = \frac{\lambda}{c_p}\nabla^2 T, \tag{2.4c}$$

where t is the time and

$$\mathcal{T} = \nabla\boldsymbol{u} + (\nabla\boldsymbol{u})^{\mathrm{T}} - \frac{2}{3}(\nabla\cdot\boldsymbol{u})\mathcal{I} \tag{2.5}$$

is (twice) the deformation rate tensor with the identity matrix $\mathcal{I} = \delta_{ij}$. In the energy equation (2.4c), the pressure contribution to the enthalpy is neglected, assuming $p/\rho \ll |c_p T|$. Likewise, we neglect the pressure work and the heat due to viscous dissipation in (2.4c).

Formally the same equations (2.4) hold for the gas phase, merely with the material parameters of the gas. To distinguish between liquid and gas we follow Stojanovic *et al.* (2022) and introduce the set of coefficients

$$\boldsymbol{\alpha} = \left(\alpha_\rho, \alpha_\mu, \alpha_\lambda, \alpha_{c_p}, \alpha_\beta\right) = \begin{cases} (1,1,1,1,1) & \text{for the liquid phase,} \\ (\tilde{\rho}, \tilde{\mu}, \tilde{\lambda}, \tilde{c_p}, \tilde{\beta}) & \text{for the gas phase,} \end{cases} \tag{2.6}$$

where $\tilde{\rho} = \rho_{\mathrm{g}0}/\rho_0$, $\tilde{\mu} = \mu_{\mathrm{g}}/\mu$, $\tilde{\lambda} = \lambda_{\mathrm{g}}/\lambda$, $\tilde{c_p} = c_{p,\mathrm{g}}/c_p$ and $\tilde{\beta} = \beta_{\mathrm{g}}/\beta$ denote the ratios of the reference densities, dynamic viscosities, thermal conductivities, specific heat capacities and the thermal expansion coefficients between the gas and the liquid. Numerical data are given in table 2.

Scaling lengths, time, velocity, pressure and temperature by d, $d^2\rho_0/\mu$, $\gamma\Delta T/\mu$, $\gamma\Delta T/d$ and ΔT, respectively, and using the same notation as for the dimensional variables, we arrive at the dimensionless version of (2.4) for both fluids

$$(1-\alpha_\beta\varepsilon\vartheta)\frac{\partial \boldsymbol{u}}{\partial t} + \mathrm{Re}(1-\alpha_\beta\varepsilon\vartheta)\boldsymbol{u}\cdot\nabla\boldsymbol{u} = -\frac{1}{\alpha_\rho}\nabla p + \alpha_\beta \mathrm{Bd}\vartheta\boldsymbol{e}_z + \alpha_\mu\nabla\cdot\mathcal{T}, \tag{2.7a}$$

$$-\frac{\alpha_\beta\varepsilon}{\mathrm{Re}}\frac{\partial \vartheta}{\partial t} - \alpha_\beta\varepsilon\nabla\cdot(\vartheta\boldsymbol{u}) + \nabla\cdot\boldsymbol{u} = 0, \tag{2.7b}$$

$$(1-\alpha_\beta\varepsilon\vartheta)\frac{\partial \vartheta}{\partial t} + \mathrm{Re}(1-\alpha_\beta\varepsilon\vartheta)\boldsymbol{u}\cdot\nabla\vartheta = \frac{\alpha_\lambda}{\alpha_{c_p}\mathrm{Pr}}\nabla^2\vartheta, \tag{2.7c}$$

where we made use of the coefficients defined in (2.6). We use cylindrical coordinates (r,φ,z) centred in the middle of the liquid bridge and a polar representation of the velocity field $\boldsymbol{u} = u\boldsymbol{e}_r + v\boldsymbol{e}_\varphi + w\boldsymbol{e}_z$. In (2.7), the reduced temperature and the reduced pressure are respectively defined as $\vartheta = (T-T_0)/\Delta T$ and $p = (d/\gamma\Delta T)(P-\rho_0 g z)$, where P indicates the dimensional pressure. Furthermore, the temperature dependence of the density is taken into

account up to linear approximation with the (small) parameter $\varepsilon = \beta\Delta T$ (and $\varepsilon_g = \beta_g \Delta T$) measuring the magnitude of the density variation in the liquid (and in the gas).

The flow is characterised by the thermocapillary Reynolds number Re, the Prandtl number Pr and the dynamic Bond number Bd, respectively defined as

$$\mathrm{Re} = \frac{\rho_0 \gamma \Delta T d}{\mu^2}, \qquad \mathrm{Pr} = \frac{\mu c_p}{\lambda} = 28, \qquad \mathrm{Bd} = \frac{\rho_0 g \beta d^2}{\gamma} = 0.41. \tag{2.8}$$

For the present silicone oil Pr = 28. Assuming terrestrial gravity conditions with $g = 9.81\,\mathrm{m/s^2}$ and a length $d = 1.65\,\mathrm{mm}$ of the liquid bridge, the dynamic Bond number is Bd = 0.41. Since ΔT can accept both, positive and negative values, the thermocapillary Reynolds number Re, the Marangoni number Ma = PrRe as well as the Rayleigh number Ra = BdMa have a sign. As most investigations of the flow in liquid bridges consider heating from above, this configuration will be associated with (Re, Ma, Ra) > 0, while (Re, Ma, Ra) < 0 indicates heating from below, even though this is an unusual convention for pure buoyancy convection.

2.2.2. *Linear stability equations*

The steady axisymmetric solution $\boldsymbol{u}_0 = u(r,z)\boldsymbol{e}_r + w(r,z)\boldsymbol{e}_z$ of (2.7) is called the basic flow. For sufficiently small driving forces the basic flow is stable. We are interested in the linear stability boundary of the basic flow when the thermocapillary Reynolds numbers Re exceeds a certain threshold. For Reynolds numbers larger in magnitude than the critical Reynolds number, i.e. $\mathrm{Re} > \mathrm{Re}_c > 0$ for heating from above, or $\mathrm{Re} < \mathrm{Re}_c < 0$ for heating from below, the flow is either time-dependent, three-dimensional or both. In order to find the critical Reynolds numbers Re_c a linear stability analysis is carried out. To that end the general three-dimensional time-dependent solution $\boldsymbol{q} = (u, v, w, p, \vartheta)$ and $\boldsymbol{q}_g = (u_g, v_g, w_g, p_g, \vartheta_g)$ of (2.7) is decomposed into an axisymmetric time-independent basic flow (subscript 0) and deviations from this basic flow (indicated by a prime $'$)

$$\boldsymbol{q} = \boldsymbol{q}_0(r,z) + \boldsymbol{q}'(r,\varphi,z,t), \qquad \boldsymbol{q}_g = \boldsymbol{q}_{g0}(r,z) + \boldsymbol{q}'_g(r,\varphi,z,t). \tag{2.9}$$

Inserting this decomposition into (2.7) and linearising the equations with respect to the perturbation quantities yields the set of linear equations

$$(1-\alpha_\beta\varepsilon\vartheta_0)\frac{\partial \boldsymbol{u}'}{\partial t} + \mathrm{Re}(1-\alpha_\beta\varepsilon\vartheta_0)(\boldsymbol{u}_0\cdot\nabla\boldsymbol{u}' + \boldsymbol{u}'\cdot\nabla\boldsymbol{u}_0) - \alpha_\beta\varepsilon\mathrm{Re}\vartheta'\boldsymbol{u}_0\cdot\nabla\boldsymbol{u}_0 = \\ = -\frac{1}{\alpha_\rho}\nabla p' + \alpha_\beta \mathrm{Bd}\vartheta'\boldsymbol{e}_z + \alpha_\mu\nabla\cdot\mathcal{T}', \tag{2.10a}$$

$$-\frac{\alpha_\beta\varepsilon}{\mathrm{Re}}\frac{\partial\vartheta'}{\partial t} - \alpha_\beta\varepsilon\nabla\cdot(\vartheta'\boldsymbol{u}_0) - \alpha_\beta\varepsilon\nabla\cdot(\vartheta_0\boldsymbol{u}') + \nabla\cdot\boldsymbol{u}' = 0, \tag{2.10b}$$

$$(1-\alpha_\beta\varepsilon\vartheta_0)\frac{\partial\vartheta'}{\partial t} + \mathrm{Re}(1-\alpha_\beta\varepsilon\vartheta_0)(\boldsymbol{u}_0\cdot\nabla\vartheta' + \boldsymbol{u}'\cdot\nabla\vartheta_0) - \alpha_\beta\varepsilon\mathrm{Re}\vartheta'\boldsymbol{u}_0\cdot\nabla\vartheta_0 = \\ = \frac{\alpha_\lambda}{\alpha_{c_p}\mathrm{Pr}}\nabla^2\vartheta', \tag{2.10c}$$

which describe the dynamics of the infinitesimal perturbation flow. Again (2.10) is valid for both phases, distinguished by $\boldsymbol{\alpha}$. Both phases are coupled through the boundary conditions on the interface.

Since the basic state is homogeneous in time t and in the azimuthal coordinate φ, the perturbations $\boldsymbol{q}'$ and $\boldsymbol{q}'_g$ can be decomposed into normal modes with azimuthal wave number

$m \in \mathbb{N}$

$$\boldsymbol{q}' = \sum_{j,m} \hat{\boldsymbol{q}}_{j,m}(r,z)e^{\psi_{j,m}t+\mathrm{i}m\varphi} + \text{c.c.}, \qquad \boldsymbol{q}'_{\mathrm{g}} = \sum_{j,m} \hat{\boldsymbol{q}}_{\mathrm{g};j,m}(r,z)e^{\psi_{j,m}t+\mathrm{i}m\varphi} + \text{c.c.}, \tag{2.11}$$

where the complex conjugate (c.c.) renders the perturbations real. The complex growth rates of the normal modes with amplitudes $\hat{\boldsymbol{q}} = (\hat{u}, \hat{v}, \hat{w}, \hat{p}, \hat{\vartheta})$ and $\hat{\boldsymbol{q}}_{\mathrm{g}} = (\hat{u}_{\mathrm{g}}, \hat{v}_{\mathrm{g}}, \hat{w}_{\mathrm{g}}, \hat{p}_{\mathrm{g}}, \hat{\vartheta}_{\mathrm{g}})$ are denoted $\psi = \psi_{j,m} \in \mathbb{C}$, where the index j numbers the different solutions for given wave number m.

Inserting the ansatz (2.11) into (2.10), we obtain linear differential equations in r and z for the perturbation amplitudes

$$\begin{aligned}\psi(\hat{u} - \alpha_\beta\varepsilon u_0\hat{\vartheta}) + \mathrm{Re}\left[\left(\frac{1}{r}+\frac{\partial}{\partial r}\right)(2u_0\hat{u}) + \frac{mu_0\hat{\hat{v}}}{r} + \frac{\partial(u_0\hat{w}+\hat{u}w_0)}{\partial z}\right] \\ - \alpha_\beta\varepsilon\mathrm{Re}\left[\left(\frac{1}{r}+\frac{\partial}{\partial r}\right)(\vartheta' u_0^2) + \frac{\partial(\vartheta' u_0 w_0)}{\partial z}\right] = -\frac{1}{\alpha_\rho}\frac{\partial\hat{p}}{\partial r} + \alpha_\mu\left[\frac{2}{r}\frac{\partial}{\partial r}\left(r\frac{\partial\hat{u}}{\partial r}\right)\right. \\ \left. -(m^2+2)\frac{\hat{u}}{r^2} + m\left(\frac{1}{r}\frac{\partial}{\partial r} - \frac{3}{r^2}\right)\hat{\hat{v}} + \left(\frac{\partial}{\partial z}+\frac{\partial}{\partial r}\right)\frac{\partial u'}{\partial z} - \frac{2}{3}\alpha_\beta\varepsilon\zeta'\right],\end{aligned} \tag{2.12a}$$

$$\begin{aligned}\psi\hat{\hat{v}} + \mathrm{Re}\left[\left(\frac{2}{r}+\frac{\partial}{\partial r}\right)(u_0\hat{\hat{v}}) + \frac{\partial(\hat{\hat{v}}w_0)}{\partial z}\right] = \frac{1}{\alpha_\rho}\frac{m}{r}\hat{p} + \alpha_\mu\left[-m\left(\frac{3}{r^2}+\frac{\partial}{\partial r}\right)\hat{u}\right. \\ \left. +\frac{1}{r}\frac{\partial}{\partial r}\left(r\frac{\partial\hat{\hat{v}}}{\partial r}\right) - (2m^2+1)\frac{\hat{\hat{v}}}{r^2} + \frac{\partial}{\partial z}\left(\frac{\partial\hat{\hat{v}}}{\partial z} - \frac{m\hat{w}}{r}\right) - \frac{2}{3}\alpha_\beta\varepsilon\zeta'\right],\end{aligned} \tag{2.12b}$$

$$\begin{aligned}\psi(\hat{w} - \alpha_\beta\varepsilon w_0\hat{\vartheta}) + \mathrm{Re}\left[\frac{1}{r}\frac{\partial[r(w_0\hat{u}+\hat{w}u_0)]}{\partial r} + \frac{mw_0\hat{\hat{v}}}{r} + 2\frac{\partial w_0\hat{w}}{\partial z}\right] \\ - \alpha_\beta\varepsilon\mathrm{Re}\left[\left(\frac{1}{r}+\frac{\partial}{\partial r}\right)(\vartheta' u_0 w_0) + \frac{\partial(\vartheta' w_0^2)}{\partial z}\right] = -\frac{1}{\alpha_\rho}\frac{\partial\hat{p}}{\partial z} + \alpha_\beta\mathrm{Bd}\hat{\vartheta} \\ + \alpha_\mu\left[\frac{1}{r}\frac{\partial}{\partial r}\left(r\frac{\partial\hat{w}}{\partial r}\right) - m^2\frac{\hat{w}}{r^2} + \frac{\partial}{\partial z}\left(\frac{1}{r}\frac{\hat{u}}{\partial r} + \frac{1}{r}\hat{\hat{v}} + 2\frac{\partial\hat{w}}{\partial z}\right) - \frac{2}{3}\alpha_\beta\varepsilon\zeta'\right],\end{aligned} \tag{2.12c}$$

$$\alpha_\beta\varepsilon\left[-\frac{\psi\hat{\vartheta}}{\mathrm{Re}} - \frac{1}{r}\frac{\partial(r\hat{\vartheta}u_0)}{\partial r} - \frac{\partial(\hat{\vartheta}w_0)}{\partial z}\right] + \frac{1}{r}\frac{\partial[(1-\alpha_\beta\varepsilon\vartheta_0)r\hat{u}]}{\partial r} + \frac{m-\alpha_\beta\varepsilon\vartheta_0}{r}\hat{\hat{v}} + \frac{\partial[(1-\alpha_\beta\varepsilon\vartheta_0)\hat{w}]}{\partial z} = 0, \tag{2.12d}$$

$$\begin{aligned}\psi(\hat{\vartheta} - \alpha_\beta\varepsilon\vartheta_0) + \mathrm{Re}\left[\frac{1}{r}\frac{\partial[r(\vartheta_0\hat{u}+\hat{\vartheta}u_0 - \alpha_\beta\varepsilon\vartheta_0 u_0\hat{\vartheta})]}{\partial r} + \frac{m\vartheta_0\hat{\hat{v}}}{r}\right. \\ \left. +\frac{\partial(\vartheta_0\hat{w}+\hat{\vartheta}w_0 - \alpha_\beta\varepsilon\vartheta_0 w_0\hat{\vartheta})}{\partial z}\right] = \frac{\alpha_\lambda}{\alpha_{c_p}\mathrm{Pr}}\left[\frac{1}{r}\frac{\partial}{\partial r}\left(r\frac{\partial\hat{\vartheta}}{\partial r}\right) - m^2\frac{\hat{\vartheta}}{r^2} + \frac{\partial^2\hat{\vartheta}}{\partial z^2}\right].\end{aligned} \tag{2.12e}$$

In these equations, the amplitudes of the azimuthal velocities have been transformed according to $\hat{\hat{v}} = \mathrm{i}\hat{v}$ and $\hat{\hat{v}}_{\mathrm{g}} = \mathrm{i}\hat{v}_{\mathrm{g}}$ in order to render the coefficient matrix real and thus save computational memory for the numerical solution (Theofilis 2003). For the sake of brevity we have abbreviated the term $\nabla\cdot\boldsymbol{u}'$ arising in the rate-of-strain tensor for the perturbation flow by $\nabla\cdot\boldsymbol{u}' = \alpha_\beta\varepsilon\zeta'$. These terms represent the deviation from a solenoidal perturbation

$m = 0:$	$\hat{u} = 0$	$\hat{v} = 0$	$\partial\hat{w}/\partial r = 0$	$\partial\hat{\vartheta}/\partial r = 0$
$m = 1:$	$\partial\hat{u}/\partial r = 0$	$\partial\hat{v}/\partial r = 0$	$\hat{w} = 0$	$\hat{\vartheta} = 0$
$m > 1:$	$\hat{u} = 0$	$\hat{v} = 0$	$\hat{w} = 0$	$\hat{\vartheta} = 0$

Table 3: Boundary conditions for the perturbation flow on $r = 0$.

flow. As can be seen from (2.10*b*) they are of the orders of $O(\varepsilon)$ and $O(\varepsilon_g)$ for the liquid and gas phase, respectively.

2.2.3. *Boundary conditions*

To solve the two-dimensional version of (2.7) for the basic flow and of (2.12) for the three-dimensional perturbation flow suitable boundary conditions must be defined for both flows.

Solid walls

The velocity fields must satisfy the no-slip boundary conditions

$$\boldsymbol{u}_0 = \boldsymbol{u}_{g0} = 0 \quad \text{and} \quad \hat{\boldsymbol{u}} = \hat{\boldsymbol{u}}_g = 0 \tag{2.13}$$

on all solid walls, namely the support rods and the cylindrical tube confining the gas radially. Since the support rods are always made from good thermal conductors (e.g. Romanò *et al.* 2017; Gotoda *et al.* 2019), constant temperatures are imposed on the rods for the basic flow, while the perturbation temperature must vanish. The shield tube, on the other hand, is typically made from a good thermal insulator to keep its thermal effect on the gas flow at a minimum. Therefore, the heat fluxes due to both the basic and the perturbation temperature field are required to vanish on the shield tube. This leads to the thermal boundary conditions

$$\text{hot rod:} \quad \vartheta_0 = \vartheta_{g0} = 1/2 \quad \text{and} \quad \hat{\vartheta} = \hat{\vartheta}_g = 0, \tag{2.14a}$$

$$\text{cold rod:} \quad \vartheta_0 = \vartheta_{g0} = -1/2 \quad \text{and} \quad \hat{\vartheta} = \hat{\vartheta}_g = 0, \tag{2.14b}$$

$$\text{shield tube:} \quad \partial\vartheta_{g0}/\partial r = 0 \quad \text{and} \quad \partial\hat{\vartheta}_g/\partial r = 0. \tag{2.14c}$$

Axis of symmetry

On the axis of symmetry at $r = 0$ the axisymmetric steady basic flow must satisfy

$$u_0 = \frac{\partial w_0}{\partial r} = \frac{\partial \vartheta_0}{\partial r} = 0. \tag{2.15}$$

The boundary conditions for the perturbation flow can be derived from uniqueness conditions for $\partial u/\partial\varphi$ and $\partial\vartheta/\partial\varphi$ as $r \to 0$ (see also Batchelor & Gill 1962; Xu & Davis 1984) and depend on the wave number m. They are given in table 3.

Liquid–gas interface

The flow in the liquid and in the gas phase are coupled through the interface. Since the location of the interface, described by $r = h(\varphi, z, t)$, is part of the solution, the flow and the location h must be computed in a coupled manner. In the following we consider the axisymmetric steady basic flow and the corresponding time-independent shape function $h_0(z)$.

Regardless of the shape of the interface, continuity of the temperature and of the heat flux across the interface at $r = h_0(z)$ require the thermal boundary conditions

$$r = h_0: \qquad \vartheta_0 = \vartheta_{g0} \tag{2.16a}$$

$$r = h_0: \qquad \boldsymbol{n} \cdot \nabla\vartheta_0 = \tilde{\lambda}\boldsymbol{n} \cdot \nabla\vartheta_{g0}, \tag{2.16b}$$

where

$$\boldsymbol{n} = \frac{\boldsymbol{e}_r - (\partial_z h_0)\boldsymbol{e}_z}{N}, \quad \text{with} \quad N = \sqrt{1 + (\partial_z h_0)^2}, \tag{2.17}$$

is the unit vector on the interface directed from the liquid into the gas. The tangent vector is defined as $\boldsymbol{t} = [(\partial_z h_0)\boldsymbol{e}_r + \boldsymbol{e}_z]/N$.

The velocity fields must satisfy kinematic and dynamic boundary conditions. The kinematic boundary conditions

$$r = h_0: \quad \boldsymbol{u}_0 = \boldsymbol{u}_{g0} \quad \text{and} \quad \frac{u_0}{w_0} = \partial_z h_0, \tag{2.18}$$

ensure the continuity of the velocity and guarantee that a fluid element on the interface remains on the interface. The dynamic boundary condition is decomposed into a normal and a tangential stress balance by projecting the equilibrium of forces onto the normal ($\boldsymbol{n}$) and tangential ($\boldsymbol{t}$) directions. The normal stress balance

$$-(p_0 - p_{g0}) + \boldsymbol{n}\cdot\mathcal{T}_0\cdot\boldsymbol{n} + \left(\frac{1}{\mathrm{Ca}} - \vartheta_0\right)\nabla\cdot\boldsymbol{n} = -\frac{\mathrm{Bo}}{\mathrm{Ca}}z - (\vartheta - \tilde{\rho}\tilde{\beta}\vartheta_{g0})\mathrm{Bd}z + \tilde{\mu}\boldsymbol{n}\cdot\mathcal{T}_{g0}\cdot\boldsymbol{n}, \tag{2.19}$$

must be satisfied on $r = h_0(z)$. It is affected by the static Bond number Bo and the Capillary number Ca defined as

$$\mathrm{Bo} = \frac{(\rho_0 - \rho_{g0})gd^2}{\sigma_0}, \qquad \mathrm{Ca} = \frac{\gamma\Delta T}{\sigma_0}. \tag{2.20}$$

They measure the relative importance of static and of hydrodynamic pressure differences, respectively, to the characteristic capillary pressure σ_0/d. Note that the ratio $\tau = \mathrm{Bd}/\mathrm{Bo} = \rho_0\beta\sigma_0/[\gamma(\rho_0 - \rho_{g0})]$ is a material constant and almost a proportionality factor between ε and Ca, since $\varepsilon = (1 - \tilde{\rho})\tau\mathrm{Ca}$ and typically $\tilde{\rho} \ll 1$. In addition to (2.19) the tangential stress balance

$$\boldsymbol{t}\cdot\mathcal{T}_0\cdot\boldsymbol{n} = -\boldsymbol{t}\cdot\nabla\vartheta_0 + \tilde{\mu}\boldsymbol{t}\cdot\mathcal{T}_{g0}\cdot\boldsymbol{n} \tag{2.21}$$

must also hold on $r = h_0(z)$. The thermocapillary stresses are represented by $-\boldsymbol{t}\cdot\nabla\vartheta_0$.

The stationary axisymmetric version of the differential equations (2.7) and the above boundary conditions for the basic state must be solved in a coupled way to yield the basic flow including the interfacial shape $h_0(z)$. The numerical solution is described in section 3. To be able to solve the problem two additional constraints for h_0 are required, because the normal stress balance is second order in z. These are provided by the interface $h_0(z = \pm 1/2) = 1/\Gamma$ being pinned to the sharp edges of the heated rods. In addition, for a non-volatile liquid the mass of the liquid bridge must be conserved. Since 2-cSt silicone oil is slightly volatile, accurate experiments (e.g. Yano *et al.* 2016; Yasnou *et al.* 2018; Gotoda *et al.* 2019) control the volume of the liquid rather than the mass. Therefore, we impose the volume constraint

$$\Gamma^2\int_{-1/2}^{1/2} h_0^2(z)\mathrm{d}z = \mathcal{V}, \tag{2.22}$$

where $\mathcal{V} = V_l/V_0$ is the liquid volume V_l normalised by the volume $V_0 = \pi r_i^2 d$ of an upright cylindrical liquid bridge. Throughout this investigation the liquid volume $\mathcal{V}$ is prescribed, not the mass of the liquid $M = \int_{V_l}\rho(\boldsymbol{x})\mathrm{d}V$.

In order to identify the flow-induced contribution to the surface shape resulting from (2.19), and of its effect on the flow stability, we also consider the hydrostatic case ($\boldsymbol{u}_0 = \boldsymbol{u}_{g,0} = 0$) in which (2.19) becomes the Young–Laplace equation

$$\Delta p_h = \frac{\nabla\cdot\boldsymbol{n}}{\mathrm{Ca}} + \frac{\mathrm{Bo}}{\mathrm{Ca}}z, \tag{2.23}$$

where Δp_h is a constant overpressure (Kuhlmann 1999). The resulting static surface shape is denoted $h_{0,s}$ (subscript s: static). As long as the effect of the flow on the shape of the interface is weak, $h_{0,s}$ represents a good approximation to the true dynamic surface shape $h_{0,d}$ (subscript d: dynamic) which results from (2.19). To assess the influence of the flow on the shape of the interface we define the dynamic surface *deformation* $\Delta h_0 = h_{0,d} - h_{0,s}$ as the difference between both surface *shapes*. Similarly, $\mathrm{Re}_{c,s}$ and $\mathrm{Re}_{c,d}$ denote the critical Reynolds numbers assuming a static or a dynamic interfacial shape, respectively, for the basic flow.

Finally, interfacial coupling conditions must be provided for the perturbation flow. To reduce the computational effort, and motivated by the results of Carrión *et al.* (2020), we neglect interfacial deformations due to the perturbation flow. In this approach the interfacial conditions

$$\hat{\boldsymbol{u}} = \hat{\boldsymbol{u}}_\mathrm{g}, \quad \hat{\vartheta} = \hat{\vartheta}_\mathrm{g}, \quad \boldsymbol{n}\cdot\nabla\hat{\vartheta} = \tilde{\lambda}\boldsymbol{n}\cdot\nabla\hat{\vartheta}_\mathrm{g} \quad \text{and} \quad \boldsymbol{t}\cdot\hat{\mathcal{T}}\cdot\boldsymbol{n} = -\boldsymbol{t}\cdot\nabla\hat{\vartheta} + \tilde{\mu}\boldsymbol{t}\cdot\hat{\mathcal{T}}_\mathrm{g}\cdot\boldsymbol{n}, \tag{2.24}$$

where $\hat{\mathcal{T}} = \nabla\hat{\boldsymbol{u}} + (\nabla\hat{\boldsymbol{u}})^\mathrm{T} - 2/3(\nabla\cdot\hat{\boldsymbol{u}})\mathcal{I}$, are imposed at $r = h_0(z)$. This approximation a priori precludes surface-wave instabilities which could possibly be triggered by the shear flow due to thermocapillary and/or mechanical stresses from the gas phase. However, such surface-wave instabilities have not yet been observed experimentally in the present flow system.

Inlet and outlet

The gas enters the annular duct through the inlet located at $z = z_\mathrm{in}$ with a dimensional mean inlet velocity $\bar{w}_\mathrm{g,in}$. It leaves the chamber through the outlet at $z = z_\mathrm{out}$ on the opposite side. The oriented mean value $\bar{w}_\mathrm{g,in}$ can be either positive or negative depending on the direction of the through flow. To measure the intensity of the gas flow we define the gas flow Reynolds number

$$\mathrm{Re}_\mathrm{g} = \frac{\rho_0 \bar{w}_\mathrm{g,in} d}{\mu}. \tag{2.25}$$

It can take positive and negative values. The Reynolds number (2.25) describes the forcing of the *liquid* flow due to the gas motion. As shown in Appendix A, Re_g is better suited to correlate the effect of the gas motion on the liquid phase than the conventional Reynolds number Re'_g based on the gap width $r_\mathrm{o} - r_\mathrm{i}$ and the kinematic viscosity of the gas $\mu_\mathrm{g}/\rho_\mathrm{g0}$.

For $\mathrm{Re}_\mathrm{g} > 0$ ($\mathrm{Re}_\mathrm{g} < 0$) the forced flow is directed in positive (negative) z direction. Accordingly, the locations of the inlet and the outlet

$$z_\mathrm{in} = \pm\,(1/2 + \Gamma_\mathrm{rod}/\Gamma) = -z_\mathrm{out} \quad \text{for} \quad \mathrm{Re}_\mathrm{g} \lessgtr 0. \tag{2.26}$$

are determined by the sign of Re_g. To avoid entrance-length effects we assume a fully developed annular Poiseuille flow at $z = z_\mathrm{in}$

$$\boldsymbol{u}_\mathrm{g0}(r) = \frac{\mathrm{Re}_\mathrm{g}}{\mathrm{Re}}\frac{2\ln(\eta)}{(\eta^2+1)\ln(\eta) - \eta^2 + 1}\left[1 - \Gamma^2 r^2 + \left(\eta^2 - 1\right)\frac{\ln(\Gamma r)}{\ln(\eta)}\right]\boldsymbol{e}_z, \tag{2.27}$$

where the factor Re^{-1} arises due to the scaling. At the outlet $z = z_\mathrm{out}$, kinematic outflow conditions

$$\frac{\partial u_\mathrm{g0}}{\partial z} = \frac{\partial v_\mathrm{g0}}{\partial z} = \frac{\partial w_\mathrm{g0}}{\partial z} = 0 \tag{2.28}$$

are imposed. Since the in- and outflow boundaries in a planned space experiment are realised by thermally conducting metallic porous media in contact with the support cylinders (S. Matsumoto, private communication), the gas enters/leaves the chamber with a homogeneous

temperature

$$z = \pm\,(1/2 + \Gamma_{\rm rod}/\Gamma): \quad \vartheta_{\rm g0} = \pm 1/2\ \mathrm{sgn}(\mathrm{Re}), \tag{2.29}$$

corresponding to the temperature of the rod next to the inlet/outlet. In the limit $\mathrm{Re_g} \uparrow\downarrow 0$ (2.27) and (2.28) are replaced by rigid boundary conditions.

Since the in- and outflow conditions are taken care of by the basic flow, the amplitudes of the perturbation flow must satisfy the homogeneous conditions

$$z = z_{\rm in}: \quad \hat{u}_{\rm g} = \hat{v}_{\rm g} = \hat{w}_{\rm g} = \hat{\vartheta}_{\rm g} = 0, \tag{2.30a}$$

$$z = z_{\rm out}: \quad \partial\hat{u}_{\rm g}/\partial z = \partial\hat{v}_{\rm g}/\partial z = \partial\hat{w}_{\rm g}/\partial z = \hat{\vartheta}_{\rm g} = 0. \tag{2.30b}$$

2.3. *Energetics*

The instability mechanism is investigated by the *a posteriori* energy analysis of the perturbation flow (Wanschura *et al.* 1995). The equations for the rates of change of the normalised kinetic and thermal perturbation energies in the liquid and in the gas phase

$$\frac{\mathrm{d}E_{\rm kin}}{\mathrm{d}t} = \frac{1}{\mathcal{D}_{\rm kin}}\frac{\mathrm{d}}{\mathrm{d}t}\int_{V_i}\frac{\boldsymbol{u}'^2}{2}\mathrm{d}V = -1 + M_r + M_\varphi + M_z + \sum_{j=1}^{5} I_j + B + K_{\rm g} + \Lambda_\rho, \tag{2.31a}$$

$$\frac{\mathrm{d}E_{\rm th}}{\mathrm{d}t} = \frac{1}{\mathcal{D}_{\rm th}}\frac{\mathrm{d}}{\mathrm{d}t}\int_{V_i}\frac{\vartheta'^2}{2}\mathrm{d}V = -1 + \sum_{j=1}^{2} J_j + H_{\rm fs} + K_{\rm th,g} + \Pi_\rho, \tag{2.31b}$$

can be derived by multiplying (2.10*a*) and (2.10*c*) with $\boldsymbol{u}'$ and ϑ', respectively, integrating separately over the volume occupied by the liquid and by the gas, and normalising by the dissipation $\mathcal{D}_{\rm kin}$ and $\mathcal{D}_{\rm th}$, respectively. In contrast to the perturbation energy budget resulting from the OB approximation (Nienhüser & Kuhlmann 2002), the additional terms

$$\Lambda_\rho = -\alpha_\beta\varepsilon\frac{\mathrm{Re}}{2\mathcal{D}_{\rm kin}}\int_{V_i}\vartheta'\boldsymbol{u}'\cdot(\boldsymbol{u}_0\cdot\nabla\boldsymbol{u}_0)\mathrm{d}V + \alpha_\beta\varepsilon\frac{1}{\mathcal{D}_{\rm kin}}\int_{V_i}p'\zeta'\mathrm{d}V - (\alpha_\beta\varepsilon)^2\frac{1}{3\mathcal{D}_{\rm kin}}\int_{V_i}\zeta'^2\mathrm{d}V, \tag{2.32a}$$

$$\Pi_\rho = -\alpha_\beta\varepsilon\frac{\mathrm{Re}}{\mathcal{D}_{\rm th}}\int_{V_i}\vartheta_0\boldsymbol{u}_0\cdot\nabla\vartheta'^2\mathrm{d}V - (\alpha_\beta\varepsilon)^2\frac{\mathrm{Re}}{2\mathcal{D}_{\rm th}}\int_{V_i}\vartheta'^2\boldsymbol{u}_0\cdot\nabla\vartheta_0^2\mathrm{d}V \tag{2.32b}$$

arise in the energy budgets, accounting for non-Oberbeck–Boussinesq effects due to the temperature dependence of the fluid densities in all terms. The expressions Λ_ρ and Π_ρ represent the rates of change of kinetic and, respectively, thermal perturbation energy, caused by the non-uniform density distribution in the weakly compressible flow. Both terms are of the order of $O(\alpha_\beta\varepsilon)$ and small compared to the other $O(1)$ terms in (2.31). In the presence of an external gas flow, the additional terms

$$K_{\rm g} = -\frac{2\pi\mathrm{Re}}{\mathcal{D}_{\rm kin}}\int_{1/\Gamma}^{\eta/\Gamma}\hat{w}_{\rm g}^2(z_{\rm out})w_{\rm g0}(z_{\rm out})\mathrm{d}r, \tag{2.33a}$$

$$K_{\rm th,g} = -\frac{2\pi\mathrm{Re}}{\mathcal{D}_{\rm kin}}\int_{1/\Gamma}^{\eta/\Gamma}\hat{\vartheta}_{\rm g}^2(z_{\rm out})w_{\rm g0}(z_{\rm out})\mathrm{d}r \tag{2.33b}$$

appear in the kinetic and, respectively, thermal energy budget. For open gas tubes, $K_{\rm g}$ represents the loss of kinetic energy of the perturbation flow by transport out of the gas domain. For a closed gas container ($\mathrm{Re_g} = 0$), $K_{\rm g} = 0$ vanishes. Similarly, $K_{\rm th,g}$ can

only be non-zero for open gas tubes. However, owing to the prescribed temperatures at the in- and outlet, $\hat{\vartheta}_g(z_{out}) = 0$ (2.30). Thus $K_{th,g} = 0$ vanishes also for open gas tubes. Detailed expressions and descriptions of the remaining terms appearing in (2.31) can be found in Stojanovic *et al.* (2022), who used the same notation. For a derivation of (2.31) for a full temperature dependence of all thermophysical parameters, we refer to Stojanović *et al.* (2023*a*).

To monitor the conservation of perturbation energy, we consider the normalised residuals of the kinetic and thermal energy balances as given in Nienhüser & Kuhlmann (2002), supplemented with the new terms,

$$\delta E_{kin} := \left| -\frac{dE_{kin}}{dt} - 1 + M_r + M_\varphi + M_z + \sum_{j=1}^{5} I_j + B + \Lambda_\rho + K_g \right|, \tag{2.34a}$$

$$\delta E_{th} := \left| -\frac{dE_{th}}{dt} - 1 + \sum_{j=1}^{2} J_j + H_{fs} + \Pi_\rho \right|. \tag{2.34b}$$

Throughout, we find $\delta E_{kin} = O(10^{-2})$ and $\delta E_{th} = O(10^{-3})$, signaling conservation of kinetic and thermal perturbation energy.

3. Numerical Methods

3.1. *Basic flow*

The computation of the steady axisymmetric basic flow depends on the treatment of the liquid–gas interface (see section 2.2.3). In the simplified approach in which the shape of the liquid–gas interface is independent of the flow, the static surface shape $h_{0,s}(z)$ is computed beforehand by solving the Young–Laplace equation (2.23). Thereafter, the volume equations are solved using finite volumes and body-fitted coordinates ($\xi = r/h_0, z$) as described in Stojanovic *et al.* (2022). In the case of flow-induced free surface deformations, the volume equations are discretized by the same method, but now the normal stress balance (2.19) is solved fully coupled to the basic flow. After each iteration the body-fitted coordinates are updated, since the transformed coordinate ξ is based on the current surface shape.

Regardless of the treatment of the interface, the nonlinear algebraic equations resulting from the discretisation of the Navier–Stokes equations (2.7) are solved iteratively using the Newton–Raphson method. If $\boldsymbol{q}_0^{(k)}$ is a known approximation to the solution of (2.7) at the k-th iteration step, an improved approximation is

$$\boldsymbol{q}_0^{(k+1)} = \boldsymbol{q}_0^{(k)} + \delta\boldsymbol{q}, \tag{3.1}$$

where the increment $\delta\boldsymbol{q}$ satisfies

$$\boldsymbol{J}\left(\boldsymbol{q}_0^{(k)}\right) \cdot \delta\boldsymbol{q} = -\boldsymbol{f}\left(\boldsymbol{q}_0^{(k)}\right), \tag{3.2}$$

with $\boldsymbol{J}\left(\boldsymbol{q}_0^{(k)}\right)$ being the Jacobian operator and $\boldsymbol{f}\left(\boldsymbol{q}_0^{(k)}\right)$ the nonlinear residual of the Navier-Stokes equations. Equation (3.2) is obtained by inserting the ansatz (3.1) into the steady

axisymmetric version of (2.7) and linearising with respect to $\delta\boldsymbol{q}$. We obtain

$$\begin{aligned}\mathrm{Re}\left(1-\alpha_\beta\varepsilon\vartheta_0^{(k)}\right)\left(\delta\boldsymbol{u}\cdot\nabla\boldsymbol{u}_0^{(k)}+\boldsymbol{u}_0^{(k)}\cdot\nabla\delta\boldsymbol{u}\right)-\alpha_\beta\varepsilon\mathrm{Re}\boldsymbol{u}_0^{(k)}\cdot\nabla\boldsymbol{u}_0^{(k)}\delta\vartheta+\frac{1}{\alpha_\rho}\nabla\delta p-\alpha_\beta\mathrm{Bd}\,\delta\vartheta\boldsymbol{e}_z\\ -\alpha_\mu\nabla\delta\mathcal{T}=-\mathrm{Re}\left(1-\alpha_\beta\varepsilon\vartheta_0^{(k)}\right)\boldsymbol{u}_0^{(k)}\cdot\nabla\boldsymbol{u}_0^{(k)}-\frac{1}{\alpha_\rho}\nabla p_0^{(k)}+\alpha_\beta\mathrm{Bd}\,\vartheta_0^{(k)}\boldsymbol{e}_z+\alpha_\mu\nabla\mathcal{T}_0^{(k)},\end{aligned}\tag{3.3a}$$

$$\nabla\cdot\delta\boldsymbol{u}-\alpha_\beta\varepsilon\nabla\cdot\left(\boldsymbol{u}_0^{(k)}\delta\vartheta\right)-\alpha_\beta\varepsilon\nabla\cdot\left(\vartheta_0^{(k)}\delta\boldsymbol{u}\right)=-\nabla\cdot\boldsymbol{u}_0^{(k)}+\alpha_\beta\varepsilon\nabla\cdot\left(\vartheta_0^{(k)}\boldsymbol{u}_0^{(k)}\right),\tag{3.3b}$$

$$\begin{aligned}\left(1-\alpha_\beta\varepsilon\vartheta_0^{(k)}\right)\left(\delta\boldsymbol{u}\cdot\nabla\vartheta_0^{(k)}+\boldsymbol{u}_0^{(k)}\cdot\nabla\delta\vartheta\right)-\alpha_\beta\varepsilon\boldsymbol{u}_0^{(k)}\cdot\nabla\vartheta_0^{(k)}\delta\vartheta-\frac{\alpha_\lambda}{\alpha_{c_p}\mathrm{Ma}}\nabla^2\delta\vartheta\\ =-\left(1-\alpha_\beta\varepsilon\vartheta_0^{(k)}\right)\boldsymbol{u}_0^{(k)}\cdot\nabla\vartheta^{(k)}+\frac{\alpha_\lambda}{\alpha_{c_p}\mathrm{Ma}}\nabla^2\vartheta^{(k)}.\end{aligned}\tag{3.3c}$$

In case of dynamic surface deformations the general solution vector of the basic flow $\boldsymbol{q}_0=(u_0,0,w_0,p_0,\vartheta_0,h_0)$ also contains the free surface shape h_0. Therefore, the linearised version of the normal stress balance (2.19)

$$\begin{aligned}&-(\delta p-\delta p_\mathrm{g})+\boldsymbol{n}^{(k)}\cdot\delta\mathcal{T}\cdot\boldsymbol{n}^{(k)}+\boldsymbol{n}^{(k)}\cdot\mathcal{T}_0^{(k)}\cdot\delta\boldsymbol{n}+\delta\boldsymbol{n}\cdot\mathcal{T}_0^{(k)}\cdot\boldsymbol{n}^{(k)}+\left(\frac{1}{\mathrm{Ca}}-\vartheta_0^{(k)}\right)\nabla\cdot\delta\boldsymbol{n}-\nabla\cdot\boldsymbol{n}^{(k)}\delta\vartheta\\ &+(\delta\vartheta-\tilde\rho\tilde\beta\delta\vartheta_\mathrm{g})\mathrm{Bd}z-\tilde\mu\left(\boldsymbol{n}^{(k)}\cdot\delta\mathcal{T}_\mathrm{g}\cdot\boldsymbol{n}^{(k)}+\boldsymbol{n}^{(k)}\cdot\mathcal{T}_{\mathrm{g}0}\cdot\delta\boldsymbol{n}+\delta\boldsymbol{n}\cdot\mathcal{T}_{\mathrm{g}0}\cdot\boldsymbol{n}^{(k)}\right)=p_0^{(k)}-p_{\mathrm{g}0}^{(k)}\\ &-\boldsymbol{n}^{(k)}\cdot\mathcal{T}_0^{(k)}\cdot\boldsymbol{n}^{(k)}-\left(\frac{1}{\mathrm{Ca}}-\vartheta_0^{(k)}\right)\nabla\cdot\boldsymbol{n}^{(k)}+\frac{\mathrm{Bo}}{\mathrm{Ca}}z-\left(\vartheta^{(k)}-\tilde\rho\tilde\beta\vartheta_{\mathrm{g}0}^{(k)}\right)\mathrm{Bd}z+\tilde\mu\boldsymbol{n}^{(k)}\cdot\mathcal{T}_{\mathrm{g}0}^{(k)}\cdot\boldsymbol{n}^{(k)}\end{aligned}\tag{3.4}$$

enters the Newton–Raphson method, where the increment

$$\delta h=h_{0,d}^{(k+1)}-h_{0,d}^{(k)}\tag{3.5}$$

appears implicitly in the increment of the normal vector

$$\delta\boldsymbol{n}=\boldsymbol{n}^{(k+1)}-\boldsymbol{n}^{(k)}\tag{3.6}$$

with

$$\delta\boldsymbol{n}=-\frac{1}{N^{(k)^3}}\frac{\mathrm{d}h_{0,d}^{(k)}}{\mathrm{d}z}\frac{\mathrm{d}\delta h}{\mathrm{d}z}\boldsymbol{e}_r-\frac{1}{N^{(k)}}\left[1-\frac{1}{N^{(k)^2}}\left(\frac{\mathrm{d}h_{0,d}^{(k)}}{\mathrm{d}z}\right)^2\right]\frac{\mathrm{d}\delta h}{\mathrm{d}z}\boldsymbol{e}_z\tag{3.7}$$

and its divergence

$$\begin{aligned}&\nabla\cdot\delta\boldsymbol{n}=\\ &\frac{1}{h_{0,d}^{(k)^3}N^{(k)^3}}\left[-h_{0,d}^{(k)^3}\frac{\mathrm{d}^2\delta h}{\mathrm{d}z^2}+\left(\frac{3h_{0,d}^{(k)^3}}{N^{(k)^2}}\frac{\mathrm{d}^2h_{0,d}^{(k)}}{\mathrm{d}z^2}-h_{0,d}^{(k)^2}\right)\frac{\mathrm{d}h_{0,d}^{(k)}}{\mathrm{d}z}\frac{\mathrm{d}\delta h}{\mathrm{d}z}-h_{0,d}^{(k)}N^{(k)^2}\delta h\right].\end{aligned}\tag{3.8}$$

The iteration is considered converged after both, the infinity norm $\|\delta\boldsymbol{q}_0\|_\infty$ and the L_2 norm $\|\delta\boldsymbol{q}_0\|_2$ of the residual, have dropped below 10^{-6}. Using a standard initialisation ($u_0=w_0=\vartheta_0=0$ and $h_0=1/\Gamma$), this typically requires around twelve Newton iteration steps.

3.2. *Linear stability analysis*

To carry out a linear stability analysis of the basic flow, the set of linear equations (2.12) for the amplitudes of the normal modes $\hat{\boldsymbol{q}}$ and $\hat{\boldsymbol{q}}_{\mathrm{g}}$ (2.11) are discretized exactly as for the basic state. The resulting large system of algebraic equations is a generalised eigenvalue problem, where the eigenvalues are identified as the complex growth rates $\psi_{j,m}$. The perturbation amplitudes $\hat{\boldsymbol{q}}_{j,m}$ and $\hat{\boldsymbol{q}}_{\mathrm{g};j,m}$ represent the corresponding eigenvectors. For a given wave number m, a vanishing growth rate $\Re(\psi_{j,m}) = 0$ defines a neutral hypersurface in parameter space. With respect to a variation of Re, this condition provides a neutral Reynolds number $\mathrm{Re}_n^{j,m}$. Minimisation with respect to j and m then yields the critical Reynolds number $\mathrm{Re}_c = \min_{j,m\geqslant 0} \mathrm{Re}_n^{j,m}$. The imaginary part of the growth rate represents the angular frequency $\omega_c = \Im[\psi_{j,m}(\mathrm{Re}_c)]$ of the critical mode. To find the eigenvalues with the largest real part we follow the method described in Stojanovic *et al.* (2022), using an implicitly restarted Arnoldi method provided by ARPACK (Lehoucq *et al.* 1998).

As we are interested in the dependence of the critical thermocapillary Reynolds number Re_c on the gas flow Reynolds number Re_{g}, the envelope of the neutral curves in the $(\mathrm{Re}, \mathrm{Re}_{\mathrm{g}})$ plane are constructed by arclength continuation (Keller 1977) for prescribed step sizes $\Delta\mathrm{Re}_{\mathrm{g}} = 10$ and $\Delta\mathrm{Re} = 15$.

3.3. *Implementation*

All necessary numerical operations are implemented in the MATLAB code `MaranStable` which was initially developed by M. Lukasser (Kuhlmann *et al.* 2011). It is available from https://github.com/fromano88/MaranStable. Early results have been published in Shevtsova *et al.* (2014) and Stojanovic & Kuhlmann (2020*b*). Here we employ a revised version of the code to solve for the basic state, perform the linear stability analysis and to evaluate the perturbation energy balances. For statically deformed liquid bridges, the grid convergence of `MaranStable` has been extensively tested by Stojanovic *et al.* (2022), who also verified and validated the code for closed chambers. Additional verifications of `MaranStable` regarding the dynamic interface shape and the coaxial through flow in the gas phase, are provided in Appendices C and D. The solver has recently been introduced by Stojanović *et al.* (2023*b*). Further documentation is shared on https://github.com/fromano88/MaranStable/tree/main/docs.

4. Results

The linear stability problem involves numerous parameters. Here we focus on the dependence of the critical thermocapillary Reynolds number $\mathrm{Re}_c = \mathrm{Re}_c(\mathrm{Re}_{\mathrm{g}})$ on the through flow in the gas phase, parameterised by Re_{g}. The gas flow Reynolds number is varied in the range $\mathrm{Re}_{\mathrm{g}} \in [-3500,\ 1500]$, including the closed chamber configuration ($\mathrm{Re}_{\mathrm{g}} = 0$). All other non-dimensional parameters are kept constant at values of the reference case defined in Stojanovic *et al.* (2022), namely, $\mathrm{Pr} = 28$, $\tau = \mathrm{Bd}/\mathrm{Bo} = 0.32$, $\Gamma = 0.66$, $\Gamma_{\mathrm{rod}} = 0.4$, $\eta = 4$ and $\mathcal{V} = 1$. The liquid bridge is heated from above or below under terrestrial gravity such that $\mathrm{Bd} = 0.41$, corresponding to the radius $r_{\mathrm{i}} = 2.5\,\mathrm{mm}$ used in the experiments of Romanò *et al.* (2017) and others (e.g. Yano *et al.* 2018*a*; Oba *et al.* 2019).

We consider two models: (a) A simplified model in which the shape of the liquid bridge is independent of the flow and given by its static shape, and (b) a model in which the flow-induced interfacial deformations are taken into account for the basic flow, but not for the perturbation flow. For both models the effect of the forced gas flow on the critical Reynolds number and the critical mode is computed and analysed. Furthermore, both models are

	$\mathrm{Re}_g^{m_1,m_2}$		$\mathrm{Re}_c(\mathrm{Re}_g^{m_1,m_2})$	
m	static	dynamic	static	dynamic
$3 \leftrightarrow 2$	−2618	−2625	1765	1753
$2 \leftrightarrow 1$	−2670	−2672	1952	1932
$1 \leftrightarrow 0$	−2547	−2564	2094	2068
$0 \leftrightarrow 2$	−2113	−2114	2319	2311
$2 \leftrightarrow 1$	−1997	−1898	2260	2207
$1 \leftrightarrow 0$	−131	−123	2043	2046
$0 \leftrightarrow 1$	−78	−74	1993	1998
$1 \leftrightarrow 2$	−70	−65	1981	1986
$2 \leftrightarrow 3$	−61	−57	1951	1957

Table 4: Codimension-two points $(\mathrm{Re}_g, \mathrm{Re}_c)^{m_1,m_2}$ for heating from above ($\mathrm{Re} > 0$). Data are given for a static as well as for a dynamically deformed free surface of the basic flow.

compared with each other and the relevance of dynamic surface deformations in the basic state is assessed.

4.1. *Hydrostatic surface shape*

4.1.1. *Linear stability boundary*

The dependence of the neutral and critical Reynolds numbers and oscillation frequencies on the gas flow Reynolds number Re_g for a static interface shape are shown in figure 2. The wave number of the critical mode is colour coded. For zero gravity conditions ($\mathrm{Bd} = 0$) the critical Reynolds numbers must be symmetric with respect to $(\mathrm{Re}_g, \mathrm{Re}_c) \to -(\mathrm{Re}_g, \mathrm{Re}_c)$ and $\omega_c(\mathrm{Re}_g) = -\omega_c(-\mathrm{Re}_g)$ (not shown). For the present Bond number $\mathrm{Bd} = 0.41$ this symmetry is broken. Due to the combined effect of thermocapillarity, buoyancy and gas flow the critical Reynolds number exhibits a complex behaviour. Throughout, the instability is time-dependent.

For heating from above ($\mathrm{Re} > 0$) and if the liquid bridge is exposed to a cold, upward gas flow opposing the thermocapillary-driven surface flow (first quadrant in figure 2(a)), the critical wave number is $m_c = 3$ and Re_c decreases from $\mathrm{Re}_c(\mathrm{Re}_g = 0) = 616$ when Re_g is increased. Except for a very shallow minimum of Re_c at $\mathrm{Re}_g = 450$, the critical Reynolds number $\mathrm{Re}_c(\mathrm{Re}_g)$ almost saturates near $\mathrm{Re}_c \approx 390$, already for $\mathrm{Re}_g \gtrsim 100$. If, on the other hand, Re_g is decreased from zero (hot, downward gas flow parallel to the thermocapillary surface flow, second quadrant in figure 2(a)), the critical Reynolds number strongly increases up to $\mathrm{Re}_c \approx 2000$ for $\mathrm{Re}_g = -60$. For a stronger flow of the hot gas ($\mathrm{Re} < -60$) different modes become critical and the critical curve is made of segments of neutral modes with different azimuthal wave numbers. This is illustrated in figure 3 by zooming into the region $(\mathrm{Re}_g, \mathrm{Re}_c) \in [-200, 20] \times [1700, 2200]$. Most notable is the local minimum of Re_c at $\mathrm{Re}_g = -414$ for wave number $m = 1$ (blue). A similar local minimum of Re_c for hot co-flow and a mode with $m = 1$ arises for long liquid bridges with $\Gamma = 1.8$ of $\mathrm{Pr} = 68$ under zero gravity (Stojanovic & Kuhlmann 2020*b*). The mode with $m = 1$ (blue) is critical in the range $\mathrm{Re}_g \in [-1850, -100]$. The codimension-two points $(\mathrm{Re}_g, \mathrm{Re}_c)^{m_1,m_2}$ at which two neutral curves for different wave numbers m_1 and m_2 intersect are listed in table 4 (columns labelled 'static'). Interestingly, the critical Reynolds number for strong gas flow is not a unique function of Re_g in the range $\mathrm{Re}_g \in [-2672, -1920]$. In this region the most dangerous mode has a wave number $m = 3$ (green). For even larger downward flow rates ($\mathrm{Re}_g < -2672$), the critical Reynolds number saturates near $\mathrm{Re}_c \approx 400$, within the range of Re_g considered.

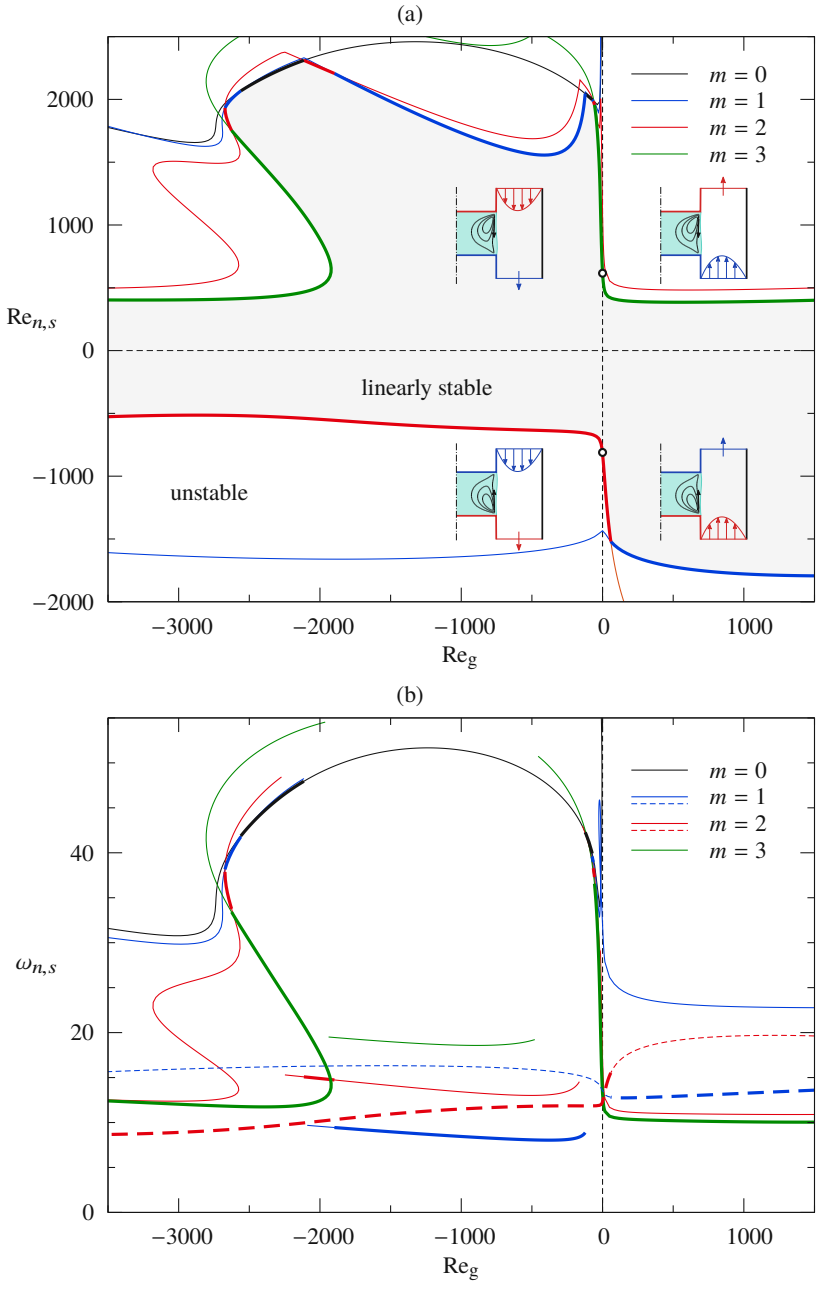

Figure 2: (a) Neutral (thin lines) and critical (thick lines) Reynolds numbers $\mathrm{Re}_{n,s}$ as functions of the gas flow Reynolds number $\mathrm{Re_g}$. The neutral and critical wave numbers are coded by colour (legend). The region of linear stability is filled in gray. The insets serve to symbolise the direction and the temperature (hot/cold) of the mean gas flow. The vertical dashed line indicates a vanishing gas flow (closed chamber) and the circles represent the associated critical points. (b) Corresponding neutral and critical frequencies ω_s (for modes propagating in the negative φ direction). Full and dashed lines correspond to $\mathrm{Re}_{n,s} > 0$ and $\mathrm{Re}_{n,s} < 0$, respectively.

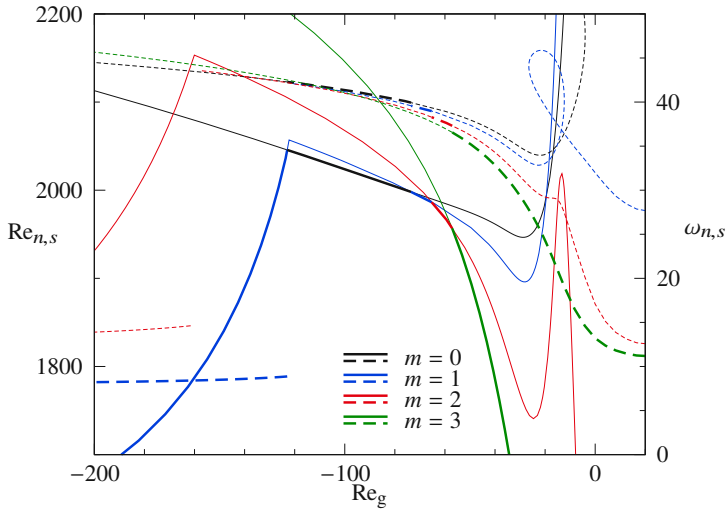

Figure 3: Neutral Reynolds numbers $\mathrm{Re}_{n,s}$ (thin solid lines) and neutral frequencies (thin dashed lines) as functions of the gas flow Reynolds number $\mathrm{Re}_g \in [-200,\ 20]$ for heating from above ($\mathrm{Re}_{n,s} > 0$). Critical Reynolds numbers $\mathrm{Re}_{c,s}$ and frequencies $\omega_{n,s}$ as shown as thick lines.

In case of heating from below ($\mathrm{Re}_c < 0$ in figure 2(a)) the critical Reynolds number for a closed chamber is $\mathrm{Re}_c(\mathrm{Re}_g = 0) = -811$ with $m_c = 2$. Like for heating from above, the critical threshold near $\mathrm{Re}_g \approx 0$ is very sensitive with respect to a variation of the gas flow rate. When the liquid bridge is exposed to a cold gas flow from above opposing the thermocapillary flow direction (third quadrant in figure 2(a)), the basic flow is destabilised and the critical Reynolds number readily saturates near $\mathrm{Re}_c \approx -580$. For a hot gas flow from below ($\mathrm{Re}_g > 0$, co-flow direction, fourth quadrant in figure 2(a)), the basic flow ist strongly stabilised, the critical wave number changes to $m_c = 1$ at $\mathrm{Re}_g = 58.5$ and, for $1000 \lesssim \mathrm{Re}_g \leqslant 1500$, the critical Reynolds number seems to saturate near $\mathrm{Re}_c \approx -1800$.

For an open shield tube and outflow boundary conditions (2.28) for the basic flow we find slightly different critical Reynolds numbers as $\mathrm{Re}_g = 0$ is approached from above or from below. For heating from above, for instance, we obtain $\mathrm{Re}_c(\mathrm{Re}_g \to 0^-) = 622$ and $\mathrm{Re}_c(\mathrm{Re}_g \to 0^+) = 620$. Both these values deviate less than 1% from the critical Reynolds number $\mathrm{Re}_c(\mathrm{Re}_g \equiv 0) = 616$ for a closed tube, using rigid boundary conditions ($\boldsymbol{u}_{g0} = 0$) at the outlet. Therefore, and due to the practical relevance of a truly closed ambient gas space, we used rigid boundary conditions only for $\mathrm{Re}_g \equiv 0$. Graphically, the minute discontinuity at $\mathrm{Re}_g = 0$ is not visible with the bare eye in fig. 3 (see dashed lines close to $\mathrm{Re}_g = 0$). Moreover, the discontinuity disappears for $\Gamma_{\mathrm{rod}} \to \infty$, which is consistent with the critical Reynolds numbers being rather insensitive with respect to increasing Γ_{rod}. In Appendix B it is shown that for $|\mathrm{Re}_g| > 90$, the critical Reynolds number varies by less than 2% when Γ_{rod} is increased from 0.4 to 8. The results obtained are thus applicable for a wide range of experimental designs with different Γ_{rod}.

4.1.2. *Sensitivity of Re_c with respect to the direction of the gas flow*

Basic state

In order to understand the strong sensitivity of the critical Reynolds number with respect to the direction and strength of a weak axial gas flow we inspect the basic flows for four cases, each in one of the four quadrants of figure 2(a). For heating from above we consider $(\mathrm{Re}_g, \mathrm{Re}) = (\pm 40, 616)$, where $\mathrm{Re} = \mathrm{Re}_c(\mathrm{Re}_g = 0) = 616$. For heating from below we

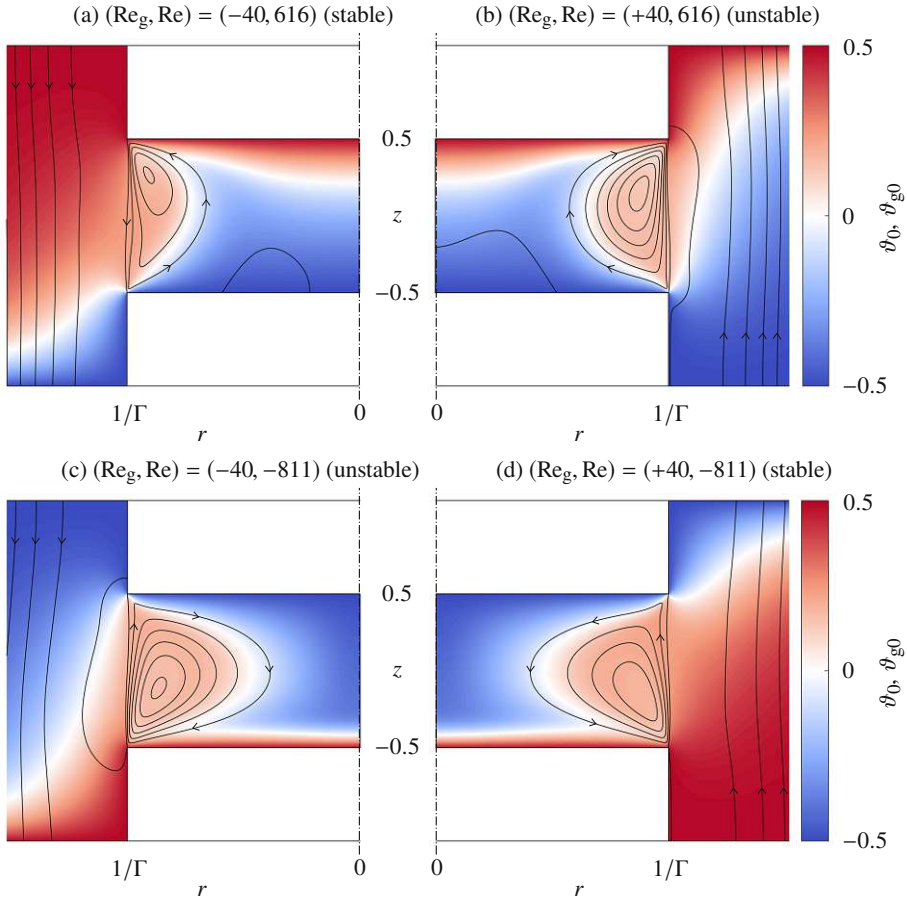

Figure 4: Streamlines and temperature fields of four basic states for Reynolds numbers Re and $\mathrm{Re_g}$ as indicated. Streamlines are drawn equidistantly. The steps size $\Delta\psi$ is pairwise identical in the liquids of (a,b) and in the gases of (a,b). The same applies to (c,d), but with different levels due to the different Reynolds number Re. Note the flow separates from the cold wall in (a,b).

similarly select $(\mathrm{Re_g}, \mathrm{Re}) = (\pm 40, -811)$, where $\mathrm{Re} = \mathrm{Re}_c(\mathrm{Re_g} = 0) = -811$. The basic flows for the four parameter sets are shown in figure 4. For the counterflow configurations in figures 4(b,c) a weak recirculation zone is created in the gas phase next to the free surface, visible by the separation streamline shown. This type of separated flow in the gas phase has been confirmed experimentally by Irikura *et al.* (2005) and Ueno *et al.* (2010).

For the present Prandtl number Pr = 28 the thermal conditions in the gas phase are much more important for the stability than the viscous stresses exerted on the interface by the gas flow. In particular, the flow along the free surface is primarily driven by thermocapillary forces near the hot corner (Kamotani & Ostrach 1998; Kuhlmann 1999). The cold corner region is of lesser importance, because the strong gradients of the surface temperature near the cold corner are located very close to the rigid wall. Therefore, they cannot contribute significantly to the global flow.

Figure 5(a) shows velocity (blue) and temperature profiles (red) of the basic flow along the free surface for the case of heating from above (Re > 0). The direction of the gas flow is distinguished by line type. For a hot (cold) gas flow the interface is heated (cooled) for

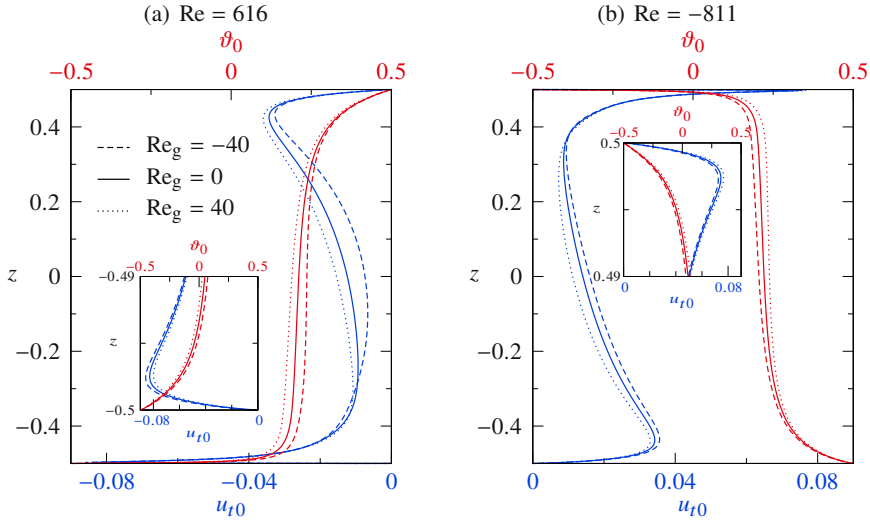

Figure 5: Tangential velocity $u_{t0} = \boldsymbol{t} \cdot \boldsymbol{u}_0$ (blue) and temperature distribution ϑ_0 (red) of the basic flow along the free surface (parameterised by z). (a) Heating from above with Re = 616. (b) Heating from below with Re = −811. The gas Reynolds number is distinguished by line type: $\mathrm{Re_g} = -40$ (dashed lines), $\mathrm{Re_g} = 0$ (full lines) and $\mathrm{Re_g} = 40$ (dotted lines). The insets resolve the velocity peaks near the cold wall.

$\mathrm{Re_g} = -40$ ($\mathrm{Re_g} = 40$) as compared to the case of a closed chamber ($\mathrm{Re_g} = 0$, full line). For a hot downward flow with $\mathrm{Re_g} = -40$ (dashed lines), the plateau temperature is increased. This reduces the thermocapillary stresses near the hot corner. As a result, the magnitude of the surface velocity decreases. The cooling of the interface for $\mathrm{Re_g} = 40$ (dotted lines), on the other hand, reduces the surface temperature in the plateau region and increases the thermocapillary stresses near the hot corner. This gives rise to a larger surface velocity as compared to $\mathrm{Re_g} = 0$. Viscous stresses from the gas phase would have the opposite effect, but for $\mathrm{Re_g} = \pm 40$ they are of minor importance compared to thermocapillary stresses. The stronger flow for $\mathrm{Re_g} = 40$ as compared to $\mathrm{Re_g} = 0$ (both at Re = 616) is equivalent to a stronger effective thermocapillary driving and can thus be identified as the reason for the instability of this flow (shown in figure 4(b)). Likewise, the weaker thermocapillary driving is responsible for the stability of the flow for $(\mathrm{Re_g}, \mathrm{Re}) = (-40, 616)$ (figure 4(a)).

Apart from the strength of the surface flow, the whole structure of the vortex in the liquid phase and the associated temperature field changes: the radial extent of the stronger vortex (cold upward counter-flow, $\mathrm{Re_g} = 40$, figure 4(b)) is significantly larger than that of the weaker vortex (hot downward co-flow, $\mathrm{Re_g} = -40$, figure 4(a)). This effect results from the interplay between buoyancy and inertia forces. Heating the liquid bridge from above, hot liquid is transported downward along the free surface and returns upward in the bulk. Since the upward motion in the bulk is assisted by buoyancy forces, the radial extension of the vortex is reduced compared to the case of zero gravity. This effect is most pronounced when the thermocapillary-driven vortex flow is weak $\mathrm{Re_g} = -40$ (figure 4(a)). For the stronger basic flow at $\mathrm{Re_g} = 40$, inertia prevents a premature buoyant rise of the liquid in the bulk and the vortex has a larger extent in the radial direction (figure 4(b)). Associated with this change of the vortex structure, the region of large (mainly radial) internal temperature gradients is displaced radially inward for $\mathrm{Re_g} = 40$ (figure 4(b)) and radially outward for $\mathrm{Re_g} = -40$ (figure 4(a)). This structural change has implications for the respective critical mode and the

stability boundary, because a hydrothermal wave draws its energy primarily from the internal basic state temperature gradients (Wanschura *et al.* 1995; Smith & Davis 1983*a*).

For heating from below (figure 4(c,d) and figure 5(b)) similar arguments hold. For example, for $\mathrm{Re_g} = 40 > 0$ (figure 4(d)), the free surface is heated (dotted red line in figure 5(b)), which reduces the thermocapillary driving near the hot wall. As a result, the flow for $\mathrm{Re_g} = 40$ is much weaker and more stable than the one for $\mathrm{Re_g} = 0$ and $\mathrm{Re_g} = -40$ (both at $\mathrm{Re} = -811$). While the structure of the basic vortices is similar for both directions of the gas flow ($\mathrm{Re_g} = \pm 40$, figures 4(c,d)) and heating from below, they differ markedly from those for heating from above: For heating from below buoyancy is assisting the upward free surface flow but tends to prevent the hot return flow from descending. This leads to a much larger radial width of the vortices (figures 4(a,b)) associated with a further inward displacement of the internal temperature gradients than for heating from above (figures 4(a,b)).

In summary, for a weak gas flow, the basic flow is stronger in the counter-flow configuration, due to the heat transfer between liquid and gas. Furthermore, buoyancy forces cause the flow structures to be located closer to the free surface for heating from above, while they are displaced radially inward for heating from below.

Critical modes

The instability for $\mathrm{Re_g} = 0$ is due to hydrothermal waves (Smith & Davis 1983*a*; Wanschura *et al.* 1995). They are generated in the liquid phase and depend on the structure of the flow in the liquid. Taking into account the gas phase, Stojanovic *et al.* (2022) have shown that the temperature amplitude of the hydrothermal wave is very weak in the gas phase. Therefore, the gas phase only plays an indirect role for the instability process by affecting the basic velocity and temperature fields in the liquid phase. Since the hydrothermal waves depend on the particular basic flow structure, we consider representative critical modes with $\omega_c > 0$, corresponding to waves propagating in the negative φ direction.

Let us compare the critical mode for heating from above and $\mathrm{Re}_c(\mathrm{Re_g} = -40) = 1786$ (hot downward gas co-flow) with the one for $\mathrm{Re}_c(\mathrm{Re_g} = 40) = 431$ (cold upward gas counter-flow). Both modes have the wave number $m_c = 3$. From figure 6(a,b) the location of the regions of high basic state temperature gradients is qualitatively similar as in figure 4(a,b) for $\mathrm{Re} = 616$. However, for cold upward gas counter-flow (figure 6(b), $(\mathrm{Re_g}, \mathrm{Re}_c) = (40, 431)$), the temperature gradients of the basic flow from which the hydrothermal wave draws its energy are located more distant from the free surface than for hot downward gas co-flow (figure 6(a), $(\mathrm{Re_g}, \mathrm{Re}_c) = (-40, 1786)$). This provides more space for the evolution of the perturbation vortices which feed the perturbation temperature extrema by advecting basic state temperature (Wanschura *et al.* 1995). Figures 6(a–d) show that the perturbation vortices at criticality are well developed for $\mathrm{Re_g} = 40$, whereas they are more confined to the free surface region for $\mathrm{Re_g} = -40$. Therefore, the critical mode for $(\mathrm{Re_g}, \mathrm{Re}_c) = (40, 431)$ can draw its energy from a larger region of high basic state temperature gradients than the critical mode for $(\mathrm{Re_g}, \mathrm{Re}_c) = (-40, 1786)$ and the perturbation temperature field for $\mathrm{Re_g} = 40$ is more compact, presumably suffering less thermal dissipation than the less compact one for $\mathrm{Re_g} = -40$. While the structures of the two critical modes differ in the bulk, their footprints on the free surface are very similar (figure 6(e,f)).

For heating from below the critical modes for $(\mathrm{Re_g}, \mathrm{Re}_c) = (-40, -686)$ and $(\mathrm{Re_g}, \mathrm{Re}_c) = (40, -1348)$ are shown in figure 7(a,c,e) and figure 7(b,d,f), respectively. In contrast to heating from above, both critical modes have wave number $m_c = 2$ and they may appear very similar for $\mathrm{Re_g} = \pm 40$ (figure 4(c,d)). But the stronger basic vortex at constant Re for $\mathrm{Re_g} = -40$ as compared to $\mathrm{Re_g} = 40$ explains why the former is more unstable than the latter. Another contributing factor, visible from figure 4(a–d), is the radial temperature gradients of the basic flow arise closer to the axis for $\mathrm{Re_g} = 40$ as compared to $\mathrm{Re_g} = -40$. Therefore, the coupling

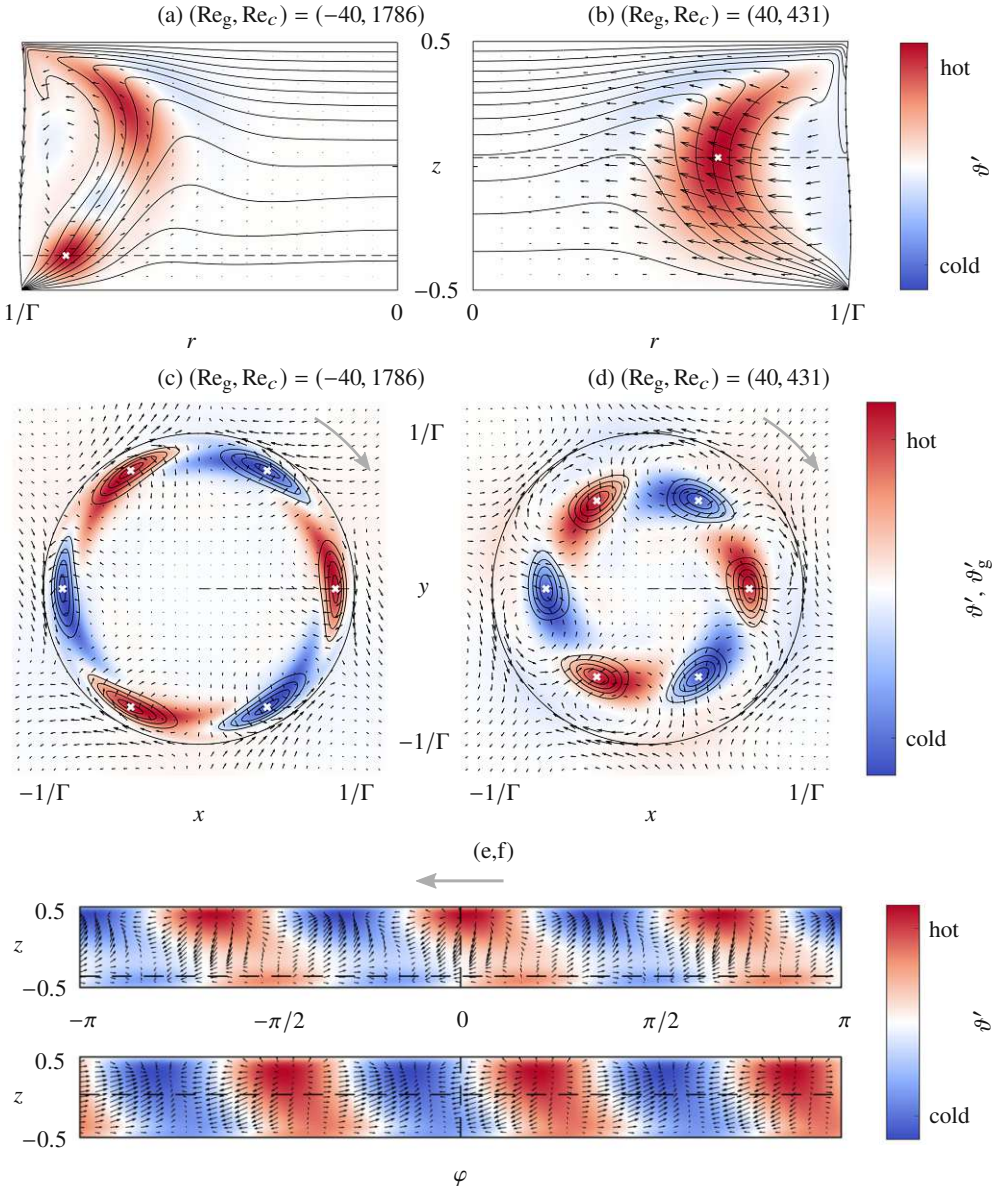

Figure 6: Critical velocity (black arrows) and temperature fields (colour) for heating from above and hot co-flow $(\mathrm{Re}_g, \mathrm{Re}_c) = (-40, 1786)$ (a,c,e) and cold counter-flow $(\mathrm{Re}_g, \mathrm{Re}_c) = (40, 431)$ (b,d,f). The critical wave number is $m_c = 3$. (a,b) Vertical (r, z) planes in which the local thermal production (not shown) takes its maximum (white cross) in the bulk. Lines in (a,b) indicate equidistant isotherms of the basic state. (c,d) Horizontal cross sections in the planes $z = -0.36$ (c) and $z = 0.03$ (d) in which the respective total local thermal production $-\vartheta' \boldsymbol{u}' \cdot \nabla \vartheta_0$ (isolines) takes its maximum (white crosses) in the bulk. (e,f) Radial projections of the free surface velocity and temperature. The gray arrows in (c,d,e) indicate the direction of propagation of the critical mode. The dashed lines represent the location of the vertical and horizontal cut planes.

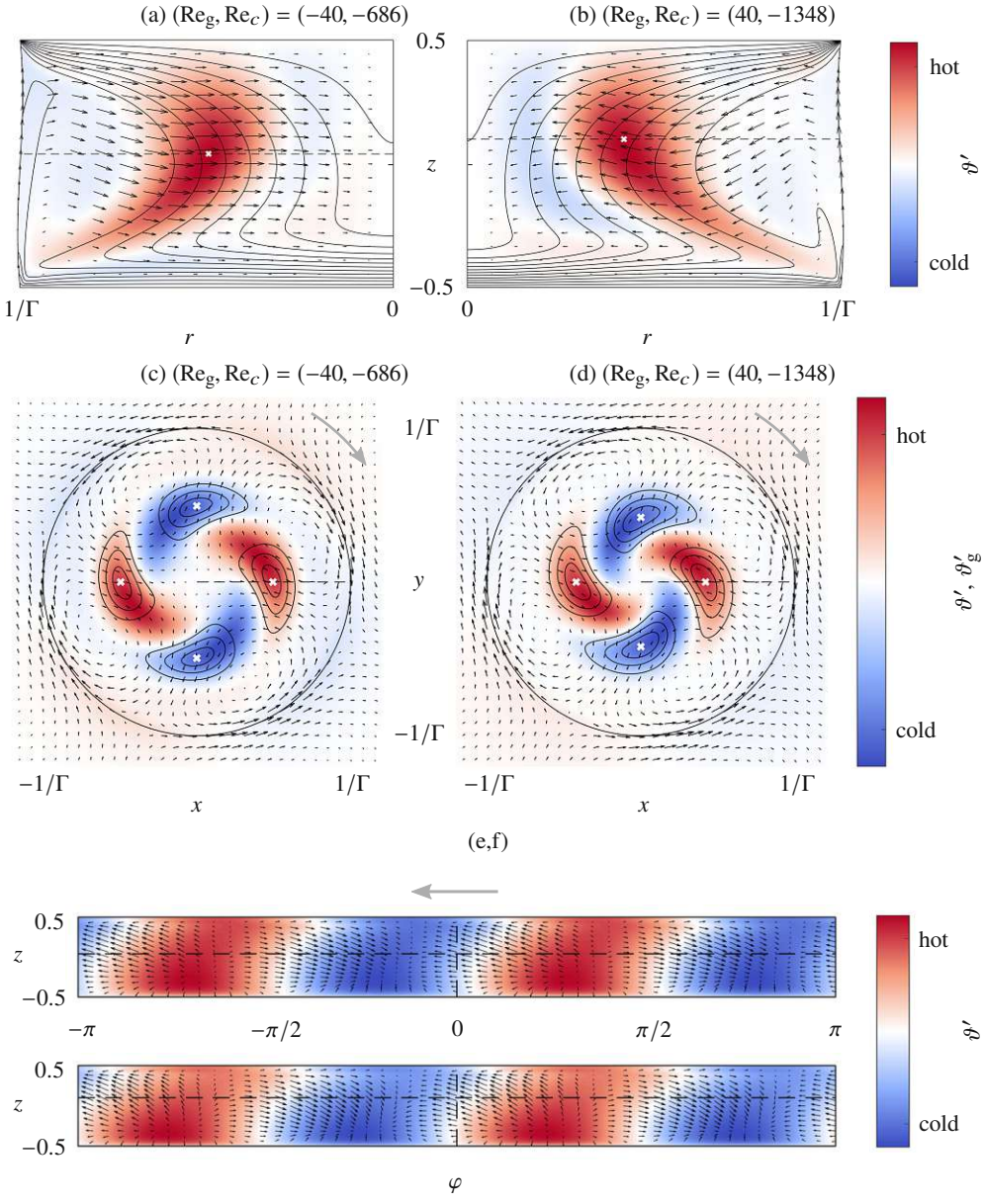

Figure 7: Critical modes for heating from below and for $(\mathrm{Re}_g, \mathrm{Re}_c) = (-40, -686)$ (a,c,e) and for $(\mathrm{Re}_g, \mathrm{Re}_c) = (40, -1348)$ (b,d,f). Lines, arrows and colours as in figure 6. The horizontal cuts are located at $z = 0.04$ (a,e) and $z = 0.1$(b,f). The critical wave number is $m_c = 2$.

between internal temperature extrema and the surface temperature fluctuations driving the perturbation velocity field is weaker for $\mathrm{Re}_g = 40$.

The thermal energy budgets for the four critical modes considered are presented in figure 8. From figure 8(a) all critical modes are hydrothermal waves for which the perturbation energy is mainly created by radial advection of basic state temperature, represented by the

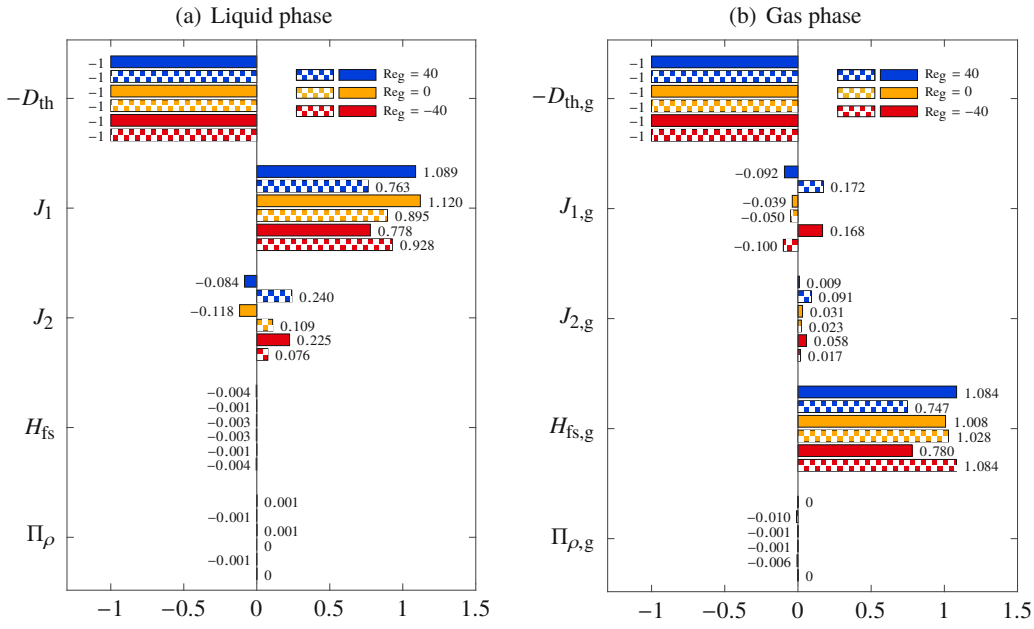

Figure 8: Thermal energy budgets of the critical modes for $\mathrm{Re_g} \in \{-40; 0; 40\}$. Full bars: heating from above with $\mathrm{Re}_c \in \{1786; 616; 431\}$ and $m_c = 3$. Checkered bars: heating from below with $\mathrm{Re}_c \in \{-686; -811; -1348\}$ and $m_c = 2$. (a) Liquid phase. (b) Gas phase.

total normalised production term $J_1 := -\mathrm{Re}\mathcal{D}_{\mathrm{th}}^{-1}\int_{V_i} j_1 \mathrm{d}V = -\mathrm{Re}\mathcal{D}_{\mathrm{th}}^{-1}\int_{V_i} \vartheta' u' \partial_r \vartheta_0 \mathrm{d}V$. The thermal production by axial advection $J_2 := -\mathrm{Re}\mathcal{D}_{\mathrm{th}}^{-1}\int_{V_i} j_2 \mathrm{d}V = -\mathrm{Re}\mathcal{D}_{\mathrm{th}}^{-1}\int_{V_i} \vartheta' w' \partial_z \vartheta_0 \mathrm{d}V$ plays a minor role. For heating from above (solid colours) the critical mode for $\mathrm{Re_g} = -40$, which is confined to the very vicinity of the free surface, has the smallest production $J_1 = 0.778$ (full red bar) and deviates the most from the reference value of J_1 for $\mathrm{Re_g} = 0$ (full orange bar). It is also seen that the heat loss of the liquid phase through the free surface, i.e. the thermal coupling, is generally vanishingly small compared to the thermal production due to advection (J_1, J_2) in the liquid (figure 8(a)). This small heat loss of the perturbation flow in the liquid $H_{\mathrm{fs}} := 2\pi\mathcal{D}_{\mathrm{th}}^{-1}\mathrm{Pr}^{-1}\int_{-0.5}^{0.5} h(\partial_r\hat{\vartheta}^2 - \partial_z h_0 \partial_z \hat{\vartheta}^2)\mathrm{d}z$ appears as a heat gain $H_{\mathrm{fs,g}} = -\tilde{\lambda} H_{\mathrm{fs}}$ of the perturbation flow in the gas phase. There it is the main source of thermal energy. But this gain is almost completely balanced by the thermal dissipation in the gas phase $D_{\mathrm{th},g}$. This proves quantitatively the gas phase does not play an active role in the instability mechanism. As a side, the relative thermal production rates $\Pi_\rho < 0.1\%$ and $\Pi_{\rho,\mathrm{g}} < 1\%$ associated with the density variations in the liquid and in the gas, respectively, are negligible.

In conclusion, we find the sensitivity of the critical Reynolds number with respect to a weak axial gas flow is mainly related to the changed strength of the basic flow, caused by the heating or cooling of the free surface by the gas flow. The strength of the basic flow affects the strength of the basic state temperature gradients and thus the stability boundary. The critical wave numbers differ for heating from above ($m_c = 3$) and from below ($m_c = 2$). But the spatial structures of the critical modes do not change very much, except for heating from above with $\mathrm{Re_g} < 0$ in which the weaker vortex is also radially more confined to the interface as a result of buoyancy.

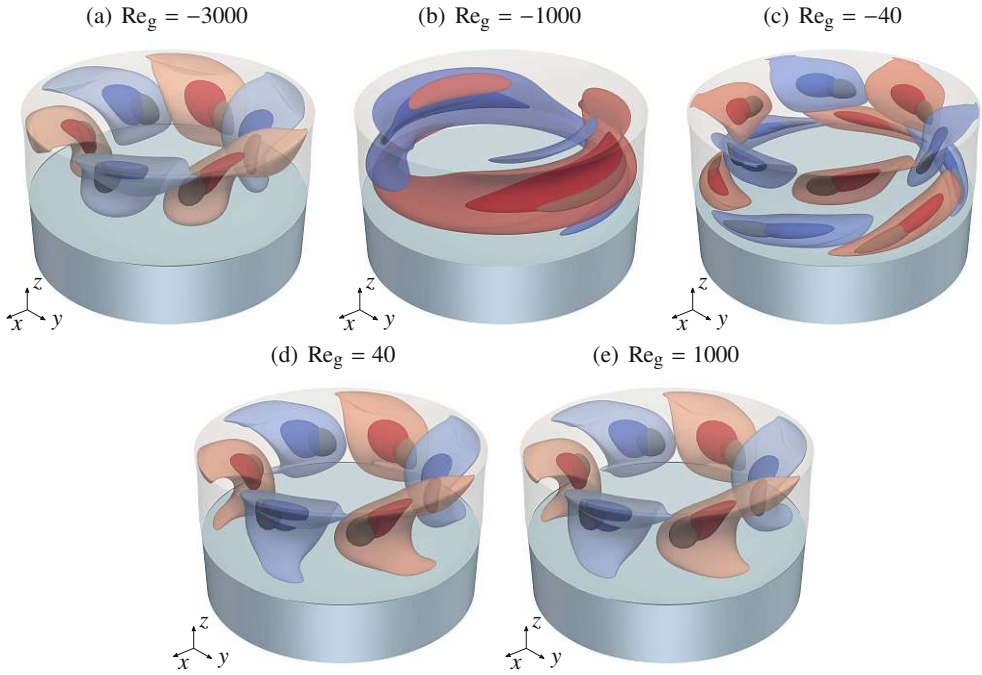

Figure 9: Isosurfaces of the critical perturbation temperature ϑ' in the liquid for heating from above: (a) $\mathrm{Re}_c = 404$, (b) $\mathrm{Re}_c = 1733$, (c) $\mathrm{Re}_c = 1786$, (d) $\mathrm{Re}_c = 431$, (e) $\mathrm{Re}_c = 389$. The isosurface values are $\pm 0.25 \times \max|\vartheta'|$ (light colours) and $\pm 0.75 \times \max|\vartheta'|$ (dark colours). A single isosurface of the total local thermal production rate at $j_1 + j_2 = \vartheta' \boldsymbol{u}' \cdot \nabla\vartheta_0 = 0.7 \times \max|\vartheta' \boldsymbol{u}' \cdot \nabla\vartheta_0|$ is shown in gray.

4.1.3. *Critical modes for large gas flow rates: Heating from above*

Three-dimensional views of the critical modes for heating from above are shown in figure 9(a–e) by isosurfaces of the perturbation temperature ϑ' for $\mathrm{Re}_g = (-3000, -1000, -40, 40, 1000)$, covering the full range of gas flow Reynolds numbers. All waves propagate in clockwise, i.e., in the negative φ direction. Since the dynamic Bond number is constant with $\mathrm{Bd} = 0.41$, buoyancy forces are proportional to the thermocapillary forces. The critical wave number of the modes shown is $m_c = 3$, except for $\mathrm{Re}_g = -1000$ for which $m_c = 1$. Throughout, the temperature perturbations exhibit the typical behaviour of a hydrothermal wave. Merely, for $\mathrm{Re}_g = -1000$ (b) and $\mathrm{Re}_g = -40$ (c) where the critical Reynolds numbers are relatively large with $\mathrm{Re}_c \approx 1750$, the critical modes differ. In these cases buoyancy forces are strong as well, while the surface flow is weakened due to the hot gas co-flow ($\mathrm{Re}_g < 0$). In these cases the Rayleigh number $\mathrm{Ra} = 11.48 \times \mathrm{Re}$ can reach values of the order of $O(10^4)$ (stabilising thermal stratification). Thus buoyancy shapes the basic vortex close to the free surface to have a much smaller radial extend (for $\mathrm{Re}_g < 0$) than for smaller Reynolds (and Rayleigh) numbers and the temperature extrema of the hydrothermal wave for $\mathrm{Re} = -1000$ and -40 arise much closer to the free surface (see e.g., figure 6(a,c)). These perturbation modes also have a more spiral behaviour such that the perturbation temperature field exhibits a more complex structure in a plane $\varphi = \text{const.}$ with temperature minima and maxima, visible in figure 6(a).

For a discussion of the saturation of the critical Reynolds numbers seen in figure 2(a), we note that the viscous stress from the gas phase has very little influence on the basic flow for the range of gas Reynolds numbers considered. Estimating the magnitude of the thermocapillary

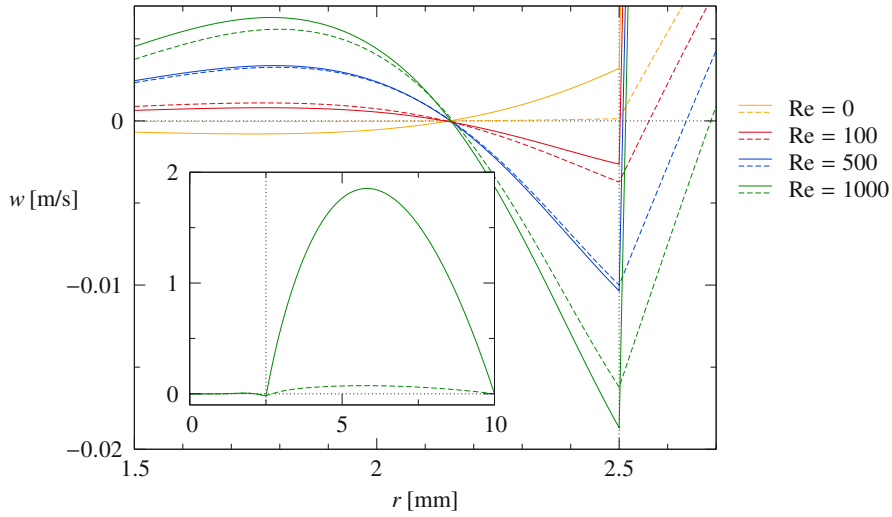

Figure 10: Dimensional axial velocity component $w(r, z = 0)$ at midplane for different thermocapillary Reynolds numbers (colours) and for gas flow Reynolds numbers $\mathrm{Re_g} = 40$ (dashed lines) and $\mathrm{Re_g} = 1000$ (full lines). The inset serves to show the scale of the gas flow relative to the liquid flow for $\mathrm{Re} = 1000$. The location of the interface is at $h_0(z = 0) = 2.5\,\mathrm{mm}$.

stress by $\gamma\Delta T/d$ and the viscous stress due to the gas flow by $\mu_g \bar{w}_\mathrm{g}/(r_\mathrm{o} - r_\mathrm{i})$, the order of magnitude of the ratio of the viscous gas stress to the thermocapillary stress is $\Gamma\tilde{\mu}(\mathrm{Re_g}/3\mathrm{Re})$. For $\mathrm{Re_g} = 3000$ and $\mathrm{Re} = 500$ this amounts to about 1%. Therefore, within the range of $\mathrm{Re_g}$, the effect of the gas flow on the basic state is essentially a thermal one.

For heating from above and cold counter-flow ($\mathrm{Re_g} > 0$) the critical Reynolds number saturates at relatively small gas flow rates of $\mathrm{Re_g} \approx 100$ at a value of $\mathrm{Re}_c \approx 390$. For this Reynolds number the basic vortex flow and temperature field in the liquid are almost independent of the gas Reynolds number in the range $\mathrm{Re_g} \in [100, 500]$. This can be explained by two opposing thermal effects of the gas flow on the strength of the vortex which nearly balance each other at $\mathrm{Re} = 390$. To understand these effects, radial profiles of the vertical velocity $w(r)$ at midplane $z = 0$ are shown in figure 10 for several thermocapillary Reynolds numbers (colour coded) and $\mathrm{Re_g} = 40$ (dashed lines) and 1000 (full lines).

For a vanishing thermocapillary Reynolds number $\mathrm{Re} = 0$, the flow in the liquid is only driven by the gas (orange lines) and the interface moves in the positive z direction with $w(r = h_0(0)) > 0$. As Re is increased the surface flow becomes readily dominated by thermocapillary forces and for $\mathrm{Re} = 100$ the direction of the surface velocity is downward with $w(r = h_0(0)) < 0$ (red lines). For $\mathrm{Re} = 100$ and weak gas counter-flow ($\mathrm{Re_g} = 40$, dashed red line) a sizable separation bubble exists in the gas phase next to the free surface (see e.g. figure 4(b)), visible in figure 10 by the downward gas flow between the free surface ($r \approx 2.50\,\mathrm{mm}$) and the zero of $w_{\mathrm{g}0}(r)$ in the gas phase at $r \approx 2.53\,\mathrm{mm}$. For the stronger gas counterflow ($\mathrm{Re_g} = 1000$, full red line) the region in which $w_{\mathrm{g}0} < 0$ in the gas phase adjacent to the free surface has become very thin due to the higher shear stress in the gas phase. The zero of $w_{\mathrm{g}0}$ has moved very close to the free surface (almost invisible on the scale shown) and $w_{\mathrm{g}0}$ (full red line) increases nearly vertically for $r > h_0(0)$. As expected, the stronger gas flow has a retarding effect on the downward surface flow due to the increased viscous stresses from the gas on the interface. Associated with the reduced surface velocity is a weaker vortex in the liquid. As the thermocapillary Reynolds number is increased to $\mathrm{Re} \approx 400$

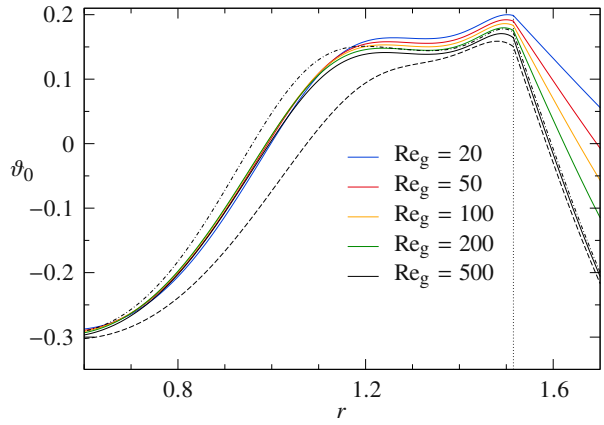

Figure 11: Radial basic temperature profiles $\vartheta_0(r, z = 0)$ for Re = 400 and different gas Reynolds numbers $\mathrm{Re_g} = 20, 50, 100, 200, 500$ (full lines colour coded, see legend). In addition, the temperature profiles are shown for $\mathrm{Re_g} = 500$ and Re = 200 (black dashed) and Re = 600 (black dash-dotted). The vertical dotted line marks the free surface.

(blue lines), which roughly coincides with the saturation of $\mathrm{Re}_c(\mathrm{Re_g})$, the retardation of the surface velocity diminishes. And for $\mathrm{Re} \gtrsim 400$ the gas flow has an augmenting effect on the magnitude of the interfacial velocity, despite of the retarding action of the viscous shear stresses from the gas side. As a result, the magnitude of the surface velocity for Re = 1000 is larger for $\mathrm{Re_g} = 1000$ (full green line) than for $\mathrm{Re_g} = 40$ (dashed green line). The reason for the augmenting action of the counterflow is related to the characteristic surface temperature profile when the thermocapillary Reynolds number is large and the flow is mainly driven near the hot corner (the argument was used above in explaining the velocity profiles in figure 5): The gas has a cooling effect such that the plateau temperature for large-thermocapillary-Reynolds-number flows is decreased. Along with a decrease of the plateau temperature the thermocapillary driving force near the hot wall increases and reinforces the thermocapillary flow, overcompensating the viscous retardation effect. For $\mathrm{Re} \gtrsim 400$ the increase of the surface velocity at midplane by the cooling effect is larger than the decrease of the surface velocity due to viscous stresses from the gas side which, on the other hand, dominates for $\mathrm{Re} \lesssim 400$.

The Reynolds number $\mathrm{Re} \approx 400$ at which both effects on the surface velocity $w(r = h_0(0), 0)$ balance seems to be almost independent of $\mathrm{Re_g} \in [100, 500]$. Therefore, the whole basic flow for $\mathrm{Re} \approx 400$ is almost independent of $\mathrm{Re_g}$ in this range, and a critical Reynolds number $\mathrm{Re}_c \approx 400$ will also be independent within $\mathrm{Re_g} \in [100, 500]$. In fact, the radial temperature gradients for Re = 400 from which the hydrothermal-wave instability draws its energy are almost independent $\mathrm{Re_g} \in [100, 500]$. This is demonstrated in figure 11 which shows basic temperature profiles $\vartheta_0(r, z = 0)$ at midplane for Re = 400 ($\approx$ saturation level of Re_c) and different gas Reynolds numbers $\mathrm{Re_g} = 20, 50, 100, 200, 500$. In the region $r \leqslant 1.1$ of largest slopes, the temperature profiles are almost identical, regardless of the temperature gradients in the gas phase. This indicates the perturbation mode finds the same basic-flow conditions for the major energy production term J_1 which builds on $\partial_r \vartheta_0$ in the liquid phase, independent of $\mathrm{Re_g}$. On the other hand, the slopes for $\mathrm{Re_g} = 500$ and Re = 200 (black dashed line) is smaller, while the one for $\mathrm{Re_g} = 500$ and Re = 600 (black dash-dotted) is larger. These flow states are stable and unstable, respectively. From figure 11 one can also identify the continuous decrease of the surface temperature as $\mathrm{Re_g}$ is increased.

The major integral (global) energy production terms J_1 and J_2 for the liquid phase are

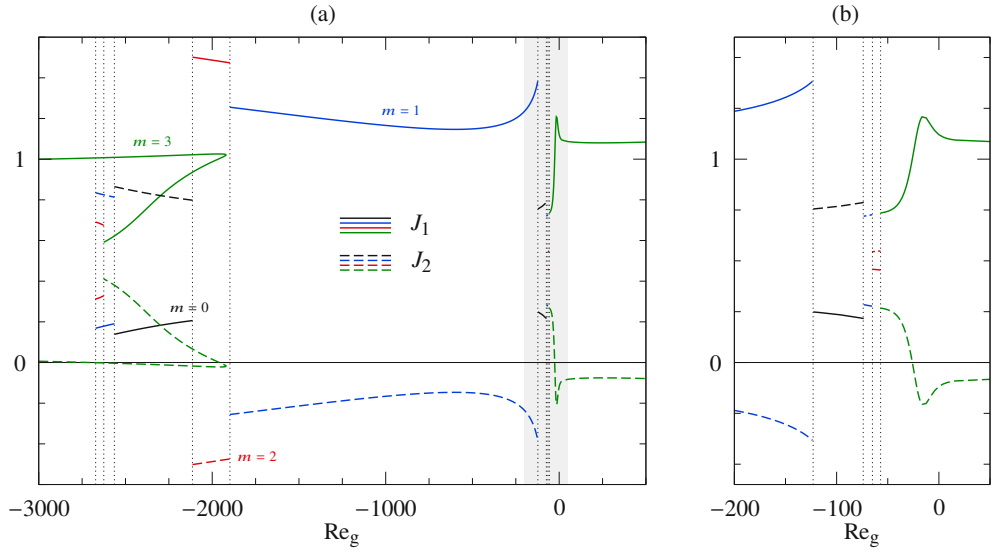

Figure 12: (a) Normalised global energy production rates J_1 (full lines) and J_2 (dashed lines) of the critical (and neutral) modes in the liquid phase for heating from above shown as functions of $\mathrm{Re_g}$. The colour indicates the wave number. The vertical dotted lines indicate the codimension-two points listed in table 4. (b) Zoom into the grey rectangle shown in (a).

displayed in figure 12 as functions of $\mathrm{Re_g}$. For the major critical modes with $m_c = 1$ (blue), $m_c = 2$ (red) and $m_c = 3$ (green), the thermal energy is mainly produced by radial advection of basic state temperature J_1 (full lines). The axial advection (dashed lines) is almost negligible or even acts stabilising. This applies to both gas flow directions. Hence, the instability mechanism as such is not much affected by the direction of the gas flow, i.e. by the heating or cooling of the liquid through the gas in the basic flow. The peak values of the total local energy production $j_1 + j_2$ are located inside the grey isosurfaces shown in figure 9. Typically, the production maxima are azimuthally displaced from the temperature extrema with the displacement direction determining the direction of propagation of the wave.

For all $\mathrm{Re_g}$ considered, $|\Pi_\rho| < 0.002$ and $-0.007 < H_{\mathrm{fs}} < 0$ in the liquid phase. The greatest impact of the density variation on the thermal energy budget is observed in the gas phase and for heating from above with $\Pi_{\rho,\mathrm{g}} = -0.021$ for $m_c = 2$, $\mathrm{Re_g} = -2114$, $\mathrm{Re}_c = 2311$. This conditions corresponds to $\Delta T = 70\,\mathrm{K}$ and $\varepsilon = 0.087$. For heating from below, the maximum impact of $\Pi_{\rho,\mathrm{g}}$ on the thermal energy is found to be even smaller (not shown).

4.1.4. *Critical modes for large gas flow rates: Heating from below*

Figure 13 shows temperature isosurfaces of the critical modes for heating from below and for the same gas flow Reynolds numbers as in figure 9. Now the dominant critical wave number is $m_c = 2$ and most critical modes have the expected structure with strong internal temperature extrema in the shear layer of the return flow of the basic vortex. Only for stronger hot co-flow from below with $\mathrm{Re} = 1000$ the wave number changes to $m_c = 1$ and the critical mode is very different from the others with a pronounced spiral character and temperature extrema very close to the axis. In this case the basic flow is affected by the gas flow in an opposite manner than for hot co-flow when heating from above: Instead of a small radial extent of the basic vortex for heating from above, the basic vortex is radially extended for heating from below,

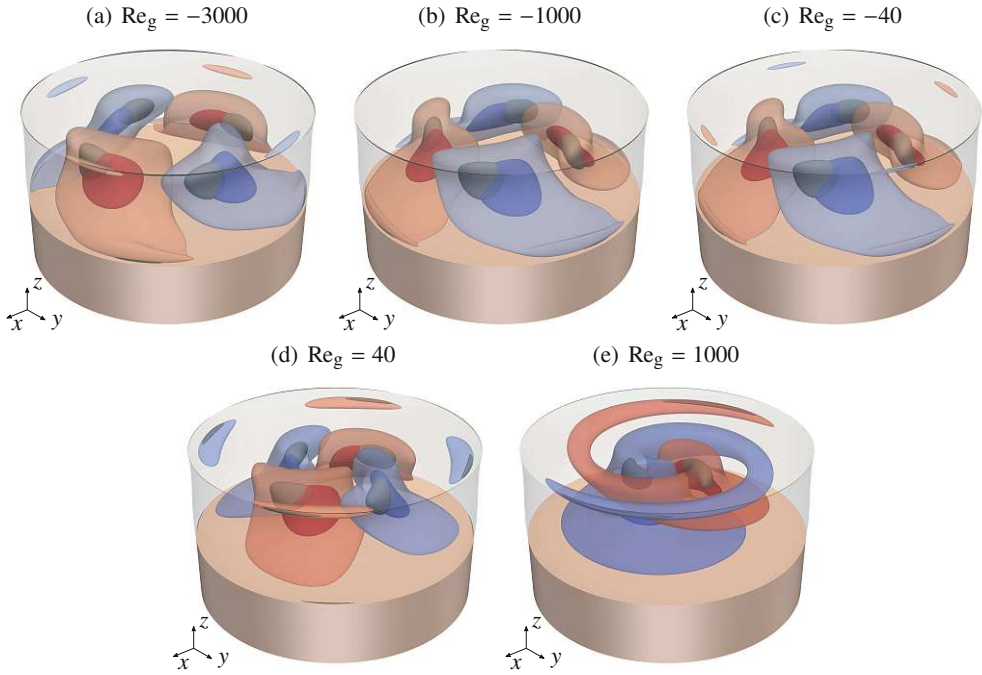

Figure 13: Isosurfaces of the critical perturbation temperature ϑ' in the liquid for heating from below: (a) Re$_c$ = −515, (b) Re$_c$ = −615, (c) Re$_c$ = −686, (d) Re$_c$ = −1348, (e) Re$_c$ = −1778. Colours and isosurface values as in figure 9.

because the hot fluid transported upward along the free surface has the tendency to stay near in the upper half of the liquid bridge such that the return flow arises closer to the axis. This facilitates an $m_c = 1$ mode with a flow across the axis to extract thermal energy from the basic temperature field. The trend that the temperature extrema move closer to the axis (following the location of high basic temperature gradients) is already visible for Re$_g$ = 40 in figure 13(e).

The critical modes for Re$_g$ = 40 and Re$_g$ = 1000 are displayed in figure 14. It can be seen that the critical velocity field for Re$_g$ = 1000 is oblique to the basis state isotherms near the point of maximum thermal energy production (white cross). Therefore, the critical mode can also gain energy from the vertical temperature gradients such that J_2 has a bigger share in the thermal energy budget, which is shown in figure 15. Remarkable is the spiral character of the isosurfaces of the perturbation temperature near the upper cold wall in figure 13(e). These spiral arms show in figure 14(b) as a sequence of hot and cold spots in the upper part of the region with high temperature gradients. A similar hydrothermal wave with an even more pronounced spiral character arises in liquid bridges with the still higher Prandtl number Pr = 68 (Stojanovic & Kuhlmann 2020*a*).

4.2. *Dynamic surface shape*

In this section we first discuss the causes for and the properties of the dynamic surface shape of the liquid bridge in the basic state. Thereafter, the influence of the dynamic deformability of the interface on the linear stability is discussed.

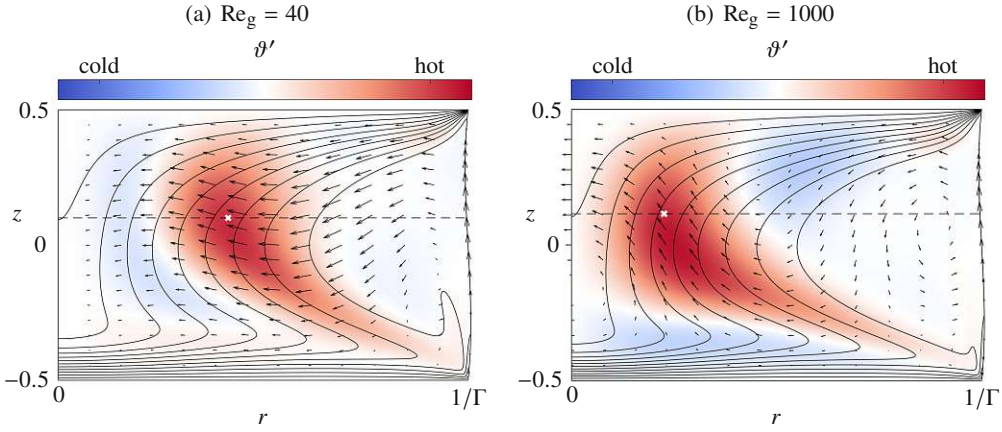

Figure 14: Critical modes for heating from below and hot co-flow with $\mathrm{Re_g} = 40$ (a) and $\mathrm{Re_g} = 1000$ (b) in planes $\varphi = \text{const.}$ in which the local thermal energy production has its maximum (white cross). Shown are the perturbation velocity fields (arrows) and the perturbation temperatures (colour). Isolines of the basic temperature field are drawn in black.

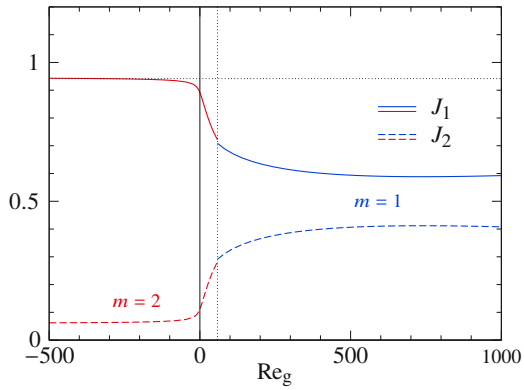

Figure 15: Normalised global energy production rates J_1 (full lines) and J_2 (dashed lines) of the critical mode in the liquid phase for heating from below shown as functions of $\mathrm{Re_g}$. The colour indicates the wave number. The vertical dotted line marks the codimension-two point at $\mathrm{Re_g} = 58.5$. The horizontal dotted line represents $J_1(\mathrm{Re_g} = -3000)$.

4.2.1. *Static surface shape and dynamic deformation due to the gas flow alone*

Static shapes $h_{0,s}$ of an isothermal liquid bridge, i.e. solutions of (2.23), are shown in figure 16(a) for different filling factors $\mathcal{V}$ (colour) and gravity levels (line type) in the absence of any flow. When an axial flow is imposed in the gas phase, with the liquid bridge still being isothermal ($\mathrm{Re} = 0$), the dynamic pressure and the normal stresses along the interface modify the static shape. The dynamic deformation Δh_0 of the static shape under zero gravity (0g) due to a vertically upward gas flow with $\mathrm{Re_g} = 825$ is shown in figure 16(b) for an underfilling ($\mathcal{V} \leqslant 1$) and in figure 16(c) for an overfilling ($\mathcal{V} > 1$) of the liquid bridge. It can be seen that a constant gas flow rate induces a dynamic deformation which is more than ten times larger in case of an overfilling as compared to an underfilling. Nevertheless, for this gas flow rate and volume ratios up to $\mathcal{V} = 1$ (full blue line figure 16(a)) the dynamic deformation Δh_0 is at least three orders of magnitude smaller than the axial variation $h_{0,s}(z, 1g) - h_{0,s}(z, 0g)$

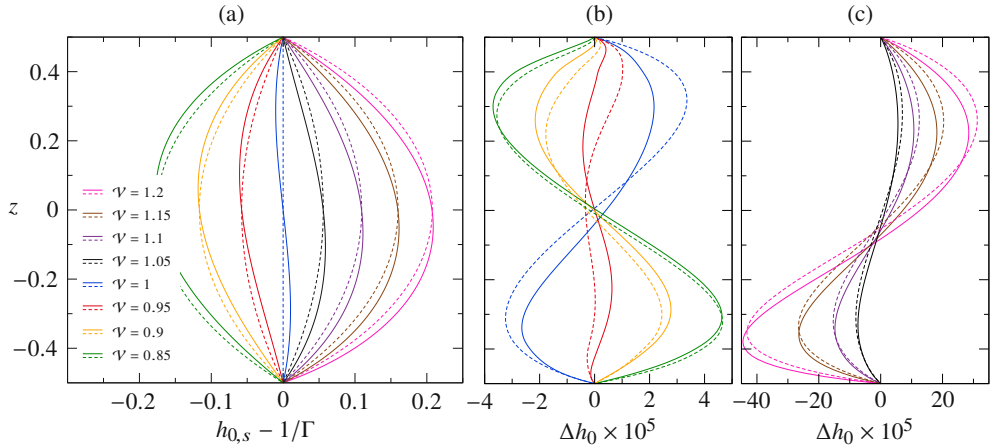

Figure 16: (a) Hydrostatic shape $h_{0,s} - 1/\Gamma$ of a liquid bridge for the present geometry, different liquid volumes $\mathcal{V}$ (colour), zero gravity (0g, dashed lines) and normal gravity (1g, full lines). (b,c) Dynamic surface deformation Δh_0 of the static shape in zero gravity due to a gas flow in positive z direction with $\mathrm{Re_g} = 825$ ($\mathrm{Re} = 0$). Colours and line types as in (a). (b) $\mathcal{V} \leqslant 1$. (c) $\mathcal{V} > 1$.

of the hydrostatic shape due to gravity. A gas flow with $\mathrm{Re_g} = 825$ thus hardly perturbs the interface. For an upright cylindrical liquid bridge ($\mathcal{V} = 1$ and zero gravity, blue dashed line in figure 16(a)) the shape perturbation Δh_0 (dynamic deformation) is caused by the streamwise pressure drop in the gas flow and leads to a constriction of the bridge in the upstream half and a bulging in the downstream half. The same holds true under gravity conditions. Due to the hydrostatic surface deformation for normal gravity (1g), the isobars in the gas phase shown in figure 17(a) are more distorted than for zero gravity (0g). As the volume ratio deviates from $\mathcal{V} = 1$, the contact angles change and the pressure in the gas in the immediate vicinity of the liquid bridge can be strongly affected (figure 17). Typically, a local minimum and a local maximum of the pressure arise. For a large volume ($\mathcal{V} > 1$) with contact angles $\alpha > \pi/2$ on the liquid side, these pressure extrema lead to qualitatively the same dynamic deformation as expected from the pressure drop in the gas far from the liquid bridge: bulging in the downstream half of the liquid bridge and necking in the upstream half (figure 16(c)). For small volume ratios ($\mathcal{V} < 1$) with contact angles $\alpha < \pi/2$ on the liquid side, the locations of the maximum and minimum pressures in the gas are approximately exchanged and the resulting dynamic deformation Δh_0 exhibits the opposite behaviour: the interface is bulging upstream and constricting downstream (figure 16(b)). The gravity level does not play an important role for the dynamic deformation, but moderately changes the hydrostatic shape of the bridge.

For contact angles $\alpha < \pi/2$ on the liquid side (contact angles $\alpha_\mathrm{g} > \pi$ on the gas side) the pressure distribution in the gas is strongly affected by the flow singularities which arise due to the sharp corners. The singularity of the pressure along the inner boundary of the gas space is clearly seen in figure 18. While a detailed analysis would have to include also the liquid phase, we note that the pressure distribution does not change much if the liquid phase is artificially replaced by an indeformable solid with the same shape as the hydrostatic shape (not shown). The reason is viscosity of the liquid ($\tilde{\mu} = 0.010597$) is almost a hundred-times higher than that of the gas. This observation suggests a comparison with the local flow over a corner with opening angle $\alpha_\mathrm{g} > \pi$ made by two plane rigid walls. The pressure which results from the Stokes flow asymptotics close to the corner (Moffatt 1964) diverges and makes a

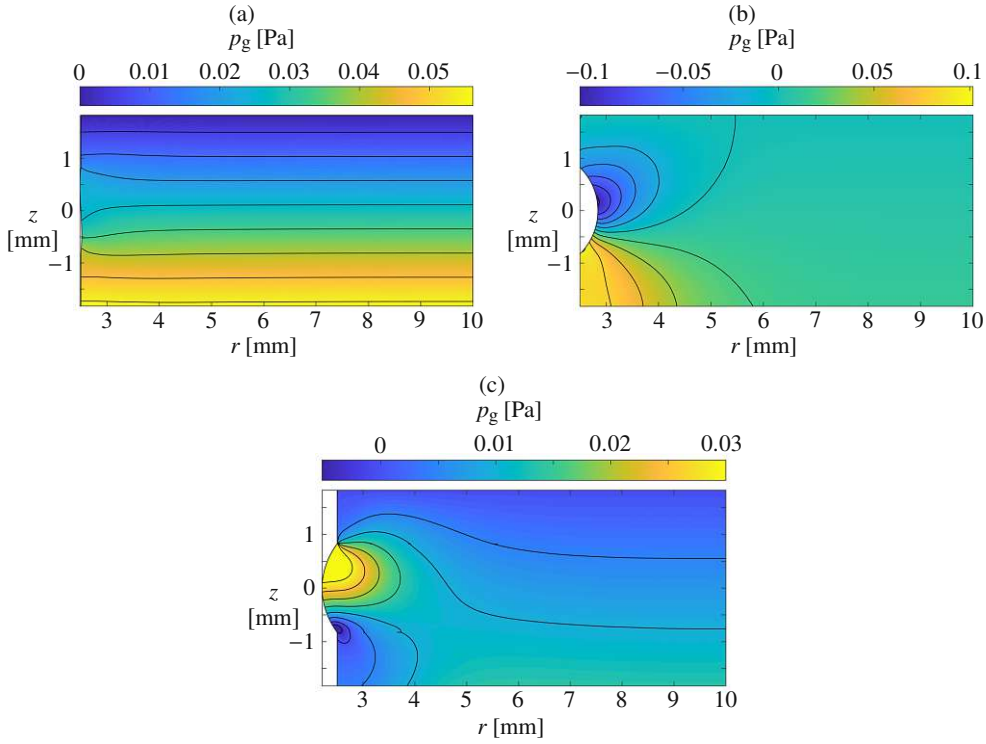

Figure 17: Isobars in the gas phase for Re = 0 and $\mathrm{Re_g}$ = 850. (a) $\mathcal{V}$ = 1 and 1g, (b) $\mathcal{V}$ = 1.2 and 0g, (c) $\mathcal{V}$ = 0.85 and 0g.

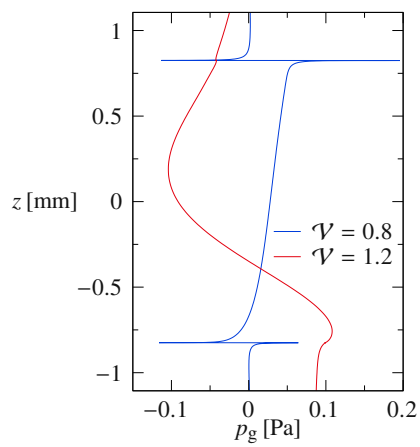

Figure 18: Profiles of the pressure p_g along the free surface and the solid rods for a dynamically deformable liquid bridge. The parameters are: 0g, Re = 0, $\mathrm{Re_g}$ = 825 and volume ratios V as indicated.

jump when the corner is passed. For the present liquid bridge, we find qualitatively the same behaviour for $\alpha_g > \pi$. The signs of the pressure divergence near the contact lines obviously determine the pressure gradient in the gas and along the interface leading to the pressure

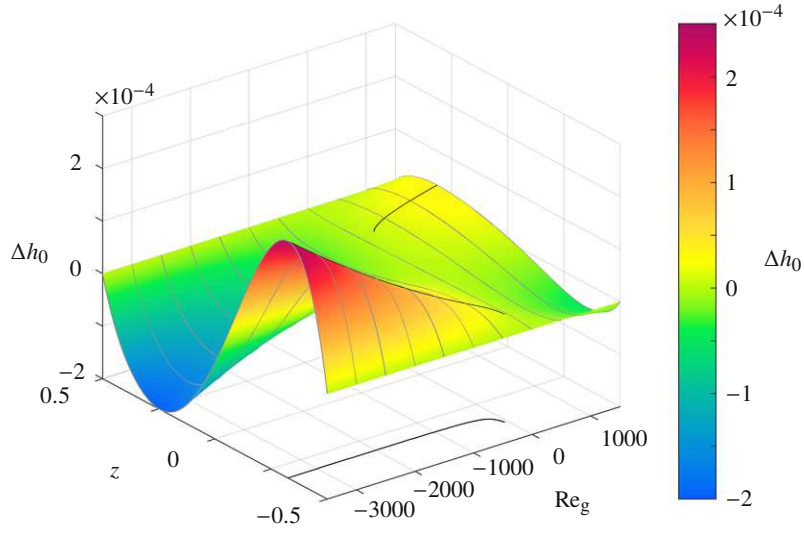

Figure 19: Dynamic surface deformation Δh_0 as function of z and $\mathrm{Re_g}$ for $\mathcal{V} = 1$, $\mathrm{Re} = 0$ and 1g. The gray contour lines indicate surface deformations for constant $\mathrm{Re_g} \in [-3500;\ 1500]$ incremented by $\Delta\mathrm{Re_g} = 500$. The black lines show the loci of maximum of Δh_0 and its projection to the $(z, \mathrm{Re_g})$ plane.

extrema shown in figure 17. The pressure variation in the gas flow due to the expansion of the cross-section of the gas flow contributes as well.

For large volume ratios $\mathcal{V} > 1$ with $\alpha_g < \pi$, the corner flow analysis of Moffatt (1964) does not yield corner singularities. In fact, the flow over the contact lines for $V > 1$ is smooth (figure 18), except for a small indentation in the pressure profile for $\mathcal{V} = 1.2$ at the upper corner. Therefore, the pressure distribution is mainly due to the gas flow deceleration near the upstream half of the liquid bridge and the acceleration near the downstream half. While these considerations can explain the gross features of the pressure distribution and thus the qualitative shape of the dynamic deformation Δh_0, the details are also affected by the liquid flow (driven by the gas flow) and the pressure singularities which exist on the liquid side as the contact lines are approached.

An overview of the dynamic deformation Δh_0 due to the isothermal gas flow over a liquid bridge with $\mathcal{V} = 1$ in the absence of the thermocapillary effect ($\mathrm{Re} = 0$) and for normal gravity condition (1g) is shown in figure 19. For downward gas flow ($\mathrm{Re_g} < 0$) parallel to the acceleration of gravity the dynamic deformation leads to a very slight necking tendency of the liquid bridge for $z \gtrsim 0$ and slight bulging tendency for $z \lesssim 0$, since the pressure gradient in the gas phase along the interface (not shown) has the same sign as the pressure difference between the inlet and the outlet. Upon a reversal of the gas flow direction, the slight necking tendency arises for $z \lesssim 0$ and the bulging for $z \gtrsim 0$. The black lines in figure 19 indicate the locus $z_{\max}$ of the maximum of the dynamic deformation Δh_0 and its projection to the $(z, \mathrm{Re_g})$ plane. The line is interrupted near $\mathrm{Re_g} = 0$, where the maximum dynamic deformation drops below $\Delta h_0(z) < 5 \times 10^{-6}$, which marks the precision by which the dynamic deformation can be computed by the present numerical approach.

Even though the dynamic deformation is insignificant on the scale of the hydrostatic deformation in the gravity field, the dynamic deformation for $\mathcal{V} = 1$ and 1g slightly amplifies the static deformation for $\mathrm{Re_g} < 0$ such that $\max h_{0,d} > \max h_{0,s}$ and $\min h_{0,d} < \min h_{0,s}$. For $\mathrm{Re_g} > 0$ the reverse holds true (see also figure 16).

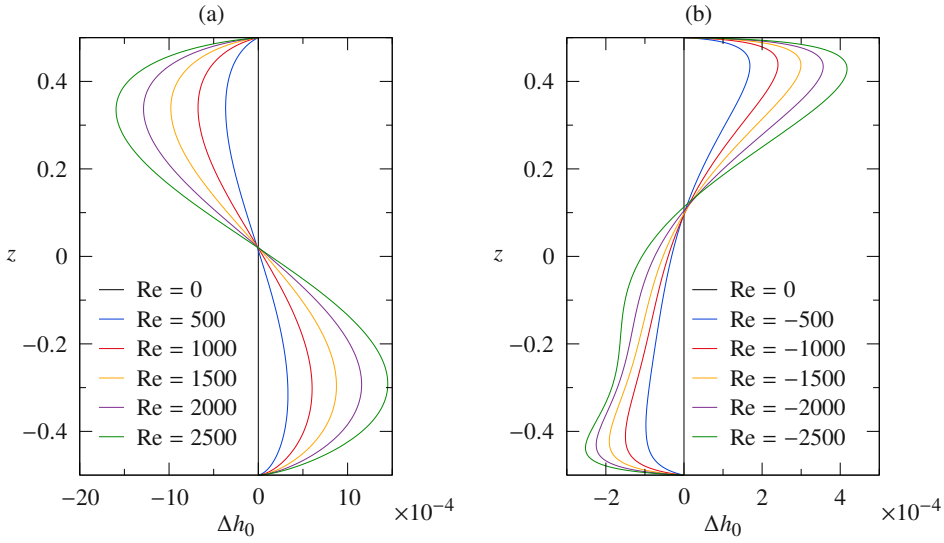

Figure 20: Dynamic surface deformation Δh_0 in the absence of an imposed gas flow ($\mathrm{Re_g} = 0$), for $\mathcal{V} = 1$, normal gravity (1g) and different Re as indicated. (a) Heating from above. (b) Heating from below.

4.2.2. *Dynamic surface deformation due to the thermocapillary flow alone*

The dynamic surface shape $h_{0,d}$ strongly depends on both, Re and Pr, examples are given in figure 30 in Appendix B. For the present liquid with Pr = 28, Re ≠ 0, zero gravity (0g), $\mathcal{V} = 1$ and neglect of the gas phase (single phase flow) the dynamic shape $h_{0,d} = h_{0,s} + \Delta h_0$ is always S-shaped, i.e., the dynamic deformation Δh_0 is negative (positive) close to the hot (cold) corner with the extrema of $h_{0,d}$ depending on the magnitude of the Reynolds number Re (not shown).

Here we investigate the influence of the thermocapillary flow alone on the dynamic surface deformation Δh_0 under normal gravity (1g) and in the presence of the gas phase (two-phase flow), but for $\mathrm{Re_g} = 0$, i.e. for a closed gas container. The dynamic surface deformation is shown in figure 20 for heating from above (Re > 0, figure 20(a)) and for heating from below (Re < 0, figure 20(b)). The dynamic deformation amplifies (reduces) the static deformation for heating from above (below). For heating from above (Re > 0, figure 20(a)), the dynamic deformation has a sinusoidal shape and its strength, measured by its maximum value, depends approximately linearly on Re. The maximum of Δh_0 arises near the lower cold wall. For heating from below (Re < 0, figure 20(b)) the maximum of Δh_0 also arises near the cold wall, which is now the upper wall. But the extrema of Δh_0 arise much closer to the wall such that the dynamic deformation for large absolute values of Re < 0 takes a more complex shape.

The maximum dynamic deformation due to the thermocapillary flow for Reynolds numbers of the order of $O(2000)$ and heating from above is approximately four times larger than the maximum dynamic deformation when the heating is from below. For heating from above with $\mathrm{Re} = O(2000)$ the thermocapillary-flow-induced dynamic deformation for $\mathrm{Re_g} = 0$ is also about four times larger than the dynamic deformation due to a downward gas flow alone with Re = 0 and $|\mathrm{Re_g}| = O(2000)$ (figure 19).

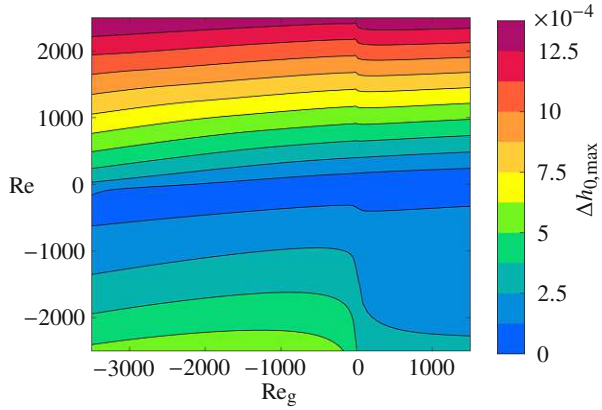

Figure 21: Maximum of the dynamic surface deformation $\Delta h_{0,\max} = \max_z(\Delta h_0)$ as function of $\mathrm{Re_g}$ and Re (equal scales) for $\mathcal{V} = 1$ and normal gravity (1g). Isolines are equidistant with step size 1.25×10^{-4} (colour bar).

4.2.3. *Dynamic surface deformation: Dependence on Re and Re_g*

Both the flow in the liquid and in the gas contribute to the flow-induced interfacial shape deformation Δh_0. To quantify this dynamic deformation we show in figure 21 the absolute maximum of the dynamic deformation $\Delta h_{0,\max} = \max_z(\Delta h_0) > 0$ for $\mathcal{V} = 1$ and normal gravity (1g). The minimum dynamic deformation $\Delta h_0 = \min_z(\Delta h_0) < 0$ is not monitored. From figure 19 the locus $z_{\max}$ of the maximum dynamic deformation can jump upon a variation of $\mathrm{Re_g}$. Therefore, first derivative $\partial[\Delta h_{0,\max}]/\partial \mathrm{Re_g}$ is discontinuous at this locus. As will become clear later, this discontinuity is not visible by the eye in figure 21. As expected from the foregoing, the Reynolds number Re has a larger influence on Δh_0 than $\mathrm{Re_g}$. While this depends on the definition of the Reynolds numbers, such behaviour is expected because the density of the liquid, which enters the pressure scale, is much higher than that of the gas ($\tilde{\rho} = 1.359 \times 10^{-3}$). From figure 21 the maximum dynamic deformation $\Delta h_{0,\max}$ depends approximately linearly on Re for $\mathrm{Re} > 0$ (heating from above). Moreover, $\Delta h_{0,\max}$ depends monotonically on $\mathrm{Re_g}$ for $\mathrm{Re} > 0$, except near $\mathrm{Re_g} \approx 0$ where a wiggle arises which can be smoothly resolved. The wiggle on the isolines of $\Delta h_{0,\max}(\mathrm{Re_g})$ near $\mathrm{Re_g} = 0$ becomes more pronounced as Re increases. It arises due to the sensitivity of the thermal conditions in the gas phase due to a weak gas flow. Depending on the direction of the gas flow the interface is heated or cooled, where the heating/cooling effect on the surface temperature rapidly saturates for increasing $|\mathrm{Re_g}|$ when the gas temperature changes from a conductive to a convective regime (see e.g. section 4.1.3).

The maximum dynamic surface deformation $\Delta h_{0,\max}$ is smaller for heating from below ($\mathrm{Re} < 0$) than for heating from above ($\mathrm{Re} > 0$), as already observed for the closed chamber in figure 20. For heating from above ($\mathrm{Re} > 0$), the dynamic deformation due to the thermocapillary flow is dominant and the dynamic deformation caused by the gas flow for comparable Reynolds numbers $|\mathrm{Re}| \approx |\mathrm{Re_g}|$ can be considered a small perturbation of the already small deformation due to the thermocapillary flow. This is illustrated in figure 22 for heating from above with $\mathrm{Re} = 1700$ and different gas flow rates. For $\mathrm{Re} = 1700$, the smallest value which the maximum positive deformation takes arises for $\mathrm{Re_g} = -19$ (full red line in figure 22(b)). This marks the above mentioned transition from the conductive to the convective regime in the gas phase.

For heating from below ($\mathrm{Re} < 0$) the dynamic surface deformation due to the thermocapillary flow and the one due to the gas flow have comparable magnitudes. This

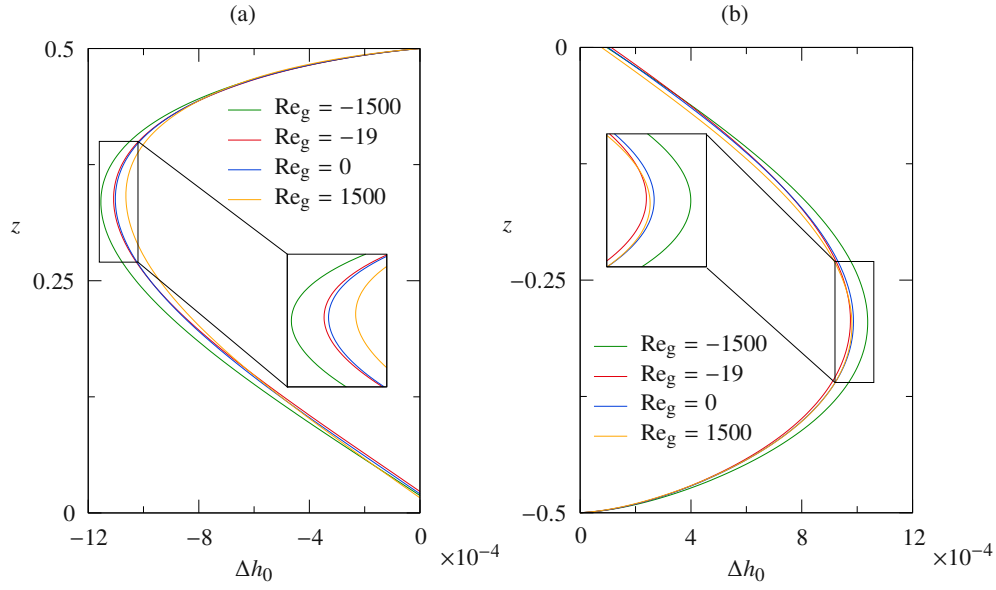

Figure 22: Dynamic surface deformations Δh_0 for Re = 1700 and different $\mathrm{Re_g}$ with a zoom into the black rectangle. (a) Upper half of the liquid bridge $z \in [0; 0.5]$. (b) Lower half of the liquid bridge $z \in [-0.5; 0]$

leads to qualitatively different dynamic surface deformation profiles as compared to heating from above. This is demonstrated in figure 23(a) for heating from below with Re = −1700 and different gas flow rates in the range $\mathrm{Re_g} \in [-3500, 1500]$. For a weak heating from below with Re = −100, a strong gas flow from above leads to a bulging near the hot and the cold corner, where the two relative maxima arise with comparable magnitudes. Figure 23(b) shows typical profiles for Re ≈ −1605 at which the locus $z_{\max}$ of $\Delta h_{0,\max}$ makes a jump. Comparing figures 22(a) and 23(a), we notice that Δh_0 is considerably more sensitive to the strength of the gas flow when heating from below as compared to heating from above.

The vertical coordinate $z_{\max}$ at which the maximum surface deformation $\Delta h_{0,\max}$ arises is shown in figure 24 as a function of the gas flow Reynolds number $\mathrm{Re_g}$ for $\mathcal{V} = 1$ and normal gravity (1g). The black lines correspond to the projected black lines in figure 19 for Re = 0, taking into account the gas flow alone. The effect of the thermocapillary-buoyant flow on $z_{\max}$ is shown by coloured lines for different values of Re. For heating from above (full coloured lines), we observe a small smooth wiggle near $\mathrm{Re_g} \approx 0$ that is related to the already discussed transition from the conductive to the convective regime in the gas phase. Besides, for small Reynolds numbers $0 < \mathrm{Re} \leqslant 50$ (blue and red full lines) a strong gas flow from below sizably affects $z_{\max}$, because the dynamic deformations due to the thermocapillary and the gas flow are of comparable magnitude, but of different shape. For heating from below (coloured dashed lines), the locus $z_{\max}$ makes a jump from near the upper cold wall to near the lower hot wall when the cold counter-flow is intensified. For Re = −100 this jump occurs near $\mathrm{Re_g} \approx -1605$, as illustrated in figure 23(b). The stronger the thermocapillary flow (the larger |Re|), the stronger the cold downward counter-flow of the gas ($\mathrm{Re_g} < 0$) must be for the maximum bulging to occur on the lower (hot) side of the liquid bridge.

4.2.4. *Linear stability of the basic flow with a dynamically deformed free surface*

The linear stability boundary for a static interface $\mathrm{Re}_{c,s}$ as function of the gas flow rate $\mathrm{Re_g}$ for heating from above and from below has been presented in figure 2(a). Since the dynamic

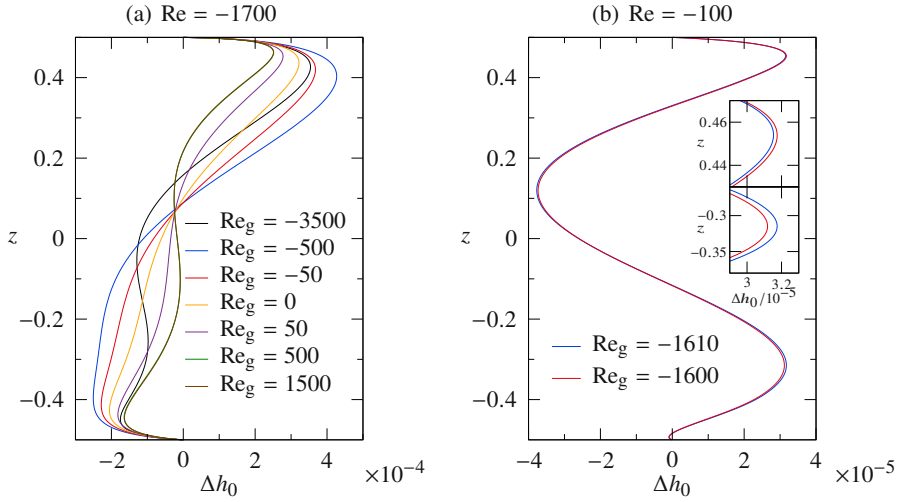

Figure 23: Dynamic surface deformations Δh_0 for $\mathcal{V} = 1$, normal gravity (1g) and different $\mathrm{Re_g}$ as indicated. Heating is from below with $\mathrm{Re} = -1700$ (a) and $\mathrm{Re} = -100$ (b).

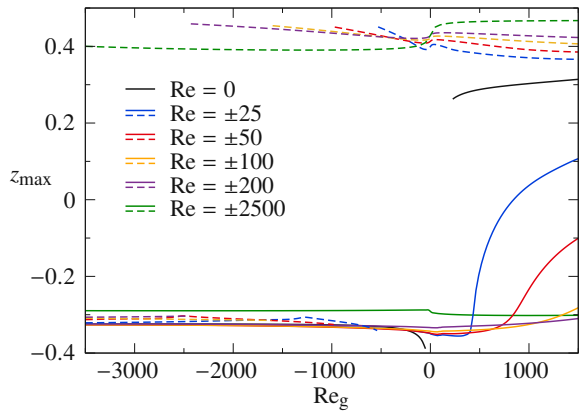

Figure 24: Axial position $z_{\max}$ of the maximum dynamic surface deformation $\Delta h_{0,\max} = \max_z(\Delta h_0)$ for $\mathcal{V} = 1$ and normal gravity (1g) as function of $\mathrm{Re_g}$ for several Re (indicated by colour and line type).

deformations are small, they are expected to have only a weak influence on the linear stability boundary. This was already noticed for the test case considered during the code validation (figure 33) in Appendix C.4.

Two regions within which the critical Reynolds number for a static interface $\mathrm{Re}_{c,s}(\mathrm{Re_g})$ deviates the most from the one for a dynamically deformed interface $\mathrm{Re}_{c,d}(\mathrm{Re_g})$ are shown in figure 25. To quantify the small difference between the two critical curves we define the deviations

$$\hat{\epsilon}(\mathrm{Re_g}) := \mathrm{Re}_{c,d}(\mathrm{Re_g}) - \mathrm{Re}_{c,s}(\mathrm{Re_g}), \tag{4.1a}$$

$$\check{\epsilon}(\mathrm{Re}) := \mathrm{Re_g}^{c,d}(\mathrm{Re}) - \mathrm{Re_g}^{c,s}(\mathrm{Re}), \tag{4.1b}$$

where $\mathrm{Re_g}^{c,d}$ and $\mathrm{Re_g}^{c,s}$ are the critical gas Reynolds numbers for given Re and dynamic and static interface, respectively. The meaning of $\hat{\epsilon}$ and $\check{\epsilon}$ is graphically indicated in figure 25.

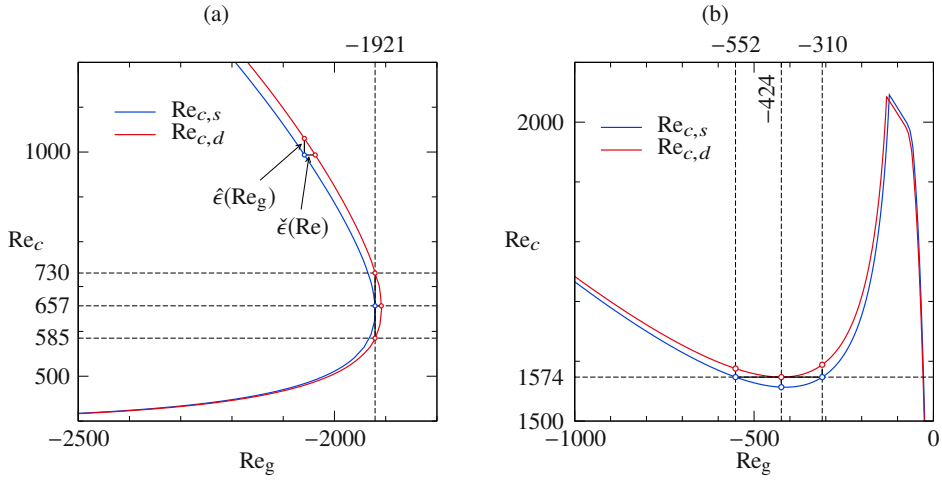

Figure 25: Critical Reynolds numbers for $\mathcal{V} = 1$ and normal gravity (1g). Shown are $\mathrm{Re}_{c,s}$ (blue, static interface) and $\mathrm{Re}_{c,d}$ (red, dynamic deformable interface) for heating from above and $\mathrm{Re}_g \in [-2500; -1800]$ (a) and $\mathrm{Re}_g \in [-1000; 0]$ (b). The deviation $\hat{\epsilon}$ and $\check{\epsilon}$ between the two critical curves are defined graphically in (a).

We also define the relative deviation

$$\hat{\tilde{\epsilon}}(\mathrm{Re}_g) := \frac{\hat{\epsilon}(\mathrm{Re}_g)}{\mathrm{Re}_{c,s}(\mathrm{Re}_g)}. \tag{4.2}$$

We do not the corresponding relative deviation $\check{\tilde{\epsilon}}(\mathrm{Re})$, because the normalising denominator $\mathrm{Re}_g^{c,s}(\mathrm{Re})$ would vanish at the critical point $\mathrm{Re} = \mathrm{Re}_{c,s}(\mathrm{Re}_g = 0)$, i.e. for a closed container. The deviations $\hat{\tilde{\epsilon}}$ (blue) and $\check{\epsilon}$ (red) are shown in figure 26 over the full range of gas Reynolds numbers considered, where $\check{\epsilon}(\mathrm{Re})$ is evaluated as $\check{\epsilon}[\mathrm{Re}_{c,s}(\mathrm{Re}_g)]$. Naturally, $\hat{\tilde{\epsilon}}$ becomes largest when the slope of the critical curve $\partial\mathrm{Re}_{c,s}/\partial\mathrm{Re}_g \to \infty$ diverges. The deviation of $\hat{\tilde{\epsilon}}$ at such points, which is also illustrated in figure 25(a) for $\mathrm{Re}_g = -1921$, can be larger than 10%. Similarly, $\check{\epsilon}$ becomes large at extrema of the critical curve, i.e. when $\partial\mathrm{Re}_{c,s}/\partial\mathrm{Re}_g \to 0$. An example is shown in figure 25(b) for $\mathrm{Re}_g = -424$. Near extrema of $\mathrm{Re}_{c,d}$ the deviation normal to the critical curve represents the meaningful measure. From figure 26, the relative deviation $\hat{\tilde{\epsilon}}$ typically amounts to a few percent, except possibly at the mentioned extrema. Since the deviation $\hat{\tilde{\epsilon}}$ can take positive and negative signs for either heating direction, the dynamic surface deformation can act slightly stabilising or slightly destabilising. The absolute deviation $\check{\epsilon}$ is typically less than 25, a value which must be compared with the gas Reynolds number which varies over a much wider range ($O(10^3)$). The weak effect of a dynamically deformable interface in the basic flow on the stability boundary is also reflected in the minute displacement of the codimension-two points seen from table 4.

5. Summary and Conclusions

The thermocapillary flow in a liquid bridge made from 2-cSt silicone oil (Pr = 28) has been investigated for heating from above and from below under axial gravity. The thermal and mechanical coupling between the liquid bridge and the surrounding air is fully accounted for, including the hydrostatic shape of the liquid–gas interface and its flow-induced dynamic deformation. The flow in the liquid is driven by three mechanisms: (a) the thermocapillary stress on the liquid–gas interface, (b) buoyancy forces in the bulk, and (c) an axial gas flow

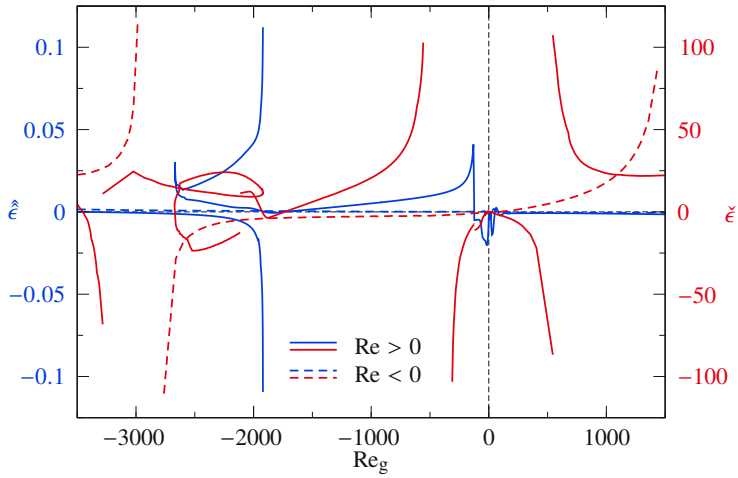

Figure 26: Relative deviation of the critical Reynolds number $\hat{\tilde{\epsilon}} = (\mathrm{Re}_{c,d} - \mathrm{Re}_{c,s})/\mathrm{Re}_{c,s}$ (blue lines) and absolute deviation of the critical gas Reynolds number $\check{\epsilon} = \mathrm{Re}_{\mathrm{g}}^{c,d}(\mathrm{Re}) - \mathrm{Re}_{\mathrm{g}}^{c,s}(\mathrm{Re})$ (red lines), both as functions of $\mathrm{Re_g}$. Full and dashed lines correspond to heating from above ($\mathrm{Re}_c > 0$) and from below ($\mathrm{Re}_c < 0$), respectively.

imposed on the annular inlet of the gas space which is confined between the liquid bridge and an out shield cylinder. Thermocapillary and buoyancy forces (a,b) depend on the applied temperature difference, while the gas flow (c) can be imposed independently. The steady axisymmetric multiphase flow problem is solved numerically, fully taking into account the dependence of the density on the temperature. Thereafter, this basic flow is analysed with respect to its linear stability.

The linear stability boundary of the axisymmetric flow for $\mathrm{Pr} = 28$ and $\mathcal{V} = 1$ has been established as a function of the gas flow rate, which can take positive or negative values, and for both heating from above and from below. Throughout, the instability is due to hydrothermal waves (Smith & Davis 1983*a*; Wanschura *et al.* 1995; Stojanovic *et al.* 2022). The waves can have different wave numbers and exhibit different structures. For a moderate gas flow the linear stability boundary depends sensitively on the imposed gas flow in the range of gas flow Reynolds numbers $\mathrm{Re_g} \in [-50,\ 50]$. This sensitivity was noted before by Kamotani *et al.* (1996), Kamotani *et al.* (2003) and, more recently, by Yano *et al.* (2016) and Gaponenko *et al.* (2021). The sensitivity results from the heating or cooling of the free surface due to the gas flow such that the plateau temperature near midplane changes. This affects the strength and structure of the basic vortex, and thus the basic temperature field from which the hydrothermal wave extracts its energy. These changes modify the energy supply to the temperature field of the hydrothermal wave via the advection of basic state temperature by the perturbation flow. Typically, radial advection of basic state temperature is by far the most important instability mechanism. The heat exchange through the free surface between the liquid and the gas due to the perturbation flow itself is unimportant.

For larger gas flow rates, but still within $\mathrm{Re_g} \in [-3500,\ 1500]$, the linear stability boundary approximately saturates, independent of its direction. In all cases, the reason for the saturation of the critical Reynolds number is an insensitivity of the flow and temperature field inside the liquid phase with respect to an increase of the gas flow rate. The critical thermocapillary Reynolds number for large gas flow rates is of the order of $\mathrm{Re}_c = O(500)$, except for heating from below and a hot co-flow of the gas, for which the stability boundary saturates at $\mathrm{Re}_c = O(1800)$. The saturation of the critical Reynolds number is reached monotonically

with an increase of the strength of the gas flow, except for heating from above and a hot co-flow of the gas. In this case the basic flow is very stable up to about $\mathrm{Re}_c \approx 2000$ in the range approximately $\mathrm{Re}_g \in [-2000, -100]$ before saturation occurs for $\mathrm{Re}_g \lesssim -2000$. In the range $\mathrm{Re}_g \in [-2672, -1921]$ and heating from above the linear stability boundary is not unique. Therefore, the unstable basic flow is possibly stabilised again at higher Reynolds numbers within a certain range of Re. In the full range of gas flow rates considered the mechanical driving of the flow in the liquid phase by viscous stresses on the interface exerted by the gas motion is insignificant.

The linear stability boundaries have been computed for a constant volume fraction $\mathcal{V} = 1$ and a liquid–gas interface which is statically determined by the mean surface tension and by the hydrostatic pressure. In addition, the stability boundaries have been computed taking into account the flow-induced dynamic interface deformation due to the basic flow, while neglecting the dynamic deformation due to the perturbation flow. Dynamic deformations of the interface are caused by the variation of the surface tension with temperature, viscous normal stresses from the gas and the liquid, and by the dynamic pressure in the gas and the liquid. The dynamic deformation of an isothermal liquid bridge caused by the gas flow alone was found to be consistent with the pressure distribution in the gas near the interface. The distribution of the pressure in the gas is mainly determined by the shape of the static interface and the corner singularities which arise in the gas flow when the liquid contact angle is less than $\pi/2$. For non-isothermal liquid bridges and heating from above the dynamic surface deformation due to the thermocapillary forcing is typically dominant over the gas-flow-induced deformation and leads to a sinusoidal dynamic deformation supporting bulging near the cold wall and necking near the hot wall, superimposed to the static shape. But for heating from below, the dynamic deformation due to the thermocapillary flow can have the same order of magnitude as the one due to the gas flow (for comparable Reynolds numbers). Therefore, the shape of the dynamic deformation can be more complicated. Regardless of the shape of the dynamic surface deformation, its effect on the critical threshold is weak.

With the present study we have accurately established the dependence on a forced gas flow of the linear stability boundary of the axisymmetric thermocapillary flow in liquid bridge of $\mathrm{Pr} = 28$. We have incorporated in the analysis static and dynamic interface deformations, the presence of a gas phase, a forced flow in the gas phase, and non-Oberbeck–Boussinesq effects due to the linear dependence of the density on temperature in all terms. Even though the Bond number was considered constant, the analysis should guide the interpretation of data measured or computed in future investigations of similar flow problems.

As was already pointed out by Shevtsova *et al.* (2014), the sensitivity of the critical onset of three-dimensional hydrothermal wave on the flow rate and direction of the hot or cold gas bares the potential to controlling the critical onset of flow oscillations. Their linear stability boundaries for 5-cSt silicone oil, $\eta = 2$ and zero gravity (figure 7 of Shevtsova *et al.* (2014)) are similar to the present stability boundaries (figure 2(a)) for heating from above: a very stable basic flow for a certain range of $\mathrm{Re}_g < 0$ and an approximate saturation of Re_c for $\mathrm{Re}_g > 0$. The details, however, are more complicated. In particular, we did not find the stationary $m_c = 1$ mode at very low Reynolds number of the order of 200 for $\mathrm{Re}_g > 0$. This may partly be related to the relatively tight air gap with $\eta = 2$ considered by Shevtsova *et al.* (2014). Probably for the same reason the two-dimensional instability found for $\eta = 1.\bar{6}$ by Shevtsova *et al.* (2013) for $\mathrm{Re}_g > 0$ does not arise in the present system. We also did not find indications for a classical Marangoni instability (different from Shevtsova *et al.* 2013), even though the production of thermal perturbation energy is dominated by radial advection of basic state temperature (J_1): The region below the free surface in the plateau region of the surface temperature profile is found to be almost isothermal. For the Pearson mechanism (Pearson 1958) to arise the basic temperature field should exhibit a significant temperature

gradient next to the interface. But for the range of parameters investigated, as in the classical hydrothermal wave (Wanschura *et al.* 1995), the radial temperature gradients arise only deep inside the liquid bridge due to the return flow of the basic toroidal vortex which is absent in the Pearson problem.

Owing to the large parameter space, other important influence factors have not been included in the present analysis. Among these are the dependence of the viscosity on the temperature (Kozhoukharova *et al.* 1999; Shevtsova *et al.* 2001) and evaporative cooling for large ΔT (Yano *et al.* 2016; Simic-Stefani *et al.* 2006). Also, an extension of the analysis to other Prandtl numbers and volume fractions of the liquid would be of interest. With respect to future space experiments which allow for larger liquid bridges it would also be desirable to take into account dynamic surface deformations in the perturbation flow. The would allow for surface wave instabilities which have been found to become critical for pure thermocapillary flow in plane layers of low Prandtl number (Smith & Davis 1983*b*) and in flat migrating droplets (Hu *et al.* 2023). At higher gas flow rates, for which the shape of the liquid bridge is sizably affected by dynamic deformations, surface waves can also be triggered by the Kelvin–Helmholtz mechanism. These effects suggest corresponding extensions of the present work.

Acknowledgements

This work has been supported by the Austrian Research Promotion Agency (FFG) in the framework of the ASAP14 programme under contract number 866027.

Appendix A. Reynolds number for the gas motion

The motion of the gas resembles the flow through an annular pipe for which the Reynolds number is usually defined as $\mathrm{Re}'_\mathrm{g} = 2\bar{w}_{\mathrm{g,in}}\rho_{\mathrm{g}0}(r_\mathrm{o} - r_\mathrm{i})/\mu_\mathrm{g}$, based on the kinematic viscosity of the gas and the width of the annular gap. In the thermocapillary liquid bridge under investigation, however, the flow instability is triggered in the liquid phase, while the gas phase is mainly passive. Therefore, the effect of the gas motion on the liquid phase is better represented by using the kinematic viscosity of the liquid μ/ρ_0 and the length scale d of the liquid phase, leading to $\mathrm{Re}_\mathrm{g} = \bar{w}_{\mathrm{g,in}}d\rho_0/\mu$. Both Reynolds numbers are related to each other by

$$\mathrm{Re}'_\mathrm{g} = \frac{2(\eta-1)}{\Gamma}\frac{\tilde{\rho}}{\tilde{\mu}}\mathrm{Re}_\mathrm{g}, \tag{A.1}$$

through the ratio of the kinematic viscosities $\tilde{\rho}/\tilde{\mu}$ and twice the ratio of the length scales $2(\eta-1)/\Gamma$.

The relevance of Re_g for the flow instability can also be inferred from table 5 which shows the critical thermocapillary Reynolds number $\mathrm{Re}_{c,d}$ when the liquid–gas interface of the basic state is dynamically deformable (subscript d). Based on the reference case (ref) for $\mathrm{Re}_\mathrm{g} = -40$ and $\mathrm{Re}'_\mathrm{g} = -46.65$, we consider the deviation of the critical Reynolds number $\hat{\delta} = \mathrm{Re}_c - \mathrm{Re}_c^{\mathrm{ref}}$ from the reference value $\mathrm{Re}_{c,d}^{\mathrm{ref}} = 1786$ when the dimensional radius of the gas tube r_o, and thus the gap width η, is varied. Keeping Re_g constant (data shown in blue) the critical Reynolds numbers deviate much less from the reference value than when Re'_g is kept constant (data shown in red). For that reason we used Re_g to characterise the strength of the gas flow.

case	r_o [mm]	η	$\bar{w}_{g,in}$ [mm/s]	Re_g	Re'_g	$Re_{c,d}$	$\hat{\delta}$[%]
ref	10	4	−48.48	−40	−46.65	1786	–
1	17.5	7	−24.24	−20	−46.65	1215	−31.9
2	6.25	2.5	−96.97	−80	−46.65	2212	23.9
3	17.5	7	−48.48	−40	−93.29	1605	−10.1
4	6.25	2.5	−48.48	−40	−23.32	1952	9.3

Table 5: Critical thermocapillary Reynolds number $Re_{c,d}$ for different tube radii r_o and mean inlet velocities $\bar{w}_{g,in}$ under zero gravity. The remaining parameters correspond to the reference parameters specified in section 4. Also given are the gas flow Reynolds numbers Re'_g and Re_g and the percentage deviation $\hat{\delta}$ of the critical Reynolds number from the one for the reference case (denoted 'ref'). Equal values of Re'_g (Re_g) are shown in red (blue).

Appendix B. Dependence of the critical Reynolds number on the rod length Γ_{rod}

The temperatures at the in- and outlet of the gas space as well as the inlet velocity profile are prescribed. To estimate the length l over which the downstream boundary conditions affect the velocity field upstream the equilibrium between momentum advection and diffusion over the influence length l can be estimated by the condition

$$\mathrm{Pe} = \frac{\bar{w}_{g,in}\rho_{g0}l}{\mu_g} \approx 1 \tag{B.1}$$

for the Peclet number Pe. Expressed by the gas flow Reynolds number Re_g, this yields

$$\frac{l}{d} \approx \frac{\tilde{\mu}}{\tilde{\rho}\mathrm{Re}_g} \approx \frac{7.8}{\mathrm{Re}_g}. \tag{B.2}$$

Thus, in order that the dimensionless influence length l/d is less than the dimensionless rod length $d_{rod}/d = \Gamma_{rod}/\Gamma = 0.606$, the gas flow Reynolds number should satisfy $|Re_g| \gtrsim 13$. With $Pr_g = \mu_g c_{pg}/\lambda_g = 0.704$ a similar estimate, $|Re_g| \gtrsim 13/Pr = 18$, holds for the thermal influence length. Thus the critical Reynolds number should not be affected by the relatively short length of the rods with $\Gamma_{rod} = 0.4$, except for very small gas flow rates.

This is confirmed by figure 27 which shows the critical Reynolds number as a function of Γ_{rod} is independent of Γ_{rod} for $\Gamma_{rod} > 0.4$ and $Re_g = \pm 500$ with heating from above (full lines) and heating from below (dashed lines). The deviations of $Re_c(\Gamma_{rod} = 0.4)$ from $Re_c(\Gamma_{rod} = 8)$ are less than 1%. Even for $Re_g = 0$ and heating from above independence from Γ_{rod} is achieved for $\Gamma_{rod} \gtrsim 0.5$ with $Re_c(\Gamma_{rod} = 0.4)$ deviating from $Re_c(\Gamma_{rod} = 8)$ by less than 8%. For $Re_g = 0$ and heating from below, however, the critical Reynolds number exhibits a strong dependence on Γ_{rod} with changes of the critical mode (dashed orange lines in figure 27). The critical mode for small Γ_{rod} is due to a hydrothermal wave in the liquid with $m_c = 2$ (see figure 2(a)). The critical mode changes at $\Gamma_{rod} = 1.77$ to a stationary mode with $m_c = 2$ which is triggered in the gas phase. At $\Gamma_{rod} = 2.85$ a further change is found to another stationary mode with $m_c = 1$. Since the latter instabilities were the only ones found where the flow becomes unstable in the gas phase, the instability for $\Gamma_{rod} = 8$ is briefly described.

The critical Reynolds number for $\Gamma_{rod} = 8$ is $Re_c = -146$ (corresponding to $\Delta T_c = -4.4$K). The basic state and a cross section of the critical mode are shown in figure 28. The critical mode involves a large-scale circulation in the full annular gas space (figure 28(b)). The air rises on one side of the annular pipe and descends on the other side. The critical velocity and temperature fields in the liquid are much weaker than in the gas phase. Obviously, the instability is due to buoyancy. To estimate the magnitude of the buoyancy in the gas phase we

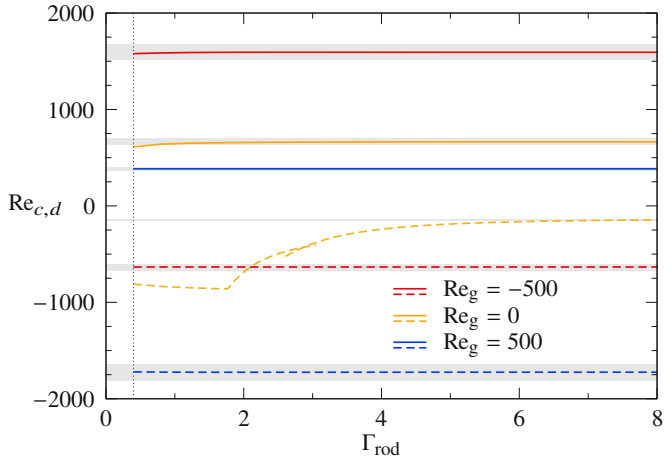

Figure 27: Dependence of the critical Reynolds numbers $\mathrm{Re}_{c,d}$ for $\mathcal{V} = 1$ and 1g on the dimensionless rod length Γ_{rod} for $\mathrm{Re_g} \in \{-500;\ 0;\ 500\}$ and heating from above (full lines) and heating from below (dashed lines). The gray stripes indicate an error of ±5% with respect to $\mathrm{Re}_{c,d}(\Gamma_{\mathrm{rod}} = 8)$. The vertical dotted line marks the rod aspect ratio $\Gamma_{\mathrm{rod}} = 0.4$ employed.

evaluate the Rayleigh number in the gas based on the height of the gas tube. For the present reference parameters the Rayleigh number is

$$\mathrm{Ra_g} = \frac{\tilde{\rho}^2 \tilde{\beta} \tilde{c}_p}{\tilde{\mu}\tilde{\lambda}} \left(1 + 2\frac{\Gamma_{\mathrm{rod}}}{\Gamma}\right)^3 \mathrm{PrBdRe} \approx 1.30 \times 10^{-2} \left(1 + 3.03 \times \Gamma_{\mathrm{rod}}\right)^3 \mathrm{Re}. \tag{B.3}$$

For the rod aspect ratio $\Gamma_{\mathrm{rod}} = 8$ and for $|\mathrm{Re}| = |\mathrm{Re}_{c,d}(\Gamma_{\mathrm{rod}} = 8)| = 146$, the Rayleigh number is $\mathrm{Ra}_c = \mathrm{Ra}(\mathrm{Re}_{c,d}) \approx 30500$ which is of the same order of magnitude as the critical value of $\mathrm{Ra}_c \approx 51000$ according to the correlation of D'Orazio *et al.* (2004) for the onset of convection in a rectangular two-dimensional container heated from below with adiabatic sidewall and the same aspect ratio $(d + 2d_{\mathrm{rod}})/(r_{\mathrm{o}} - r_{\mathrm{i}}) = 5.55$.

The presence of the buoyant instability in the gas phase shows that the above estimate based on advection and diffusion is incomplete to estimate the effect of Γ_{rod} in the presence of gravity. Therefore, we compare in figure 29 the neutral curves $\mathrm{Re}_n(\mathrm{Re_g})$ for $\Gamma_{\mathrm{rod}} = 0.4$ (dashed lines) with those for $\Gamma_{\mathrm{rod}} = 8$ (full lines) for both heating from above (red curves) and below (blue curves). For sufficiently strong gas flow, the rod aspect ratio (up to $\Gamma_{\mathrm{rod}} = 8$) does not significantly affect the instability. For weak gas flow in the range $\mathrm{Re_g} \in [-80, 20]$ and for heating from below (blue lines, $\mathrm{Re_{n,d}} < 0$), however, stationary buoyant instabilities (as in figure 28) can arise in the gas phase and break the axisymmetry before hydrothermal waves become unstable.

Considering $\Gamma_{\mathrm{rod}} = 8$ sufficiently large to suppress effects due to the inlet and outlet length on the basic flow, we define a tolerance of ±2% for the critical Reynolds number for hydrothermal waves (gray shaded region in figure 27). Comparing $\mathrm{Re}_{c,d}(\Gamma_{\mathrm{rod}} = 0.4)$ (dashed lines) with $\mathrm{Re}_{c,d}(\Gamma_{\mathrm{rod}} = 8)$ (full lines), we find that using $\Gamma_{\mathrm{rod}} = 0.4$ provides a good approximation of the critical Reynolds number for hydrothermal waves in the axially extended system with $\Gamma_{\mathrm{rod}} = 8$, if $|\mathrm{Re_g}| > 17$ in case of heating from below (blue lines). For heating from above (red lines) the restriction is similar with $\mathrm{Re_g} > 21$ for hot downward co-flow, whereas for cold upward counter-flow the restriction is more severe and $\mathrm{Re_g} < -90$ must be satisfied. Since the length of the support rods in typical experiments is limited and the heating is usually from above, buoyant instabilities like the one shown in figure 28 do not

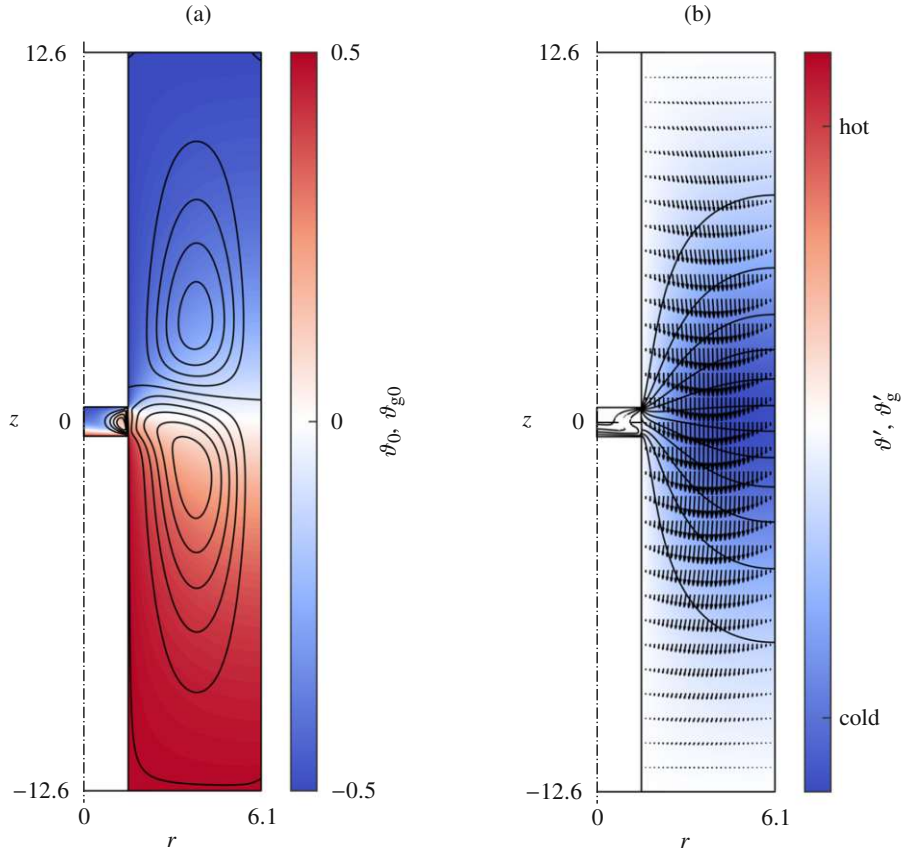

Figure 28: (a) Basic state at criticality $\mathrm{Re}_{c,d} = -146$ for $\Gamma_{\mathrm{rod}} = 8$, $\mathcal{V} = 1$, 1g, $\mathrm{Re}_{\mathrm{g}} = 0$ and heating from below. (b) Corresponding stationary critical mode with $m = 1$, shown in the plane $\varphi = \text{const.}$ in which the local thermal energy production has its maximum.

arise. Therefore, $\Gamma_{\mathrm{rod}} = 0.4$, also employed by Romanò *et al.* (2017), is a reasonable choice for the length of the support rods, if one keeps in mind that the critical Reynolds numbers for weak gas flows depends on Γ_{rod}.

Appendix C. Verification and validation of the dynamic surface deformation

To check the implementation of dynamic free-surface deformation the surface shapes obtained using the code `MaranStable` are compared with available experimental and numerical results. Some comparisons are made for the single-fluid model in which viscous stresses from the gas phase are absent. In most tests a quantitative agreement is found.

C.1. *Comparison with Kuhlmann & Nienhüser (2002)*

Kuhlmann & Nienhüser (2002) have carried out an asymptotic expansion of the thermocapillary flow and interface shape for the limit $\mathrm{Ca} \to 0$. The same approach was used by Shevtsova *et al.* (2008). For a comparison with the results of Kuhlmann & Nienhüser (2002) we consider a liquid bridge with $\Gamma = 1$, $\mathcal{V} = 1$, an adiabatic free surface, zero gravity and a Capillary number $\mathrm{Ca} = 10^{-6}$. Under zero gravity ($\mathrm{Bd} = \mathrm{Bo} = 0$) the static shape is cylindrical with $h_{0,s}(z) \equiv 1/\Gamma$. Figure 30 shows the deviation Δh_0 of the surface

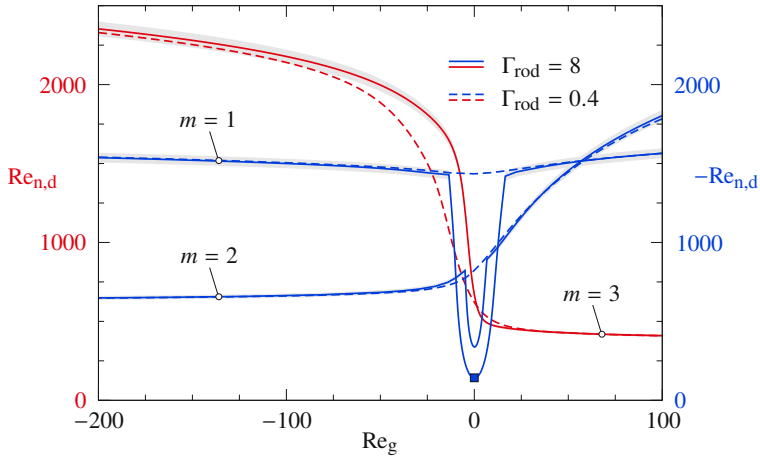

Figure 29: Neutral Reynolds numbers as functions of Re_g for $\Gamma_{rod} = 0.4$ (dashed lines) and $\Gamma_{rod} = 8$ (full lines). Results are shown for heating from above (red lines, left axis) and for heating from below (blue lines, right axis, $Re_{n,d} < 0$). The neutral wave numbers $m = 1$, $m = 2$ and $m = 3$ are indicated by labels. The gray region indicates a deviation of ±2% with respect to the neutral curves for $\Gamma_{rod} = 8$. The blue square indicates the conditions of figure 28.

shape from cylindrical obtained by `MaranStable` (lines) in comparison with the first-order correction $h^{(1)}$Ca to the cylindrical shape computed by Kuhlmann & Nienhüser (2002) (dots) for different combinations of Re and Pr. Our results agree very well with the literature data, particularly for the viscous–conductive case Re = 10^{-4}, Pr = 0.02 (blue). Deviations among the two results slightly increase for larger Marangoni numbers, i.e. for Re = 2130, Pr = 0.02 (red, near the hot wall at $z = 1/2$) and for Re = 951, Pr = 4.38 (orange near the midplane). A plausible reason for these minor deviations is the absence of higher-orders corrections in Ca of the interface shapes provided by Kuhlmann & Nienhüser (2002).

C.2. *Comparison with Montanero* et al. *(2008)*

To validate the dynamic deformations obtained by `MaranStable` for larger dynamic surface deformations we also compare with the experimental results obtained by Montanero *et al.* (2008). While the experimental data are obtained in the presence of the gas phase, it is neglected in our calculations. The reason is Montanero *et al.* (2008) did not provide any information about the ambient gas and the complimentary numerical computations by Carrión *et al.* (2020) were made for a single-fluid model. Following Carrión *et al.* (2020) we assume the thermal boundary condition can be modelled by Newton's law of cooling

$$\boldsymbol{n} \cdot \nabla\vartheta = -\mathrm{Bi}\left(\vartheta + \frac{1}{2}\right), \tag{C.1}$$

with a Biot number $\mathrm{Bi} = h_q d/\lambda = 0.15$, where h_q is the heat-transfer coefficient between the liquid and the gas.

We consider a liquid bridge of length $d = 3.69$ mm made from 5-cSt silicone oil (Pr = 67) for $\Gamma = 1.23$ and $\mathcal{V} = 0.82$ (underfilling) under normal gravity and heated from above. Figure 31(a) shows the static surface shape computed using `MaranStable`. The horizontal axes show both the dimensional $(h_{0,s} - r_i)$ and the non-dimensional deviation $(h_{0,s} - 1/\Gamma)$ of the static surface shape from cylindrical. The (additional) flow-induced dynamic deformation

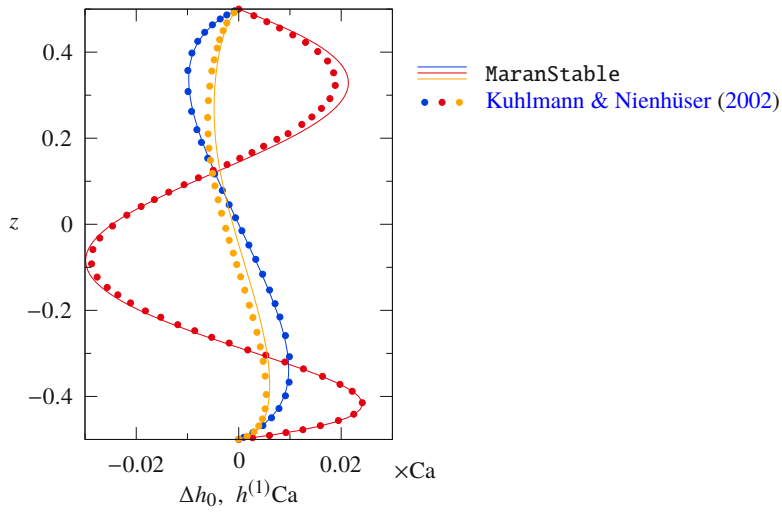

Figure 30: Comparison of the scaled dynamic surface deformations Δh_0 (lines) with the first-order correction $h^{(1)}\mathrm{Ca}$ of Kuhlmann & Nienhüser (2002) (dots, taken from their figure 2(a)) for $\Gamma = 1$, $\mathcal{V} = 1$, $\mathrm{Bd} = \mathrm{Bo} = 0$, $\mathrm{Ca} = 10^{-6}$, adiabatic free surface and $(\mathrm{Pr}, \mathrm{Re}) = (0.02, 10^{-4})$ (blue), $(0.02, 2130)$ (red) and $(4.38, 951)$ (orange). Viscous stresses from the gas phase are neglected.

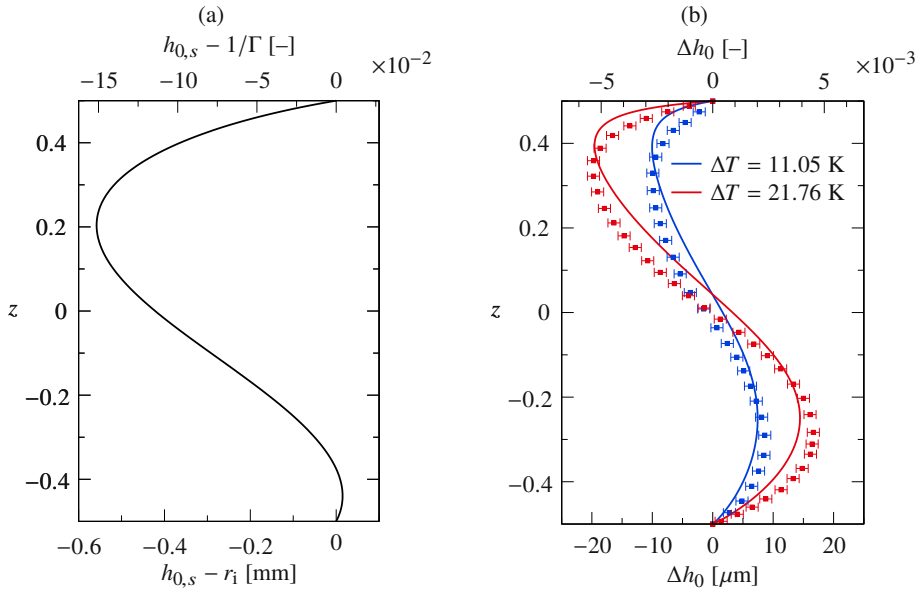

Figure 31: (a) Static surface shape $h_{0,s}$ of a tall liquid bridge made from 5-cSt silicone oil under normal gravity with length $d = 3.691$ mm, aspect ratio $\Gamma = 1.23$ and volume $\mathcal{V} = 0.82$. (b) Dynamic surface deformation Δh_0 for the same liquid bridge for $\Delta T = 11.05$ K ($\mathrm{Re} = 113.9$, blue) and $\Delta T = 21.76$ K ($\mathrm{Re} = 224.4$, red). Lines show results of `MaranStable`, while squares represent experimental data of Montanero *et al.* (2008). The experimental error bars ($\pm 1\ \mu$m) were estimated by Montanero *et al.* (2008).

$\Delta h_0 = h_{0,d} - h_{0,s}$ is shown in figure 31(b). The results obtained with `MaranStable` are in a reasonable agreement with the experimental data.

Deviations between our numerical results (lines) and the experimental data (solid squares) are expected. Notwithstanding the measurement error, the heat flux through the interface is not correctly described by (C.1) when using a constant Biot number (Romanò & Kuhlmann 2019).

C.3. *Comparison with Matsunaga* et al. *(2012)*

Dynamic surface deformations arise not only due to a temperature gradient along the interface, but also due to viscous shear stresses from the gas phase. To test the dynamic surface deformation caused solely by an axial gas flow, we also compare with the experimental results of Matsunaga *et al.* (2012). Again, we consider a liquid bridge of 5-cSt silicone oil, but with nitrogen as the ambient gas. Moreover, the geometry of the setup was adapted to that of Matsunaga *et al.* (2012) by selecting $\Gamma = 1$, $\Gamma_{\mathrm{rod}} = 2/3$ and $\eta = 5/3$. The liquid bridge of length $d = 3\,\mathrm{mm}$ and relative volume $\mathcal{V} = 0.8$ is isothermal, and the gas enters the shield tube from below ($\mathrm{Re_g} > 0$).

Figure 32(a) shows the deviation $h_{0,s} - 1/\Gamma$ of the static shape from cylindrical. The flow induced dynamic part of the deformation $\Delta h_0 = h_{0,d} - h_{0,s}$ is shown in fig. 32(b) for $\mathrm{Re} = 0$. Shown are profiles computed by `MaranStable` for $\mathrm{Re_g} = 600$ (blue line), 900 (red line) and 1200 (orange line). For $\mathrm{Re_g} = 600$ and 900 an excellent agreement is found with the corresponding experimental results (symbols).

Even though Matsunaga *et al.* (2012) estimated the measurement error of $h_{0,\mathrm{d}}$ as $\pm 0.1\ \mu$m, we show error bars for $\pm 0.6\ \mu$m. The reason is Matsunaga *et al.* (2012) found that the deviation between their measured static interfacial shape $h_{0,s}$ for $\mathrm{Re_g} = 0$ and their numerical solution of the Young-Laplace equation (our solution is shown in figure 32(a)) was $\pm 0.6\ \mu$m on average, with a maximum deviation of $\pm 1.5\ \mu$m. Since only the total dynamic shape $h_{0,d}$ is observed experimentally, the dynamic part of the deformation Δh_0 is also affected by the error in the static shape $h_{0,s}$. This may explain the large deviation between our result and the measured data of Matsunaga *et al.* (2012) for $\mathrm{Re_g} = 1200$ (orange in figure 32(b)).

C.4. *Code validation regarding the critical Reynolds number with and without dynamic surface deformation of the basic flow*

Finally, we validate `MaranStable` in terms of the critical onset of three-dimensional flow by comparison with the measurements of Yano *et al.* (2016) for a liquid bridge of 2-cSt silicone oil in air with length $r_{\mathrm{i}} = d = 2.5\,\mathrm{mm}$ and $\mathrm{Pr} = 28$, $\mathrm{Bd} = 0.41$, $\Gamma = 1$, $\Gamma_{\mathrm{rod}} = 4.8$ and $\eta = 5$. Figure 33 shows the neutral and critical Marangoni numbers as functions of the volume ratio $\mathcal{V}$ for a mean gas inlet velocity of $\bar{w}_{\mathrm{g,in}} = -20\,\mathrm{mm/s}$ corresponding to a gas flow Reynolds number of $\mathrm{Re_g} = -25$ (cold counter-flow, heating from above, 1g). The numerical neutral curves obtained for a static ($h_{0,s}$, dashed lines) and for a dynamic surface shape ($h_{0,d}$, full lines) do not deviate much from each other, indicating the weak influence of the dynamic deformability on the critical Marangoni number for such a weak gas flow.

Both numerical results are in good agreement with the experimental data for all volume ratios $\mathcal{V}$ sampled. The only exception is the volume $\mathcal{V} = 1.05$ for which the critical wave numbers deviate qualitatively. Given the experimental error bar, a possible reason could be the large slope of the neutral curve for $m = 1$ with respect to $\mathcal{V}$, such that small deviations of $\mathcal{V}$ cause a large change of the critical Marangoni number. Also a subcritical instability at $\mathcal{V} = 1.05$ cannot currently be ruled out.

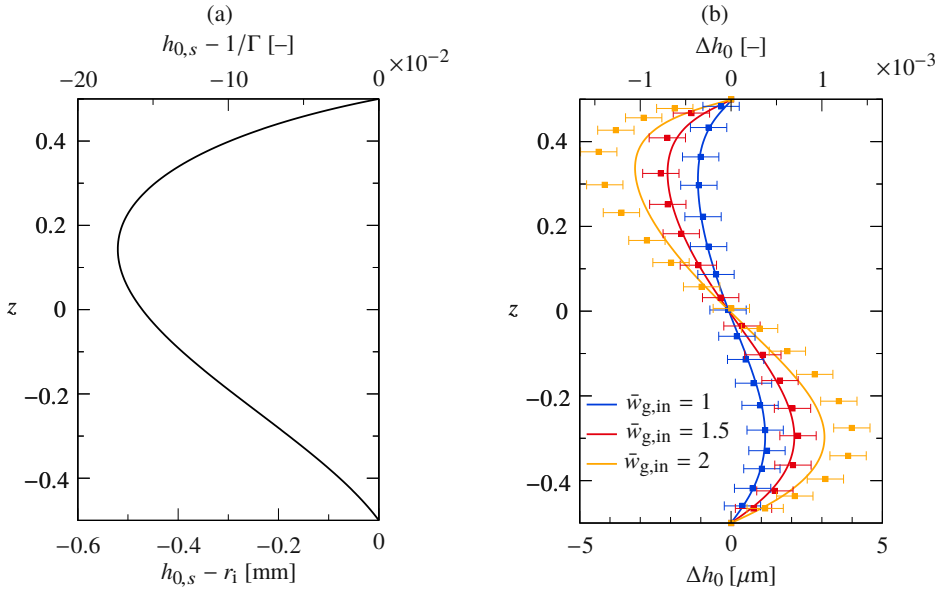

Figure 32: (a) Deviation $h_{0,s} - 1/\Gamma$ of the static interface shape from cylindrical for a liquid bridge of length $d = 3$ mm made from 5-cSt silicone oil in nitrogen. The essential non-dimensional parameters are: $\Gamma = 1$, $\mathcal{V} = 0.8$, Bo = 4.075 (ground condition) and Re = 0 (see the text for the remaining geometry parameters). (b) Dynamic part of the interfacial deformation Δh_0 computed using `MaranStable` (lines) in comparison with the measurements of Matsunaga *et al.* (2012) (squares) for different through flows: $\bar{w}_{g,in} = 1$ m/s ($\mathrm{Re_g} = 600$, blue), $\bar{w}_{g,in} = 1.5$ m/s ($\mathrm{Re_g} = 900$, red) and $\bar{w}_{g,in} = 2$ m/s ($\mathrm{Re_g} = 1200$, orange). Error bars show an uncertainty of ±0.6 μm.

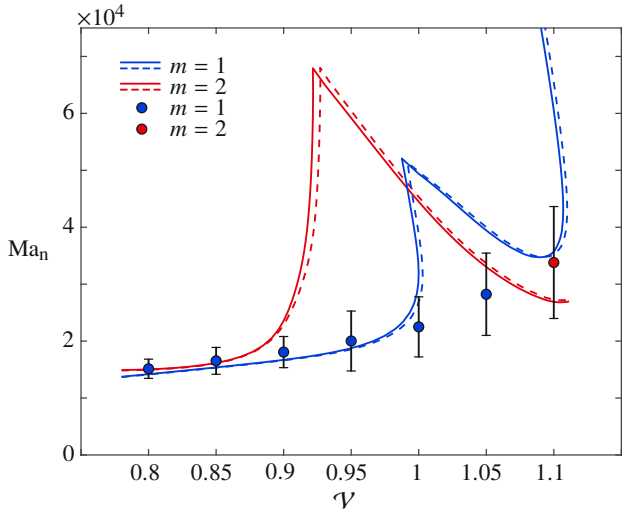

Figure 33: Neutral Marangoni numbers Ma_n (lines) as functions of the volume ratio $\mathcal{V}$ for a liquid bridge of 2-cSt silicone oil in air with length $d = 2.5$ mm and Pr = 28, $\Gamma = 1$, Bd = 0.41 and $\eta = 5$. Dashed lines: Static surface shape $h_{0,s}$, full lines: Dynamic surface shape $h_{0,d}$. A comparison is made with experimental data of Yano *et al.* (2016) (their figure 6(a)) for a gas inlet velocity of −20 mm/s ($\mathrm{Re_g} = -25$). Colour indicates the neutral wave number: $m = 1$ (blue) and $m = 2$ (red).

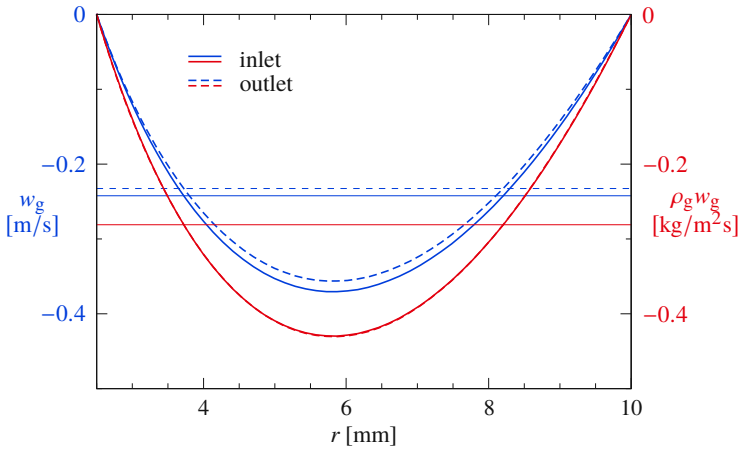

Figure 34: Volumetric flow rate density (left, blue) and mass flow rate density (right, red) at the inlet (full lines) and at the outlet (dashed lines) of the gas tube for Re = 400 and a hot downward flow ($\mathrm{Re_g} = -200$). The horizontal lines represent averaged values over the cross section.

Appendix D. Verification of the density variation

Different from the OB approximation, our code takes into account a linear variation of the density with temperature in all terms. To verify the correct implementation we consider the present standard configuration with Pr = 28. The liquid bridge is heated from above with Re = 400 and exposed to a hot downward flow with $\mathrm{Re_g} = 200$. In figure 34 we show the volume flow density w_g (left axis, blue) and the mass flow density $\rho_g w_g$ (right axis, red) as functions of r at the in- and outlet. The incoming hot air slows down from an averaged value of $\bar{w}_g = -0.242$ m/s (full horizontal blue line) to $\bar{w}_g = -0.233$ m/s (dashed horizontal blue line). As expected, the volume flux cannot be constant and independent of z, since the gas must have cooled down at the outlet. The total mass flux $\dot{m} = \int_A \rho_g w_g \mathrm{d}A$, however, must be independent of z. The almost invisible discrepancies between the mass flow densities at the inlet (full red curve) and the outlet (dashed red curve) arise, because the gas leaves the tube with a velocity profile which is slightly perturbed due to the thermocapillary flow along the liquid–gas interface. However, the total mass balance long the tube is satisfied up to machine precision: The average mass flow densities $\overline{\rho_g w_g} = -0.281\,[\mathrm{kg/m^2 s}]$ (red horizontal line) deviate by less than $10^{-12}\%$ from each other.

REFERENCES

Bach, C. & Schwabe, D. 2015 Surface waves in thermocapillary flow–revisited. *The European Physical Journal Special Topics* **224** (2), 319–340.

Batchelor, G. K. & Gill, A. E. 1962 Analysis of the stability of axisymmetric jets. *J. Fluid Mech.* **14**, 529–551.

Carrión, Luis M., Herrada, Miguel A. & Montanero, José M. 2020 Influence of the dynamical free surface deformation on the stability of thermal convection in high-Prandtl-number liquid bridges. *Intl J. Heat Mass Transfer* **146**, 118831 (10pp).

Chang, Ch. E. & Wilcox, W. R. 1975 Inhomogeneities due to thermocapillary flow in floating zone melting. *J. Crystal Growth* **28**, 8–12.

Davis, S. H. 1987 Thermocapillary instabilities. *Annu. Rev. Fluid Mech.* **19**, 403–435.

D'Orazio, Maria Cappelli, Cianfrini, Claudio & Corcione, Massimo 2004 Rayleigh–Bénard convection in tall rectangular enclosures. *Int. J. Thermal Sci.* **43**, 135–144.

Ferrera, C., Montanero, J. M., Mialdun, A., Shevtsova, V. M. & Cabezas, M.G. 2008 A new

experimental technique for measuring the dynamical free surface deformation in liquid bridges due to thermal convection. *Meas. Sci. Technol.* **19**, 015410–1–015410–10.

Gaponenko, Y., Glockner, S., Mialdun, A. & Shevtsova, V. 2011*a* Study of a liquid bridge subjected to interface shear stresses. *Acta Astronaut.* **69**, 119–126.

Gaponenko, Y., Miadlun, A. & Shevtsova, V. 2011*b* Liquid entrainment by gas flow along the interface of a liquid bridge. *Eur. Phys. J. Special Topics* **192** (1), 63–70.

Gaponenko, Yuri, Mialdun, Aliaksandr & Shevtsova, Valentina 2012 Shear driven two-phase flows in vertical cylindrical duct. *Int. J. Multiphase Flow* **39**, 205–215.

Gaponenko, Y., Mialdun, V. Yasnouand A., Nepomnyashchy, A. & Shevtsova, V. 2021 Hydrothermal waves in a liquid bridge subjected to a gas stream along the interface. *J. Fluid Mech.* **908**, A34 (36pp).

Gaponenko, Yu, Nepomnyashchy, A & Shevtsova, V 2011*c* Thermocapillary and shear driven flows in gas/liquid system in annular duct. *J. Phys. Conf. Ser.* **327**, 012030.

Gaponenko, Yuri & Shevtsova, Valentina 2012 Heat transfer through the interface and flow regimes in liquid bridge subjected to co-axial gas flow. *Microgravity Sci. Technol.* **24**, 297–306.

Gaponenko, Y., Yasnou, V., Mialdun, A., Bou-Ali, M. M., Nepomnyashchy, A. & Shevtsova, V. 2023 Variety of flow patterns in a liquid bridge subjected to a gas stream. *Philosophical Transactions of the Royal Society A: Mathematical, Physical and Engineering Sciences* **381** (2245).

Gotoda, Masakazu, Toyama, Aro, Ishimura, Misa, Sano, Tomoaki, Suzuki, Mizuki, Kaneko, Toshihiro & Ueno, Ichiro 2019 Experimental study of coherent structures of finite-size particles in thermocapillary liquid bridges. *Phys. Rev. Fluids* **4**, 094301–1–094301–22.

Hu, Kai-Xin, Zhang, Shao-Neng & Chen, Qi-Sheng 2023 Surface wave instability in the thermocapillary migration of a flat droplet. *Journal of Fluid Mechanics* **958**.

Hurle, D. T. J., ed. 1994 *Handbook of Crystal Growth*. North Holland.

Irikura, Motoki, Arakawa, Yoshihiko, Ueno, Ichiro & Kawamura, Hiroshi 2005 Effect of ambient fluid flow upon onset of oscillatory thermocapillary convection in half-zone liquid bridge. *Microgravity Sci. Technol.* **16** (1), 176–180.

Kamotani, Y., Chang, A. & Ostrach, S. 1996 Effects of heating mode on steady axisymmetric thermocapillary flows in microgravity. *ASME J. Heat Transfer* **118**, 191–197.

Kamotani, Y. & Ostrach, S. 1998 Theoretical analysis of thermocapillary flow in cylindrical columns of high Prandtl number fluids. *ASME J. Heat Transfer* **120**, 758–764.

Kamotani, Y., Wang, L., Hatta, S., Wang, A. & Yoda, S. 2003 Free surface heat loss effect on oscillatory thermocapillary flow in liquid bridges of high Prandtl number fluids. *Intl J. Heat Mass Transfer* **46**, 3211–3220.

Keller, H. B. 1977 *Numerical solution of bifurcation and nonlinear eigenvalue problems*, pp. 359–384. New York: Academic Press.

Kozhoukharova, Zh., Kuhlmann, H. C., Wanschura, M. & Rath, H. J. 1999 Influence of variable viscosity on the onset of hydrothermal waves in thermocapillary liquid bridges. *Z. Angew. Math. Mech.* **79**, 535–543.

Kuhlmann, H. C. 1999 *Thermocapillary Convection in Models of Crystal Growth*, *Springer Tracts in Modern Physics*, vol. 152. Berlin, Heidelberg: Springer.

Kuhlmann, Hendrik C., Lukasser, Michael & Muldoon, Frank H. 2011 Engineering Marangoni flows (EMA). ASAP6 819714. FFG.

Kuhlmann, H. C. & Nienhüser, C. 2002 Dynamic free-surface deformations in thermocapillary liquid bridges. *Fluid Dyn. Res.* **31**, 103–127.

Kuhlmann, H. C. & Rath, H. J. 1993 Hydrodynamic instabilities in cylindrical thermocapillary liquid bridges. *J. Fluid Mech.* **247**, 247–274.

Landau, L. D. & Lifschitz, E. M. 1959 *Fluid Mechanics*. New York: Pergamon Press.

Lehoucq, R. B., Sorensen, D. C. & Yang, C. 1998 *ARPACK Users' Guide: Solution of Large-Scale Eigenvalue Problems with Implicitly Restarted Arnoldi Methods*. Philadelphia: SIAM.

Levenstam, M. & Amberg, G. 1995 Hydrodynamic instabilities of thermocapillary flow in a half-zone. *J. Fluid Mech.* **297**, 357–372.

Matsunaga, T., Mialdun, A., Nishino, K. & Shevtsova, V. 2012 Measurements of gas/oil free surface deformation caused by parallel gas flow. *Phys. Fluids* **24** (6), 062101 (17pp).

Melnikov, D. E. & Shevtsova, V. M. 2014 The effect of ambient temperature on the stability of thermocapillary flow in liquid column. *Int. J. Heat Mass Transfer* **74**, 185–195.

Mihaljan, J. M. 1962 A rigorous exposition of the Boussinesq approximation applicable to a thin layer of fluid. *Astrophys. J.* **136**, 1126–1133.

Mills, K. C., Keene, B. J., Brooks, R. F. & Shirali, A. 1998 Marangoni effects in welding. *Phil. Trans. Roy. Soc. London A* **356**, 911–925.

Moffatt, H. K. 1964 Viscous and resistive eddies near a sharp corner. *J. Fluid Mech.* **18**, 1–18.

Montanero, J. M., Ferrera, C. & Shevtsova, V. M. 2008 Experimental study of the free surface deformation due to thermal convection in liquid bridges. *Exp. Fluids* **45**, 1087–1101.

Neitzel, G. P., Chang, K.-T., Jankowski, D. F. & Mittelmann, H. D. 1992 Linear stability theory of thermocapillary convection in a model of float-zone crystal growth. 30th Aerospace Sciences Meeting and Exhibit, Reno, NV.

Nienhüser, C. & Kuhlmann, H. C. 2002 Stability of thermocapillary flows in non-cylindrical liquid bridges. *J. Fluid Mech.* **458**, 35–73.

Oba, Takeru, Toyama, Aro, Hori, Takuma & Ueno, Ichiro 2019 Experimental study on behaviors of low-Stokes number particles in weakly chaotic structures induced by thermocapillary effect within a closed system with a free surface. *Phys. Rev. Fluids* **4**, 104002–1–104002–15.

Pearson, J. R. A. 1958 On convection cells induced by surface tension. *J. Fluid Mech.* **4**, 489–500.

Pfann, W. G. 1962 Zone melting. *Science* **135**, 1101–1109.

Preisser, F., Schwabe, D. & Scharmann, A. 1983 Steady and oscillatory thermocapillary convection in liquid columns with free cylindrical surface. *J. Fluid Mech.* **126**, 545–567.

Romanò, F. & Kuhlmann, H. C. 2019 Heat transfer across the free surface of a thermocapillary liquid bridge. *Tech. Mech.* **39**, 72–84.

Romanò, Francesco, Kuhlmann, Hendrik C., Ishimura, Misa & Ueno, Ichiro 2017 Limit cycles for the motion of finite-size particles in axisymmetric thermocapillary flows in liquid bridges. *Phys. Fluids* **29** (9), 093303 (14pp), arXiv: http://dx.doi.org/10.1063/1.5002135.

Ryzhkov, Ilya I. & Shevtsova, Valentina M. 2012 Thermocapillary instabilities in liquid columns under co- and counter-current gas flows. *Intl J. Heat Mass Transfer* **55**, 1236–1245.

Schwabe, D., Scharmann, A., Preisser, F. & Oeder, F. 1978 Experiments on surface tension driven flow in floating zone melting. *J. Crystal Growth* **43**, 305–312.

Shevtsova, V., Gaponenko, Y., Kuhlmann, H. C., Lappa, M., Lukasser, M., Matsumoto, S., Mialdun, A., Montanero, J. M., Nishino, K. & Ueno, I. 2014 The JEREMI-project on thermocapillary convection in liquid bridges. Part B: Overview on impact of co-axial gas flow. *Fluid Dyn. Mat. Proc.* **10**, 197–240.

Shevtsova, V., Gaponenko, Y. A. & Nepomnyashchy, A. 2013 Thermocapillary flow regimes and instability caused by a gas stream along the interface. *J. Fluid Mech.* **714**, 644–670.

Shevtsova, V., Mialdun, A., Ferrera, Ermakov, M., Cabezas, M. G. & Montanero, J. M. 2008 Subcritical and oscillatory dynamic surface deformations in non-cylindrical liquid bridges. *Fluid Dyn. Mat. Proc.* **4**, 43–54.

Shevtsova, V. M., Melnikov, D. E. & Legros, J. C. 2001 Three-dimensional simulations of hydrodynamic instability in liquid bridges: Influence of temperature-dependent viscosity. *Phys. Fluids* **13**, 2851–2865.

Simanovskii, Ilya B. & Nepomnyashchy, Alexandre A. 1993 *Convective Instabilities in systems with interface*. Amsterdam: Gordon and Breach.

Simic-Stefani, S., Kawaji, M. & Yoda, S. 2006 Onset of oscillatory thermocapillary convection in acetone liquid bridges: The effect of evaporation. *Intl J. Heat Mass Transfer* **49**, 3167–3179.

Smith, M. K. & Davis, S. H. 1983*a* Instabilities of dynamic thermocapillary liquid layers. Part 1. Convective instabilities. *J. Fluid Mech.* **132**, 119–144.

Smith, M. K. & Davis, S. H. 1983*b* Instabilities of dynamic thermocapillary liquid layers. Part 2. Surface-wave instabilities. *J. Fluid Mech.* **132**, 145–162.

Stojanovic, Mario & Kuhlmann, Hendrik C. 2020*a* Flow instability in high-Prandtl-number thermocapillary liquid bridges exposed to a coaxial ambient gas stream. *PAMM* **20**, e202000123.

Stojanovic, Mario & Kuhlmann, Hendrik C. 2020*b* Stability of thermocapillary flow in high-Prandtl-number liquid bridges exposed to a coaxial gas stream. *Microgravity Sci. Technol.* **32**, 953–959.

Stojanovic, Mario, Romanò, Francesco & Kuhlmann, Hendrik C. 2022 Stability of thermocapillary flow in liquid bridges fully coupled to the gas phase. *J. Fluid Mech.* **949**, A5 (51pp).

Stojanović, Mario, Romanò, Francesco & Kuhlmann, Hendrik C. 2023*a* Instability of axisymmetric flow in thermocapillary liquid bridges: Kinetic and thermal energy budgets for two-phase flow with temperature-dependent material properties (accepted). *Eur. J. Appl. Math.* .

Stojanović, Mario, Romanò, Francesco & Kuhlmann, Hendrik C. 2023*b* MaranStable: A linear stability solver for multiphase flows in canonical geometries. *SoftwareX* **23**, 101405.

Theofilis, V. 2003 Advances in global linear instability analysis of nonparallel and three-dimensional flows. *Prog. Aerospace Sci.* **39**, 249–315.

Ueno, I., Kawazoe, A. & Enomoto, H. 2010 Effect of ambient-gas forced flow on oscillatory thermocapillary convection of half-zone liquid bridge. *Fluid Dyn. Mat. Processing* **6** (1), 99–108.

Wanschura, M., Kuhlmann, H. C. & Rath, H. J. 1997 Linear stability of two-dimensional combined buoyant-thermocapillary flow in cylindrical liquid bridges. *Phys. Rev. E* **55**, 7036–7042.

Wanschura, M., Shevtsova, V. S., Kuhlmann, H. C. & Rath, H. J. 1995 Convective instability mechanisms in thermocapillary liquid bridges. *Phys. Fluids* **7**, 912–925.

Xu, J.-J. & Davis, S. H. 1984 Convective thermocapillary instabilities in liquid bridges. *Phys. Fluids* **27**, 1102–1107.

Yano, Taishi, Hirotani, Makoto & Nishino, Koichi 2018*a* Effect of interfacial heat transfer on basic flow and instability in a high-Prandtl-number thermocapillary liquid bridge. *Intl J. Heat Mass Transfer* **125**, 1121–1130.

Yano, Taishi, Maruyama, Kaname, Matsunaga, Takuya & Nishino, Koichi 2016 Effect of ambient gas flow on the instability of Marangoni convection in liquid bridges of various volume ratios. *Intl J. Heat Mass Transfer* **99**, 182–191.

Yano, Taishi & Nishino, Koichi 2020 Numerical study on the effects of convective and radiative heat transfer on thermocapillary convection in a high-Prandtl-number liquid bridge in weightlessness. *Adv. Space Res.* **66**, 2047–2061.

Yano, Taishi, Nishino, Koichi, Matsumoto, Satoshi, Ueno, Ichiro, Komiya, Atsuki, Kamotani, Yasuhiro & Imaishi, Nobuyuki 2018*b* Report on microgravity experiments of dynamic surface deformation effects on Marangoni instability in high-Prandtl-number liquid bridges. *Microgravity Sci. Technol.* **30**, 599–610.

Yano, T., Nishino, K., Ueno, I., Matsumoto, S. & Kamotani, Y. 2017 Sensitivity of hydrothermal wave instability of Marangoni convection to the interfacial heat transfer in long liquid bridges of high Prandtl number fluids. *Phys. Fluids* **29** (4), 044105 (11pp).

Yasnou, V., Gaponenko, Y., Mialdun, A. & Shevtsova, V. 2018 Influence of a coaxial gas flow on the evolution of oscillatory states in a liquid bridge. *Int. J. Heat Mass Transfer* **123**, 747–759.

Yasnou, V., Mialdun, A. & Shevtsova, V. 2012 Preparation of JEREMI experiment: Development of the ground based prototype. *Microgravity Sci. Technol.* **24**, 411–418.

Paper 3

Stojanović, M., Romanò, F., Kuhlmann, H. C. (2023), 'Instability of axisymmetric flow in thermocapillary liquid bridges: Kinetic and thermal energy budgets for two-phase flow with temperature-dependent material properties', *Eur. J. Appl. Math.*, pp. 1–27

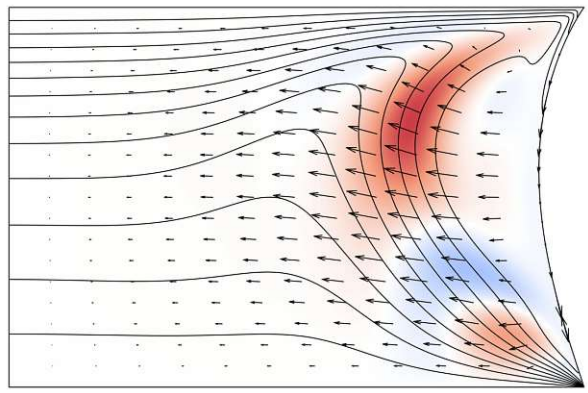

European Journal of Applied Mathematics (2023), 1–27
doi:10.1017/S0956792523000189

CAMBRIDGE UNIVERSITY PRESS

PAPER

Instability of axisymmetric flow in thermocapillary liquid bridges: Kinetic and thermal energy budgets for two-phase flow with temperature-dependent material properties

Mario Stojanović[1], Francesco Romanò[2] and Hendrik C. Kuhlmann[1]

[1]Institute of Fluid Mechanics and Heat Transfer, TU Wien, Getreidemarkt 9, 1060 Vienna, Austria and [2]Univ. Lille, CNRS, ONERA, Arts et Métiers Institute of Technology, Centrale Lille, UMR 9014-LMFL-Laboratoire de Mécanique des Fluides de Lille - Kampé de Fériet, F-59000, Lille, France
Corresponding author: Mario Stojanović; Email: mario.stojanovic@tuwien.ac.at

Received: 05 January 2023; **Revised:** 05 May 2023; **Accepted:** 10 June 2023

Keywords: Thermocpaillary flow; liquid bridge; temperature-dependent properties; linear stability; multiphase flows

2020 Mathematics Subject Classification: 76E19, 76T10, 76E09 (Primary); 80A19, 76D45 (Secondary)

Abstract

In numerical linear stability investigations, the rates of change of the kinetic and thermal energy of the perturbation flow are often used to identify the dominant mechanisms by which kinetic or thermal energy is exchanged between the basic and the perturbation flow. Extending the conventional energy analysis for a single-phase Boussinesq fluid, the energy budgets of arbitrary infinitesimal perturbations to the basic two-phase liquid–gas flow are derived for an axisymmetric thermocapillary bridge when the material parameters in both phases depend on the temperature. This allows identifying individual transport terms and assessing their contributions to the instability if the basic flow and the critical mode are evaluated at criticality. The full closed-form energy budgets of linear modes have been derived for thermocapillary two-phase flow taking into account the temperature dependence of all thermophysical parameters. The influence of different approximations to the temperature dependence on the linear stability boundary of the axisymmetric flow in thermocapillary liquid bridges is tested regarding their accuracy. The general mechanism of symmetry breaking turns out to be very robust.

1. Introduction

Thermocapillary flow in axisymmetric liquid bridges which are heated differentially represents one of the most popular paradigms of thermocapillary flow [8]. It originated from the desire to better understand the formation of striations in crystals grown by the floating-zone method [18]. One intriguing aspect is the spontaneous breaking of the steady axisymmetric flow and the relevant physical mechanisms at work. The onset of the three-dimensional flow in high-Prandtl-number liquids is characterised by a thermocapillary Reynolds number $Re \sim \Delta T d/\mu^2$ which scales linearly with the length of the liquid bridge d and the temperature difference ΔT applied between the supporting rods or, equivalently, with the total variation of the surface tension. Since the length d under normal gravity is limited by the Rayleigh–Plateau instability causing a mechanical breaking of the bridge, driving the system into a three-dimensional flow state can require a relatively large temperature difference ΔT, in particular if the dynamic viscosity μ is large. Hence, the temperature dependence of the material properties, like the dynamic viscosity, may not be negligible. For that reason, a temperature-dependent viscosity has been taken into account in stability analyses [7] and numerical simulations [22, 23]. However, most numerical results have been obtained for constant material properties [4, 9, 12, 14, 15, 16, 29].

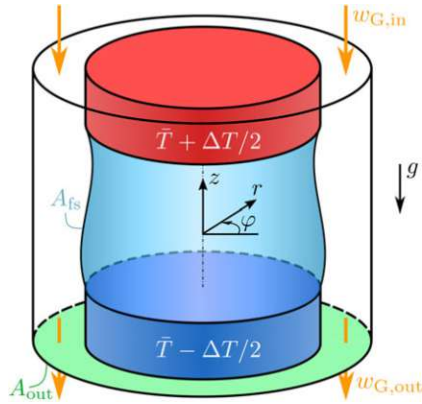

Figure 1. *Sketch of the thermocapillary liquid bridge held in place between the hot rod at temperature $\bar{T} + \Delta T/2$ and the cold rod at temperature $\bar{T} - \Delta T/2$. The flow is driven by (i) the thermocapillary effect, (ii) buoyancy forces in the gravity field $\boldsymbol{g}$ and (iii) a gas flow with a given inlet velocity $w_{G,in}$. A_{fs} and A_{out} denote the liquid–gas interface and the outlet section, respectively. Polar coordinates are indicated.*

Since the work of Reynolds [19], Orr [17] and, for thermocapillary flows, Smith [25], the balance of kinetic and thermal perturbation energies of the (infinitesimal) perturbation flow has proven a valuable tool to determine the total amount and the spatial distribution of the energy production and dissipation. Knowledge of these properties can be key to understanding the physical mechanisms of linear instability of the flow. For instance, the thermocapillary instability for low-Prandtl-number liquids is caused by the lift-up mechanism in the free surface shear layer [10, 33], similar to the vortex-ring instability [34], while the temperature field is passive with respect to the instability. The temperature field is only required to drive the basic flow. For large Prandtl numbers, on the other hand, the temperature field is important and the flow instability arises in form of a pair of azimuthally propagating hydrothermal waves [33], similar as for plane layers [26]. The hydrothermal waves draw their energy from temperature gradients of the basic flow in the bulk. The strong internal temperature gradients arise due to the basic recirculation, driven by thermocapillary forces, which transports hot fluid from the free surface over the cold wall deep into the bulk.

Uncertainties in the computation of the critical Reynolds number are mainly caused by (a) discretisation errors, (b) neglect of the temperature dependence of the material properties and (c) simplifying assumptions about the ambient conditions like the assumption of Newtons's law of heat transfer. As numerical capabilities have improved, the discretisation errors can be well controlled. Moreover, it has become feasible to take into account temperature-dependent material properties as well as the flow in the ambient atmosphere. Due to its usefulness for the understanding of the physical instability mechanics as well as for a check of the energy preservation of the numerically computed critical mode, we establish the Reynold–Orr equations governing the temporal evolution of the kinetic and thermal energy budgets of the critical perturbation mode of the linear theory for an axisymmetric liquid bridge surrounded by a gas. The energy balances obtained take into account the temperature dependence of all thermophysical material properties and are valid both in the liquid and in the gas phase, of which the latter is confined to a concentric tube surrounding the liquid bridge.

2. Geometrical configuration

The flow in a liquid droplet suspended between two coaxial cylindrical rods is considered, assuming that the physical properties of the liquid and gas phases are temperature-dependent (Figure 1). The two rods are kept at constant temperatures with $T_{\mathrm{hot}} = \bar{T} + \Delta T/2$ (hot rod) and $T_{\mathrm{cold}} = \bar{T} - \Delta T/2$ (cold rod),

https://doi.org/10.1017/S0956792523000189 Published online by Cambridge University Press

where $\bar{T} = (T_{\text{hot}} + T_{\text{cold}})/2$ denotes the arithmetic mean temperature which is assumed as reference temperature. The liquid bridge is surrounded by a gas confined to a coaxial cylindrical tube, intended to prevent uncontrollable circulations from the ambience in experiments. The flow is driven (i) by thermocapillary forces acting on the interface due to a variable surface tension $\sigma(T)$, (ii) buoyancy forces in the presence of the acceleration of gravity which is assumed to be directed in the negative axial direction (Figure 1) and (iii) by an externally imposed gas flow ($w_{\text{G,in}}$ in Figure 1), assumed to be axisymmetric and non-swirling. The external gas flow affects the flow in the liquid phase via viscous shear stresses acting on the liquid–gas interface and by the thermal coupling between liquid and gas.

On all solid walls of the support rods and the tube, we assume no-slip boundary conditions. On the surfaces of the rods, the temperatures T_{hot} and T_{cold} are imposed as indicated by colour in Figure 1, while the cylindrical tube is assumed adiabatic. Gas may enter the system with a given axial velocity profile $w_{\text{G,in}}(r)$ and a given temperature, also satisfying outflow conditions at the outlet (denoted A_{out} in Figure 1). Alternatively, the gas tube may be closed ($w_{\text{G,in}} \equiv w_{\text{G,out}} \equiv 0$) and confined by either adiabatic or conductive walls. The thermocapillary flow is driven along the interface A_{fs} by the thermocapillary effect which creates the tangential stress [11]

$$\begin{aligned}\nabla_{\parallel}\sigma(T) &= \frac{\partial\sigma}{\partial T}\nabla_{\parallel}T = \frac{\partial}{\partial T}\left[\sigma(\bar{T}) - \gamma(T-\bar{T}) + \delta(T-\bar{T})^2 + \ldots\right]\nabla_{\parallel}T \\ &= \left[-\gamma + 2\delta(T-\bar{T}) + \ldots\right]\nabla_{\parallel}T, \end{aligned} \tag{2.1}$$

where $\nabla_{\parallel}$ denotes the tangential Nabla operator. For the overwhelming majority of liquids, the surface tension decreases with temperature ($\gamma > 0$). Therefore, the thermocapillary effect will typically generate a flow which is directed along the interface away from the hot rod (low surface tension) and towards the cold rod (high surface tension). The usual approximation is to neglect quadratic terms in the Taylor expansion of the surface tension leading to $\nabla_{\parallel}\sigma(T) \approx -\gamma\nabla_{\parallel}T$. We note that the present analysis is independent of the exact functional dependence of $\sigma(T)$. While the Taylor coefficients γ, δ, etc. in (2.1) crucially affect the flow fields by coupling the velocity and temperature fields on the interface, they do not explicitly appear in the energy budgets of a given linear instability mode.

3. Governing equations

The general flow problem is governed by the Navier–Stokes and energy equations in both the liquid and the gas phase. We consider the strong conservative forms

$$\partial_t\rho + \nabla\cdot\left(\rho\hat{\boldsymbol{U}}\right) = 0, \tag{3.1a}$$

$$\partial_t\left(\rho\hat{\boldsymbol{U}}\right) + \nabla\cdot\left(\rho\hat{\boldsymbol{U}}\hat{\boldsymbol{U}}\right) = -\nabla\hat{P} + \rho\boldsymbol{g} + \nabla\cdot\boldsymbol{\mathcal{T}}, \tag{3.1b}$$

$$\partial_t\left(\rho c_p\hat{T}\right) + \nabla\cdot\left(\rho c_p\hat{T}\hat{\boldsymbol{U}}\right) = \nabla\cdot\left(\lambda\nabla\hat{T}\right), \tag{3.1c}$$

where $\hat{\boldsymbol{U}}$, $\hat{P}$ and $\hat{T}$ are the velocity, pressure and temperature fields. Henceforth, the hat ($\hat{}$) indicates the total flow fields, including a basic flow and a perturbation. Equations (3.1a)–(3.1c) describe the transport in both the liquid and the gas phase. As long as the formulation for both phases is the same, we do not distinguish between them. We assume the fluids are Newtonian with stress tensor

$$\boldsymbol{\mathcal{T}} = \mu\left[\nabla\hat{\boldsymbol{U}} + \left(\nabla\hat{\boldsymbol{U}}\right)^{\mathrm{T}}\right] - \frac{2}{3}\mu\left(\nabla\cdot\hat{\boldsymbol{U}}\right)\boldsymbol{I}, \tag{3.2}$$

where $\boldsymbol{I}$ is the identity matrix. The temperature-dependent density, dynamic viscosity, thermal conductivity and specific heat at constant pressure are denoted $\rho(\hat{T})$, $\mu(\hat{T})$, $\lambda(\hat{T})$ and $c_p(\hat{T})$, respectively. Since the density is treated as temperature-dependent, the velocity field is not solenoidal. The formulation used for the temperature equation (3.1c) neglects the pressure work and the viscous dissipation. These assumptions are justified, respectively, if the conditions

$$\chi\frac{\bar{T}}{\Delta T} \le 0.1 \quad \text{and} \quad \chi Pr \le 0.1 \quad \text{with} \quad \chi = \frac{\bar{\beta}gd}{\bar{c}_p} \tag{3.3}$$

https://doi.org/10.1017/S0956792523000189 Published online by Cambridge University Press

are satisfied, where $Pr = \bar{\mu}\bar{c}_p/\bar{\lambda}$ is the Prandtl number and $\beta = -\rho^{-1}(\partial\rho/\partial T)_p$ is the thermal expansion coefficient [3]. The overbar indicates reference values at the reference temperature $\bar{T}$. Similarly, we disregard the pressure contribution to the enthalpy in (3.1c) assuming $p/\rho \ll |c_p T|$. In Section 6, we verify the conditions (3.3) for two different cases, confirming the validity of (3.1c).

For equations (3.1a)–(3.1c) and for the assumed steady axisymmetric boundary conditions a steady axisymmetric basic flow $(\boldsymbol{u}_0, T_0, p_0, h_0)$ exists. The axisymmetric shape function $h_0(z)$ marks the radial coordinate of the location of the liquid–gas interphase in the axisymmetric steady flow which is assumed to be pinned to the sharp circular edges of the supporting rods. The shape $h_0(z)$ is determined by the flow-induced normal stresses and the Laplace pressure, which also depends on the full surface tension $\sigma(\hat{T})$ and the hydrostatic pressure difference.

Here we are not concerned with computing the basic flow. We assume it has been obtained numerically, taking into account the full temperature dependence of the material properties. Therefore, the exact form of the boundary conditions and forcing terms for the basic flow does not enter the present problem. Furthermore, we assume a linear stability analysis has been carried out by solving the associated eigenvalue problem (see e.g. Stojanović et al. [27]) such that the neutrally stable linear mode $(\boldsymbol{u}, T, p, h)$ is available as well. We consider the formal decomposition

$$\hat{\boldsymbol{U}} = \boldsymbol{u}_0(r, z) + \boldsymbol{u}(r, \varphi, z, t), \tag{3.4a}$$

$$\hat{T} = T_0(r, z) + T(r, \varphi, z, t), \tag{3.4b}$$

$$\hat{P} = p_0(r, z) + p(r, \varphi, z, t), \tag{3.4c}$$

$$\hat{H} = h_0(z) + h(\varphi, z, t), \tag{3.4d}$$

of the total flow ($\hat{}$) into the basic state (index 0) and a perturbation $(\boldsymbol{u}, T, p, h)$. All flow fields are described using cylindrical coordinates (r, φ, z) and associated velocity components (u, v, w) such that $\boldsymbol{u} = u\boldsymbol{e}_r + v\boldsymbol{e}_\varphi + w\boldsymbol{e}_z$, where $\boldsymbol{e}$ denotes a unit vector.

The neutral mode is typically obtained by a linearisation of the governing equations which requires the perturbation quantities to be asymptotically small. We do not explicitly introduce a smallness parameter ϵ, but keep in mind that the perturbation quantities $(\boldsymbol{u}, T, p, h)$ are all of the order of $O(\epsilon)$ in the sense of the linearisation required for the linear stability analysis. For convenience, we shall not express the perturbation quantities by normal modes. This is easily accomplished a posteriori.

In order to keep the effort required in deriving the energy budgets for the neutral mode at a meaningful level, we make the ad hoc assumption that the perturbation flow does not affect the interfacial shape. This is motivated by the experimental observations that the interfacial deformations due to the supercritical three-dimensional flow are very small under typical laboratory conditions [36]. We note, however, that this simplification precludes surface waves from the range of critical modes. With the assumption $h = 0$, the outward pointing unit vector normal to the free surface is

$$\boldsymbol{n} = \frac{1}{N}\left(\boldsymbol{e}_r - h_{0z}\boldsymbol{e}_z\right), \tag{3.5}$$

with the normalising denominator $N = \sqrt{1 + h_{0z}^2}$, where we use the notation $h_{0z} = \mathrm{d}h_0/\mathrm{d}z$. Likewise, we define $h_{0zz} = \mathrm{d}^2 h_0/\mathrm{d}z^2$.

Let us assume the basic flow has been computed from the axisymmetric steady version of (3.1a)–(3.1c). Furthermore, we assume the perturbation flow has been computed by solving (3.1a)–(3.1c) linearised about the basic state. Within a postprocessing step, we are then interested in the temporal evolution of the kinetic and thermal perturbation energy densities

$$\varepsilon_{\mathrm{kin}}(\boldsymbol{x}, t) = \frac{1}{2}\rho(T_0)\boldsymbol{u}^2, \tag{3.6a}$$

$$\varepsilon_{\mathrm{therm}}(\boldsymbol{x}, t) = \frac{1}{2}\rho(T_0)c_p(T_0)T^2, \tag{3.6b}$$

in the liquid and the gas phase. These energy densities must be considered measures of the perturbation flow in the sense of Joseph [5]. With the perturbations being of $O(\epsilon)$, the above energy densities are of $O(\epsilon^2)$. The aim is to express $\partial_t \varepsilon_{\mathrm{kin}}(\boldsymbol{x}, t)$ and $\partial_t \varepsilon_{\mathrm{therm}}(\boldsymbol{x}, t)$ by a sum of contributions which describe

https://doi.org/10.1017/S0956792523000189 Published online by Cambridge University Press

individual transport processes and can be interpreted in physical terms. While the local rates of change of the energy densities (3.6a) and (3.6b) are generally non-zero and depend on $\boldsymbol{x}$, the total change rates obtained by integration over the volume occupied by the respective fluid must vanish, if the perturbation flow field represents a critical or a neutral mode for which the growth rate vanishes.

In the following, we assume that the fluid properties depend solely on the temperature and not on the pressure. This simplifying assumption is commonly made by the manufacturers of batch liquids employed for silicone oil liquid bridges [24] and for liquids in general far from their phase-change critical points. To take into account the temperature dependence of the material parameters, we assume the parameters, as well as their first and second derivatives $\rho'(\hat{T})$, $\mu'(\hat{T})$, $\lambda'(\hat{T})$, $c_p'(\hat{T})$ and $\rho''(\hat{T})$, $\mu''(\hat{T})$, $\lambda''(\hat{T})$, $c_p''(\hat{T})$, respectively, are available in closed-form expressions as functions of the temperature $\hat{T}$. The functional dependence on $\hat{T}$ could be established, for instance, by fitting discrete data by suitable ansatz functions (polynomials, exponentials, etc.) or spline functions. With this information available, all material parameters can be expanded about the local temperature $T_0(r,z)$ of the basic flow and up to second order

$$\rho\big(\hat{T}\big) = \rho(T_0+T) \approx \rho(T_0) + \partial_T\rho|_{T_0}\, T + \frac{1}{2}\,\partial_T^2\rho\big|_{T_0}\, T^2 := \rho_0 + \rho_0' T + \frac{1}{2}\rho_0'' T^2, \tag{3.7a}$$

$$\mu\big(\hat{T}\big) = \mu(T_0+T) \approx \mu(T_0) + \partial_T\mu|_{T_0}\, T + \frac{1}{2}\,\partial_T^2\mu\big|_{T_0}\, T^2 := \mu_0 + \mu_0' T + \frac{1}{2}\mu_0'' T^2, \tag{3.7b}$$

$$\lambda\big(\hat{T}\big) = \lambda(T_0+T) \approx \lambda(T_0) + \partial_T\lambda|_{T_0}\, T + \frac{1}{2}\,\partial_T^2\lambda\big|_{T_0}\, T^2 := \lambda_0 + \lambda_0' T + \frac{1}{2}\lambda_0'' T^2, \tag{3.7c}$$

$$c_p\big(\hat{T}\big) = c_p(T_0+T) \approx c_p(T_0) + \partial_T c_p\big|_{T_0}\, T + \frac{1}{2}\,\partial_T^2 c_p\big|_{T_0}\, T^2 := c_{p0} + c_{p0}' T + \frac{1}{2}c_{p0}'' T^2. \tag{3.7d}$$

The Taylor coefficients $(\rho_0, \mu_0, \lambda_0, c_{p0})$, $(\rho_0', \mu_0', \lambda_0', c_{p0}')$ and $(\rho_0'', \mu_0'', \lambda_0'', c_{p0}'')$ are scalar fields which depend continuously on the basic temperature T_0. Note all the above thermophysical properties and coefficients depend on the phase.

Before deriving the rates of change of the kinetic energies, it is useful to consider the continuity equation. Inserting expansions (3.7a)–(3.7d) into the continuity equation (3.1a) and neglecting quadratic terms yields

$$\partial_t(\rho_0' T) + \nabla\cdot(\rho_0\boldsymbol{u}_0) + \nabla\cdot(\rho_0\boldsymbol{u}) + \nabla\cdot(\rho_0' T\boldsymbol{u}_0) = 0. \tag{3.8}$$

As this equation involves different orders of magnitude, the terms of each order of magnitude in this equation must vanish separately,

$$O(\epsilon^0): \qquad \nabla\cdot(\rho_0\boldsymbol{u}_0) = 0, \tag{3.9a}$$

$$O(\epsilon^1): \qquad \rho_0'\partial_t T + \nabla\cdot(\rho_0\boldsymbol{u}) + \nabla\cdot(\rho_0' T\boldsymbol{u}_0) = 0. \tag{3.9b}$$

The terms of order $O(\epsilon^0)$ arise in the equations for the basic flow and thus do not enter the equations of order $O(\epsilon^1)$ for the perturbation flow. Equation (3.9b), on the other hand, balances the terms of $O(\epsilon^1)$ and thus represents the continuity equation in linear order entering the linear stability analysis.

4. Thermal energy budget

The basic flow $(\boldsymbol{u}_0, T_0, p_0, h_0)$ is assumed stationary and of order $O(\epsilon^0)$. Since the perturbation flow is of order $O(\epsilon^1)$, it has no effect on the energy budget of the basic flow which is also $O(\epsilon^0)$. Nevertheless, the rates of change of the perturbation energies (3.6a) and (3.6b), which are of order $O(\epsilon^2)$, contain terms which describe an energy exchange with the basic flow.

To derive the local thermal energy budget, we first derive the linear equation governing the evolution of the perturbation temperature. To that end, the flow decomposition (3.4a)–(3.4d) is inserted into the temperature equation (3.1c) to obtain

$$\partial_t(\rho c_p T_0) + \partial_t(\rho c_p T) + \nabla\cdot\big[\rho c_p(T_0+T)(\boldsymbol{u}_0+\boldsymbol{u})\big] = \nabla\cdot(\lambda\nabla T_0) + \nabla\cdot(\lambda\nabla T), \tag{4.1}$$

https://doi.org/10.1017/S0956792523000189 Published online by Cambridge University Press

which contains both the basic state and the perturbation flow. Neglecting terms of order $O(\epsilon^2)$ yields

$$\partial_t(\rho c_p T_0) + \partial_t(\rho c_p T) + \nabla\cdot(\rho c_p T_0 \boldsymbol{u}_0) + \nabla\cdot(\rho c_p T_0 \boldsymbol{u}) + \nabla\cdot(\rho c_p T \boldsymbol{u}_0) = \nabla\cdot(\lambda\nabla T_0) + \nabla\cdot(\lambda\nabla T). \quad (4.2)$$

Inserting the Taylor expansions (3.7a)–(3.7d) of ρ, c_p and λ we obtain, after linearisation,

$$\begin{aligned} T_0\ \partial_T(\rho c_p)\big|_{T_0}\,\partial_t T + \rho_0 c_{p0}\partial_t T + \nabla\cdot(\rho_0 c_{p0} T_0 \boldsymbol{u}_0) + \nabla\cdot(\rho_0' c_{p0} T_0 \boldsymbol{u}_0 T) + \nabla\cdot(\rho_0 c_{p0}' T_0 \boldsymbol{u}_0 T) \\ + \nabla\cdot(\rho_0 c_{p0} T \boldsymbol{u}_0) + \nabla\cdot(\rho_0 c_{p0} T_0 \boldsymbol{u}) = \nabla\cdot(\lambda_0\nabla T_0) + \nabla\cdot(\lambda_0' T\nabla T_0) + \nabla\cdot(\lambda_0\nabla T), \end{aligned} \quad (4.3)$$

where the coefficients, like $\lambda_0 = \lambda(T_0)$, are functions of the basic state temperature field T_0. Separating the orders of magnitude, the terms of order $O(\epsilon^0)$ enter the basic state equation for T_0

$$\nabla\cdot(\rho_0 c_{p0} T_0 \boldsymbol{u}_0) = \nabla\cdot(\lambda_0\nabla T_0), \quad (4.4)$$

while the terms of order $O(\epsilon^1)$

$$\begin{aligned} \left[T_0(\rho_0' c_{p0} + \rho_0 c_{p0}') + \rho_0 c_{p0}\right]\partial_t T + \nabla\cdot(\rho_0' c_{p0} T_0 \boldsymbol{u}_0 T) + \nabla\cdot(\rho_0 c_{p0}' T_0 \boldsymbol{u}_0 T) \\ + \nabla\cdot(\rho_0 c_{p0} T \boldsymbol{u}_0) + \nabla\cdot(\rho_0 c_{p0} T_0 \boldsymbol{u}) = \nabla\cdot(\lambda_0' T\nabla T_0) + \nabla\cdot(\lambda_0\nabla T) \end{aligned} \quad (4.5)$$

constitute the linear perturbation equation for T.

To obtain the rate of change of the thermal energy density (3.6b), equation (4.5) is multiplied by T to yield

$$\begin{aligned} \underbrace{\rho_0 c_{p0} T\partial_t T}_{\mathtt{T1}} = &-\underbrace{(\rho_0' c_{p0} + \rho_0 c_{p0}')T_0 T\partial_t T}_{\mathtt{T2}} - \underbrace{T\nabla\cdot(\rho_0' c_{p0} T_0 \boldsymbol{u}_0 T)}_{\mathtt{T3}} - \underbrace{T\nabla\cdot(\rho_0 c_{p0}' T_0 \boldsymbol{u}_0 T)}_{\mathtt{T4}} \\ &- \underbrace{T\nabla\cdot(\rho_0 c_{p0} T \boldsymbol{u}_0)}_{\mathtt{T5}} - \underbrace{T\nabla\cdot(\rho_0 c_{p0} T_0 \boldsymbol{u})}_{\mathtt{T6}} + \underbrace{T\nabla\cdot(\lambda_0' T\nabla T_0)}_{\mathtt{T7}} + \underbrace{T\nabla\cdot(\lambda_0\nabla T)}_{\mathtt{T8}}. \end{aligned} \quad (4.6)$$

As far as the transport mechanisms are concerned, we recognise that the term T1 represents the rate of change of thermal perturbation energy density $\partial_t \varepsilon_{\text{therm}}$. Moreover, the term T2 describes an additional rate of change of thermal perturbation energy density due to the dependence of ρ and c_p on the temperature T_0.

The remaining divergence terms describe the rates of change of thermal perturbation energy density due to the divergence of thermal perturbation energy flux densities. These thermal perturbation energy flux densities are caused by the basic state velocity $\boldsymbol{u}_0$ and the thermal energy densities given by $(\rho_0' T_0)c_{p0}T$ in T3, $(c_{p0}' T_0)\rho_0 T$ in T4 and $\rho_0 c_{p0} T$ in T5, where the first and second terms are due to the variation with T_0 of ρ and c_p, respectively. The term T6 is due to the thermal perturbation energy flux density which is caused by the transport of basic state thermal energy $\rho_0 c_{p0} T_0$ by the perturbation velocity $\boldsymbol{u}$.

Finally, the term T8 describes the dissipation of thermal energy due to Fourier's diffusive perturbation heat flux $-\lambda_0\nabla T$, and T7 is due to the diffusive heat flux caused by gradients of the basic temperature in combination with the temperature dependence of λ which is not taken care of in the $O(\epsilon^0)$ equations for the basic state.

To arrive at the total, that is integral, thermal energy budget for each fluid phase, the rate of change of the thermal energy density (4.6) must be integrated over the volume V_i occupied by the respective phase (liquid or gas), where the subscript $i \in [\mathrm{L}, \mathrm{G}]$ indicates the phase. Moreover, we define the coefficient

$$\alpha_i = \begin{cases} 1 & i = \mathrm{L}, \\ -1 & i = \mathrm{G}. \end{cases} \quad (4.7)$$

Since the integration is rather technical, the derivation of the integral thermal energy budget is made in Appendix A. As a result, we obtain the total rate of change of thermal energy $\partial_t E_T = \partial_t \int_{V_i} \varepsilon_{\text{therm}}\,\mathrm{d}V$ in the phase i

$$\partial_t E_T = -D_{\text{th}} + J + H_{\text{fs}} + K_{\text{G,th}} + \Pi_\rho + \Pi_{c_p} + \Pi_\lambda - \partial_t E_T', \quad (4.8)$$

https://doi.org/10.1017/S0956792523000189 Published online by Cambridge University Press

with the abbreviations

$$D_{\mathrm{th}} = \int_{V_i} \lambda_0 (\nabla T)^2 \,\mathrm{d}V, \tag{4.9a}$$

$$J = \sum_{j=1}^{2} J_j = -\int_{V_i} \rho_0 T \left[u\partial_r (c_{p0} T_0) + w \partial_z (c_{p0} T_0) \right] \,\mathrm{d}V, \tag{4.9b}$$

$$H_{\mathrm{fs}} = \alpha_i \int_{A_{\mathrm{fs}}} \lambda_0 T \nabla T \cdot \boldsymbol{n} \,\mathrm{d}S, \tag{4.9c}$$

$$K_{\mathrm{G,th}} = -\frac{1-\alpha_i}{4} \int_{A_{\mathrm{out}}} \rho_0 c_{p0} T^2 w_0 \,\mathrm{d}S, \tag{4.9d}$$

$$\begin{aligned} \Pi_\rho = &\int_{V_i} \rho_0' c_{p0} T_0 \boldsymbol{u}_0 \cdot \nabla T^2 \,\mathrm{d}V - \frac{1}{2} \int_{V_i} \left(\frac{\rho_0'^2}{\rho_0} - \rho_0'' \right) c_{p0} T^2 \boldsymbol{u}_0 \cdot \nabla T_0^2 \,\mathrm{d}V \\ &- \frac{1-\alpha_i}{2} \int_{A_{\mathrm{out}}} \rho_0' c_{p0} T_0 T^2 w_0 \,\mathrm{d}S, \end{aligned} \tag{4.9e}$$

$$\begin{aligned} \Pi_{c_p} = &\frac{1}{2} \int_{V_i} \rho_0 c_{p0}' T_0 \boldsymbol{u}_0 \cdot \nabla T^2 \,\mathrm{d}V - \frac{1}{2} \int_{V_i} \rho_0 c_{p0}' T^2 \boldsymbol{u}_0 \cdot \nabla T_0 \,\mathrm{d}V \\ &- \frac{1-\alpha_i}{2} \int_{A_{\mathrm{out}}} \rho_0 c_{p0}' T_0 T^2 w_0 \,\mathrm{d}S, \end{aligned} \tag{4.9f}$$

$$\Pi_\lambda = \alpha_i \int_{A_{\mathrm{fs}}} \lambda_0' T^2 \nabla T_0 \cdot \boldsymbol{n} \,\mathrm{d}S - \frac{1}{2} \int_{V_i} \lambda_0' \nabla T_0 \cdot \nabla T^2 \,\mathrm{d}V, \tag{4.9g}$$

$$\partial_t E_T' = \frac{1}{2} \int_{V_i} T_0 \rho_0 c_{p0}' \partial_t T^2 \,\mathrm{d}V, \tag{4.9h}$$

where the index i has been suppressed for the thermophysical properties of the two phases.

The terms (4.9a)–(4.9c) are well known from the energy budget for constant material properties (see e.g. Nienhuser and Kuhlmann [16]). The surface integrals in (4.9d)–(4.9f) represent rates of change of thermal energy of the gas phase ($\alpha_i = -1$) due to convective heat fluxes through the outlet boundary A_{out} of the gas container. These fluxes vanish if the gas container is closed ($w_0|_{A_{\mathrm{out}}} = 0$) or if the temperature is prescribed at the outlet ($T|_{A_{\mathrm{out}}} = 0$). Since we assume the gas enters the container with a prescribed (basic state) temperature, no perturbation energy is introduced through the inlet. The terms Π_ρ, Π_{c_p} and Π_λ arise due to the temperature dependence of the material parameters. They vanish, respectively, if $\rho = \text{const.}$, $c_p = \text{const.}$ or $\lambda = \text{const.}$ Similar to the thermal perturbation energy density (3.6b), the term (4.9h) also depends on the temporal evolution of the perturbation temperature.

5. Kinetic energy budget

The rate of change of the kinetic energy density $\partial_t \varepsilon_{\mathrm{kin}}$ is derived by linearising the momentum equation with respect to the perturbation quantities followed by a scalar multiplication of the linearised momentum equation with the perturbation velocity $\boldsymbol{u}$. Inserting (3.4a) and (3.4c) in (3.1b), we obtain

$$\begin{aligned} &\partial_t(\rho \boldsymbol{u}_0) + \partial_t(\rho \boldsymbol{u}) + \nabla \cdot [\rho(\boldsymbol{u}_0 + \boldsymbol{u})(\boldsymbol{u}_0 + \boldsymbol{u})] = -\nabla p_0 - \nabla p + \rho_0 \boldsymbol{g} + \rho_0' T \boldsymbol{g} \\ &\quad + \nabla \cdot \left\{ \mu \left[\nabla \boldsymbol{u}_0 + (\nabla \boldsymbol{u}_0)^{\mathrm{T}} \right] \right\} - \frac{2}{3} \nabla \cdot [\mu (\nabla \cdot \boldsymbol{u}_0) \boldsymbol{I}] + \nabla \cdot \left\{ \mu \left[\nabla \boldsymbol{u} + (\nabla \boldsymbol{u})^{\mathrm{T}} \right] \right\} - \frac{2}{3} \nabla \cdot [\mu (\nabla \cdot \boldsymbol{u}) \boldsymbol{I}] . \end{aligned} \tag{5.1}$$

Linearising this equation with respect to the perturbation quantities by neglecting terms of $O(\epsilon^2)$ yields

$$\begin{aligned} &\partial_t(\rho \boldsymbol{u}_0) + \partial_t(\rho \boldsymbol{u}) + \nabla \cdot (\rho \boldsymbol{u}_0 \boldsymbol{u}_0) + \nabla \cdot [\rho(\boldsymbol{u}_0 \boldsymbol{u} + \boldsymbol{u}\boldsymbol{u}_0)] = -\nabla p_0 - \nabla p + \rho_0 \boldsymbol{g} + \rho_0' T \boldsymbol{g} \\ &\quad + \nabla \cdot \left\{ \mu \left[\nabla \boldsymbol{u}_0 + (\nabla \boldsymbol{u}_0)^{\mathrm{T}} \right] \right\} - \frac{2}{3} \nabla \cdot [\mu (\nabla \cdot \boldsymbol{u}_0) \boldsymbol{I}] + \nabla \cdot \left\{ \mu \left[\nabla \boldsymbol{u} + (\nabla \boldsymbol{u})^{\mathrm{T}} \right] \right\} - \frac{2}{3} \nabla \cdot [\mu (\nabla \cdot \boldsymbol{u}) \boldsymbol{I}] . \end{aligned} \tag{5.2}$$

https://doi.org/10.1017/S0956792523000189 Published online by Cambridge University Press

Now the Taylor expansion of the material parameters (3.7a)–(3.7d) is inserted in (5.2) to obtain, after linearisation,

$$\begin{aligned}\boldsymbol{u}_0\ \partial_T\rho|_{T_0}\,\partial_t T+\rho_0\partial_t\boldsymbol{u}+\nabla\cdot(\rho_0\boldsymbol{u}_0\boldsymbol{u}_0)+\nabla\cdot(\rho_0'T\boldsymbol{u}_0\boldsymbol{u}_0)+\nabla\cdot[\rho_0(\boldsymbol{u}_0\boldsymbol{u}+\boldsymbol{u}\boldsymbol{u}_0)]\\ =-\nabla p_0-\nabla p+\nabla\cdot\left\{\mu_0\left[\nabla\boldsymbol{u}_0+(\nabla\boldsymbol{u}_0)^{\mathrm{T}}\right]\right\}-\frac{2}{3}\nabla\cdot[\mu_0(\nabla\cdot\boldsymbol{u}_0)\boldsymbol{I}]+\nabla\cdot\left\{\mu_0'T\left[\nabla\boldsymbol{u}_0+(\nabla\boldsymbol{u}_0)^{\mathrm{T}}\right]\right\}\\ +\rho_0\boldsymbol{g}+\rho_0'T\boldsymbol{g}-\frac{2}{3}\nabla\cdot\left[\mu_0'T(\nabla\cdot\boldsymbol{u}_0)\boldsymbol{I}\right]+\nabla\cdot\left\{\mu_0\left[\nabla\boldsymbol{u}+(\nabla\boldsymbol{u})^{\mathrm{T}}\right]\right\}-\frac{2}{3}\nabla\cdot[\mu_0(\nabla\cdot\boldsymbol{u})\boldsymbol{I}]\,.\end{aligned}\tag{5.3}$$

Separating again the orders of magnitude yields the basic state momentum equation at $O(\epsilon^0)$

$$\nabla\cdot(\rho_0\boldsymbol{u}_0\boldsymbol{u}_0)=-\nabla p_0+\rho_0\boldsymbol{g}+\nabla\cdot\left\{\mu_0\left[\nabla\boldsymbol{u}_0+(\nabla\boldsymbol{u}_0)^{\mathrm{T}}\right]\right\}-\frac{2}{3}\nabla\cdot[\mu_0(\nabla\cdot\boldsymbol{u}_0)\boldsymbol{I}]\,,\tag{5.4}$$

and the momentum perturbation equation at $O(\epsilon^1)$

$$\begin{aligned}\boldsymbol{u}_0\rho_0'\partial_t T+\rho_0\partial_t\boldsymbol{u}+\nabla\cdot(\rho_0'T\boldsymbol{u}_0\boldsymbol{u}_0)+\nabla\cdot[\rho_0(\boldsymbol{u}_0\boldsymbol{u}+\boldsymbol{u}\boldsymbol{u}_0)]\\ =-\nabla p+\rho_0'T\boldsymbol{g}+\nabla\cdot\left\{\mu_0'T\left[\nabla\boldsymbol{u}_0+(\nabla\boldsymbol{u}_0)^{\mathrm{T}}\right]\right\}-\frac{2}{3}\nabla\cdot\left[\mu_0'T(\nabla\cdot\boldsymbol{u}_0)\boldsymbol{I}\right]\\ +\nabla\cdot\left\{\mu_0\left[\nabla\boldsymbol{u}+(\nabla\boldsymbol{u})^{\mathrm{T}}\right]\right\}-\frac{2}{3}\nabla\cdot[\mu_0(\nabla\cdot\boldsymbol{u})\boldsymbol{I}]\,.\end{aligned}\tag{5.5}$$

Finally, the scalar product between the momentum perturbation equation (5.5) is taken with the perturbation velocity field $\boldsymbol{u}$, yielding

$$\begin{aligned}\underbrace{\rho_0\boldsymbol{u}\cdot\partial_t\boldsymbol{u}}_{\mathtt{K1}}=\underbrace{-\rho_0'\boldsymbol{u}_0\cdot\boldsymbol{u}\partial_t T}_{\mathtt{K2}}\underbrace{-\boldsymbol{u}\cdot\{\nabla\cdot[\rho_0(\boldsymbol{u}_0\boldsymbol{u}+\boldsymbol{u}\boldsymbol{u}_0)]\}}_{\mathtt{K3}}\underbrace{-\boldsymbol{u}\cdot\left[\nabla\cdot(\rho_0'T\boldsymbol{u}_0\boldsymbol{u}_0)\right]}_{\mathtt{K4}}\\ \underbrace{-\boldsymbol{u}\cdot\nabla p}_{\mathtt{K5}}\underbrace{+\rho_0'T\boldsymbol{u}\cdot\boldsymbol{g}}_{\mathtt{K6}}\underbrace{+\boldsymbol{u}\cdot\left\{\nabla\cdot\left\{\mu_0\left[\nabla\boldsymbol{u}+(\nabla\boldsymbol{u})^{\mathrm{T}}\right]\right\}\right\}}_{\mathtt{K7}}\underbrace{-\frac{2}{3}\boldsymbol{u}\cdot\left\{\nabla\cdot[\mu_0(\nabla\cdot\boldsymbol{u})\boldsymbol{I}]\right\}}_{\mathtt{K8}}\\ \underbrace{+\boldsymbol{u}\cdot\left\{\nabla\cdot\left\{\mu_0'T\left[\nabla\boldsymbol{u}_0+(\nabla\boldsymbol{u}_0)^{\mathrm{T}}\right]\right\}\right\}}_{\mathtt{K9}}\underbrace{-\frac{2}{3}\boldsymbol{u}\cdot\left\{\nabla\cdot\left[\mu_0'T(\nabla\cdot\boldsymbol{u}_0)\boldsymbol{I}\right]\right\}}_{\mathtt{K10}}.\end{aligned}\tag{5.6}$$

Equation (5.6) represents the balance of kinetic energy density at order $O(\epsilon^2)$. The first term K1 is recognised as the rate of change of the kinetic energy density of the perturbation flow $\partial_t\varepsilon_{\mathrm{kin}}$. The physical processes leading to the change of energy density appear on the right-hand side of (5.6). Similar to the thermal budget, the term K2 describes a rate of change of the kinetic perturbation energy density due to the temperature dependence of the density. This term is conservative in the sense that it vanishes when integrated over the volume, as explained in Appendix B.

The terms K3 and K4 describe the rate of change of kinetic perturbation energy density due to the divergence of kinetic perturbation energy flux densities. These fluxes arise due to the transfer of momentum between the basic and the perturbation flow (K3) and due to the second-order density dependence on the temperature (K4), after evaluation of the divergence ($\nabla\rho_0'=\rho_0''\nabla T$). The term K5 describes the work per volume and time done by pressure forces which is enabled by the weak compressibility of the perturbation flow due to spatial variation of ρ. The term K6 represents the work done by buoyancy forces. It also arises in the framework of the Oberbeck–Boussinesq approximation.

The remaining terms K7 to K10 describe the rate of change of kinetic perturbation energy density due to viscous dissipation of the perturbation flow (K7), corrected by the effects due to the spatial variation of the density (K8), the spatial variation of the dynamic viscosity (K9) and the spatial variation of both, density and dynamic viscosity (K10).

As for the thermal energy budget, the integral kinetic energy budget is detailed in Appendix B. Integration over the volume occupied by the liquid and the gas separately yields the total rate of change of kinetic energy $\partial_t E_{\mathrm{kin}}=\partial_t\int_{V_i}\varepsilon_{\mathrm{kin}}\,\mathrm{d}V$ in the phase i

$$\partial_t E_{\mathrm{kin}}=-D_{\mathrm{kin}}+M_r+M_\varphi+M_z+I+B+K_{\mathrm{G}}+\Lambda_\rho+\Lambda_\mu+\Lambda_{\rho\mu},\tag{5.7}$$

https://doi.org/10.1017/S0956792523000189 Published online by Cambridge University Press

where we introduced the abbreviations

$$D_{\mathrm{kin}} = \int_{V_i} \mu_0 (\nabla \boldsymbol{u}) : (\nabla \boldsymbol{u}) \, \mathrm{d}V + \alpha_i \int_{A_{\mathrm{fs}}} \mu_0 (h_0 h_{0zz} w^2 - v^2) \, \mathrm{d}\varphi \, \mathrm{d}z, \tag{5.8a}$$

$$M_r = \alpha_i \int_{A_{\mathrm{fs}}} \mu_0 h_0 h_{0z} u \, (\partial_r w - \partial_z u) \, \mathrm{d}\varphi \, \mathrm{d}z, \tag{5.8b}$$

$$M_\varphi = \alpha_i \int_{A_{\mathrm{fs}}} \mu_0 h_0 v \left(\partial_r v - \frac{v}{h_0} - h_{0z} \partial_z v \right) \mathrm{d}\varphi \, \mathrm{d}z, \tag{5.8c}$$

$$M_z = \alpha_i \int_{A_{\mathrm{fs}}} \mu_0 h_0 w \, (\partial_r w + h_{0zz} w - h_{0z} \partial_z w) \, \mathrm{d}\varphi \, \mathrm{d}z, \tag{5.8d}$$

$$I = \sum_{j=1}^{5} I_j = - \int_{V_i} \rho_0 \left(u_0 \frac{v^2}{r} + u^2 \partial_r u_0 + u w \partial_z u_0 + u w \partial_r w_0 + w^2 \partial_z w_0 \right) \mathrm{d}V, \tag{5.8e}$$

$$B = - \int_{V_i} \rho_0' T g w \, \mathrm{d}V, \tag{5.8f}$$

$$K_{\mathrm{G}} = - \frac{1 - \alpha_i}{4} \int_{A_{\mathrm{out}}} \rho_0 w^2 w_0 \, \mathrm{d}S, \tag{5.8g}$$

$$\Lambda_\rho = - \int_{V_i} \rho_0' T \boldsymbol{u} \cdot (\boldsymbol{u}_0 \cdot \nabla \boldsymbol{u}_0) \, \mathrm{d}V + \int_{V_i} \zeta \left(p - \frac{1}{3} \mu_0 \zeta \right) \mathrm{d}V, \tag{5.8h}$$

$$\begin{aligned} \Lambda_\mu = & \int_{V_i} \mu_0' \boldsymbol{u} \cdot [\mathcal{S} + (\nabla \boldsymbol{u})^{\mathrm{T}}] \cdot \nabla T_0 \, \mathrm{d}V + \int_{V_i} (\mu_0' + \mu_0'' T_0) \boldsymbol{u} \cdot [\mathcal{S}_0 + (\nabla \boldsymbol{u}_0)^{\mathrm{T}}] \cdot \nabla T \, \mathrm{d}V \\ & - \int_{V_i} \mu_0' T (\nabla \boldsymbol{u}_0) : (\nabla \boldsymbol{u}) \, \mathrm{d}V + \alpha_i \int_{A_{\mathrm{fs}}} \mu_0' w T \left(N^2 \partial_r w_0 - N^2 h_{0z} \partial_z w_0 - h_{0z}^2 h_{0zz} w_0 \right) \mathrm{d}\varphi \, \mathrm{d}z, \end{aligned} \tag{5.8i}$$

$$\Lambda_{\rho\mu} = - \int_{V_i} \mu_0' \zeta_0 \left(\frac{1}{3} T \zeta + \boldsymbol{u} \cdot \nabla T \right) \mathrm{d}V - \int_{V_i} \left(\mu_0' \zeta + \mu_0'' T \right) \boldsymbol{u} \cdot \nabla T_0 \, \mathrm{d}V, \tag{5.8j}$$

and

$$\zeta_0 = \nabla \cdot \boldsymbol{u}_0 = - \frac{\rho_0'}{\rho_0} \boldsymbol{u}_0 \cdot \nabla T_0, \tag{5.9a}$$

$$\zeta = \nabla \cdot \boldsymbol{u} = - \frac{1}{\rho_0} \left[\rho_0' \boldsymbol{u} \cdot \nabla T_0 + \rho_0' \partial_t T + \nabla \cdot (\rho_0' \boldsymbol{u}_0 T) \right], \tag{5.9b}$$

$$\mathcal{S}_0 = \nabla \boldsymbol{u}_0 + (\nabla \boldsymbol{u}_0)^{\mathrm{T}}, \tag{5.9c}$$

$$\mathcal{S} = \nabla \boldsymbol{u} + (\nabla \boldsymbol{u})^{\mathrm{T}}. \tag{5.9d}$$

As before, the index i indicating the phase (liquid or gas) has been suppressed for the thermophysical properties.

The terms (5.8a)–(5.8e) are the known terms for an incompressible flow and constant material properties [16]. D_{kin} denotes the viscous dissipation, I the kinetic energy production including effects like, for example, the lift-up process, and M_r, M_φ and M_z represent the work per time done by thermocapillary forces on the interface A_{fs} in the radial, azimuthal and axial direction, respectively. The well-known buoyancy production term B also enters the kinetic energy budget within the Boussinesq approximation. K_{G} represents the advection with the basic flow of perturbation kinetic energy through the outlet of the gas A_{out}. It vanishes for a closed container holding the gas ($w_0|_{A_{\mathrm{out}}} = 0$). Note we assume that no perturbation momentum is introduced by advection through the inlet of the gas. The new terms (5.8h)–(5.8j) arise due to the temperature dependence of the material parameters. Λ_ρ and Λ_μ vanish, if $\rho = \text{const.}$ or $\mu = \text{const.}$, respectively, while $\Lambda_{\rho\mu}$ vanishes if either $\rho = \text{const.}$ or $\mu = \text{const.}$

https://doi.org/10.1017/S0956792523000189 Published online by Cambridge University Press

6. Discussion

The orders of magnitude of the terms arising in the energy budgets (4.8) and (5.7) depend on the physicochemical properties of the two fluids as well as on their variability. To estimate the effect of fully temperature-dependent (FTD) properties on the linear stability boundary, we compare the results computed with those obtained using the Oberbeck–Boussinesq approximation (OB) in which all material parameters are assumed constant except for the density in the buoyancy term $\rho \boldsymbol{g}$ of (3.1b), which is considered up to first order in $\hat{T} - \bar{T}$.

By considering a Taylor expansion up to first order around the reference values, Gray and Giorgini [3] found that a deviation of 5% of the thermophysical parameters from the value at the reference temperature is an acceptable tolerance to use the OB approximation. Here we make the same assumption, but keep the higher-order terms of the Taylor expansion. The condition that the absolute relative deviation of any quantity $f \in \{\rho, \lambda, c_p, \mu\}$ from its value at the reference temperature is less than or equal to the threshold value $\xi/2 = 0.05$ leads to

$$\left| \frac{f(\hat{T}) - f(\bar{T})}{f(\bar{T})} \right| = \left| \frac{f'(\bar{T})}{f(\bar{T})}(\hat{T} - \bar{T}) + \frac{1}{2}\frac{f''(\bar{T})}{f(\bar{T})}(\hat{T} - \bar{T})^2 + \dots \right| \leq \frac{\xi}{2}, \tag{6.1}$$

where $\hat{T}$ can be any temperature arising in the system, bounded by $\bar{T} \pm \Delta T/2$. Assuming $f(\hat{T})$ is a monotonic function and using the algebraic mean temperature $\bar{T}$ as the reference temperature (as in Gray and Giorgini [3]), we consider the extreme case when $\hat{T} - \bar{T} = \pm \Delta T/2$. Then we get the restriction of the maximum tolerable relative deviation from the reference value

$$\psi_f := \max \left| \pm \frac{f'(\bar{T})}{f(\bar{T})}\Delta T + \frac{1}{4}\frac{f''(\bar{T})}{f(\bar{T})}\Delta T^2 \pm \dots \right| \leq \xi. \tag{6.2}$$

In lowest order and for $\xi = 0.1$, we recover the criterion of Gray and Giorgini [3]. If the series is truncated at second order, we obtain ($\Delta T > 0$)

$$\psi_f = \psi_f^{\mathrm{I}} + \psi_f^{\mathrm{II}} = \left| \frac{f'(\bar{T})}{f(\bar{T})} \right| \Delta T + \frac{1}{4} \left| \frac{f''(\bar{T})}{f(\bar{T})} \right| \Delta T^2 \leq \xi. \tag{6.3}$$

Therefore, if the second-order contribution ψ_f^{II} is significant, the criterion of Gray and Giorgini [3] is tightened.

If, instead of the OB approximation, a linearised model for a quantity f is used, it makes sense to ensure that the relative deviation of the quantity f due to its second-order variation from the linear model is sufficiently small. Assuming a threshold of $\xi/2 = 0.05$ as in Gray and Giorgini [3], this leads to the condition

$$\left| \frac{f(\hat{T}) - \left[f(\bar{T}) + f'(\bar{T})(\hat{T} - \bar{T}) \right]}{f(\bar{T}) + f'(\bar{T})(\hat{T} - \bar{T})} \right| = \frac{1}{2} \left| \frac{f''(\bar{T})(\hat{T} - \bar{T})^2 + \dots}{f(\bar{T}) + f'(\bar{T})(\hat{T} - \bar{T})} \right| \leq \frac{\xi}{2}. \tag{6.4}$$

Assuming a monotonic variation with $\hat{T}$, by setting $\hat{T} - \bar{T} = \pm \Delta T/2$ as above, and by neglecting cubic terms, we obtain

$$\frac{1}{4} \left| \frac{f''(\bar{T})\Delta T^2}{f(\bar{T}) \pm f'(\bar{T})\Delta T} \right| = \frac{1}{4} \left| \frac{[f''(\bar{T})/f(\bar{T})]\Delta T^2}{1 \pm [f'(\bar{T})/f(\bar{T})]\Delta T} \right| = \frac{\psi_f^{\mathrm{II}}}{\left| 1 \pm [f'(\bar{T})/f(\bar{T})]\Delta T \right|} \leq \xi, \tag{6.5}$$

Maximising the left-hand side, we get the condition

$$\frac{\psi_f^{\mathrm{II}}}{\left| 1 - \psi_f^{\mathrm{I}} \right|} \leq \xi. \tag{6.6}$$

It is well known that in experiments on thermocapillary liquid bridges even the first-order bound $\psi^{\mathrm{I}} \leq 0.1$ provided by Gray and Giorgini [3] can be violated by the viscosity ($f = \mu$). Therefore, the dependence of the liquid viscosity on the temperature has already been taken into account up to first order

https://doi.org/10.1017/S0956792523000189 Published online by Cambridge University Press

Table 1. *Thermophysical reference quantities of 2-cSt silicone oil and air at 25°C*

Property	Dimension	KF96L-2cs	Air
density $\bar{\rho}$	[kg/m^3]	873.25	1.1837
dynamic viscosity $\bar{\mu}$	[Pa s]	1.7465×10^{-3}	1.8460×10^{-5}
thermal conductivity $\bar{\lambda}$	[W/(mK)]	0.10904	2.6374×10^{-2}
specific heat $\bar{c}_p$	[J/(kgK)]	1800.8	1005.7
surface tension $\bar{\sigma}$	[N/m]	18.3×10^{-3}	
surface tension coefficient γ	[N/(mK)]	7×10^{-5}	

in the stability analysis of Kozhoukharova et al. [7] ($Pr_{\mathrm{L}} = \bar{\mu}_{\mathrm{L}}\bar{c}_{p\mathrm{L}}/\bar{\lambda}_{\mathrm{L}} = 4$). In their numerical simulations for $Pr_{\mathrm{L}} \in [1, 5]$ Melnikov et al. [13] found a significant impact of the linear temperature dependence of the viscosity on the linear stability boundary.

Since the functional dependence of the thermophysical properties on the temperature is not restricted in our investigation, also the effect of a higher-order temperature dependence is of interest. It is difficult, however, to quantify the effect of the FTD approach on the stability boundary without specifying the fluids, owing to the wide range of different fluids employed for liquid bridges. Therefore, we focus on two different cases: a high- and a low-Prandtl-number liquid bridge being heated from above.

6.1 High-Prandtl-number instability

Linear stability analyses have been carried out for the following setting. The length and radius of the liquid bridge are $d = 1.65$ mm and $R = d/\Gamma$, respectively, where $\Gamma = 0.66$ is the aspect ratio. The liquid is 2-cSt silicone oil (KF96L-2cs, Shin-Etsu Chemical, Co., Ltd., Japan) which has a Prandtl number of $Pr_{\mathrm{L}} = 28.84$ at the arithmetic mean (reference) temperature $\bar{T} = 25°\mathrm{C}$. The discrete data of ρ_{L}, λ_{L} and $c_{p\mathrm{L}}$ for 2-cSt silicone oil provided by Shin-Etsu [24] have been fitted by least-squares to polynomials of second order. A low polynomial order is used to avoid non-physical oscillations. Since the manufacturer does not specify the temperature dependence of the surface tension, we have to stick to the linear dependence provided in Romanò et al. [20] (see Table 1). The function $\mu_{\mathrm{L}}(\hat{T})$ is constructed from the exponential temperature dependence of the kinematic viscosity as in Ueno et al. [31] and by a quadratic fit of the density. The volume ratio of the liquid is kept constant at $\mathcal{V} = V_{\mathrm{L}}/\pi R^2 d = 0.9$. The liquid bridge is placed in a wide test chamber filled with air and confined by no-penetration ($w_{\mathrm{G}} \equiv 0$) adiabatic walls. The temperature dependence of the properties of the gas is based on explicit formulae of *VDI Heat Atlas* [32]. The reference values of all physical properties are given in Table 1 for both working fluids. The geometry of the test chamber (subscript tc) is defined through the radius ratio $\eta = R_{\mathrm{tc}}/R = 4$, and the total height of the gas space is $d_{\mathrm{tc}} = 3.65$ mm within which the liquid bridge is positioned coaxially and vertically centred. Further details on the numerical methods and the explicit temperature dependence of the fluid properties will be provided in Stojanović et al. [28].

Fixing $\bar{T} = 25°\mathrm{C}$, the condition (6.3) can be rewritten in terms of maximum allowable temperature differences for the OB approximation. Truncating (6.2) after the first and second order, we define the temperature thresholds (symmetric about $\bar{T}$), respectively, as

$$\Delta T_{\mathrm{OB}}^{\mathrm{I}} := \xi \left| \frac{\bar{f}}{\bar{f}'} \right| \quad \text{and} \quad \Delta T_{\mathrm{OB}}^{\mathrm{II}} := 2\frac{\sqrt{|\bar{f}'|^2 + \xi|\bar{f}''||\bar{f}|} - |\bar{f}'|}{|\bar{f}''|}, \tag{6.7}$$

where $\bar{f} = f(\bar{T})$, $\bar{f}' = f'(\bar{T})$ and $\bar{f}'' = f''(\bar{T})$. Similarly, the temperature limit of validity for a model accounting for linearly temperature-dependent (LTD) properties can be derived by solving (6.6) for ΔT to yield

https://doi.org/10.1017/S0956792523000189 Published online by Cambridge University Press

Table 2. *Maximum allowable temperature differences ΔT^{I}_{OB}, ΔT^{II}_{OB} and ΔT_{LTD} based on a tolerance of $\xi = 0.1$ and a reference temperature of $\bar{T} = 25°C$ for different thermophysical parameters. ΔT^{I}_{OB} and ΔT^{II}_{OB} represent the validity thresholds for the applied temperature difference when using the OB approximation and assuming a first-order (up to linear) or, respectively, a second-order (up to quadratic) dependence of the thermophysical quantity on the temperature. ΔT_{LTD} is the validity threshold when using the linear temperature model (LTD). All temperature differences are given in Kelvin for 2-cSt silicone oil (L) and air (G)*

f	i	$\Delta T^{\mathrm{I}}_{\mathrm{OB}}$	$\Delta T^{\mathrm{II}}_{\mathrm{OB}}$	ΔT_{LTD}	i	$\Delta T^{\mathrm{I}}_{\mathrm{OB}}$	$\Delta T^{\mathrm{II}}_{\mathrm{OB}}$	ΔT_{LTD}
ρ	L	91.9	89.3	395.7	G	29.8	28.5	106.8
λ	L	38.4	38.4	365.5	G	35.1	34.7	218.3
c_p	L	121.8	121.6	1096	G	1601	578.0	706.9
μ	L	4.8	4.6	20.2	G	37.9	37.4	213.8

$$\Delta T_{\mathrm{LTD}} := \begin{cases} -2\xi \dfrac{|\bar{f}'|}{|\bar{f}''|} + 2\sqrt{\xi \dfrac{|\bar{f}|}{|\bar{f}''|} + \xi^2 \dfrac{|\bar{f}'|^2}{|\bar{f}''|^2}}, & \psi_f^{\mathrm{I}} < 1, \\ 2\xi \dfrac{|\bar{f}'|}{|\bar{f}''|} - 2\sqrt{-\xi \dfrac{|\bar{f}|}{|\bar{f}''|} + \xi^2 \dfrac{|\bar{f}'|^2}{|\bar{f}''|^2}}, & \psi_f^{\mathrm{I}} > 1. \end{cases} \tag{6.8}$$

The temperature differences $\Delta T^{\mathrm{I}}_{\mathrm{OB}}$, $\Delta T^{\mathrm{II}}_{\mathrm{OB}}$ and ΔT_{LTD} are assigned to each thermophysical property of each phase, and they are given in Table 2 for $\xi = 0.1$. The most severe restriction of ΔT for the validity of the OB approximation is imposed by the condition $\psi^{\mathrm{I}}_{\mu\mathrm{L}} + \psi^{\mathrm{II}}_{\mu\mathrm{L}} < 0.1$, not allowing ΔT to exceed $\Delta T^{\mathrm{II}}_{\mathrm{OB}} = 4.6$ K. Furthermore, temperature differences greater than 20.2 K would violate condition (6.6) on the viscosity of the liquid. In this case, assuming a linear dependence $\mu_{\mathrm{L}}(\hat{T}) \sim (\hat{T} - \bar{T})$ would not be sufficient to accurately describe the flow inside the liquid bridge. Besides, the criteria ψ^{II}_f on $c_{p\mathrm{L}}$ and $c_{p\mathrm{G}}$ get violated for $\Delta T > 121.6$ K and $\Delta T > 578$ K, respectively. The latter condition is unrealistic and could only be realised by a phase change.

In addition, a minimum temperature difference $\Delta T_{\min} = 10\chi\bar{T}$ can be obtained from the first condition of (3.3), which is required to justify the omission of the pressure work in (3.1c). For the present liquid and gas, this condition certainly holds true at $\bar{T} = 25°$C, since the minimum required temperature differences are negligibly small with $\Delta T_{\min,\mathrm{L}} = 2 \times 10^{-6}$ K and $\Delta T_{\min,\mathrm{G}} = 10^{-5}$ K, respectively. The second condition of (3.3) does not involve ΔT, but rather turns into a condition for the length of the liquid bridge, which is $d \leq 585$ m in the present case. Thus, neglecting viscous dissipation in (3.1c) is also reasonable for liquid bridges, which confirms the validity of (3.1c).

In Table 3, we compare the critical temperature differences of the linear stability analyses for different approximations of the governing equations. The linear stability boundary for the onset of hydrothermal waves obtained by the present FTD approach is taken as a reference. It is compared with the result obtained using the OB approximation. To demonstrate the effect of the temperature dependence on the stability boundary of a single thermophysical property, we also combine the OB approximation with the temperature dependence of only one property at a time, keeping the remaining thermophysical properties at their reference values. For instance, within the approximation 'OB + $\rho(\hat{T})$' the temperature dependence of the fluid densities is taken into account in all the governing equations (3.1a)–(3.1c). From Table 3, it is seen that critical Reynolds number $Re_c = Ma_c/Pr_{\mathrm{L}} = \gamma d \Delta T_c \bar{\rho}_{\mathrm{L}}/\bar{\mu}^2_{\mathrm{L}}$ for the OB approximation deviates strongly (by $\epsilon_c = 24.7\%$) from the reference result (FTD). The main reason is that the relatively large change of the liquid viscosity in the range $\bar{T} \pm \Delta T_c/2$ is not taken care of by the OB approximation, resulting in strongly violated conditions with $\psi^{\mathrm{I}}_{\mu\mathrm{L}} = 1.16$ and $\psi^{\mathrm{I}}_{\mu\mathrm{L}} + \psi^{\mathrm{II}}_{\mu\mathrm{L}} = 1.59$. Given the exponential behaviour of $\mu_{\mathrm{L}}(\hat{T})$, also condition (6.6) gets violated for $\Delta T_c = 55.5$ K with $\psi^{\mathrm{II}}_{\mu}/|1 - \psi^{\mathrm{I}}_{\mu}| = 2.8$. Other than that, the OB approximation slightly fails to satisfy the conditions for $\psi^{\mathrm{I}}_{\lambda\mathrm{L}} = 0.14$, $\psi^{\mathrm{I}}_{\lambda\mathrm{G}} = 0.16$, $\psi^{\mathrm{I}}_{\rho\mathrm{G}} = 0.19$ and $\psi^{\mathrm{I}}_{\mu\mathrm{G}} = 0.15$. This explains why the critical Reynolds number

https://doi.org/10.1017/S0956792523000189 Published online by Cambridge University Press

Table 3. *Critical temperature difference ΔT_c and critical Reynolds number $Re_c = \gamma\bar{\rho}_L\Delta T_c d/\bar{\mu}_L^2$ for a slender liquid bridge with $\Gamma = 0.66$ and $\mathcal{V} = 0.9$ made of 2-cSt silicone oil (see text). Results are given for different approximations. For all models, the critical wave number is $m_c = 3$. The relative deviation $\epsilon_c = (Re_c - Re_c^{FTD})/Re_c^{FTD}$ is given in [%]*

Approximation	ΔT_c [K]	Re_c	ϵ_c [%]
FTD	44.49	1471	0
OB	55.50	1835	24.7
OB + $\rho(\hat{T})$	54.63	1806	22.8
OB + $\lambda(\hat{T})$	54.33	1797	22.1
OB + $c_p(\hat{T})$	54.28	1795	22.0
OB + $\mu(\hat{T})$	45.60	1509	2.5

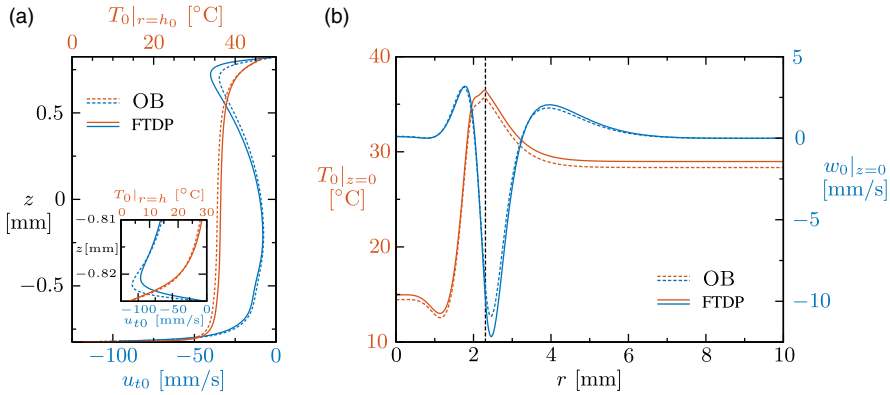

Figure 2. *Temperature and velocity distributions of the basic state for $\Delta T = 44.49$ K along the free surface (a) and across the midplane at $z = 0$ mm (b). Solid lines: FTD approach. Dashed lines: OB approximation. In (a), $u_{t0} = \boldsymbol{t}\cdot\boldsymbol{u}_0$ denotes the tangential velocity, where $\boldsymbol{t}$ is the unit vector tangent to the interface. The vertical black dashed line in (b) represents the position of the interface $h_0(z = 0)$.*

for the case 'OB + $\mu(\hat{T})$' is the best approximation to the reference value Re_c^{FTD}. The small deviation of 2.5% from FTD is due to the remaining approximations made. In contrast, the relative error in Re_c of $\epsilon_c \approx 22\%$ with respect to the FTD model is very large if, instead, the model accounts for the full temperature dependence of only ρ, λ or c_p at a time.

The question arises as to why the critical Reynolds number using the OB approximation is larger than the one for the FTD approach. Inspecting both basic flows in Figure 2, it seems that the dimensional basic flow fields for $\Delta T = 44.49$ K do not differ much. The main differences concern the higher plateau temperature (full red line in Figure 2(a)) and the faster surface velocity (full blue line in Figure 2(a), in particular for $z > 0$) for the FTD model as compared to the OB approximation. These deviations are caused by a liquid viscosity $\mu[T_0(r, z)]$ which is reduced in the hotter regions with $T_0(r, z) > \bar{T}$ from the constant reference viscosity $\bar{\mu}_L$ in the OB approximation. The relative local viscosity deviation in the liquid (subscript L)

$$\Delta\mu_{\mathrm{L}} = \frac{\mu_{\mathrm{L}}[T_0(r, z)] - \bar{\mu}_{\mathrm{L}}}{\bar{\mu}_{\mathrm{L}}}. \tag{6.9}$$

is illustrated by colour in Figure 3(a). In the FTD model, the local viscosity is more than 60% larger than nominal near the cold wall, whereas near the hot wall and the free surface it is up to 30% smaller than nominal. The reduced viscosity near the hot wall and along the free surface provides less resistance to

https://doi.org/10.1017/S0956792523000189 Published online by Cambridge University Press

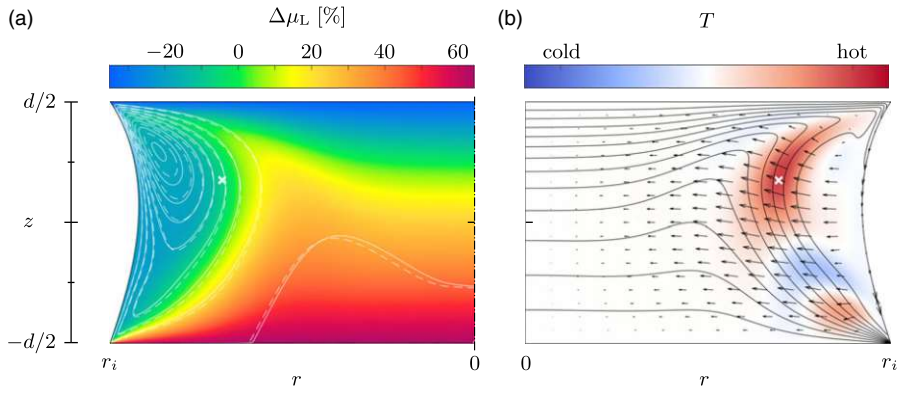

Figure 3. *Basic state (a) and critical mode (b) for $\Delta T = 44.49$ K using the FTD model. (a) Local deviation of the viscosity $\Delta\mu_L = [\mu_L(r,z) - \bar{\mu}_L]/\bar{\mu}_L$ (colour) and streamlines (full white lines) in the liquid. The dashed white lines show streamlines obtained with the OB approximation. (b) Critical velocity field (arrows) and critical temperature field (colour) for $m_c = 3$ in the (r,z) plane in which the local thermal production $j_1 + j_2 = -\rho_0 T\boldsymbol{u} \cdot \nabla(c_{p0}T_0)$ takes one of its maxima (white crosses in (a, b) located at $(r,\ z) = (1.73,\ 0.28)$ mm) in the bulk. Black lines indicate isotherms of the basic state.*

the flow such that the basic vortex for the FTD model is stronger than for the OB approximation. This is confirmed by the equidistant streamlines in Figure 3(a), where the full/dashed white lines correspond to the FTD/OB model obtained for the same temperature difference. From Figure 3(b), the critical mode arises in the region where the basic temperature gradients are large, and extends further into the region $\mu_L < \bar{\mu}_L$ of lower viscosity. This is confirmed by the loci of maximum thermal production (white crosses in Figure 3) in a region of slightly reduced viscosity $\mu_L < \bar{\mu}_L$.

These properties favour the instability by two mechanisms: (a) The stronger basic vortex leads to larger internal temperature gradients in the upper half of the liquid bridge. Therefore, the hydrothermal wave can extract more energy from the basic temperature field than in the case of the OB model. (b) The perturbation vortices which created the temperature perturbations of the hydrothermal wave arise in a region of reduced viscosity and experience less resistance. For these reasons, the critical Reynolds number for the FTD model is significantly lower than for the OB approximation.

To study the instability mechanism itself, we investigate the budget of the thermal perturbation energy which is crucial for the present hydrothermal wave instability and typical for high-Prandtl-number liquids [25, 27, 33]. Figure 4 shows the main contributions to the integral thermal energy budget of the critical mode for the liquid phase (a) and for the gas phase (b). The tilde indicates that the quantities have been normalised by the dissipation term D_{th}, as usual. The integral rates of change of thermal energy by the most important transfer processes are almost identical among the FTD method (red) and the OB approximation (blue). This is consistent with the integral contributions $\tilde{\Pi}_\rho$, $\tilde{\Pi}_{c_p}$ and $\tilde{\Pi}_\lambda$ to the thermal energy budget being very small in the present FTD approximation (Table 4). They are thus negligible. Within the OB approximation, they vanish by definition. Therefore, the temperature dependence of the material parameters does not alter the general instability mechanism discussed, for example, in Stojanović et al. [27]. Note the close agreement of the energy budgets between the FTD and OB models on the stability boundary does not preclude different critical Reynolds numbers, as the terms in the energy budgets are only relative (normalised) quantities.

6.2 Low-Prandtl-number instability

For low-Prandtl-number liquids, the instability mechanism is inertial and the critical mode is stationary [33]. In that case, the kinetic energy budget of the perturbation flow is relevant for the instability. As an

https://doi.org/10.1017/S0956792523000189 Published online by Cambridge University Press

Table 4. *Minor contributions to the thermal energy budgets of the critical mode for the FTD approach*

i	$\tilde{\Pi}_\rho$	$\tilde{\Pi}_\lambda$	$\tilde{\Pi}_{c_p}$	$\partial_t \tilde{E}'_T$
L	1.5×10^{-4}	-3.1×10^{-4}	-1.2×10^{-4}	-1.8×10^{-8}
G	-1.4×10^{-3}	4.0×10^{-3}	3.6×10^{-5}	-2.2×10^{-11}

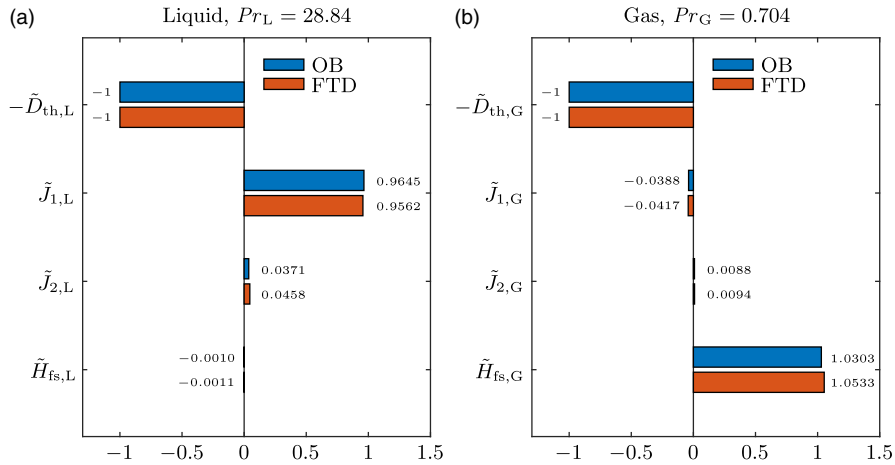

Figure 4. *Main contributions to the thermal energy budget of the critical mode in the liquid phase (a) and the gas phase (b). Results are given for the OB approximation (blue) and FTD approach (red). J_1 and J_2 are defined in (4.9b).*

example, we consider a liquid bridge made of molten tin and use the reference temperature $\bar{T} = 250°\text{C}$ which is slightly above the melting temperature $T_m = 231.97°\text{C}$ [21]. Thus, the Prandtl number is $Pr_L = 0.0185$. The functional dependence of the thermophysical properties of molten tin on the temperature is taken from Gancarz et al. [1] and Savchenko et al. [21], either through explicitly given correlations or by fitting quadratic polynomials to tabulated data. Since buoyancy plays a lesser role for low-Prandtl-number liquids [16], we assume weightlessness conditions. Moreover, we select $\Gamma = \mathcal{V} = 1$ which allows for a comparison of the critical parameters with data from the literature. The length of the liquid bridge, the chamber geometry, the boundary conditions, and the gas are the same as for the high-Prandtl-number liquid bridge from Section 6.1.

The main contributions, normalised by D_{kin}, to the kinetic energy budgets of the critical modes are shown in Figure 5 for both approximations FTD (red) and OB (blue). The tilde sign is here employed to denote the terms of the kinetic energy budget normalised by D_{kin}. Both methods yield almost the same result, which is consistent with the kinetic energy budget obtained by Wanschura et al. [33]. This is consistent with Table 5 , where the obtained critical temperature differences safely fall into the validity range of the OB approximation given in Table 6. Note that increasing the reference temperature to $\bar{T} = 500°\text{C}$ leads to an extension of the validity range as the variability of the viscosity decreases for higher reference temperatures. Owing to the extremely small dynamic surface deformations, the radial Marangoni production terms $\tilde{M}_r$, $\tilde{M}_{r,G} < 10^{-4}$ are negligible. The production due to buoyancy $\tilde{B}$ vanishes by definition and, for the closed chamber considered, $\tilde{K}_G = 0$. It is clear from Figure 5(a) that most kinetic energy is produced by the inertial process described by $\tilde{I}_4$ with the work done by Marangoni forces (mainly $\tilde{M}_\varphi$) being very small. As can be seen from Figure 5(b), practically no inertial energy production takes place in the gas phase ($\tilde{I}_{1,G}, \ldots, \tilde{I}_{5,G} < 10^{-2}$). The perturbation flow in the gas is driven by axial ($\tilde{M}_{z,G}$) and mainly azimuthal thermocapillary forces ($\tilde{M}_{\varphi,G}$), but the produced kinetic energy is readily dissipated ($\tilde{D}_{kin,G}$). Thus, in the present two-phase system, the gas phase only plays a passive role for the instability mechanism. This also holds true for high-Prandl-number liquids [27]. Owing

https://doi.org/10.1017/S0956792523000189 Published online by Cambridge University Press

Table 5. *Critical temperature differences and Reynolds numbers for the first instability in a liquid bridge made from tin at $\bar{T} = 250°C$ with $Pr_L = 0.0185$, $\Gamma = 1$ and $\mathcal{V} = 1$. For the other parameters, see the text. Results are given for different approximations. The critical Reynolds number of Wanschura et al. [33] was obtained by linear interpolation of their data for different Pr_L (their table 3)*

Approximation	ΔT_c [K]	Re_c
FTD	7.06	2033
constant properties (OB)	7.15	2057
[33]		2038

Table 6. *Validity ranges $\Delta T \le \Delta T^{I}_{OB}(\bar{T})$ and $\Delta T \le \Delta T^{II}_{OB}(\bar{T})$ of the OB approximation for each thermophysical property of molten tin at $\bar{T} = 250°C$ and at $\bar{T} = 500°C$, respectively, using $\xi = 0.1$. All temperature differences are given in K*

f	$\Delta T^{\mathrm{I}}_{\mathrm{OB}}(250°\mathrm{C})$	$\Delta T^{\mathrm{II}}_{\mathrm{OB}}(250°\mathrm{C})$	$\Delta T^{\mathrm{I}}_{\mathrm{OB}}(500°\mathrm{C})$	$\Delta T^{\mathrm{II}}_{\mathrm{OB}}(500°\mathrm{C})$
ρ_{L}	1074	1074	1049	1049
λ_{L}	100.8	100.8	125.8	125.8
$c_{p\mathrm{L}}$	311.7	242.1	1223	574.4
μ_{L}	30.3	28.8	66.2	62.2

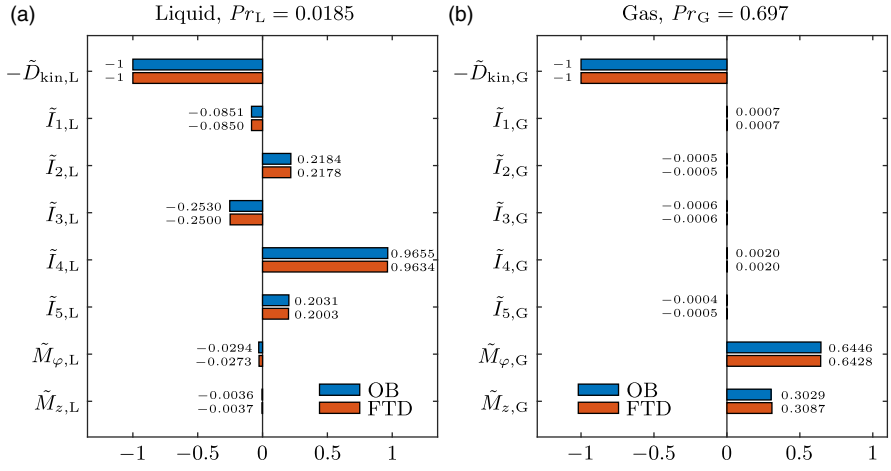

Figure 5. *Main contributions to the kinetic energy budgets of the critical modes assuming constant properties (OB approximation) and fully temperature-dependent fluid properties (FTD). (a) Liquid phase. (b) Gas phase. I_1 to I_5 are defined in (5.8e).*

to the small critical temperature difference ΔT_c, the new contributions (5.8h)–(5.8j) remain negligibly small.

7. Conclusions

Variable material properties are important in high-Prandtl-number liquid bridges, because the temperature difference is typically large such that the viscosity can vary over a wide range. This variation is particularly important for very small-scale liquid bridges for which the critical temperature difference $\Delta T_c \sim d^{-1}$ must be even larger. In that case, there is some ambiguity (through the reference temperature) in defining the Reynolds, Prandtl and Marangoni numbers, and the critical Reynolds numbers for different approximations of the governing equations may deviate significantly. The

https://doi.org/10.1017/S0956792523000189 Published online by Cambridge University Press

dependence of the critical Marangoni number on the choice of the reference temperature has already been noted by Melnikov et al. [13] who demonstrated that using the cold wall temperature as the reference temperature, $\bar{T} = T_{\text{cold}}$, leads to a significant reduction of the critical Marangoni number (depending on the amount of variation of the viscosity) as compared to when the mean temperature is used as a reference. While using $\bar{T} = T_{\text{cold}}$ is convenient from an experimental point of view, because ΔT_c is initially unknown and the reference Prandtl number does not depend on the (varying) temperature difference, it is not so well suited to correlate the critical Marangoni numbers for different experimental realisations with different critical temperature differences.

Another aspect is the use of the OB approximation beyond its strict range of validity. Even when using the algebraic mean temperature to define the reference material parameters [7], the critical Reynolds number can still significantly depend on the approximation made. It was shown that in the high-Prandtl-number case considered, higher-order variations of the liquid's viscosity need to be taken into account beyond a certain value for ΔT. On the other hand, it is more than sufficient to assume a linear dependence of ρ and λ on $\hat{T}$ for silicone oil and for air near room temperature. Moreover, the temperature dependence of c_{pL} and c_{pG} is negligible. Finally, we note that the free surface temperature depends on the thermal conditions in the gas phase. For instance, a weak forced axial gas flow can strongly affect the critical conditions [2, 6, 30, 35, 37].

In the future, it would be interesting to investigate the linear stability of very small-scale liquid bridges under extreme temperature gradients. In this case, the model needs to be extended by including the effects of evaporation to correctly describe the physics close to the liquid's boiling temperature.

Competing interests. None.

References

[1] Gancarz, T., Moser, Z., Gasior, W., Pstruś, J. & Henein, H. (2011) A comparison of surface tension, viscosity, and density of sn and sn–ag alloys using different measurement techniques. *Int. J. Thermophys.* **32** (6), 1210–1233.

[2] Gaponenko, Y., Mialdun, V. Y. A., Nepomnyashchy, A. & Shevtsova, V. (2021) Hydrothermal waves in a liquid bridge subjected to a gas stream along the interface. *J. Fluid Mech.* **908**: A34–36pp.

[3] Gray, D. D. & Giorgini, A. (1976) The validity of the Boussinesq approximation for liquids and gases. *Int. J. Heat Mass Transf.* **19** (5), 545–551.

[4] Imaishi, N., Yasuhiro, S., Akiyama, Y. & Yoda, S. (2001) Numerical simulation of oscillatory Marangoni flow in half-zone liquid bridge of low Prandtl number fluid. *J. Cryst. Growth* **230** (1-2), 164–171.

[5] Joseph, D. D. (1976) *Stability of Fluid Motions I*, Springer Tracts in Natural Philosophy, Vol. **27**, Springer, Berlin/Heidelberg.

[6] Kamotani, Y., Wang, L., Hatta, S., Wang, A. & Yoda, S. (2003) Free surface heat loss effect on oscillatory thermocapillary flow in liquid bridges of high Prandtl number fluids. *Int. J. Heat Mass Transf.* **46** (17), 3211–3220.

[7] Kozhoukharova, Z., Kuhlmann, H. C., Wanschura, M. & Rath, H. J. (1999) Influence of variable viscosity on the onset of hydrothermal waves in thermocapillary liquid bridges. *Z. Angew. Math. Mech.* **79**: 535–543.

[8] Kuhlmann, H. C. (1999) *Thermocapillary Convection in Models of Crystal Growth*, Springer Tracts in Modern Physics, Vol. **152**, Springer, Berlin/Heidelberg.

[9] Lappa, M. (2003) Three-dimensional numerical simulation of Marangoni flow instabilities in floating zones laterally heated by an equatorial ring. *Phys. Fluids* **15** (3), 776–789.

[10] Levenstam, M. & Amberg, G. (1995) Hydrodynamic instabilities of thermocapillary flow in a half-zone. *J. Fluid Mech.* **297**: 357–372.

[11] Levich, V. G. (1962). *Physicochemical Hydrodynamics*. Prentice-Hall, Englewood Cliffs, NJ.

[12] Leypoldt, J., Kuhlmann, H. C. & Rath, H. J. (2000) Three-dimensional numerical simulation of thermocapillary flows in cylindrical liquid bridges. *J. Fluid Mech.* **414**: 285–314.

[13] Melnikov, D. E., Shevtsova, V. M. & Legros, J. C. (2002) Numerical simulation of hydro-thermal waves in liquid bridges with variable viscosity. *Adv. Space Res.* **29** (4), 661–666.

[14] Motegi, K., Fujimura, K. & Ueno, I. (2017) Floquet analysis of spatially periodic thermocapillary convection in a low-Prandtl-number liquid bridge. *Phys. Fluids* **29** (7), 074104 (14pp). DOI: 10.1063/1.4993466.

[15] Motegi, K., Kudo, M. & Ueno, I. (2017) Linear stability of buoyant thermocapillary convection for a high-Prandtl number fluid in a laterally heated liquid bridge. *Phys. Fluids* **29** (4), 044106 (10pp).

[16] Nienhüser, C. & Kuhlmann, H. C. (2002) Stability of thermocapillary flows in non-cylindrical liquid bridges. *J. Fluid Mech.* **458**: 35–73.

[17] Orr, W. M. (1907) The stability or instability of the steady motions of a perfect liquid and of a viscous liquid, part II: A viscous liquid. *Proc. R. Irish Acad.* **27**: 69–138.

https://doi.org/10.1017/S0956792523000189 Published online by Cambridge University Press

[18] Pfann, W. G. (1962) Zone melting. *Science* **135** (3509), 1101–1109.
[19] Reynolds, O. (1895) On the dynamical theory of incompressible viscous fluids and the determination of the criterion. *Philos. Trans. R. Soc. A* **186**: 123–164.
[20] Romanò, F., Kuhlmann, H. C., Ishimura, M. & Ueno, I. (2017) Limit cycles for the motion of finite-size particles in axisymmetric thermocapillary flows in liquid bridges. *Phys. Fluids* **29** (9), 093303 (14pp). DOI: 10.1063/1.5002135.
[21] Savchenko, I. V., Stankus, S. V. & Agadjanov, A. S. (2011) Measurement of liquid tin heat transfer coefficients within the temperature range of 506-1170 k. *High Temp.* **49** (4), 506–511.
[22] Shevtsova, V. M., Melnikov, D. E. & Legros, J. C. (2001) Three-dimensional simulations of hydrodynamic instability in liquid bridges: Influence of temperature-dependent viscosity. *Phys. Fluids* **13**: 2851–2865.
[23] Shevtsova, V., Melnikov, D. E. & Nepomnyashchy, A. (2009) New flow regimes generated by mode coupling in buoyant-thermocapillary convection. *Phys. Rev. Lett.* **102** (13), 134503-1–134503-4.
[24] Shin-Etsu (2004). *Silicone Fluid KF-96 – Performance Test Results, 6-1, Ohtemachi 2-chome*, 6-1, Ohtemachi 2-chome, Chioda-ku, Tokyo, Japan.
[25] Smith, M. K. (1986) Instability mechanisms in dynamic thermocapillary liquid layers. *Phys. Fluids* **29** (10), 3182–3186.
[26] Smith, M. K. & Davis, S. H. (1983) Instabilities of dynamic thermocapillary liquid layers. Part 1. Convective instabilities. *J. Fluid Mech.* **132**: 119–144.
[27] Stojanović, M., Romanò, F. & Kuhlmann, H. C. (2022) Stability of thermocapillary flow in liquid bridges fully coupled to the gas phase. *J. Fluid Mech.* **949**: A5-1–A5-51.
[28] Stojanović, M., Romanò, F. & Kuhlmann, H. C. (n.d.). Flow instability of high-Prandtl-number liquid bridges with fully temperature-dependent thermo-physical properties. In preparation.
[29] Tang, Z. M., Hu, W. R. & Imaishi, N. (2001) Two bifurcation transitions of the floating half zone convection in a fat liquid bridge of larger Pr. *Int. J. Heat Mass Transf.* **44** (7), 1299–1307.
[30] Ueno, I., Kawazoe, A. & Enomoto, H. (2010) Effect of ambient-gas forced flow on oscillatory thermocapillary convection of half-zone liquid bridge. *Fluid Dyn. Mater. Process.* **6** (1), 99–108. http://www.techscience.com/fdmp/v6n1/24474
[31] Ueno, I., Tanaka, S. & Kawamura, H. (2003) Oscillatory and chaotic thermocapillary convection in a half-zone liquid bridge. *Phys. Fluids* **15** (2), 408–416.
[32] VDI Heat Atlas (2010) Springer, Berlin/Heidelberg.
[33] Wanschura, M., Shevtsova, V. S., Kuhlmann, H. C. & Rath, H. J. (1995) Convective instability mechanisms in thermocapillary liquid bridges. *Phys. Fluids* **7** (5), 912–925.
[34] Widnall, S. E. & Tsai, C.-Y. (1977) The instability of the thin vortex ring of constant vorticity. *Proc R. Soc. Lond.* **287**: 273–305.
[35] Yano, T. & Nishino, K. (2020) Numerical study on the effects of convective and radiative heat transfer on thermocapillary convection in a high-Prandtl-number liquid bridge in weightlessness. *Adv. Space Res.* **66** (8), 2047–2061.
[36] Yano, T., Nishino, K., Matsumoto, S., et al. (2018) Report on microgravity experiments of dynamic surface deformation effects on Marangoni instability in high-Prandtl-number liquid bridges. *Microgravity Sci. Technol.* **30** (5), 599–610. DOI: 10.1007/s12217-018-9614-9.
[37] Yasnou, V., Gaponenko, Y., Mialdun, A. & Shevtsova, V. (2018) Influence of a coaxial gas flow on the evolution of oscillatory states in a liquid bridge. *Int. J. Heat Mass Transf.* **123**: 747–759. http://www.sciencedirect.com/science/article/pii/S0017931018303521

Appendix A: Integral thermal energy budget

The integral version of the rate of change of thermal energy is obtained by integrating all terms of (4.6), T1 through T8, over the volume V_i.

T1

Integrating T1 over the volume yields

$$\int_{V_i} \mathrm{T1}\,\mathrm{d}V = \int_{V_i} \rho_0 c_{p0} T \partial_t T\,\mathrm{d}V = \frac{1}{2}\int_{V_i} \rho_0 c_{p0} \partial_t T^2\,\mathrm{d}V := \partial_t E_T. \tag{A1}$$

T2

The term T2 can be written as

$$\mathrm{T2} = \frac{1}{2}(\rho_0' c_{p0} + \rho_0 c_{p0}')T_0 \partial_t T^2. \tag{A2}$$

https://doi.org/10.1017/S0956792523000189 Published online by Cambridge University Press

Since the first term on the r.h.s. of (A2) is compensated by the same term but with the opposite sign in T6, we are left with

$$\int_{V_i} \mathtt{T2'}\,\mathrm{d}V = \frac{1}{2}\int_{V_i} T_0\rho_0 c'_{p0}\partial_t(T^2)\,\mathrm{d}V := \partial_t E'_T, \tag{A3}$$

where T2' represents T2 except for the cancelled term.

T3

With

$$\mathtt{T3} = T\nabla\cdot(\rho'_0 c_{p0} T_0 \boldsymbol{u}_0 T) = \nabla\cdot\left(\rho'_0 c_{p0} T_0 \boldsymbol{u}_0 T^2\right) - \rho'_0 c_{p0} T_0 \boldsymbol{u}_0 T\cdot\nabla T \tag{A4}$$

the volume integral yields

$$\int_{V_i} \mathtt{T3}\,\mathrm{d}V = \int_{\partial V_i} \rho'_0 c_{p0} T_0 T^2 \boldsymbol{u}_0\cdot\boldsymbol{n}\,\mathrm{d}S - \int_{V_i} \rho'_0 c_{p0} T_0 T\boldsymbol{u}_0\cdot\nabla T\,\mathrm{d}V. \tag{A5}$$

Taking advantage of the coefficient α_i defined in (4.7), we obtain

$$\int_{V_i} \mathtt{T3}\,\mathrm{d}V = \frac{1-\alpha_i}{2}\int_{A_{\mathrm{out}}} \rho'_0 c_{p0} T_0 T^2 w_0\,\mathrm{d}S - \frac{1}{2}\int_{V_i} \rho'_0 c_{p0} T_0 \boldsymbol{u}_0\cdot\nabla T^2\,\mathrm{d}V. \tag{A6}$$

Note that the velocity and temperature perturbations vanish at the chamber inlet owing to the prescribed velocity and temperature profile for the basic state.

T4

Integrating

$$\mathtt{T4} = T\nabla\cdot(\rho_0 c'_{p0} T_0 \boldsymbol{u}_0 T) = \nabla\cdot\left(\rho_0 c'_{p0} T_0 \boldsymbol{u}_0 T^2\right) - \rho_0 c'_{p0} T_0 \boldsymbol{u}_0 T\cdot\nabla T \tag{A7}$$

over the volume yields

$$\begin{aligned}\int_{V_i} \mathtt{T4}\,\mathrm{d}V &= \int_{\partial V_i} \rho_0 c'_{p0} T_0 T^2 \boldsymbol{u}_0\cdot\boldsymbol{n}\,\mathrm{d}S - \int_{V_i} \rho_0 c'_{p0} T_0 T\boldsymbol{u}_0\cdot\nabla T\,\mathrm{d}V \\ &= \frac{1-\alpha_i}{2}\int_{A_{\mathrm{out}}} \rho_0 c'_{p0} T_0 T^2 w_0\,\mathrm{d}S - \frac{1}{2}\int_{V_i} \rho_0 c'_{p0} T_0 \boldsymbol{u}_0\cdot\nabla T^2\,\mathrm{d}V.\end{aligned} \tag{A8}$$

T5

The term T5 can either be written as

$$\begin{aligned}\mathtt{T5} &= T\nabla\cdot(\rho_0 c_{p0} T\boldsymbol{u}_0) = \nabla\cdot(\rho_0 c_{p0} T^2\boldsymbol{u}_0) - \rho_0 c_{p0} T\boldsymbol{u}_0\cdot\nabla T \\ &= \nabla\cdot(\rho_0 c_{p0} T^2\boldsymbol{u}_0) - \rho_0 T\boldsymbol{u}_0\cdot\nabla(c_{p0}T) + \rho_0 T^2\boldsymbol{u}_0\cdot\nabla c_{p0}\end{aligned} \tag{A9}$$

or as

$$T\nabla\cdot(\rho_0 c_{p0} T\boldsymbol{u}_0) = \underbrace{c_{p0} T^2\nabla\cdot(\rho_0\boldsymbol{u}_0)}_{=0} + \rho_0 T\boldsymbol{u}_0\cdot\nabla(c_{p0}T), \tag{A10}$$

where the first term on the r.h.s. vanishes because of (3.9a). Combining (A9) and (A10) leads to

$$2T\nabla\cdot(\rho_0 c_{p0} T\boldsymbol{u}_0) = \nabla\cdot(\rho_0 c_{p0} T^2\boldsymbol{u}_0) + \rho_0 T^2\boldsymbol{u}_0\cdot\nabla c_{p0}. \tag{A11}$$

Making use of the chain rule yields

$$T\nabla\cdot(\rho_0 c_{p0} T\boldsymbol{u}_0) = \frac{1}{2}\nabla\cdot(\rho_0 c_{p0} T^2\boldsymbol{u}_0) + \frac{1}{2}\rho_0 c'_{p0} T^2\boldsymbol{u}_0\cdot\nabla T_0. \tag{A12}$$

https://doi.org/10.1017/S0956792523000189 Published online by Cambridge University Press

Finally, by integrating over the volume, we obtain

$$\begin{aligned}\int_{V_i} \mathtt{T5}\,\mathrm{d}V &= \frac{1}{2}\int_{\partial V_i} \rho_0 c_{p0} T^2 \boldsymbol{u}_0 \cdot \boldsymbol{n}\,\mathrm{d}S + \frac{1}{2}\int_{V_i} \rho_0 c'_{p0} T^2 \boldsymbol{u}_0 \cdot \nabla T_0\,\mathrm{d}V \\ &= \frac{1-\alpha_i}{4}\int_{A_{\mathrm{out}}} \rho_0 c_{p0} T^2 w_0\,\mathrm{d}S + \frac{1}{2}\int_{V_i} \rho_0 c'_{p0} T^2 \boldsymbol{u}_0 \cdot \nabla T_0\,\mathrm{d}V \\ &= -K_{\mathrm{G,th}} + \frac{1}{2}\int_{V_i} \rho_0 c'_{p0} T^2 \boldsymbol{u}_0 \cdot \nabla T_0\,\mathrm{d}V. \end{aligned} \tag{A13}$$

T6

Transforming the term T6 to

$$\mathtt{T6} = T\nabla\cdot(\rho_0 c_{p0} T_0 \boldsymbol{u}) = \rho_0 T\boldsymbol{u}\cdot\nabla(c_{p0}T_0) + c_{p0}T_0 T\nabla\cdot(\rho_0\boldsymbol{u}) \tag{A14}$$

and inserting (3.9b) into (A14) gives us

$$\begin{aligned} T\nabla\cdot(\rho_0 c_{p0} T_0\boldsymbol{u}) &= \rho_0 T\boldsymbol{u}\cdot\nabla(c_{p0}T_0) - c_{p0}T_0 T\nabla\cdot(\rho'_0 T\boldsymbol{u}_0) - c_{p0}\rho'_0 T_0 T\partial_t T \\ &= \rho_0 T\left[u\partial_r(c_{p0}T_0) + w\partial_z(c_{p0}T_0)\right] - c_{p0}T_0 T\nabla\cdot(\rho'_0 T\boldsymbol{u}_0) \\ &\quad - \frac{1}{2}c_{p0}\rho'_0 T_0\partial_t T^2, \end{aligned} \tag{A15}$$

where the last term in (A15) cancels with the same term but with the opposite sign in (A1). Integrating over the volume, we remain with

$$\begin{aligned}\int_{V_i} \mathtt{T6'}\,\mathrm{d}V &= \int_{V_i} \rho_0 T\left[u\partial_r(c_{p0}T_0) + w\partial_z(c_{p0}T_0)\right]\mathrm{d}V - \int_{V_i} c_{p0}T_0 T\nabla\cdot(\rho'_0 T\boldsymbol{u}_0)\,\mathrm{d}V \\ &= -J - \int_{V_i} c_{p0}T_0 T\nabla\cdot(\rho'_0 T\boldsymbol{u}_0)\,\mathrm{d}V \\ &= -J - \int_{V_i} c_{p0}\rho''_0 T_0 T^2\boldsymbol{u}_0\cdot\nabla T_0\,\mathrm{d}V - \int_{V_i} c_{p0}\rho'_0 T_0 T^2\nabla\cdot\boldsymbol{u}_0\,\mathrm{d}V \\ &\quad - \int_{V_i} c_{p0}\rho'_0 T_0 T\boldsymbol{u}_0\cdot\nabla T\,\mathrm{d}V, \end{aligned} \tag{A16}$$

where T6' represents T6 except for the cancelled term. Using (3.9a), we finally find

$$\int_{V_i} \mathtt{T6'}\,\mathrm{d}V = -J + \int_{V_i}\left(\frac{\rho_0'^2}{\rho_0} - \rho''_0\right) c_{p0}T_0 T^2\boldsymbol{u}_0\cdot\nabla T_0\,\mathrm{d}V - \frac{1}{2}\int_{V_i}\rho'_0 c_{p0}T_0\boldsymbol{u}_0\cdot\nabla T^2\,\mathrm{d}V. \tag{A17}$$

T7

Integrating

$$\mathtt{T7} = T\nabla\cdot(\lambda'_0 T\nabla T_0) = \nabla\cdot(\lambda'_0 T^2\nabla T_0) - \lambda'_0 T\nabla T_0\cdot\nabla T \tag{A18}$$

over the volume yields

$$\int_{V_i}\mathtt{T7}\,\mathrm{d}V = \alpha_i\int_{A_s}\lambda'_0 T^2\nabla T_0\cdot\boldsymbol{n}\,\mathrm{d}S - \frac{1}{2}\int_{V_i}\lambda'_0\nabla T_0\cdot\nabla T^2\,\mathrm{d}V. \tag{A19}$$

T8

Finally, integrating

$$\mathtt{T8} = T\nabla\cdot(\lambda_0\nabla T) = \nabla\cdot(\lambda_0 T\nabla T) - \lambda_0(\nabla T)^2 \tag{A20}$$

https://doi.org/10.1017/S0956792523000189 Published online by Cambridge University Press

over the volume, we obtain

$$\int_{V_i} \mathtt{T8}\,\mathrm{d}V = \alpha_i \int_{A_{\mathrm{fs}}} \lambda_0 T \nabla T \cdot \boldsymbol{n}\,\mathrm{d}S - \int_{V_i} \lambda_0 (\nabla T)^2\,\mathrm{d}V := H_{\mathrm{fs}} - D_{\mathrm{th}}. \tag{A21}$$

Appendix B: Integral kinetic energy budget

As done for the thermal energy budget, the ten terms identified in the rate of change of the kinetic energy density (5.6) are integrated over the volume one by one.

K1

Integrating the term

$$\mathtt{K1} = \rho_0 \boldsymbol{u} \partial_t \boldsymbol{u} = \frac{1}{2} \rho_0 \partial_t \boldsymbol{u}^2 \tag{B1}$$

over the volume V_i yields

$$\int_{V_i} \mathtt{K1}\,\mathrm{d}V = \frac{1}{2} \int_{V_i} \rho_0 \partial_t \boldsymbol{u}^2\,\mathrm{d}V := \partial_t E_{\mathrm{kin}}. \tag{B2}$$

K2

The term

$$\mathtt{K2} = \rho_0' \boldsymbol{u}_0 \cdot \boldsymbol{u} \partial_t T \tag{B3}$$

cancels with the first term on the r.h.s. of (B6).

K3

Using the Einstein notation (l, m, n) for expanding the terms in braces of K3, we get

$$\begin{aligned}
&\nabla \cdot [\rho_0 (\boldsymbol{u}_0 \boldsymbol{u} + \boldsymbol{u}\boldsymbol{u}_0)] \\
&\quad = \partial_m (\rho_0 u_{0l} u_m + \rho_0 u_l u_{0m}) = \partial_m (\rho_0 u_{0l} u_m) + \partial_m (\rho_0 u_l u_{0m}) \\
&\quad = u_{0l} \partial_m (\rho_0 u_m) + \rho_0 u_m \partial_m u_{0l} + u_l \partial_m (\rho_0 u_{0m}) + \rho_0 u_{0m} \partial_m u_l \\
&\quad = \boldsymbol{u}_0 \nabla \cdot (\rho_0 \boldsymbol{u}) + \rho_0 \boldsymbol{u} \cdot \nabla \boldsymbol{u}_0 + \boldsymbol{u} \underbrace{\nabla \cdot (\rho_0 \boldsymbol{u}_0)}_{=0} + \rho_0 \boldsymbol{u}_0 \cdot \nabla \boldsymbol{u},
\end{aligned} \tag{B4}$$

where the second-last term vanishes due to the continuity equation (3.9a) at $O(\epsilon^0)$. Inserting (3.9b) into (B4) leads to

$$\nabla \cdot [\rho_0 (\boldsymbol{u}_0 \boldsymbol{u} + \boldsymbol{u}\boldsymbol{u}_0)] = -\rho_0' \boldsymbol{u}_0 \partial_t T - \boldsymbol{u}_0 \nabla \cdot (\rho_0' T \boldsymbol{u}_0) + \rho_0 \boldsymbol{u} \cdot \nabla \boldsymbol{u}_0 + \rho_0 \boldsymbol{u}_0 \cdot \nabla \boldsymbol{u}. \tag{B5}$$

Scalar multiplication with $\boldsymbol{u}$ yields

$$\begin{aligned}
\mathtt{K3} = \boldsymbol{u} \cdot \{\nabla \cdot [\rho_0 (\boldsymbol{u}_0 \boldsymbol{u} + \boldsymbol{u}\boldsymbol{u}_0)]\} &= -\rho_0' \boldsymbol{u}_0 \cdot \boldsymbol{u} \partial_t T - (\boldsymbol{u} \cdot \boldsymbol{u}_0) \nabla \cdot (\rho_0' T \boldsymbol{u}_0) \\
&+ \rho_0 \boldsymbol{u} \cdot (\boldsymbol{u} \cdot \nabla \boldsymbol{u}_0) + \rho_0 \boldsymbol{u} \cdot (\boldsymbol{u}_0 \cdot \nabla \boldsymbol{u}),
\end{aligned} \tag{B6}$$

https://doi.org/10.1017/S0956792523000189 Published online by Cambridge University Press

where the first term on the r.h.s. is compensated with K2. Furthermore, the second term on the r.h.s. cancels with the last term in (B13) for K4. It remains

$$\begin{aligned}\texttt{K3'} &= \rho_0 \boldsymbol{u}\cdot(\boldsymbol{u}_0\cdot\nabla\boldsymbol{u}) + \rho_0\boldsymbol{u}\cdot(\boldsymbol{u}\cdot\nabla\boldsymbol{u}_0)\\ &= \frac{1}{2}\rho_0\boldsymbol{u}_0\cdot\nabla\boldsymbol{u}^2 + \rho_0\boldsymbol{u}\cdot(\boldsymbol{u}\cdot\nabla\boldsymbol{u}_0)\\ &= \frac{1}{2}\nabla\cdot(\rho_0\boldsymbol{u}_0\boldsymbol{u}^2) - \frac{1}{2}\boldsymbol{u}^2\underbrace{\nabla\cdot(\rho_0\boldsymbol{u}_0)}_{=0} + \rho_0\boldsymbol{u}\cdot(\boldsymbol{u}\cdot\nabla\boldsymbol{u}_0),\end{aligned} \tag{B7}$$

where K3' represents K3 without the cancelled terms. The second term in K3' vanishes due to the continuity equation in $O(\epsilon^0)$. Expressing

$$\nabla\boldsymbol{u}_0 = \begin{pmatrix}\partial_r u_0 & 0 & \partial_z u_0\\ 0 & u_0/r & 0\\ \partial_r w_0 & 0 & \partial_z w_0\end{pmatrix} \tag{B8}$$

through the components of basic velocity field, we obtain

$$\texttt{K3'} = \frac{1}{2}\nabla\cdot(\rho_0\boldsymbol{u}_0\boldsymbol{u}^2) + \rho_0\left(u_0\frac{v^2}{r} + u^2\partial_r u_0 + uw\partial_z u_0 + uw\partial_r w_0 + w^2\partial_z w_0\right). \tag{B9}$$

By integration over the volume, we get

$$\begin{aligned}\int_{V_i}\texttt{K3'}\,\mathrm{d}V &= \frac{1}{2}\int_{\partial V_i}\rho_0\boldsymbol{u}^2\boldsymbol{u}_0\cdot\boldsymbol{n}\,\mathrm{d}S\\ &\quad+\int_{V_i}\rho_0\left(u_0\frac{v^2}{r} + u^2\partial_r u_0 + uw\partial_z u_0 + uw\partial_r w_0 + w^2\partial_z w_0\right)\mathrm{d}V.\end{aligned} \tag{B10}$$

Finally, using α_i from (4.7), we arrive at

$$\begin{aligned}\int_{V_i}\texttt{K3'}\,\mathrm{d}V &= \frac{1-\alpha_i}{4}\int_{A_{\mathrm{out}}}\rho_0 w^2 w_0\,\mathrm{d}S\\ &\quad+\int_{V_i}\rho_0\left(u_0\frac{v^2}{r} + u^2\partial_r u_0 + uw\partial_z u_0 + uw\partial_r w_0 + w^2\partial_z w_0\right)\mathrm{d}V\\ &:= -K_{\mathrm{G}} - \sum_{j=1}^{5} I_j := -K_{\mathrm{G}} - I.\end{aligned} \tag{B11}$$

K4

We use the index notation for expanding the part in square brackets of K4

$$\begin{aligned}\nabla\cdot(\rho_0' T\boldsymbol{u}_0\boldsymbol{u}_0) &= \partial_m(\rho_0' T u_{0l}u_{0m}) = u_{0l}\partial_m(\rho_0' T u_{0m}) + \rho_0' T u_{0m}\partial_m u_{0l}\\ &= \boldsymbol{u}_0\nabla\cdot(\rho_0' T\boldsymbol{u}_0) + \rho_0' T\boldsymbol{u}_0\cdot\nabla\boldsymbol{u}_0.\end{aligned} \tag{B12}$$

After taking the dot product with $\boldsymbol{u}$, we obtain

$$\boldsymbol{u}\cdot\left[\nabla\cdot(\rho_0' T\boldsymbol{u}_0\boldsymbol{u}_0)\right] = \rho_0' T\boldsymbol{u}\cdot(\boldsymbol{u}_0\cdot\nabla\boldsymbol{u}_0) + (\boldsymbol{u}\cdot\boldsymbol{u}_0)\nabla\cdot(\rho_0' T\boldsymbol{u}_0). \tag{B13}$$

As aforementioned, the last term in (B13) compensates with one of the terms of K3 in (B6). Using $\boldsymbol{u}_0\cdot\nabla\boldsymbol{u}_0$ in components

$$\boldsymbol{u}_0\cdot\nabla\boldsymbol{u}_0 = \begin{pmatrix}\partial_r u_0 & 0 & \partial_z u_0\\ 0 & \dfrac{u_0}{r} & 0\\ \partial_r w_0 & 0 & \partial_z w_0\end{pmatrix}\cdot\begin{pmatrix}u_0\\ 0\\ w_0\end{pmatrix} = \begin{pmatrix}u_0\partial_r u_0 + w_0\partial_z u_0\\ 0\\ w_0\partial_z w_0 + u_0\partial_r w_0\end{pmatrix}, \tag{B14}$$

https://doi.org/10.1017/S0956792523000189 Published online by Cambridge University Press

and integrating over the volume yields

$$\int_{V_i} \mathtt{K4'}\,\mathrm{d}V = \int_{V_i} \rho_0' T\boldsymbol{u}\cdot(\boldsymbol{u}_0\cdot\nabla\boldsymbol{u}_0)\,\mathrm{d}V$$
$$= \int_{V_i} \rho_0' u_0\,(u\partial_r u_0 + w\partial_r w_0)\;\mathrm{d}V + \int_{V_i} \rho_0' w_0\,(u\partial_z u_0 + w\partial_z w_0)\;\mathrm{d}V. \tag{B15}$$

K5

The term K5 can be written as

$$\mathtt{K5} = \boldsymbol{u}\cdot\nabla p = \nabla\cdot(p\boldsymbol{u}) - p\nabla\cdot\boldsymbol{u}. \tag{B16}$$

Using the continuity equation in $O(\epsilon)$ (3.9b), we can express

$$\nabla\cdot\boldsymbol{u} = -\frac{1}{\rho_0}\left[\boldsymbol{u}\cdot\nabla\rho_0 + \rho_0'\partial_t T + \nabla\cdot(\rho_0'\boldsymbol{u}_0 T)\right]$$
$$= -\frac{1}{\rho_0}\left[\rho_0'\boldsymbol{u}\cdot\nabla T_0 + \rho_0'\partial_t T + \nabla\cdot(\rho_0'\boldsymbol{u}_0 T)\right] := \zeta, \tag{B17}$$

where the abbreviation ζ indicates the deviations from a solenoidal perturbation flow, which is primarily determined by the temperature dependence of ρ. Inserting (B17) in (B16) gives

$$\int_{V_i} \mathtt{K5}\,\mathrm{d}V = \underbrace{\int_{\partial V_i} p\boldsymbol{u}\cdot\boldsymbol{n}\,\mathrm{d}S}_{=0} - \int_{V_i} \zeta p\,\mathrm{d}V. \tag{B18}$$

Note that the integrand in the first integral of (B18) vanishes at the chamber outlet because of the vanishing pressure perturbation. It also vanishes on the walls, at the inlet and along the axis because of the vanishing normal velocity perturbation.

K6

Integrating

$$\mathtt{K6} = \rho_0' T\boldsymbol{u}\cdot\boldsymbol{g} = -\rho_0' T g w \tag{B19}$$

over the volume yields

$$\int_{V_i} \mathtt{K6}\,\mathrm{d}V = -\int_{V_i} \rho_0' T g w\,\mathrm{d}V := B. \tag{B20}$$

K7

Considering the terms in the braces of K7

$$\nabla\cdot\{\mu_0\left[\nabla\boldsymbol{u} + (\nabla\boldsymbol{u})^{\mathrm{T}}\right]\} = \mu_0\nabla\cdot\left[\nabla\boldsymbol{u} + (\nabla\boldsymbol{u})^{\mathrm{T}}\right] + \left[\nabla\boldsymbol{u} + (\nabla\boldsymbol{u})^{\mathrm{T}}\right]\cdot\nabla\mu_0 \tag{B21}$$

and using the index notation, the first term on the r.h.s. of (B21) can be written as

$$\nabla\cdot\left[\nabla\boldsymbol{u} + (\nabla\boldsymbol{u})^{\mathrm{T}}\right] = \partial_l\left(\partial_l u_m + \partial_m u_l\right) = \partial_l\partial_l u_m + \partial_m\partial_l u_l = \Delta\boldsymbol{u} + \nabla(\nabla\cdot\boldsymbol{u}). \tag{B22}$$

Thus, (B21) turns into

$$\nabla\cdot\{\mu_0\left[\nabla\boldsymbol{u} + (\nabla\boldsymbol{u})^{\mathrm{T}}\right]\} = \mu_0\Delta\boldsymbol{u} + \mu_0\nabla(\nabla\cdot\boldsymbol{u}) + \left[\nabla\boldsymbol{u} + (\nabla\boldsymbol{u})^{\mathrm{T}}\right]\cdot\nabla\mu_0. \tag{B23}$$

https://doi.org/10.1017/S0956792523000189 Published online by Cambridge University Press

Scalar multiplication of (B23) with the perturbation velocity field $\boldsymbol{u}$, we can express the term K7 as

$$\begin{aligned}\mathtt{K7} &= \boldsymbol{u}\cdot\left\{\nabla\cdot\left\{\mu_0\left[\nabla\boldsymbol{u}+(\nabla\boldsymbol{u})^{\mathrm{T}}\right]\right\}\right\}\\ &= \underbrace{\mu_0\boldsymbol{u}\cdot\Delta\boldsymbol{u}}_{\mathtt{K7a}}+\underbrace{\mu_0\boldsymbol{u}\cdot\nabla(\nabla\cdot\boldsymbol{u})}_{\mathtt{K7b}}+\underbrace{\boldsymbol{u}\cdot\left[\nabla\boldsymbol{u}+(\nabla\boldsymbol{u})^{\mathrm{T}}\right]\cdot\nabla\mu_0}_{\mathtt{K7c}}.\end{aligned} \tag{B24}$$

The three terms K7a, K7b and K7c are considered separately. Using the index notation, the integral over the term K7a can be written as

$$\begin{aligned}\int_{V_i}\mathtt{K7a}\,\mathrm{d}V &= \int_{V_i}\mu_0 u_l\partial_m\partial_m u_l\,\mathrm{d}V\\ &= \underbrace{\alpha_i\int_{A_{\mathrm{fs}}}\mu_0 u_l n_m\partial_m u_l\,\mathrm{d}S}_{\coloneqq M}-\int_{V_i}\mu_0(\partial_m u_l)^2\,\mathrm{d}V+\int_{V_i}u_l(\partial_m\mu_0)(\partial_m u_l)\,\mathrm{d}V\\ &= -\int_{V_i}\mu_0(\partial_m u_l)^2\,\mathrm{d}V+M+\int_{V_i}u_l(\partial_m u_l)(\partial_m\mu_0)\,\mathrm{d}V\\ &= -\int_{V_i}\mu_0(\partial_m u_l)^2\,\mathrm{d}V+M_r+M_\varphi+M_z\\ &\quad-\alpha_i\int_{A_{\mathrm{fs}}}\mu_0(h_0w^2h_{0zz}-v^2)\,\mathrm{d}\varphi\,\mathrm{d}z+\int_{V_i}\mu_0'\boldsymbol{u}\cdot(\nabla\boldsymbol{u})^{\mathrm{T}}\cdot\nabla T_0\,\mathrm{d}V.\end{aligned} \tag{B25}$$

Identifying the terms that characterise the kinetic energy dissipation D_{kin} and the energy transfer due to thermocapillary stresses in r-, φ- and z-direction (see M_r, M_φ, and M_z, respectively), we obtain

$$\int_{V_i}\mathtt{K7a}\,\mathrm{d}V=-D_{\mathrm{kin}}+M_r+M_\varphi+M_z+\frac{1}{2}\int_{V_i}\mu_0'\cdot(\nabla\boldsymbol{u}^2)\cdot\nabla T_0\,\mathrm{d}V, \tag{B26}$$

with

$$D_{\mathrm{kin}}=\int_{V_i}\mu_0(\partial_l u_m)^2\,\mathrm{d}V+\alpha_i\int_{A_{\mathrm{fs}}}\mu_0(h_0h_{0zz}w^2-v^2)\,\mathrm{d}\varphi\,\mathrm{d}z, \tag{B27}$$

which reads in component notation

$$\begin{aligned}D_{\mathrm{kin}}=\int_{V_i}\mu_0\Bigg[&(\partial_r u)^2+\left(\frac{1}{r}\partial_\varphi u-\frac{v}{r}\right)^2+(\partial_z u)^2+(\partial_r v)^2+\left(\frac{1}{r}\partial_\varphi v+\frac{u}{r}\right)^2\\ &+(\partial_z v)^2+(\partial_r w)^2+\frac{(\partial_\varphi w)^2}{r^2}+(\partial_z w)^2\Bigg]\,\mathrm{d}V+\alpha_i\int_{A_{\mathrm{fs}}}\mu_0(h_0w^2h_{0zz}-v^2)\,\mathrm{d}\varphi\,\mathrm{d}z.\end{aligned} \tag{B28}$$

The integral production terms of kinetic energy by thermocapillary stresses are

$$M_r=\alpha_i\int_{A_{\mathrm{fs}}}\mu_0h_0u(\partial_r w-\partial_z u)h_{0z}\,\mathrm{d}\varphi\;\mathrm{d}z, \tag{B29a}$$

$$M_\varphi=\alpha_i\int_{A_{\mathrm{fs}}}\mu_0h_0v\left(\partial_r v-\frac{v}{h_0}-h_{0z}\partial_z v\right)\,\mathrm{d}\varphi\;\mathrm{d}z, \tag{B29b}$$

$$M_z=\alpha_i\int_{A_{\mathrm{fs}}}\mu_0h_0w\left(\partial_r w+wh_{0zz}-h_{0z}\partial_z w\right)\,\mathrm{d}\varphi\;\mathrm{d}z. \tag{B29c}$$

https://doi.org/10.1017/S0956792523000189 Published online by Cambridge University Press

Expanding the term K7b and integrating over the volume results in

$$\begin{aligned}\int_{V_i} \mathtt{K7b}\,\mathrm{d}V &= \int_{V_i} \mu_0 u_l \partial_l \partial_n u_n \,\mathrm{d}V = \int_{V_i} \mu_0 \partial_l (u_l \partial_n u_n)\,\mathrm{d}V - \int_{V_i} \mu_0 (\partial_n u_n)(\partial_l u_l)\,\mathrm{d}V \\ &= \underbrace{\int_{\partial V_i} \mu_0 (\partial_n u_n)(n_l u_l)\,\mathrm{d}S}_{=0} - \int_{V_i} \mu_0' (\partial_n u_n) u_l \partial_l T_0 \,\mathrm{d}V \\ &\quad - \int_{V_i} \mu_0 (\partial_n u_n)(\partial_l u_l). \end{aligned} \tag{B30}$$

Note that the first integral on the r.h.s. vanishes, because the normal vector $\boldsymbol{n}$ is perpendicular to the velocity vector $\boldsymbol{u}$ along the interface such that $\boldsymbol{n}\cdot\boldsymbol{u}=0$. Using (B17), we find

$$\int_{V_i} \mathtt{K7b}\,\mathrm{d}V = -\int_{V_i} \mu_0 \zeta^2\,\mathrm{d}V - \int_{V_i} \mu_0' \zeta \boldsymbol{u}\cdot\nabla T_0\,\mathrm{d}V. \tag{B31}$$

Finally, expanding the term K7c and integrating over the volume we get

$$\int_{V_i} \mathtt{K7c}\,\mathrm{d}V = \int_{V_i} \boldsymbol{u}\cdot\left[\nabla\boldsymbol{u} + (\nabla\boldsymbol{u})^{\mathrm{T}}\right]\cdot\nabla\mu_0\,\mathrm{d}V = \int_{V_i} \mu_0' \boldsymbol{u}\cdot\mathcal{S}\cdot\nabla T_0\,\mathrm{d}V, \tag{B32}$$

where the stress tensor of the perturbation velocity field reads

$$\mathcal{S} = \nabla\boldsymbol{u} + (\nabla\boldsymbol{u})^{\mathrm{T}} = \begin{pmatrix} 2\partial_r u & \frac{1}{r}\partial_\varphi u - \frac{v}{r} + \partial_r v & \partial_z u + \partial_r w \\ \frac{1}{r}\partial_\varphi u - \frac{v}{r} + \partial_r v & \frac{2}{r}\partial_\varphi v + \frac{2u}{r} & \partial_z v + \frac{1}{r}\partial_\varphi w \\ \partial_z u + \partial_r w & \partial_z v + \frac{1}{r}\partial_\varphi w & 2\partial_z w \end{pmatrix}. \tag{B33}$$

K8

The l-th component of $\nabla\cdot[\mu_0(\nabla\cdot\boldsymbol{u})\boldsymbol{I}]$ reads

$$\left\{\nabla\cdot[\mu_0(\nabla\cdot\boldsymbol{u})\boldsymbol{I}]\right\}_l = \partial_m(\mu_0\partial_n u_n)\delta_{ml}, \tag{B34}$$

where $\delta_{ml}=\delta_{lm}$ is the symmetric Kronecker delta. Taking the scalar product with $\boldsymbol{u}$, we obtain

$$\begin{aligned}\boldsymbol{u}\cdot\left\{\nabla\cdot[\mu_0(\nabla\cdot\boldsymbol{u})\boldsymbol{I}]\right\} &= u_l\partial_m(\mu_0\partial_n u_n)\delta_{ml} \\ &= \partial_m(\mu_0 u_l\delta_{lm}\partial_n u_n) - \mu_0\partial_n u_n\partial_m(u_l\delta_{lm}) \\ &= \partial_m(\mu_0 u_m\partial_n u_n) - \mu_0(\partial_n u_n)(\partial_m u_m) \\ &= \nabla\cdot[\mu_0(\nabla\cdot\boldsymbol{u})\boldsymbol{u}] - \mu_0(\nabla\cdot\boldsymbol{u})^2. \end{aligned} \tag{B35}$$

Integrating the term K8 over the volume, we find

$$\int_{V_i} \mathtt{K8}\,\mathrm{d}V = \frac{2}{3}\underbrace{\int_{\partial V_i} \mu_0(\nabla\cdot\boldsymbol{u})(\boldsymbol{u}\cdot\boldsymbol{n})\,\mathrm{d}S}_{=0} - \frac{2}{3}\int_{V_i}\mu_0\zeta^2\,\mathrm{d}V. \tag{B36}$$

The first term vanishes for the same arguments as in (B30) during the treatment of K7b.

K9

Similarly to (B23), for the terms in braces of K9 we have

$$\nabla\cdot\left\{\mu_0' T\left[\nabla\boldsymbol{u}_0 + (\nabla\boldsymbol{u}_0)^{\mathrm{T}}\right]\right\} = \mu_0' T\Delta\boldsymbol{u}_0 + \mu_0' T\nabla(\nabla\cdot\boldsymbol{u}_0) + \left[\nabla\boldsymbol{u}_0 + (\nabla\boldsymbol{u}_0)^{\mathrm{T}}\right]\cdot\nabla(\mu_0' T). \tag{B37}$$

https://doi.org/10.1017/S0956792523000189 Published online by Cambridge University Press

Scalar multiplication with $\boldsymbol{u}$ yields

$$\boldsymbol{u}\cdot\left\{\nabla\cdot\left\{\mu_0' T\left[\nabla\boldsymbol{u}_0+(\nabla\boldsymbol{u}_0)^{\mathrm{T}}\right]\right\}\right\}=\underbrace{\mu_0' T\boldsymbol{u}\cdot\Delta\boldsymbol{u}_0}_{\texttt{K9a}}+\underbrace{\mu_0' T\boldsymbol{u}\cdot\nabla(\nabla\cdot\boldsymbol{u}_0)}_{\texttt{K9b}}+\underbrace{\boldsymbol{u}\cdot\left[\nabla\boldsymbol{u}_0+(\nabla\boldsymbol{u}_0)^{\mathrm{T}}\right]\cdot\nabla(\mu_0' T)}_{\texttt{K9c}}. \tag{B38}$$

The three terms K9a, K9b and K9c are treated separately. The term K9a can be written as

$$\begin{aligned}\int_{V_i}\texttt{K9a}\,\mathrm{d}V&=\int_{V_i}\mu_0' T u_l\partial_m\partial_m u_{0l}\,\mathrm{d}V=\alpha_i\int_{A_{\mathrm{fs}}}\mu_0' T u_l n_m\partial_m u_{0l}\,\mathrm{d}S-\int_{V_i}(\partial_m u_{0l})(\partial_m\mu_0' T u_l)\,\mathrm{d}V\\&=\alpha_i\int_{A_{\mathrm{fs}}}\mu_0' T u_l n_m\partial_m u_{0l}\,\mathrm{d}S-\int_{V_i}\mu_0' T(\partial_m u_{0l})(\partial_m u_l)\,\mathrm{d}V+\int_{V_i}u_l(\partial_m u_{0l})(\partial_m\mu_0' T)\,\mathrm{d}V\\&=\alpha_i\int_{A_{\mathrm{fs}}}\mu_0' T u_l n_m\partial_m u_{0l}\,\mathrm{d}S-\int_{V_i}\mu_0' T(\partial_m u_{0l})(\partial_m u_l)\,\mathrm{d}V\\&\quad+\int_{V_i}u_l(\partial_m u_{0l})(\mu_0'+\mu_0'' T)\partial_m T\,\mathrm{d}V.\end{aligned} \tag{B39}$$

Expressing the tensor $\partial_m u_{0l}$ in cylindrical coordinates yields

$$\begin{aligned}\partial_m u_{0l}&=(\boldsymbol{e}_r\partial_r+\boldsymbol{e}_z\partial_z)\,(u_0\boldsymbol{e}_r+w_0\boldsymbol{e}_z)\\&=\boldsymbol{e}_r(\partial_r u_0\boldsymbol{e}_r+\partial_r w_0\boldsymbol{e}_z)+\frac{\boldsymbol{e}_\varphi}{r}u_0\boldsymbol{e}_\varphi+\boldsymbol{e}_z(\partial_z u_0\boldsymbol{e}_r+\partial_z w_0\boldsymbol{e}_z).\end{aligned} \tag{B40}$$

This is projected onto $n_m=N^{-1}(\boldsymbol{e}_r-h_{0z}\boldsymbol{e}_z)$ to obtain

$$n_m\partial_m u_{0l}=\frac{1}{N}(\partial_r u_0\boldsymbol{e}_r+\partial_r w_0\boldsymbol{e}_z)-\frac{h_{0z}}{N}(\partial_z u_0\boldsymbol{e}_r+\partial_z w_0\boldsymbol{e}_z). \tag{B41}$$

Further projection onto u_l yields

$$u_l n_m\partial_m u_{0l}=\frac{1}{N}(u\partial_r u_0+w\partial_r w_0-h_{0z}u\partial_z u_0-h_{0z}w\partial_z w_0). \tag{B42}$$

On the liquid–gas interface, we can use the relations

$$u=h_{0z}w, \tag{B43a}$$
$$\partial_r u=h_{0z}\partial_r w, \tag{B43b}$$
$$\partial_z u=h_{0zz}w+h_{0z}\partial_z w, \tag{B43c}$$
$$u_0=h_{0z}w_0, \tag{B43d}$$
$$\partial_r u_0=h_{0z}\partial_r w_0, \tag{B43e}$$
$$\partial_z u_0=h_{0zz}w_0+h_{0z}\partial_z w_0, \tag{B43f}$$

to obtain

$$u_l n_m\partial_m u_{0l}=\frac{w}{N}(N^2\partial_r w_0-N^2h_{0z}\partial_z w_0-h_{0z}^2h_{0zz}w_0). \tag{B44}$$

Combining the above relations, the integral over the term K9a reads

$$\begin{aligned}\int_{V_i}\texttt{K9a}\,\mathrm{d}V&=\alpha_i\int_{A_{\mathrm{fs}}}\mu_0' Tw(N^2\partial_r w_0-N^2h_{0z}\partial_z w_0-h_{0z}^2h_{0zz}w_0)\,\mathrm{d}\varphi\,\mathrm{d}z\\&\quad-\int_{V_i}\mu_0' T(\nabla u_0):(\nabla u)\,\mathrm{d}V+\int_{V_i}(\mu_0'+\mu_0'' T_0)\boldsymbol{u}\cdot[(\nabla\boldsymbol{u}_0)^{\mathrm{T}}\cdot\nabla T]\,\mathrm{d}V.\end{aligned} \tag{B45}$$

https://doi.org/10.1017/S0956792523000189 Published online by Cambridge University Press

We now focus on the term K9b. Its integral over the volume is expressed as

$$\int_{V_i} \texttt{K9b}\,\mathrm{d}V = \int_{V_i} \mu_0' T u_l \partial_l \partial_n u_{0n}\,\mathrm{d}V = \int_{V_i} \mu_0' T \partial_l (u_l \partial_n u_{0n})\,\mathrm{d}V - \int_{V_i} \mu_0' T (\partial_n u_{0n}) (\underbrace{\partial_l u_l}_{=\zeta})\,\mathrm{d}V$$
$$= \underbrace{\int_{\partial V_i} \mu_0' T (\partial_n u_{0n})(u_l n_l)\,\mathrm{d}S}_{=0} - \int_{V_i} (\partial_n u_{0n}) u_l \partial_l (\mu_0' T)\,\mathrm{d}V - \int_{V_i} \mu_0' T \zeta (\partial_n u_{0n})\,\mathrm{d}V$$
$$= -\int_{V_i} (\partial_n u_{0n})(\mu_0' u_l \partial_l T + \mu_0'' T u_l \partial_l T_0)\,\mathrm{d}V - \int_{V_i} \mu_0' T \zeta (\partial_n u_{0n})\,\mathrm{d}V. \tag{B46}$$

Considering the $O(\epsilon^0)$ continuity equation, one can recast the divergence of $\boldsymbol{u}_0$ as

$$\nabla \cdot \boldsymbol{u}_0 = -\frac{1}{\rho_0} \boldsymbol{u}_0 \cdot \nabla \rho_0 = -\frac{\rho_0'}{\rho_0} \boldsymbol{u}_0 \cdot \nabla T_0 := \zeta_0. \tag{B47}$$

Analogous to (B17), we define ζ_0 to be an indicator for the deviation of the basic state velocity field from being solenoidal. Thus, the integral over K9b is obtained as

$$\int_{V_i} \texttt{K9b}\,\mathrm{d}V = -\int_{V_i} \zeta_0 (\mu_0' \boldsymbol{u} \cdot \nabla T + \mu_0'' T \boldsymbol{u} \cdot \nabla T_0)\,\mathrm{d}V - \int_{V_i} \mu_0' T \zeta_0 \zeta\,\mathrm{d}V. \tag{B48}$$

Finally, the term K9c reads

$$\boldsymbol{u} \cdot \left[\nabla \boldsymbol{u}_0 + (\nabla \boldsymbol{u}_0)^{\mathrm{T}}\right] \cdot \nabla (\mu_0' T) = (\mu_0' + \mu_0'' T) \boldsymbol{u} \cdot \left[\nabla \boldsymbol{u}_0 + (\nabla \boldsymbol{u}_0)^{\mathrm{T}}\right] \cdot \nabla T. \tag{B49}$$

Integrating over the volume, we obtain

$$\int_{V_i} \texttt{K9c}\,\mathrm{d}V = \int_{V_i} (\mu_0' + \mu_0'' T) \boldsymbol{u} \cdot \mathcal{S}_0 \cdot \nabla T\,\mathrm{d}V, \tag{B50}$$

with

$$\mathcal{S}_0 = \nabla \boldsymbol{u}_0 + (\nabla \boldsymbol{u}_0)^{\mathrm{T}} = \begin{pmatrix} 2\partial_r u_0 & 0 & \partial_z u_0 + \partial_r w_0 \\ 0 & 2u_0/r & 0 \\ \partial_z u_0 + \partial_r w_0 & 0 & 2\partial_z w_0 \end{pmatrix}. \tag{B51}$$

K10

Similarly to (B35), the term K10 can be expressed as

$$\boldsymbol{u} \cdot \left\{\nabla \cdot \left[\mu_0' T (\nabla \cdot \boldsymbol{u}_0) \boldsymbol{I}\right]\right\} = \nabla \cdot \left[\mu_0' T (\nabla \cdot \boldsymbol{u}_0) \boldsymbol{u}\right] - \mu_0' T (\nabla \cdot \boldsymbol{u})(\nabla \cdot \boldsymbol{u}_0). \tag{B52}$$

Integrating over the volume yields

$$\int_{V_i} \texttt{K10}\,\mathrm{d}V = \frac{2}{3} \underbrace{\int_{\partial V_i} \mu_0' T (\nabla \cdot \boldsymbol{u}_0)(\boldsymbol{u} \cdot \boldsymbol{n})\,\mathrm{d}S}_{=0} - \frac{2}{3} \int_{V_i} \mu_0' T \zeta \zeta_0\,\mathrm{d}V. \tag{B53}$$

Cite this article: Stojanović M., Romanò F. and Kuhlmann H. C. Instability of axisymmetric flow in thermocapillary liquid bridges: Kinetic and thermal energy budgets for two-phase flow with temperature-dependent material properties. *European Journal of Applied Mathematics*, https://doi.org/10.1017/S0956792523000189

Paper 4

Stojanović, M., Romanò, F., Kuhlmann, H. C., 'Flow instability in high-Prandtl-number liquid bridges with fully temperature-dependent thermo-physical properties (submitted)', *J. Fluid Mech.*

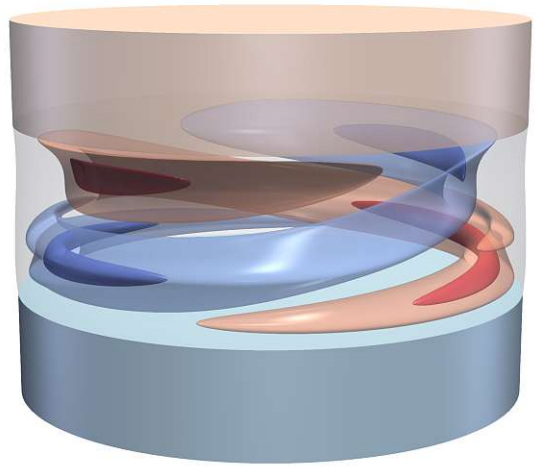

Flow instability in high-Prandtl-number liquid bridges with fully temperature-dependent thermo-physical properties

Mario Stojanović[1] †, Francesco Romanò[2] ‡ and Hendrik C. Kuhlmann[1] ¶

[1]Institute of Fluid Mechanics and Heat Transfer, TU Wien, Getreidemarkt 9-BA, 1060 Vienna, Austria
[2]Univ. Lille, CNRS, ONERA, Arts et Métiers Institute of Technology, Centrale Lille, UMR 9014 - LMFL - Laboratoire de Mécanique des Fluides de Lille - Kampé de Fériet, F-59000, Lille, France

(Received xx; revised xx; accepted xx)

The axisymmetric steady two-phase flow of a differentially heated thermocapillary liquid bridge in air and its linear stability is investigated numerically, taking into account dynamic interfacial deformations in the basic flow. Since most experiments require a high temperature difference to drive the flow into the three-dimensional regime, the temperature dependence of the material properties must be taken into account. Three different models are investigated for a high-Prandtl number thermocapillary liquid bridge with nominal Prandtl number Pr = 28.8: the Oberbeck–Boussinesq approximation, a linear temperature dependence of all material properties, and a full nonlinear temperature dependence of all material properties. For all models critical Reynolds numbers are computed as functions of the volume of the liquid bridge, its aspect ratio, its dimensional size and as a function of the strength of a forced axial flow in the ambient air. Under most circumstances the Oberbeck–Boussinesq approximation over-predicts and the linear model under-predicts the critical Reynolds number, compared to the model based on the full temperature dependence of the material properties. Among the main influence factors are the proper selection of the reference temperature and, at larger temperature differences, the temperature dependence of the viscosity of the liquid.

Key words: Liquid bridges; Thermocapillarity; Instability; Gas/liquid flow

1. Introduction

Thermocapillary flows are driven by tangential shear stresses acting on non-isothermal liquid–gas interfaces. They are due to the thermocapillary effect which describes the variation of the surface tension with temperature (Scriven & Sternling 1960). These flows are important in a number of applications, like crystal growth from the melt (Schwabe 1981), welding (Amberg & Do-Quang 2008) or droplet evaporation from inkjet printing (Ristenpart *et al.* 2007). The flow in thermocapillary liquid bridges, originally devised as a model system for the floating-zone crystal-growth process (Pfann 1962) has evolved as a paradigm. In particular, the critical conditions for the onset of a time-dependent flow in transparent high-Prandtl-number liquids has received considerable interest (Kuhlmann 1999), since an oscillator flow is known to cause crystal striation (Cröll *et al.* 1991). In these model systems,

† Email address for correspondence: mario.stojanovic@tuwien.ac.at
‡ Email address for correspondence: francesco.romano@ensam.eu
¶ Email address for correspondence: hendrik.kuhlmann@tuwien.ac.at

an axisymmetric liquid bridge between two coaxial support rods is heated differentially from the rods such that axial thermocapillary stresses drive a toroidal vortex in the liquid.

Transparent liquids with a moderate Prandtl, but still $\mathrm{Pr} > 1$, tend to be volatile which makes experimental investigations difficult (Simic-Stefani *et al.* 2006). Therefore, molten salts (Preisser *et al.* 1983) or silicone oils with a high Prandtl number $\mathrm{Pr} = 28$ or larger (Ueno *et al.* 2003; Kamotani *et al.* 2003) are frequently used in experiments. Since the viscosity of silicone oils increases with Prandtl number, the required temperature difference $\Delta T = T_{\mathrm{hot}} - T_{\mathrm{cold}}$ to drive the flow into the time-dependent regime increases. For length scales of millimetres and a Prandtl number of $\mathrm{Pr} = 28$ the critical temperature difference can easily amount to $\Delta T_c = 30\,\mathrm{K}$ or larger. Under such temperature variation the thermophysical properties of the liquid may vary considerably and the often used assumption of constant material parameters may no longer yield reliable numerical results for the critical Reynolds number. The present work is intended to overcome the limitations imposed by assuming constant material properties by taking into account the full, in general nonlinear, dependence of all material properties of the liquid and the gas on the temperature.

The first linear stability analysis of the flow in single-phase adiabatic thermocapillary liquid bridges for variable material properties is due to Kozhoukharova *et al.* (1999). For a liquid bridge with $\mathrm{Pr} = 4$ under zero gravity and a radius-to-height ratio of one, they numerically computed the critical Reynolds number for the onset of three-dimensional (and oscillatory) flow, assuming a linear variation with temperature of the kinematic viscosity $\nu(T) = \nu^* + \zeta(T - T_*)$, with reference viscosity $\nu^* = \nu(T^*)$ and $\zeta = (\partial\nu/\partial T)_{T^*}$. Evaluating the reference viscosity ν^* at the arithmetic mean temperature of the heaters $T^* = (T_{\mathrm{hot}} - T_{\mathrm{cold}})/2$, they found the critical temperature difference ΔT_c, or the critical Reynolds number $\mathrm{Re}_c \sim \Delta T_c/\nu^{*2}$, is typically reduced in liquids ($\zeta < 0$) as compared to the case of a constant kinematic viscosity ($\zeta = 0$). The reduction of ΔT_c (or Re_c) for $\zeta < 0$ was interpreted to be due to a reduction of the effective viscosity which was taken as the kinematic viscosity averaged over the interface $\nu_S(\zeta < 0) < \nu^*$. Under the hypothesis that a modified Reynolds number $\widetilde{\mathrm{Re}}_c = \Delta T_c/\nu_S^2$ using the effective kinematic viscosity (mean surface viscosity) would be almost independent of ζ, they suggested a correction factor $(\nu_S/\nu^*)^2$ to estimate the variable viscosity effect as $\mathrm{Re}_c(\zeta) = (\nu_S/\nu^*)^2\mathrm{Re}_c(\zeta = 0)$. While this correction always yields a reduction of the critical Reynolds number with $\mathrm{Re}_c(\zeta < 0) < \mathrm{Re}_c(\zeta = 0)$, the estimate $(\nu_S/\nu^*)^2\mathrm{Re}_c(\zeta = 0)$ can over- or under-predict the exact result $\mathrm{Re}_c(\zeta < 0)$ by about 10%.†

Shevtsova & Melnikov (2000) and Shevtsova *et al.* (2001) investigated the effect of a linear temperature dependence of the kinematic viscosity on the critical temperature difference through numerical simulation for a liquid bridge with $\mathrm{Pr} = 35$. They also found a reduction of the critical temperature difference. Different from Kozhoukharova *et al.* (1999), however, they defined the Reynolds number $\mathrm{Re} \sim \Delta T/\nu_{\mathrm{cold}}^2$ using a reference kinematic viscosity evaluated at the cold-wall temperature $\nu_{\mathrm{cold}} = \nu(T_{\mathrm{cold}})$. This leads to a much larger reduction of the critical Reynolds number with ζ, because the correction of $\mathrm{Re}_c(\zeta = 0)$ is much stronger with $1 < (\nu_S/\nu^*)^2 < (\nu_S/\nu_{\mathrm{cold}})^2$ for $\zeta < 0$. In other words, the kinematic viscosity ν_{cold} is not a good estimate of the effective viscosity, which is much better approximated by the mean viscosity ν^*. Regardless of the viscosity contrast, both Kozhoukharova *et al.* (1999) and Shevtsova & Melnikov (2000) found the instability arises as a hydrothermal wave (Smith 1986; Wanschura *et al.* 1995). Owing to the influence of the viscosity variation on the critical temperature difference a linear dependence of ν on T was also employed in succeeding simulations (see e.g. Melnikov *et al.* 2004; Shevtsova *et al.* 2009). Also Saifi *et al.* (2022) and

† The right hand side of (34) in Kozhoukharova *et al.* (1999) is lacking a factor ν_0^{-2}.

Shitomi *et al.* (2019) used a temperature-dependent viscosity, albeit assuming an exponential dependence on T.

On the experimental side Ueno *et al.* (2003), as well as most other investigators (see e.g. Nishino *et al.* 2015; Yano *et al.* 2015), took into account an exponential variation of the kinematic viscosity in order to determine the reference viscosity for the definition of the Reynolds or the Marangoni number. Like Kozhoukharova *et al.* (1999) they selected the reference viscosity ν_0, evaluated at the algebraic mean temperature.

While the critical Reynolds number of the thermocapillary flow in liquid bridges depends on the temperature dependence of the kinematic viscosity, the critical Rayleigh number in the Rayleigh–Bénard problem does not, because the basic flow is at rest. However, the sign of ζ has a qualitative influence on the planform of the supercritical convection. This was demonstrated experimentally by v. Tippelskirch (1956) who found polygonal convection cells in open layers of liquid sulfur heated from below. In temperature ranges in which $\partial_T \mu < 0$ the cells had upflow in their centres, whereas for temperature ranges with $\partial_T \mu > 0$ the flow in the cell centres was directed downwards. His findings confirmed the earlier observations of Graham (1933) for water and air according to which the flow in the centre of the cells is always directed towards increasing viscosity. The flow direction in the convection cells has been explained theoretically by Palm (1960) and Segel & Stuart (1962). According to Busse (1978) and Busse & Frick (1985) the flow direction minimizes the viscosity in the highly strained region near the cell centres.

Except for Kozhoukharova *et al.* (1999) and Carrión *et al.* (2020) most stability analyses have been carried out assuming a constant viscosity (e.g. Wanschura *et al.* 1995; Chen & Hu 1998; Nienhüser & Kuhlmann 2002; Stojanović *et al.* 2022). Therefore, the influence of the temperature dependence of the material properties on the critical conditions has not been thoroughly investigated. In this work we extend the previous analyses by carrying out linear stability analyses for the two-phase flow of a commonly used liquid–gas combination (2-cSt silicone oil and air) confined to a cylindrical tube. The full (nonlinear) temperature dependence of all thermophysical properties in the liquid and in the gas phase is taken into account. The critical Reynolds numbers obtained are then compared with results for a linear dependence of all thermophysical parameters and with those for the Oberbeck–Boussinesq approximation. For all calculations the basic state is computed for a dynamically deforming interface.

In § 2 the geometry is described and the mathematic problem is formulated. The numerical methods to solve the governing equations are discussed in § 3. In § 4 the reference parameters are defined and the temperature-dependence of the fluid properties are provided. Results are presented in § 5. In a first step the linear stability is computed for a sealed cylindrical tube surrounding the liquid bridge. The effects of the volume ratio of the liquid, the aspect ratio of the liquid bridge, and the length scale are discussed separately. Thereafter, the effect of an imposed axial flow in the gas phase on the linear stability boundary is considered. Finally, the results obtained are summarised in § 6 and conclusions are drawn.

2. Problem Formulation

2.1. *Setup*

We consider a droplet of an incompressible Newtonian silicone oil captured between two coaxial, cylindrical rods of radius r_i and length d_rod. The rods supporting the liquid bridge are separated axially by a distance d as shown in figure 1. Short liquid bridges can be hydrostatically stable, even in a terrestrial gravity field, depending on the wetting conditions and the geometry. Here we consider an axisymmetric geometry with the axial acceleration of

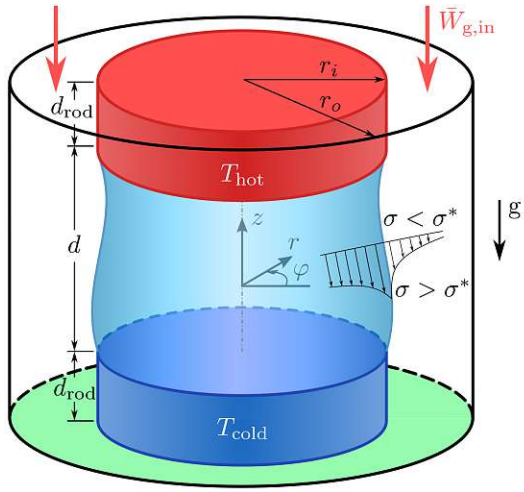

Figure 1: Schematic of the axisymmetric thermocapillary liquid bridge including the coordinate system. The sketch shows the situation when the liquid bridge is exposed to a hot gas stream with mean axial velocity $\bar{W}_{\mathrm{g,in}}$. The gravity vector $\boldsymbol{g}$ is always aligned with the negative z-axis. The thermocapillary effect is illustrated schematically through velocity vectors close to the interface.

gravity $\boldsymbol{g} = -g\boldsymbol{e}_z$, where $\boldsymbol{e}_z$ is the axial unit vector, while the liquid is heated from above. We assume the liquid bridge is pinned to the sharp circular edges of the two support rods. The gas phase (air) is Newtonian as well and it is bounded radially by a cylindrical tube of radius $r_{\mathrm{o}} > r_{\mathrm{i}}$ and height $2d_{\mathrm{rod}} + d$, placed coaxially around the liquid bridge and the support rods. The shield cylinder was first used in experiments by Preisser *et al.* (1983) and, more recently, by e.g. Simic-Stefani *et al.* (2006) and Gaponenko *et al.* (2021). To a good approximation, it can be considered thermally insulating. Thus the geometry of the problem is characterised by

$$\Gamma = \frac{d}{r_{\mathrm{i}}}, \qquad \Gamma_{\mathrm{rod}} = \frac{d_{\mathrm{rod}}}{r_{\mathrm{i}}}, \qquad \eta = \frac{r_{\mathrm{o}}}{r_{\mathrm{i}}}, \tag{2.1}$$

where Γ and Γ_{rod} describe the aspect ratios of the liquid bridge and the rods, respectively, and η is the radius ratio of the annular space between the tube and the support rods.

The support rods are kept at different but constant temperatures $T_{\mathrm{hot}} = \bar{T} + \Delta T/2$ and $T_{\mathrm{cold}} = \bar{T} - \Delta T/2$, respectively, where $\Delta T = T_{\mathrm{hot}} - T_{\mathrm{cold}} > 0$ is an imposed temperature difference. The mean temperature $\bar{T} = (T_{\mathrm{hot}} + T_{\mathrm{cold}})/2$ is used as the reference temperature $T^* = \bar{T}$. Owing to the imposed temperature difference the surface tension $\sigma(T)$ varies along the interface. Tangential surface tension gradients create surface stresses (Levich 1962) which drive a flow on both sides of the interface via the thermocapillary effect, as sketched in figure 1. Taylor expansion of $\sigma(T)$ about T^* yields the surface tension gradient

$$\begin{aligned} \nabla_{\parallel}\sigma(T) &= \frac{\partial\sigma}{\partial T}\nabla_{\parallel}T = \frac{\partial}{\partial T}\left[\sigma^* - \gamma^*(T - T^*) + \ \ldots\right]\nabla_{\parallel}T \\ &= \left\{-\gamma^* + O\left[(T - T^*)\right]\right\}\nabla_{\parallel}T \end{aligned} \tag{2.2}$$

where $\nabla_{\parallel} = \boldsymbol{t}(\boldsymbol{t}\cdot\nabla)$ is the Nabla operator in the plane tangent to the interface, $\boldsymbol{t}$ an arbitrary unit tangent vector, $\gamma^* = -\partial\sigma/\partial T|_{T=T^*}$ is the negative linear surface-tension coefficient and $\sigma^* = \sigma(T^*)$ is the reference (mean) surface tension. The asterisk indicates reference values of temperature-dependent thermophysical properties evaluated at T^*. The Taylor expansion in (2.2) is truncated after the linear term, since literature data on the coefficients of the higher-

order-terms for silicone oil in air are lacking. Within our modelling, we take into account the full temperature dependence of all other thermophysical properties and neglect the pressure dependence, assuming reference conditions far from phase-change critical points.

The flow in the liquid phase is driven by surface stresses which depend on the conditions in the gas phase. Thus, imposing a gas flow allows to passively control the flow in the liquid phase by varying the temperature and velocity (magnitude, profile) of the forced gas flow at the inlet, which is located either at the upper or the lower end of the tube. Owing to the low viscosity of gases under standard conditions, the gas flow affects the motion in the liquid phase primarily by altering the surface temperature and thus the thermocapillary stresses, and to a lesser degree by mechanical stresses on the interface. In addition, buoyancy forces drive the flow due to horizontal density gradients. For very small liquid bridges (thermocapillary) surface forces typically dominate (buoyant) volume forces. But for millimetric liquid bridges investigated under terrestrial conditions, buoyancy can significantly affect the interfacial shape and the fluid motion.

2.2. *Governing equations and boundary conditions*

2.2.1. *Transport equations*

Due to the axisymmetric geometry, we use cylindrical coordinates (r, φ, z) with the corresponding unit vectors $(\boldsymbol{e}_r, \boldsymbol{e}_\varphi, \boldsymbol{e}_z)$, and an origin centred in the middle of the liquid bridge. The velocity field is represented as $\boldsymbol{u} = u\boldsymbol{e}_r + v\boldsymbol{e}_\varphi + w\boldsymbol{e}_z$.

The fluid motion inside the liquid bridge is governed by the Navier–Stokes, continuity, and energy equations. For a Newtonian fluid with variable properties, they read in strong conservative form

$$\frac{\partial(\rho\boldsymbol{u})}{\partial t} + \nabla\cdot(\rho\boldsymbol{u}\boldsymbol{u}) = -\nabla P + \rho g\boldsymbol{e}_z + \nabla\cdot(\mu\boldsymbol{\mathcal{T}}), \tag{2.3a}$$

$$\frac{\partial\rho}{\partial t} + \nabla\cdot(\rho\boldsymbol{u}) = 0, \tag{2.3b}$$

$$\frac{\partial(\rho c_p T)}{\partial t} + \nabla\cdot(\rho c_p\boldsymbol{u}T) = \nabla\cdot(\lambda\nabla T), \tag{2.3c}$$

where t is time, P is the pressure and $\boldsymbol{\mathcal{T}} = \nabla\boldsymbol{u} + (\nabla\boldsymbol{u})^{\mathrm{T}} - (2/3)(\nabla\cdot\boldsymbol{u})\boldsymbol{\mathcal{I}}$ the deformation rate tensor with the identity matrix $\boldsymbol{\mathcal{I}}$. In contrast to most previous numerical studies on liquid bridges, we consider the dynamic viscosity $\mu(T)$, the density $\rho(T)$, the specific heat capacity $c_p(T)$, and the thermal conductivity $\lambda(T)$ to be fully temperature-dependent and call this the *FTD approach* (**F**ully **T**emperature-**D**ependent material properties) in contrast to, e.g., the Oberbeck–Boussinesq approximation (OB). The equations governing the gas phase are formally identical to (2.3). The material parameters relating to the gas phase ρ_g, μ_g, λ_g and $c_{p\mathrm{g}}$ are indicated by the subscript 'g'.

Using the reference material parameters of the liquid (superscript '*') evaluated at the reference temperature T^*, equations (2.3) are made dimensionless by the length, time, velocity, pressure and temperature scales d, $d^2\rho^*/\mu^*$, $\gamma^*\Delta T/\mu^*$, $\gamma^*\Delta T/d$ and ΔT, respectively. This yields

$$\frac{\partial(\alpha_\rho\boldsymbol{u})}{\partial t} + \mathrm{Re}\nabla\cdot(\alpha_\rho\boldsymbol{u}\boldsymbol{u}) = -\nabla p - \mathrm{Bd}\frac{\alpha_\rho - \alpha_\rho^*}{\varepsilon}\boldsymbol{e}_z + \nabla\cdot(\alpha_\mu\boldsymbol{\mathcal{T}}), \tag{2.4a}$$

$$\frac{\partial\alpha_\rho}{\partial t} + \mathrm{Re}\nabla\cdot(\alpha_\rho\boldsymbol{u}) = 0, \tag{2.4b}$$

$$\frac{\partial(\alpha_\rho\alpha_{cp}\vartheta)}{\partial t} + \mathrm{Re}\nabla\cdot\left(\alpha_\rho\alpha_{cp}\boldsymbol{u}\vartheta\right) = \frac{1}{\mathrm{Pr}}\nabla\cdot(\alpha_\lambda\nabla\vartheta), \tag{2.4c}$$

where $p = (d/\gamma^*\Delta T)(P - \rho^* g z)$ is the reduced pressure and

$$\vartheta = \frac{T - T^*}{\Delta T} \tag{2.5}$$

the reduced temperature. The Reynolds, Prandtl, and dynamic Bond numbers are respectively defined as

$$\mathrm{Re} = \frac{\rho^*\gamma^*\Delta T d}{\mu^{*2}}, \qquad \mathrm{Pr} = \frac{\mu^* c_p^*}{\lambda^*}, \qquad \mathrm{Bd} = \frac{\rho^* g \beta^* d^2}{\gamma^*}. \tag{2.6}$$

Equations (2.4) hold for both the liquid and the gas phase. They are distinguished by the functions $\alpha(\vartheta)$ and the parameter ε. The parameters $\varepsilon = \beta^*\Delta T$ and $\varepsilon_g = \beta_g^*\Delta T$ measure the magnitude of the density variation in the respective phase, where $\beta^* = -(1/\rho^*)(\partial\rho/\partial T)_P^*$ and β_g^* are the thermal expansion coefficients of the liquid and the gas, respectively, evaluated at $\vartheta^* = 0$. As in Stojanović *et al.* (2022) the phase is distinguished by selecting the respective set of thermophysical shape functions

$$\boldsymbol{\alpha} = \left[\alpha_\rho(\vartheta), \alpha_\mu(\vartheta), \alpha_\lambda(\vartheta), \alpha_{cp}(\vartheta)\right] = \begin{cases} \left[\dfrac{\rho(\vartheta)}{\rho^*}, \dfrac{\mu(\vartheta)}{\mu^*}, \dfrac{\lambda(\vartheta)}{\lambda^*}, \dfrac{c_p(\vartheta)}{c_p^*}\right] & \text{for the liquid phase,} \\ \left[\dfrac{\rho_g(\vartheta)}{\rho^*}, \dfrac{\mu_g(\vartheta)}{\mu^*}, \dfrac{\lambda_g(\vartheta)}{\lambda^*}, \dfrac{c_{pg}(\vartheta)}{c_p^*}\right] & \text{for the gas phase,} \end{cases} \tag{2.7}$$

which represent the temperature dependent material parameters, normalised by the values which the parameters take in the liquid at the reference temperature. A shape function evaluated at the reference point is indicated by an asterisk, i.e., $\alpha_\rho^* = \alpha_\rho(\vartheta^*) = 1$ for the liquid and $\alpha_\rho^* = \rho_g^*/\rho^*$ for the gas. The shape functions α_j with $j \in [\rho, \mu, \lambda, c_p]$ used will be specified in section 4. Note that in (2.4*a*) $(\alpha_\rho - \alpha_\rho^*)/\varepsilon = -\vartheta + O(\vartheta^2)$, recovering the buoyancy term in Boussinesq approximation at linear order. In a model assuming constant material parameters

$$\boldsymbol{\alpha} = \begin{cases} [1, 1, 1, 1] & \text{for the liquid phase,} \\ \left[\dfrac{\rho_g^*}{\rho^*}, \dfrac{\mu_g^*}{\mu^*}, \dfrac{\lambda_g^*}{\lambda^*}, \dfrac{c_{pg}^*}{c_p^*}\right] & \text{for the gas phase,} \end{cases} \tag{2.8}$$

and the bulk equations only depend Re, Pr and Bd.

2.2.2. *Linear stability equations*

For sufficiently small driving forces, measured either by the Reynolds number Re or the Marangoni number Ma = RePr, an axisymmetric and time-independent solution $\boldsymbol{q}_0(r, z) = (u_0, 0, w_0, p_0, \vartheta_0)$ (liquid) and $\boldsymbol{q}_{g0}(r, z) = (u_{g0}, 0, w_{g0}, p_{g0}, \vartheta_{g0})$ (gas) of (2.4) exists. This basic flow is indicated by a subscript '0'. The shape of the interface $h_0(z)$, separating the gas from the liquid phase, is part of the basic flow solution.

To investigate the linear stability of the basic flow the dynamics of small deviations from the basic solution must be considered. These deviations also concern the interfacial shape. Recent experiments (Yano *et al.* 2018*b*) revealed that the dynamic interfacial deformation caused by the perturbation flow is negligible. Therefore, we only consider perturbations of $\boldsymbol{q}_0$ and $\boldsymbol{q}_{g0}$ within their domains separated by the phase boundary $h_0(z)$. To carry out the linear stability analysis the general three-dimensional and time-dependent solution $[\boldsymbol{q}, \boldsymbol{q}_g]$ of (2.4) is decomposed into

$$\boldsymbol{q} = \boldsymbol{q}_0(r, z) + \tilde{\boldsymbol{q}}(r, \varphi, z, t) \quad \text{and} \quad \boldsymbol{q}_g = \boldsymbol{q}_{g0}(r, z) + \tilde{\boldsymbol{q}}_g(r, \varphi, z, t). \tag{2.9}$$

separating the perturbation flow $[\tilde{\boldsymbol{q}}, \tilde{\boldsymbol{q}}_\mathrm{g}]$ (indicated by a tilde) from the basic flow $[\boldsymbol{q}_0, \boldsymbol{q}_{\mathrm{g}0}]$.

The linear dynamics is obtained by inserting (2.9) in (2.4) and linearising all terms with respect to all perturbation quantities, in particular, with respect to $\tilde{\vartheta}$. This requires linearising the shape functions $\alpha_j(\vartheta)$ about their local values $\alpha_j[\vartheta_0(r,z)]$ determined by the basic flow. Taylor expansion about the local basic state temperature $\vartheta_0(r,z)$ yields

$$\alpha_j(\vartheta) = \alpha_j(\vartheta_0+\tilde{\vartheta}) = \alpha_j(\vartheta_0) + \left.\frac{\partial \alpha_j}{\partial \vartheta}\right|_{\vartheta_0} \tilde{\vartheta} + O(\tilde{\vartheta}^2) = \alpha_{j0} + \alpha'_{j0}\tilde{\vartheta} + O(\tilde{\vartheta}^2), \tag{2.10}$$

where the zeroth- and first-order Taylor coefficients $\alpha_{j0}[\vartheta_0(r,z)]$ and $\alpha'_{j0}[\vartheta_0(r,z)]$ are scalar fields that depend continuously on (r,z) through the basic temperature field $\vartheta_0(r,z)$. Using (2.10) we obtain the linearised version of (2.4) as

$$\alpha_{\rho0}\frac{\partial \tilde{\boldsymbol{u}}}{\partial t} + \alpha'_{\rho0}\boldsymbol{u}_0\frac{\partial \tilde{\vartheta}}{\partial t} + \mathrm{Re}\nabla\cdot\left(\alpha_{\rho0}\boldsymbol{u}_0\tilde{\boldsymbol{u}} + \alpha_{\rho0}\tilde{\boldsymbol{u}}\boldsymbol{u}_0 + \alpha'_{\rho0}\boldsymbol{u}_0\boldsymbol{u}_0\tilde{\vartheta}\right) = -\nabla\tilde{p} - \frac{\mathrm{Bd}}{\varepsilon}\alpha'_{\rho0}\tilde{\vartheta}\boldsymbol{e}_z + \nabla\cdot\left(\alpha_{\mu0}\tilde{\boldsymbol{\mathcal{T}}} + \alpha'_{\mu0}\boldsymbol{\mathcal{T}}_0\tilde{\vartheta}\right), \tag{2.11a}$$

$$\alpha'_{\rho0}\frac{\partial \tilde{\vartheta}}{\partial t} + \mathrm{Re}\nabla\cdot\left(\alpha_{\rho0}\tilde{\boldsymbol{u}} + \alpha'_{\rho0}\boldsymbol{u}_0\tilde{\vartheta}\right) = 0, \tag{2.11b}$$

$$\left[\alpha_{\rho0}\alpha_{cp0} + \vartheta_0(\alpha'_{\rho0}\alpha_{cp0} + \alpha_{\rho0}\alpha'_{cp0})\right]\frac{\partial \tilde{\vartheta}}{\partial t} + \mathrm{Re}\nabla\cdot\left(\alpha_{\rho0}\alpha_{cp0}\boldsymbol{u}_0\tilde{\vartheta} + \alpha_{\rho0}\alpha_{cp0}\vartheta_0\tilde{\boldsymbol{u}} + \alpha'_{\rho0}\alpha_{cp0}\vartheta_0\boldsymbol{u}_0\tilde{\vartheta} + \nabla\cdot\alpha_{\rho0}\alpha'_{cp0}\vartheta_0\boldsymbol{u}_0\tilde{\vartheta}\right) = \frac{1}{\mathrm{Pr}}\nabla\cdot\left(\alpha'_{\lambda0}\tilde{\vartheta}\nabla\vartheta_0 + \alpha_{\lambda0}\nabla\tilde{\vartheta}\right), \tag{2.11c}$$

where $\tilde{\boldsymbol{\mathcal{T}}} = \nabla\tilde{\boldsymbol{u}} + (\nabla\tilde{\boldsymbol{u}})^\mathrm{T} - (2/3)(\nabla\cdot\tilde{\boldsymbol{u}})\boldsymbol{\mathcal{I}}$ and $\boldsymbol{\mathcal{T}}_0 = \nabla\boldsymbol{u}_0 + (\nabla\boldsymbol{u}_0)^\mathrm{T} - (2/3)(\nabla\cdot\boldsymbol{u}_0)\boldsymbol{\mathcal{I}}$. The basic state solution enters parametrically in the linear disturbance equations for $\tilde{\boldsymbol{q}}$.

Since (2.11) is linear in $\tilde{\boldsymbol{q}}$ with coefficients which do not depend on φ and t, the general solution $\tilde{\boldsymbol{q}}$ of (2.11) can be constructed by a superposition of normal modes

$$\tilde{\boldsymbol{q}} = \sum_{j,m}\hat{\boldsymbol{q}}_{j,m}(r,z)\exp(\psi_{j,m}t + \mathrm{i}m\varphi) + \mathrm{c.c.}, \quad \tilde{\boldsymbol{q}}_\mathrm{g} = \sum_{j,m}\hat{\boldsymbol{q}}_{\mathrm{g}j,m}(r,z)\exp(\psi_{j,m}t + \mathrm{i}m\varphi) + \mathrm{c.c.}, \tag{2.12}$$

where the complex conjugates terms (c.c.) render the solution real. The normal modes are harmonic in φ with wave number $m \in \mathbb{N}_0$. The time dependence of each mode is exponential with the complex growth $\psi_{j,m} \in \mathbb{C}$. The index j numbers the discrete set of solutions for fixed m which arise due to the finite domain in r and z. Inserting the ansatz (2.12) into (2.11) yields partial differential equations for the complex amplitudes $\hat{\boldsymbol{q}}_{j,m}$ and $\hat{\boldsymbol{q}}_{\mathrm{g}j,m}$

$$\psi\left(\boldsymbol{u}_0\alpha'_{\rho0}\hat{\vartheta} + \alpha_{\rho0}\hat{\boldsymbol{u}}\right) + \mathrm{Re}\nabla\cdot\left[\alpha'_{\rho0}\hat{\vartheta}\boldsymbol{u}_0\boldsymbol{u}_0 + \alpha_{\rho0}(\boldsymbol{u}_0\hat{\boldsymbol{u}} + \hat{\boldsymbol{u}}\boldsymbol{u}_0)\right] + \mathrm{Re}\frac{\alpha_{\rho0}\mathrm{i}\hat{v}m\boldsymbol{u}_0}{r} = -\nabla\hat{p} - \frac{\mathrm{Bd}}{\varepsilon}\alpha'_{\rho0}\hat{\vartheta}\boldsymbol{e}_z + \nabla\cdot\left(\alpha'_{\mu0}\hat{\vartheta}\boldsymbol{\mathcal{T}}_0 + \alpha_{\mu0}\hat{\boldsymbol{\mathcal{T}}}\right) + \left(\alpha'_{\mu0}\hat{\vartheta}\boldsymbol{\mathcal{T}}_0 + \alpha_{\mu0}\hat{\boldsymbol{\mathcal{T}}} - \hat{p}\right)\frac{\mathrm{i}m\boldsymbol{e}_\varphi}{r} \tag{2.13a}$$

$$\psi\alpha'_{\rho0}\hat{\vartheta} + \mathrm{Re}\nabla\cdot\left(\alpha_{\rho0}\hat{\boldsymbol{u}} + \alpha'_{\rho0}\boldsymbol{u}_0\hat{\vartheta}\right) + \mathrm{Re}\frac{\alpha_{\rho0}\mathrm{i}\hat{v}m}{r} = 0, \tag{2.13b}$$

$$\psi\left[\vartheta_0(\alpha'_{\rho0}\alpha_{cp0}+\alpha_{\rho0}\alpha'_{cp0})+\alpha_{\rho0}\alpha_{cp0}\right]\hat{\vartheta} + \mathrm{Re}\nabla\cdot\left[(\alpha'_{\rho0}\alpha_{cp0} + \alpha_{\rho0}\alpha'_{cp0})\vartheta_0\boldsymbol{u}_0\hat{\vartheta} + \alpha_{\rho0}\alpha_{cp0}\hat{\vartheta}\boldsymbol{u}_0 + \alpha_{\rho0}\alpha_{cp0}\vartheta_0\hat{\boldsymbol{u}}\right] + \mathrm{Re}\frac{\alpha_{\rho0}\alpha_{cp0}\mathrm{i}\hat{v}m}{r} = \frac{1}{\mathrm{Pr}}\nabla\cdot\left[(\alpha'_{\lambda0}\hat{\vartheta}\nabla\vartheta_0 + \alpha_{\lambda0}\nabla\hat{\vartheta}) - \frac{\alpha_{\lambda0}\hat{\vartheta}m^2}{r^2}\right]. \tag{2.13c}$$

Discretisation of (2.13) leads to a large linear eigenvalue problem which must be solved to determine the stability boundary (section 3).

$m = 0:$	$\hat{u} = 0$	$\hat{v} = 0$	$\partial\hat{w}/\partial r = 0$	$\partial\hat{\vartheta}/\partial r = 0$
$m = 1:$	$\partial\hat{u}/\partial r = 0$	$\partial\hat{v}/\partial r = 0$	$\hat{w} = 0$	$\hat{\vartheta} = 0$
$m > 1:$	$\hat{u} = 0$	$\hat{v} = 0$	$\hat{w} = 0$	$\hat{\vartheta} = 0$

Table 1: Boundary conditions for the perturbation flow on $r = 0$.

2.2.3. *Boundary conditions*

The equations for the steady two-dimensional basic flow $\boldsymbol{q}_0$ satisfying (2.4) and those for the perturbation amplitudes $\hat{\boldsymbol{q}}$ according to the linear stability equations (2.11) must be solved subject to boundary and coupling conditions.

Solid walls: On all solid walls, the liquid and the gas must satisfy the no-slip conditions

$$\boldsymbol{u}_0 = \boldsymbol{u}_{g0} = 0 \quad \text{and} \quad \hat{\boldsymbol{u}} = \hat{\boldsymbol{u}}_g = 0, \tag{2.14}$$

In contrast to the outer shield, which is thermally insulated in the radial direction, the cylindrical support rods are assumed to be perfect heat conductors, leading to

$$\text{hot rod:} \quad \vartheta_0 = \vartheta_{g0} = 1/2 \quad \text{and} \quad \hat{\vartheta} = \hat{\vartheta}_g = 0, \tag{2.15a}$$

$$\text{cold rod:} \quad \vartheta_0 = \vartheta_{g0} = -1/2 \quad \text{and} \quad \hat{\vartheta} = \hat{\vartheta}_g = 0, \tag{2.15b}$$

$$\text{shield tube:} \quad \partial\vartheta_{g0}/\partial r = 0 \quad \text{and} \quad \partial\hat{\vartheta}_g/\partial r = 0. \tag{2.15c}$$

The amplitudes of the temperature perturbations vanish on the hot and cold walls since the imposed constant temperatures are taken care of by the basic state.

Axis of symmetry: On the axis $r = 0$ the symmetry of the basic state requires

$$u_0 = \frac{\partial w_0}{\partial r} = \frac{\partial \vartheta_0}{\partial r} = 0. \tag{2.16}$$

The boundary conditions for the perturbation amplitudes depend on the azimuthal wave number m and are given in table 1.

Liquid–gas interface: The liquid and the gas flow are coupled via the interface at $r = h_0(z)$ which is assumed to be determined by the basic flow only. Therefore, we first consider the basic flow. The continuity of the basic temperature and the basic heat flux requires

$$r = h_0: \quad \vartheta_0 = \vartheta_{g0}, \tag{2.17a}$$

$$r = h_0: \quad \alpha_{\lambda 0}\boldsymbol{n} \cdot \nabla\vartheta_0 = \alpha_{\lambda g0}\boldsymbol{n} \cdot \nabla\vartheta_{g0}, \tag{2.17b}$$

where

$$\boldsymbol{n} = \frac{1}{N}\left(\boldsymbol{e}_r - \frac{\mathrm{d}h_0}{\mathrm{d}z}\boldsymbol{e}_z\right) \quad \text{with} \quad N = \sqrt{1 + \left(\frac{\mathrm{d}h_0}{\mathrm{d}z}\right)^2}, \tag{2.18}$$

is the outward-pointing unit normal vector to the interface. The kinematic coupling conditions

$$r = h_0: \quad \boldsymbol{u}_0 = \boldsymbol{u}_{g0} \quad \text{and} \quad \frac{u_0}{w_0} = \frac{\mathrm{d}h_0}{\mathrm{d}z} \tag{2.19}$$

guarantee no slip on the interface and also enforce the basic streamlines to be parallel to the interface $h_0(z)$.

The dynamic coupling condition is represented by the stress balance on the interface. It is

decomposed into a normal stress balance

$$-(p_0 - p_{g0}) + \alpha_{\mu 0}\boldsymbol{n}\cdot\mathcal{T}_0\cdot\boldsymbol{n} + \left(\frac{1}{\mathrm{Ca}} - \vartheta_0\right)\nabla\cdot\boldsymbol{n} = -(\alpha_{\rho 0} - \alpha_{\rho g0})\frac{\mathrm{Bo}}{\mathrm{Ca}}z + \alpha_{\mu g0}\boldsymbol{n}\cdot\mathcal{T}_{g0}\cdot\boldsymbol{n}, \tag{2.20a}$$

and a tangential stress balance

$$\alpha_{\mu 0}\boldsymbol{t}\cdot\mathcal{T}_0\cdot\boldsymbol{n} = -\boldsymbol{t}\cdot\nabla\vartheta_0 + \alpha_{\mu g0}\boldsymbol{t}\cdot\mathcal{T}_{g0}\cdot\boldsymbol{n}, \tag{2.20b}$$

where $\boldsymbol{t}\perp\boldsymbol{n}$ is the unit tangent vector, and the basic-state shape functions, like $\alpha_{\mu g0}(r,z)$, depend on (r,z). In these non-dimensional equations

$$\mathrm{Ca} = \frac{\gamma^*\Delta T}{\sigma^*} \quad \text{and} \quad \mathrm{Bo} = \frac{\rho^* g d^2}{\sigma^*} \tag{2.21}$$

denote the capillary number and the static Bond number, respectively. Since the term $(\alpha_{\rho 0} - \alpha_{\rho g0})$ in (2.20*a*) takes care of the static pressure distribution in the gas phase, the reference density of the gas ρ_g^* does not enter Bo. This way, the non-dimensional material parameter

$$\tau = \frac{\rho^*\beta^*\sigma^*}{\gamma^*} = \frac{\mathrm{Bd}}{\mathrm{Bo}} = \frac{\varepsilon}{\mathrm{Ca}} \tag{2.22}$$

serves as a proportionality factor between the dynamic and static Bond numbers and also between ε and Ca.

Since the location $h_0(z)$ is part of the basic flow solution it is obtained iteratively by solving simultaneously the Navier–Stokes equations for both phases and imposing the coupling and boundary conditions. To that end, we assume the contact lines are pinned to the edges of the support rods, $h_0(\pm 1/2) = 1/\Gamma$, and impose the volume constraint

$$\Gamma^2\int_{-1/2}^{1/2} h_0(z)^2\mathrm{d}z = \mathcal{V}, \tag{2.23}$$

where $\mathcal{V} = V/\pi r_i^2 d$ is the ratio between the volume V occupied by the liquid and the upright cylindrical volume between the two support rods.

To assess the influence of the dynamic deformability of a dynamic interface (DI), we also consider a static interface (SI) whose shape $h(z)$, instead of the normal stress balance (2.20*a*), is determined by the solution of the Young–Laplace equation

$$\Delta p_h = \frac{\nabla\cdot\boldsymbol{n}}{\mathrm{Ca}} + \frac{\mathrm{Bo}}{\mathrm{Ca}}z, \tag{2.24}$$

where Δp_h is a constant pressure jump across the interface. For more details, see Stojanović *et al.* (2022).

Once the interface shape $h_0(z)$ and the basic state are computed, the coupling conditions for the perturbation amplitudes

$$\hat{\vartheta} = \hat{\vartheta}_g, \quad \alpha_{\lambda 0}\boldsymbol{n}\cdot\nabla\hat{\vartheta} = \alpha_{\lambda g0}\boldsymbol{n}\cdot\nabla\hat{\vartheta}_g, \quad \hat{\boldsymbol{u}} = \hat{\boldsymbol{u}}_g \tag{2.25}$$

and

$$\alpha_{\mu 0}\boldsymbol{t}\cdot\hat{\mathcal{T}}\cdot\boldsymbol{n} = -\boldsymbol{t}\cdot\nabla\hat{\vartheta} + \alpha_{\mu g0}\boldsymbol{t}\cdot\hat{\mathcal{T}}_g\cdot\boldsymbol{n} \tag{2.26}$$

can readily be imposed to solve the perturbation equations (2.13).

Inlet and outlet conditions: The boundary conditions at the ends of the shield tube, $z = \pm(1/2 + \Gamma_{\mathrm{rod}}/\Gamma)$, depend on whether the tube is sealed or open. In the case of a sealed tube, we prescribe no-slip and adiabatic conditions on both plane end walls

$$\boldsymbol{u}_{g0} = \hat{\boldsymbol{u}}_g = 0 \quad \text{and} \quad \partial\vartheta_{g0}/\partial z = \partial\hat{\vartheta}_g/\partial z = 0. \tag{2.27}$$

For an open tube, up-flow in the positive z direction and down-flow in the negative z direction are distinguished by the sign of the Reynolds number $\mathrm{Re_g} = \bar{W}_{\mathrm{g,in}}\rho^* d/\mu^*$, defined as in Stojanović *et al.* (2023*a*), which is taken positive for up-flow and negative for down-flow. The inlet (z_{in}) and outlet locations (z_{out}) are thus defined as

$$z_{\mathrm{in}} = \pm\,(1/2 + \Gamma_{\mathrm{rod}}/\Gamma) = -z_{\mathrm{out}} \quad \text{for} \quad \mathrm{Re_g} \lessgtr 0. \tag{2.28}$$

At the inlet, we prescribe a fully developed axial velocity profile

$$w_{\mathrm{g,in}}(r) = \frac{\mathrm{Re_g}}{\mathrm{Re}} \frac{2\ln(\eta)}{(\eta^2+1)\ln(\eta) - \eta^2 + 1}\left[1 - \Gamma^2 r^2 + \left(\eta^2 - 1\right)\frac{\ln(\Gamma r)}{\ln(\eta)}\right], \tag{2.29}$$

where the factor Re^{-1} arises due to the scaling. At the outlet, outflow conditions are used such that

$$z = z_{\mathrm{in}}\text{:} \qquad w_{\mathrm{g0}} = w_{\mathrm{g,in}}(r) \quad \text{and} \quad u_{\mathrm{g0}} = \hat{u}_{\mathrm{g}} = \hat{v}_{\mathrm{g}} = \hat{w}_{\mathrm{g}} = 0, \tag{2.30a}$$

$$z = z_{\mathrm{out}}\text{:} \quad \partial u_{\mathrm{g0}}/\partial z = \partial w_{\mathrm{g0}}/\partial z = 0 \quad \text{and} \quad \partial \hat{u}_{\mathrm{g}}/\partial z = \partial \hat{v}_{\mathrm{g}}/\partial z = \partial \hat{w}_{\mathrm{g}}/\partial z = 0. \tag{2.30b}$$

Following Stojanović *et al.* (2023*a*), constant temperatures are imposed at both ends of the tube

$$z = \pm\,(1/2 + \Gamma_{\mathrm{rod}}/\Gamma)\text{:} \quad \vartheta_{\mathrm{g0}} = \pm 1/2 \quad \text{and} \quad \hat{\vartheta}_{\mathrm{g}} = 0, \tag{2.31}$$

which are equal to the temperature of the respective adjacent support rod.

3. Numerical Methods

All numerical calculations required to compute the basic flow and its linear stability are carried out using the code `MaranStable` (Stojanović *et al.* 2023*b*). It is written in MATLAB and is available as open source from https://github.com/fromano88/MaranStable. The stability analysis implemented in `MaranStable` has been verified and validated extensively for statically and dynamically deformed liquid bridges, for single and two-phase flows where the gas phase is confined to a cylindrical tube about the liquid bridge being either closed or subject to through flow (Stojanović *et al.* 2022; Stojanovic *et al.* 2023). Grid convergence of `MaranStable` has been proven for a Boussinesq fluid of $\mathrm{Pr} = 28$ (Stojanović *et al.* 2022). Additional verifications and validations of `MaranStable` regarding the fully temperature-dependent properties (FTD) are provided in Appendix B.

3.1. *Basic flow*

In `MaranStable` the governing equations (2.4) and the boundary and coupling conditions are discretised by finite volumes using body-fitted coordinates. The physical mesh fitted to the interface shape is mapped to an orthogonal computational mesh using the surface shape $h_0(z)$. It is computed together with the flow field updating the physical and computational meshes after every iteration step. The resulting set of nonlinear algebraic equations is linearised and solved iteratively using the Newton-Raphson method. At the k-th iteration the known approximation $\boldsymbol{q}_0^{(k)}$ is updated by the increment $\delta\boldsymbol{q}$ to obtain the improved approximation

$$\boldsymbol{q}_0^{(k+1)} = \boldsymbol{q}_0^{(k)} + \delta\boldsymbol{q}. \tag{3.1}$$

Within the present fully temperature-dependent parameter approach, the nonlinear shape functions as well need to be linearised about their basic state value according to

$$\alpha_j\left(\vartheta_0^{(k+1)}\right) = \alpha_j\left(\vartheta_0^{(k)} + \delta\vartheta\right) \approx \alpha_j\left(\vartheta_0^{(k)}\right) + \left.\frac{\partial\alpha_j}{\partial\vartheta}\right|_{\vartheta_0^{(k)}} \delta\vartheta := \alpha_{j0}^{(k)} + \alpha_{j0}^{\prime(k)}\delta\vartheta, \tag{3.2}$$

where the increment $\delta\vartheta$ is contained in $\delta\boldsymbol{q}$. Inserting (3.1) and (3.2) into (2.4) yields the set of linear equations

$$\boldsymbol{J}\left(\boldsymbol{q}_0^{(k)}\right)\cdot\delta\boldsymbol{q} = -\boldsymbol{f}\left(\boldsymbol{q}_0^{(k)}\right), \tag{3.3}$$

where $\boldsymbol{J}\left(\boldsymbol{q}_0^{(k)}\right)$ and $\boldsymbol{f}\left(\boldsymbol{q}_0^{(k)}\right)$ are the Jacobian operator and the nonlinear residual of the Navier–Stokes equations, respectively. This leads to the linearised momentum, continuity and energy equations

$$\begin{aligned}
&\mathrm{Re}\nabla\cdot\left[\alpha_{\rho0}^{(k)}\left(\boldsymbol{u}_0^{(k)}\delta\boldsymbol{u}+\delta\boldsymbol{u}\boldsymbol{u}_0^{(k)}\right)+\alpha_{\rho0}^{\prime(k)}\boldsymbol{u}_0^{(k)}\boldsymbol{u}_0^{(k)}\delta\vartheta\right]\\
&\qquad+\nabla\delta p+\frac{\mathrm{Bd}}{\varepsilon}\alpha_{\rho0}^{\prime(k)}\delta\vartheta-\nabla\cdot\left(\alpha_{\mu0}^{(k)}\delta\boldsymbol{\mathcal{T}}-\alpha_{\mu0}^{\prime(k)}\boldsymbol{\mathcal{T}}_0^{(k)}\delta\vartheta\right)\\
&\quad=-\mathrm{Re}\nabla\cdot\left(\alpha_{\rho0}^{(k)}\boldsymbol{u}_0^{(k)}\boldsymbol{u}_0^{(k)}\right)-\nabla p_0^{(k)}-\frac{\mathrm{Bd}}{\varepsilon}\left(\alpha_{\rho0}^{(k)}\boldsymbol{e}_z-\alpha_\rho^*\right)+\nabla\cdot\left(\alpha_{\mu0}^{(k)}\boldsymbol{\mathcal{T}}_0^{(k)}\right),
\end{aligned} \tag{3.4a}$$

$$\nabla\cdot\left(\alpha_{\rho0}^{(k)}\delta\boldsymbol{u}+\alpha_{\rho0}^{\prime(k)}\boldsymbol{u}_0^{(k)}\delta\vartheta\right)=-\nabla\cdot\left(\alpha_{\rho0}^{(k)}\boldsymbol{u}_0^{(k)}\right), \tag{3.4b}$$

$$\begin{aligned}
&\mathrm{Ma}\nabla\cdot\left[\alpha_{\rho0}^{(k)}\alpha_{cp0}^{(k)}\left(\boldsymbol{u}_0^{(k)}\delta\vartheta+\vartheta_0^{(k)}\delta\boldsymbol{u}\right)+\left(\alpha_{\rho0}^{\prime(k)}\alpha_{cp0}^{(k)}+\alpha_{\rho0}^{(k)}\alpha_{cp0}^{\prime(k)}\right)\vartheta_0^{(k)}\boldsymbol{u}_0^{(k)}\delta\vartheta\right]\\
&-\nabla\cdot\left(\alpha_{\lambda0}^{\prime(k)}\delta\vartheta\nabla\vartheta_0^{(k)}+\alpha_{\lambda0}^{(k)}\nabla\delta\vartheta\right)=\nabla\cdot\left(\alpha_{\lambda0}^{(k)}\nabla\vartheta_0^{(k)}\right)-\mathrm{Ma}\nabla\cdot\left(\alpha_{\rho0}^{(k)}\alpha_{cp0}^{(k)}\boldsymbol{u}_0^{(k)}\vartheta_0^{(k)}\right),
\end{aligned} \tag{3.4c}$$

where $\delta\boldsymbol{\mathcal{T}}=\nabla\delta\boldsymbol{u}+(\nabla\delta\boldsymbol{u})^{\mathrm{T}}-(2/3)(\nabla\cdot\delta\boldsymbol{u})\boldsymbol{\mathcal{I}}$. An additional iteration loop arising from the normal stress balance (2.20*a*) is embedded in the Newton-Raphson iteration that updates the surface shape $h_0(z)$ after each iteration step. Neglecting terms of order $O(\vartheta^2)$ in $\sigma(\vartheta)$, the linearised normal stress balance becomes

$$\begin{aligned}
&-(\delta p-\delta p_{\mathrm{g}})+\alpha_{\mu0}^{(k)}\boldsymbol{n}^{(k)}\cdot\delta\boldsymbol{\mathcal{T}}\cdot\boldsymbol{n}^{(k)}+\alpha_{\mu0}^{(k)}\boldsymbol{n}^{(k)}\cdot\boldsymbol{\mathcal{T}}_0^{(k)}\cdot\delta\boldsymbol{n}+\alpha_{\mu0}^{(k)}\delta\boldsymbol{n}\cdot\boldsymbol{\mathcal{T}}_0^{(k)}\cdot\boldsymbol{n}^{(k)}\\
&+\alpha_{\mu0}^{\prime(k)}\boldsymbol{n}^{(k)}\cdot\boldsymbol{\mathcal{T}}_0^{(k)}\cdot\boldsymbol{n}^{(k)}\delta\vartheta+\left(\frac{1}{\mathrm{Ca}}-\vartheta_0^{(k)}\right)\nabla\cdot\delta\boldsymbol{n}-\nabla\cdot\boldsymbol{n}^{(k)}\delta\vartheta+\left(\alpha_{\rho0}^{\prime(k)}-\alpha_{\rho\mathrm{g}0}^{\prime(k)}\right)\frac{\mathrm{Bo}}{\mathrm{Ca}}\delta\vartheta z\\
&-\alpha_{\mu\mathrm{g}0}^{(k)}\boldsymbol{n}^{(k)}\cdot\delta\boldsymbol{\mathcal{T}}_{\mathrm{g}}\cdot\boldsymbol{n}^{(k)}-\alpha_{\mu\mathrm{g}0}^{(k)}\boldsymbol{n}^{(k)}\cdot\boldsymbol{\mathcal{T}}_{\mathrm{g}0}^{(k)}\cdot\delta\boldsymbol{n}-\alpha_{\mu\mathrm{g}0}^{(k)}\delta\boldsymbol{n}\cdot\boldsymbol{\mathcal{T}}_{\mathrm{g}0}^{(k)}\cdot\boldsymbol{n}^{(k)}\\
&-\alpha_{\mu\mathrm{g}0}^{\prime(k)}\boldsymbol{n}^{(k)}\cdot\boldsymbol{\mathcal{T}}_{\mathrm{g}0}^{(k)}\cdot\boldsymbol{n}^{(k)}\delta\vartheta=p_0^{(k)}-p_{\mathrm{g}0}^{(k)}-\left(\alpha_{\rho0}^{(k)}-\alpha_{\rho\mathrm{g}0}^{(k)}\right)\frac{\mathrm{Bo}}{\mathrm{Ca}}z-\alpha_{\mu0}^{(k)}\boldsymbol{n}^{(k)}\cdot\boldsymbol{\mathcal{T}}_0^{(k)}\cdot\boldsymbol{n}^{(k)}\\
&\qquad-\left(\frac{1}{\mathrm{Ca}}-\vartheta_0^{(k)}\right)\nabla\cdot\boldsymbol{n}^{(k)}+\alpha_{\mu\mathrm{g}0}^{(k)}\boldsymbol{n}^{(k)}\cdot\boldsymbol{\mathcal{T}}_{\mathrm{g}0}^{(k)}\cdot\boldsymbol{n}^{(k)},
\end{aligned} \tag{3.5}$$

where the surface increment

$$\delta h_0=h_0^{(k+1)}-h_0^{(k)} \tag{3.6}$$

is contained implicitly in the increment of the surface normal vector

$$\delta\boldsymbol{n}=\boldsymbol{n}^{(k+1)}-\boldsymbol{n}^{(k)} \tag{3.7}$$

with

$$\delta\boldsymbol{n}=-\frac{1}{N^{(k)^3}}\frac{\mathrm{d}h_0^{(k)}}{\mathrm{d}z}\frac{\mathrm{d}\delta h_0}{\mathrm{d}z}\boldsymbol{e}_r-\frac{1}{N^{(k)}}\left[1-\frac{1}{N^{(k)^2}}\left(\frac{\mathrm{d}h_0^{(k)}}{\mathrm{d}z}\right)^2\right]\frac{\mathrm{d}\delta h_0}{\mathrm{d}z}\boldsymbol{e}_z \tag{3.8}$$

and its divergence

$$\nabla\cdot\delta\boldsymbol{n} = \frac{1}{h_0^{(k)^3}N^{(k)^3}}\left[-h_0^{(k)^3}\frac{\mathrm{d}^2\delta h_0}{\mathrm{d}z^2}+\left(\frac{3h^{(k)^3}}{N^{(k)^2}}\frac{\mathrm{d}^2h_0^{(k)}}{\mathrm{d}z^2}-h_0^{(k)^2}\right)\frac{\mathrm{d}h_0^{(k)}}{\mathrm{d}z}\frac{\mathrm{d}\delta h_0}{\mathrm{d}z}-h_0^{(k)}N^{(k)^2}\delta h_0\right]. \tag{3.9}$$

3.2. *Linear stability analysis*

`MaranStable` executes a linear stability analysis of the basic flow by discretising the linear perturbation equations (2.13) for the amplitudes $\hat{\boldsymbol{q}}_{j,m}$ and $\hat{\boldsymbol{q}}_{g;j,m}$ on the same grid and employing the same numerical scheme as used for the basic state. The resulting large system of algebraic equations represents a generalised eigenvalue problem for the spatial structure of the perturbation flow (eigenvector) and the complex growth rate $\psi_{j,m}$ (eigenvalue) for a given wave number m. The real growth rate $\Re(\psi_{j,m})$ determines the stability of the respective mode, whereas its imaginary part $\omega_c = \Im[\psi_{j,m}(\mathrm{Re}_c)]$ represents the angular frequency. The mode whose real growth rate vanishes at a particular Reynolds number is called neutral mode and the corresponding Reynolds number is identified as the neutral Reynolds number $\mathrm{Re}_n^{j,m}$. The minimum value $\mathrm{Re}_c = \min_{j,m\geqslant 0}\mathrm{Re}_n^{j,m}$ defines the critical Reynolds number Re_c. To identify the eigenvalues with the largest real part, we follow Stojanović *et al.* (2022) and use an implicitly restarted Arnoldi method provided by ARPACK (Lehoucq *et al.* 1998). The neutral curves are obtained by arclength continuation (Keller 1977) for moderate step sizes of the dependent (Re) and independent parameters ($\mathcal{V}$, Γ, d or Re_g).

3.3. *Postprocessing: Energetics*

The Reynolds–Orr type of equations for the kinetic and thermal energies of the perturbation flow can be obtained in the usual way. For variable material properties Stojanović *et al.* (2023*a*) have derived the rates of change of the total kinetic ($\mathrm{d}E_{\mathrm{kin}}/\mathrm{d}t$) and the total thermal energy ($\mathrm{d}E_{\mathrm{th}}/\mathrm{d}t$) in the form

$$\frac{\mathrm{d}E_{\mathrm{kin}}}{\mathrm{d}t} = -1 + M_r + M_\varphi + M_z + \sum_{j=1}^{5} I_j + B + K_{\mathrm{g}} \underbrace{+\Lambda_\rho + \Lambda_\mu + \Lambda_{\rho\mu}}, \tag{3.10a}$$

$$\frac{\mathrm{d}E_{\mathrm{th}}}{\mathrm{d}t} = -1 + \sum_{j=1}^{2} J_j + H_{\mathrm{fs}} + K_{\mathrm{g,th}} \underbrace{-\frac{\mathrm{d}E'_{\mathrm{th}}}{\mathrm{d}t} + \Pi_\rho + \Pi_{cp} + \Pi_\lambda}, \tag{3.10b}$$

providing explicit expressions in dimensional from for all terms appearing on the right hand sides. Since the non-dimensionalisation of the energy budgets is straightforward, we refrain from reproducing all expression here. Most terms in (3.10) also arise in the Oberbeck–Boussinesq (OB) approximation. They have the usual meaning (see e.g. Nienhüser & Kuhlmann 2002; Stojanović *et al.* 2022). The additional terms arising in the FTD model are indicated by the underbraces in (3.10).

All terms in (3.10) are volume integrals over the space occupied by the liquid or the gas, or surface integrals over the interface or the inlet for the gas. The integrands represent local production/dissipation rates of kinetic or thermal energy of the perturbation flow which are often useful to understand the local physical mechanisms by which energy is exchanged between the basic state and the perturbation. The spatial distribution of the integrands thus serve a better understanding of the overall instability mechanism (see e.g. Wanschura *et al.* 1995; Nienhüser & Kuhlmann 2002). Stojanović *et al.* (2023*a*) have shown that the instability mechanism for $\mathrm{Pr} = 28.8$ is that of a hydrothermal wave and that the mechanism as such is hardly influenced by the temperature dependence of the material parameters. However, the critical Reynolds numbers can be significantly affected. We shall make use of (3.10) to

identify the regions of largest perturbation energy production and for the analysis of a new instability in the gas phase in section 5.1.2.

4. Geometry, fluids and temperature-dependence of their properties

Owing to the high-dimensional parameters space we consider a common reference geometry as the origin of all parameter variations to be made. Therefore, we adopt the same geometry as in Romanò *et al.* (2017) with rod radius $r_{\mathrm{i,ref}} = 2.5\,\mathrm{mm}$, $\Gamma_{\mathrm{ref}} = 0.66$, $\Gamma_{\mathrm{rod,ref}} = 0.4$, $\eta_{\mathrm{ref}} = 4$, $\mathcal{V}_{\mathrm{ref}} = 1$, $\mathrm{Re_g} = \mathrm{Re_{g,ref}} = 0$ and $\mathrm{Bd_{ref}} = 0.363$. Note the origin for the parameter space made by the geometry and forcing parameters is indicated by the subscript 'ref', while the reference point for the temperature-dependent material properties is denoted by the superscript '*'.

Owing its importance for experiments (Majima *et al.* 2001; Tanaka *et al.* 2006; Yano *et al.* 2018*a*; Ueno 2021) we consider a liquid bridge made from 2-cSt silicone oil (KF96L-2cs, Shin-Etsu Chemical Co., Ltd., Japan) in air under typical experimental conditions for $T^* = \bar{T} = 25\,^{\circ}\mathrm{C}$. The functions $\rho(T)$, $\mu(T)$, $\lambda(T)$ and $c_p(T)$ required in (2.3) can be obtained either through explicitly given correlations or by fitting tabulated data to suitable ansatz functions. The functional dependencies used herein are provided in Appendix A for each property of both the working fluids. Once the continuous functions have been constructed, the reference quantities are evaluated (table 2) and the non-dimensional shape function $\alpha_j(T)$ defined in (2.7) are obtained for both phases. Finally, the shape functions are expressed in terms of the reduced temperature: $\alpha_j(T) \to \alpha_j(\vartheta)$ such that $\alpha_j^* = \alpha_j(\vartheta = 0)$. For the present liquid–gas couple, the shape functions read

$$\alpha_\rho(\vartheta) = \begin{cases} \xi_{\mathrm{I}} - \xi_{\mathrm{II}}\mathrm{Ca}\vartheta + \xi_{\mathrm{III}}\mathrm{Ca}^2\vartheta^2, \\ \dfrac{\zeta_{\mathrm{I}}}{1 + \zeta_{\mathrm{II}}\mathrm{Ca}\vartheta}, \end{cases} \tag{4.1a}$$

$$\alpha_\mu(\vartheta) = \begin{cases} (\xi_{\mathrm{I}} - \xi_{\mathrm{II}}\mathrm{Ca}\vartheta + \xi_{\mathrm{III}}\mathrm{Ca}^2\vartheta^2)\exp[\xi_{\mathrm{IV}}\mathrm{Ca}\vartheta/(\xi_{\mathrm{V}} + \mathrm{Ca}\vartheta)], \\ \zeta_{\mathrm{I}} + \zeta_{\mathrm{II}}\mathrm{Ca}\vartheta + \zeta_{\mathrm{III}}\mathrm{Ca}^2\vartheta^2 + \zeta_{\mathrm{IV}}\mathrm{Ca}^3\vartheta^3 + \zeta_{\mathrm{V}}\mathrm{Ca}^4\vartheta^4, \end{cases} \tag{4.1b}$$

$$\alpha_\lambda(\vartheta) = \begin{cases} \xi_{\mathrm{I}} + \xi_{\mathrm{II}}\mathrm{Ca}\vartheta + \xi_{\mathrm{III}}\mathrm{Ca}^2\vartheta^2, \\ \zeta_{\mathrm{I}} + \zeta_{\mathrm{II}}\mathrm{Ca}\vartheta + \zeta_{\mathrm{III}}\mathrm{Ca}^2\vartheta^2 + \zeta_{\mathrm{IV}}\mathrm{Ca}^3\vartheta^3 + \zeta_{\mathrm{V}}\mathrm{Ca}^4\vartheta^4, \end{cases} \tag{4.1c}$$

$$\alpha_{cp}(\vartheta) = \begin{cases} \xi_{\mathrm{I}} + \xi_{\mathrm{II}}\mathrm{Ca}\vartheta + \xi_{\mathrm{III}}\mathrm{Ca}^2\vartheta^2, \\ \zeta_{\mathrm{I}} + (\zeta_{\mathrm{II}} - \zeta_{\mathrm{I}})G^2(\vartheta)\left[1 - F(\vartheta)\left(\zeta_{\mathrm{III}} + \zeta_{\mathrm{IV}}G(\vartheta) + \zeta_{\mathrm{V}}G^2(\vartheta) + \zeta_{\mathrm{VI}}G^3(\vartheta)\right)\right], \end{cases} \tag{4.1d}$$

where the first line of each subequation specifies the property of the liquid, while the second line represents the property of the gas. The coefficients ξ_n and ζ_n ($n = \mathrm{I}, \mathrm{II}, \mathrm{III}, \ldots$) in (4.1) are constants specific to the respective thermophysical property, and

$$G(\vartheta) = \frac{c_{\mathrm{I}} + \mathrm{Ca}\vartheta}{c_{\mathrm{II}} + \mathrm{Ca}\vartheta}, \qquad F(\vartheta) = \frac{c_{\mathrm{II}} - c_{\mathrm{I}}}{c_{\mathrm{II}} + \mathrm{Ca}\vartheta}, \tag{4.2}$$

with $c_{\mathrm{I}} = 1.14046$ and $c_{\mathrm{II}} = 10.89048$. All constant coefficients are collected in tables 3 and 4 for the liquid and the gas, respectively. Except for α_{cp} for the gas, all coefficients ζ_{I} represent the reference quantities, e.g., $\zeta_{\mathrm{I}} = \alpha_\rho^* = \alpha_\rho(0) = \rho_{\mathrm{g}}(25^{\circ}\mathrm{C})/\rho(25^{\circ}\mathrm{C})$.

The shape functions α_j of the four thermophysical parameters for the liquid and the gas are shown in figure 2(a) and 2(b), respectively. Shown is the relative variation within each fluid phase of the density, viscosity, thermal conductivity and specific heat as function of ϑ for a relatively large temperature difference of $\Delta T = 50\,\mathrm{K}$. For this temperature difference, most

Property	KF96L-2cs	air	Dimension
ρ^*	873.25	1.1837	[kg/m^3]
μ^*	1.7465×10^{-3}	1.8460×10^{-5}	[Pa s]
λ^*	0.10904	2.6374×10^{-2}	[W/(mK)]
c_p^*	1800.76	1005.70	[J/(kgK)]
β^*	1.0879×10^{-3}	3.3540×10^{-3}	[1/K]
σ^*	18.3×10^{-3}		[N/m]
γ^*	7×10^{-5}		[N/(mK)]
Pr	28.84	0.704	

Table 2: Reference quantities evaluated at $T^* = 25°\mathrm{C}$.

α_j	ξ_I	ξ_II	ξ_III	ξ_IV	ξ_V
α_ρ	1	0.2844	0.049714		
α_μ	1	0.2844	0.049714	-5.892	1.1405
α_λ	1	−0.6807	−0.004936		
α_{cp}	1	0.2147	0.001134		

Table 3: Coefficients ξ_n appearing in the shape functions for 2-cSt silicone oil.

α_j	ζ_I	ζ_II	ζ_III	ζ_IV	ζ_V	ζ_VI
α_ρ	0.001356	0.876838				
α_μ	0.010570	0.007286	−0.001378	0.00033808	−0.00003712	
α_λ	0.241886	0.180413	−0.026150	0.00627974	−0.00066962	
α_{cp}	0.561961	−0.101493	−3.4281	49.8238	−120.3466	98.8658

Table 4: Coefficients ζ_n appearing in the shape functions for air.

parameters vary almost linearly with a variation of about $\approx 10\%$. An exception is the shape function α_μ for the viscosity of the silicone oil (figure 2(a)). It varies by $\approx 100\%$ relative to $\alpha_\mu^* = 1$ and has significant nonlinear contributions. This observation indicates the need to take these variations into account.

Ideally, the full temperature dependence of all parameters as shown in figure 2 is taken into account (FTD model). A less demanding approach is the LTD model (**L**inear **T**emperature **D**ependence) in which all thermophysical parameters are approximated by linear functions

$$\frac{\alpha_j(\vartheta)}{\alpha_j^*} = 1 + \frac{\alpha_j'^*}{\alpha_j^*}\vartheta + O(\vartheta^2) \tag{4.3}$$

and terms of $O(\vartheta^2)$ are neglected. Within the well-known **O**berbeck–**B**oussinesq model (OB) only the density $\rho(\vartheta)$ in the buoyancy term is approximated according to (4.3) while all the other parameters are assumed constant. At times, we also investigate the influence of a single parameter only on the stability boundary, as in Stojanović *et al.* (2023*a*), keeping the remaining parameters constant.

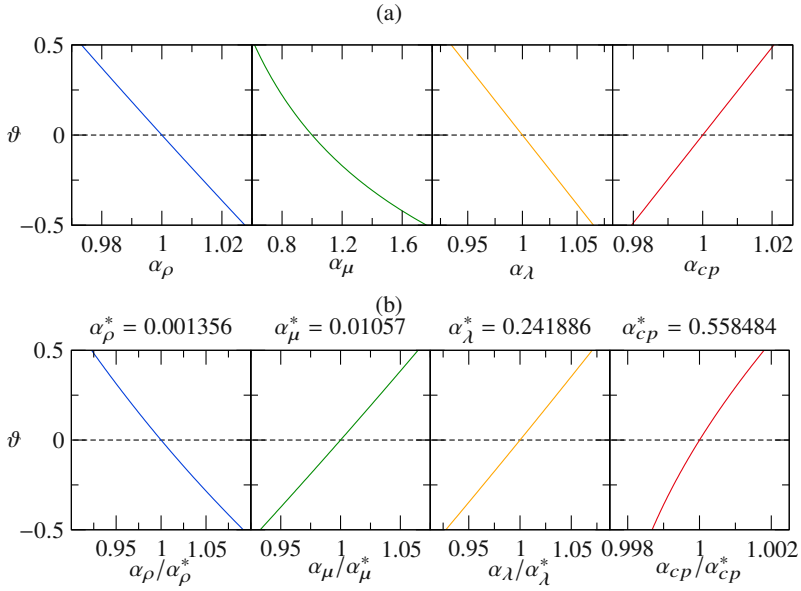

Figure 2: Normalised shape functions α_j/α_j^* for 2-cSt silicone oil ($\alpha_j^* = 1$) (a) and for air (b) evaluated at the reference temperature $T^* = 25\,^\circ\mathrm{C}$ and for $\Delta T = 50\,\mathrm{K}$. The reference parameters α_j^* for air are shown as subcaptions in (b).

A systematic quantification of the variability of the thermophysical parameters has been provided by Stojanović *et al.* (2023*a*), in particular their tables 1 and 2. In linear approximation (4.3), a maximum relative deviation of $c/2$ of a particular thermophysical parameter leads to the requirement ($\vartheta \in [-0.5,\ 0.5]$)

$$\left|\frac{\alpha_j'^*}{\alpha_j^*}\right| < c. \tag{4.4}$$

The most severe restriction on ΔT is posed by the viscosity of the liquid. To satisfy (4.4) with $c = 0.1$ (Gray & Giorgini 1976), for instance, restricts the allowable temperature difference to $\Delta T = c\mu^*/(\partial\mu/\partial T)^* \leqslant 4.8\,\mathrm{K}$.

5. Results

Originating from the reference values of the geometry and driving parameters (subscript ref) the critical thermocapillary Reynolds number Re_c is calculated as function of the relative volume $\mathcal{V}$ of the liquid bridge, the aspect ratio Γ, the size of the system (length scale d) and the gas flow Reynolds number Re_g. These parameters are varied over the following ranges.

(i) The volume ratio is varied within $\mathcal{V} \in [0.66,\ 1.3]$ for $\Gamma = \Gamma_\mathrm{ref}$, $\mathrm{Re}_\mathrm{g} = \mathrm{Re}_\mathrm{g,ref}$ and $\mathrm{Bd} = \mathrm{Bd}_\mathrm{ref}$.

(ii) The aspect ratio of the liquid bridge is changed in the range $\Gamma \in [0.5,\ 1.8]$ by varying the distance d between the rods for $\mathcal{V} = \mathcal{V}_\mathrm{ref}$ and $\mathrm{Re}_\mathrm{g} = \mathrm{Re}_\mathrm{g,ref}$. The change of d also affects the dynamic Bond number $\mathrm{Bd} \sim d^2$. In order to enable a comparison of the numerical results with laboratory experiments, by varying d we do not keep the dynamic Bond number constant but simultaneously vary $\mathrm{Bd} \in [0.208,\ 3.70]$ such that $\mathrm{Bd} = \mathrm{Bd}_\mathrm{ref}(\Gamma/\Gamma_\mathrm{ref})^2$.

(iii) The size of the system is varied by changing $d \in [0.1,\ 3]\,\mathrm{mm}$ for $\Gamma = \Gamma_\mathrm{ref}$, $\mathcal{V} = \mathcal{V}_\mathrm{ref}$

and $\mathrm{Re_g} = \mathrm{Re_{g,ref}}$. As for the variation of Γ, the dynamic Bond number varies $\sim d^2$ and we vary the Bond number accordingly in the range $\mathrm{Bd} \in [0.016,\ 1.20]$.

(iv) The strength of the gas flow is varied within $\mathrm{Re_g} \in [-3500,\ 1500]$ for $\Gamma = \Gamma_{\mathrm{ref}}$, $\mathcal{V} = \mathcal{V}_{\mathrm{ref}}$ and $\mathrm{Bd} = \mathrm{Bd_{ref}}$.

While the first, second, and fourth variations are often conducted in experiments (see e.g. Melnikov *et al.* 2015; Yano *et al.* 2016; Gaponenko *et al.* 2021), the third variation is intended to reveal the length scale below which the flow in the thermocapillary liquid bridge becomes independent of buoyancy forces under terrestrial conditions.

5.1. *Liquid bridge inside a sealed tube*

5.1.1. *Effect of the volume ratio on the stability boundary*

Figure 3 shows the dependence of the critical Reynolds number Re_c (a) and frequency ω_c (b) as a functions of the volume ratio $\mathcal{V}$ taking into account a dynamically deforming interface in the basic flow. Three different flow models are considered: (a) full temperature dependence of all parameters (FTD, full lines), (b) linear temperature dependence of all parameters (LTD, dashed lines) and (c) the Oberbeck–Boussinesq approximation (OB, dash-dotted lines). In addition, the black dash-dotted curves are reproduced from Stojanović *et al.* (2022) who used the OB model, but for slightly different reference parameters and an indeformable, hydrostatic interface according to (2.24) (see Section 5.1.2). Note that this line does not distinguish between different wave numbers.

The larger the temperature difference the larger are the deviations among the three models. Based on the usual criterion $c = 0.1$ the OB approximation should be valid only for temperature differences up to $\Delta T \leqslant 4.8\,\mathrm{K}$ (due to the variability of μ). Nevertheless, the OB approximation yields critical Reynolds numbers Re_c which deviate less than ±5% (grey region in figure 3(a)) from those obtained using the FTD model as long as $\Delta T \lesssim 28\,\mathrm{K}$. The linearised model (LTD, dashed) compares overall better with the FTD model, yet the dashed line (LTD) leaves the grey 5% tolerance region in the range $\mathcal{V} \in [0.752, 0.785]$ at $\Delta T \approx 27\,\mathrm{K}$. The difference in Re_c between the linearised (dashed) and the FTD model (full) becomes more significant in the range $\mathcal{V} \in [0.842, 0.898]$ for $\Delta T \gtrsim 45\,\mathrm{K}$.

The volume ratio $\mathcal{V}$ has a strong effect on the stability boundary. The slope of $\mathrm{Re}_c(\mathcal{V})$ is particularly large and changes its sign at the peak near $\mathcal{V} = 0.85$. Moreover, the wave number and the structure of the critical mode changes along the critical curve. This indicates the value of Re_c is sensitive with respect to small variations of $\mathcal{V}$ in this region. This sensitivity exists in addition to the sensitivity of Re_c with respect to the model (OB, LTD or FTD) used. For most volume ratios the critical Reynolds number for the OB model $\mathrm{Re}_c^{\mathrm{OB}} > \mathrm{Re}_c^{\mathrm{FTD}}$ is larger than the one of the FTD model which itself is slightly larger than the one of the LTD model. To the right of the peak the critical oscillation frequencies in figure 3(b) exhibit a similar trend as critical Reynolds number. For lower volume ratios, however, the critical frequencies are much lower.

As an example we consider $\mathcal{V} = 0.88$ (green square in figure 3) for which $m_c = 3$ for all models. We find that the structure of the basic flow (full and dashed lines in figure 4) and of the respective most dangerous modes (comparison not shown) for all three parameter models are almost identical for $\mathcal{V} = 0.88$. The higher critical Reynolds number for the OB model in comparison to the ones for the FTD and LTD models in this case might be related to the strong variation of the local viscosity, more precisely, the local kinematic viscosity. Owing to the relatively weak variation of α_ρ compared to α_μ (c.f. blue and green curve in figure 2(a)) for the liquid, we focus on the local kinematic viscosity

$$\nu(\vartheta) = \frac{\mu}{\rho} = \frac{\alpha_\mu}{\alpha_\rho}\nu^*. \tag{5.1}$$

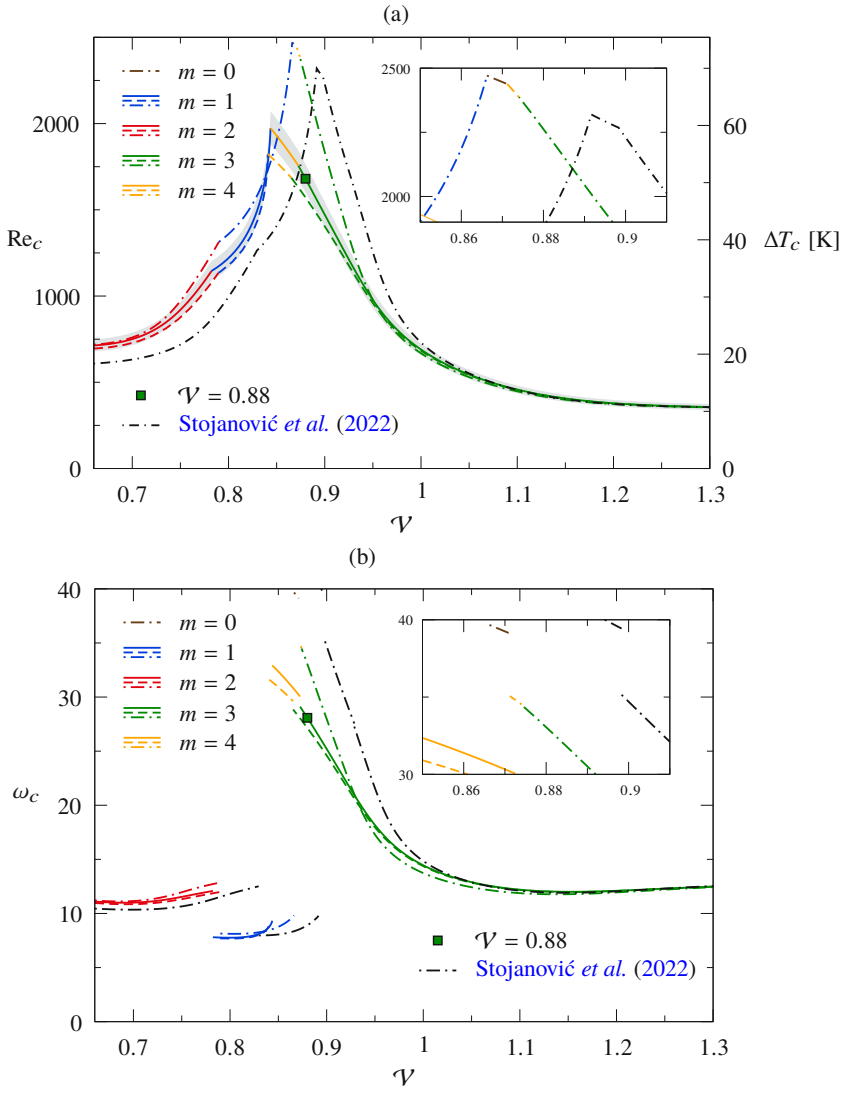

Figure 3: (a) Critical Reynolds number Re_c (left side) and critical temperature difference ΔT_c (right side) as functions of the volume ratio $\mathcal{V}$ for $\Gamma = 0.66$, $\mathrm{Bd} = \mathrm{Bd}_{\mathrm{ref}}$ and a sealed tube: FTD model (full lines), OB model (dash-dotted lines) and LTD model (dashed lines). The gray-shaded region indicates a deviation of ±5% from the FTD model. Critical wave number are indicated by colour (see legend). Inserts show zooms into the regions in which $m_c = 0$. (b) Critical frequencies.

Its relative deviation from the nominal value $\nu^* = 2 \times 10^{-6}\,\mathrm{m}^2/\mathrm{s}$ is given by

$$\epsilon_\nu(\vartheta) = \frac{\nu - \nu^*}{\nu^*} = \frac{\alpha_\mu}{\alpha_\rho} - 1. \tag{5.2}$$

From figure 4(a) the local kinematic viscosity ν near the cold wall is larger by more than 60% than the nominal value, while near the hot wall and the free surface it is more than 20% smaller than nominal, due to the high surface temperature $\vartheta > 0$. As a result the azimuthal perturbation temperature variations associated with the hydrothermal wave (HTW) lead to

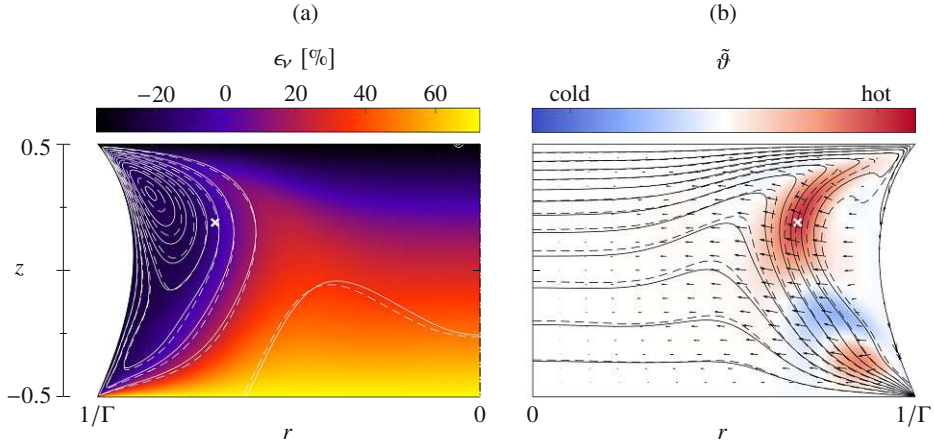

Figure 4: Basic state streamlines (a) and isotherms (b) for $(\Gamma, \mathrm{Re_g}, \mathrm{Bd}) = (\Gamma, \mathrm{Re_g}, \mathrm{Bd})_{\mathrm{ref}}$ and $\mathcal{V} = 0.88$ at $\mathrm{Re}_c = 1680$ using the FTD model. In (b) also the critical velocity field (arrows) and the critical temperature field (colour) for $m_c = 3$ is shown in the (r, z) plane in which the local thermal production $\alpha_{\rho 0}\tilde{\vartheta}\tilde{\boldsymbol{u}} \cdot \nabla\vartheta_0$ takes one of its maxima (white crosses in (a,b) at $(r_{\max}, z_{\max}) = (1.05, 0.19)$). Colour in (a) indicates the local viscosity deviation $\epsilon_\nu(\vartheta_0)$. The dashed lines show basic state streamlines and isotherms for the same set of parameters, but using the OB approximation.

larger azimuthal velocity gradients compared to those in the OB model in which the kinematic viscosity on the interface is ν^*, or $\epsilon_\nu = 0$. Since the azimuthal perturbation velocity drives the HTW (Wanschura *et al.* 1995), this effect enhances the velocity field of the critical mode and thus may explain the lower critical Reynolds number for the FTD model as compared to the OB model for $\mathcal{V} = 0.88$.

The slightly lower critical Reynolds number of the LTD model in comparison to the FTD model for $\mathcal{V} = 0.88$ is consistent with the effective kinematic viscosity

$$\nu_{\mathrm{eff}} = \left\{ \int_V \rho[T_0(\boldsymbol{x})]\hat{\boldsymbol{u}}^2 \mathrm{d}V \right\}^{-1} \int_V \nu[T_0(\boldsymbol{x})]\rho[T_0(\boldsymbol{x})]\hat{\boldsymbol{u}}^2 \mathrm{d}V, \tag{5.3}$$

which is defined as kinematic viscosity weighted by the kinetic energy density of the critical mode (see appendix C). We find that the ordering of the critical Reynolds numbers $\mathrm{Re}_c^{\mathrm{LTD}} < \mathrm{Re}_c^{\mathrm{FTD}} < \mathrm{Re}_c^{\mathrm{OB}}$ coincides with the one of the effective viscosities $\nu_{\mathrm{eff}}^{\mathrm{LTD}} < \nu_{\mathrm{eff}}^{\mathrm{FTD}} < \nu_{\mathrm{eff}}^{\mathrm{OB}}$, namely $0.853\nu^* < 0.880\nu^* < \nu^*$ at the respective critical points of each model. Comparing the three models for a constant Reynolds number at e.g. $\mathrm{Re} = \mathrm{Re}_c^{\mathrm{FTD}} = 1680$ yields the same ordering with $0.832\nu^* < 0.880\nu^* < \nu^*$.

While the above interpretation seems plausible for $\mathcal{V} = 0.88$, this argument cannot generally proven valid, because the critical curves for the OB approximation of the FTD model intersect. Thus for certain ranges of $\mathcal{V}$ the basic flow is slightly more stable within the FTD model than within the OB model. This indicates that the influence of the changed volume is much more important, not only changing the critical Reynolds number, but also the structure and wave number of the critical mode. Regardless of the explanation of the mechanisms at work, the results in figure 3 show that it is important to take into account the variation of the thermophysical parameters (in particular that of the viscosity of the liquid) in order to arrive at accurate critical data when the temperature difference is large, here approximately in the range $\mathcal{V} \in [0.75, 0.95]$.

In table 5 we compare the critical data obtained for $\mathcal{V} = 0.88$ using different approximations. Within the OB + $\rho(T)$ model, the temperature dependence of the fluid

Approximation	Re_c	ΔT_c [K]	ϵ_c [%]
FTD	1679	50.79	0
LTD	1572	47.53	−6.4
OB	2263	68.45	34.8
OB + $\rho(T)$	2218	67.09	32.1
OB + $\mu(T)$	1716	51.89	2.2
OB + $\mu_\mathrm{L}(T)$	1717	51.93	2.2

Table 5: Critical Reynolds numbers Re_c and critical temperature differences ΔT_c for $\mathcal{V} = 0.88$ and different model equations (approximations). The relative deviation $\epsilon_c = (\mathrm{Re}_c - \mathrm{Re}_c^{\mathrm{FTD}})/\mathrm{Re}_c^{\mathrm{FTD}}$ is given in [%].

densities is taken into account in all the governing equations (2.4) according to (2.10), whereas the OB + $\mu(T)$ model combines the OB approximation with a fully temperature dependent dynamic viscosity, while the OB + $\mu_\mathrm{L}(T)$ model indicates that only the liquid's viscosity is fully temperature dependent. The OB + $\mu(T)$ and OB + $\mu_\mathrm{L}(T)$ models yield the smallest deviation of the critical Reynolds number from the one of the FTD model. This confirms the importance of taking into account the temperature dependence of $\mu(T)$ of the fluids, in particular that of the liquid.

5.1.2. *Comparison with the results of Stojanović* et al. *(2022)*

Stojanović *et al.* (2022) have also computed the linear stability boundary $\mathrm{Re}_c(\mathcal{V})$ using the OB approximation and the same geometry parameters. However, there are small differences compared to the present investigation: (a) Stojanović *et al.* (2022) neglected dynamic surface deformations and (b) the reference quantities α_j differ slightly: In the present work they are determined by quadratic least-squares fits of the discrete manufacturer's data (cf. section 4), while Stojanović *et al.* (2022) implemented the discrete values specified for the reference temperature, except for the thermal expansion coefficient which was taken from Romanò *et al.* (2017), because it is not contained in the data sheet provided by the manufacturer.

Tests have shown that the dynamic surface deformation $\Delta h_0 = h_{0,\mathrm{d}} - h_{0,\mathrm{s}}$ in the basic flow, where $h_{0,\mathrm{d}}$ and $h_{0,\mathrm{s}}$ are the *dynamic* and *static* surface shapes, respectively, has a weak influence on the critical Reynolds number near the peak of $\mathrm{Re}_c(\mathcal{V})$ at $\mathcal{V} \approx 0.9$. For these volume ratios, differences between the present results using the OB approximation and those of Stojanović *et al.* (2022) are mainly due to the different reference values α_j used, in particular due to the difference in β^* for the liquid phase: Stojanović *et al.* (2022) used the same value for β^* as did Romanò *et al.* (2017). This value is 11.4% larger than the current value used (table 2). The impact is visible from figure 3, where the critical Reynolds number obtained by Stojanović *et al.* (2022) (black dash-dotted) significantly deviates from current result using the OB approximation (coloured dash-dotted) for $\mathcal{V} \lesssim 1$. In particular, an axisymmetric $m = 0$ mode is critical in the present investigation in the narrow range $\mathcal{V} \in [0.8663, 0.8712]$ (brown dash-dotted line, upper inset of figure 3(a)), whereas the axisymmetric critical mode arises for $\mathcal{V} \in [0.8917, 8983]$ in Stojanović *et al.* (2022) (full black line in their figure 17(a)). The different thermophysical reference parameters are also responsible for the significant reduction of the volume ratio range within which the wave number $m = 4$ is critical: $\mathcal{V} \in [0.871, 0.874]$ (orange dotted line in figure 3(a)) as compared to $\mathcal{V} \in [0.898, 0.929]$ (full purple line in figure 17a of Stojanović *et al.* (2022)). The changes indicate the sensitivity of the critical Reynolds number on the thermophysical reference parameters α_j, not only for the OB approximation but in general.

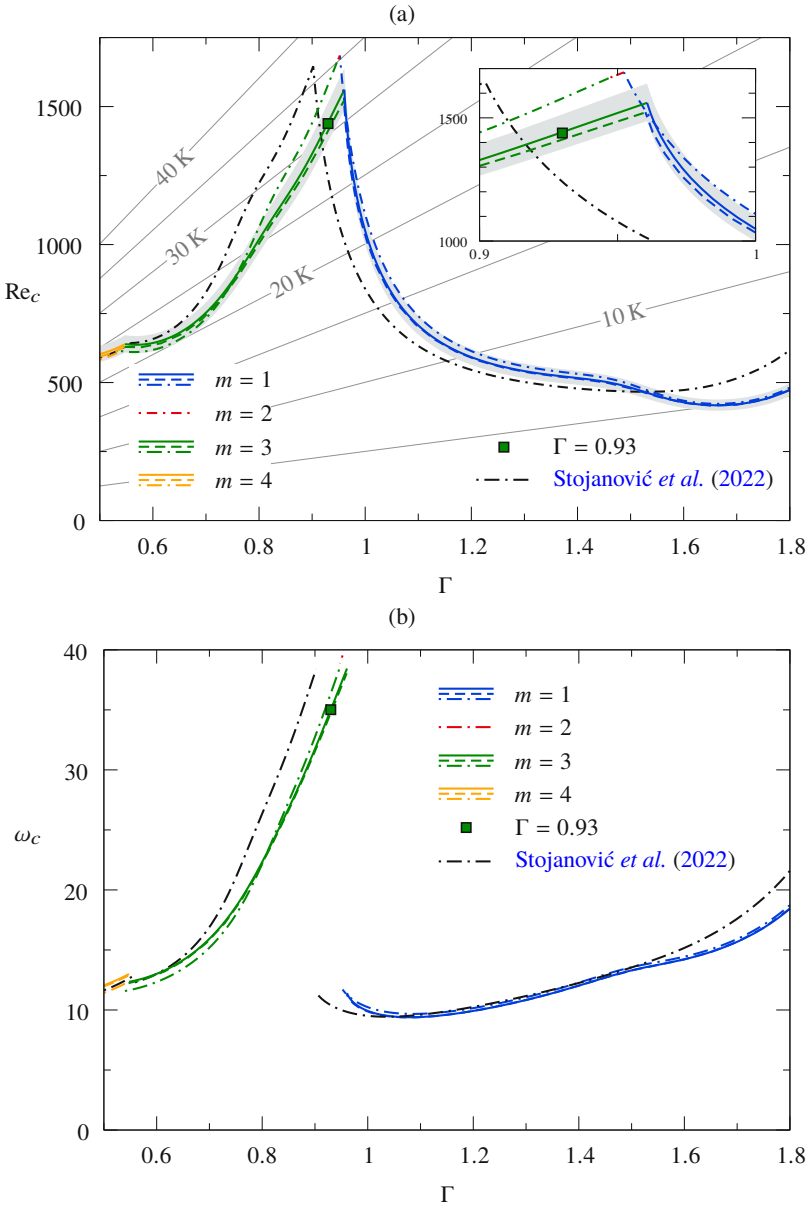

Figure 5: Critical Reynolds number Re_c (left axis) and critical temperature difference ΔT_c (right axis) as functions of the aspect ratio Γ for $\mathcal{V} = 1$, $\mathrm{Bd} = \mathrm{Bd}_{\mathrm{ref}} \times (\Gamma/\Gamma_{\mathrm{ref}})^2$ and a closed chamber. The curves related to the left and right vertical axis, respectively, are indicated by the additional label in the right corner of the graph. Shown are the results for FTD (full lines), LTD (dashed lines), and OB (dash-dotted lines) models. The gray shaded region indicates a deviation of ±5% from the reference FTD model.

5.1.3. *Effect of the aspect ratio on the stability boundary*

The aspect ratio $\Gamma = d/r_{\mathrm{i}}$ can easily be adjusted in experiments and is an important parameter determining the critical wave number. Therefore, we vary the length d, as in experiments, keeping $r_{\mathrm{i}} = r_{\mathrm{i,ref}}$ constant. The Bond number is adjusted accordingly $\mathrm{Bd} = \mathrm{Bd}_{\mathrm{ref}} \times (\Gamma/\Gamma_{\mathrm{ref}})^2$.

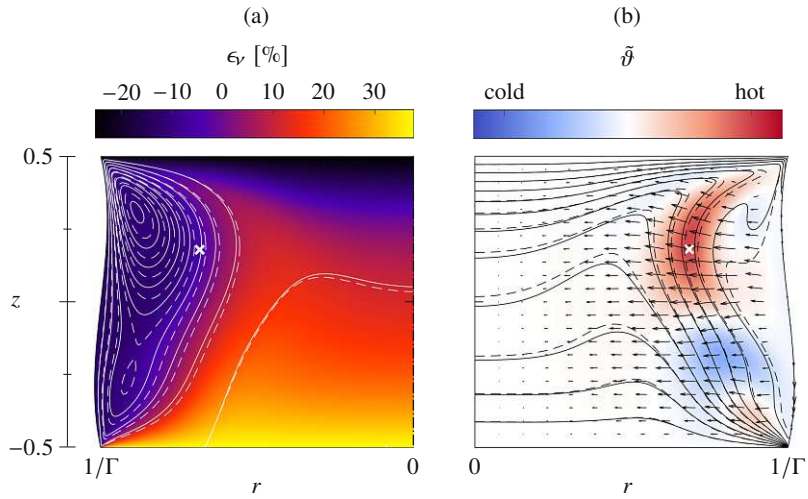

Figure 6: Same as figure 4 but for $(\mathcal{V}, \mathrm{Re_g}) = (\mathcal{V}, \mathrm{Re_g})_{\mathrm{ref}}$, $\Gamma = 0.93$ and $\mathrm{Re}_c = 1438$

The dependence of the critical conditions on d is displayed in figure 5(a), where the critical Reynolds number Re_c is shown as a function of the aspect ratio Γ for $\mathcal{V} = 1$ and the three models employed (OB, LTD, FTP). Figure 5(b) shows the corresponding critical frequencies. While the critical frequencies increase with the critical Reynolds number to the left of the peak of Re_c (small Γ), the opposite behaviour is found for the frequency of the critical $m = 1$ mode to the right of the peak of Re_c (larger Γ). In addition, we reproduce in figure 5 $\mathrm{Re}_c(\Gamma)$ and $\omega_c(\Gamma)$ (black dash-dotted curves) obtained by Stojanović *et al.* (2022) for the OB model, but for slightly different reference parameters and an indeformable interface. Since for the present parameter variation $\Delta T_c \sim \mathrm{Re}_c/d$ scales differently from Re_c, straight grey lines in 5(a) refer to constant values of ΔT.

For most aspect ratios all present critical Reynolds numbers lie within the 5% tolerance level about the result for the FTD model (full line). However, similar as for the variation of $\mathcal{V}$ above, the OB model (coloured dash-dotted lines) overestimates the critical Reynolds number by more than 5% in the range $\Gamma \in [0.806, 1.086]$. The sensitivity of the critical Reynolds number on the reference parameters α_j is again confirmed when comparing the OB model of Stojanović *et al.* (2022) (black dash-dotted) with the current OB model results (coloured dash-dotted). In Stojanović *et al.* (2022), buoyancy forces have been overestimated due to the larger selected β^*. This also explains the increasing discrepancy of Re_c for long liquid bridges (large Γ). Numerical tests have shown including dynamic surface deformations in the model of Stojanović *et al.* (2022) have only a very minor effect on the black dash-dotted curves. The comparison thus underlines that the selection of the reference quantities (here β^*) has a profound effect on Re_c which can be large when the slope of $\mathrm{Re}_c(\Gamma)$ is large.

As a minor detail, the OB approximation predicts the critical wave number $m_c = 2$ (red) within a very small window of Γ at the peak of Re_c (inset of figure 5(a)), whereas the FTD model yields $m_c = 3$ (green). Likewise, the critical mode with $m_c = 2$ does not arise in the OB model used by Stojanović *et al.* (2022), but from their calculations neutral modes with different wave numbers arise at very close Reynolds numbers near the peak of $\mathrm{Re}_c(\Gamma)$.

Close to the peak of Re_c which coincides with a maximum of the critical temperature difference the distribution of the kinematic viscosity $\nu(\boldsymbol{x})$ exhibits a similar structure as for $(\Gamma, \mathrm{Re_g}, \mathrm{Bd}) = (\Gamma, \mathrm{Re_g}, \mathrm{Bd})_{\mathrm{ref}}$ and $\mathcal{V} = 0.88$. This is evident when comparing figure 6(a) for $\Gamma = 0.93$ (green square in figure 5) with figure 4(a). Despite of quantitative differences

of ν, the effective viscosities based on the result for $\mathrm{Re} = \mathrm{Re}_c^{\mathrm{FTD}}(\Gamma = 0.93) = 1438$ are ordered with $\nu_{\mathrm{eff}}^{\mathrm{LTD}} = 0.911 < \nu_{\mathrm{eff}}^{\mathrm{FTD}} = 0.923 < \nu_{\mathrm{eff}}^{\mathrm{OB}} = 1$, just like the Reynolds numbers are ($\mathrm{Re}_c^{\mathrm{LTD}} < \mathrm{Re}_c^{\mathrm{FTD}} < \mathrm{Re}_c^{\mathrm{OB}}$). The impact of the effective viscosity is demonstrated in figure 6(b), where the basic state isotherms of the FTD model (full black lines) are compared with the ones obtained by the OB model (dashed black lines) at the same Reynolds number $\mathrm{Re} = \mathrm{Re}_c^{\mathrm{FTD}} = 1438$. At this Reynolds number the most dangerous mode of the OB model (not shown) is linearly stable. The slightly stronger basic flow in the FTD model compared to the OB model (c.f. dashed and full white lines in figure 6(a)) yields a slightly stronger basic state thermal advection (c.f. dashed and full black isotherms in figure 6(b)). This enhances the energy supply from the basic state to the perturbation flow, which destabilises the flow.

5.1.4. *Effect of the length scale on the linear stability boundary*

The size of a liquid bridge, parameterised by the length scale d, is perhaps the most important design parameter for experiments. It affects the static shape of the liquid bridge through the hydrostatic pressure difference and determines its mechanical stability (see e.g. Meseguer *et al.* 1995). Apart from these mechanical aspects, the size affects the critical thermocapillary Reynolds number, because (a) the strength of buoyancy forces to thermocapillary forces depends on size, and (b) the range of variation of the material parameters depends on size through the size-dependence of the critical temperature difference.

To investigate these influence factors we consider $\Gamma = 0.66$, $\Gamma_{\mathrm{rod}} = 0.4$, $\eta = 4$, $\mathcal{V} = 1$ and take into account the dynamic surface shape of the liquid bridge in the basic state. While the FTD model is the most realistic one, it is instructive to compare the size dependence of the critical Reynolds number of the different models with the OB approximation under zero gravity conditions (OB-0g). For zero gravity and the absence of a forced flow in the gas phase deviations of the shape from cylindrical are only due to the basic flow (DI). If dynamic deformations are suppressed (SI), the length scale and the temperature difference would only appear in the Reynolds number $\mathrm{Re} \sim \Delta T d$. Therefore, the stability boundary for the OB-0g model and a static interface (SI) is simply $\mathrm{Re}_c(d) = 627 = \text{const}$ with $\Delta T_c \sim d^{-1}$. In the present case of a dynamic interface (DI) the effect of the dynamic surface deformation in the basic state only becomes relevant for small values of d, thus large values of ΔT_c, because a high temperature difference significantly increases the capillary number entering the normal stress balance (2.20*a*), which makes the interface more deformable dynamically. The effect is visible in figure 7 by the minute reduction of $\mathrm{Re}_c^{\mathrm{OB\text{-}0g}}$ (black curve, DI) from $\mathrm{Re} = 627$ (SI) for $d \lesssim 0.25\,\mathrm{mm}$. The critical wave number for the case OB-0g is $m_c = 2$ in the full range of d investigated.

The critical Reynolds number $\mathrm{Re}_c^{\mathrm{OB\text{-}0g}}(d)$ for OB-0g represents the reference. The grey strip indicates a ±5% deviation from $\mathrm{Re}_c^{\mathrm{OB\text{-}0g}}$. The effect of the terrestrial gravity level and of the full temperature dependence of the material parameters on the critical Reynolds number when the length scale d is varied is shown in figure 7 for the OB and FTD models and for 0g and 1g.

In the framework of the OB approximation (OB-1g) the buoyancy force in the liquid phase in (2.4) becomes in our scaling

$$-\mathrm{Bd}\frac{\alpha_\rho - \alpha_\rho^*}{\varepsilon} = \frac{\rho^* g \beta^* d^2}{\gamma^*}\vartheta = \frac{U_{\mathrm{diff}}}{U_{\mathrm{TC}}}\mathrm{Ra}\vartheta, \tag{5.4}$$

where $U_{\mathrm{diff}} = \lambda^*/(\rho^* c_p^* d)$ and $U_{\mathrm{TC}} = \gamma^* \Delta T/\mu^*$ are the characteristic velocity scales for

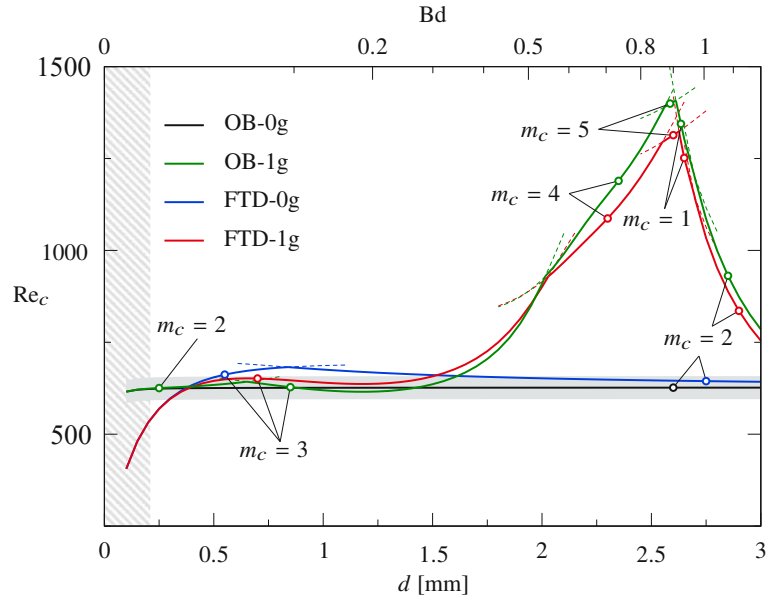

Figure 7: Critical Reynolds number as function of the size of the setup expressed through d for constant geometrical proportions $\Gamma = 0.66$, $\Gamma_{\text{rod}} = 0.4$, $\eta = 4$ and $\mathcal{V} = 1$. Different gravity conditions and flow models are considered (see the legend). The gray hatched region corresponds to inaccessible critical temperature differences with $\Delta T_c > 126\,\text{K}$. The gray shaded region indicates a deviation of 5% from the zero-gravity reference case (blue lines). Full lines: critical Reynolds numbers. Dashed line: neutral Reynolds numbers close to the intersection of critical curves. The wave number m is given for each segment of the critical curve.

thermal diffusion in the liquid and for thermocapillary convection, respectively, and

$$\text{Ra} = \frac{g\beta^*\Delta T d^3}{(\lambda^*/\rho^* c_p^*)(\mu^*/\rho^*)} \tag{5.5}$$

is the Rayleigh number. Due to the dependence $\text{Ra} \sim d^3$, buoyancy forces rapidly diminish in the liquid phase as the length scale d is reduced and if approximately $\Delta T \sim d^{-1}$. Therefore, the critical Reynolds number Re_c under terrestrial gravity within the OB approximation (OB-1g, green in figure 7) approaches the zero gravity case (OB-0g, black) in the limit of vanishing d. As d increases beyond $d \approx 0.4\,\text{mm}$, the basic flow first becomes slightly stabilised due to buoyancy within the OB-1g model. The change of the critical wave number from $m_c = 2$ to $m_c = 3$ at $d = 0.65\,\text{mm}$ leads to a slight reduction of the critical Reynolds number below the one for the case OB-0g until, for $d \gtrsim 1.6\,\text{mm}$, buoyancy forces again strongly stabilise the basic flow. Further increasing d the critical Reynolds number grows significantly and a more complicated switching of critical modes arises. Based on the OB approximation, the influence of buoyancy forces on the critical Reynolds number for the present couple of fluids and geometry remains less than $\approx 4.5\%$ as long as $d < 1.6\,\text{mm}$. A relation similar to (5.4) holds for the buoyancy force in the gas phase. However, the Rayleigh number would not scale like $\sim d^3$ for the present parameter variation with constant values of Γ_{rod} and η.

The picture changes when the full temperature dependence of the material parameters are taken into account. Under zero gravity, the FTD model (FTD-0g, blue) yields a critical Reynolds number larger than $\text{Re}_c^{\text{OB-0g}}$ for $d \gtrsim 0.37\,\text{mm}$. Figure 8 shows the critical mode using the FTD-0g model (a) and the OB-0g model (b) for $d = 1\,\text{mm}$. The isotherms of

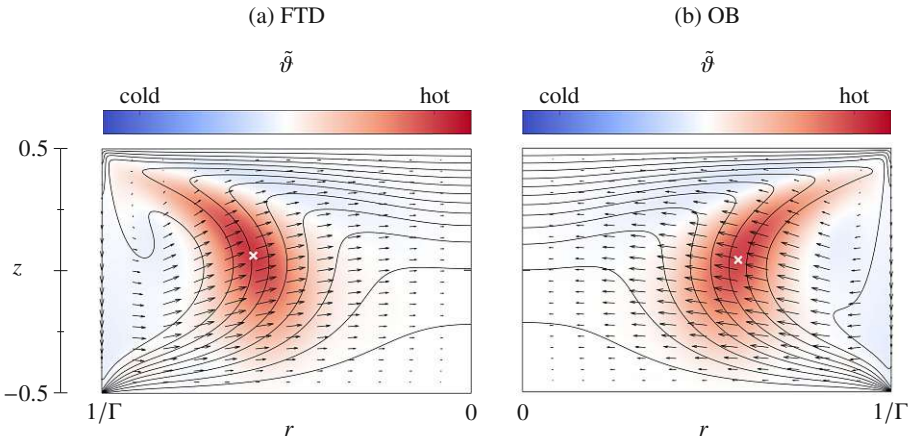

Figure 8: Linear stability results for $(\mathcal{V}, \Gamma, \mathrm{Re_g}) = (\mathcal{V}, \Gamma, \mathrm{Re_g})_{\mathrm{ref}}$, $\mathrm{Bd} = 0$ and $d = 1\,\mathrm{mm}$ using the FTD model (a) and the OB model (b). Shown are the critical velocity field (arrows) and critical temperature field (colour) in the (r, z) plane in which the local production $\alpha_{\rho 0}\tilde{\vartheta}\tilde{\boldsymbol{u}} \cdot \nabla\vartheta_0$ takes one of its maxima (white crosses) in the bulk. Black lines indicate isotherms of the basic state. (a) $\mathrm{Re}_c = 676$, $m_c = 2$. (b) $\mathrm{Re}_c = 627$, $m_c = 2$.

the basic state (black lines) indicate again a higher temperature close to the free surface for FTD-0g. However, in contrast to the case shown in figure 4, the FTD-0g model is more stable than the OB-0g model, i.e. $\mathrm{Re}_c^{\text{FTD-0g}} > \mathrm{Re}_c^{\text{OB-0g}}$. This finding is consistent with figure 3 (for $\mathcal{V} = 1$) in the presence of buoyancy forces.

The difference between OB-0g and FTD-0g vanishes asymptotically as d becomes larger, because the critical temperature difference decreases $\sim d^{-1}$, provided $\mathrm{Re}_c \approx \text{const}$. Therefore, the material properties hardly vary anymore within their respective domains. This also becomes clear when taking the limit $\Delta T \to 0$ in (2.7) in which the shape functions for the liquid reduce to $\alpha_j \equiv 1$. Asymptotically, $\mathrm{Ca} \sim d^{-1}$ such that the Laplace pressure dominates and the liquid bridge takes a perfect cylindrical shape. If, on the other hand, the size of the bridge is reduced, the critical wave number for the FTD-0g model changes from $m_c = 2$ to $m_c = 3$ at $d = 0.84\,\mathrm{mm}$. For even smaller sizes the basic flow is strongly destabilised for $d < 0.25\,\mathrm{mm}$ within the FTD-0g model. This effect is due to the increased range of variation of the material properties when the critical temperature difference increases due to the reduction of the length scale. In this region (gray hatched in figure 7) other effects like evaporation become important which are not taken into consideration here. In any case, the maximum theoretical temperature difference is bounded by the pour point and the boiling temperature which, for 2-cSt silicone oil, are −120°C and 88°C, respectively. The latter restricts the experimentally realisable temperature differences to $\Delta T < 2 \times (88 - 25)°\mathrm{C} = 126°\mathrm{C}$, assuming that the mean temperature is kept at 25°C. Temperature differences above this threshold fall into the gray hatched region.

For small length scales $0.35\,\mathrm{mm} \leqslant d \lesssim 0.5\,\mathrm{mm}$, deviations of Re_c from the reference case $\mathrm{Re}_c^{\text{OB-0g}}$ are primarily caused by the temperature dependence of the material properties and neither by buoyancy nor dynamic deformations of the interface. Therefore, the critical Reynolds number under terrestrial gravity conditions for the FTD model (FTD-1g, red) hardly deviates from Re_c under zero gravity (FTD-0g, blue) for $d \lesssim 0.5\,\mathrm{mm}$ with $m_c = 3$. For larger system sizes the critical Reynolds number for FTD-1g remains closer to the results for OB-0g and OB-1g and the critical wave number $m_c = 3$ for the FTD-1g model does not

change before Re_c for the terrestrial conditions (red, green) starts increasing strongly from the 0g cases (black, blue) for $d \gtrsim 1.6\,\mathrm{mm}$.

In summary, the critical data (Re_c and m_c) under terrestrial gravity modelled by the FTD-1g model (red) is comparable (up to 5%) to the OB-1g model (green) as long as $d \geqslant 0.69\,\mathrm{mm}$. For smaller lengths, the OB-1g model yields a different critical wave number m_c. For zero gravity conditions, the critical Reynolds numbers of the FTD-0g model (blue) can be predicted by the simpler OB-0g model (black) with an accuracy better than 5% if $d \leqslant 1.64\,\mathrm{mm}$. Moreover, in the range $d \in [0.35, 1.5]\,\mathrm{mm}$, all four models yield comparable results since Re_c is almost constant and bounded by $\mathrm{Re}_c \in [615,\ 683]$. It is remarkable that for $d \geqslant 1.64\,\mathrm{mm}$ the large critical Reynolds numbers and the mode switching leading to the peak of Re_c for the OB-1g and FTD-1g models are essentially caused by the increasing buoyancy forces in the bulk when heating from above and by the increasing static shape deformation ($\mathrm{Bo} \sim d^2$). Dynamic deformation are of minor importance for increasing d, indicated by the small deviation of $\mathrm{Re}_c^{\text{OB-0g}}$ (black in figure 7) from the constant value $\mathrm{Re}_c^{\text{OB-0g,SI}} = 627$.

5.2. *Effect of temperature-dependent thermophysical properties in the presence of an axial gas flow*

A concentric circular tube about the liquid bridge, originally designed to minimise ambient air effects on the flow in the liquid, can be utilised to impose an axial flow in the gas phase which bears some potential to control the onset of a time-dependent and/or three-dimensional flow in the liquid phase (Shevtsova *et al.* 2013, 2014; Yano *et al.* 2016, 2017; Yasnou *et al.* 2018; Stojanovic & Kuhlmann 2020; Gaponenko *et al.* 2021). Following Stojanovic *et al.* (2023), we impose an axial gas flow at the inlet of the annular space around the liquid bridge. The velocity profile $w_{\mathrm{g,in}}(r)$ is fully developed according to (2.29) and its strength is measured by the gas flow Reynolds number $\mathrm{Re}_\mathrm{g} = \bar{W}_{\mathrm{g,in}}\rho^* d/\mu^*$ as defined in Stojanović *et al.* (2022). The gas at the inlet has a homogeneous temperature corresponding to that of the adjacent support rod. Thus for an upward flow with $\mathrm{Re}_\mathrm{g} > 0$ the gas is cold ($\vartheta_{0,\mathrm{in}} = -0.5$), while for a downward flow with $\mathrm{Re}_\mathrm{g} < 0$ it is hot ($\vartheta_{0,\mathrm{in}} = 0.5$).

Critical Reynolds numbers Re_c and frequencies ω_c as functions of the gas flow Reynolds number Re_g are shown in figure 9(a,b) for the FTD (solid), LTD (dashed) and OB model (dash-dotted line). The sensitivity of the critical Reynolds number with respect to the gas flow for small values $|\mathrm{Re}_\mathrm{g}| \lesssim 50$ has been explained by Stojanovic *et al.* (2023). The critical curves for all models behave qualitatively similar as reported in figure 2(a) of Stojanovic *et al.* (2023) for an extended OB model which almost agrees with the current standard OB model. Also for upward flow ($\mathrm{Re}_\mathrm{g} \gtrsim 50$) and strong downward flow ($\mathrm{Re}_\mathrm{g} \lesssim -2000$) the critical Reynolds numbers are almost independent of Re_g and in the range of $\mathrm{Re}_c \approx 400$. For these conditions, the three models yield comparable results well within the 5% tolerance margin (grey). However, for downward flow in the intermediate range of $-2000 \lesssim \mathrm{Re}_\mathrm{g} \lesssim -50$ the three material parameter models yield very different results. This is due to the large critical temperature difference for which the dependence of the thermophysical parameters on the flow becomes important.

The critical Reynolds numbers obtained using the OB approximation (dash-dotted) are typically much larger in the range $-2000 \lesssim \mathrm{Re}_\mathrm{g} < -50$ than the reference data for FTD. An exception is the $m = 1$ OB mode which is responsible for a local minimum $\mathrm{Re}_c^{\mathrm{OB}}(m = 1) = 1727$ of the critical Reynolds number at $\mathrm{Re}_\mathrm{g} = -480$. Within $\mathrm{Re}_\mathrm{g} \in [-767, -345]$ the critical Reynolds number for the OB model is even slightly less than the one for the FTD model, $\mathrm{Re}_c^{\mathrm{OB}} < \mathrm{Re}_c^{\mathrm{FTD}}$. Despite of similar critical Reynolds numbers near $\mathrm{Re}_\mathrm{g} = -480$ the wave numbers, oscillation frequencies and flow structures of the critical modes of the two models differ. The linear LTD model (dashed) represents a better approximation to the FTD

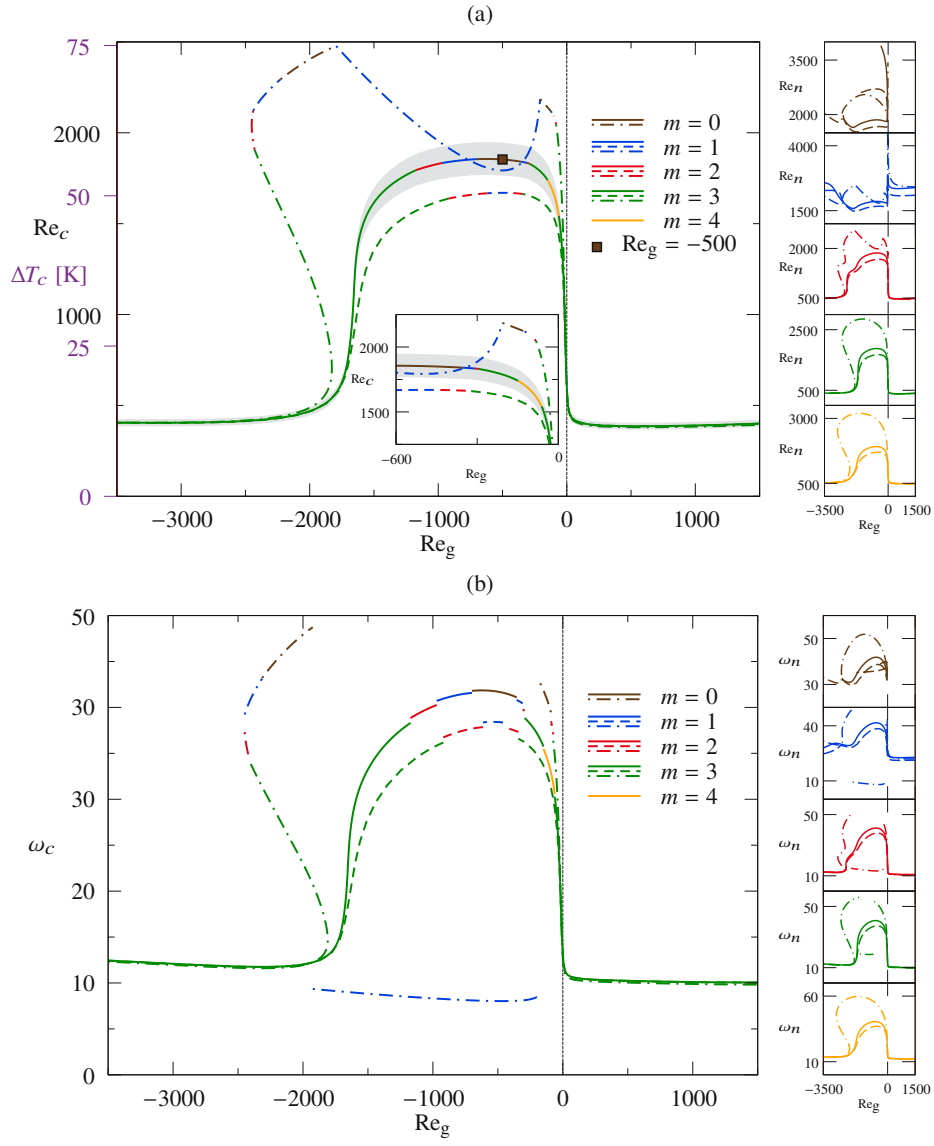

Figure 9: Left panel: Critical Reynolds number Re_c (black axis labels) and critical temperature difference ΔT_c (purple axis labels) as functions of the gas flow Reynolds number Re_g for $\Gamma = 0.66$, $\mathcal{V} = 1$ and $\mathrm{Bd} = \mathrm{Bd}_{\mathrm{ref}}$. Results are shown for the FTD model (full lines), the LTD model (dashed lines), and the OB approximation (dash-dotted lines). The gray-shaded region indicates a deviation of ±5% from the reference FTD model. The wave numbers are coded by colour. Right panel: Full neutral Reynolds numbers for individual wave numbers.

model (full) than the OB model (dash-dotted). Like for the FTD model, the critical curve $\mathrm{Re}_c^{\mathrm{LTD}}(\mathrm{Re}_g)$ is unique and has the same shape as $\mathrm{Re}_c^{\mathrm{FTD}}(\mathrm{Re}_g)$. However, the LTD model underestimates the critical threshold by more than 10% in the range $\mathrm{Re}_g \in [-1705, -32]$. Noteworthy, there exists a considerable range of Re_g around $\mathrm{Re}_g \approx -500$ in which the most dangerous mode of the FTD model is axisymmetric (brown line). Furthermore, a critical

$\mathrm{Re_g}$	$\mathrm{Re_c^{FTD}}$	$\mathrm{Re_c^{LTD}}$	$\mathrm{Re_c^{OB}}$	$\epsilon_c^{\mathrm{LTD}}$ [%]	ϵ_c^{OB} [%]
−1500	1616	1351	2185	−16.4	35.2
−500	1853	1670	1728	−9.9	−6.7
−250	1813	1642	1860	−9.4	2.6

Table 6: Critical Reynolds number Re_c and critical temperature difference ΔT_c for $\mathrm{Re_g} = -1500$, $\mathrm{Re_g} = -500$ and $\mathrm{Re_g} = -250$. Results are given for different approximations. The relative deviation $\epsilon_c = (\mathrm{Re}_c - \mathrm{Re}_c^{\mathrm{FTD}})/\mathrm{Re}_c^{\mathrm{FTD}}$ is given in [%].

$\mathrm{Re_g}$	LTD		FTD		OB	
	$\lvert\check{\psi}_{\min}\rvert$	ν_{eff}/ν^*	$\lvert\check{\psi}_{\min}\rvert$	ν_{eff}/ν^*	$\lvert\check{\psi}_{\min}\rvert$	ν_{eff}/ν^*
−250	1.147	0.8320	1.084	0.9135	0.9746	1
−500	1.123	0.8444	1.058	0.8406	0.9450	1
−1000	1.155	0.8219	1.083	0.8981	0.9498	1
−1500	1.263	0.8124	1.178	0.8499	0.9995	1

Table 7: Scaled streamfunction extrema $|\check{\psi}_{\min}| = |\psi_{\min}| \times 10^3$ of the basic flow and effective viscosities ν_{eff} for $\mathrm{Re} = 1500$ and different $\mathrm{Re_g}$ for the three models LTD, FTD, and OB.

mode with wave number $m_c = 4$ can be critical within the FTD model, but not for the other models.

The larger critical Reynolds numbers for the OB model (except for the $m = 1$ mode) and the smaller ones for the LTD model as compared to $\mathrm{Re}_c^{\mathrm{FTD}}$ are caused by the considerable viscosity variation for large ΔT. For most values of $\mathrm{Re_g}$, we find the effective kinetic-energy-weighted viscosity (5.3) is ordered like $\nu_{\mathrm{eff}}^{\mathrm{LTD}} < \nu_{\mathrm{eff}}^{\mathrm{FTD}} < \nu_{\mathrm{eff}}^{\mathrm{OB}}$. Therefore, it is reasonable to assume that the perturbation flow experiences the most dissipation for the OB model and the least for the LTD model. But also the magnitude of the stream function extrema of the basic flows for a constant Reynolds number $\mathrm{Re} = 1500$ provided in table 7 show the same ordering. Thus a higher Reynolds number is required in the OB model to establish the characteristic internal temperature gradients by advection, from which the hydrothermal wave can draw its thermal perturbation energy. This effect is assisted by the lower surface temperature in the OB model as compared to the FTD model at the same thermocapillary Reynolds number as shown in figure 10.

Figure 11 shows the most important integral thermal energy production terms J_1 (blue) and J_2 (red) for the FTD model as functions of the gas flow Reynolds number. We note the heat transfer through the interface is always negligible compared to the bulk thermal production rates J_1 and J_2, since $-1.3 \times 10^{-3} < H_{\mathrm{fs}} < 0$. For $\mathrm{Re_g} < -1750$ and for $\mathrm{Re_g} > 0$ the critical Reynolds number is low and the thermal perturbation energy is almost entirely provided by radial advection of basic state temperature described the term J_1 (blue). The variation of the relative importance of J_1 and J_2 indicates changes of the model structure or the critical wave number. The changes of the critical mode along $\mathrm{Re}_c(\mathrm{Re_g})$ are illustrated in the supplementary video for the FTD model: For strong downward flow of the hot gas ($\mathrm{Re_g} = -3500$) the region of basic state temperature gradients (full black lines) is located at about one half of the radius of the liquid bridge ($r \approx 1/2\Gamma$). The temperature perturbations spots extend from top to

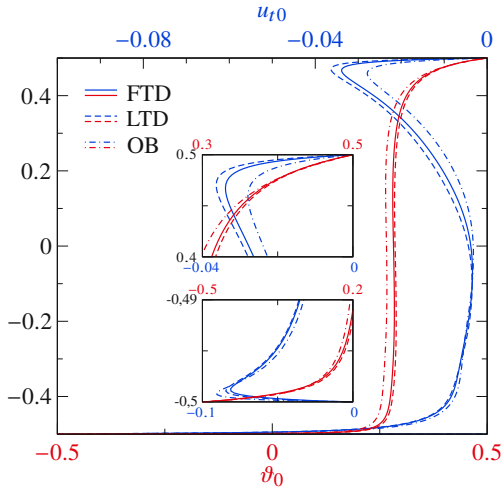

Figure 10: Tangential velocity $u_{t0} = \boldsymbol{t} \cdot \boldsymbol{u}_0$ (blue) and temperature distribution ϑ_0 (red) of the basic flow along the free surface (parameterised by z) for $(\mathrm{Re_g}, \mathrm{Re}) = (-1500, 1616)$. The models FTD, LTD and OB are distinguished by line type (see legend). The insets show the velocity peaks near the hot and cold corners.

bottom and the perturbation flow arises in form of six vortices ($m = 3$) which are almost aligned with the z axis. In this region the temperature perturbation spot are almost exclusively created by the radial perturbation flow sucht that $J_1 \approx 1$ and $J_2 \approx 0$. Increasing $\mathrm{Re_g}$ from -1750 to -1500 the basic flow becomes more stable (figure 9(a)). Due to the larger critical temperature difference at the critical point the hot fluid transported along the free surface downward to the cold end of the bridge has an increasing tendency to rise due to buoyancy. As a result the basic state temperature gradients move closer to the interface and becomes thinner. This is accompanied with a structural change of the critical mode (see also figure 11) such that the temperature perturbations increasingly spiral about the axis. In the cross section shown in the video this is visible by the temperature spots of alternating sign which seem to grow out of the cold corner as $\mathrm{Re_g}$ increases.

In the plateau region of Re_c, approximately for $\mathrm{Re_g} \in [-1500, -300]$, the basic temperature field does not change much. But the critical wave number changes monotonically from $m = 3$ to $m = 0$. With each reduction of m the importance of J_2 (axial advection) over J_1 grows (figure 11). Due to the radially quite localized basic state temperature gradients also the critical modes are confined to this radial region. The radial confinement of the critical modes may explain why the azimuthal wave number (if not too large) is not very important for the instability such that the segments of the critical curve in figure 9(a) merge relatively smoothly. In the range $\mathrm{Re_g} \in [-300, 230]$, the region of basic state temperature gradients becomes wider again and the perturbation flow undergoes a reverse evolution as for the transition region $\mathrm{Re_g} \in [-1750, -1500]$. This is due to the reduced heating from the free surface (even cooling for $\mathrm{Re_g} > 0$) and a reduction of the buoyant rise of the return flow in the bulk.

We shall now focus on the region between $\mathrm{Re_g} \approx\in [-2000, 0]$, where most of the deviations between the OB, LTD and FTD models are observed. For a given $\mathrm{Re_g}$, the basic flow structure remains qualitatively very similar upon a change of the model (either OB, LTD, or FTD), however the critical thermocapillary Reynolds number can be significantly different. The difference in Re_c between the FTD and LTD model can be explained via the effective viscosity for all modes, except for the $m = 1$ mode of the OB model. In this sense the $m = 1$

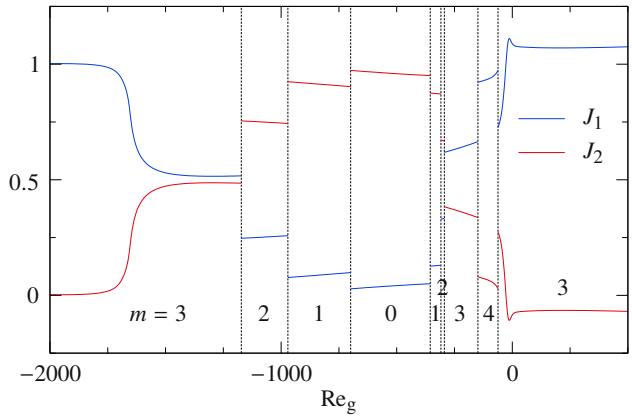

Figure 11: Normalised thermal perturbation energy production rates J_1 (blue) due to radial advection and J_2 (red) due to axial advection in the liquid phase according to (3.10*b*) as functions of $\mathrm{Re_g}$ along the critical curve of the FTD model (full lines in figure 9(a)). The vertical dotted lines indicate changes of the critical wave number m_c as indicated.

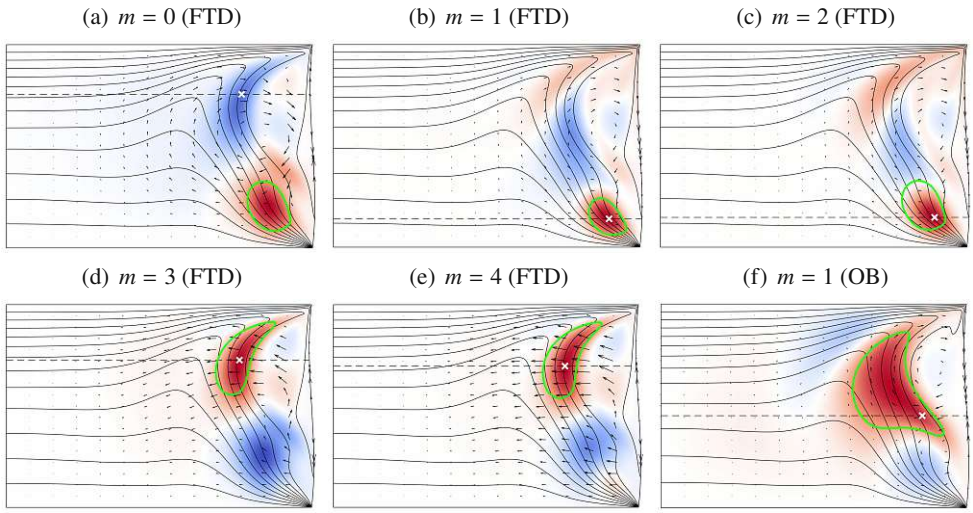

Figure 12: Basic state isotherms (black lines), perturbation temperature field (colour) and perturbation velocity field (arrows) in the plane $\varphi = \text{const.}$ in wich the local thermal production $\alpha_{\rho 0}\tilde{\vartheta}\tilde{\boldsymbol{u}} \cdot \nabla\vartheta_0$ is maximised (white crosses). Shown are (a) the critical mode with $m = 0$ of the FTD model for $(\mathcal{V}, \Gamma, \mathrm{Bd}) = (\mathcal{V}, \Gamma, \mathrm{Bd})_{\mathrm{ref}}$, $\mathrm{Re_g} = -500$ and $\mathrm{Re}_c = 1853$ (brown square in figure 9(a)). Also shown for the same parameters are the stable modes with $m = 1$ to $m = 4$, in (b) to (e)), and the unstable most dangerous mode with $m = 1$ for the OB model in (f). The dashed black lines indicate horizontal cuts shown in figure 13. The green lines represent the isosurfaces $\tilde{\vartheta} = 0.5 \times \max(\tilde{\vartheta})$ projected onto the respective plane.

OB mode is atypical and has a much lower frequency than all other modes. To investigate more in depth the difference between the OB $m = 1$ instability and the peculiar plateau of the critical stability curve for the FTD and LTD models, figures 12 and 13 compare the basic state isotherms (lines) and the perturbation velocity (arrows) and temperature (colour) fields of the OB for $m = 1$ and the FTD model for $m = 0$ (at criticality) and for $m \in [1,\ 4]$ at $\mathrm{Re_g} = -500$ and $\mathrm{Re} = \mathrm{Re}_c = 1853$ (brown square in figure 9(a)). It is observed that the most dangerous

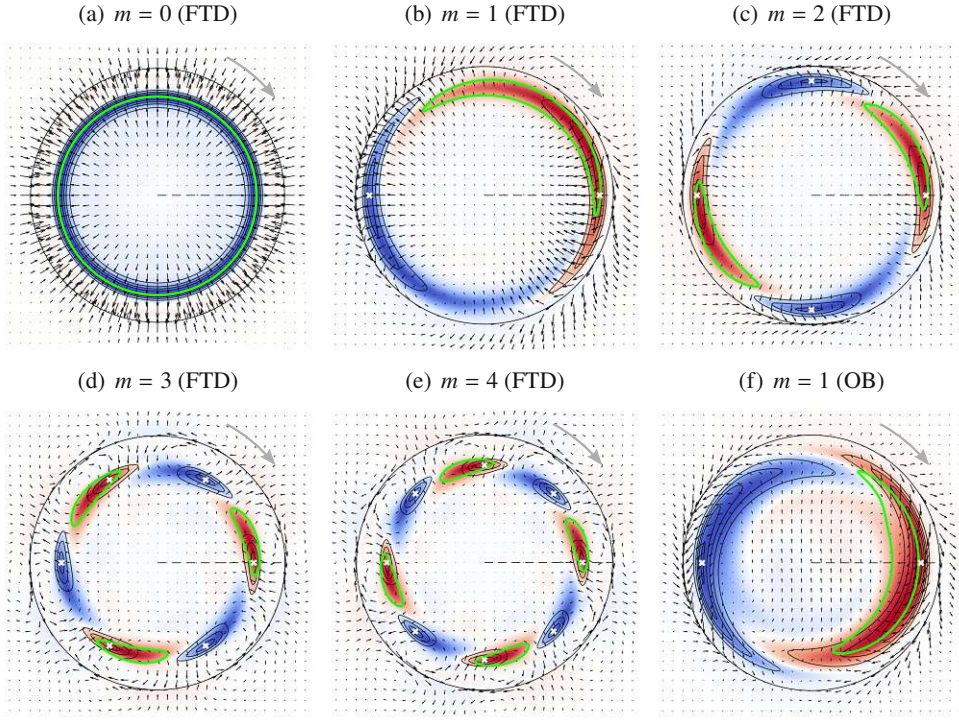

Figure 13: Same as figure 12 but for constant z. The grey arrows in indicate the direction of propagation of the mode.

mode for the OB model ($m = 1$) is qualitatively different from the other modes observed for the fully-temperature dependent perturbations. The most dangerous $m = 1$ mode of the OB model is promoted by a radially narrow perturbation vortex near the top right corner of the liquid bridge. This cannot well exploit the basic state temperature gradient, hence it requires a perturbation temperature developed over a thicker annular region in order to produce enough energy to feed the $m_c = 1$ HTW perturbation (see figure 12(f)). On the other hand, for FTD (as well as for LTD, not shown), the velocity perturbation is strongest where the basic state temperature gradient is most intense. This allows the most dangerous perturbation to concentrate its temperature peaks in a thin toroidal blade (see figs. 12(a–e)). The radial confinement of the temperature perturbation is illustrated by the green lines in figures 12 and 13 indicating the projection of the isosurfaces $\tilde{\vartheta} = 0.5 \times \max(\tilde{\vartheta})$ onto the respective planes. As the radial extension of the production region for FTD and LTD (not shown) is relatively small, the instability mechanism becomes almost insensitive to the perturbation wave number. This explains the plateau of the neutral stability curves (see panels on the right of figure 9) for the FTD and LTD models, that signifies that the flow in the liquid bridge can be driven towards an unstable state at Re $\approx$ 1850 for FTD and Re $\approx$ 1700 for LTD for all azimuthal wave numbers m considered. The supplementary video confirms this interpretation.

6. Discussion and Conclusions

The linear stability of a differentially heated thermocapillary liquid bridge has been investigated numerically. Three distinct models were analysed for a silicone oil liquid bridge

in air: the Oberbeck–Boussinesq approximation (OB), a linear temperature dependence of all material properties (LTD), and a full nonlinear dependence of all material parameters on temperature (FTD). The critical stability curves have been computed as functions of the volume ratio $\mathcal{V}$ of the liquid bridge, its aspect ratio Γ, it size d and for a forced axial flow in the surrounding air measured by $\mathrm{Re_g}$. The Oberbeck–Boussinesq approximation tends to overestimate the critical Reynolds number, while the linear model underestimated it. This trend can be explained by an effective viscosity ν_{eff}, because the viscosity is by far the most temperature-dependent material property. If the effective viscosity rules the critical onset, then the modified Reynolds number of the FTD model $(\nu^*/\nu_{\mathrm{eff}})^2\,\mathrm{Re}_c^{\mathrm{FTD}} \approx \mathrm{Re}_c^{\mathrm{OB}}$ should be comparable to the one of the OB model. This correlation holds true approximately if ν_{eff} is defined as the perturbation kinetic-energy-weighted kinematic viscosity of the FTD model at criticality. Defining ν_{eff} this way was found to be more suitable than the surface-averaged viscosity proposed by Kozhoukharova *et al.* (1999), because the surface averaged viscosity only accounts for the driving of the basic and perturbation velocity fields, but does not take care of the thermal perturbation energy production of the HTW due to the advection across basic-state temperature gradients in the bulk. Unlike Kozhoukharova *et al.* (1999) and Shevtsova & Melnikov (2000) who have reported a reduction of Re_c due to the linearly temperature-dependent viscosity, we have found parameter ranges where this general conclusion is not valid. Therefore, a Reynolds number based on the effective viscosity cannot correlate the critical points for all governing parameters, but it represents a rough estimate in most cases considered.

The variable material properties have a particular strong effect on the critical Reynolds number when the liquid bridge is heated or cooled from the gas phase by an imposed axial gas flow. For a hot downward gas flow in the range $\mathrm{Re_g} \in [-1750,\ -250]$ the critical curves for all three models exhibit broad maxima. The maximum values differ significantly due to the high critical temperature difference. In range of $\mathrm{Re_g}$ the segments of the critical curve which belong to different azimuthal wave numbers merge almost smoothly. This can be explained by the production of the thermal perturbation energy of the hydrothermal wave being confined to a narrow radial zone. Therefore, the neutral Reynolds numbers for different (not too large) azimuthal wave numbers do not vary much. Owing to the crowding of neutral modes in this range of $\mathrm{Re_g}$ a complex interplay between these modes can be expected slightly supercritically. The only exception to the smooth merging of critical modes is the $m = 1$ mode of the OB model within $\mathrm{Re_g} \in [-1960,\ -250]$. This perturbation mode is extended towards the liquid bridge axis and the energy production is more widespread inside the (r, z)-plane travelling at untypical low rotational frequencies.

From a practical perspective, the dependence of the critical Reynolds numbers on the length scale d, shown in figure 7 for various models, could be useful for experimentalists who aim to predict Re_c and m_c for zero gravity conditions by conducting experiments on the ground. Our results show that a reliable prediction of the critical wave number under zero gravity by using the same experimental setup on the ground requires the size of the liquid bridge not to exceed $d = 0.8\,\mathrm{mm}$ (for the parameters selected). Based on the FTD model this size restriction should also keep the deviation between the critical Reynolds numbers for 1g and 0g below 5%, e.g., for $d = 0.75\,\mathrm{mm}$ $\Delta T_c(1\mathrm{g}) = 40.6\,\mathrm{K}$, while $\Delta T_c(0\mathrm{g}) = 42.7\,\mathrm{K}$. For smaller length scales d the relative deviations diminish, but the large absolute value of ΔT_c may lead to technical or safety issues for 0g space experiments and create undesired side effects. For this reason and for a better optical access space experiments are typically carried out using large liquid bridges ($d > 3\,\mathrm{mm}$). Due the dependence of the material properties on T similarity cannot be exploited for predictions by small scale terrestrial experiments. According to our linear stability analysis, the HTW instability for FTD-0g for $d > 3\,\mathrm{mm}$ cannot be predicted by simply employing smaller liquid bridges on the ground (FTD-1g):

The wave number of the critical mode under 0g is $m_c = 2$ for $d \gtrsim 0.84$ mm, while on ground the critical wave number is $m_c = 3$ for $d \lesssim 2.1$ mm.

With increasing temperature difference the deviations among Re_c for the three thermophysical models (OB, LTD, FTD) become larger. Large temperature difference, furthermore, typically require an increased maximum temperature T_{hot}. Under these conditions evaporation of the liquid can become significant. Using acetone (Pr = 4.3) as the liquid phase evaporative cooling can strongly stabilise the basic flow by reducing radial temperature gradients in the liquid phase (Simic-Stefani *et al.* 2006). Therefore, it is expected that including evaporative cooling in the modelling will reduce the difference between the OB, LTD and FTD models. Since the FTD model accounts for higher-order corrections of all thermo-physical properties, it would be desirable to also include higher-order terms in the temperature dependence of the surface tension (for an example, see Villers & Platten 1988). To do so, corresponding accurate measurements of $\sigma(T)$ for the present fluids are required. Finally, it would be of interest to extend the present models to include dynamic surface deformation due to the perturbation flow. It is expected that dynamic deformation due to the perturbation flow lead to only small corrections to the hydrothermal wave instabilities, but this approach would be more general, also allowing for surface wave instabilities. To date, surface wave instabilities in thermocapillary flows have been only observed in plane layers of low-Prandtl-number liquids (Smith & Davis 1983) and in flat migrating droplets (Hu *et al.* 2023).

Appendix A. Temperature dependence of the working fluids

Polynomials of second order have been fitted to the discrete data of ρ, λ and c_p for 2-cSt silicone oil provided by Shin-Etsu (2004) using least-squares. The low polynomial order was employed to avoid non-physical oscillations of the fit function. The functional dependence of $\mu(T)$ is constructed from the quadratic fit of the density and an exponential temperature dependence of the kinematic viscosity (as in Ueno *et al.* 2003). The explicit functions read

$$\rho(T) = \rho^* \left[1 - \beta^*(T - T^*) + 7.27 \times 10^{-7}(T - T^*)^2\right] \quad \mathrm{kg/m^3}, \tag{A 1a}$$

$$\mu(T) = \mu^* \mathrm{e}^{-5.892(T-T^*)/(T+273.15)} \left[1 - \beta^*(T - T^*) + 7.27 \times 10^{-7}(T - T^*)^2\right] \quad \mathrm{Pa\,s}, \tag{A 1b}$$

$$\lambda(T) = \lambda^* \left[1 - 0.0026(T - T^*) - 7.22 \times 10^{-8}(T - T^*)^2\right] \quad \mathrm{W/m\,K}, \tag{A 1c}$$

$$c_p(T) = c_p^* \left[1 + 0.000821(T - T^*) + 1.66 \times 10^{-8}(T - T^*)^2\right] \quad \mathrm{J/kg\,K}, \tag{A 1d}$$

where T is measured in °C. The reference quantities for $T^* = 25$°C denoted by the asterisk are given in table 2. Since the manufacturer does not specify the temperature dependence of the surface tension σ, we assume the linear dependence

$$\sigma(T) = \sigma^* - \gamma^*(T - T^*) \tag{A 2}$$

provided by Romanò *et al.* (2017) and also specified in table 2. The functional dependence of the gas properties

$$\rho_{\mathrm{g}}(T) = \rho_{\mathrm{g}}^* \frac{T^* + 273.15}{T + 273.15} \quad \mathrm{kg/m^3}, \tag{A 3a}$$

$$\mu_{\mathrm{g}}(T) = \mu_{\mathrm{g}}^* \left[1 + 0.0026(T - T^*) - 1.9 \cdot 10^{-6}(T - T^*)^2 + 1.78 \cdot 10^{-9}(T - T^*)^3 - 7.51 \cdot 10^{-13}(T - T^*)^4\right] \quad \mathrm{Pa\,s}, \tag{A 3b}$$

$$\lambda_{\mathrm{g}}(T) = \lambda_{\mathrm{g}}^* \left[1 + 0.0028(T - T^*) - 1.58 \times 10^{-6}(T - T^*)^2 + 1.28 \times 10^{-9}(T - T^*)^3 - 5.91 \times 10^{-13}(T - T^*)^4\right] \quad \mathrm{W/m\,K}, \tag{A 3c}$$

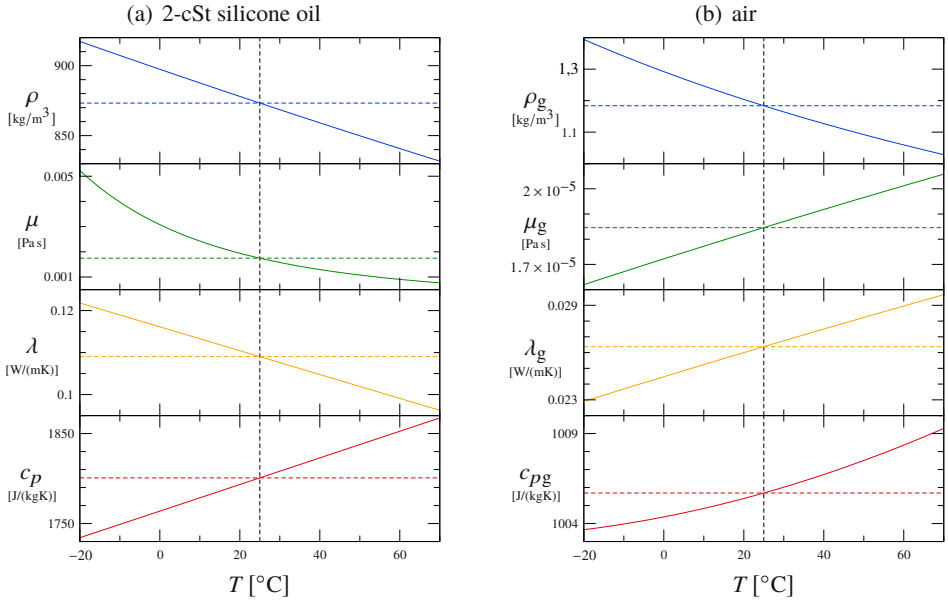

Figure 14: Temperature dependence of the thermophysical properties of the working liquid (a) and working gas (b). The coloured horizontal dashed lines represent the reference values specified in table 2. The vertical black dashed lines represent the reference mean temperature $T^* = 25°\mathrm{C}$.

$$c_{pg}(T) = 1011.96 - 1194.72G^2\left[1 - F\left(-3.428 + 49.824G - 120.35G^2 + 98.867G^3\right)\right] \quad \mathrm{J/kg\,K}, \qquad (\mathrm{A}\,3d)$$

are based on explicit formulae of VDI e.V. (2010), where

$$G(T) = \frac{T + 273.15}{T + 2822.08}, \quad \text{and} \quad F(T) = \frac{2548.93}{T + 2822.08}. \qquad (\mathrm{A}\,4)$$

In figure 14, all functions (A 1) and (A 3) are evaluated and plotted in the range $T \in [-20,\ 70]\,°\mathrm{C}$.

Appendix B. Verification and validation of the linear stability analysis for temperature-dependent material properties

For the verification of the LTD model, we adopt the setup of Melnikov *et al.* (2002), where the liquid's viscosity $\alpha_\mu(\vartheta) = \alpha_\mu^* + \alpha_\mu'^*\vartheta$ is assumed to be a linear function of the temperature. The remaining thermophysical properties ρ, λ and c_p are assumed to be constant. In figure 15, a comparison is made between the critical data Re_c and ω_c obtained by `MaranStable` (circles) and Melnikov *et al.* (2002) (squares). Results are given as functions of the non-dimensional viscosity variation $\alpha_\mu'^*$. A good agreement is found for all $\alpha_\mu'^*$ considered. The critical Reynolds numbers Re_c reported by Melnikov *et al.* (2002) (blue squares) are about 5% larger than those obtained by `MaranStable` (blue circles), but the slopes with respect to $\alpha_\mu'^*$ agree very well. The maximum deviation of 2% in ω_c is even smaller than for Re_c. The slightly higher critical Reynolds numbers found by Melnikov *et al.* (2002) might be related to their numerical treatment of the problem, using a three-dimensional time-dependent simulation rather than a stability analysis. Their mesh of 24×16 grid points in the (r, z) plane

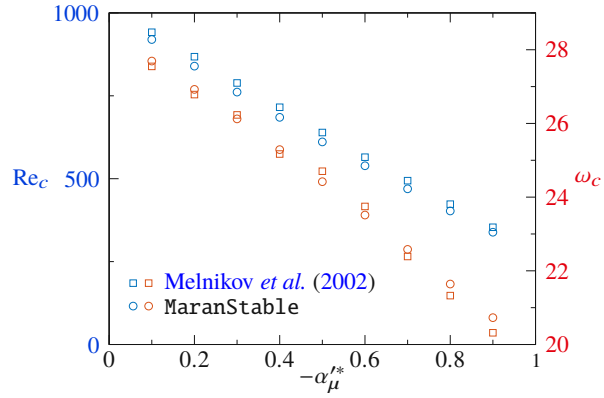

Figure 15: Critical Reynolds numbers Re_c (blue symbols) and critical oscillation frequencies ω_c (red symbols) as functions of α'^*_μ under weightlessness conditions with $\Gamma = 1$, $\mathcal{V} = 1$ and $\mathrm{Pr} = 4$. Squares: data taken from Melnikov *et al.* (2002); circles: results of `MaranStable`. The critical wave number is $m_c = 2$.

was much coarser than the one used in `MaranStable`. Furthermore, some regularization of the thermocapillary stresses near the hot and cold corners might have been applied, as was done by Wanschura *et al.* (1995).

We are not aware of numerical investigations taking into account the full temperature dependence of all thermophysical parameters. Therefore, we compare the results from `MaranStable` for the basic flow with the ones from the code of Romanò *et al.* (2017) in which only the full temperature dependence of the kinematic viscosity (main effect) and of the thermal diffusivity were taken into account. Figure 16 shows the basic temperature ϑ_0 (a) and the basic axial velocity component w_0 (b) on the free surface. The parameters have been selected according to Barmak *et al.* (2021), i.e. $d = 5\,\mathrm{mm}$, $\Gamma = 1$, $\Gamma_{\mathrm{rod}} = \eta = 3\,\mathrm{mm}$, $T^* = 25°\mathrm{C}$, $\Delta T = 40\,\mathrm{K}$ and a closed gas tube. The present results are shown as red dots, while those of Romanò *et al.* (2017) are represented by black lines. Both results agree up to the line's thickness, even when using different grid resolutions in the z direction. Also shown are the surface quantities obtained using the OB approximation (blue dots). Their deviation from the FTD approach demonstrates the importance of taking into account the temperature dependence of the material properties.

To validate the linear stability analysis for the FTD approach the geometry was adapted to match the experimental setup of Yano *et al.* (2016). We consider two liquid bridges made of 2-cSt and 5-cSt silicone oil, but the same geometry with $d = 2.5\,\mathrm{mm}$ and $\Gamma = 1$. Both liquid bridges are surrounded by air in a tube with $\Gamma_{\mathrm{rod}} = 4.8$ and $\eta = 5$. Figure 17 shows the neutral and critical Marangoni numbers as functions of the volume ratio $\mathcal{V}$ for a closed tube (figure 17(a)) and for a hot vertically downward gas flow through an open tube (figs. 17(b,c)). In the experiments of Yano *et al.* (2016) the air enters the tube through a porous medium. Therefore, we prescribe in the numerics a constant gas velocity at the inlet with the same mean velocity $w_{\mathrm{g}}(r) \equiv \bar{w}_{\mathrm{g}} = -35\,\mathrm{mm/s}$ as in the experiment, corresponding to $\mathrm{Re}_{\mathrm{g}} = 43.75$. To demonstrate the importance of using the FTD model (full lines), we also include in figure 17 the results of the LTD (dashed lines) and the OB models (dash-dotted lines).

Considering the 2-cSt liquid bridge (figure 17(a,b)), the numerical critical Marangoni numbers obtained with the linearised model and with the FTD model agree very well with the experimental data within the experimental error bar for both, closed and open gas tubes. Merely for $\mathcal{V} = 1$ some deviations exist owing to the huge slope of the critical curve for $m = 1$ with respect to $\mathcal{V}$. For moderate temperature differences ΔT, the OB approximation

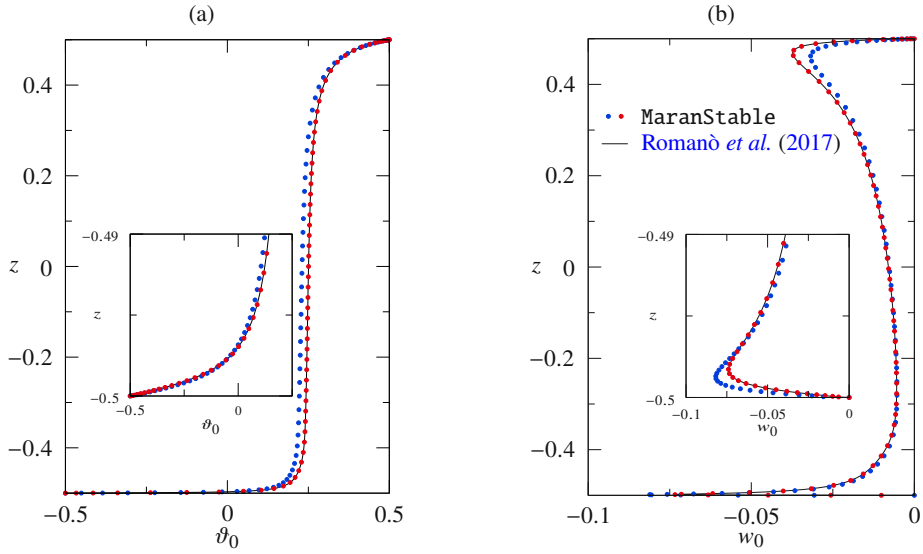

Figure 16: Basic-state surface temperature ϑ_0 (a) and axial component of the surface velocity w_0 (b) for $d = 5$ mm, $\Gamma = 1$, $\Gamma_{\text{rod}} = \eta = 3$ mm, $T^* = 25°\text{C}$, $\Delta T = 40$ K, a closed gas tube and an indeformable upright cylindrical interface. Sown are results of Romanò *et al.* (2017) (full line), present FTD results (red dots) and present OB results (blue dots).

is sufficient to predict the critical Marangoni number. However, for the largest measured ΔT in figure 17(a), i.e. $\Delta T \approx 27°\text{C}$ for $\mathcal{V} = 0.95$, the critical Marangoni number predicted by the OB approximation would be too large.

For the 5-cSt liquid bridge, the critical temperature differences are larger (see figure 17(c)), resulting in more significant deviations among the critical Marangoni numbers obtained using different material laws. For $\mathcal{V} < 1$ the FTD yields results closest to the experimental data. However, for $\mathcal{V} \gtrsim 0.97$ the FTD model predicts a critical mode with $m = 2$, whereas $m = 1$ is found in the experiments. This indicates that certain influence factors are not accounted for within the FTD model. Possible candidates are evaporative cooling effects or experimental imperfections (a slightly non-axisymmetric gas flow could have also favoured an $m = 1$ mode).

In view of the very good agreement with the results of Melnikov *et al.* (2002) and Romanò *et al.* (2017) our code can be considered verified. Despite of the relatively large error bar of the experimental data of Yano *et al.* (2016) our code can be also considered validated for 2-cSt silicone oil which is used as the working liquid in the present work.

Appendix C. Correlation between the variable-material-property effect and an effective kinematic viscosity

Since the dynamic viscosity of the liquid phase has the largest range of variation in the FTD calculations, it is tempting to correlate the difference between the critical Reynolds numbers for the FTD and the OB approaches with a suitably defined effective kinematic viscosity ν_{eff} of the liquid, similar as in Kozhoukharova *et al.* (1999). It is based on the assumption that the modified Reynolds number $\widetilde{\text{Re}}$ based on the critical temperature difference ΔT_c^{FTD} and on the effective kinematic viscosity ν_{eff} yields the same critical Reynolds number as the OB

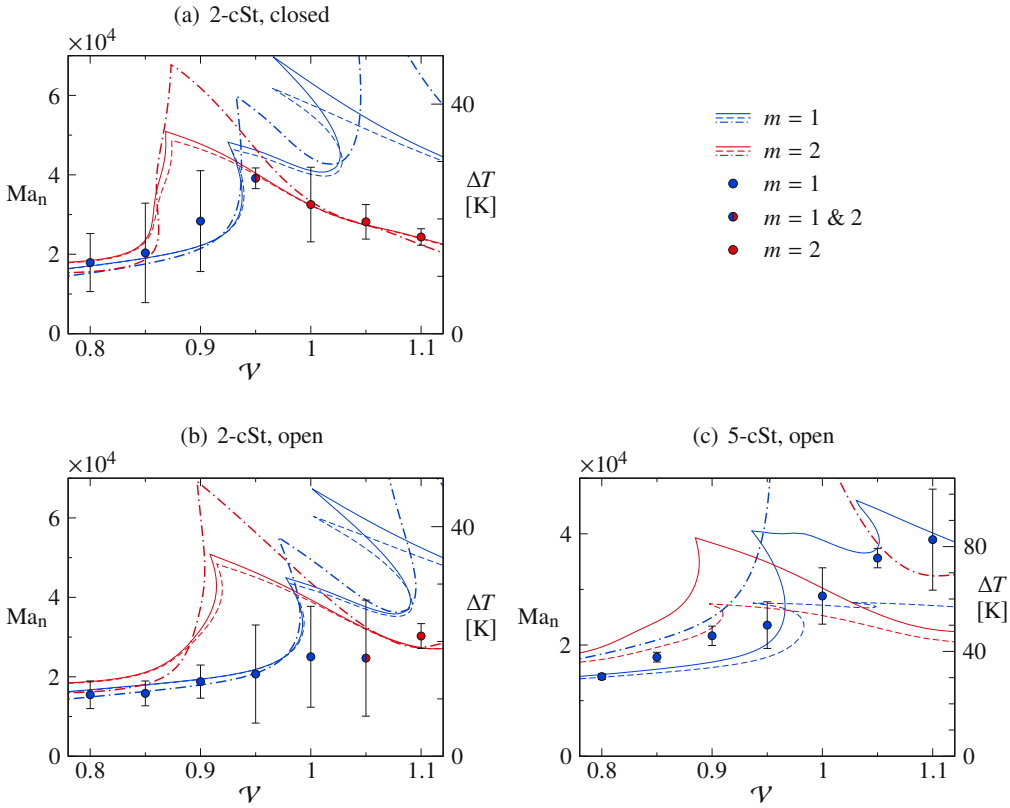

Figure 17: Neutral Marangoni numbers (lines) and temperature difference ΔT as functions of the volume ratio $\mathcal{V}$ for a liquid bridge of 2-cSt (a,b) and 5-cSt (c) silicone oil in air with $d = r_\mathrm{i} = 2.5\,\mathrm{mm}$, $d_\mathrm{rod} = 12\,\mathrm{mm}$ and $r_\mathrm{o} = 12.5\,\mathrm{mm}$ under normal gravity conditions. The gas tube is closed in (a) and open in (b,c) with $\bar{w}_\mathrm{g} = -35\,\mathrm{mm/s}$. Shown are the experimental data taken from figs. 6(a) and 6(b) of Yano *et al.* (2016) (dots) in comparison to the FTD model (full lines), the LTD model (dashed lines) and the OB model (dash-dotted lines). Color indicates the neutral wave number: $m = 1$ (blue) and $m = 2$ (red).

approach. This leads to the hypothesis

$$\widetilde{\mathrm{Re}}_c := \frac{\gamma^* d}{\rho^*}\frac{\Delta T_c^\mathrm{FTD}}{\nu_\mathrm{eff}^2} = \left(\frac{\nu^*}{\nu_\mathrm{eff}}\right)^2 \mathrm{Re}_c^\mathrm{FTD} \stackrel{!}{=} \mathrm{Re}_c^\mathrm{OB}. \tag{C 1}$$

From the space-dependent variable viscosity $\nu[T_0(\boldsymbol{x})]$ of the of the liquid in the basic flow at the critical point $\mathrm{Re}_c^\mathrm{FTD}$ different mean kinematic viscosities can be constructed. Among these are the volume-averaged viscosity ν_V, the volume-averaged viscosity with kinetic-energy weighting ν_E, and the surface averaged viscosity ν_S (used by Kozhoukharova *et al.* 1999), defined as

$$\nu_V = \frac{1}{V}\int_V \nu[T_0(\boldsymbol{x})]\mathrm{d}V, \tag{C 2a}$$

$$\nu_E = \left\{\int_V \rho[T_0(\boldsymbol{x})]\hat{\boldsymbol{u}}^2\mathrm{d}V\right\}^{-1} \int_V \nu[T_0(\boldsymbol{x})]\rho[T_0(\boldsymbol{x})]\hat{\boldsymbol{u}}^2\mathrm{d}V, \tag{C 2b}$$

$$\nu_S = \frac{1}{S}\int_S \nu[T_0(\boldsymbol{x})]\mathrm{d}S. \tag{C 2c}$$

The corresponding relative mean liquid viscosities ν_i/ν^* ($i \in [V, E, S]$) are shown in figure 18 for three parameter variations carried out in the main text. Quite generally, we find $\nu_V > \nu^*$ and $\nu_E, \nu_S < \nu^*$.

Given $\mathrm{Re}_c^{\mathrm{FTD}}$ and $\mathrm{Re}_c^{\mathrm{OB}}$ equation (C 1) can be tested using the above effective viscosities. Since typically $\mathrm{Re}_c^{\mathrm{OB}} > \mathrm{Re}_c^{\mathrm{FTD}}$ the effective viscosity should satisfy $\nu_{\mathrm{eff}} < \nu^*$. Therefore, ν_V does not qualify for an effective viscosity. Using $\nu_{\mathrm{eff}} = \nu_S$ we find the shift of $\mathrm{Re}_c^{\mathrm{FTD}}$ is too large. The modified Reynolds number based on the kinetic-energy-weighted kinematic viscosity $\widetilde{\mathrm{Re}}_c = \gamma^* d\Delta T_c^{\mathrm{FTD}}/(\rho^* \nu_E^2)$ is shown in figure 19 for the volume variation. The general trend and the order of magnitude of the shift $\widetilde{\mathrm{Re}}_c - \mathrm{Re}_c^{\mathrm{FTD}}$ is well captured in some ranges of $\mathcal{V}$, while the correction is too strong in other ranges of $\mathcal{V}$ (e.g. where $m_c = 1$). Obviously, other factors like the temperature dependence of other thermophysical parameters, the dependence of the basic flow on ΔT or the structure of the perturbation flow on r and φ are not taken into account. The qualitative agreement between $\widetilde{\mathrm{Re}}_c$ and $\mathrm{Re}_c^{\mathrm{OB}}$ suggests, however, that an important reason for the difference between the critical Reynolds number is the reduced dissipation the perturbation flow experiences in regions where the perturbation flow is significant, i.e. where the kinetic-energy-weighting factor in (C 2)(b) is large.

We mention that the correction factor $(\nu^*/\nu_{\mathrm{eff}})^2$ has the right order of magnitude also in the case of an imposed flow in the gas phase (not shown), except for the range of $\mathrm{Re_g}$ in which the critical $m = 1$ mode arises for the OB model (figure 9(a)). In this range the structures of the critical curves $\mathrm{Re}_c^{\mathrm{FTD}}(\mathrm{Re_g})$ and $\mathrm{Re}_c^{\mathrm{OB}}(\mathrm{Re_g})$ are too different to allow for the simple correlation according to (C 1). Regarding the aspect ratio variation the correction $\widetilde{\mathrm{Re}}_c - \mathrm{Re}_c^{\mathrm{FTD}}(\Gamma)$ is too large for $\Gamma \lesssim 0.95$ but fits nicely for $\Gamma \gtrsim 0.95$.

REFERENCES

Amberg, G. & Do-Quang, M. 2008 Thermocapillary convection and phase change in welding. *Int. J. Num. Meth. Heat Fluid Flow* **18**, 378–386.

Barmak, Ilya, Romanò, Francesco & Kuhlmann, Hendrik C. 2021 Finite-size coherent particle structures in high-Prandtl-number liquid bridges. *Phys. Rev. Fluids* **6**, 084301 (36pp).

Busse, F. H. 1978 Non-linear properties of thermal convection. *Rep. Prog. Phys.* **41**, 1929–1967.

Busse, F. H. & Frick, H. 1985 Square-pattern convection in fluids with strongly temperature-dependent viscosity. *J. Fluid Mech.* **150**, 451–465.

Carrión, Luis M., Herrada, Miguel A. & Montanero, José M. 2020 Influence of the dynamical free surface deformation on the stability of thermal convection in high-Prandtl-number liquid bridges. *Intl J. Heat Mass Transfer* **146**, 118831 (10pp).

Chen, Q. S. & Hu, W. R. 1998 Influence of liquid bridge volume on instability of floating half zone convection. *Intl J. Heat Mass Transfer* **41**, 825–837.

Cröll, A., Müller-Sebert, W., Benz, K. W. & Nitsche, R. 1991 Natural and thermocapillary convection in partially confined silicon melt zones. *Microgravity Sci. Technol.* **3**, 204–215.

Gaponenko, Y., Mialdun, V. Yasnouand A., Nepomnyashchy, A. & Shevtsova, V. 2021 Hydrothermal waves in a liquid bridge subjected to a gas stream along the interface. *J. Fluid Mech.* **908**, A34 (36pp).

Graham, A. 1933 Shear patterns in an unstable layer of air. *Philos. Trans. Roy. Soc. London A* **232**, 285–296.

Gray, D. D. & Giorgini, A. 1976 The validity of the Boussinesq approximation for liquids and gases. *Intl J. Heat Mass Transfer* **19**, 545.

Hu, Kai-Xin, Zhang, Shao-Neng & Chen, Qi-Sheng 2023 Surface wave instability in the thermocapillary migration of a flat droplet. *J. Fluid Mech.* **958**, A22 (22pp).

Kamotani, Y., Wang, L., Hatta, S., Wang, A. & Yoda, S. 2003 Free surface heat loss effect on oscillatory thermocapillary flow in liquid bridges of high Prandtl number fluids. *Intl J. Heat Mass Transfer* **46**, 3211–3220.

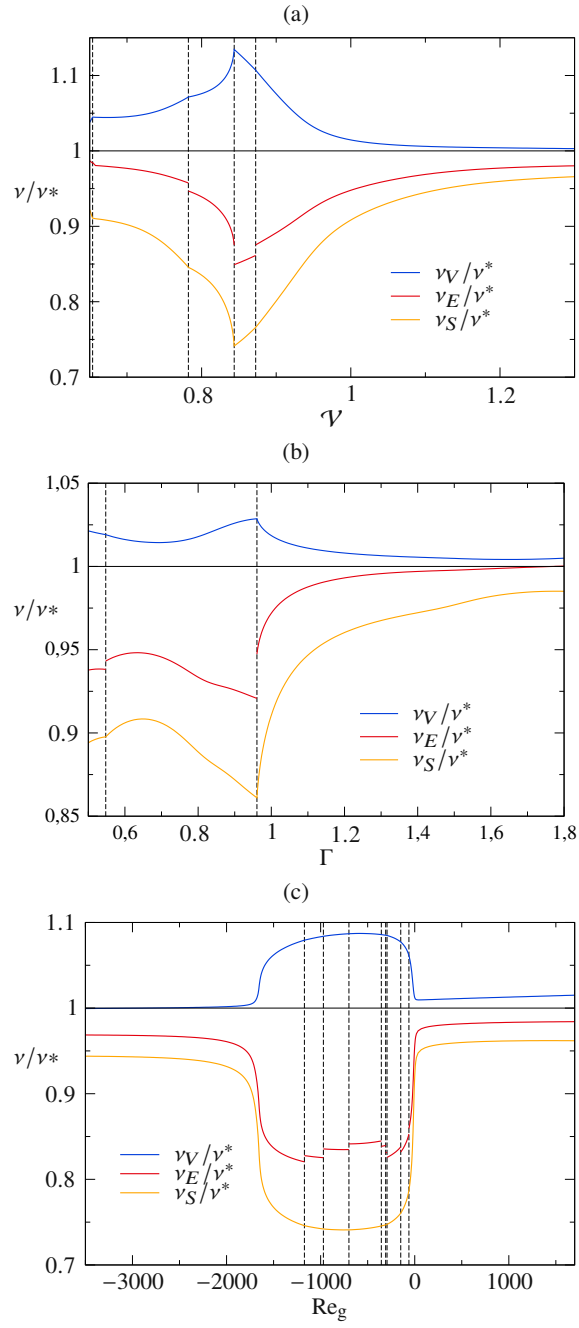

Figure 18: Different relative mean liquid viscosities according to (C 2) evaluated on the stability boundary $\mathrm{Re}_c^{\mathrm{FTD}}$.

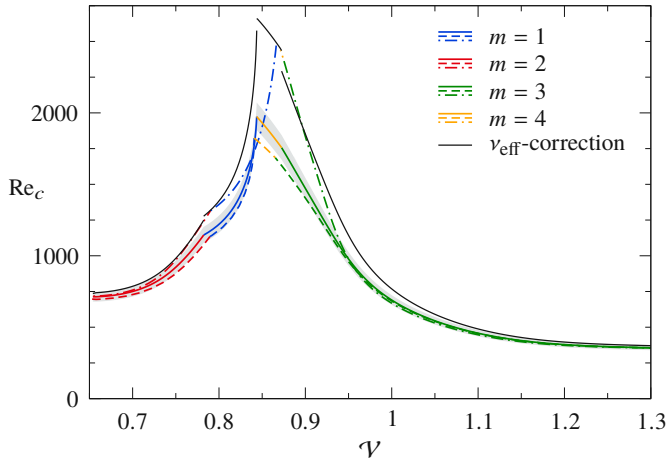

Figure 19: Prediction of Re_c^{OB} (dash-dotted lines) by $\text{Re}_c^{\text{OB},\nu_{\text{eff}}}$ (black lines) based on Re_c^{FTD} and the kinetic-energy-weighted viscosity ν_{eff}, for all non-zero critical wave numbers.

Keller, H. B. 1977 *Numerical solution of bifurcation and nonlinear eigenvalue problems*, pp. 359–384. New York: Academic Press.

Kozhoukharova, Zh., Kuhlmann, H. C., Wanschura, M. & Rath, H. J. 1999 Influence of variable viscosity on the onset of hydrothermal waves in thermocapillary liquid bridges. *Z. Angew. Math. Mech.* **79**, 535–543.

Kuhlmann, H. C. 1999 *Thermocapillary Convection in Models of Crystal Growth*, *Springer Tracts in Modern Physics*, vol. 152. Berlin, Heidelberg: Springer.

Lehoucq, R. B., Sorensen, D. C. & Yang, C. 1998 *ARPACK Users' Guide: Solution of Large-Scale Eigenvalue Problems with Implicitly Restarted Arnoldi Methods*. Philadelphia: SIAM.

Levich, V. G. 1962 *Physicochemical Hydrodynamics*. Prentice-Hall.

Majima, S., Kawamura, H., Otsubo, F., Kuwahara, K. & Doi, T. 2001 Oscillatory thermocapillary flow in encapsulated liquid column. *Phys. Fluids* **13**, 1517–1520.

Melnikov, D.E., Shevtsova, V., Yano, T. & Nishino, K. 2015 Modeling of the experiments on the marangoni convection in liquid bridges in weightlessness for a wide range of aspect ratios. *Int. J. Heat Mass Transfer* **87**, 119 – 127.

Melnikov, D. E., Shevtsova, V. M. & Legros, J. C. 2002 Numerical simulation of hydro-thermal waves in liquid bridges with variable viscosity. *Adv. Space Res.* **29**, 661–666.

Melnikov, D. E., Shevtsova, V. M. & Legros, J. C. 2004 Onset of temporal aperiodicity in high Prandtl number liquid bridge under terrestrial conditions. *Phys. Fluids* **16**, 1746–1757.

Meseguer, J., Slobozhanin, L. A. & Perales, J. M. 1995 A review on the stability of liquid bridges. *Adv. Space Res.* **16**, 5–14.

Nienhüser, C. & Kuhlmann, H. C. 2002 Stability of thermocapillary flows in non-cylindrical liquid bridges. *J. Fluid Mech.* **458**, 35–73.

Nishino, Koichi, Yano, Taishi, Kawamura, Hiroshi, Matsumoto, Satoshi, Ueno, Ichiro & Ermakov, Michael K. 2015 Instability of thermocapillary convection in long liquid bridges of high Prandtl number fluids in microgravity. *J. Crystal Growth* **420**, 57–63.

Palm, Enok 1960 On the tendency towards hexagonal cells in steady convection. *J. Fluid Mech.* **8** (2), 183–192.

Pfann, W. G. 1962 Zone melting. *Science* **135**, 1101–1109.

Preisser, F., Schwabe, D. & Scharmann, A. 1983 Steady and oscillatory thermocapillary convection in liquid columns with free cylindrical surface. *J. Fluid Mech.* **126**, 545–567.

Ristenpart, W. D., Kim, P. G., Domingues, C., Wan, J. & Stone, H. A. 2007 Influence of substrate conductivity on circulation reversal in evaporating drops. *Phys. Rev. Lett.* **99**, 234502.

Romanò, Francesco, Kuhlmann, Hendrik C., Ishimura, Misa & Ueno, Ichiro 2017 Limit cycles for the

motion of finite-size particles in axisymmetric thermocapillary flows in liquid bridges. *Phys. Fluids* **29** (9), 093303 (14pp), arXiv: http://dx.doi.org/10.1063/1.5002135.

Saifi, A. H., Mundhada, V. M. & Tripathi, M. K. 2022 Thermocapillary convection in liquid-in-liquid capillary bridges due to a heating/cooling ring. *Phys. Fluids* **34**, 032112 (11pp).

Schwabe, D. 1981 Marangoni effects in crystal growth melts. *Physicochem. Hydrodyn.* **2**, 263–280.

Scriven, L. E. & Sternling, C. V. 1960 The Marangoni effects. *Nature* **187**, 186–188.

Segel, L. A. & Stuart, J. T. 1962 On the question of the preferred mode in cellular thermal convection. *J. Fluid Mech.* **13** (2), 289–306.

Shevtsova, V., Gaponenko, Y., Kuhlmann, H. C., Lappa, M., Lukasser, M., Matsumoto, S., Mialdun, A., Montanero, J. M., Nishino, K. & Ueno, I. 2014 The JEREMI-project on thermocapillary convection in liquid bridges. Part B: Overview on impact of co-axial gas flow. *Fluid Dyn. Mat. Proc.* **10**, 197–240.

Shevtsova, V., Gaponenko, Y. A. & Nepomnyashchy, A. 2013 Thermocapillary flow regimes and instability caused by a gas stream along the interface. *J. Fluid Mech.* **714**, 644–670.

Shevtsova, V., Melnikov, D. E. & Nepomnyashchy, A. 2009 New flow regimes generated by mode coupling in buoyant-thermocapillary convection. *Phys. Rev. Lett.* **102**, 134503–1–134503–4.

Shevtsova, V. M. & Melnikov, D. E. 2000 Influence of variable viscosity on convective flow in liquid bridges. 3-D simulations of ground based experiments. In *1st Symposium on Microgravity Research and Applications in Physical Science and Biotechnology, Sorrento, Italy*.

Shevtsova, V. M., Melnikov, D. E. & Legros, J. C. 2001 Three-dimensional simulations of hydrodynamic instability in liquid bridges: Influence of temperature-dependent viscosity. *Phys. Fluids* **13**, 2851–2865.

Shin-Etsu 2004 *Silicone Fluid KF-96 – Performance Test Results*. 6-1, Ohtemachi 2-chome, Chioda-ku, Tokyo, Japan.

Shitomi, Nobuhiro, Yano, Taishi & Nishino, Koichi 2019 Effect of radiative heat transfer on thermocapillary convection in long liquid bridges of high-prandtl-number fluids in microgravity. *International Journal of Heat and Mass Transfer* **133**, 405 – 415.

Simic-Stefani, S., Kawaji, M. & Yoda, S. 2006 Onset of oscillatory thermocapillary convection in acetone liquid bridges: The effect of evaporation. *Intl J. Heat Mass Transfer* **49**, 3167–3179.

Smith, M. K. 1986 Instability mechanisms in dynamic thermocapillary liquid layers. *Phys. Fluids* **29**, 3182–3186.

Smith, M. K. & Davis, S. H. 1983 Instabilities of dynamic thermocapillary liquid layers. Part 2. Surface-wave instabilities. *J. Fluid Mech.* **132**, 145–162.

Stojanovic, Mario & Kuhlmann, Hendrik C. 2020 Stability of thermocapillary flow in high-Prandtl-number liquid bridges exposed to a coaxial gas stream. *Microgravity Sci. Technol.* **32**, 953–959.

Stojanović, Mario, Romanò, Francesco & Kuhlmann, Hendrik C. 2022 Stability of thermocapillary flow in liquid bridges fully coupled to the gas phase. *J. Fluid Mech.* **949**, A5 (51pp).

Stojanovic, Mario, Romanò, Francesco & Kuhlmann, Hendrik C. 2023 High-Prandtl-number thermocapillary liquid bridges with dynamically deformed interface: Effect of an axial gas flow on the linear stability. *(submitted)* .

Stojanović, M., Romanò, F. & Kuhlmann, H. C. 2023*a* Instability of axisymmetric flow in thermocapillary liquid bridges: Kinetic and thermal energy budgets for two-phase flow with temperature-dependent material properties. *Eur. J. Appl. Math.* p. 100000.

Stojanović, M., Romanò, F. & Kuhlmann, H. C. 2023*b* MaranStable: A linear stability solver for multiphase flows in canonical geometries. *Software X* **23**, 101405 (6pp).

Tanaka, S., Kawamura, H., Ueno, I. & Schwabe, D. 2006 Flow structure and dynamic particle accumulation in thermocapillary convection in a liquid bridge. *Phys. Fluids* **18**, 067103 (11pp).

v. Tippelskirch, H. 1956 Über konvektionszellen, insbesondere im flüssigen schwefel. *Beitr. Phys. Atmos.* **29**, 37–54.

Ueno, Ichiro 2021 Experimental study on coherent structures by particles suspended in half-zone thermocapillary liquid bridges: Review. *Fluids* **6**, 105–1–105–16.

Ueno, I., Tanaka, S. & Kawamura, H. 2003 Oscillatory and chaotic thermocapillary convection in a half-zone liquid bridge. *Phys. Fluids* **15**, 408–416.

VDI e.V. 2010 *VDI Heat Atlas*. Springer Berlin Heidelberg.

Villers, D. & Platten, J. K. 1988 Temperature dependence of the interfacial tension between water and long-chain alcohols. *J. Phys. Chem.* **92**, 4023–4024.

Wanschura, M., Shevtsova, V. S., Kuhlmann, H. C. & Rath, H. J. 1995 Convective instability mechanisms in thermocapillary liquid bridges. *Phys. Fluids* **7**, 912–925.

Yano, Taishi, Hirotani, Makoto & Nishino, Koichi 2018*a* Effect of interfacial heat transfer on basic flow and instability in a high-Prandtl-number thermocapillary liquid bridge. *Intl J. Heat Mass Transfer* **125**, 1121–1130.

Yano, Taishi, Maruyama, Kaname, Matsunaga, Takuya & Nishino, Koichi 2016 Effect of ambient gas flow on the instability of Marangoni convection in liquid bridges of various volume ratios. *Intl J. Heat Mass Transfer* **99**, 182–191.

Yano, T., Nishino, K., Kawamura, H., Ueno, I. & Matsumoto, S. 2015 Instability and associated roll structure of Marangoni convection in high Prandtl number liquid bridge with large aspect ratio. *Phys. Fluids* **27** (2), 024108.

Yano, Taishi, Nishino, Koichi, Matsumoto, Satoshi, Ueno, Ichiro, Komiya, Atsuki, Kamotani, Yasuhiro & Imaishi, Nobuyuki 2018*b* Report on microgravity experiments of dynamic surface deformation effects on Marangoni instability in high-Prandtl-number liquid bridges. *Microgravity Sci. Technol.* **30**, 599–610.

Yano, T., Nishino, K., Ueno, I., Matsumoto, S. & Kamotani, Y. 2017 Sensitivity of hydrothermal wave instability of Marangoni convection to the interfacial heat transfer in long liquid bridges of high Prandtl number fluids. *Phys. Fluids* **29** (4), 044105 (11pp).

Yasnou, V., Gaponenko, Y., Mialdun, A. & Shevtsova, V. 2018 Influence of a coaxial gas flow on the evolution of oscillatory states in a liquid bridge. *Int. J. Heat Mass Transfer* **123**, 747–759.

Paper 5

Romanò, F., Stojanović, M., Kuhlmann, H. C. (2023), 'Scaling and modeling of the heat transfer across the free surface of a thermocapillary liquid bridge (submitted)', *Int. J. Numer. Method H.*

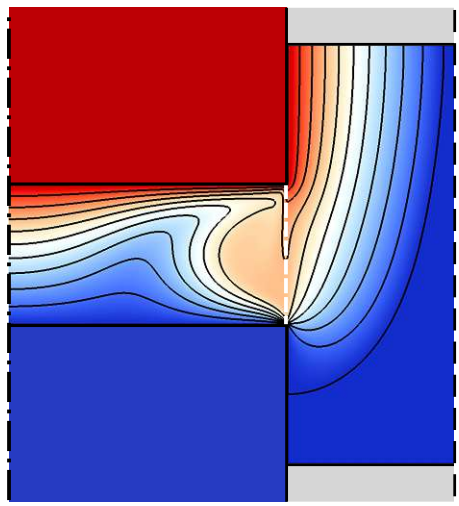

Scaling and modeling of the heat transfer across the free surface of a thermocapillary liquid bridge

Abstract

Purpose – A reduced-order model for the heat transfer across the interface between a millimetric thermocapillary liquid bridge from silicone oil and the surrounding ambient gas is derived.
Design/methodology/approach – Numerical solutions for the two-fluid model are computed covering a wide parametric space, making a total of 2800 numerical flow simulations. Based on the computed data, a reduced single-fluid model for the liquid phase is devised, in which the heat transfer between the liquid and the gas is modeled by Newton's law of heat transfer, albeit with a space-dependent Biot function $\mathrm{Bi}(z)$, instead of a constant Biot number Bi.
Findings – An explicit robust fit of $\mathrm{Bi}(z)$ is obtained covering the whole range of parameters considered. The single-fluid model together with the Biot function derived yields very accurate results at much lesser computational cost than the corresponding two-phase fully-coupled simulation required for the two-fluid model.
Practical implications – Using our novel Biot function approach instead of a constant Biot number, the critical Reynolds number can be predicted much more accurately within single-phase linear stability solvers.
Originality/value – The Biot function for thermocapillary liquid bridges is derived from the full multiphase problem by a robust multi-stage fit procedure. The Biot function derived reproduces very well the theoretical boundary layer scalings.
Keywords Biot number, Heat transfer, Liquid bridge, Multiphase flow, Boundary layer, Multi-stage polynomial fit
Paper type Research paper

1. Introduction

When the temperature varies along a fluid–fluid interface a surface stress is created due to the thermocapillary effect and a fluid motion tangential to the interface is established [1]. In non-isothermal two-phase microfluidic systems surface forces are often more important than volume forces. Examples are small droplets [2] or thin films [3], where thermocapillary forces can drive significant steady flows. These flows may become unstable to symmetry-breaking perturbations from which hydrothermal waves can evolve [4]. Beside the scientific interest, thermocapillary convection is also relevant for several industrial applications involving fluid interfaces and large temperature gradients. Examples are crystal growth from the melt [5], welding [6] and combustion of fuels [7]. Therefore, quite a large body of publications exists devoted to thermocapillary convection. To study the physical mechanisms of flow instabilities, simple geometries have been investigated, such as liquid bridges [8], liquid films [3], annular pools [9] and open liquid-filled cavities [10, 11, 12].

Schwabe et al. [13] and Hurle and Jakeman [14] proposed to model the floating-zone crystal-growth process considering one half of the full liquid zone. Many subsequent theoretical and numerical studies, aiming at further simplifying the model or at reducing the computational cost,

considered only the liquid phase and neglected its coupling to the surrounding gas. Typically, the mechanical stresses from the gas phase acting on the liquid–gas interface are neglected owing to the small viscosity of the gas, while the more important thermal coupling between the two phases was treated by Newton's law of heat transfer. Within this approach the flow in the gas phase does not need to be computed.

Although the single-phase approach is appealing from a computational economy or theoretical point of view, it might only be reasonably accurate. This conjecture is supported by experimental investigations which indicated that the surrounding gas has an important effect on the flow in the liquid phase. For instance, the critical Reynolds number for the onset of three-dimensional flow and the azimuthal structure (mode) of the flow above the threshold depends on the thermal environment [26, 28]. Nevertheless, current numerical investigations are routinely assuming an adiabatic free surface [15], a given heat transfer [16], or a fictitious temperature distribution in the gas phase together with a constant Biot number [17]. The same simplified modeling approach is currently used to deal with particle-laden flow in liquid bridges and cavities [18, 19, 20, 21]. We shall demonstrate the deficits of such approximations and propose a more refined single-phase model which includes the leading-order (i.e. axisymmetric) thermal coupling derived from a two-phase model. To that end the investigation of [22] is extended, following their modeling approach and methodology.

For typical experimental parameters, numerical simulations of the liquid and gas flow are carried out in the framework of the half-zone model using a full coupling between both phases. Within the multiphase computations, the heat transfer across the liquid–gas interface is part of the solution and can be evaluated a-posteriori. Based on a post-processing of the data a new heat-transfer model is proposed, recasting the interfacial heat flux in the form of Newton's cooling law, but with a space-dependent Biot number, the Biot function $\mathrm{Bi}(z)$. The Biot function $\mathrm{Bi}(z)$ is evaluated for a large parameter set and an explicit heat-transfer model based on fitting all Biot functions computed is proposed and tested using a single-phase solver.

The paper is structured as follows. Section 2 defines the mathematical model of the multiphase flow, Sec. 3 presents the discretization employed to numerically solve the Navier–Stokes system and Sec. 4 explains the method to derive a robust heat transfer model. The results, including the boundary layer scaling and the fitting procedure for the Biot function, are presented and tested in Sec. 5. Finally, in Sec. 6 the results are summarized and conclusions are drawn.

2. Two-phase flow: Problem formulation

The geometry of the problem is shown in fig. 1. Two thermally conducting rods of radius R are placed coaxially at a mutual distance d. A liquid bridge, surrounded by a gas, is formed in the gap between the two rods. The liquid is kept in place by surface tension and by contact lines pinned to the sharp circular edges of the rods. The liquid is Newtonian with temperature-dependent density $\rho(T)$, and dynamic viscosity $\mu(T)$, specific heat capacity $c_p(T)$ and thermal conductivity $\lambda(T)$. The top and the bottom rods are kept at different constant temperatures $T_{\mathrm{hot}} = T_0 + \Delta T/2$ and $T_{\mathrm{cold}} = T_0 - \Delta T/2$, respectively, where ΔT is the temperature difference between the two rods and T_0 the arithmetic mean, kept constant at $T_0 = 25\,^{\circ}\mathrm{C}$. For $\Delta T \neq 0$ an axial temperature gradient is created along the free surface of the liquid bridge, which leads to a varying surface tension $\sigma(T)$ with gradient

$$\begin{aligned}\nabla_{\parallel}\sigma(T) &= \frac{\partial\sigma}{\partial T}\nabla_{\parallel}T = \frac{\partial}{\partial T}\left[\sigma(T_0) - \gamma(T-T_0) + \ldots\right]\nabla_{\parallel}T \\ &= \left[-\gamma + O(T-T_0)\right]\nabla_{\parallel}T, \end{aligned} \tag{1}$$

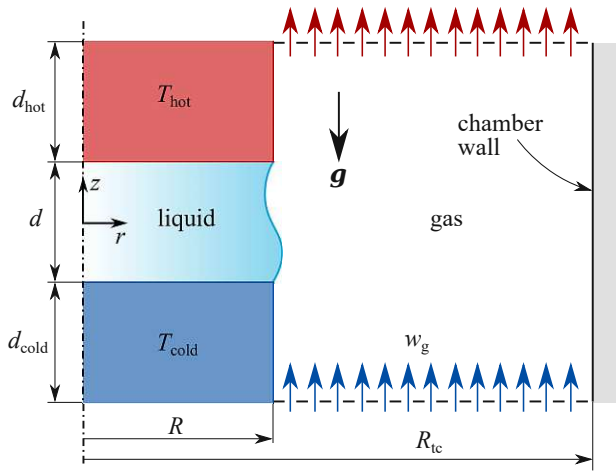

Figure 1: Schematics of the liquid bridge held in place between the hot and cold rods and surrounded by an ambient gas in an adiabatic mantel chamber. The blue arrows symbolize an imposed gas flow (here at the bottom), while the red arrows represent the resulting outflow.

where $\nabla_{\parallel} = \boldsymbol{t}(\boldsymbol{t}\cdot\nabla)$ is the nabla operator in direction of the unit vector tangent to the interface $\boldsymbol{t}$, $\gamma = -\partial\sigma/\partial T|_{T=T_0}$ is the negative surface-tension coefficient and $\sigma_0 = \sigma(T_0)$ denotes the surface tension at the mean temperature T_0. Owing to the thermocapillary effect, the varying surface tension leads to a tangential stress which acts on the liquid–gas interface and generates a thermocapillary flow in both phases.

The gas phase is made by a Newtonian gas (air or argon). As for the liquid, the density $\rho_{\mathrm{g}}(T)$ of the gas, its thermal conductivity $\lambda_{\mathrm{g}}(T)$, its dynamic viscosity $\mu_{\mathrm{g}}(T)$ and its specific heat capacity $c_{p\mathrm{g}}(T)$ are assumed temperature-dependent. The gas is confined to an annular mantel chamber of outer radius R_{tc} and height $d_{\mathrm{tc}} = d_{\mathrm{cold}} + d + d_{\mathrm{hot}}$ (see fig. 1), where the subscript 'tc' stands for 'test chamber' and the length of the rods $d_{\mathrm{cold}} = d_{\mathrm{hot}} = d$ equals the length of the liquid bridge. The cylindrical chamber wall at R_{tc} is either assumed thermally insulating or perfectly conducting, and the bottom and top boundaries of the test chamber are either non-penetration adiabatic walls or open boundaries on which a fully developed axial inlet flow $w_{\mathrm{g}}(r)$ is imposed with a constant inlet temperature T_{g} on one side and convective boundary conditions on the other side. In case of gravity, the acceleration of gravity $\boldsymbol{g} = -g\boldsymbol{e}_z$ is aligned axially and in the negative z direction (fig. 1).

The steady flow in the liquid phase is governed by the non-dimensional Navier–Stokes, continuity, and energy equations

$$\mathrm{Re}\nabla\cdot\left[\frac{\rho(T)}{\rho_0}\boldsymbol{u}\boldsymbol{u}\right] = -\nabla p - \frac{\mathrm{Bd}}{\varepsilon}\frac{\rho(T)}{\rho_0}\boldsymbol{e}_z + \nabla\cdot\left[\frac{\mu(T)}{\mu_0}\mathcal{T}\right], \tag{2a}$$

$$\nabla\cdot\left[\frac{\rho(T)}{\rho_0}\boldsymbol{u}\right] = 0, \tag{2b}$$

$$\mathrm{Ma}\nabla\cdot\left[\frac{\rho(T)c_p(T)}{\rho_0 c_{p0}}\boldsymbol{u}\theta\right] = \nabla\cdot\left[\frac{\lambda(T)}{\lambda_0}\nabla\theta\right], \tag{2c}$$

where $\boldsymbol{u}$, p and $\theta = (T - T_0)/\Delta T$ represent the velocity vector field, the pressure and the reduced temperature, respectively. The non-dimensional parameter ε is defined as $\varepsilon = \beta \Delta T$, where β is the thermal expansion coefficient of the liquid, i.e. $\beta = -\rho_0^{-1}(\partial\rho/\partial T)_p$. The deformation rate tensor is denoted $\mathcal{T} = [\nabla \boldsymbol{u} + (\nabla \boldsymbol{u})^{\mathrm{T}} - \frac{2}{3}(\nabla \cdot \boldsymbol{u})\boldsymbol{I}]$, where $\boldsymbol{I}$ is the identity matrix.

All variables have been made dimensionless using the length, velocity, pressure and temperature scales d, $\gamma\Delta T/\mu_0$, $\gamma\Delta T/d$ and ΔT, respectively, where $\mu_0 = \mu(T_0)$ is the reference dynamic viscosity, $\rho_0 = \rho(T_0)$ the reference density, $\lambda_0 = \lambda(T_0)$ is the reference thermal conductivity and $c_{p0} = c_p(T_0)$ the reference specific heat at constant pressure, all evaluated at the mean temperature T_0. For the gas phase corresponding equations hold. Here we use cylindrical coordinates (r, φ, z) centered in the middle of the liquid bridge and represent the velocity field as $\boldsymbol{u} = u\boldsymbol{e}_r + v\boldsymbol{e}_\varphi + w\boldsymbol{e}_z$ where $\boldsymbol{e}_r$, $\boldsymbol{e}_\varphi$ and $\boldsymbol{e}_z$ are the polar unit vectors.

From equations (2) governing the liquid phase it is useful to define the conventional non-dimensional thermocapillary Reynolds number Re, Marangoni number Ma and dynamic Bond number Bd

$$\mathrm{Re} = \frac{\rho_0 \gamma \Delta T d}{\mu_0^2}, \quad \mathrm{Ma} = \frac{\rho_0 c_{p0} \gamma \Delta T d}{\mu_0 \lambda_0}, \quad \mathrm{Bd} = \frac{\rho_0 g \beta d^2}{\gamma}, \tag{3}$$

where $\mathrm{Pr} = \mathrm{Ma}/\mathrm{Re} = \mu_0 c_{p0}/\lambda_0$ is the reference Prandtl number of the liquid. As is common in the literature on thermocapillary flows in liquid bridges, the pressure contribution to the enthalpy ($p/\rho \ll |c_p T|$), the pressure work and the viscous dissipation have been neglected in the energy equation (2c). The two latter assumptions are justified, respectively, if the conditions

$$\chi \frac{T}{\Delta T} \leqslant 0.1 \quad \text{and} \quad \chi \mathrm{Pr} \leqslant 0.1 \quad \text{with} \quad \chi = \frac{\beta g d}{c_p} \tag{4}$$

are satisfied [35]. After selecting the working fluids at the end of this section, we verified the conditions (4), confirming the validity of (2c).

The geometry (fig. 1) is characterized by the four aspect ratios

$$\Gamma = \frac{d}{R}, \quad \Gamma_{\mathrm{tc}} = \frac{R_{\mathrm{tc}}}{d}, \quad \Lambda_{\mathrm{hot}} = \frac{d_{\mathrm{hot}}}{d}, \quad \Lambda_{\mathrm{cold}} = \frac{d_{\mathrm{cold}}}{d}, \tag{5}$$

where we select $\Lambda_{\mathrm{hot}} = \Lambda_{\mathrm{cold}} = 1$, being constant throughout. In order to keep the Bond number constant upon a change of the geometry, we fix $d = 1.7$ mm (see e.g. [23]) and vary the radius of the rods. This corresponds to varying the aspect ratio of the liquid bridge which is set to $\Gamma = 0.5$, 0.66 and 1, values frequently considered in the literature (see e.g. [24, 25]). Furthermore, two radial aspect ratio of the test chamber are considered $\Gamma_{\mathrm{tc}} = 3$ and 10.

The a-priori unknown location of the free surface at $r = h(\varphi, z)$ is part of the solution of the problem. In the limit of asymptotically large mean surface tension σ_0, the capillary number $\mathrm{Ca} = \gamma\Delta T/\sigma_0 \to 0$ tends to zero and dynamic perturbations of the interface induced by the fluid flow vanish. Hence, the problem of determining the liquid–gas interface decouples from (2) and $h(z)$ is determined by the Young–Laplace equation

$$\Delta p_{\mathrm{fs}} = \nabla \cdot \boldsymbol{n} + \mathrm{Bo} z, \tag{6}$$

where Δp_{fs} is the static pressure jump across the liquid–gas interface, $\boldsymbol{n}$ the unit normal vector on the free surface directed from the liquid to the gas phase, and

$$\mathrm{Bo} = \frac{\rho_0 g d^2}{\sigma_0} \tag{7}$$

the static Bond number. Considering the axisymmetric problem the surface normal vector $\boldsymbol{n}$ is a function of z [8, 15]. The resulting second-order problem for $h(z)$ is closed by two boundary conditions. For the present setup with sharp edges of the cylindrical rods suitable boundary conditions are pinned contact lines $h(z = \pm 1/2) = 1/\Gamma$. Furthermore, $h(z)$ must satisfy the volume constraint

$$\int_{-1/2}^{1/2} h^2(z)\mathrm{d}z = \mathcal{V}, \tag{8}$$

where $\mathcal{V} = V/(\pi R^2 d)$ with the volume V of the liquid bridge. Here we confine ourselves to $\mathcal{V} = 1$. For this volume ratio and in the absence of gravity ($\mathrm{Bo} = 0$) the liquid–gas interface is cylindrical with $h(z) = 1/\Gamma$.

After determining h, axisymmetric solutions ($\partial_\varphi = 0$) of (2) are sought. These solutions are required to satisfy constant-temperature, no-slip and no-penetration boundary conditions along the support rods

$$\text{hot rod:} \quad \boldsymbol{u} = \boldsymbol{u}_\mathrm{g} = \boldsymbol{0}, \quad \theta = \theta_\mathrm{g} = 1/2, \tag{9a}$$

$$\text{cold rod:} \quad \boldsymbol{u} = \boldsymbol{u}_\mathrm{g} = \boldsymbol{0}, \quad \theta = \theta_\mathrm{g} = -1/2. \tag{9b}$$

Regarding the chamber boundary conditions, four cases are considered.

(i) Closed axially-adiabatic, wide test chamber with outer cold wall at $T = 0°\mathrm{C}$

$$r = \Gamma_\mathrm{tc}: \quad \boldsymbol{u}_\mathrm{g} = \boldsymbol{0}, \quad \theta_\mathrm{g} = -T_0/\Delta T, \tag{10a}$$

$$z = -1/2 - \Lambda_\mathrm{cold},\ 1/2 + \Lambda_\mathrm{hot}: \quad \boldsymbol{u}_\mathrm{g} = \boldsymbol{0}, \quad \partial_z \theta_\mathrm{g} = 0. \tag{10b}$$

(ii) Closed adiabatic test chamber

$$r = \Gamma_\mathrm{tc}: \quad \boldsymbol{u}_\mathrm{g} = \boldsymbol{0}, \quad \partial_r \theta_\mathrm{g} = 0, \tag{11a}$$

$$z = -1/2 - \Lambda_\mathrm{cold},\ 1/2 + \Lambda_\mathrm{hot}: \quad \boldsymbol{u}_\mathrm{g} = \boldsymbol{0}, \quad \partial_z \theta_\mathrm{g} = 0. \tag{11b}$$

(iii) Open test chamber with cold axial flow and adiabatic outer wall

$$r = \Gamma_\mathrm{tc}: \quad \boldsymbol{u}_\mathrm{g} = \boldsymbol{0}, \quad \partial_r \theta_\mathrm{g} = 0, \tag{12a}$$

$$z = -1/2 - \Lambda_\mathrm{cold}: \quad \boldsymbol{u}_\mathrm{g} = w_\mathrm{g}(r)\boldsymbol{e}_z, \quad \theta_\mathrm{g} = -1/2, \tag{12b}$$

$$z = 1/2 + \Lambda_\mathrm{hot}: \quad \partial_z \boldsymbol{u}_\mathrm{g} = 0, \quad \partial_z \theta_\mathrm{g} = 0. \tag{12c}$$

(iv) Open test chamber with hot axial flow and adiabatic outer wall

$$r = \Gamma_\mathrm{tc}: \quad \boldsymbol{u}_\mathrm{g} = \boldsymbol{0}, \quad \partial_r \theta_\mathrm{g} = 0, \tag{13a}$$

$$z = -1/2 - \Lambda_\mathrm{cold}: \quad \partial_z \boldsymbol{u}_\mathrm{g} = 0, \quad \partial_z \theta_\mathrm{g} = 0, \tag{13b}$$

$$z = 1/2 + \Lambda_\mathrm{hot}: \quad \boldsymbol{u}_\mathrm{g} = -w_\mathrm{g}(r)\boldsymbol{e}_z, \quad \theta_\mathrm{g} = 1/2, \tag{13c}$$

where all quantities with subscript 'g' refer to the gas phase. In cases (iii) and (iv) the inlet velocity $w \geq 0$ is assumed to be fully developed with

$$w_\mathrm{g}(r) = \frac{\mathrm{Re}_\mathrm{g}}{\mathrm{Re}} \frac{2\ln(\eta)}{(\eta^2+1)\ln(\eta) - \eta^2 + 1} \left[1 - \Gamma^2 r^2 + \left(\eta^2 - 1\right) \frac{\ln(\Gamma r)}{\ln(\eta)}\right], \tag{14}$$

where $\eta = R_\mathrm{tc}/R = \Gamma_\mathrm{tc}\Gamma$, $\mathrm{Re}_\mathrm{g} = \overline{W}_\mathrm{g}\rho_0 d/\mu_0$, and $\overline{W}_\mathrm{g}$ is the mean inlet velocity. Finally, the kinematic, mechanical and thermal boundary conditions

$$\boldsymbol{t} \cdot \nabla\theta + \boldsymbol{t} \cdot \boldsymbol{\mathcal{T}} \cdot \boldsymbol{n} = [\mu_\mathrm{g}(T)/\mu(T)]\boldsymbol{t} \cdot \boldsymbol{\mathcal{T}}_\mathrm{g} \cdot \boldsymbol{n}, \tag{15a}$$

$$\boldsymbol{u} = \boldsymbol{u}_{\mathrm{g}}, \tag{15b}$$
$$\boldsymbol{n} \cdot \nabla\theta = [\lambda_{\mathrm{g}}(T)/\lambda(T)]\boldsymbol{n} \cdot \nabla\theta_{\mathrm{g}}, \tag{15c}$$
$$\theta = \theta_{\mathrm{g}}, \tag{15d}$$

are enforced on the free surface $r = h(z)$.

We are targeting experimental conditions corresponding to Shin-Etsu silicone fluids with Prandtl numbers $\mathrm{Pr} = 28.8$ and $\mathrm{Pr} = 69.2$. Under normal gravity conditions (1g) when $g = 9.81\ \mathrm{m/s^2}$. The corresponding static and dynamic Bond numbers for $\mathrm{Pr} = 28.8$ are $\mathrm{Bo} = 1.27$ and $\mathrm{Bd} = 0.40$, while for $\mathrm{Pr} = 69.2$ these are $\mathrm{Bo} = 1.24$ and $\mathrm{Bd} = 0.49$. The notation '0g' refers to conditions of weightlessness for which $\mathrm{Bd} = \mathrm{Bo} = 0$. Finally, the temperature-dependent properties of the Shin-Etsu silicone oils are represented by functions

$$\rho(T) = \xi_1[1 + \xi_2(T - T_0) + \xi_3(T - T_0)^2] \quad \mathrm{kg/m^3}, \tag{16a}$$
$$\mu(T) = \xi_1 \mathrm{e}^{-\xi_4(T-T_0)/(T+273.15)}[1 + \xi_2(T - T_0) + \xi_3(T - T_0)^2] \quad \mathrm{kg/m\,s}, \tag{16b}$$
$$\lambda(T) = \xi_1[1 + \xi_2(T - T_0) + \xi_3(T - T_0)^2] \quad \mathrm{W/m\,K}, \tag{16c}$$
$$c_p(T) = \xi_1[1 + \xi_2(T - T_0) + \xi_3(T - T_0)^2] \quad \mathrm{J/kg\,K}, \tag{16d}$$

where T is measured in °C and the coefficients represent fits to the tabulated data of the manufacturer for $T_0 = 25°\mathrm{C}$. The coefficients ξ_i for $i = 1,\ 2,\ 3,\ 4$ are listed in table 1. Note that the coefficients ξ_1 represent the reference values of each property. The properties of the gas phase

$$\rho_g(T) = \frac{\zeta_1}{T + 273.15} \quad \mathrm{kg/m^3}, \tag{17a}$$
$$\mu_g(T) = \zeta_1 + \zeta_2(T - T_0) + \zeta_3(T - T_0)^2 + \zeta_4(T - T_0)^3 + \zeta_5(T - T_0)^4 \quad \mathrm{kg/m\,s}, \tag{17b}$$
$$\lambda_g(T) = \zeta_1 + \zeta_2(T - T_0) + \zeta_3(T - T_0)^2 + \zeta_4(T - T_0)^3 + \zeta_5(T - T_0)^4 \quad \mathrm{W/m\,K}, \tag{17c}$$
$$\begin{aligned} c_{pg}(T) = \zeta_2 + (\zeta_3 - \zeta_2)\left(\frac{T + 273.15}{\zeta_1 + T + 273.15}\right)^2 \times \\ \left[1 - \frac{\zeta_1}{\zeta_1 + T + 273.15}\left(\zeta_4 + \zeta_5\frac{T + 273.15}{\zeta_1 + T + 273.15} + \right.\right. \\ \left.\left.\zeta_6\left(\frac{T + 273.15}{\zeta_1 + T + 273.15}\right)^2 + \zeta_7\left(\frac{T + 273.15}{\zeta_1 + T + 273.15}\right)^3\right)\right] \quad \mathrm{J/kg\,K}, \end{aligned} \tag{17d}$$

are taken from [36]. The coefficients ζ_i for $i = 1, ..., 7$ are given in table 2.

3. Numerical solution method

The solution procedure follows the one of Romanò et al. [25] and starts with solving (6) by means of a second-order finite difference method to compute the axisymmetric interface shape $h(z)$. To find the axisymmetric solution of (2) for a given surface shape $h(z)$, the differential equations are discretized on a body-fitted stretched grid of finite volumes which are formally of second order. The grid consists of $N_r \times N_z = 366 \times 366$ and 202×702 grid points in the liquid and the gas phase, respectively, as in [25].

With $\boldsymbol{y} = (u, w, p, \theta)^{\mathrm{T}}$, where the vector $\boldsymbol{y}$ contains all field variables of the liquid and the gas phase, the discretized equations are solved using Newton–Raphson iteration

$$\boldsymbol{J}\left(\boldsymbol{y}^k\right) \cdot \delta\boldsymbol{y} = -\boldsymbol{f}\left(\boldsymbol{y}^k\right), \tag{18a}$$

Table 1: Coefficients appearing in the temperature-dependent thermo-physical properties (16) of the working liquids.

Liquid	Prop.	ξ_1	ξ_2	ξ_3	ξ_4
2-cSt	ρ	873.25	-1.09×10^{-3}	7.27×10^{-7}	
	μ	1.75×10^{-3}	-1.09×10^{-3}	7.27×10^{-7}	5.892
	λ	1.09×10^{-1}	-2.60×10^{-3}	-7.22×10^{-8}	
	c_p	1800.76	8.21×10^{-4}	1.66×10^{-8}	
5-cSt	ρ	914.60	-1.08×10^{-3}	7.45×10^{-7}	
	μ	4.57×10^{-3}	-1.08×10^{-3}	7.45×10^{-7}	5.892
	λ	1.19×10^{-1}	-2.38×10^{-3}	-6.62×10^{-8}	
	c_p	1800.76	8.21×10^{-4}	1.66×10^{-8}	

Table 2: Coefficients appearing in the temperature-dependent thermo-physical properties (17) of the working gases.

Gas	Prop.	ζ_1	ζ_2	ζ_3	ζ_4	ζ_5	ζ_6	ζ_7
air	ρ_g	352.93						
	μ_g	1.85×10^{-5}	4.87×10^{-8}	-3.52×10^{-11}	3.30×10^{-14}	-1.39×10^{-17}		
	λ_g	2.64×10^{-2}	7.52×10^{-5}	-4.17×10^{-8}	3.83×10^{-11}	-1.56×10^{-14}		
	c_{pg}	2548.932	1011.956	-182.765	-3.4281	49.8238	-120.3466	98.8658
argon	ρ_g	486.86						
	μ_g	2.26×10^{-5}	6.08×10^{-8}	-2.78×10^{-11}	1.34×10^{-14}	-2.76×10^{-18}		
	λ_g	1.76×10^{-2}	4.24×10^{-5}	-7.78×10^{-9}				
	c_{pg}		520.294	520.294				

$$\boldsymbol{y}^{k+1} = \boldsymbol{y}^k + \delta\boldsymbol{y}, \tag{18b}$$

where $\boldsymbol{f}\left(\boldsymbol{y}^k\right)$ is the nonlinear residual at the k-th iteration step, $\boldsymbol{J}\left(\boldsymbol{y}^k\right)$ the Jacobian operator at the k-th step and $\delta\boldsymbol{y}$ the solution increment from the k-th to the $(k+1)$-th iteration.

Inserting (18b) into (2) and linearizing the equations with respect to $\delta\boldsymbol{y}$ yields

$$\begin{aligned}
\mathrm{Re}\nabla\cdot\left[\frac{\rho(T^k)}{\rho_0}(\delta\boldsymbol{u}\boldsymbol{u}^k+\boldsymbol{u}^k\delta\boldsymbol{u})+\Delta T\left.\frac{\partial\rho}{\partial T}\right|_{T^k}u^k u^k\delta\theta\right]+\nabla\delta p+\\
\Delta T\left.\frac{\partial\rho}{\partial T}\right|_{T^k}\frac{\mathrm{Bd}}{\varepsilon\rho_0}\delta\theta\boldsymbol{e}_z-\nabla\cdot\left[\frac{\mu(T^k)}{\mu_0}\delta\mathcal{T}+\Delta T\left.\frac{\partial\mu}{\partial T}\right|_{T^k}\mathcal{T}^k\delta\theta\right]=\\
-\mathrm{Re}\nabla\cdot\left[\frac{\rho(T^k)}{\rho_0}\boldsymbol{u}^k\boldsymbol{u}^k\right]-\nabla p^k-\frac{\mathrm{Bd}}{\varepsilon}\frac{\rho(T^k)}{\rho_0}\boldsymbol{e}_z+\nabla\cdot\left[\frac{\mu(T^k)}{\mu_0}\mathcal{T}^k\right],
\end{aligned} \tag{19a}$$

$$\nabla\cdot\left[\frac{\rho(T^k)}{\rho_0}\delta\boldsymbol{u}+\Delta T\left.\frac{\partial\rho}{\partial T}\right|_{T^k}\boldsymbol{u}^k\delta\theta\right]=-\nabla\cdot\left[\frac{\rho(T^k)}{\rho_0}\boldsymbol{u}^k\right], \tag{19b}$$

$$\begin{aligned}
\mathrm{Ma}\nabla\cdot\left[\frac{\rho(T^k)c_p(T^k)}{\rho_0 c_{p0}}\left(\boldsymbol{u}^k\delta\theta+\theta^k\delta\boldsymbol{u}\right)+\frac{\Delta T}{\rho_0 c_{p0}}\left(c_p(T^k)\left.\frac{\partial\rho}{\partial T}\right|_{T^k}+\right.\right.\\
\left.\left.\rho(T^k)\left.\frac{\partial c_p}{\partial T}\right|_{T^k}\right)\boldsymbol{u}^k\theta^k\delta\theta\right]-\nabla\cdot\left[\frac{\lambda(T^k)}{\lambda_0}\nabla\delta\theta+\frac{\Delta T}{\lambda_0}\left.\frac{\partial\lambda}{\partial T}\right|_{T^k}\right]=\\
\nabla\cdot\left[\frac{\lambda(T^k)}{\lambda_0}\nabla\theta^k\right]-\mathrm{Ma}\nabla\cdot\left[\frac{\rho(T^k)c_p(T^k)}{\rho_0 c_{p0}}\boldsymbol{u}^k\theta^k\right]
\end{aligned} \tag{19c}$$

where

$$\delta\mathcal{T}=[\nabla\delta\boldsymbol{u}+(\nabla\delta\boldsymbol{u})^{\mathrm{T}}-\frac{2}{3}(\nabla\cdot\delta\boldsymbol{u})\boldsymbol{I}], \tag{20a}$$

$$\mathcal{T}^k=[\nabla\boldsymbol{u}^k+(\nabla\boldsymbol{u}^k)^{\mathrm{T}}-\frac{2}{3}(\nabla\cdot\boldsymbol{u}^k)\boldsymbol{I}]. \tag{20b}$$

In (19) all quadratic term have been linearized by, e.g.,

$$\nabla\cdot\left(\boldsymbol{u}^{k+1}\boldsymbol{u}^{k+1}\right)\approx-\nabla\cdot\left(\boldsymbol{u}^k\boldsymbol{u}^k\right)+\nabla\cdot\left(\boldsymbol{u}^{k+1}\boldsymbol{u}^k\right)+\nabla\cdot\left(\boldsymbol{u}^k\boldsymbol{u}^{k+1}\right), \tag{21}$$

while the temperature dependence of all material parameters was approximated by, e.g.,

$$\rho(T^{k+1})=\rho(T^k+\delta T)\approx\rho(T^k)+\left.\frac{\partial\rho}{\partial T}\right|_{T^k}\delta T, \tag{22}$$

where $\delta T=\Delta T\delta\theta$. The same holds for the remaining thermophysical properties. For additional details on the initial guess $\boldsymbol{y}^0$, the computational grid, the finite-volume discretization and the convergence of the solver, we refer to [25].

4. Heat-transfer in the single-fluid model

4.1. Thermal boundary conditions at the interface

The two-fluid system defined in section 2 includes the full thermal and mechanical coupling between the liquid and the gas phase through the free-surface conditions (15). As a result, the heat transfer across the free surface is part of the solution and does not need to be modelled.

In a surrogate single-fluid model in which only the flow in the liquid phase is computed, only half of the boundary conditions (15) can be imposed. Since the gas velocity $\boldsymbol{u}_g$ and the gas temperature θ_g are not defined in the single-fluid model the boundary conditions (15b) and (15d) must be omitted. The no-penetration condition $\boldsymbol{u}\cdot\boldsymbol{n}=0$ is implicitly related to the indeformable interface. Since the viscosity ratio $\mu_{g0}/\mu_0 \approx \mathcal{O}(10^{-2})$, the viscous stresses S_g from the gas phase in (15a) plays a minor role for the flow inside the liquid bridge and is neglected within the single-fluid model. However, the heat flux through the interface $-\partial_n\theta = -\boldsymbol{n}\cdot\nabla\theta$ in (15c) must be modelled.

To that end we make an ansatz for $\partial_n\theta$

$$\mathrm{Bi}(z) = -\left.\frac{\partial_n\theta}{\theta-\theta_\mathrm{ref}}\right|_{r=h(z)}, \tag{23a}$$

suggested by Newton's law of heat transfer, where the reference temperature $\theta_\mathrm{ref}=\theta_\mathrm{cold}=-1/2$ is assumed to be the cold-rod temperature. The right hand side of this equation depends on z and is a priori unknown within the single-fluid model. The quantities θ and $\partial_n\theta$ can be obtained, however, from a two-fluid simulation. This defines a *Biot function* $\mathrm{Bi}(z)$. Once the Biot function is known, Newton's law can be employed for the single-fluid model, in which the conventional Biot number is replaced by

$$\mathrm{Bi}(z) = \frac{h_\mathrm{g}(z)d}{\lambda}, \tag{23b}$$

where $h_\mathrm{g}(z)$ now is a z-dependent heat-transfer coefficient between the liquid and the gas phase and λ the thermal conductivity of the liquid. The modified cooling law (23) will yield the same heat flux through free surface as does the two-fluid model, up to small corrections caused by the neglected viscous stresses from the gas phase.

4.2. Ansatz for the Biot function

In order for the above approach to make sense, it is required that the "exact" Biot function $\mathrm{Bi}(z)$, numerically determined by the two-fluid model, can be accurately approximated by a simple functional dependence $\tilde{\mathrm{Bi}}(z)\approx\mathrm{Bi}(z)$ defined by a few characteristic constants and valid for a wide range of parameters. Here and in the following the tilde ($\tilde{}$) stands for the approximation of a given quantity. It is indeed possible to find universal fit functions $\tilde{\mathrm{Bi}}(z,\Gamma,\mathrm{Re})$ approximating $\mathrm{Bi}(z,\Gamma,\mathrm{Re})$ for a given set of Pr, Bd, Bo, and given thermophysical properties of the surrounding gas.

An example for the exact Biot function $\mathrm{Bi}(z)$ from the two-fluid model is shown in fig. 2. Owing to its variation with z, the conventional assumption of a constant Biot number obviously represents a poor approximation. All Biot functions show the same characteristic shape: Since temperature gradient $\partial_n\theta$ diverges for $z\to\pm0.5$ due to the imposed temperature at the geometrical cusp point, also the Biot function $\mathrm{Bi}(z)$ diverges at these end points.

Furthermore, the Biot function for high Prandtl and Marangoni numbers exhibits a shallow relative minimum and a sharp relative maximum. For the high Prandtl numbers considered, these extrema are located near the hot and the cold wall, respectively, and reflect the thermal boundary layers on these walls [32, 33, 27]. As shown later (figs. 8 and 9), the dependence of the extremum values Bi_min and Bi_max of the Biot function and their locations z_min and z_max on the Reynolds number Re can be excellently represented by the empirical fit

$$\{z_\mathrm{min},\mathrm{Bi}_\mathrm{min},z_\mathrm{max},\mathrm{Bi}_\mathrm{max}\} \approx A_0^\dagger + A_1^\dagger\mathrm{Re} + A_2^\dagger/\mathrm{Re}^{A_3^\dagger} + A_4^\dagger\left(1-\mathrm{e}^{A_5^\dagger\mathrm{Re}}\right), \tag{24}$$

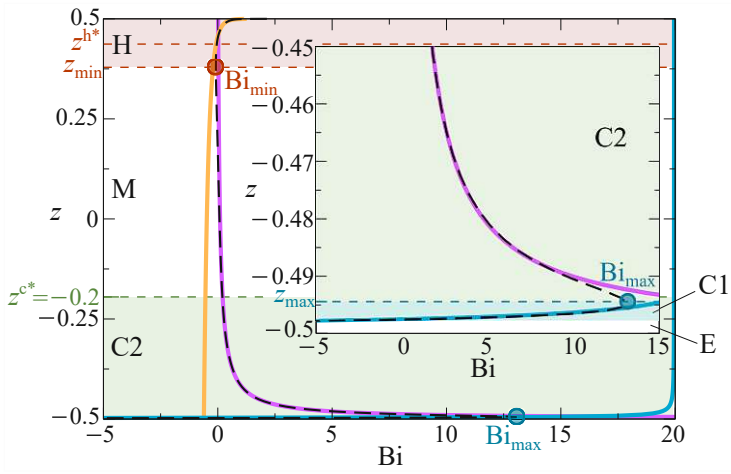

Figure 2: Local Biot number, or Biot function $\mathrm{Bi}(z)$, shown as a black dashed line for case (i) defined in (10) for $\mathrm{Pr} = 69.2$, $\Gamma = 0.5$, $\mathrm{Re} = 117$, $\mathrm{Bd} = 0.49$, $\mathrm{Bo} = 1.24$ and air as the ambient gas. Power-law fits for the thermal-boundary-layer regions near the hot and the cold supports are depicted as colored lines. The relative maximum and minimum of the Biot function are indicated by circles. The mean temperature is $T_0 = 25°\mathrm{C}$. Different regions for the fit are indicated by shading.

where the superscript † stands for *extremum value* and denotes $z_{\min}$, $\mathrm{Bi}_{\min}$, $z_{\max}$, or $\mathrm{Bi}_{\max}$. The rational behind (24) relies on the expected asymptotic trends of the thermal boundary layers. In fact, the power-law term $A_2^\dagger/\mathrm{Re}^{A_3^\dagger}$ is introduced because of the power-law scaling expected for the boundary layer thickness at high Marangoni numbers. The linear terms $A_0^\dagger + A_1^\dagger \mathrm{Re}$ are motivated by the leading-order linear growth (decay) expected for $\mathrm{Bi}_{\max}$ ($\mathrm{Bi}_{\min}$) at high Ma, when $z_{\max}$ ($z_{\min}$) vary slowly with Ma, whereas the distance between $\mathrm{Bi}_{\max}$ and $\mathrm{Bi}_{\min}$ is supposed to scale linearly with ΔT. Finally, the exponential term $A_4^\dagger \left(1 - \mathrm{e}^{A_5^\dagger \mathrm{Re}}\right)$ is employed to account for the discrepancies between the asymptotics and the exact Biot function extrema at low Ma, where the asymptotic trends do not hold. Furthermore, we find that the six coefficients $A_i^\dagger(\Gamma) \approx \tilde{A}_i^\dagger(\Gamma) = \alpha_i^\dagger + \beta_i^\dagger \Gamma$, $i = 0, 1, 2, 3, 4, 5$, for each of the four characteristic variables ($z_{\min}, \mathrm{Bi}_{\min}, z_{\max}$, and $\mathrm{Bi}_{\max}$) depend linearly on the aspect ratio Γ. Therefore, the dependence on Re and Γ of each of the four above characteristic quantities of $\mathrm{Bi}(z)$ is determined by its own set of twelve parameters $(\alpha_i^\dagger, \beta_i^\dagger)$ with $i = 0, 1, 2, 3, 4, 5$.

Once the locations $z_{\min}$ and $z_{\max}$ of the extrema have been numerically computed, the full range $z \in [-1/2, 1/2]$ is subdivided into different regions (shaded in fig. 2), and the Biot function $\mathrm{Bi}(z)$ is approximated separately within each region by

$$\text{region H,} \qquad z \in [z_{\min}, 0.5] : \quad \mathrm{Bi} \approx \tilde{\mathrm{Bi}}^{\mathrm{H}} = a_0^{\mathrm{h}} + a_1^{\mathrm{h}} (0.5 - z)^{a_2^{\mathrm{h}}}, \tag{25a}$$

$$\text{region M,} \qquad z \in \left[z^{c*}, z_{\min}\right] : \quad \mathrm{Bi} \approx \tilde{\mathrm{Bi}}^{\mathrm{M}} = a_0^{\mathrm{m}} + a_1^{\mathrm{m}} z, \tag{25b}$$

$$\text{region C2,} \qquad z \in \left[z_{\max}, z^{c*}\right] : \quad \mathrm{Bi} \approx \tilde{\mathrm{Bi}}^{\mathrm{C2}} = a_0^{\mathrm{c2}} + a_1^{\mathrm{c2}} (0.5 + z)^{a_2^{\mathrm{c2}}}, \tag{25c}$$

$$\text{region C1,} \qquad z \in \left[\frac{z_{\max} - 0.5}{2}, z_{\max}\right] : \quad \mathrm{Bi} \approx \tilde{\mathrm{Bi}}^{\mathrm{C1}} = a_0^{\mathrm{c1}} + a_1^{\mathrm{c1}} (0.5 + z)^{a_2^{\mathrm{c1}}}, \tag{25d}$$

Table 3: Parameter sets for the two-phase simulations. ⋆ Note that for case (ii) with $\Gamma_{\mathrm{tc}} = 10$ only air was considered as the gas.

Case	Pr	Gas	g	Γ_{tc}	# tests	Γ
(i)	28.8, 69.2	air	0g, 1g	10	4	0.5, 0.66, 1
(ii)	28.8, 69.2	air, argon	0g, 1g	3, 10	$8 + 4^{\star}$	0.5, 0.66, 1
(iii)	69.2	air, argon	0g, 1g	3	4	1
(iv)	69.2	air, argon	0g, 1g	3	4	1

$$\text{region E,} \qquad z \in \left[-0.5, \frac{z_{\max} - 0.5}{2}\right] : \quad \text{extrapolated from region C1,} \tag{25e}$$

where the superscripts 'h' and 'm' indicate that regions H and M are fitting domains close to the hot rod and in the middle of the liquid bridge, respectively. The superscripts 'c1' and 'c2' refer to the fitting regions C1 and C2 closest to the cold rod. The region between the two extrema is split into two at $z = z^{c*} = -0.2$, because it robustly approximates the boundary between regions C2 and M for all parameters of our study. Furthermore, region C1 covers one half of the range between the cold wall and $z_{\max}$. The other half (region E, see fig. 2) is not used for fitting the simulation data, because the fit in region C1 already captures the divergence of Bi for $z \to -0.5$ and because the fit of a diverging function (in region E) is an ill-conditioned operation which can deteriorate the robustness of the global fit. Therefore, the fit in region C1 is simply extrapolated to region E.

Since the values of the extrema of Bi and their locations can be very well represented by the ansatz (24), it is expected that the power laws (25) will admit coefficients which also scale like (24). Therefore, the fit parameters $a_j^{\ddagger}$ in (25), where the superscript $\ddagger \in [\mathrm{h}, \mathrm{m}, \mathrm{c1}, \mathrm{c2}]$ indicates the *region*, are enforced to have the same type of functional dependence (24) on Re and Γ as $\mathrm{Bi}_{\min}$, $\mathrm{Bi}_{\max}$, $z_{\min}$ and $z_{\max}$ with associated individual twelve parameters $(\alpha_{i,j}^{\ddagger}, \beta_{i,j}^{\ddagger})$, i.e. $a_j^{\ddagger} \approx \tilde{a}_j^{\ddagger}(\mathrm{Re}, \Gamma) = \alpha_{i,j}^{\ddagger} + \beta_{i,j}^{\ddagger}\Gamma$ ($\ddagger$: region, $i = 0, 1, 2, 3, 4, 5$: dependence on Re, j: sequential index). Finally, to provide a smooth differentiable fit function over the full range $z \in [-0.5, 0.5]$ the fits valid in each region are smoothly blended as described in Sec. 4.4.

4.3. Range of parameters

Two-phase simulations have been carried out for 24 different parameter sets (called *tests* in the following). They are listed in table 3. For each test the Reynolds number was varied in 50 equidistant steps over a range depending on the parameters but within $\mathrm{Ma} = \mathrm{Re} \times \mathrm{Pr} \in [850, 42750]$ (specified further below). Three values of $\Gamma \in [0.5, 0.66, 1]$ commonly employed in the literature were considered for cases (i) and (ii), while only $\Gamma = 1$ was tested for cases (iii) and (iv). This amounts to a total of 2800 two-phase flow calculations. Note that case (ii) is the only case, for which we employ two different chamber aspect ratios, i.e. $\Gamma_{\mathrm{tc}} = 3$ and 10. For the latter one, $\Gamma = 10$, we only considered a chamber filled with air in order to compare with case (i).

Once all data, i.e. all 2800 Biot functions $\mathrm{Bi}(z)$ were obtained, they were fitted by $\widetilde{\mathrm{Bi}}(z, \Gamma, \mathrm{Re})$. For each Biot function, i.e. for each test, the following fit procedure is carried out.

4.4. Representation of the global Biot function

In a first step the boundaries of the different regions $\ddagger$ must be found within which the power-law approximations (25) are made. To that end $z_{\min}$, $\mathrm{Bi}_{\min}$, $z_{\max}$ and $\mathrm{Bi}_{\max}$ are numerically

determined. Thereafter, regions C1, C2 and E are combined into a compound region C. Moreover, the additional point $z^{\mathrm{h}^*} = (0.5 + z_{\min})/2$ is introduced. The points z^{h^*} and z^{c^*} (see fig. 2) are used to smoothly blend the individual local approximations to $\mathrm{Bi}(z)$ which are obtained strictly within the regions H, M and C. Moreover, in order to provide an explicit form for the Biot function fit, $z_{\min}$, $\mathrm{Bi}_{\min}$, $z_{\max}$ and $\mathrm{Bi}_{\max}$ are approximated by the corresponding least-squares-fitted explicit functions $\tilde{z}_{\min}$, $\tilde{\mathrm{Bi}}_{\min}$, $\tilde{z}_{\max}$ and $\tilde{\mathrm{Bi}}_{\max}$, and employed in the compound function $\tilde{\mathrm{Bi}}(z)$.

Assuming all coefficients $a_i^{\ddagger}$ have been obtained and fitted to the corresponding least-squares-fitted explicit functions $\tilde{a}_i^{\ddagger}$, the final form of the Biot function approximation is constructed by smoothly blending $\tilde{\mathrm{Bi}}^{\mathrm{H}}$, $\tilde{\mathrm{Bi}}^{\mathrm{M}}$ and $\tilde{\mathrm{Bi}}^{\mathrm{C}}$ at z^{h^*} and z^{c^*} to cover the full range $z \in [-0.5, 0.5]$ such that

$$\begin{aligned}\tilde{\mathrm{Bi}}(z) = \tilde{\mathrm{Bi}}^{\mathrm{H}}(z)\mathcal{B}(z - z^{\mathrm{h}^*}, C_1) + \tilde{\mathrm{Bi}}^{\mathrm{M}}(z)\mathcal{B}(z^{\mathrm{h}^*} - z, C_1)\mathcal{B}(z - z^{\mathrm{c}^*}, C_2) \\ + \tilde{\mathrm{Bi}}^{\mathrm{C}}(z) + \mathcal{K}(z),\end{aligned} \tag{26}$$

where the blending functions are defined as

$$\mathcal{B}(z - \hat{Z}, C_i) := \frac{\tanh[2\pi C_i(z - \hat{Z})] + 1}{2}, \tag{27}$$

$\hat{Z} \in [z^{\mathrm{c}^*}, z^{\mathrm{h}^*}, \tilde{z}_{\max}]$ is any of the characteristic collocation points and the blending parameters are $C_1 = 10^2$ and $C_2 = 10^3$. In the above sum the individual local contributions according to (25) are

$$\tilde{\mathrm{Bi}}^{\mathrm{H}}(z) = \tilde{a}_0^{\mathrm{h}} + \tilde{a}_1^{\mathrm{h}}(0.5 - z)^{\tilde{a}_2^{\mathrm{h}}}, \tag{28}$$

$$\tilde{\mathrm{Bi}}^{\mathrm{M}}(z) = \tilde{a}_0^{\mathrm{m}} + \tilde{a}_1^{\mathrm{m}} z, \tag{29}$$

$$\tilde{\mathrm{Bi}}^{\mathrm{C1}}(z) = \tilde{a}_0^{\mathrm{c1}} + \tilde{a}_1^{\mathrm{c1}}(z + 0.5)^{\tilde{a}_2^{\mathrm{c1}}}, \tag{30}$$

$$\tilde{\mathrm{Bi}}^{\mathrm{C2}}(z) = \tilde{a}_0^{\mathrm{c2}} + \tilde{a}_1^{\mathrm{c2}}(z + 0.5)^{\tilde{a}_2^{\mathrm{c2}}}. \tag{31}$$

The last two regional contributions are smoothly combined to yield

$$\tilde{\mathrm{Bi}}^{\mathrm{C}}(z) = \tilde{\mathrm{Bi}}^{\mathrm{C1}}(z)\mathcal{B}(\tilde{z}_{\max} - z, C_1) + \tilde{\mathrm{Bi}}^{\mathrm{C2}}(z)\mathcal{B}(\tilde{z} - \tilde{z}_{\max}, C_3), \tag{32}$$

where $C_3 = 2 \times 10^2$. Finally, the correction term in (26)

$$\mathcal{K}(z) = \left[\tilde{\mathrm{Bi}}_{\max} - \max\left(\tilde{\mathrm{Bi}}^{\mathrm{C}}\right)\right] \times \exp\left[-\frac{(\tilde{z}_{\max} - z)^2}{C_4}\right] \tag{33}$$

takes care of reproducing the explicit fit of the maximum of the Biot function $\tilde{\mathrm{Bi}}_{\max}$, and $C_4 = 5 \times 10^{-7}$. Note that the form of the coefficients in region M

$$\tilde{a}_0^{\mathrm{m}} = \left[\tilde{a}_0^{\mathrm{c2}} + \tilde{a}_1^{\mathrm{c2}}(z^{\mathrm{c}^*} + 0.5)^{\tilde{a}_2^{\mathrm{c2}}}\right] - \tilde{a}_1^{\mathrm{m}} z^{\mathrm{c}^*}, \tag{34}$$

$$\tilde{a}_1^{\mathrm{m}} = \frac{1}{z^{\mathrm{h}^*} - z^{\mathrm{c}^*}}\left\{\left[\tilde{a}_0^{\mathrm{h}} + \tilde{a}_1^{\mathrm{h}}(0.5 - z^{\mathrm{h}^*})^{\tilde{a}_2^{\mathrm{h}}}\right] - \left[\tilde{a}_0^{\mathrm{c2}} + \tilde{a}_1^{\mathrm{c2}}(z^{\mathrm{c}^*} + 0.5)^{\tilde{a}_2^{\mathrm{c2}}}\right]\right\} \tag{35}$$

results from linearly matching the values of the explicit Biot function fit at $z = z^{\mathrm{h}^*}$ and $z = z^{\mathrm{c}^*}$.

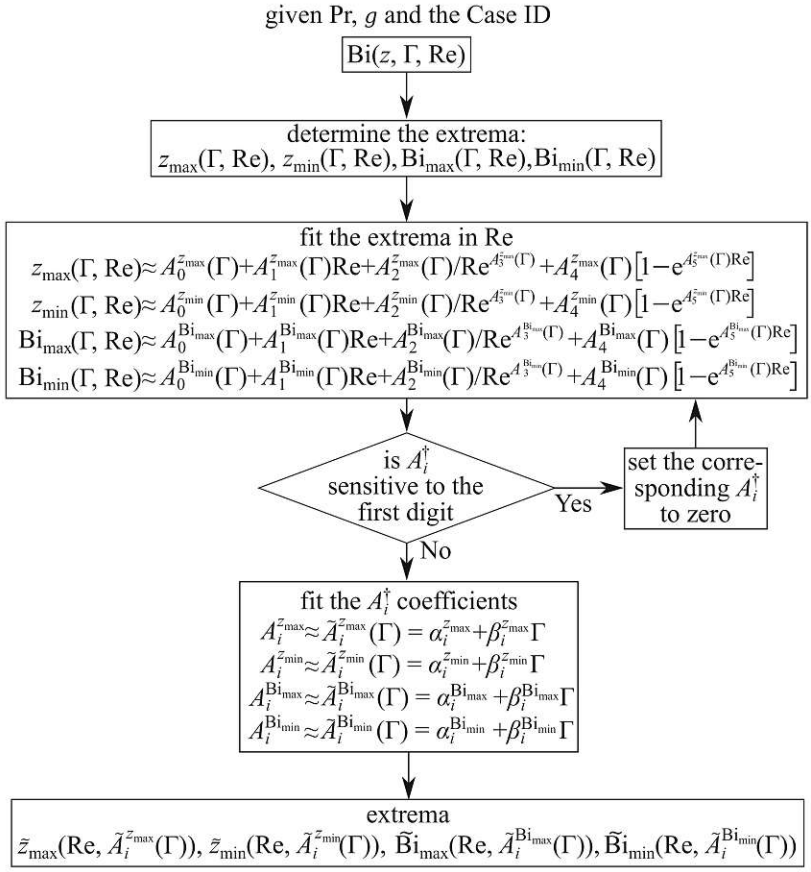

Figure 3: Flowchart of the fitting for the extrema of the Biot function, i.e. z_{min}, Bi_{min}, z_{max}, and Bi_{max}.

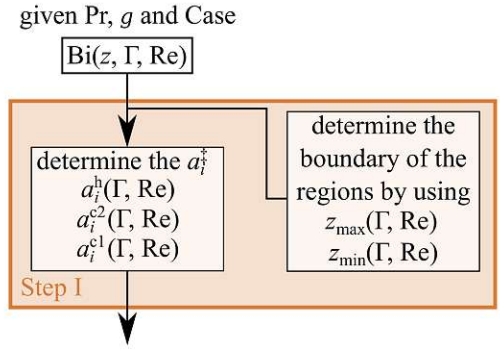

Figure 4: Flowchart of the first fitting stage for the Biot function.

4.5. Fit procedure

All coefficients required for the approximation of $\mathrm{Bi}(z)$ are obtained by minimizing the sum of the squared distances between the data and the respective fit function. Since the fit functions are nonlinear, a Newton method is employed to solve the non-linear equations governing the least-squares minimization operation. This procedure requires to provide an initial guess sufficiently close to the solution, and to define a termination criterion for the iteration. The iteration is considered converged when the residual of the fit coefficients is less than 10^{-8} in absolute norm. In each of the regions H, C1 and C2 the fit consists of four stages.

I. In the first step each numerical simulation is post-processed independently for each tuple (Γ, Re) with Γ according to table 3 and $\mathrm{Ma} = \mathrm{Re} \times \mathrm{Pr} \in [850, 42750]$. In order to find the power-law coefficients a_i^{h}, a_i^{c1}, a_i^{c2} $(i = 0, 1, 2)$ appearing in (25)(a,c,d) and their dependence on Γ and Re for each region H, C1 and C2 it is necessary to first determine numerically the boundaries of these regions. Their corresponding fits, used in (26), are obtained by the two-stage fitting of the ansatz (24) to the data for each simulation (tuple). The algorithm is explained in form of a flow chart in fig. 3. Once the regions boundaries are known the ansatz functions in (25)(a,c,d) are fitted to the numerically obtained Biot function $\mathrm{Bi}(z)$ for each tuple. This is symbolically illustrated in fig. 4.

II. In a second step only the coefficients $a_0^\ddagger$ ($\ddagger \in \{\mathrm{h}, \mathrm{c1}, \mathrm{c2}\}$) obtained in step (I) are employed to carry out a secondary fit such to determine the corresponding approximations $\tilde{a}_0^\ddagger$ that explicitly depend on Re and Γ following (24). In this step all simulation data for a given set of Pr, g, Γ_{tc}, boundary conditions (case) and type of gas are involved. To that end three sets of coefficients $A_{i,0}^\ddagger$, $i = 0, 1, 2, 3, 4, 5$, (as in (24)) are introduced, one set per each region $\ddagger \in \{\mathrm{h}, \mathrm{c1}, \mathrm{c2}\}$. The coefficients $A_{i,0}^\ddagger$ are approximated by enforcing a linear dependence on Γ as previously done for the extrema (shown in fig. 3): $A_{i,0}^\ddagger \approx \tilde{A}_{i,0}^\ddagger = \alpha_{i,0}^\ddagger + \beta_{i,0}^\ddagger \Gamma$.

   The explicit fits $\tilde{a}_0^\ddagger$, which now have the required dependence on Re and Γ, are inserted into (25)(a,c,d). The remaining six coefficients, $a_1^\ddagger$ and $a_2^\ddagger$, ($\ddagger \in \{\mathrm{h}, \mathrm{c1}, \mathrm{c2}\}$), obtained in step (I) are replaced by again fitting the numerical Biot function $\mathrm{Bi}(z)$ in each respective region and separately for each combination of $\Gamma \in \{0.5, 0.66, 1\}$ and $\mathrm{Ma} = \mathrm{Re} \times \mathrm{Pr} \in [850, 42750]$ (see the flowchart depicted in fig. 5). It remains to enforce the required dependence on Re and Γ which is achieved in the next steps.

III. In a third step the coefficients $a_1^\ddagger$ are fitted as done for $a_0^\ddagger$ in step (II) such that the corresponding fits $\tilde{a}_1^\ddagger$ explicitly depend on Re and Γ. This involves the numerical data for all tuples (Re, Γ). The fit is achieved by making an ansatz for Re dependence of $a_1^\ddagger$ as in (24). This yields the corresponding three sets of six coefficients $A_{i,1}^\ddagger$ with $i = 0, 1, 2, 3, 4, 5$ for the three regions $\ddagger$. Thereafter, the coefficients $A_{i,1}^\ddagger$ are fitted linearly in Γ to determine the coefficients $(\alpha_{i,1}^\ddagger, \beta_{i,1}^\ddagger)$, $i = 0, 1, 2, 3, 4, 5$, such that $A_{i,1}^\ddagger \approx \tilde{A}_{i,1}^\ddagger = \alpha_{i,1}^\ddagger + \beta_{i,1}^\ddagger \Gamma$. The explicit fits $\tilde{a}_1^\ddagger$ with the correct dependence on Re and Γ are then inserted into (25)(a,c,d) together with the corresponding $\mathrm{a}_0^\ddagger$ from stage (II). The remaining coefficients $a_2^\ddagger$ are then determined a third time by fitting to the numerical Biot function $\mathrm{Bi}(z)$ separately for each combination of $\Gamma \in \{0.5, 0.66, 1\}$ and $\mathrm{Ma} = \mathrm{Re} \times \mathrm{Pr} \in [850, 42750]$ (see the flowchart depicted in fig. 6).

IV. Finally, the coefficients $a_2^\ddagger$ are fitted by the ansatz in Re (24) for all Re involved. This yields the corresponding three sets of six coefficients $A_{i,2}^\ddagger$ with $i = 0, 1, 2, 3, 4, 5$ for $a_2^\ddagger$ which

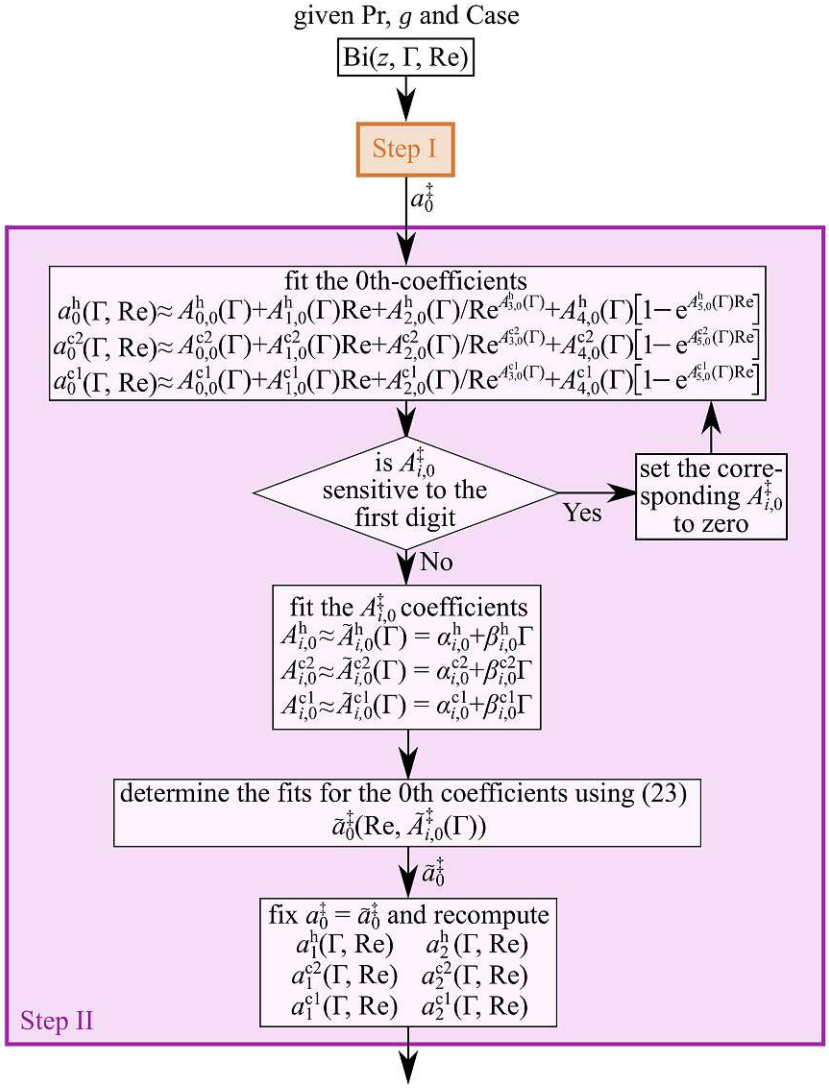

Figure 5: Flowchart of the second fitting stage for the Biot function.

are subsequently fitted linearly in Γ to obtain the corresponding coefficients $(\alpha_{i,2}^{\ddagger}, \beta_{i,2}^{\ddagger})$, $i = 0, 1, 2, 3, 4, 5$, such that $A_{i,2}^{\ddagger} \approx \tilde{A}_{i,2}^{\ddagger} = \alpha_{i,2}^{\ddagger} + \beta_{i,2}^{\ddagger}\Gamma$. The resulting coefficients lead to the explicit functions $\tilde{a}_2^{\ddagger}$ with the targeted dependence on Re and Γ (see the flow chart depicted in fig. 7).

Summarizing, by this procedure, a first set of coefficients $a_i^{\ddagger}$ (where $\ddagger \in \{\mathrm{h}, \mathrm{c1}, \mathrm{c2}\}$) is obtained in step (I) by fitting the ansatz to the simulation data for each combination (Re, Γ) separately.

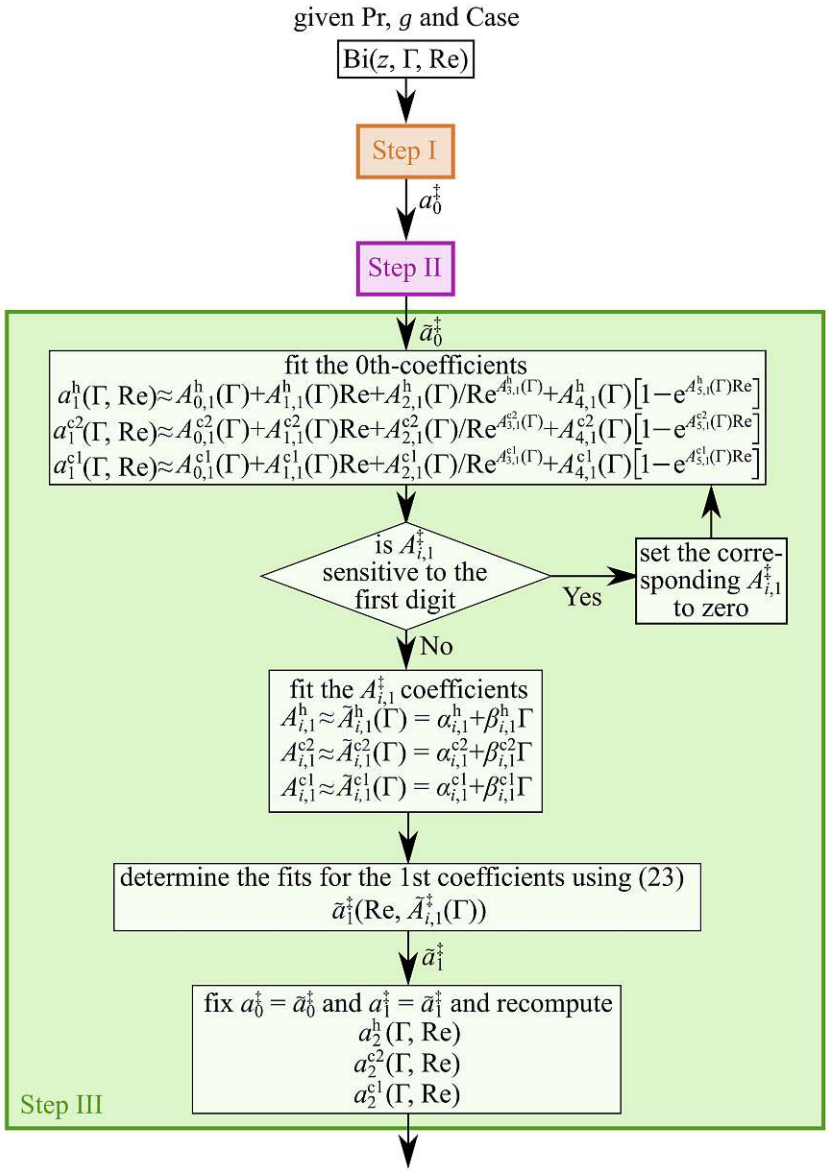

Figure 6: Flowchart of the third fitting stage for the Biot function.

The dependence of $a_i^{\ddagger}$ on Re and Γ is then subsequently introduced in steps (II), (III), and (IV) leading to $\tilde{a}_0^{\ddagger}$, $\tilde{a}_1^{\ddagger}$ and $\tilde{a}_2^{\ddagger}$, respectively.

Whenever we find that changing the first sensitive digit (first non-zero decimal place) of a coefficient $A_{i,j}^{\ddagger}$ ($A_i^{\dagger}$), where $j = 0, 1, 2$, does not affect the second relevant digit (second non-zero decimal place) of the other coefficients $A_{k,j}^{\ddagger}$ ($A_j^{\dagger}$), the fit is repeated enforcing $A_{i,j}^{\ddagger} = 0$ ($A_i^{\dagger} = 0$). After having carried out the above four steps for all three power-law ansätze, $\tilde{a}_i^{\mathrm{h}}(\mathrm{Re}, \Gamma)$, $\tilde{a}_i^{\mathrm{c1}}(\mathrm{Re}, \Gamma)$ and $\tilde{a}_i^{\mathrm{c2}}(\mathrm{Re}, \Gamma)$ are known and inserted into (26). All fit coefficients can be downloaded from `https://github.com/fromano88/BiotFunction_LB.git`, together with a Matlab code that plots the original Biot function and the corresponding fits.

5. Results

5.1. Extrema of Bi

The typical structure of the Biot function $\mathrm{Bi}(z)$ has been shown in fig. 2. Its approximation hinges on the locations $z_{\min}$ and $z_{\max}$ of the two extrema of $\mathrm{Bi}(z)$. Figure 8 shows the distance $\delta_{\max} = z_{\max} + 0.5$ of the maximum of the Biot function from the cold wall (a) and the maximum of the Biot function $\mathrm{Bi}_{\max}$ (b) as functions of the Reynolds number for a liquid Prandtl number $\mathrm{Pr} = 69.2$, normal gravity (1g) and three aspect ratios Γ (distinguished by type and color of the symbols), before introducing the continuous linear dependence on Γ. The corresponding dependence on Re of the distance of the locations of the minimum Biot function from the hot wall $\delta_{\min} = 0.5 - z_{\min}$ and the minimum Biot function $\mathrm{Bi}_{\min}$ are shown in fig. 9(a,b). It can be seen that the approximations according to the ansatz (24) for the dependence on Re (lines in figs. 8 and 9) allow for excellent comparisons with the numerical data from the two-fluid simulations (symbols) in the range $\mathrm{Re} \in [25, 250]$. These fits have been carried out in a single stage for fixed Γ.

A successive fit operation is then carried out assuming the ansatz $A_i^{\dagger} \approx \tilde{A}_i^{\dagger} = \alpha_i^{\dagger} + \beta_i^{\dagger}\Gamma$. These fits (lines) are shown in the inset panels in figs. 8 and 9, and they correspond to the lines depicted in the main panels of figs. 8 and 9. It can be seen that the linear dependence of ${A^{\dagger}}_i$ on Γ is a good approximation to the numerical data (dots) in the range $\Gamma \in [0.5, 1]$. The same fits are therefore employed in (26) for approximating the extrema of the Biot function. Whenever a coefficient ${A_i}^{\dagger}$ for some i is not included in the fit, the plot appears in solid gray. Likewise, a solid gray plot indicates that the coefficients ${A_{i,j}}^{\ddagger}$ of ${a_i}^{\ddagger}$ are not included in the fit.

Figure 10 shows the dependence on the Reynolds number of the fitted stationary points of $\tilde{\delta}_{\min} = 0.5 - \tilde{z}_{\min}$, $\tilde{\delta}_{\max} = -0.5 - \tilde{z}_{\max}$, $\tilde{\mathrm{Bi}}_{\min}$, and $\tilde{\mathrm{Bi}}_{\max}$ for $\Gamma = 0.5$. Both our Prandtl numbers are included in this comparison (left column: $\mathrm{Pr} = 28.8$, right column: $\mathrm{Pr} = 69.2$). Cases (i) and (ii) have been considered for two chamber aspect ratios $\Gamma_{\mathrm{tc}} = 3$ and 10 and air as the surrounding gas. Argon is considered for $\Gamma_{\mathrm{tc}} = 3$. The respective cases are coded by color and the gravity conditions are indicated by line type (full lines: 0g, dashed lines: 1g). Figure 11 displays the dependence on the Reynolds number of the stationary points for cases (i) to (iv), fixing $\mathrm{Pr} = 69.2$, $\Gamma = 1$, $\Gamma_{\mathrm{tc}} = 3$. Both the gravity conditions are included in the comparison, considering both, hot and cold blowing. All these parameters are tested for air and argon as surrounding gas.

The locations of the Biot function extrema $\tilde{\delta}_{\min}$ and $\tilde{\delta}_{\max}$ scale very similar as the boundary layer thicknesses $\tilde{\delta}_{\min} \sim \mathrm{Re}^{-1/2}$ (on the hot wall) and $\tilde{\delta}_{\max} \sim \mathrm{Re}^{-1}$ (on the cold wall) predicted by [33] and [27], respectively, for the single-fluid model with an adiabatic interface. Corresponding least-squares fits of the bundles for $\tilde{\delta}_{\min}$ and $\tilde{\delta}_{\max}$ are included in figs. 10 and 11 as red dotted lines. The functions $\tilde{\delta}_{\min}(\mathrm{Re})$ and $\tilde{\delta}_{\max}(\mathrm{Re})$ for different cases and parameters remain remarkably coherent for all the conditions considered in figs. 10 and 11. However, a change of the boundary

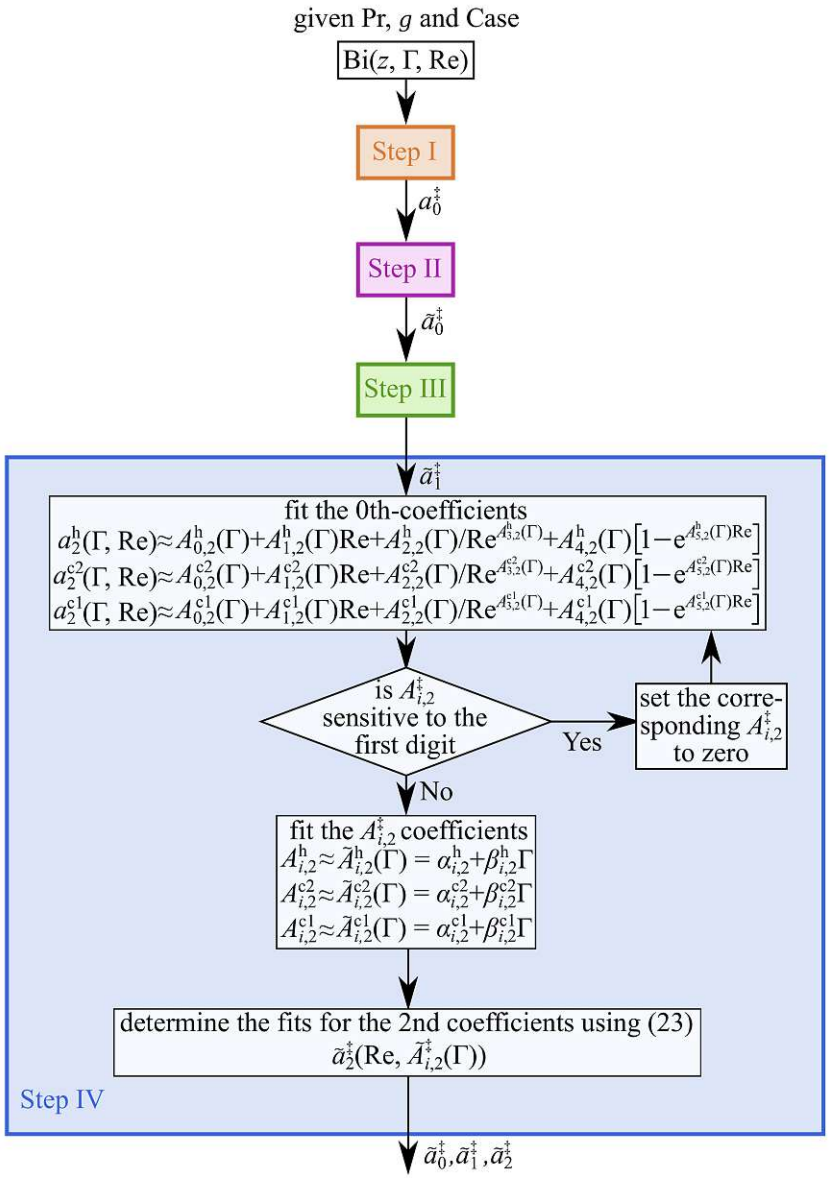

Figure 7: Flowchart of the fourth fitting stage for the Biot function.

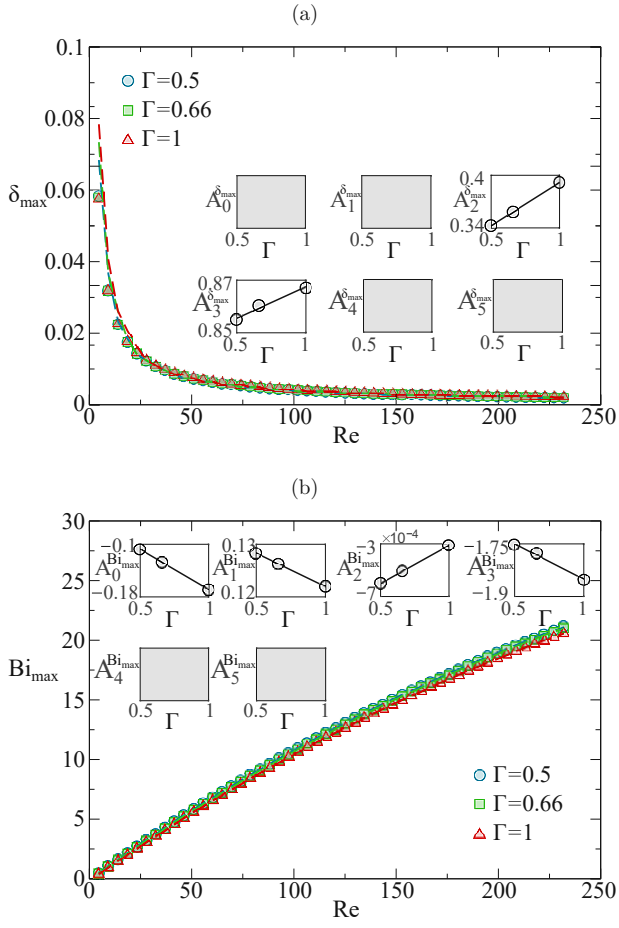

Figure 8: Fits of the location $\delta_{\max}$ (a) and the value $\mathrm{Bi}_{\max}$ (b) of the local maximum of the Biot function with respect to Re and Γ for case (ii) and (Pr = 69.2, $\Gamma_{\mathrm{tc}} = 10$, air, 1g). The markers denote the simulation data and the lines the corresponding fits: Γ = 0.5 (circles, full blue line), 0.66 (squares, dashed green line) and 1 (triangles, dash-dotted red line).

conditions on the outer wall of the gas space at $r = \Gamma_{\mathrm{tc}}$ from an adiabatic (cases (ii)–(iv)) to a cold isothermal wall (case (i)), has a strong influence on the minimum Biot number (see the blue curves in the top panels of fig. 10). The deviation becomes most pronounced for small Reynolds numbers. Also the type of the surrounding gas, air or argon, has a significant impact on $\tilde{\mathrm{Bi}}_{\min}$, as well as on $\tilde{\mathrm{Bi}}_{\max}$. The minimum Biot number is found to be almost insensitive to the gravity level (0g or 1g). The maximum Biot number as well as its location $\tilde{\mathrm{Bi}}_{\max}$, however, depend slightly on gravity. The reason is discussed in Sec. 6.

A similar behavior as for cases (i) and (ii) is found for cases (iii) and (iv) when the liquid bridge is exposed to a forced axial mean flow in the gas phase. However, independent of the direction of the forced mean flow in the gas phase, the minimum Biot number varies considerably,

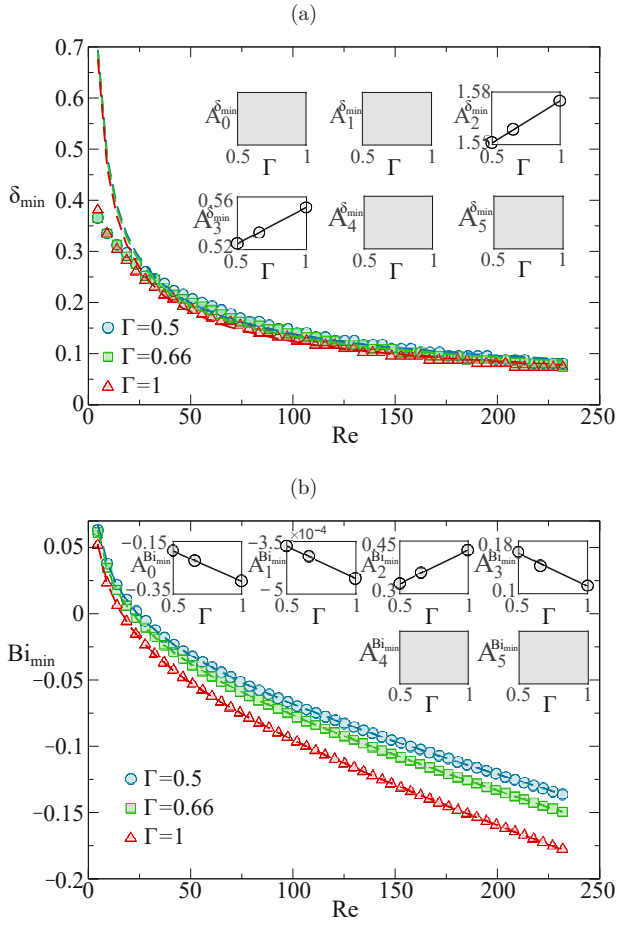

Figure 9: Fits of the location $\delta_{\min}$ (a) and value $\mathrm{Bi}_{\min}$ (b) of local minimum of the Biot function with respect to Re and Γ for case (ii) and ($\mathrm{Pr} = 69.2$, $\Gamma_{\mathrm{tc}} = 10$, air, 1g). The markers denote the simulation data and the lines the corresponding fits: $\Gamma = 0.5$ (circles, full blue line), 0.66 (squares, dashed green line) and 1 (triangles, dash-dotted red line).

and its location (near the hot rod) becomes sensitive for small Reynolds numbers. These are also the only quantities which depend sensitively on the magnitude and direction of the forced mean flow (not shown).

5.2. Evolution of fit coefficients during the multi-stage procedure

Building on the location of the extrema of $\mathrm{Bi}(z)$, a robust Biot-function model is derived by means of the multistage fitting algorithm described in Sec. 4.5. Figures 12, 13 and 14 show the coefficients $a_0^{c2}(\Gamma, \mathrm{Re})$, $a_1^{c2}(\Gamma, \mathrm{Re})$ and $a_2^{c2}(\Gamma, \mathrm{Re})$ for stages I, II and III, as well as the corresponding explicit fits $\tilde{a}_0^{c2}(\Gamma, \mathrm{Re})$, $\tilde{a}_1^{c2}(\Gamma, \mathrm{Re})$ for stages III and IV, for $\mathrm{Pr} = 69.2$, case (ii), $\Gamma_{\mathrm{tc}} = 10$, 1g and air as surrounding gas. The main graphs show the simulation data as markers, while the fits are

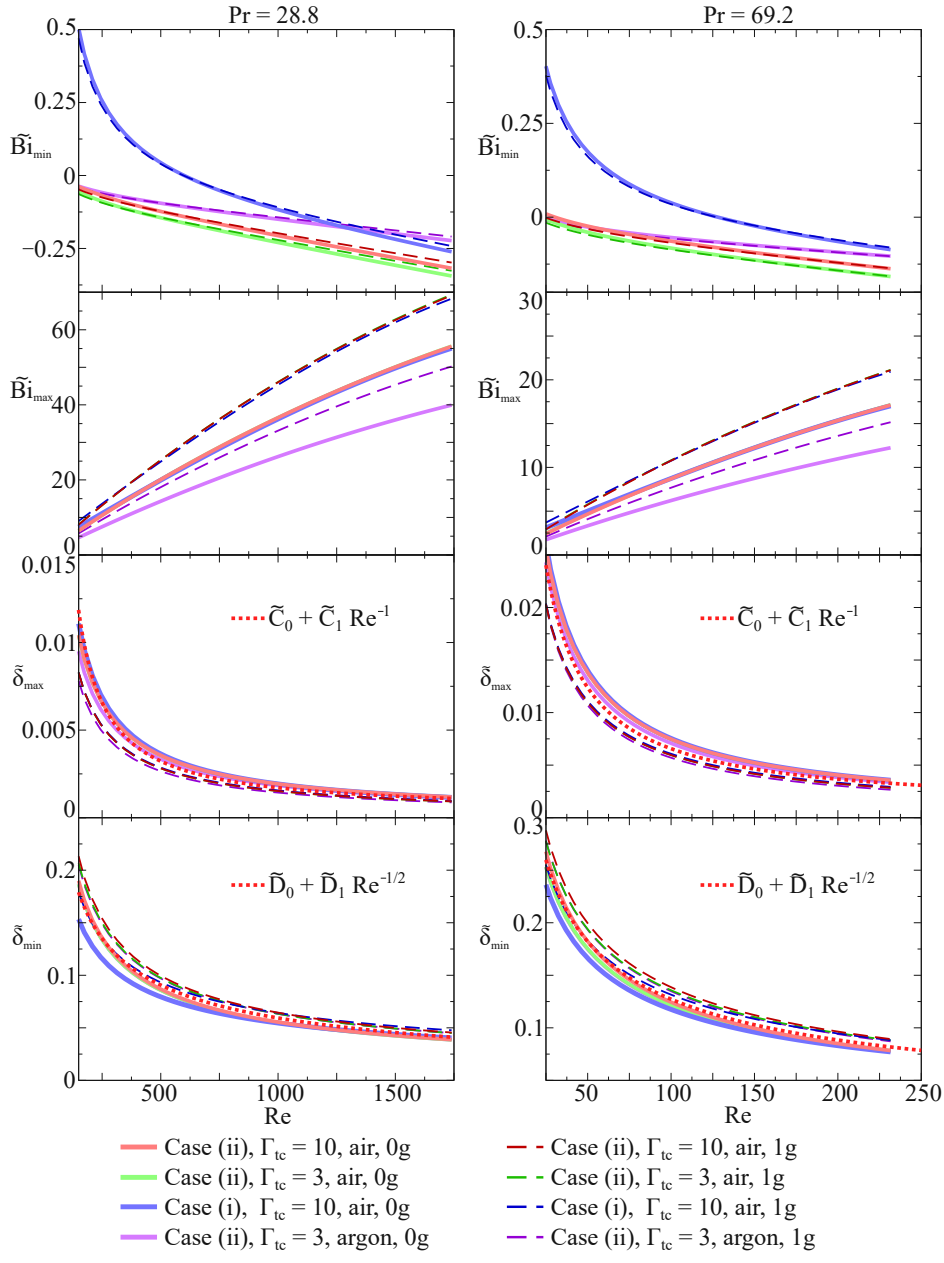

Figure 10: Comparison of the fits of the local minimum and maximum of the Biot function $\widetilde{Bi}_{min}$ and $\widetilde{Bi}_{max}$, respectively, and their location $\tilde{\delta}_{min}$ and $\tilde{\delta}_{max}$ for $\Gamma = 0.5$ and closed chambers. The theoretical fits for δ_{min} and δ_{max} are indicated by dotted red lines with $\tilde{C}_0 = 0.000289$, $\tilde{C}_1 = 1.40574$, $\tilde{D}_0 = -0.01573$, and $\tilde{D}_1 = 2.38955$ for $Pr = 28.8$, and $\tilde{C}_0 = 0.000762$, $\tilde{C}_1 = 0.580549$, $\tilde{D}_0 = -0.004265$, and $\tilde{D}_1 = 1.32588$ for $Pr = 69.2$.

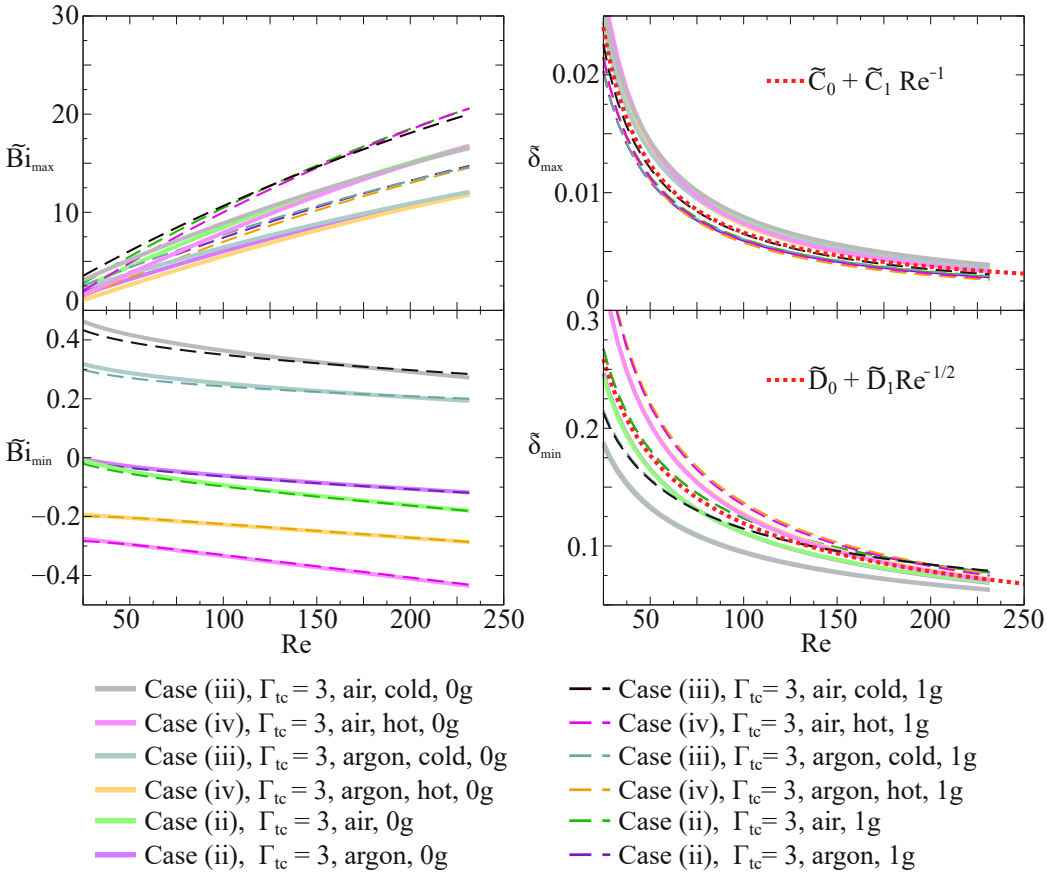

Figure 11: Comparison of the fits of the local minimum and maximum of the Biot function $\tilde{Bi}_{min}$ and $\tilde{Bi}_{max}$, respectively, and their location $\tilde{\delta}_{min}$ and $\tilde{\delta}_{max}$ for $\Gamma = 1$, $Pr = 69.2$ for open and closed chambers. The theoretical fits for δ_{min} and δ_{max} are indicated by dotted red lines with $\tilde{C}_0 = 0.000771$, $\tilde{C}_1 = 0.580637$, $\tilde{D}_0 = -0.02057$, and $\tilde{D}_1 = 1.39514$. The labels 'cold' and 'hot' used in the legend refer to cold and hot blowing boundary condition enforced at the inlet of the gas phase.

represented by lines. Depicted are fits for constant aspect ratio, i.e. $\Gamma = 0.5$ (circles, full line), $\Gamma = 0.66$ (squares, dashed line) and $\Gamma = 1$ (triangles, dash-dotted line). The inset panels collect the fit coefficients $A^{c2}_{i,j}$ (bullets) and a correcting linear fit in Γ of the coefficients $\tilde{A}^{c2}_{i,j} = \alpha^{c2}_{i,j} + \beta^{c2}_{i,j}\Gamma$ (full lines).

The trends observed for the three fitting coefficients a^{c2}_0, a^{c2}_1 and a^{c2}_2 as a function of the Reynolds number are dominated by two main contributions. We observe, in fact, a power-law decay of the absolute value of a^{c2}_0, a^{c2}_1 and a^{c2}_2 at low and moderate Re, while the coefficient a^{c2}_0 becomes linear in Re at high-enough Reynolds numbers (and potentially at asymptotic regimes). At low and moderate Reynolds numbers, the thickness of the boundary layer decays as a power law of Re (see $\delta_{\max}$ in fig. 8(a)) on the cold wall. This implies that a power-law regime must be present, and turns out to be dominant, for the three fitting coefficients a^{c2}_0, a^{c2}_1 and a^{c2}_2. In fact, they must fit the function $\mathrm{Bi}(z)$ in region C2, with the length of such a region that expands along z as a power law in Re because z^{c^*} is fixed and $z^{c^*} - z_{\max} = 0.7 - \delta_{\max}$. On the other hand, at high-enough Reynolds numbers, the rate of change of $\delta_{\max}$ is low and the quasi-linear growth of $\mathrm{Bi}_{\max}$ with Re (see fig. 8(b)) becomes dominant. Owing to the self-similarity of the

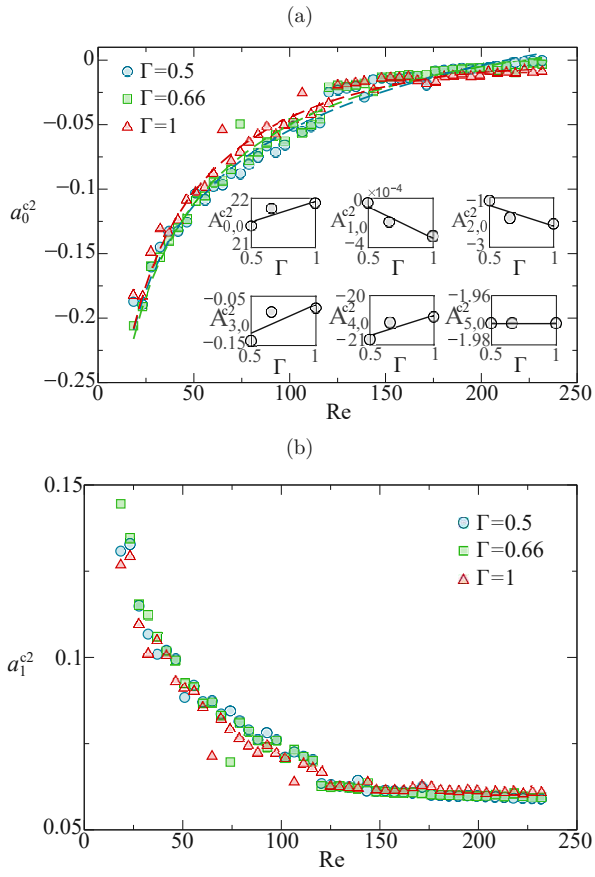

Figure 12: See next page for figure caption.

(c)

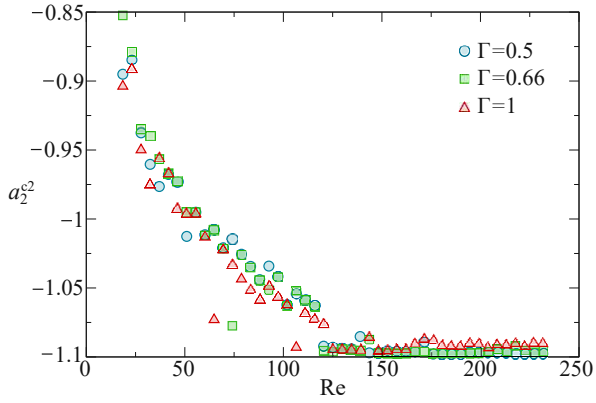

Figure 12: (a) Fit of the coefficient $a_0^{c2}(\mathrm{Re},\Gamma)$ for Case (ii), Pr = 69.2, Γ_{tc} = 10, air, 1g (stage II, $z \in [z_{max}, z_{max}+0.1]$) obtained processing the fits of the Biot function Bi(z) (stage I). The fit of a_0^{c2} depends on Re (lines) for $\Gamma = 0.5$ (circles, dashed line), 0.66 (squares, dashed line) and 1 (triangles, dashed line). The linear fits (solid lines) of the coefficients $A_{i,0}^{c2}$ (gray-filled circles) with respect to Γ are reported in the insets. The panels (b) and (c) report a_1^{c2} and a_2^{c2} at stage I.

boundary layer, the Biot function in region C1 shall experience a stretching that leads to a shift of the matching condition at Bi_{max} in region C2. Considering the only region C2, this leads to an effective shift of the function Bi(z), which must be proportional to the quasi-linear trend of Bi_{max} with Re. This explains why a linear trend is observed for the shifting coefficient of the fit $\tilde{\mathrm{Bi}}^{C2}$, i.e. a_0^{c2} has an $A_{0,1}^{c2} \neq 0$, and the coefficients $A_{1,1}^{c2}$ and $A_{1,2}^{c2}$ are null. Further considering that, at high-enough Reynolds numbers, the length of region C2 changes very slowly upon an increase of Re, the power-law effect due to the change of the matching location between C1 and C2 is not dominant and a saturation of the fitting coefficients a_1^{c2} and a_2^{c2} is observed.

(a)

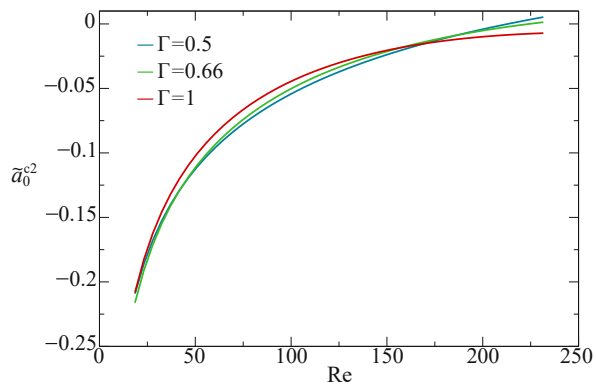

Figure 13: See next page for figure caption.

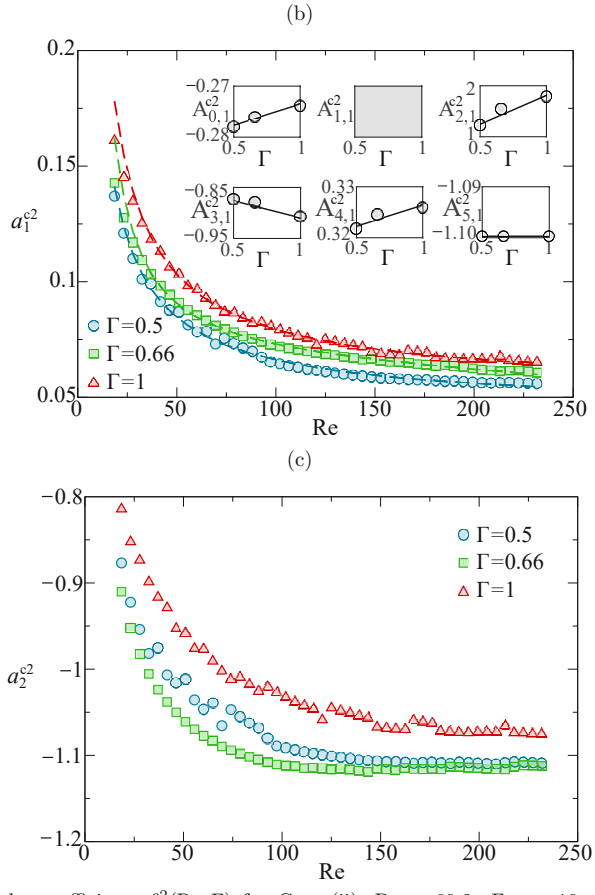

Figure 13: (a) Fit of the coefficient $a_1^{c2}(\mathrm{Re},\Gamma)$ for Case (ii), Pr = 69.2, Γ_{tc} = 10, air, 1g (stage III). The markers denote the coefficients resulting from the fits of the Biot function for Γ = 0.5 (circles), 0.66 (squares) and 1 (triangles) after fixing $a_0^{c2} = \tilde{a}_0^{c2}$ (solid lines in (b)). The dashed lines denote the power-law fits which are employed for a_1^{c2}, while the insets show the linear fits (solid lines) of the coefficients $A_{i,1}^{c2}$ (gray-filled circles) with respect to Γ. The panel (c) depicts a_2^{c2} at stage II.

5.3. Accuracy of the Biot function approximation

A comparison between the "exact" Biot function Bi(z) determined numerically from the two-fluid model (full black line) and the Biot function $\widetilde{\mathrm{Bi}}(z)$ resulting from the above fitting procedure (full brown line) is shown in fig. 15(a) for case (ii), Γ = 0.5, Γ_{tc} = 10, Bd = Bo = 0, and Pr = 28.8. The same comparison, but for Pr = 69.2, is provided in fig. 15(b). In both cases, air is considered as a surrounding gas. Throughout, the Biot function approximation $\widetilde{\mathrm{Bi}}(z)$ is in very good agreement with the "exact" Biot function Bi(z) obtained from the numerical two-phase flow simulation. The good agreement is found to hold true for all Reynolds numbers considered (right subfigures of 15). The left parts of fig. 15(a,b) show the z-dependence of Bi and $\widetilde{\mathrm{Bi}}$ in more detail for $(\mathrm{Pr},\mathrm{Re}) = (28.8,\ 383)$ (a) and $(\mathrm{Pr},\mathrm{Re}) = (69.2,\ 51)$ (b). On the global z scale both functions are almost identical. The zoom into the region near the cold wall (insets in fig. 15) reveal minor

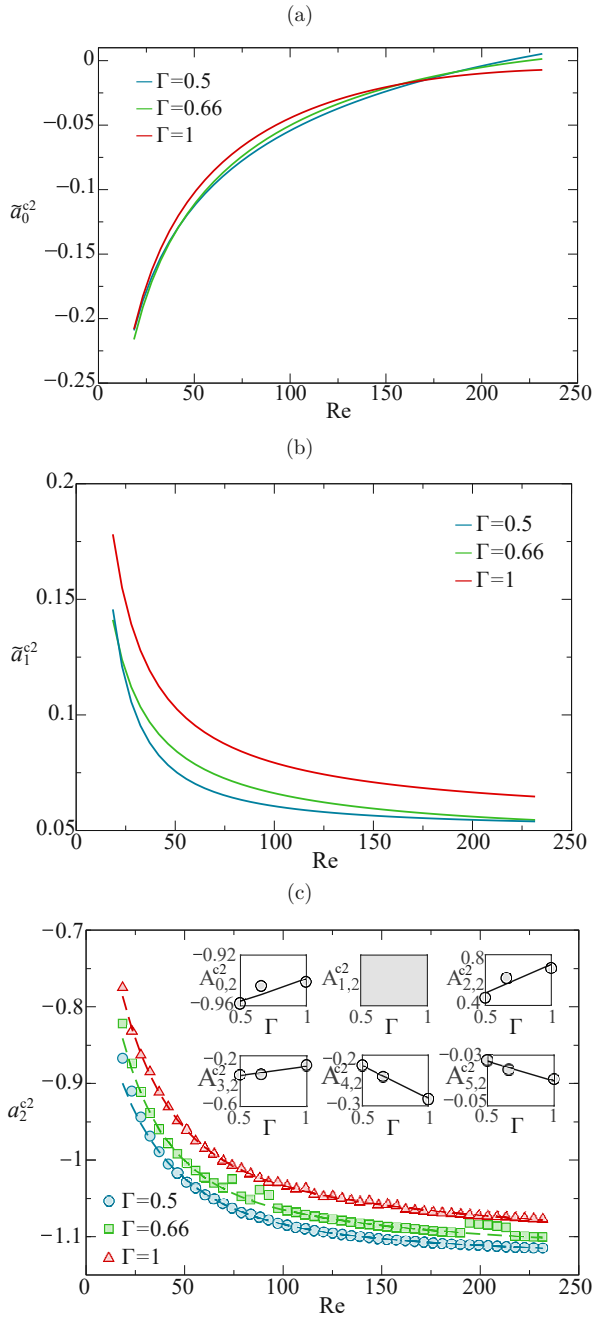

Figure 14: Fit of the coefficient $a_2^{c2}(\mathrm{Re},\Gamma)$ for Case (ii), Pr = 69.2, $\Gamma_{tc} = 10$, air, 1g (stage IV). The markers denote the coefficients resulting from the fits of the Biot function for $\Gamma = 0.5$ (circles), 0.66 (squares) and 1 (triangles) after fixing $a_0^{c2} = \tilde{a}_0^{c2}$ and $a_1^{c2} = \tilde{a}_1^{c2}$. The line and color coding is consistent with fig. 13.

deviations. Also shown as colored dash-dotted lines are the local fits to regions H, C2, and C1. Note the local fits in fig. 15 result from the final stage (IV) of the algorithm, whereas the local fits depicted in fig. 2 have not undergone a multistage fit in Re and Γ and resulted from stage I of the algorithm. For that reason, the latter is more accurate. For a detailed analysis of the structure of the Biot function, we refer to the supplementary material.

(a) Case (ii), Pr = 28.8, Bd = Bd = 0, Γ = 0.5, Γ_{tc} = 10, air. Left: Re = 383

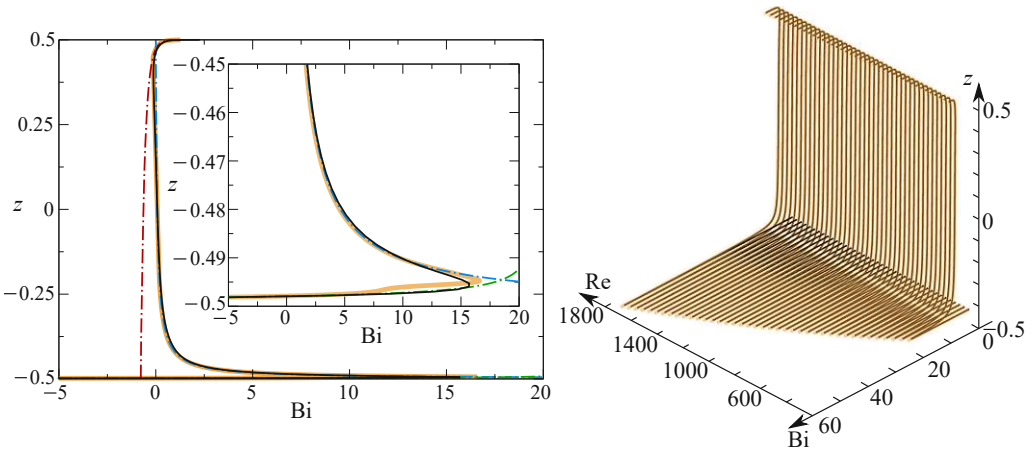

(b) Case (ii), Pr = 69.2, Bd = Bd = 0, Γ = 0.5, Γ_{tc} = 10, air. Left: Re = 51

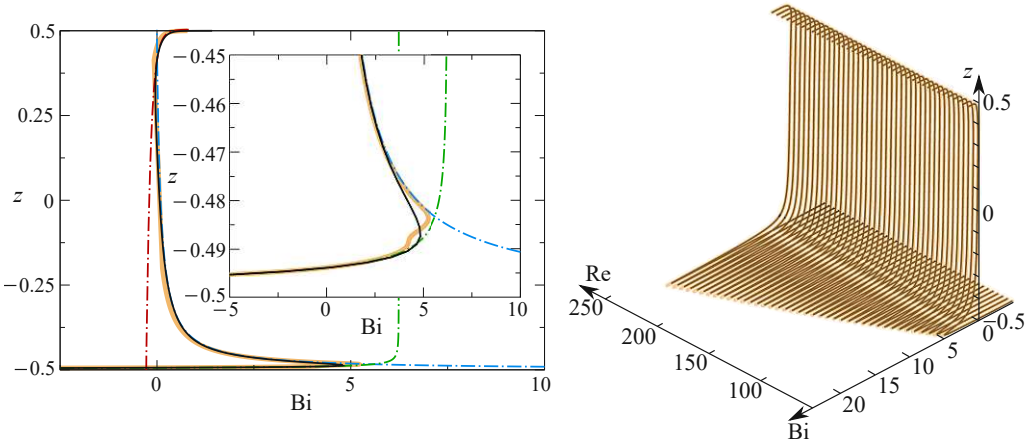

Figure 15: Biot function Bi(z) resulting from the multiphase simulation (black solid line), compared with the fit $\widetilde{\mathrm{Bi}}(z)$ obtained by the multi-stage approach of sec. 4 (orange solid line) according to (26) for Case (ii), Bd = Bo = 0, Γ = 0.5, Γ_{tc} = 10, Pr = 28.8 (a) and Pr = 69.2 (b), assuming air as surrounding gas. Power-law fits for the individual regions resulting after the four-stage fitting operation are shown as colored dash-dotted lines. The left sides show the profiles for Re = 383 (a) and Re = 51 (b), while the right sides compare $\mathrm{Bi}(z, \mathrm{Re}, \Gamma = 0.5)$ and $\widetilde{\mathrm{Bi}}(z, \mathrm{Re}, \Gamma = 0.5)$. The bumps observed at the maximum of $\widetilde{\mathrm{Bi}}$ are due to the blending between $\widetilde{\mathrm{Bi}}^{C1}$ and $\widetilde{\mathrm{Bi}}^{C2}$ performed by the hyperbolic tangent blending function $\mathcal{B}(z)$.

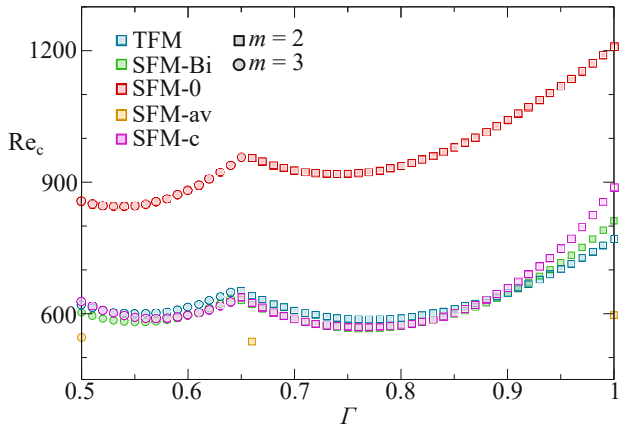

Figure 16: Critical Reynolds number for case (ii) with Pr = 28.8, Bd = 0, $\Gamma_{tc} = 3$, and $\Gamma = [0.5, 1]$. Different numerical models (color) and wave numbers m (symbol) according to the legend are explained in the text.

5.4. Application of the Biot function approximation

The heat transfer across the free surface due to the axisymmetric flow has a profound impact of the onset of three-dimensional oscillatory flow [26]. Therefore, the quality of the heat transfer model can be well assessed by comparing the linear stability boundaries of the two-dimensional axisymmetric steady flow obtained by different heat transfer models. Here we use the linear stability analysis code of Stojanović et al. [39] which is freely available at `https://github.com/fromano88/MaranStable.git` [37]. For the details of the linear stability analysis we refer to [39] and [38]. However, for the specific case of the Biot function we use an in-development version of the code not yet available for download. All other cases can be obtained by the version available on GitHub.

Linear stability analyses have been carried out for case (ii) with Pr = 28.8, Bd = 0, $\Gamma_{tc} = 3$, and $\Gamma = [0.5, 1]$. The analysis with respect to general three-dimensional perturbations is performed for different axisymmetric steady basic states and for different boundary conditions. The analysis yields the critical Reynolds number, critical frequency, critical azimuthal wave number and the critical mode. Here we only consider the results for the critical Reynolds number. It is shown as a function of the aspect ratio in fig. 16 for the different models employed. The following basic state models have been tested.

[TFM] Fully resolved two-fluid model (TFM). The TFM serves as the benchmark (blue).

[SFM-Bi] Single-fluid model (SFM) using Newton's law of heat transfer with the current Biot function approximation $\widetilde{\mathrm{Bi}}(z, \Gamma, \mathrm{Re})$ instead of a constant Biot number (green).

[SFM-0] Single-fluid model with adiabatic boundary conditions on the free surface, i.e. Bi = 0 (red).

[SFM-av] Single-fluid model using Newton's law with a constant average Biot number $\mathrm{Bi}_{av} = (1/2 - \hat{z})^{-1} \int_{\hat{z}}^{1/2} \mathrm{Bi}(z)\mathrm{d}z$ (yellow). The lower boundary $\hat{z} = -0.49$ serves to exclude the strong singularity of Bi associated with the cold corner.

[SFM-c] Single-fluid model with Newton's law and a constant Biot number selected as $\mathrm{Bi}_c = \tilde{a}_0^m(\Gamma, \mathrm{Re})$ (magenta).

Regarding the boundary conditions for the three-dimensional perturbation flow the following conditions were employed. For the reference case [TFM] we used the same boundary conditions as provided in [39]. In case of the single-fluid model the free surface boundary conditions result from (15) by neglecting the viscous stress from the gas phase and by linearizing the boundary conditions with respect to small deviations from the basic flow.

From fig. 16 the reference case [TFM] (blue) shows the instability of the basic flow arises with an azimuthal wave number $m = 3$ for $\Gamma > 0.66$ while the most dangerous mode has a wave number $m = 2$ for $\Gamma > 0.66$. Use of the Biot function fit $\tilde{\mathrm{Bi}}$ [SFM-Bi] (green) is able to very accurately reproduce the benchmark result (blue). Deviations between [SFM-Bi] and the [TFM] reference results become largest near the end points of the fitting range at $\Gamma = 0.5$ and $\Gamma = 1$. Nevertheless, the error in Re_c remains always less than 5%.

Owing to its simplicity, very often a single-fluid model together with an adiabatic free surface

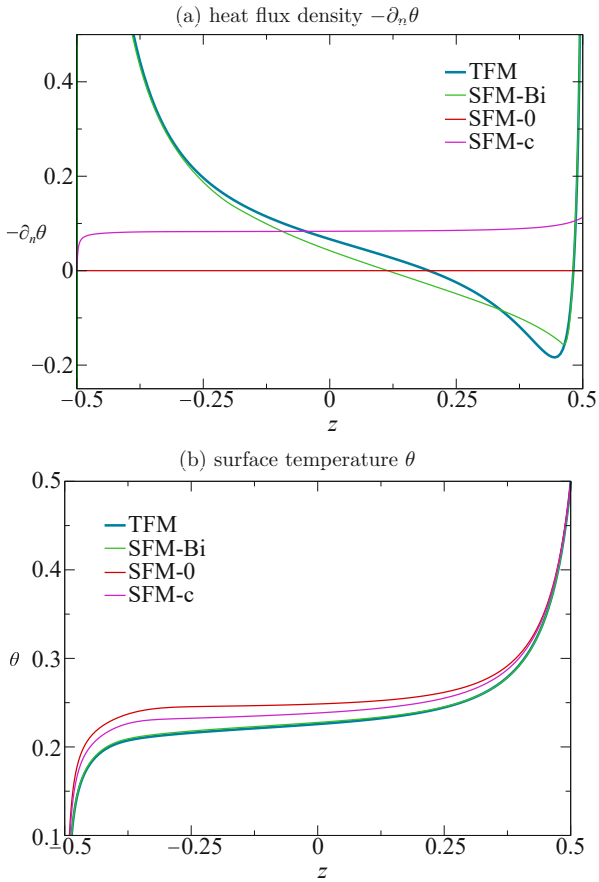

Figure 17: See next page for figure caption.

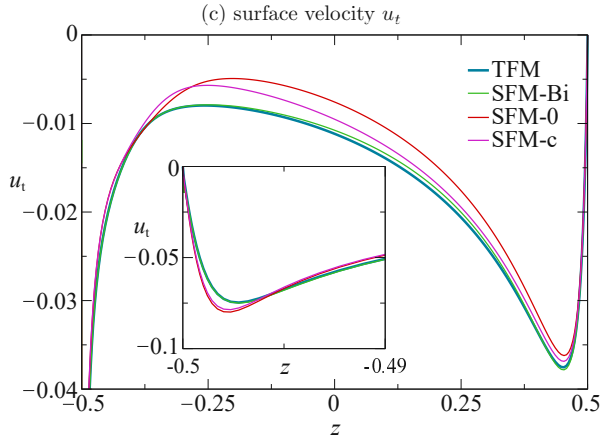

Figure 17: Heat flux density $-\partial_n\theta$ (a), temperature θ (b) and tangential velocity u_t on the free surface for case (ii) at the critical Reynolds number for the two-fluid model $\mathrm{Re} = \mathrm{Re}_c[TFM] = 771$ for $\mathrm{Pr} = 28.8$, $\mathrm{Bd} = 0$, $\Gamma_{\mathrm{tc}} = 3$ and $\Gamma = 1$. Different numerical models are coded by color. [TFM] (blue), [SFM-Bi] (green), [SFM-0] (red) and [SFM-c] with $\mathrm{c} = 0.1043$ (magenta).

has been employed [e.g. 40, 15]. However, the [SFM-0] model (purple) strongly overestimates the true [TFM] critical Reynolds number for all Γ analyzed, even though the aspect ratio at which a transition between the critical modes with $m = 3$ and $m = 2$ arises is reasonably well reproduced. Alternatively, using the constant part of the Biot function fit from region M to estimate the constant Biot number $\mathrm{Bi_c} = \tilde{a}_0^m$ of the classical Newton's law ([SFM-c]), the stability boundary (yellow triangles down) is remarkably well reproduced. Merely, towards $\Gamma = 1$ deviations from the benchmark become significant, as was the case for [SFM-Bi]. Nevertheless, the result indicates that a good guess of an appropriate constant Biot number can yield rather accurate predictions of Re_c. Finally, the model [SFM-av], using a constant Biot number obtained by averaging the Biot function over the length of the liquid bridge strongly underestimates the critical Reynolds number $\mathrm{Re_c}$ (red markers). This result, in comparison to [SFM-c], underlines that the correct value of the constant is essential. The use of a constant Biot number based on an average value has been proposed before by Gaponenko et al. [29]. They have also computed the heat flux based on a two-fluid model and suggested a Biot number based on the average temperature difference between the free surface and some ambient temperature. However, since both the Biot number and the fictitious ambient temperature difference remained unknown in their investigation, they could only estimate the Biot number. On the other hand, we base the Biot number on the actual heat flux (or quantities derived from it) and we are thus able to specify a corresponding average Biot number derived as an explicit function from our fits. We further stress the difference that they propose to use the unknown ambient temperature, while we rather suggest to employ the known cold-wall temperature as the reference temperature θ_{ref} (see (23)).

To understand which influence the different heat-transfer laws have on the surface temperature θ and the tangential surface velocity u_t, these quantities are shown in fig. 17 together with the free-surface heat flux density $-\partial_n\theta$ at the critical Reynolds number for the two-fluid model $\mathrm{Re} = \mathrm{Re}_c[\mathrm{TFM}] = 771$ for case (ii), $\mathrm{Pr} = 28.8$, $\mathrm{Bd} = 0$, $\Gamma_{\mathrm{tc}} = 3$. The data are shown for $\Gamma = 1$ at which the deviations of the different models from the reference case are the largest. The general characteristic shape of the surface temperature (fig. 17(b)) and the surface velocity (fig. 17(c))

are reproduced by all models. The single-phase solver supplied with the present Biot-function model (SFM-Bi, green) almost perfectly reproduces the surface temperature and velocity (TFM, blue) over the whole range of z. The slight mismatch seems to be due to the heat flux density of [SFM-Bi] not perfectly reproducing the heat flux dictated by the [TFM]. Apparently, the reason is the remaining error in matching the location and amplitude of the maximum Biot number near the hot wall (minimum heat flux in fig. 17(a)) by the fit function. The differences in the surface flow data are much larger for a constant Biot number, in particular for $\mathrm{Bi} = 0$ [SFM-0]. Assuming an adiabatic free surface [SFM-0] (purple) the free surface temperature in the central plateau region is too high and the magnitude of the free surface velocity is too low. If the Biot number is selected constant [SFM-c] with Biot number $\mathrm{Bi} = \mathrm{Bi_c} = 0.1043$ (orange) the deviations from the reference data are not as large, except for the surface velocity near $z \approx -0.35$. Obviously this is accomplished by the positive non-zero Biot number having a similar effect as the positive heat flux density for $z \lesssim 0.2$ in the [TFM] reference model (blue in fig. 17(a)). The fact that the velocity peaks for [SFM-0] and [SFM-c] at $z \approx -0.498$ near the cold wall are slightly stronger than for the reference case [TFM] (inset in fig. 17(c)) seems to be irrelevant due to the small distance from the solid wall.

The critical Reynolds numbers in the range $\Gamma \in [0.9, 1]$ in fig. 16 are ordered according to the surface temperature or surface velocity magnitude in the plateaus region near midplane $z \approx 0$ for $\Gamma = 1$ (fig. 17). As shown by [30] the stabilization of the basic flow that is seen when defining the Reynolds number using the thermophysical data at the reference temperature (fig. 16) is due to a reduced effective viscosity in the flow due to the elevated free surface temperature in the plateau region, which is most pronounced here for [SFM-0] (adiabatic free surface).

Similar linear stability results as in fig. 16 for $\Gamma_{\mathrm{tc}} = 3$ are obtained for the cases (i) with $\mathrm{Pr} = 28.8$ and $\mathrm{Bd} = 0$ shown in fig. 18(a) and case (ii) with $\mathrm{Pr} = 28.8$ and $\mathrm{Bd} = 0$ shown in fig. 18(b), both for a gas container geometry with $\Gamma_{\mathrm{tc}} = 10$ (radius ratio $\eta = \Gamma_{\mathrm{tc}}\Gamma$). The results of the Biot function model [SFM-Bi] compare well to the reference case [TFM] independent from the gas space (compare figs. 16 and 18(b)), as the level of tolerance is $\leqslant 5\%$ for the whole range of Γ. However, in case (i), when the gas container is kept at the cold wall temperature at its radial boundary, the deviation between [SFM-Bi] and [TFM] is $> 5\%$ for $\Gamma \in [0.52, 0.81]$ but still remains $\leqslant 8\%$. Regardless of the considered case, [SFM-Bi] yields more accurate predictions than [SFM-c].

The above comparison shows that the Biot function approach [SFM-Bi] can almost perfectly reproduce the benchmark [TFM] and it comes with a great flexibility with respect to a variations of the aspect ratio and the Reynolds number. Using a constant Biot number [SFM-c] the benchmark results can possibly be matched to some degree, but the value for $\mathrm{Bi_c}$ is not known a priori as $\mathrm{Bi_c}$ depends on the aspect ratio and Reynolds number. However, selecting the constant Biot number as $\tilde{a}_0^m$ from matching region M provides a rationale for finding a good approximation in case a constant Biot number is to be used. As a by-product of the present fitting procedure for the (variable) Biot function it is, in fact, possible to construct a constant Biot number $\tilde{\mathrm{Bi}} \approx \mathrm{Bi_c} = \tilde{a}_0^{\mathrm{m}}(\mathrm{Re}, \mathrm{Pr}, \Gamma, \Gamma_{\mathrm{tc}}, \mathrm{Bd}, \mathrm{Bo}, \mathrm{gas}, \mathrm{Case})$ which is a function of all major parameters governing the flow. A corresponding Matlab code that provides $\mathrm{Bi_c} = \tilde{a}_0^{\mathrm{m}}$ can be downloaded at https://github.com/fromano88/BiotFunction_LB.git.

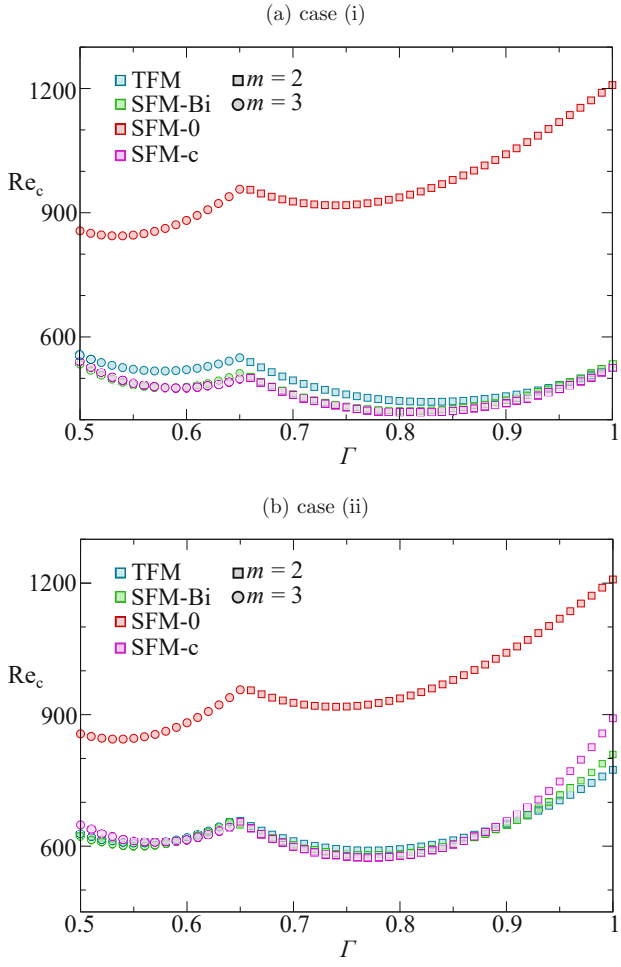

Figure 18: Linear stability boundary of the basic steady flow for Pr = 28.8, Bd = 0, $\Gamma_{tc} = 10$, and $\Gamma = [0.5, 1]$. (a) case (i), (b) case (ii). Different numerical models are indicated by color (see legend) and explained in the text.

6. Discussion and conclusion

The heat transfer across the interface between a thermocapillary liquid bridge from silicone oil and the surrounding ambient gas has been investigated by means of fully-resolved, fully-coupled multiphase numerical simulations. Steady axisymmetric flow and temperature fields have been computed for two different liquids, 2- and 5-cSt silicone oil, and for zero and normal gravity conditions. The length of the liquid bridge was kept fixed at 1.7 mm. Calculations have been carried out for all tests and aspect ratios Γ listed in table 3, and for Marangoni numbers $Ma \in [850, 42750]$, covering three orders of magnitude, resulting in a total of 2800 simulations.

The computed surface temperature and heat flux across the free surface were then introduced in Newton's law of cooling assuming the cold-wall temperature as the ambient refer-

ence temperature. This yields the local heat flux density in form of a local Biot number, the Biot function. The Biot function $\mathrm{Bi}(z)$ exhibits two extrema, one near the hot and one near the cold wall, which reflect the boundary-layer character of the flow. Based on its extrema the numerically computed Biot function $\mathrm{Bi}(z)$ for all Γ and Re has been fitted by a function $\tilde{\mathrm{Bi}}$ using a robust multistage algorithm to arrive at closed form expressions for $\tilde{\mathrm{Bi}}(z, \mathrm{Re}, \Gamma)$ for two frequently employed high-Prandtl-number silicone oils and given geometries of the gas cavity hosting the liquid bridge. Explicit fit functions of these data are available under https://github.com/fromano88/BiotFunction_LB.git.

The knowledge of $\tilde{\mathrm{Bi}}$ allows to employ a single-fluid model to capture the true (multiphase) local heat flux with high fidelity for a wide range of Reynolds numbers and aspect ratios. This approach yields more accurate results than the classical Newton law with a constant Biot number. Moreover, for the configurations considered, the use of the Biot function is computationally less demanding, because the computational effort for the single-fluid model typically amounts to only 30% of the effort required for the two-fluid model.

The conventional approach using a constant Biot number yields temperature and velocity profiles on the free surface qualitatively similar to those obtained by the full two-fluid model. The reason is the boundary layer structure is dominated by the thermocapillary convection in the liquid phase. But deviations from the multi-phase reference results can amount to more than 10% in the L2-norm of the tangential velocity and temperature at the liquid–gas interface (see fig. 17), and deviations of the critical Reynolds number for the onset of three-dimensional oscillatory flow can be even larger. The sensitivity of the critical Reynolds number calls for a test of different heat transfer models. It is possible to obtain an accurately prediction of the critical Reynolds number by a single-phase model with a constant Biot number. The 'correct' Biot number is typically unknown a priori and needs to be guessed. However, selecting $\mathrm{Bi} = \tilde{a}_0^{\mathrm{m}}$, i.e. the average of the Biot function over the free surface excluding the thermal boundary layers (region M), yields a good approximation to Re_c within the single-fluid model. Therefore, if the average heat flux in region M would be measured in experiments in addition to the critical Reynolds number, the Biot number based on the measured heat flux should provide a good approximation to the proper constant Biot number to be used in numerical single-fluid linear stability analyses. It would be interesting to test this hypothesis in future investigations.

The selection of the ansatz functions for the present Biot function approximation $\tilde{\mathrm{Bi}}(z, \Gamma, \mathrm{Re})$ and the fit procedure introduce small deviations from the numerical Biot function $\mathrm{Bi}(z)$ obtained from the two-phase flow simulations. But even $\mathrm{Bi}(z)$ deviates from the Biot function of a more precise physical model because flow-induced dynamic deformations of the interface have been neglected. However, these fine details do not have a notable effect on the heat transfer [22]. Therefore, it is hoped that the present Biot-function model will prove useful for future stability analyses. The method presented should be easily adaptable to the case of an imposed axial flow in the gas phase, which is one means of controlling the onset of three-dimensional flow [34] and which is planned to be investigated in the forthcoming space experiment JEREMI [28].

Acknowledgements

Part of this work has been supported by FFG (ASAP 14, project number 866027) and by ESA (contract 4000121111/17/NL/PG/pt).

References

[1] Scriven, L. E., and Sternling, C. V., 1960, "The Marangoni effects", *Nature*, Vol. 187, pp. 186–188.

[2] Young, N.O., Goldstein, J.S., and Block, M.J., 1959, "The motion of bubbles in a vertical temperature gradient", *J. Fluid Mech.*, Vol. 6, pp. 350–356.

[3] Oron, A., Davis, S.H., and Bankoff, S.G., 1997, "Long-scale evolution of thin liquid films", *Rev. Mod. Phys.*, Vol. 69.2, pp. 931–980.

[4] Smith, M.K., and Davis, S.H., 1983, "Instabilities of dynamic thermocapillary liquid layers. Part 1. Convective instabilities", *J. Fluid Mech.*, Vol. 132, pp. 119–144.

[5] Schwabe, D., 1981, "Marangoni effects in crystal growth melts", *Physicochem. Hydrodyn.*, Vol. 2, pp. 263–280.

[6] Mills, K.C., Keene, B.J., Brooks, R.F., and Shirali, A., 1998, "Marangoni effects in welding", *Philos. T. Roy. Soc. As*, pp. 911–926.

[7] Sirignano, W.A., and Glassman, I., 1970, "Flame spreading above liquid fuels: Surface-tension-driven flows", *Combust. Sci. Technol.*, Vol. 1, pp. 307–312.

[8] Kuhlmann, 1999, "Thermocapillary Convection in Models of Crystal Growth", *Springer*, Vol. 152.

[9] Li, Y.-R., Peng, L., Akiyama Y., and Imaishi, N., 2003, "Three-dimensional numerical simulation of thermocapillary flow of moderate Prandtl number fluid in an annular pool", *J. Cryst. Growth*, Vol. 259, pp. 374–387.

[10] Carpenter, B.M., and Homsy, G.M., 1989, "Combined buoyant-thermocapillary flow in a cavity", *J. Fluid Mech.*, Vol. 207, pp. 121–132.

[11] Xu, J., and Zebib, A., 1998, "Oscillatory two- and three-dimensional thermocapillary convection", *J. Fluid Mech.*, Vol. 364, pp. 187–209.

[12] Kuhlmann, H. C., and Albensoeder, S., 2008. "Three-dimensional flow instabilities in a thermocapillary-driven cavity". *Physical Review E*, Vol. 68, pp. 036303.

[13] Schwabe, D., Scharmann, A., Preisser, F., and Oeder, F., 1978, "Experiments on surface tension driven flow in floating zone melting", *J. Crystal Growth*, Vol. 43, pp. 305–312.

[14] Hurle, D.T.J., and Jakeman, E., 1981, "Introduction to the techniques of crystal growth", *Physicochem. Hydrodyn.*, Vol. 2, pp. 237–244.

[15] Nienhüser, C., and H. C. Kuhlmann, H. C., 2002, "Stability of thermocapillary flows in non-cylindrical liquid bridges", *J. Fluid Mech.*, Vol. 458, pp. 35–73.

[16] Motegi, K., Kudo, M., and Ueno, I., 2017, "Linear stability of buoyant thermocapillary convection for a high-Prandtl number fluid in a laterally heated liquid bridge", *Phys. Fluids*, Vol. 29, pp. 044106.

[17] Xu, J.-J. and Davis, S. H., 1984, "Convective thermocapillary instabilities in liquid bridges", *Phys. Fluids*, Vol. 27, pp. 1102–1107.

[18] Romanò, F., and Kuhlmann, H. C., 2017, "Particle–boundary interaction in a shear-driven cavity flow", *Theor. Comput. Fluid Dyn.*, Vol. 31, pp. 427–445.

[19] Romanò, F., and Kuhlmann, H. C., 2018, "Finite-size Lagrangian coherent structures in thermocapillary liquid bridges", *Phys. Rev. Fluids*, Vol. 3, pp. 094302.

[20] Romanò, F., Wu, H., and Kuhlmann, H. C., 2019, "A generic mechanism for finite-size coherent particle structures", *Int. J. Multiphase Flow*, Vol. 111, pp. 42–52.

[21] Romanò, F., and Kuhlmann, H. C., 2019, "Finite-size coherent structures in thermocapillary liquid bridges: A review", *Int. J. Microgravity Sci. Appl.*, Vol. 36, pp. 360201.

[22] Romanò, F., and Kuhlmann, H. C., 2019, "Heat transfer across the free surface of a thermocapillary liquid bridge", *Tech. Mech.*, Vol. 39, pp. 72–84.

[23] Oba, T., Toyama, A., Hori, T., and Ueno, I., 2019, "Experimental study on behaviors of low-Stokes number particles in weakly chaotic structures induced by thermocapillary effect within a closed system with a free surface", *Phys. Rev. Fluids*, Vol. 4, pp. 104002.

[24] Gotoda, M., Toyama, A., Ishimura, M., Sano, T., Suzuki, M., Kaneko, T., and Ueno, I., 2019, "Experimental study of coherent structures of finite-size particles in thermocapillary liquid bridges", *Phys. Rev. Fluids*, Vol. 4, p. 094301.

[25] Romanò, F., Kuhlmann, H. C., Ishimura, M., and Ueno, I., 2017, "Limit cycles for the motion of finite-size particles in axisymmetric thermocapillary flows in liquid bridges", *Phys. Fluids*, Vol. 29, p. 093303.

[26] Kamotani, Y., Wang, L., Hatta, S., Wang, A., and Yoda, S., 2003, "Free surface heat loss effect on oscillatory thermocapillary flow in liquid bridges of high Prandtl number fluids", *Int. J. Heat Mass Transfer*, Vol. 46, pp. 3211–3220.

[27] Kamotani, Y., Ostrach, S., 1998, "Theoretical analysis of thermocapillary flow in cylindrical columns of high Prandtl number fluids", *ASME J. Heat Transfer*, Vol. 120, pp. 758–764.

[28] Shevtsova, V., Gaponenko, Y., Kuhlmann, H. C., Lappa, M., Lukasser, M., Matsumoto, S., Mialdun, A., Montanero, J.M., Nishino, K., Ueno, I., 2014, "The JEREMI-Project on Thermocapillary Convection in Liquid Bridges. Part B: Overview on Impact of Co-axial Gas Flow.", *Fluid Dyn. Mater. Process.*, Vol. 10, pp. 197–240.

[29] Gaponenko, Y., and Shevtsova, V., 2012, "Heat transfer through the interface and flow regimes in liquid bridge subjected to co-axial gas flow", *Microgravity Sci. Technol.*, Vol. 24, pp. 297–306.

[30] M. Stojanović, F. Romanò, and H. C. Kuhlmann, 2023, "Instability of axisymmetric flow in thermocapillary liquid bridges: Kinetic and thermal energy budgets for two-phase flow with temperature-dependent material properties", *Eur. J. Appl. Math.* (submitted for publication).

[31] Nishino, K., Yano, T., Kawamura, H., Matsumoto, S., Ueno, I., and Ermakov, M.K., 2015, "Instability of thermocapillary convection in long liquid bridges of high Prandtl number fluids in microgravity", *J. Cryst. Growth*, Vol. 420, pp. 57–63.

[32] Cowley, S. J., and Davis, S. H., 1983, "Viscous thermocapillary convection at high Marangoni numbers", *J. Fluid Mech.*, Vol. 135, pp. 175-188.

[33] Canright, D., 1994, "Thermocapillary flow near a cold wall", *Phys. Fluids*, Vol. 6, pp. 1415–1424.

[34] Yasnou, V., Gaponenko, Y., Mialdun, A., and Shevtsova, V., 2018, "Influence of a coaxial gas flow on the evolution of oscillatory states in a liquid bridge", *Int. J. Heat Mass Transfer*, Vol. 123, 747–759.

[35] Gray, D.D. and Giorgini, A., 1976, "The validity of the Boussinesq approximation for liquids and gases", *Int. J. Heat Mass Transfer*, Vol. 19, 545–551.

[36] VDI e.V., 2010, "VDI Heat Atlas", *Springer Berlin Heidelberg*.

[37] Stojanović, M., Romanò, F., and Kuhlmann, H. C., (n.d.), "`MaranStable`: A linear stability solver for multiphase flows in canonical geometries", *Software X*, Submitted.

[38] Stojanović, M., Romanò, F., and Kuhlmann, H. C., (n.d.), "High-Prandtl-number thermocapillary liquid bridges with dynamically deformed interface: Effect of an axial gas flow on the linear stability", In preparation.

[39] Stojanović, M., Romanò, F., and Kuhlmann, H. C., (2022), "Stability of thermocapillary flow in liquid bridges fully coupled to the gas phase", *J. Fluid Mech.*, Vol. 949, A5-1–A5-51.

[40] Wanschura, M., Shevtsova, V., Kuhlmann, H. C., and Rath, H.J., (1995), "Convective instability mechanisms in thermocapillary liquid bridges", *Phys. Fluids*, Vol. 7, 912–925.

Paper 6

Stojanović, M., Romanò, F., Kuhlmann, H. C. (2023), '`MaranStable`: A linear stability solver for multiphase flows in canonical geometries', *Software X* **23**, 101405

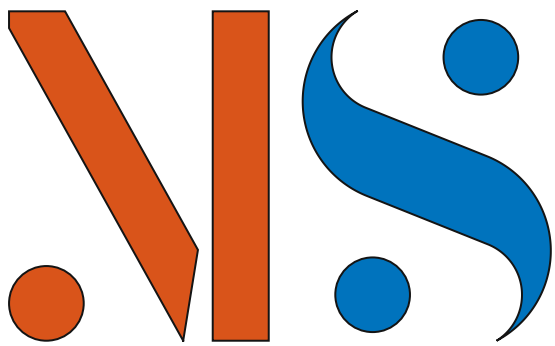

SoftwareX 23 (2023) 101405

Contents lists available at ScienceDirect

SoftwareX

journal homepage: www.elsevier.com/locate/softx

Original software publication

MaranStable: A linear stability solver for multiphase flows in canonical geometries

Mario Stojanović [a,*], Francesco Romanò [b], Hendrik C. Kuhlmann [a]

[a] TU Wien, Getreidemarkt 9-BA, 1060 Vienna, Austria

[b] Univ. Lille, CNRS, ONERA, Arts et Métiers Institute of Technology, Centrale Lille, UMR 9014 – LMFL – Laboratoire de Mécanique des Fluides de Lille – Kampé de Fériet, F-59000 Lille, France

ARTICLE INFO

Article history:
Received 27 February 2023
Received in revised form 27 April 2023
Accepted 4 May 2023

Dataset link: https://github.com/fromano88/MaranStable.git

Keywords:
Navier–Stokes equations
Multiphase flow
GUI
Thermocapillary flow

ABSTRACT

MaranStable is a software to perform three-dimensional linear stability analyses of steady two-dimensional non-isothermal multiphase flows in canonical geometries. Different approximations to the Navier–Stokes equations can be selected, which are discretized by finite volumes on a staggered grid. The stability of the basic flow, obtained by Newton—Raphson iteration, is computed by solving the linearized three-dimensional perturbation equations using normal modes. All calculations are based on MATLAB and make extensive use of the already parallelized backslash and eigs operators, and the graphical user interface eases the access to MaranStable.

Code metadata

Current code version	3.1
Permanent link to code/repository used for this code version	https://github.com/ElsevierSoftwareX/SOFTX-D-23-00135
Permanent link to Reproducible Capsule	
Legal Code License	CC-BY-NC-SA
Code versioning system used	none
Software code languages, tools, and services used	MATLAB
Compilation requirements, operating environments & dependencies	MATLAB R2022a or newer; OS tested: Windows 10, Ubuntu 18.04.6
If available Link to developer documentation/manual	https://github.com/fromano88/MaranStable/tree/main/docs
Support email for questions	maranstable@tuwien.ac.at

Software metadata

Current software version	3.1
Permanent link to executables of this version	https://github.com/fromano88/MaranStable/tree/main/bin
Permanent link to Reproducible Capsule	
Legal Software License	CC-BY-NC-SA
Computing platforms/Operating Systems	OS tested: Windows 10, Ubuntu 18.04.6
Installation requirements & dependencies	MATLAB R2022a or newer
If available, link to user manual - if formally published include a reference to the publication in the reference list	https://github.com/fromano88/MaranStable/tree/main/docs
Support email for questions	maranstable@tuwien.ac.at

1. Motivation and significance

Flow instabilities occur everywhere. They change the structure of the flow in nature and in engineering applications. Three scenarios demonstrate the crucial importance of hydrodynamic

* Corresponding author.
E-mail address: mario.stojanovic@tuwien.ac.at (Mario Stojanović).

https://doi.org/10.1016/j.softx.2023.101405

instability for the system dynamics: (a) The capillary breakup of a liquid jet initiated by the Rayleigh instability is relevant to inkjet printing. (b) Shear-flow instabilities related to the laminar–turbulence transition significantly affect the drag forces. (c) Buoyancy-driven instabilities are largely employed in thermal management of buildings with floor heating or ceiling cooling and drive geophysical circulations. While the physical mechanisms changing the flow character by instability are different, they all derive from the nonlinear character of the Navier–Stokes equations.

`MaranStable` computes the parameters (e.g. the Reynolds number) at which the flow changes by instability. The code can deal with different canonical geometries (channels, annular pipes, cavities, etc.). It thus computes the essential instability phenomenon which might be hidden by excessive details in a comprehensive engineering model. For instance, the thermocapillary instabilities of the flow in a generic liquid bridge is the origin of striation imperfections in floating-zone crystal growth.

With this paper we make `MaranStable` publicly available and thus provide the mathematics, physics, and engineering communities with software capable of computing basic two-dimensional immiscible multiphase flows involving capillary and Marangoni stresses, and static and dynamic interface deformations. The solver can also compute the most dangerous mode and the critical parameter (e.g. the Reynolds number) beyond which the mode grows exponentially in time.

2. Software description

The governing equations are discretized by second-order finite volumes on a staggered grid. Primitive variables are used to solve the Navier–Stokes equations. Discrete pressure and temperature values are located at the cell centers, while the velocities are defined normal to and in centers of the cell faces which facilitates balancing the convective fluxes. The computational mesh is generated using a `MaranStable` tool capable of combining multiple tensorial grids (blocks), face-matched at their boundaries. Whenever curved boundaries are present, the solver body-fits the grid to the boundaries to avoid errors associated with geometric approximations at the order of accuracy of the discretization. For multiphase flows all blocks across the interface are body-fitted to the sharp interface. Thus the correct thermophysical properties are assigned to each phase with pressure and shear stress discontinuities across the interface due to capillary and Marangoni stresses, respectively. The curved interface location is solved either employing a static or a dynamic stress balance. Each block of the mesh is refined along its coordinate lines either by hyperbolic tangent or geometric progression, controlled by specifying the maximum and minimum grid sizes in each tensorial direction.

The basic flow state is an equilibrium solution of the steady two-dimensional Navier–Stokes equations. It is computed by the Newton–Raphson method using the MATLAB operator `backslash` which requires a good initial guess. A computed basic state can serve as an initial guess for consecutive basic state computations in the sense of a natural continuation. Once the sought basic state is obtained, its stability is computed from the linearized equations governing small perturbations. These are represented by Fourier modes in the homogeneous spatial direction (spanwise or azimuthal) and by an exponential behavior in time. This ansatz yields a generalized eigenvalue problem for the complex growth rate (eigenvalue) and the spatial structure of the perturbation flow (eigenvector). The eigenvalue problem is solved using the MATLAB operator `eigs`, which relies on the functions implemented in the ARPACK library [1] for linear algebra, and a Cayley transform implemented in `MaranStable`. `MaranStable` either returns the normalized perturbation flow of the *most dangerous mode* together with its growth rate and frequency at the given set of parameters or seeks the *critical mode* whose growth rate vanishes at a particular value of the control parameter. The user can opt to either search for the most dangerous or the critical mode. The latter is found by an automatic variation of one of the controlling parameters which is stepwise ramped up or down until the sign of the growth rate changes. The zero of the growth rate is then determined by a regula falsi [2] and the critical mode is obtained. More details on the mathematics, implementation and validation can be found in [3]. A corresponding simulation-resuming and parameter continuation algorithm is provided in `MaranStable` and is automatically called whenever required.

2.1. Software architecture

Running the script `main.m`, the GUI of `MaranStable` is launched and guides the user through all steps to set up a simulation. This same GUI is accessible by installing the executable for Windows or Linux and launching `MaranStable` by double clicking on the desktop icon without the need of installing MATLAB. The architecture of `MaranStable` is summarized in Fig. 1. Four macro-modules can be identified: (i) solver selection (green box in Fig. 1), (ii) initialization (blue boxes), (iii) simulation (red boxes), and (iv) visualization and post-processing (yellow boxes). A single- or a two-phase flow can be selected (i). During the initialization (ii), the user specifies the thermophysical properties of the fluids, the geometry, the parameters for the mesher, the approximation of the Navier–Stokes equations and the boundary conditions for the flow. Thereafter (iii), the simulation parameters shall be set, including the convergence criteria, the initial guess and the type of simulation (basic state, linear stability analysis, optical ray tracing). A comprehensive post-processing/visualization tool (iv) is included in the GUI. The data can be exported in VTK or DAT. The latter format is suitable for external line plotting. When a simulation is resumed, the macro-modules (ii) – (iv) work independently: Instead of going through (ii), the user can either load a previous initialization data set, a previously computed basic state, or a previously computed perturbation flow (see 'Load' button in Fig. 1). If the basic state has already been computed, the user can either skip (ii) and perform a stability analysis in (iii) or also skip (iii) and visualize the results in the macro-module (iv). The user may also change the parameters in (ii) and use the loaded flow field as an initial guess for a subsequent basic state computation. If the loaded file contains a computed perturbation flow, it can also be directly transferred to the post-processing (iv). Saving and resuming is done via the GUI, which grants high flexibility in the file naming. The resuming option is implemented only for states saved in `mat`-format.

2.2. Software capabilities

`MaranStable` provides the user with a highly flexible geometry set-up, of which only a few representative combinations are illustrated as examples in Fig. 2. However, we limit the solver to the case in which $\boldsymbol{g}$ is parallel to the axis of symmetry (symmetry plane) whenever gravitational forces are present. Regarding the governing equations, three versions of the continuity, Navier–Stokes, and energy equations are implemented in `MaranStable` for immiscible multiphase flows which are, with ascending complexity,

OB: **O**berbeck–**B**oussinesq approximation

$$\nabla \cdot \boldsymbol{u} = 0, \tag{1a}$$

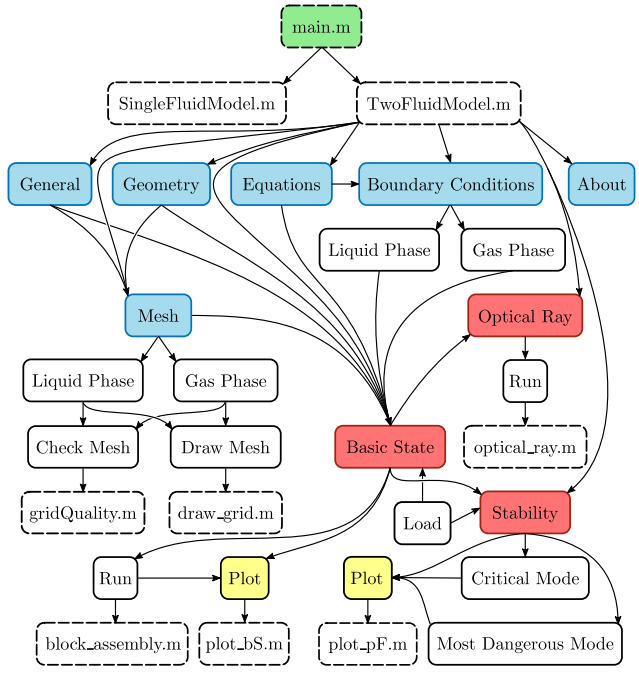

Fig. 1. Flowchart of `MaranStable`, only shown for the two-fluid model. For the single-fluid model, the flowchart is formally identical apart from the missing 'Gas Phase'. The four macro-modules are coded by color. Green: solver selection (i). Blue: initialization (ii). Red: simulation (iii). Yellow: visualization and post-processing (iv). Colored frames (blue and red) constitute the main tabs of the GUI. Black full frames indicate subordinated tabs or buttons. Black dashed frames represent source files.

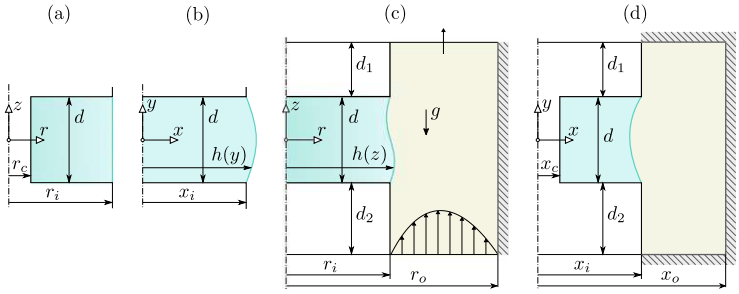

Fig. 2. Schematics of possible setups and coordinates: (a, c) cylindrical, (b, d) Cartesian. All geometrical parameters, as well as the volume ratio $\mathcal{V} = V_{\text{liquid}}/V_{\text{gap}}$, are adjustable, where V_{gap} is the upright gap between the two rods/blocks of radius r_i (or blocks of width x_i). Light blue: liquid phase. Beige: gas phase. (a, b): single-fluid model. (c, d): two-fluid model.

$$\partial_t \boldsymbol{u} + \boldsymbol{u}\cdot\nabla\boldsymbol{u} = -\frac{1}{\rho_{0i}}\nabla p + \frac{\mu_{0i}}{\rho_{0i}}\nabla^2\boldsymbol{u} - \boldsymbol{g}\alpha_{\rho i}(T - T_0), \tag{1b}$$

$$\partial_t T + \boldsymbol{u}\cdot\nabla T = \frac{\lambda_{0i}}{\rho_{0i}c_{p0i}}\nabla^2 T, \tag{1c}$$

LTD: **L**inearly **T**emperature-**D**ependent properties

$$-\rho_{0i}\alpha_{\rho i}\partial_t T + \nabla\cdot(\rho_i\boldsymbol{u}) = 0, \tag{2a}$$

$$\rho_i\left(\partial_t\boldsymbol{u} + \boldsymbol{u}\cdot\nabla\boldsymbol{u}\right) = -\nabla p + \nabla\cdot(\mu_i\boldsymbol{\tau}) - \boldsymbol{g}\alpha_{\rho i}(T - T_0), \tag{2b}$$

$$\rho_i c_{pi}\left(\partial_t T + \boldsymbol{u}\cdot\nabla T\right) = \lambda_i\nabla^2 T + \lambda_{0i}\alpha_{\lambda i}\left(\nabla T\right)^2, \tag{2c}$$

FTD: **F**ully **T**emperature-**D**ependent properties

$$\partial_t\rho_i + \nabla\cdot(\rho_i\boldsymbol{u}) = 0, \tag{3a}$$

$$\partial_t(\rho_i\boldsymbol{u}) + \nabla\cdot(\rho_i\boldsymbol{u}\boldsymbol{u}) = -\nabla p + \nabla\cdot(\mu_i\boldsymbol{\tau}) + \rho_i\boldsymbol{g}, \tag{3b}$$

$$\partial_t(\rho_i c_{pi}T) + \nabla\cdot(\rho_i c_{pi}T\boldsymbol{u}) = \nabla\cdot(\lambda_i\nabla T), \tag{3c}$$

where the index $i = 1, 2$ denotes the phase (only for the two-fluid model), t is the time, $\boldsymbol{u}$, p and T denote the velocity, pressure and temperature fields, $\boldsymbol{\tau} = \nabla\boldsymbol{u} + (\nabla\boldsymbol{u})^{\mathrm{T}} - 2(\nabla\cdot\boldsymbol{u})\mathcal{I}/3$ and $\mathcal{I}$ are (twice) the deformation rate tensor and the identity matrix, respectively. The thermo-physical properties ρ, μ, c_p and λ are the temperature-dependent density, dynamic viscosity, specific heat at constant pressure and thermal conductivity, respectively.

The physical model among OB, LTD and FTD is selected in the macro-module (ii) inside the main tab 'General'.

In the Boussinesq approximation OB all thermo-physical material parameters are assumed constant and evaluated at a reference temperature T_0 (subscript '0'), except for the linear dependence of the density in the buoyancy term. Within the LTD model, the material parameters

$$\mu_i = \mu_{0i}\left[1 - \alpha_{\mu i}(T - T_0)\right], \tag{4a}$$
$$\rho_i = \rho_{0i}\left[1 - \alpha_{\rho i}(T - T_0)\right], \tag{4b}$$
$$\lambda_i = \lambda_{0i}\left[1 + \alpha_{\lambda i}(T - T_0)\right], \tag{4c}$$
$$c_{pi} = c_{p0i}\left[1 + \alpha_{cpi}(T - T_0)\right], \tag{4d}$$

depend linearly on T, where $c_{p0}\alpha_{cp}$, $\lambda_0\alpha_\lambda$, $-\rho_0\alpha_\rho$ and $-\mu_0\alpha_\mu$ are the linear coefficients of the Taylor expansions about $T = T_0$. Finally, within the FTD model, the user can choose among various implemented fluids, whose material properties depend nonlinearly on T. When choosing the OB or the LTD model, the user has the possibility to create a new fluid with custom material properties.

At the interface between two fluids, the balance of tangential and normal stresses, as well as the heat transfer across the interface is imposed. The capillary and Marangoni stresses are included in the interfacial conditions. Concerning the location of the interface h, we neglect dynamic surface deformations due to the three-dimensional perturbation flow, i.e., the stationary surface shape h of the basic state is prescribed while solving the perturbation equations. In that case, the interface location h depends only on the vertical coordinate (y for Cartesian and z for cylindrical coordinates, see Fig. 2). Within this constraint, three approximations are implemented in `MaranStable` with ascending complexity which can be selected in the macro-module (ii) inside 'Boundary Conditions':

RI: Straight indeformable surface shape (**R**igid **I**nterface) and linearized surface tension σ

$$h \equiv \begin{cases} x_i & \text{for Cartesian coordinates,} \\ r_i & \text{for cylindrical coordinates,} \end{cases} \tag{5a}$$
$$\sigma = \sigma_0 - \gamma(T - T_0), \tag{5b}$$

SI: Indeformable hydrostatic surface shape (**S**tatic **I**nterface) (limit of asymptotically large surface tension at reference temperature σ_0) and linearized surface tension

$$\Delta p_h = \sigma_0 \nabla \cdot \boldsymbol{n} + \Delta\rho_h g z, \tag{6a}$$
$$\sigma = \sigma_0 - \gamma(T - T_0), \tag{6b}$$

DI: Dynamically deformed surface shape (**D**ynamic **I**nterface) and full temperature-dependent surface tension

$$\Delta p_h = \sigma \nabla \cdot \boldsymbol{n} + \Delta\rho_h g z + \mu_1 \boldsymbol{n} \cdot \tau_1 \cdot \boldsymbol{n} - \mu_2 \boldsymbol{n} \cdot \tau_2 \cdot \boldsymbol{n}, \tag{7a}$$
$$\sigma = \sigma(T). \tag{7b}$$

Here $\gamma = -\partial_T \sigma|_{T_0}$ is the negative surface tension coefficient evaluated at the reference temperature T_0, Δp_h the interfacial pressure jump, $\Delta\rho_h$ the interfacial density jump and $\boldsymbol{n} = \boldsymbol{n}(h)$ the unit normal vector directed from phase 1 to phase 2. Selecting SI, the general stress balance on the interface (7a) reduces to the Young–Laplace Eq. (6a) which can be solved independently from the flow field [3]. However, in DI, the interface shape h is part of the numerical solution, since flow-induced deformations are taken into account in the basic state. This is taken care of by an additional iteration loop embedded in the Newton–Raphson iteration for the basic state.

A dedicated tab of the GUI guides the user through the boundary conditions. They can be chosen among: '`no-penetration`' (free-slip or no-slip boundary with either adiabatic conditions or a given temperature profile), '`free-surface`' (free-slip with user-specified heat flux, only for single-phase simulations) and '`outflow`' (constant-pressure with homogeneous Neumann conditions for velocity and temperature). Under the '`inflow`' conditions, the user can define a combination of non-homogeneous Dirichlet and homogeneous Neumann conditions allowing for case-specific inlet velocity and temperature profiles. Finally, `MaranStable` provides a module dedicated to optical ray tracing in axisymmetric, non-homogeneous diffraction index fields $\mathcal{N}$. This is coupled with the Navier–Stokes solver, as the user can provide a temperature-dependent $\mathcal{N}(T)$ index and trace the optical path in the liquid of a ray with normal incidence on a (transparent) wall.

2.3. Visualization, post-processing and customization

Several visualization and data post-processing features are implemented in `MaranStable`. The GUI provides a dedicated button for a post-processing of the data (velocity, pressure, and temperature fields) and visualization of the two-dimensional basic state and the three-dimensional critical mode. The computation of the Stokes stream function is implemented for planar and axisymmetric basic states. Beside of the embedded visualization toolbox, an export feature is available to save the flow in VTK and DAT formats. The exported data can be readily imported in third-party software for a more advanced graphical post-processing, like `ParaView` (VTK) or, for line graphs, `gnuplot`, `xmgrace`, etc. (DAT).

`MaranStable` can be further customized. One can switch from planar to axisymmetric geometries (Fig. 2). Moreover, by box-ticking one can select the physical model, activate/deactivate Marangoni stresses, use the creeping flow approximation (inertia terms in the OB, LTD and FTD models are set to zero) or skip the energy equation. Several fluids with their thermo-physical properties are already implemented in `MaranStable`. Additional fluids can be defined, but $\rho(T)$, $c_p(T)$, $\lambda(T)$, and $\mu(T)$ must either be constant or depend linearly on T. Fluids can also be defined as to enable a fully non-dimensional formulation, cf. Section 3.1.

3. Illustrative examples

3.1. Rayleigh-Bénard instability

In an infinitely extended layer of a Boussinesq fluid heated from below the conducting basic state becomes unstable due to buoyancy forces when a critical Rayleigh number is exceeded. To set up this problem, we use a single-fluid model governed by the OB model in a finite Cartesian domain with free-slip conditions on the horizontal top and bottom walls which are heated from below with a temperature difference ΔT. The domain (layer) has a thickness of $d = 1$ mm and the acceleration of gravity $\boldsymbol{g} = -g\boldsymbol{e}_y$ acts in the negative y direction. Since convection in plane layers arises in form of stationary periodic counter-rotating rolls with rectangular cross-section, periodic boundary conditions are equivalent, in this case, to adiabatic free-slip conditions on the cell boundaries. These conditions are thus imposed on the side walls of the present finite domain, whose length represents one wavelength $2\pi/k$ of the flow pattern, where k is the wave number in units of d^{-1}. The control parameter is the Rayleigh number $\mathrm{Ra} = g\alpha_\rho \Delta T d^3 \rho_0^2 c_{p0}/\mu_0\lambda_0$.

Neutral Rayleigh numbers Ra_n are defined by a vanishing growth rate. Results for Ra_n are shown in Fig. 3(a) as function of the wave number k. For the selected range of k, `MaranStable` (red crosses) reproduces the exact solution $\mathrm{Ra}_n^{\mathrm{exact}} = (k^2 + \pi^2)^3/k^2$ [4,5] (full line) up to 0.01% using a uniformly distributed

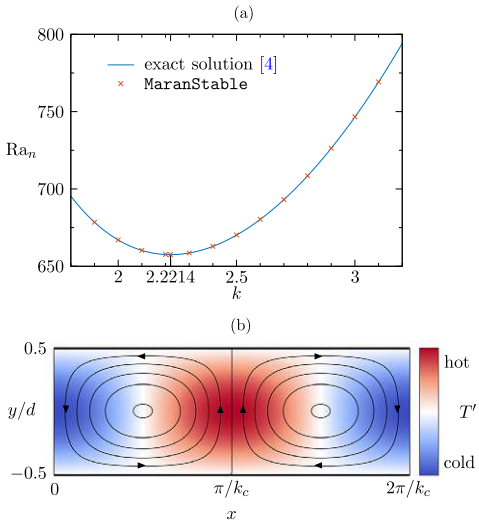

Fig. 3. (a) Neutral curve for the Rayleigh-Bénard problem with free-slip conditions at the top and bottom boundaries; crosses: `MaranStable`, line: exact solution. (b) Streamlines and temperature field T' (color) of the critical mode ($k = k_c = 2.2214$).

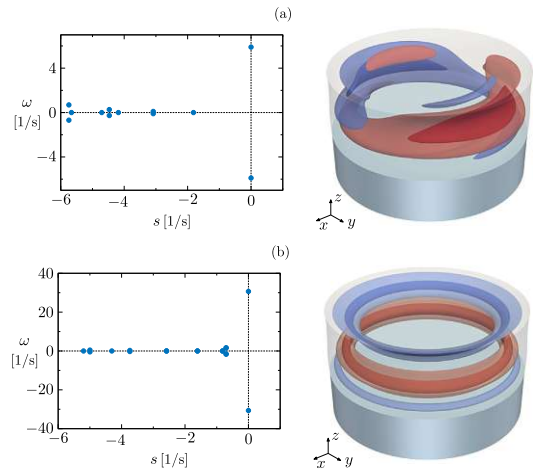

Fig. 4. Leading eigenvalues (left) and critical temperature field (right) for the same parameters, but different computational models. (a) Oberbeck–Boussinesq approximation OB with $m_c = 1$ and $\Delta T_c = 52.2$ °C. (b) Full temperature-dependent properties FTD with $m_c = 0$ and $\Delta T_c = 56.1$ °C.

grid with 28 300 grid points. The critical wave number k_c (minimum of Ra$_n$) found by `MaranStable` deviates by less than 10^{-4} % from $k_c^{\text{exact}} = \pi/\sqrt{2}$. The critical mode obtained by `MaranStable` is shown in Fig. 3(b).

3.2. Thermocapillary liquid bridge with a coaxial gas flow

An example for a multiphase problem with temperature-dependent fluid properties is the flow instability in an axisymmetric liquid bridge from silicone oil, which is treated using cylindrical coordinates. The liquid bridge is heated differentially with ΔT via cylindrical support rods and surrounded by air which is concentrically confined by a cylindrical tube. The basic flow is driven along the liquid–gas interface by the thermocapillary effect and by a steady forced nominally axial flow in the air. For more information, the reader is referred to [6].

Results of linear stability analyses are shown in Fig. 4. `MaranStable` can visualize the eigenvalue spectrum (left), where ω is the frequency and s the growth rate of the critical mode. The temperature field of one of the two oscillatory critical modes is shown on the right. Figures 4(a) and 4(b) are obtained for the same parameters, but for flow models OB and FTD, respectively, which yields different critical temperature differences ΔT_c. In both cases the critical mode is a wave, but it travels azimuthally with $m = 1$ for the OB model, while it is axisymmetric ($m = 0$) traveling axially for the FTD model.

3.3. Optical ray tracing

Finally, we demonstrate the ray tracing capability of `MaranStable`. The axisymmetric basic flow in a thermocapillary liquid bridge made from 2-cSt silicone oil with volume ratio $\Gamma = 0.9$ and aspect ratio $\Gamma = d/r_i = 0.5$ is computed using the two-fluid model FTD for a temperature difference $\Delta T = 70$ °C ($T_0 = 25$ °C) under weightlessness. This corresponds to typical experimental conditions [8] for tracking particles in the liquid bridge through a transparent top rod. `MaranStable` can correct the hypothetical particle position (along the straight dashed line in Fig. 5) for a constant index of refraction $\mathcal{N}$ of the liquid to take into account the temperature dependence of $\mathcal{N}(T)$ (red line).

4. Impact and conclusions

`MaranStable` aims to provide the mathematics, physics and engineering community with a flexible and easy-to-use GUI-integrated code for performing linear stability analyses in immiscible multiphase flows.

The canonical geometries implemented in `MaranStable` cover many paradigmatic setups used to investigate flow instabilities. Examples were presented in Section 3. The range of Navier–Stokes (OB, LTD, FTD) and interfacial models (RI, SI, DI) implemented provides a large flexibility for carrying out state-of-the-art research in complex multiphase hydrodynamic stability. Several articles based on `MaranStable` have recently been published by the authors who developed the software [3,9,10]. This paper aims at broadening the user community to foster progress in multiphase flow instabilities.

The software enables new research opportunities. To the best of our knowledge, no other open-source linear stability solver is capable of directly comparing the three Navier–Stokes models OB, LTD and FTD implemented. This enables, e.g., an assessment of the accuracy and the validity of the Oberbeck–Boussinesq approximation OB, which is an active research topic [11]. Moreover, the three interface models RI, SI and DI allow to study the role of dynamic interface deformations, which are often neglected. In ongoing work [6] regimes have been identified near the mechanical stability limit in which the flow-induced interface deformations have a significant impact on the basic state, hence on the stability of the system. The nonlinear temperature-dependence of the surface tension, implemented in DI, is important for large temperature differences. It allows users to investigate the effect of Marangoni stresses beyond the classic approximation SI.

`MaranStable` bears a great potential for significant extensions of its already advanced capabilities. Including evaporation and phase change would be of great interest. Moreover, including dynamic deformations caused by the perturbation flow would

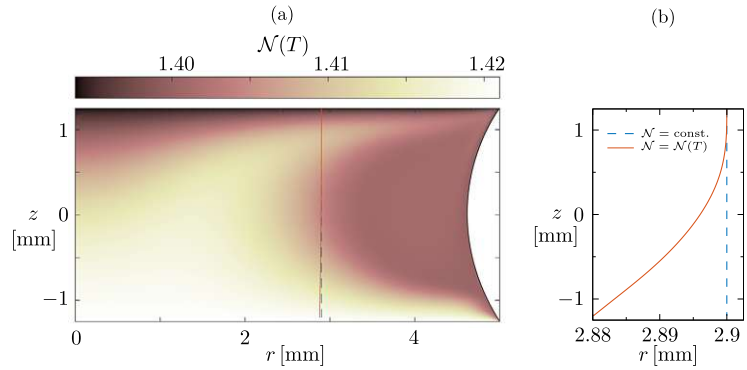

Fig. 5. Ray tracing in a non-isothermal liquid bridge: (a) Spatial distribution of the index of refraction $\mathcal{N}(T)$ [7] and optical path (red line) of a ray which enters or leaves the liquid perpendicular to the top (hot) transparent wall at $r = 2.9$ mm (blue dashes). (b) Close-up of the optical path.

allow the detection of surface wave instabilities. Adding the computation of the kinetic and thermal energy budgets of the critical mode to the post-processing tools would considerably support the physical understanding of the instabilities. Future extensions of `MaranStable` concern embedding implicit and explicit reduced-order models for heat transfer and wetting, including surfactant dynamics in the bulk and on the interface, and a generalization of the optical module.

Declaration of competing interest

The authors declare the following financial interests/personal relationships which may be considered as potential competing interests: Mario Stojanović reports financial support was provided by Austrian Research Promotion Agency. Hendrik C. Kuhlmann reports a relationship with Austrian Research Promotion Agency that includes: funding grants.

Data availability

Our data/code is available on https://github.com/fromano88/MaranStable.git.

Acknowledgments

This work has been supported by the Austrian Research Promotion Agency (FFG) in the framework of the ASAP14 programme under contract no. 866027. The first version of the `MaranStable` has been developed by Michael Lukasser in the framework of the project Engineering Marangoni Flows (EMA), which was also supported by FFG, Austria under contract no. 819714.

References

[1] Lehoucq RB, Sorensen DC, Yang C. ARPACK users' guide: Solution of large-scale eigenvalue problems with implicitly restarted Arnoldi methods. Philadelphia: SIAM; 1998.
[2] Gottlieb RG, Thompson BF. Bisected direct quadratic regula falsi. Appl Math Sci 2010;4:709–18.
[3] Stojanović M, Romanò F, Kuhlmann HC. Stability of thermocapillary flow in liquid bridges fully coupled to the gas phase. J Fluid Mech 2022;949:A5.
[4] Rayleigh, Lord. On convection currents in a horizontal layer of fluid, when the higher temperature is on the under side. Phil Mag 1916;32:529–46.
[5] Chandrasekhar S. Hydrodynamic and hydromagnetic stability. Oxford: Oxford University Press; 1961.
[6] Stojanović M, Romanò F, Kuhlmann HC. Flow instability of high-Prandtl-number liquid bridges accounting for the full temperature dependence of the thermo-physical properties (unpublished).
[7] He J, Liu W, Huang Y-X. Simultaneous determination of glass transition temperatures of several polymers. PLoS One 2016;11:1–12.
[8] Romanò F, Kuhlmann HC, Ishimura M, Ueno I. Limit cycles for the motion of finite-size particles in axisymmetric thermocapillary flows in liquid bridges. Phys Fluids 2017;29:093303.
[9] Stojanović M, Kuhlmann HC. Stability of thermocapillary flow in high-Prandtl-number liquid bridges exposed to a coaxial gas stream. Microgravity Sci Technol 2020;32:953–9.
[10] Stojanović M, Romanò F, Kuhlmann HC. Instability of axisymmetric flow in thermocapillary liquid bridges: Kinetic and thermal energy budgets for two-phase flow with temperature-dependent material properties. Eur J Appl Math [submitted for publication].
[11] Zonta F, Soldati A. Stably stratified wall-bounded turbulence. Appl Mech Rev 2018;70:040801.